A. Leger
M. Deschamps
Editors

SPRINGER PROCEEDINGS IN PHYSICS 128

Ultrasonic Wave Propagation in Non Homogeneous Media

Springer

SPRINGER PROCEEDINGS IN PHYSICS 128

SPRINGER PROCEEDINGS IN PHYSICS

113 **Theoretical and Numerical Unsaturated Soil Mechanics**
Editor: T. Schanz

114 **Advances in Medical Engineering**
Editor: T.M. Buzug

115 **X-Ray Lasers 2006**
Proceedings
of the 10th International Conference,
August 20–25, 2006, Berlin, Germany
Editors: P.V. Nickles, K.A. Janulewicz

116 **Lasers in the Conservation of Artworks**
LACONA VI Proceedings,
Vienna, Austria, Sept. 21–25, 2005
Editors: J. Nimmrichter, W. Kautek,
M. Schreiner

117 **Advances in Turbulence XI**
Proceedings of the 11th EUROMECH
European Turbulence Conference,
June 25–28, 2007, Porto, Portugal
Editors: J.M.L.M. Palma and A. Silva Lopes

118 **The Standard Model and Beyond**
Proceedings of the 2nd International
Summer School in High Energy Physics,
Mğla, 25–30 September 2006
Editors: M. Serin, T. Aliev, N.K. Pak

119 **Narrow Gap Semiconductors 2007**
Proceedings
of the 13th International Conference,
8–12 July, 2007, Guildford, UK
Editors: B. Murdin, S. Clowes

120 **Microscopy**
of Semiconducting Materials 2007
Proceedings of the 15th Conference,
2–5 April 2007, Cambridge, UK
Editors: A.G. Cullis, P.A. Midgley

121 **Time Domain Methods**
in Electrodynamics
A Tribute to Wolfgang J. R. Hoefer
Editors: P. Russer, U. Siart

122 **Advances in Nanoscale Magnetism**
Proceedings of the International
Conference on Nanoscale Magnetism
ICNM-2007, June 25–29, Istanbul, Turkey
Editors: B. Aktas, F. Mikailov

123 **Computer Simulation Studies**
in Condensed-Matter Physics XIX
Editors: D.P. Landau, S.P. Lewis,
and H.-B. Schüttler

124 **EKC2008 Proceedings**
of the EU-Korea Conference
on Science and Technology
Editor: S.-D. Yoo

125 **Computer Simulation Studies**
in Condensed-Matter Physics XX
Editors: D.P. Landau, S.P. Lewis,
and H.-B. Schüttler

126 **Vibration Problems ICOVP 2007**
Editors: E. Inan, D. Sengupta,
M.M. Banerjee, B. Mukhopadhyay,
and H. Demiray

127 **Physics and Engineering**
of New Materials
Editors: D.T. Cat, A. Pucci,
and K.R. Wandelt

128 **Ultrasonic Wave Propagation**
in Non Homogeneous Media
Editors: A. Leger, M. Deschamps

Volumes 90–112 are listed at the end of the book.

Alain Leger
Marc Deschamps
Editors

Ultrasonic Wave Propagation in Non Homogeneous Media

With 168 Figures

Springer

Professor Dr. Alain Leger
CNRS Labo. Mécanique et d'Acoustique,
31 chemin Joseph-Aiguier, 13402 Marseille CX 20, France
E-mail: leger@lma.cnrs-mrs.fr

Professor Marc Deschamps
Université Bordeaux 1, Lab. de Mécanique Physique,
351 Cours de la Libération, 33405 Talence cedex, France
E-mail: m.deschamps@lmp.u-bordeaux1.fr

ISBN 978-3-540-89104-8 e-ISBN 978-3-540-89105-5

DOI 10.1007/978-3-540-89105-5

Springer Proceedings in Physics ISSN 0930-8989

Library of Congress Control Number: 2008938545

Cover design: eStudio Calamar Steinen

Printed on acid-free paper

9 8 7 6 5 4 3 2 1

springer.com

Preface

The Research Network GDR 2501 deals with Ultrasonic wave propagation in non-homogeneous media for Non Destructive Testing applications. This group gathers researchers of various backgrounds in applied mathematics as well as in experimental physics. Founded in January 2002 as a CNRS unit, it became Anglo-French in January 2006. Now, it consists of 32 departments or laboratories evenly distributed between France and UK. Different research institutions and industrial departments support the network: CEA, EDF, EADS, Dassault Aviation, Renault, ONERA, LCPC, INRIA from the French side, EPSRC and English companies through RCNDE from the British side.

The fifth meeting of the GDR was held in Anglet, France, from June 2nd to June 6th 2008. Forty oral presentations and ten posters made at the meeting have been devoted to the following research topics:

- bonding,
- propagation in composites,
- guided waves,
- contact or damage non-linearities in acoustics,
- inverse problems and imaging,
- structural noise.

The program offered a wide-ranging view of the present state of the art in the research for Non Destructive Testing and Non Destructive Evaluation applications. Four keynote lectures have been chosen either precisely in the field of the GDR:

– Ultrasonic arrays: the post processing approach, by Professor Bruce Drinkwater,
– Reverse time migration technique coupling with finite element methods, by Dr Hélène Barucq,

or in the near fields of interest:

– Acoustic cloaking theory, by Professor Andrew Norris,
– On the use of (static) digital image correlation for identifying material heterogeneities and non linear behaviors, by Professor Stéphane Roux.

This volume gives a comprehensive account of the presentations made at the conference. The sequence of papers follows the meeting schedule, which has been intentionally arranged to mingle talks on the theory and on various applications. It reflects a strong link between different aspects of the research scope of the conference. With a view to foster interaction and cohesion between the theoretical and applied communities, each paper has been reviewed in real-time during the conference by two participants, one theoretician and one experimentalist or engineer.

The organizers and the 85 participants have been pleased to observe that the conference has provided an excellent opportunity for exchanging ideas and developing collaborations. It was also beneficial for the PhD student participants who could gain an overview of the cutting-edge research in the field.

The editors would like to stress the fact that this volume could not have been published had not Beatrice Desoudin been so efficient in her work. All the material organization of the meeting has rested on her shoulders and she also has found time to help in the compilation of articles presented herein.

The next meeting will be held in the Lake District in UK. We hope for the same success as at the present one, and we are looking forward to reaching a next step in active co-operation within the GDR 2501, the network of British and French Laboratories.

Marseille/Talence, October 2008 Alain Leger, Marc Deschamps

Contents

Preface ..... **v**

The WBK method applied to the refection-transmission by a depth-varying random distribution of cylinders in a fluid slab-like region **1**

J.-M. Conoir, S. Robert, A. El Mouhtadi, F. Luppé

Advances in ultrasonic testing of autenitic stainless steel welds. Towards a 3-d description af the material including attenuation and optimisation by inversion **15**

J. Moysan, C. Gueudre, M.-A. Ploix, G. Corneloup, P. Guy, B. Chassignole

Imaging of defects in autenitic steel welds using an ultrasonic array **25**

G. Connolly, M. Lowe, S. Roklin, A. Temple

Material and mechanical aspects of bonded joints **39**

M. Shanahan

The causal differential scattering approach to calculating the effective properties of random composite materials with a particle size distribution .. **49**

A. Young, A. Mulholland, R. O'Leary

Modeling of scattering of ultrasounds by flaws for NDT **61**

M. Darmon, N. Leymarie, S. Chatillon, S. Mahaut

Finite element computation of leaky modes in stratified waveguides **73**

A.-S. Bonnet-Bendhia, B. Goursaud, C. Hazard, A. Pietro

Ultrasonic bulk wave propagation in concentrated heterogeneous slurries ... **87**

R. Challis, A. Holmes, V. Pinfield

Dynamics of elastic bodies connected by o thin adhesive layer 99

C. Licht, F. Lebon, A. Léger

Acoustic wave attenuation in a rough-walled waveguide filled with a dissipative fluid 111

T. Valier-Brasier, C. Potel, M. Bruneau, C. Depollier

Some advances towards a better understanding of wave propagation in civil engineering multi-wire strand 123

L. Laguerre, F. Treyssède

A numerical method for the simulation of NDT experiments in an elastic waveguide 137

V. Baronian, A.-S. Bonnet-Bendhia, A. Lhemery, E. Luneville

Finite element for a beam system with nonlinear contact under periodic excitation 149

H. Hazim, B. Rousselet

Nonlinear acoustic fast and slow dynamics of damaged composite materials : correlation with acoustic emission..... 161

M. Bentahar, A. Marec, R. El Guerjouma, J.H. Thomas

Asymptotic expansions of vibrations with small unilateral contact 173

S. Junca, B. Rousselet

Propagation of compressional elastic waves through a 1-d medium with contact nonlinearities..... 183

B. Lombard, J. Piraux

3-d Finite element simulations of an air-coupled ultrasonic NDT system 195

W. Ke, M. Castaings, C. Bacon

The reverse time migration technique coupled with finite element methods 207

C. Baldassari, H. Barucq, H. Calandra, B. Denel, J. Diaz

Modelling of corner echo ultrasonic inspection with bulk and creeping waves..... 217

G. Huet, M. Darmon, A. Lhémery, S. Mahaut

Attenuation of Lamb waves in the vincinity of a forbidden band in a phononic crystal 227

M. Bavencoffe, A.-C. Hladky-Hennion, B. Morvan, J.-L. Izbicki

3-d orthogonality relations for the surface waves and the far field evaluation in viscoelastic layered solids with or without fluid loading 237

D. D. Zakharov

Damage detection in foam core sandwich structures using guided waves.... 251

N. Terrien, D. Osmont

Sensitivity of the guided waves to the adhesion of lap joints : Finite elements modeling and experimental investigations 261

H. Lourme, B. Hosten, P. Brassier

Guided waves in empty and filled pipes with optimized magnetostrictive transduction 271

A. Phang, R. Challis

Piezoelectric material characterization by acoustic methods 283

E. Le Clezio, T. Delaunay, M. Lam, G. Feuillard

Ultrasound characterization of aggregated red blood cells : towards *in vivo* application 293

E. Franceschini, F. Yu, G. Cloutier

A 3-d semi-analytical model to predict the behavior of ultrasonic bounded beam traveling in cylindrical solid bar embedded in a solid matrix 303

S. Yaacoubi, L. Laguerre, E. Ducasse, M. Deschamps

Comparison between a multiple scattering method and direct numerical simulations for elastic wave propagation in concrete 317

M. Chekroun, L. Le Marec, B. Lombard, J. Piraux, O. Abraham

Investigation of a novel polymer foam material for air coupled ultrasonic transducer applications..... 329

L. Satyanarayan, J.-M. Vander Weide, N.-F. Declercq, Y. Berthelot

Dual signal processing approach for Lamb wave analysis 341

J. Assaad, S. Grondel, F. El Yaoubi, E. Moulin, C. Delebarre

Structural health monitoring of bonded composite patches using Lamb waves 355

B. Chapuis, N. Terrien, D. Royer, A. Déom

Simulation of structural noise and attenuation occuring in ultrasonic NDT of polycrystalline materials 365

V. Dorval, F. Jenson, G. Corneloup, J. Moysan

Ultrasonic array reconstruction methods for the localization and the characterization of defects in complex NDT configurations 377

A. Fidahoussen, P. Calmon, M. Lambert

Ultrasonic nonlinear parameter measurement : critical investigation of the instrumentation 387

L. Haumesser, J. Fortineau, D. Parenthoine, T. Goursolle, F. Vander Meulen

Investigation of damage mechanisms of composite materials : multivariable analysis based on temporal and wavelet features extracted from acoustic emission signals 399

A. Marec, J.-H. Thomas, R. El Guerjouma, R. Berbaoui

Propagation of elastic waves in a fluid-loades anisotropic functionally graded waveguide : application to ultrasound characterization of cortical bone 411

C. Baron, S. Naili

Coherent wave propagation in solids containing spatially varying distributions of finite-size cracks 423

C. Aristégui, M. Caleap, O. Poncelet, A.-L. Shuvalov, Y.-C. Angel

The WKB method applied to the reflection-transmission by a depth-varying random distribution of cylinders in a fluid slab-like region

J.M. Conoir, S. Robert, A. El Mouhtadi and F. Luppé

Abstract This paper deals with multiple scattering by a random arrangement of parallel circular elastic cylinders immersed in a fluid. The cylinders are distributed in a region called « slab » that is located between two parallel planes orthogonal to a given x-direction. The disorder inside the slab is not uniform but depends on the x-variable. The goal is to calculate the reflection and transmission coefficients by this space-varying slab. The spatial variations of the random distribution are assumed smooth enough in order to use the WKB (Wentzel-Kramers-Brillouin) method. For this method, a crucial point is the knowledge of the boundary conditions at the interfaces between the homogeneous fluid and the space-varying slab. These boundary conditions are shown to be the usual continuity of pressure and normal displacement. The relation between pressure and normal displacement is given by Euler's equation and the introduction of an effective mass density.

1 Introduction: results for the uniform slab

Multiple scattering by random arrangements of scatterers is a topic with an extensive literature. See, for example, the recent book by Martin [1]. A typical problem is the following. The space is filled with a homogeneous compressible fluid of density ρ and sound speed c, and a fluid slab-like region,

J.M.Conoir
UPMC Univ Paris 06, UMR 7190, Institut Jean Le Rond d'Alembert, F-75005 Paris, France, e mail: conoir@lmm.jussieu.fr

S.Robert
Laboratoire Ondes et Acoustique, UMR 7587, ESPCI, 10 rue Vauquelin, 75231 Paris Cedex 05, France, e mail: sebastien.robert@espci.fr

A.El Mouhtadi, F.Luppé
LOMC, FRE 3102, Groupe Onde Acoustique, Université du Havre, place R.Schuman, 76610 Le Havre, France, e mail: francine.luppe@univ-lehavre.fr

$0 \leq x \leq d$, contains many randomly spaced scatterers. In the following, the scatterers are elastic parallel circular cylinders. As their axes are normal to the x direction, the problem is a two-dimensional one (cf. Fig. 1). As a time harmonic plane wave with wavenumber $k = \mathrm{w}/c$ (w is the angular frequency) is incident upon the slab (cf. Fig. 1), what are the reflected and transmitted waves? The acoustic fields cannot be computed exactly for a large number of cylinders. This is the reason why another problem is solved. The slab is replaced by a homogeneous effective medium in which coherent plane waves propagate. After Twersky [2], coherent plane waves can be interpreted as the average of the exact fields calculated for a great number of random configurations of the scatterers. They are characterised by a complex wave number K_{eff} usually called *effective wave number*. The earliest modern work on such a problem is due to Foldy [3] and a large number of papers have been published yet [4-7]. Most of them are mainly focused on the effective wave number calculation, while few of them actually deal with the reflected and transmitted fields [8-12]. This point is important to notice because it is not obvious to relate the reflection and transmission coefficients of the slab, R_{slab} and T_{slab}, to the effective wave number. Nonetheless, it has been shown in Refs. [8-12] that

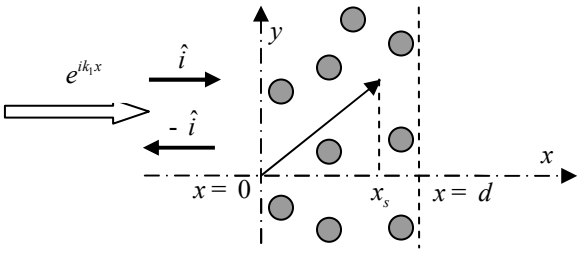

Fig. 1 Geometry of the slab.

$$R_{slab} = R_{12} + \frac{T_{12}e^{iK_{eff}d}R_{21}e^{iK_{eff}d}T_{21}}{1 - R_{21}^2 e^{2iK_{eff}d}} = R_{12} + T_{12}e^{iK_{eff}d}R_{21}e^{iK_{eff}d}T_{21} + \ldots \qquad (1.1)$$

$$T_{slab} = \frac{T_{12}e^{iK_{eff}d}T_{21}}{1 - R_{21}^2 e^{2iK_{eff}d}} = T_{12}e^{iK_{eff}d}T_{21} + T_{12}e^{iK_{eff}d}R_{21}^2 e^{2iK_{eff}d}T_{21} + \ldots \quad . \qquad (1.2)$$

where R_{12} is the specular reflection coefficient at the first interface of the slab, T_{12} (T_{21}) is the transmission coefficient at the interfaces between the homogeneous fluid, labelled 1, (slab, labelled 2) and the slab, labelled 2, (homogeneous fluid, labelled 1), and R_{21} the specular reflection coefficient inside the slab (*cf.* Fig.2). Eqs. (1.1,1.2) correspond to Eq. (21) in Ref. [8], to Eqs. (74,75) in Ref. [10], to Eqs. (12,13) in Ref [11], and to Eqs. (42,46) in Ref. [9], with $-R_{12} = R_{21} = Q = Q'$ and $T_{12}T_{21} = 1 - Q^2$. Of course, the analytic expression of Q depends on the theory used: Q is defined in Ref. [8,10,11] for

Twersky's or Waterman & Truell's theory (*cf.* Eq. (3.12), Eq.(76), Eq. (17) respectively), and in Ref. [9] for Fikioris & Waterman's one (*cf.* Eq. (4.12)). The physical meaning of Eqs. (1.1,1.2) is clear. First, the slab looks like a fluid plate in which waves propagate with wave number K_{eff} . Second, the slab can be considered as an usual Fabry-Perrot interferometer.
If the concentration of scatterers is low enough, it is possible with a bit of luck never to encounter a cylinder while walking through the boundaries of the slab. In this case, the impedance ratio between the homogeneous fluid and the slab is close to 1, so that $|R_{21}| \approx 0$ and $|T_{12}| \approx |T_{21}| \approx 1$. It follows that T_{slab} can be approximated by

$$T_{slab} \approx e^{iK_{eff}d} \tag{1.3}$$

so that

$$\mathrm{Im}(K_{eff}) \approx -\frac{1}{d} Log|T_{slab}| \ . \tag{1.4}$$

This last relation has indeed been successfully used, at low concentration, in order to evaluate the attenuation of the coherent waves that propagate through the slab from experimental transmission data [13,14].

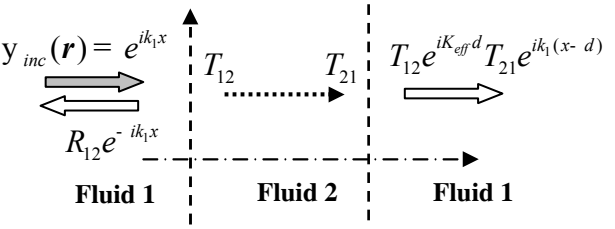

Fig. 2 Reflection and transmission by the uniform slab.

Contrary to previous studies, this paper deals with the reflected and transmitted waves by a slab in which the concentration and/or the size of the scatterers, rather than uniform, depends on the *x*-space variable. The goal is the generalisation of Eqs. (1.1,1.2) to such a space-varying slab. In the method we use, the spatial variations of the random distribution are assumed smooth enough for the relevancy of the WKB method [15]. For this method, a crucial point is the knowledge of the boundary conditions at the interfaces between the fluid and the slab. The continuity of pressure is naturally respected but that of the normal displacement is checked after introduction of an effective mass density for the uniform slab, that allows the derivation of the displacement expression from that of pressure.
The effective mass density of a uniform slab is defined in section 2. The Foldy-Twersky's integral equations that govern the average acoustic pressure fields are shown in section 3. Section 4 presents the WKB method for a slab of

smooth spatial variations. Section 5 shows numerical results before to conclude.

2 Effective mass density of a uniform slab

In linear acoustics, Euler's relation relates the time harmonic acoustic displacement $\boldsymbol{u}_f$ in a fluid medium to the time harmonic pressure p :

$$\boldsymbol{u}_f = -\frac{1}{\rho_f \omega^2} \boldsymbol{\nabla} p \ , \tag{2.1}$$

with ρ_f the mass density of the fluid. This is the reason why the mass density is needed in order to write the continuity of normal displacement at the interface between two different fluids. While the mass density ρ_f of a homogeneous fluid is a known characteristic of the fluid, that of a uniform slab has yet to be defined. In order to do so, let consider the R_{12} specular refection coefficient at the interface between two fluids, labelled 1 and 2 respectively; its expression is given by [15]

$$R_{12} = \frac{\rho_2 k_1 - \rho_1 k_2}{\rho_2 k_1 + \rho_1 k_2} \tag{2.2}$$

with k_1, k_2 the wavenumbers in fluids 1 and 2, and ρ_1, ρ_2 the mass densities of the fluids. If fluid 2 contains a uniform distribution of scatterers, this specular reflection is obtained from Eq. (1.1) by letting the depth d of the slab tend to infinity: $R_{12} = \lim_{d \to +\infty} R_{slab} = -Q$ (the imaginary part of the effective wavenumber K_{eff} being positive). As k_2 is to be replaced with K_{eff} in Eq.(2.2) and ρ_2 with ρ_{eff}, it follows straightaway that

$$\rho_{eff} = \rho_1 \frac{K_{eff}}{k_1} \frac{1-Q}{1+Q} \ . \tag{2.3}$$

Consequently, the mass density of a homogeneous fluid with a uniform distribution of scatterers is complex and depends on frequency, as K_{eff} and Q do.

3 Foldy-Twersky's integral equations

The method developed to calculate the reflection and transmission coefficients of a space-varying slab is based on a set of coupled integral equations derived by Twersky [8]. As the incident wave and the geometry of the varying slab are

supposed to be independent of the *y*-co-ordinate, parameters and acoustic fields only depend on the *x*-co-ordinate. According to Twersky, the average acoustic field $\langle \psi \rangle$ can be split into two fields, y_+ associated to the propagation in the $\hat{i}$ direction and y_- associated to the propagation in the opposite direction $-\hat{i}$

$$\langle \mathrm{y} \rangle = \mathrm{y}_+ + \mathrm{y}_- \tag{3.1}$$

which are solutions of the set of coupled integral equations

$$\psi_+(x) = e^{ik_1 x} + e^{ik_1 x} \int_0^x \left[T(x_s)\psi_+(x_s) + R(x_s)\psi_-(x_s) \right] e^{-ik_1 x_s} n(x_s) dx_s \tag{3.2-a}$$

$$\psi_-(x) = e^{-ik_1 x} \int_x^d \left[R(x_s)\psi_+(x_s) + T(x_s)\psi_-(x_s) \right] e^{+ik_1 x_s} n(x_s) dx_s \tag{3.2-b}$$

with

$$T(x_s) = \frac{2}{k_1} f(\hat{i}, \hat{i}; x_s) \qquad \text{and} \qquad R(x_s) = \frac{2}{k_1} f(\hat{i}, -\hat{i}; x_s) \,. \tag{3.3}$$

In Eq. (3.2), $\exp(ik_1 x)$ is the spatial dependence of the incident harmonic pressure wave and $n(x_S)dx_s$ the average number of scatterers in the dx_s small region around x_S. $f(\hat{i}, \hat{i}; x_s)$ and $f(\hat{i}, -\hat{i}; x_s)$ are the forward and backward scattering amplitudes associated to the scattering of a plane wave by a cylinder located at x_S (*cf.* Fig. 1). They can be expressed as modal sums, *cf.* [16], and calculated numerically. It must be noted here that $f(\hat{i}, -\hat{i}; x)$ and $f(\hat{i}, \hat{i}; x)$ depend on the *x*-co-ordinate because they depend on the radius (size) $a(x)$ of the cylinders

4 The WKB method applied to the smooth-varying slab

The variations of $n(x)$, $R(x)$, and $T(x)$ are supposed smooth, and

$$n'(x) \ll n(x), \; R'(x) \ll R(x) \text{ and } T'(x) \ll T(x) \,. \tag{4.1}$$

In other words, both the concentration and size of the cylinders are slow varying parameters. When derived, Eqs. (3.2) become

$$\psi'_+(x) = \left[ik_1 + n(x)T(x) \right] \psi_+(x) + n(x)R(x)\psi_-(x) \tag{4.2-a}$$

$$\psi'_-(x) = -\left[ik_1 + n(x)T(x) \right] \psi_-(x) - n(x)R(x)\psi_+(x) \,. \tag{4.2-b}$$

Taking into account the assumptions in Eq. (4.1), the derivation of Eqs. (4.2) leads to

$$\psi_{\pm}''(x) + K_{eff}^{2}(x)\psi_{\pm}(x) \cong 0 \tag{4.3}$$

with

$$K_{eff}^{2}(x) = n^{2}(x)R^{2}(x) - \left[ik_{1} + n(x)T(x)\right]^{2} \tag{4.4}$$

where $R(x)$ and $T(x)$ are defined in Eq. (3.3). According to Eqs. (3.3), Eq. (4.4) is clearly Waterman & Truell'one [4] for a concentration and a size of the cylinders depending on the *x*-co-ordinate. After Eq. (4.1), it follows that

$$K'_{eff}(x) \ll K_{eff}(x) \ , \tag{4.5}$$

which is the reason why the WKB method can be used. The WKB solution of Eqs. (4.3) is well known [15]

$$\psi_{\pm}(x) = A_{\pm} e^{i\int_{0}^{x} K_{eff}(x_s)dx_s} / \sqrt{K_{eff}(x)} + B_{\pm} e^{-i\int_{0}^{x} K_{eff}(x_s)dx_s} / \sqrt{K_{eff}(x)} \tag{4.6}$$

with $A_{\pm}$ and $B_{\pm}$ the unknown constants. The only way to determine them is to use the boundary conditions at $x = 0$ and $x = d$. In order to do so, the following notations are introduced

$$n(x=0) = n_0 \qquad \text{and} \qquad n(x=d) = n_d \tag{4.7}$$

$$K_{eff}(x=0) = K_{eff}^{(0)} \qquad \text{and} \qquad K_{eff}(x=d) = K_{eff}^{(d)} \tag{4.8}$$

$$\left\langle K_{eff} \right\rangle = \frac{1}{d}\int_{0}^{d} K_{eff}(x_s)dx_s \tag{4.9}$$

with $\left\langle K_{eff} \right\rangle$ the average effective wave number of the varying slab. Continuity of pressure reads

$$\psi_{+}(0) + \psi_{-}(0) = 1 + R_{slab} \qquad \text{and} \qquad \psi_{+}(d) + \psi_{-}(d) = T_{slab} \tag{4.10}$$

with

$$\psi_{-}(0) = R_{slab} \qquad \text{and} \qquad \psi_{+}(d) = T_{slab} \ . \tag{4.11}$$

It follows that

$$\psi_{+}(0) = 1 \qquad \text{and} \qquad \psi_{-}(d) = 0 \ . \tag{4.12}$$

Inserting Eqs. (4.6) into Eqs. (4.12) gives

$$A_{+} + B_{+} = \sqrt{K_{eff}^{(0)}} \qquad \text{and} \qquad A_{-}\, e^{i\left\langle K_{eff}\right\rangle d} + B_{-}\, e^{-i\left\langle K_{eff}\right\rangle d} = 0 \tag{4.13}$$

Two equations do not allow to calculate the four parameters $A_{\pm}$ and $B_{\pm}$. Two others are required. As expected, these ones must be the continuity of normal displacements. But the question is how to write them? In the following, the effective mass density is supposed to be dependent on the x-co-ordinate. It is introduced as a generalisation of that of references [8,10,11]. Then, the continuity of normal displacement is written and the reflection and transmission coefficients of the space-varying slab are calculated. Finally, as they look like the usual reflection and transmission coefficients of a fluid plate, we validate *a posteriori* the continuity of normal displacements and the way the effective mass density is defined. Continuity of normal displacement gives

$$\frac{1}{\rho_{eff}^{(0)}}\left[\frac{\partial \psi_{+}}{\partial x}(0)+\frac{\partial \psi_{-}}{\partial x}(0)\right]=\frac{1}{\rho_1}\left[\frac{\partial \psi_{inc}}{\partial x}(0)+\frac{\partial \psi_{R}}{\partial x}(0)\right] \tag{4.14-a}$$

$$\frac{1}{\rho_{eff}^{(d)}}\left[\frac{\partial \psi_{+}}{\partial x}(d)+\frac{\partial \psi_{-}}{\partial x}(d)\right]=\frac{1}{\rho_1}\left[\frac{\partial \psi_{T}}{\partial x}(d)\right], \tag{4.14-b}$$

where $r_{eff}^{(0)}=r_{eff}(x=0)$ and $r_{eff}^{(d)}=r_{eff}(x=d)$ are the effective mass densities at the beginning and at the end of the slow-varying slab. Starting from the Twersky's formalism, the x-dependence of the effective mass density is quite naturally the generalization of Eq. (2.3)

$$\rho_{eff}(x)=\rho_1\frac{K_{eff}(x)}{k_1}\frac{1-Q(x)}{1+Q(x)} \tag{4.15}$$

with (*cf.* Eqs. (3.3, 4.4))

$$Q(x)=\frac{n(x)T(x)+i(k_1-K_{eff}(x))}{n(x)R(x)}\ . \tag{4.16}$$

Of course, the function $Q(x)$ is formally the same that of references [8,10,11] with n,R,T,K_{eff} depending on the x-co-ordinate. The impedance ratios

$$\tau_0=\frac{\rho_{eff}^{(0)}k_1}{\rho_1 K_{eff}^{(0)}}=\frac{1-Q_0}{1+Q_0}\qquad\text{and}\qquad\tau_d=\frac{\rho_{eff}^{(d)}k_1}{\rho_1 K_{eff}^{(d)}}=\frac{1-Q_d}{1+Q_d}\ , \tag{4.17}$$

are also introduced, with $Q(x=0)=Q_0$ and $Q(x=d)=Q_d$.

In the field of the WKB approximation, k_1 is assumed to be large, and, as $\langle K_{eff}\rangle$ is of the same order as k_1, one has

$$\frac{\partial}{\partial x}\left(e^{\pm i\int_0^x K_{eff}(x_s)dx_s}\Big/\sqrt{K_{eff}(x)}\right)\cong\pm i\sqrt{K_{eff}(x)}\,e^{\pm i\int_0^x K_{eff}(x_s)dx_s}\ . \tag{4.18}$$

As a consequence, once Eq. (4.6) introduced in Eqs. (4.14), and Eq. (4.18) taken into account, one gets

$$\left(1+Q_0\right)A_+ - \left(1+Q_0\right)B_+ + 2A_- - 2Q_0 B_- = \sqrt{K_{eff}^{(0)}}\left(1-Q_0\right) \ , \tag{4.19-a}$$

$$2Q_d A_+ e^{i\langle K_{eff}\rangle d} - 2B_+ e^{-i\langle K_{eff}\rangle d} + \left(1+Q_d\right)A_- e^{i\langle K_{eff}\rangle d} - \left(1+Q_d\right)B_- e^{-i\langle K_{eff}\rangle d} = 0 \ . \tag{4.19-b}$$

Once the solution of the set of linear equations Eqs. (4.13,4.19) obtained, the reflection and transmission coefficients can be calculated from Eqs. (4.6,4.11), it comes

$$R_{slab} = \frac{-Q_0 + Q_d e^{2i\langle K_{eff}\rangle d}}{1 - Q_0 Q_d e^{2i\langle K_{eff}\rangle d}} = \frac{(\tau_0 - 1)(1+\tau_d) + (\tau_0 + 1)(1-\tau_d)e^{2i\langle K_{eff}\rangle d}}{(\tau_0 + 1)(1+\tau_d) + (\tau_0 - 1)(1-\tau_d)e^{2i\langle K_{eff}\rangle d}} \tag{4.20-a}$$

$$\begin{aligned} T_{slab} &= \frac{\sqrt{K_{eff}^{(0)}}}{\sqrt{K_{eff}^{(d)}}} \frac{(1+Q_d)(1-Q_0)e^{i\langle K_{eff}\rangle d}}{1 - Q_0 Q_d e^{2i\langle K_{eff}\rangle d}} \\ &= \frac{\sqrt{K_{eff}^{(0)}}}{\sqrt{K_{eff}^{(d)}}} \frac{4\tau_0 e^{i\langle K_{eff}\rangle d}}{(\tau_0 + 1)(1+\tau_d) + (\tau_0 - 1)(1-\tau_d)e^{2i\langle K_{eff}\rangle d}} \ . \end{aligned} \tag{4.20-b}$$

In the case where the features of the slab are the same at the beginning and at the end, *i.e.* $n_d = n_0$, $K_{eff}^{(d)} = K_{eff}^{(0)}$, $r_{eff}^{(d)} = r_{eff}^{(0)}$ and $Q_d = Q_0$, Eqs. (4.20) comes down to

$$R_{slab} = \frac{-Q_0 + Q_0 e^{2i\langle K_{eff}\rangle d}}{1 - Q_0^2 e^{2i\langle K_{eff}\rangle d}} = \frac{(\tau_0^2 - 1) + (1-\tau_0^2)e^{2i\langle K_{eff}\rangle d}}{(1+\tau_0)^2 - (1-\tau_0)^2 e^{2i\langle K_{eff}\rangle d}} \tag{4.21-a}$$

$$T_{slab} = \frac{(1-Q_0^2)e^{i\langle K_{eff}\rangle d}}{1 - Q_0^2 e^{2i\langle K_{eff}\rangle d}} = \frac{4\tau_0 e^{i\langle K_{eff}\rangle d}}{(1+\tau_0)^2 - (1-\tau_0)^2 e^{2i\langle K_{eff}\rangle d}} \ . \tag{4.21-b}$$

These expressions are formally identical to those given in Ref. [8-11] for a uniform slab. The difference lies in the introduction of $\left\langle K_{eff}\right\rangle$ instead of K_{eff}, as the latter is not a constant. The varying slab is thus equivalent to a uniform slab characterized by the impedance ratio t_0 at the interfaces and by the average effective wave number $\left\langle K_{eff}\right\rangle$ that describes the propagation of the average coherent wave.

Let consider now the reflection-refraction coefficients at the two interfaces of the slab (the homogeneous fluids $[x \le 0]$ and $[x \ge d]$ are labelled 0 and *d*, the varying slab is labelled 1)

$$R_{01} = -R_{10} = \frac{\tau_0 - 1}{1+\tau_0},\ T_{01} = \frac{2\tau_0}{1+\tau_0} \quad \text{and} \quad T_{10} = \frac{2}{1+\tau_0} \tag{4.22-a}$$

$$R_{1d} = -R_{d1} = \frac{\tau_d - 1}{1+\tau_d},\ T_{1d} = \frac{2\tau_d}{1+\tau_d} \quad \text{and} \quad T_{d1} = \frac{2}{1+\tau_d}\ . \tag{4.22-b}$$

The reflection and transmission coefficients in Eqs. (4.20) can be written as

$$R_{slab} = R_{01} + \frac{T_{01}R_{1d}T_{10}e^{2i\langle K_{eff}\rangle d}}{1 - R_{10}R_{1d}e^{2i\langle K_{eff}\rangle d}} \tag{4.23-a}$$

$$T_{slab} = \frac{T_{01}T_{1d}e^{i\langle K_{eff}\rangle d}}{1 - R_{10}R_{1d}e^{2i\langle K_{eff}\rangle d}}\ . \tag{4.23-b}$$

The varying slab can still be considered as an interferometer. As discussed in the introduction, the impedance ratios τ_0 and τ_d are close to unity at low concentration, so that $R_{01} \cong R_{1d} \cong 0$ and $T_{01} \cong T_{1d} \cong 1$ (*cf.* Eqs (4.22)), and (*cf.* Eqs (4.23-b))

$$T_{slab} \cong e^{i\langle K_{eff}\rangle d}\ . \tag{4.24}$$

This means that transmission experiments can bring no information on $K_{eff}(x)$, but only on its average $\langle K_{eff} \rangle$. Two different varying-slabs, with $K_{eff}^{(1)}(x) \neq K_{eff}^{(2)}(x)$, can give rise to the same average transmitted field, provided that $\langle K_{eff}^{(1)} \rangle = \langle K_{eff}^{(2)} \rangle$. It seems thus rather hopeless to try and identify the profile $(n(x), R(x), T(x))$ of a varying-slab with the help of a theory based on coherent wave propagation.

5 Numerical results

Computations are performed for a space-varying slab characterised by

$$n(x) = \begin{cases} n_{\max} e^{-(x-d/2)^2/\sigma^2} & 0 \le x \le d \\ 0 & otherwise \end{cases} \quad \text{with} \quad \sigma^2 = \left(\frac{d}{2}\right)^2 \Big/ \log\left(\frac{n_{\max}}{n_{\min}}\right), \tag{5.1}$$

and $a(x)$=1 mm the radius of all cylinders. In Eq.(5.1), $n_{\max} = 10^4 / m^2$ and $n_{\min} = n_{\max}/3$ are respectively the maximum and minimum numbers of steel cylinders per unit surface. Eq.(5.1) describes a truncated Gaussian function for which $n(d/2) = n_{\max}$ and $n(0) = n(d) = n_{\min}$. The thickness of the slab is

d=0.1m. As the size of the cylinders is constant all over the slab, so are the forward and backward scattering amplitudes $f(\hat{i},\pm\hat{i})$. Steel is characterised by its density r_s =7916 kg/m^3, the velocity of the longitudinal waves c_L =6000 m/s, and that of the shear waves c_T =3100 m/s. The cylinders are immersed in water, characterized by its density r_1 =1000 kg/m^3 and the velocity of sound c_1 =1470 m/s.

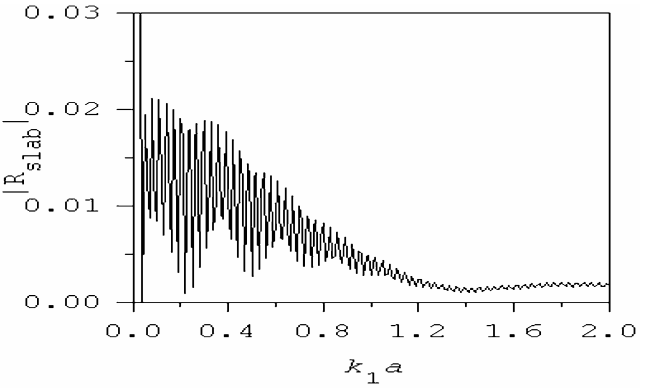

Fig. 3 Modulus of the reflection of the space varying slab for $0 \le k_1 a \le 2$.

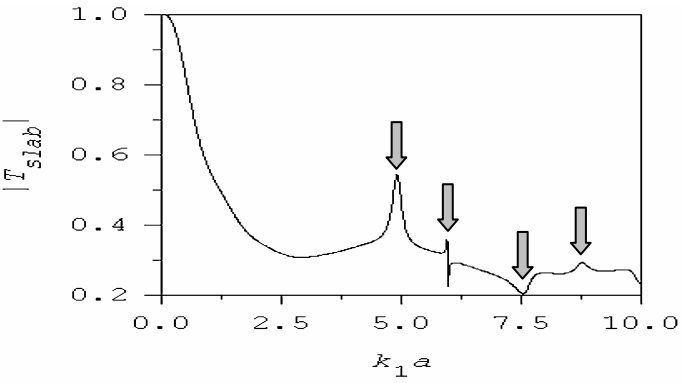

Fig. 4 Modulus of the transmission coefficient of the space varying slab. Arrows indicate the resonance frequencies of the steel cylinders.

First, it can be observed in Figs. 3 and 4 that the reflection is small compared to the transmission and vanishes with the increase of the frequency. Second, it has been checked that the two first terms of Eq. (4.24-a) approximate very well R_{slab}. So, the reflection is only due to the specular reflection at the first

interface and to the wave which propagate back after one reflection on the second interface. This explains the oscillations observed on the reflection due to interferences between the two waves. Same way, T_{slab} is very well approximated by the first term of Eq. (4.24-b). Consequently, the transmission through the slab is merely reduced to a direct transmission.
In order to get shorter computation times, consider now a uniform slab, characterized only by the average number of cylinders:

$$\langle n \rangle = \frac{1}{d} \int_0^d n(x_s) dx_s . \tag{5.2}$$

Is that new-defined slab equivalent to the space-varying one? The coherent waves in that slab propagate with a wavenumber $\langle K_{eff} \rangle$ given by Eq.(5.3) [4]

$$\langle K_{eff} \rangle^2 = \left(k_1 + \frac{2\langle n \rangle}{ik_1} f(\hat{i}, \hat{i}) \right)^2 - \left(\frac{2\langle n \rangle}{ik_1} f(\hat{i}, -\hat{i}) \right)^2, \tag{5.3}$$

and its mass density is supposed to be

$$\rho_{eff} \cong \rho_1 \frac{\langle K_{eff} \rangle}{k_1} \frac{1 - \langle Q \rangle}{1 + \langle Q \rangle} \tag{5.4}$$

with

$$\langle Q \rangle @ \frac{\langle T \rangle + i(k_1 - \langle K_{eff} \rangle)}{\langle R \rangle} \ , \ \langle T \rangle \cong \frac{2\langle n \rangle}{k_1} f(\hat{i}, \hat{i}) \text{ and } \langle R \rangle \cong \frac{2\langle n \rangle}{k_1} f(\hat{i}, -\hat{i}) . \tag{5.5}$$

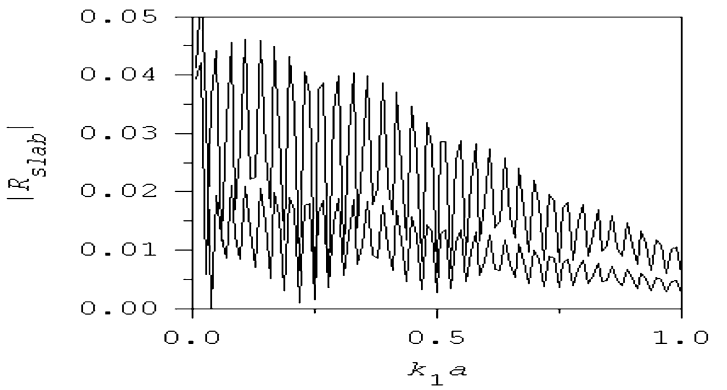

Fig. 5 Modulus of the reflection coefficient of the space varying slab. Lower curve: exact value. Upper curve: Approximate value corresponding to Eq. (5.3).

Its transmission and reflection coefficients can be calculated therefrom. The modulus of the transmission coefficient obtained is pretty much the same than that plotted in Fig. 4, but Fig.5 shows that the reflection coefficient is larger than that of the original space-varying slab. The average effective wave number $\left\langle K_{eff} \right\rangle$ is well approximated from Eq. (5.3), which is the reason why the oscillations of the two reflection coefficients are practically in phase. Consequently, it is the effective mass density ρ_{eff} given by Eq. (5.4) that is not correct. As shown by the WKB method, it is the effective masse densities $r_{eff}^{(0)}$ and $r_{eff}^{(d)}$ at the beginning and at the end of the varying slab which must be taken into account. In our case, ρ_{eff} given by Eq. (5.4) overestimates the effective masse density $r_{eff}^{(0)} = r_{eff}^{(d)}$.

Summary

It has been shown that the use of the WKB method is relevant for the study of the propagation of coherent waves through a smooth space-varying slab. Once the effective mass density is defined correctly, it has been shown that the boundary conditions at the interface between a homogeneous fluid and an effective medium are fulfilled. These are the continuity of pressure and of normal displacement.

References

1. P.A. Martin, *MULTIPLE SCATTERING, Interaction of Time-Harmonic Waves with N Obstacles*, Cambridge University Press (2006).
2. V. Twersky, *On propagation in random media of discrete scatterers*, Proc. Am. Math. Soc. Symp. Stochas. Proc. Math. Phys. Eng. **16** (1964) pp. 84-116.
3. L.L. Foldy, *The Multiple Scattering of Waves. Part. I: General theory of isotropic scattering by randomly distributed scatterers*, Physical Review **67** (1945) pp. 107-119.
4. P.C. Waterman, R. Truell, *Multiple Scattering of Waves,* Journal of Mathematical Physics **2** (1961) pp. 512-537.
5. J.G. Fikioris, P.C. Waterman, *Multiple Scattering of Waves. Part. II: 'Hole corrections in the scalar case*, Journal of Mathematical Physics **5** (1964) pp. 1413-1420.
6. C. Aristégui, Y.C. Angel, *New results for isotropic point scatterers: Foldy revisited*, Wave Motion **36** (2002) pp. 383-399.
7. C.M. Linton, P.A. Martin, *Multiple scattering by random configurations of circular cylinders: second-order corrections for the effective wavenumber*, J. Acoust. Soc. Am. **117** (2005) pp. 3413-3423.
8. V. Twersky, *On Scattering of Waves by Random Distributions. I. Free-Space Scatterer Formalism*, Journal of Mathematical Physics **3** (1962) pp. 700-715.
9. P.Y. Le Bas, F. Luppé, J.M. Conoir, *Reflection and transmission by randomly spaced elastic cylinders in a fluid slab-like region*, J. Acoust. Soc. Am. **117** (2005) pp. 1088-1097.

10. Y.C. Angel, C. Aristegui, *Analysis of sound propagation in a fluid through a screen of scatterers*, J. Acoust. Soc. Am. **118** (2005) pp. 72-82.
11. C. Aristegui, Y.C. Angel, *Effective mass density and stiffness derived from P-wave multiple scattering*, Wave Motion **44** (2007) pp. 153-164.
12. S. Robert, J.M. Conoir, *Reflection and transmission process from a slab-like region containing a random distribution of cylindrical scatterers in an elastic matrix*, ACTA ACUSTICA united with ACUSTICA **93** (2007) pp. 1-12.
13. V. Tournat, V. Pagneux, D. Lafarge, L. Jaouen, *Multiple scattering of acoustic waves and porous absorbing media*, Phys.Rev.E **70** (2004) pp. 026609.1-026609.10.
14. A. Derode, V. Mamou, A. Tourin, *Influence of correlations between scatterers on the attenuation of the coherent wave in a random medium*, Pys.Rev.E **74** (2006) pp. 036606.1-036606.9.
15. L.M. Brekhovskikh, O.A. Godin, *Acoustics of Layered Media I*, Springer-Verlag (1990).
16. N.D. Veksler, *Resonance Acoustic Spectroscopy*, Springer-Verlag (1993).

Advances in ultrasonic testing of austenitic stainless steel welds. Towards a 3D description of the material including attenuation and optimisation by inversion

J. Moysan , C. Gueudré , M.-A. Ploix , G. Corneloup , Ph. Guy , R. El Guerjouma , B. Chassignole

Abstract In the case of multi-pass welds, the material is very difficult to describe due to its anisotropic and heterogeneous properties. Anisotropy results from the metal solidification and is correlated with the grain orientation. A precise description of the material is one of the key points to obtain reliable results with wave propagation codes. A first advance is the model MINA which predicts the grain orientations in multi-pass 316-L steel welds. For flat position welding, good predictions of the grains orientations were obtained using 2D modelling. In case of welding in position the resulting grain structure may be 3D oriented. We indicate how the MINA model can be improved for 3D description. A second advance is a good quantification of the attenuation. Precise measurements are obtained using plane waves angular spectrum method together with the computation of the transmission coefficients for triclinic material. With these two first advances, the third one is now possible: developing an inverse method to obtain the material description through ultrasonic measurements at different positions.

J. Moysan, C. Gueudré, M.-A. Ploix, G. Corneloup

LCND, Université de la Méditerranée, Av. G. Berger, 13625 Aix en Provence, France, joseph.moysan@univmed.fr

Ph. Guy

MATEIS, INSA Lyon, 7 Avenue Jean Capelle, 69621 Villeurbanne, France, philippe.guy@insa-lyon.fr

R. El-Guerjouma

LAUM, Avenue Olivier Messiaen, 72085 Le Mans Cedex 9, France, rachid.elguerjouma@univ-lemans.fr

B. Chassignole

Département MMC, EDF R&D, Site des Renardières, 77818 Moret-sur-Loing, France, bertrand.chassignole@edf.fr

1 Introduction

Austenitic steel multi-pass welds exhibit a heterogeneous and anisotropic structure that causes difficulties in the ultrasonic testing (UT) understanding. Increasing the material knowledge has been an international large and long term research field. Some years ago works aiming at giving a precise description of the material provided significant progresses [1].This paper acquaints firstly with a synthesis of several research works aiming at modelling UT inspection in multipass welds. In all these previous works the UT modelling is considered as 2D case. In a second part the question of a 3D representation of the material resulting from the welding in position arises. New modelling ideas are presented to improve 2D MINA model towards a 3D material description. Modelling is done with the final goal to use inverse methodology in UT testing. The paper syntheses other milestones obtained along this way: attenuation measurements and results with inverse methodology.

2 The context: UT modelling for welds inspection

The main specificity of the weld material is its oriented grain structure which has to be described as an anisotropic and heterogeneous material. The description of the grain structure regularly progresses from simplified and symmetrical structures to more realistic descriptions. Ogilvy [2] proposes to calculate the central ray in a grain structure described by mathematical functions. Schmitz et al [3] use the ray tracing code 3D-Ray-SAFT with an empirical grain structure described by orientation vectors with three coordinates. The EFIT (Element Finite Integration Technique) code is used by Halkjaer et al [4] with Ogilvy's grain structure. Langerberg et al [5] also simulate a simplified symmetrical structure. Spies [6] uses a Gaussian beam approach to calculate the transducer field and to ensure faster modelling. The author simulates the heterogeneity by splitting up the weld into several layers of transverse isotropic material [7]. X. Zhao et al [8] also use a ray tracing approach to determine optimal configuration for flaw detection. Corresponding material descriptions do not always reach the complexity of the heterogeneous structure resulting from manual arc welding. The structure of the real material is non symmetrical and UT modelling may exhibit strong differences [9]. Our modelling approach couples MINA model and ATHENA code [10].
Heterogeneous and anisotropic structure is defined by introducing a mesh containing the grain orientations calculated by MINA model (cf. § 3). This permits to define the appropriate coordinate systems of the elasticity constants at any point of the weld. A result of the coupling between ATHENA and MINA is presented on figure 1. The UT testing is modelled using a 60° longitudinal wave at 2.25 MHz. The corresponding echodynamic curves are calculated using ATHENA results in transmission at the bottom of the weld. In the right part of this figure the result of the coupling MINA-ATHENA is compared with an ATHENA modelling

using the “real” grain structure. This real grain structure is obtained by image analysis of the macrographs [11].

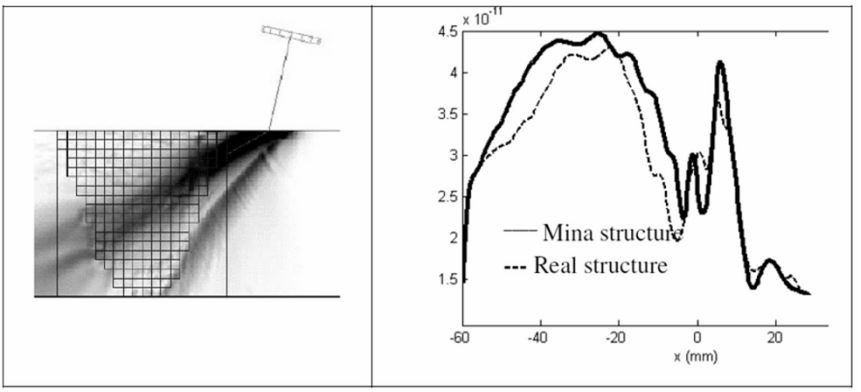

Fig. 1 Example of results from coupling ATHENA and MINA codes.

3 MINA model parameters for flat welding

The MINA model (Modelling anIsotropy from Notebook of Arc welding) was planned to describe the material resulting from flat position arc welding with shielded electrode at a functional scale for UT modeling. It predicts the result of the grain growth [12]. Three physical phenomena are involved: the epitaxial growth, the influence of temperature gradient, and the competition between the grains (selective growth). Epitaxial growth implies that the melt metal takes in each point the crystallographic orientations of the underlying pass. The grain may turn during the growth but the crystallographic orientation is kept. When the temperature gradient changes of direction, grains have a propensity to align themselves with the gradient direction. In the case of multi-pass welding, temperature gradient direction changes within the welding pass and also from one pass to the other. A competition between grains exists as they preferentially grow if their longitudinal axis is close to the direction of the temperature gradient.

The challenge of creating a model reproducing the result of these phenomena has been successfully won with MINA model. The difficulty was to use only knowledge reported in the welding notebook and, in order to complete this knowledge, to find representative parameters of the variation in the deposit of passes. Macrographs analysis was widely used to build the model. The model is dedicated to predict material resulting from flat welding. In that case the grain structure is reputed to be 2D. A complete description of the model can be found in [12]. Main MINA model parameters are recalled here in order to introduce how MINA model may be improved for welding in position. A pass is represented by a parabolic shape. Pass heights are calculated proportionally to the diameters of the

electrodes. A partial remelting is created when a new pass is laid. The two most important parameters are the lateral and the vertical remelting rates, respectively noted R_L and R_V. Two angles are used to imitate the operator's tilt of the electrode. In fact the operator has to modify the way he deposes a pass along the welded joint. This causes an incline of the welding pool. In Figure 2a, weld pool shape and incline of the pass are sketched on a macrograh. Two cases are considered. When a pass leans on the chamfer the angle of rotation θ_B reproduces the influence of the weld geometric chamfer. This angle is considered to be the same for the two sides of the weld due to its symmetry. When a pass leans on a previous pass, the temperature gradient is rotated by an angle noted θ_C. For example in the case where a pass leans to its left and its right on other passes, the angle θ_C equals to zero. All angles are automatically calculated in relation to the location of each pass written in the welding notebook.
With these four parameters (R_L, R_V, θ_B, θ_C) the grain orientation in a mesh is calculated using an algorithm which reproduces the three physical phenomena previously mentioned. The temperature gradient direction is deduced from the parabolic weld pool description [12]. MINA model output is a matrix whose elements represent the local orientation of the grains resulting from the complete solidification process due to the remelting of passes (see figure 2). The matrix elements are calculated pass after pass in the order written down in the book.

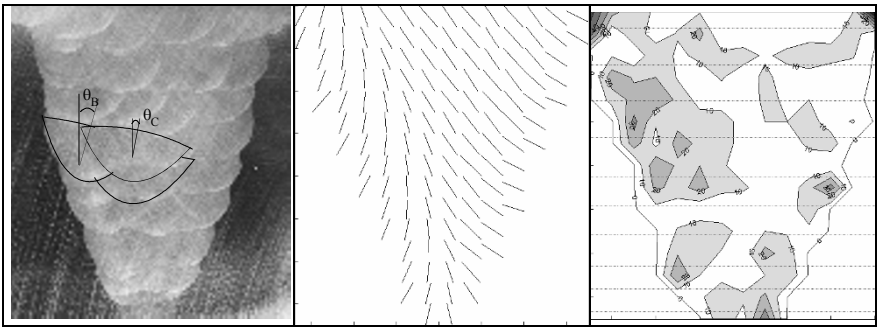

Figure 2. (left to right) Macrographs, resulting grain structure, differences map in the case of an horizontal-vertical weld

4 Improving MINA for welding in position

Welding in position corresponds to several standardized positions: the overhead position, the vertical position (vertical up or vertical down), or the horizontal-vertical position. For this study specific welds have been made with the same base material and the same electrodes. Macrographs were achieved in two perpendicular planes in order to study 3D effects on grain solidification. The conclusions give us clear indications to improve MINA model towards a more

general model: new parameters are then proposed to be able to reproduce grain structure for welds in position. The figure 2 represents one of the new macrographs used for this study. Figure 2b presents resulting grain structure with a mesh-size of 2x2 mm². It could be compared with the corresponding macrograph in Figure 3b. Figure 2c shows the map of orientation differences. Differences are presented with level lines where grain orientations are gathered by about ten degrees. The real grain orientations are measured by an image analysis system. In comparison with previous studies for flat welding position, the resulting of grain structure for horizontal-vertical welding is truly very different. A strong non-symmetrical grain structure can be observed. In figure 2 the differences are localized on the left side of the weld. This demonstrates that the MINA model parameter θ_B which aims at representing the incline of the weld pass on the chamfer could no more be used in the same way as for flat welding (symmetrical behavior). We propose to introduce another parameter called θ_D to take into account this significant difference.

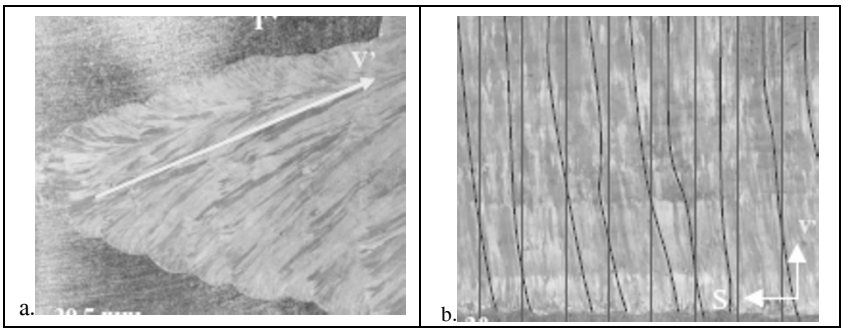

Figure 3. Macrographs of grain structure for horizontal-vertical weld (TV and SV' cuts)

New knowledge is also obtained by considering macrographs in the SV or SV' plane (cf. figure 3b). SV' plane corresponds to a cut along the main grain orientation. These macrographs were done to study disorientations in the welding direction. For flat welding position, no disorientation is observed. A slight disorientation, about 5°, could be observed for welding in overhead position and in horizontal-vertical position. A major one is observed in the case of vertical position welding, it is about 20° to 25°. In figure 3b the grains disorientations were underlined by additional lines following biggest grains. For further studies we propose to introduce a new parameter called Φ corresponding to these disorientations. This parameter should be used to improve the MINA model, but it supposes at first that a fully 3D material is also needed in propagation code.

Another parametric study was done in this work to analyse modelling behaviour when welding in position is considered. The shape of a pass is a very important aspect in the MINA approach as it determines the temperature gradient. The ratio of the width (w) and the height (h) of passes could be an interesting descriptive

parameter to compare passes shape. This ratio w/h is measured on macrographs and could be automatically calculated by MINA. The MINA model gives very satisfactory w/h ratios, with a average difference of 10% with measured ratios on macrographs. The exception is the vertical welding position for which modelled and measured ratios are more different, about 20%. This difference may result from a higher difficulty to estimate with accuracy the remelting parameters on macrographs. If remelting parameters are correct, a modification of the weld pool could be suggested. A large previous experience with macrographs for flat position welding allows assessing that grain structure behaviour is similar if welding conditions keep the same. It enables to conclude that the MINA model could be used with few adaptations for most of the welding positions. In the case of vertical welding, more important differences are observed between the real grain structure and the modelled one. The shape of the weld pool should be modified. For this welding position it would be useful to verify the conclusions on another weld. The most important conclusion for this welding position is the 3D aspect of the grain structure. If this property is not taken into account in modelling, misunderstanding of the UT testing can rapidly occurs. In case of finite element modelling, only 3D codes would correctly predict beam deviation.

5 Attenuation measurements

The second advance which is required for wave propagation codes is a good quantification of the attenuation. The coupling of the MINA-ATHENA codes demonstrated good results when comparing measured and predicted amplitudes at the bottom of the weld (UT in transmission) [10]. Differences are observed when considering the amplitudes. The origin of these differences is the real attenuation, not reproduced with the finite element modelling. The attenuation can reach 0,3 dB/mm for such grain structures [13]. The origin of the attenuation in welded materials is for the most part caused by scattering effect on the columnar grains. The value of this attenuation depends on the size, shape and orientation of the grains. An experimental set up is designed in order to study the ultrasonic attenuation as a function of the grain orientation [14]. A measurement in transmission is used in a water tank. The emitter is a 1/2" in diameter wideband transducer of 2.25 MHz central frequency, and the receiver is a hydrophone.
The welded samples were cut in a flat position and shielded metal arc welding mock-up. The samples are considered macroscopically homogeneous and orthotropic. The real orientations that are obtained are 0°, 10°, 35°, 45°, 60°, 80° and 85° relatively to the normal to the samples surface. Samples are placed in the farfield of the emitter. The beam decomposition into plane waves angular spectrum is used to correct the effects of beam divergence [15]. With this approach, deviations and mode conversions could be taken into account. The hydrophone scans a plane $z=z_o$ parallel to the emitter surface and acquires a signal $s(t,x,y,z_o)$ at each point (x,y). The angular frequency spectrum $S(x,y,\omega_o,z_o)$ is

calculated for each signal by Fourier-transform. For an angular frequency ω_o, a 2D spatial Fourier-transform gives the so called plane waves angular spectrum $U(kx,ky,\omega_o,z_o)$ in the k-space domain. Firstly the incident field is mapped without any sample. The hydrophone moves in the plane containing the front face of the sample ($z_o=0$). Then the sample is inserted and the transmitted field is mapped in a second plane in the proximity of the sample's back face ($z_o>d$). For the angular frequency ω_o corresponding to a frequency of 2.25MHz, the plane waves angular spectra $U(kx,ky,\omega_o,z_o=0) = U_{inc}$ and $U(kx,ky,wo,z_o=d+\varepsilon) = U_{tra}$ are calculated. A "semi-theoretical" transmitted plane waves angular spectrum U'_{tra} is obtained by multiplying experimental U_{inc} with the transmission coefficients calculated in the k-space domain.

Transmission coefficients computation was solved in the orthotropic case [15] and was then extended to the monoclinic case. In fact the elastic description of an orthotropic material disorientated according to an axis of the fixed coordinate system becomes monoclinic. So, except for samples with 0° and 90° grain orientation that present an orthotropic description, all other samples are described as monoclinic materials. For some samples a deviation in two directions is observed (sample 10°). It confirms the result of the first study where little deviation in plane SV are observed (§ 4). If these two deviations are considered, the material exhibits triclinic elastic properties for the ultrasonic beam. Transmitted coefficients have to be calculated for this case. The attenuation for each direction of propagation (kx,ky) is calculated by comparing simulated transmitted beam and real one. The attenuation is expressed as the ratio between the experimental transmitted energy and the theoretical transmitted energy.

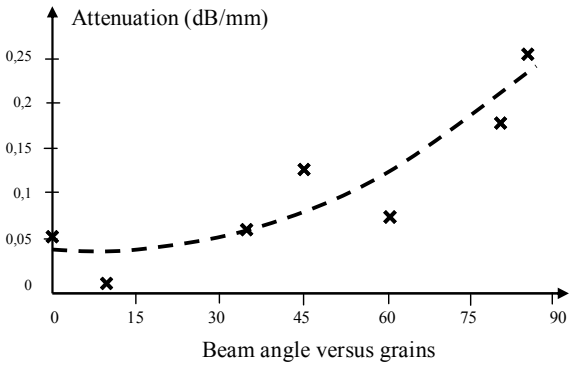

Figure 4. Experimental results of attenuation

Experimental results in figure 4 are in good agreement with theoretical calculations using Ahmed's modelling [16]. The double correction of beam deviation is used to obtain a good transmitted energy. This double correction reveals to be important for the 0° sample as a grain deviation in SV plane of about

5° was observed. With this correction a global monotonic increase of the attenuation is observed. Without this correction the attenuation value at 0° would be equal to 0,18 dB/mm. This result confirms once more that it is valuable to describe precisely the material. Slight 3D disorientations may give significant variations in the UT modelling. In part 4, it was observed that such order of 3D disorientations is possible for welding in position.

6 Inverse methodoly

The inverse problems are nowadays regularly encountered in the field of ultrasonic nondestructive testing [17]. The principle consists in comparing data obtained from experimental measurements with those obtained from a mathematical model known as the direct model. Results depend on the parameters assigned to the model (parameters of interest p). In this study the direct model corresponds to the coupling of MINA and ATHENA. The parameters of interest (input data) are the remelting and pass inclination parameters $p = (R_L, R_V, \theta_B, \theta_C)$. The output data is the full transmitted echodynamic curve at the bottom of the weld. The echodynamic curve corresponds to the maximum wave amplitude measured by a receiver scanning the bottom of the weld. In the interest of sensitivity, five transmitter positions are used so that the ultrasonic beam crosses most of the weld. The dissemblance criterion used to quantify the comparison is the estimator in the least squares sense.

Current ATHENA code does not yet take the attenuation into account. As a consequence, the amplitudes of the echodynamic curves simulated by ATHENA and those of the experimental curves can notably differ. Inversion of experimental data is not possible at this time. To overcome this difficulty experimental data are obtained by simulation using MINA and ATHENA. The main advantage is that the inversion can be done without the errors inherent in experimental measurements. All the parameters are completely known. The sensitivity of the cost function J and the presence of local minima can be studied in that case. This process is a useful first step before inversion with real data to demonstrate that a model is sufficiently well established to be inversible. Figure 5 shows an example of the evolution of the estimated parameters.

The genetic algorithm GA-Toolbox from MATLAB® is used. The main algorithm parameters are therefore the population size (N), the number of bits used to code parameters (Preci), the crossover rate (0<PcCros<1) and the replacement rate (0<Ggap<1). The tournament selection and the double point crossover are used. The search domain must be well-defined. These limits have been determined for each parameter experimentally from macrographs. This gives a realistic precision of the parameters.The inversion solution is found in commonly 16 generations, for a computation time of 4 hours on a Pentium IV @2.4 GHz [17]. The estimated parameters R_L = 0.471, R_V = 0.263, θ_B = 18.18° and θ_C = 12.25° are independent from the initialisation and are very close to the solution.

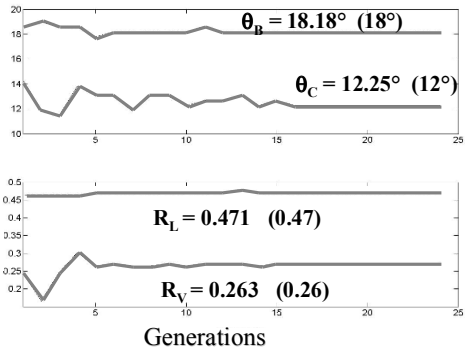

Figure 5. Inverse Methodology Results

The demonstration is done that inversion of this kind of direct problem is now possible.

7 Conclusion

Several advances in the field of ultrasonic modelling are presented. They are related to the ultrasonic testing of austenitic stainless steel welds which were reputed to be very difficult to be qualified by ultrasound. Advances were conducted with the intention to model the complete ultrasonic beam propagation in multi-pass welds. The foundation of all these advances is to be able to have a good material description for wave propagation. The MINA model allows a solid foundation regarding this objective. In this paper new elements are brought to enlarge the range of application of the MINA model. Another important element for the material description is a good evaluation of the attenuation, a solution for accurate measurement is presented and results are in good agreement with modelling. The direct model is settled using MINA and ATHENA. The inverse crime is solved; as a result it demonstrates the soundness of this coupling.
Further prospects are planned. The first one is related to an inversion which takes into account experimental data. Future works are planned with the new ATHENA code taking attenuation into account. A second immediate prospect is to use this inversion method to verify the sequencing order of the passes. The order of passes is used in the MINA model to calculate the value of θ_B and θ_C parameters. Several modelling results demonstrated that there is a great influence of this sequencing order in the final resulting grain structure. Ultrasonic testing of complex welds may now be studied using this direct model as [19].

Acknowledgments : All the works presented in this paper were supported by Electricité de France (EDF).

References

[1] B. Chassignole, D. Villard, M. Dubuget, J.C. Baboux, R. El Guerjouma, 'Characterization of austenitic stainless steel welds for ultrasonic NDT', Review of Progress in QNDE, Vol.20, 2000, pp.1325-1332.

[2] J.A. Ogilvy, Computerized ultrasonic ray tracing in austenitic steel, NDT&E International 18 (2) (1985) 67–77.

[3] V. Schmitz, F. Walte, S.V. Chakhlov, 3D ray tracing in austenite materials, NDT&E International 32 (1999) 201–213.

[4] S. Halkjaer, M.P. Sorensen, W.D. Kristensen, The propagation of ultrasound in a austenitic weld, Ultrasonics 38 (2000) 256–261.

[5] K.J. Langenberg, R. Hannemann, T. Kaczorowski, R. Marklein, B. Koehler, C. Schurig, F. Walte, Application of modeling techniques for ultrasonic austenitic weld inspection, NDT&E International 33 (2000) 465–480.

[6] M. Spies, Elastic waves in homogeneous and layered transversaly isotropic media: plane waves and Gaussian wave packets. A general approach, JASA 95 (1994) 1748–1760.

[7] M. Spies, Modeling of transducer fields in inhomogeneous anisotropic materials using Gaussian beam superposition, NDT&E International 33 (2000) 155–162.

[8] X. Zhao, S.J. Song, H.J. Kim, T. Gang, S.C. Kang, Y. H. Choi, K. Kim, S.S. Kang, Determination of incident angle and position of optimal mode ultrasonic beam for flaw detection in anisotropic and inhomogeneous weldments by ray tracing, J. of the Korean Society for Nondestructive Testing, Vol. 27, N°3, 2007, pp 231-238

[9] A. Apfel, J. Moysan, G. Corneloup, B. Chassignole, Simulations of the influence of the grains orientations on ultrasounds, 16th WCNDT, Montreal, 2004

[10] A. Apfel, J. Moysan, G. Corneloup, t. Fouquet, B. Chassignole, Coupling an ultrasonic propagation code with a model of the heterogeneity of multipass welds to simulate the ultrasonic testing. Ultrasonics, Volume 43, Issue 6, May 2005,pp 447-456

[11] B. Chassignole, Influence of the Metallurgical Structure of Austenitic Stainless Steel Welds on the Ultrasonic Non Destructive Testing, PhD Thesis, ISAL 0107, 2000, 207 p (fr).

[12] J. Moysan, A. Apfel, G. Corneloup, B. Chasssignole, Modelling the Grain Orientation of Austenitic Stainless Steel Multipass Welds to Improve Ultrasonic Assessment of Structural Integrity, International Journal of Pressure Vessels and Piping, Vol. 80 n°2, 2003, pp 77 - 85

[13] T. Seldis, C. Pecorari, M. Bieth, Measurements of longitudinal wave attenuation in austenitic steel, 1st International Conference on NDE in Relation to Structural Integrity for Nuclear and Pressurised Components, Amsterdam (Netherlands), 1998, pp 769-777.

[14] M.A. Ploix et al., Attenuation Assessment for NDT of Austenitic Stainless Steel Welds, 9 th European Conference on NDT, Berlin, 25-29 sept. 2006

[15] B. Hosten, Reflection and Transmission of Acoustic Plane Waves on an Immersed Orthotropic and Viscoelastic Solid Layer, JASA, Vol. 89, No. 6, 1991, pp. 2745-2752

[16] S. Ahmed and R.B. Thompson, Propagation of elastic waves in equiaxed stainless-steel polycrystals with aligned [001] axes, J. Acoust. Soc. Am. 99, 1996, 2086-2096.

[17] G. Haïat, P. Calmon, A. Lhémery, F. Lasserre, A model-based inverse method for positioning scatterers in a cladded component inspected by ultrasonic waves, Ultrasonics, Vol. 43 (8), 2005, p.619-628.

[18] C. Gueudré, L. Le Marrec, J. Moysan, B. Chassignole, Ultrasonic data inversion for characterization of heterogeneous welds, Conf. COFREND 2008, Toulouse, 20-23 May, 2008

[19] B. Chassignole, O. Paris, E. Abittan, Ultrasonic examination of a CVCS weld, 6th ICNDE, Budapest, 8 – 10 October 2007

Imaging of defects within austenitic steel welds using an ultrasonic array

G. D. Connolly, M. J. S. Lowe, S. I. Rokhlin, and J. A. G. Temple

Abstract The use of ultrasonic arrays has increased dramatically within recent years due to their ability to perform multiple types of inspection and due to the fact that phased arrays allow the immediate production of images of the structure through post-processing of received signals. These arrays offer great potential to the inspection of austenitic steel welds in safety-critical applications, where it is important to be able to detect and size any crack-like defects that may occur during service or may have occurred during welding. This paper outlines the procedure behind the generation of images of simple planar defects within a previously developed weld model. Particular attention will be given to the principles of the modelling of elastic wave propagation through anisotropic and inhomogeneous media. Images of simulated defects within the structure produced from two inspection setups will be shown.

1 Introduction

Austenitic steels are favoured for use in engineering applications within the petro-chemical and nuclear industries, particularly for the fabrication of piping

G. Connolly
UK Research Centre in NDE, Imperial College, London SW7 2AZ, UK, e-mail: g.connolly@imperial.ac.uk

M. J. S. Lowe
UK Research Centre in NDE, Imperial College, London SW7 2AZ, UK, e-mail: m.lowe@imperial.ac.uk

S. I. Rokhlin
The Ohio State University, Edison Joining Technology Center, 1248 Arthur E Adams Drive, Columbus OH 43221, e-mail: rokhlin.2@osu.edu

J. A. G. Temple
UK Research Centre in NDE, Imperial College, London SW7 2AZ, UK, e-mail: a.temple@imperial.ac.uk

and pressure vessels. They have demonstrated high strength and toughness as compared to typical carbon steels and have the advantage that post-welding heat treatment need not be applied due to the high resistance to brittle fracture. These components will usually see cyclic and heavy loading, and as such, any crack-like defects that have been formed during the welding process may propagate during service. It is important to be able to monitor the location, shape and size of these defects to evaluate the condition of the weld, since failure would result in both physical damage of the plant with safety implications, and economic damage whilst repair or replacement is under way.

A reliable method of ultrasonic inspection is sought to remove the need for radiography and its high associated cost. In recent years, the use of ultrasonic arrays has increased due to their flexibility, rapidity and ease of inspection when compared to single element transducers. Some researchers have taken advantage of the superior imaging performance of the ultrasonic array to generate images of internal defects [1], including those within scattering and inhomogeneous materials [2]. However, since the 1970s [3], it has been known that there are limitations in the capabilities of inspection of austenitic steels due to scattering and beam-steering. Studies of micrographs of welds have revealed that the grains tend to develop curved shapes, elongated in the direction of maximum heat flow, thus resulting in the formation of an anisotropic inhomogeneous material. Fig. 1 shows a typical weld microstructure.

It is also difficult to generalise the microstructure of the weld, since it is a function of the metallurgical composition of the parent metal and the weld metal, the welding temperature and orientation of the weld during formation. Many researchers have proposed weld models to account for material inhomogeneity. These models open possibilities for the improved understanding of wave behaviour within, for instance, austenitic steel V-welds through propagation of simulated rays. A concise introduction to this problem is found in Halmshaw [4].

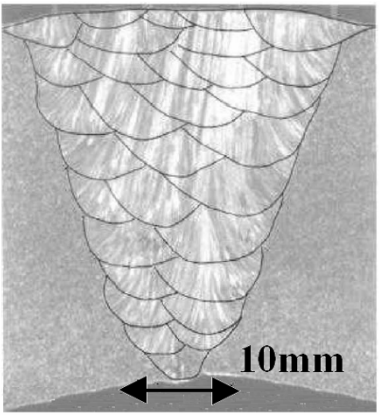

Fig. 1 Typical weld microstructure, showing both weld pass boundaries and grain boundaries. Image taken from [5].

This paper will take a similar approach based on a weld model proposed by Ogilvy [6]. Rays will be traced through the model, will interact with point or crack-like defects and simulated signals will be generated using common post-processing imaging techniques. The next section will present an introduction to the behaviour of bulk waves in both isotropic and anisotropic media, focusing on how fundamental wave properties would be determined from material data. The factors that would decide how waves interact with interfaces are then presented, followed by a brief treatment of the computation of delay laws and of several basic imaging algorithms. Finally, examples of typical simulated images will be shown using two different algorithms.

2 Theory of elastic wave propagation

In this section, a brief description of the nature of elastic waves is given. Excellent detailed treatments may be found in chapter 2 of Harker [7] or chapters 4-5 of Cheeke [8]. In an unbounded elastic solid, the propagation of waves causes particles of the medium to become displaced linearly from their resting positions in a periodic fashion. The phase of the wave is a property that describes where along the displacement cycle is a particular point of this medium. Lines that join points of constant phase describe wavefronts and the velocity at which these wavefronts propagate shall be called c, the magnitude of which shall be known as the phase velocity c_P.

The idea of a group velocity may have first been proposed by Russel [9], who spoke of the velocity of a group of waves (which will be called the group velocity c_G) as distinct from the velocity "of the individual waves of which it is composed". A relationship between the group velocity, the wavevector (the vector that points in the direction of wave propagation and whose magnitude is the wavenumber) k, and the angular frequency ω in elastic waves in terms of c was specified by Lord Rayleigh:

$$c_G = c + k\frac{dc}{dk} \tag{1}$$

Most widely known propagating elastic waves in elastic solids are classed as either longitudinal or transverse. In a plane longitudinal wave, the particles are given a displacement parallel to the direction of propagation of the phase velocity and in a transverse wave the particles are displaced perpendicularly. Surface waves are not considered in this paper. A third type of wave that is relevant to the calculations is the evanescent wave, which may be generated at interfaces. Where such a wave is present, the periodic motion of the particles of the medium will be elliptical rather than linear. The polarisation vector p then becomes complex, where the imaginary components represent the phase shift between the motions along the principal axes of the vector.

Here a method of determining wave properties given only the phase vector is summarised. Using the implied summation convention, we will begin with the Christoffel equation

$$\left(\rho c_P^2 \delta_{ik} - \Gamma_{ik}\right) p_k = 0 \tag{2}$$

where ρ is the density and $\Gamma = C_{ijkl} n_j n_k$, called the Green-Christoffel acoustic tensor, n being a vector describing the direction cosines of the wavevector. If we apply the eigensystem method to (2), we find that the eigenvalues λ and eigenvectors v are, for given direction cosines of the wavevector

$$\lambda_a = \rho c_{Pa}^2 \; ; \; v_a = p_a \tag{3}$$

where a represents the index of a particular wave. The group velocity c_G can be determined from:

$$c_G = \frac{1}{\rho} C_{ijkl} k_l p_j p_k \tag{4}$$

The prediction of properties of waves reflected and refracted from an interface is fundamental to this study. Only well-bonded solid-solid interfaces are dealt with in this paper. Further reading upon this approach may be found in, for instance, chapter 9 of Auld [10].

In a system of three spatial dimensions, three waves will be reflected and three will be transmitted. Here the approach used by Rokhlin et al. [11] is followed, where a sextic equation is constructed whose solutions yield the component of the phase vector normal to the interface. Since all phase velocity vectors lie in a single plane perpendicular to the interface, the other two components are already known. Complex conjugate pairs produced from this equation indicate the presence of evanescent waves. Once the unit phase vectors are found, the methods described earlier are used to compute the polarisation vector, the phase vector and the phase and group velocities.

At this point, the remaining unknown quantities are the amplitudes and phases relative to the incident wave. To find these, we consider six boundary conditions to enforce continuity of displacement and stress at the interface, which are rearranged to form a matrix. If we assume that there is only one incident wave striking the interface, we may write

$$A^i p_j^i + \sum_{a=1}^{6} A^a p_j^a = 0 \tag{5}$$

$$\frac{A^i C_{l3jk} p_j^i k_k^i}{c_P^i} + \sum_{a=1}^{6} \frac{A^a C_{l3jk} p_j^a k_k^a}{c_P^a} = 0 \tag{6}$$

where superscript a is the wave index and superscript i indicates a property of the incoming wave, the interface is the 12 plane and all waves lie in the 13 plane. The system of above equations can be represented in matrix form, where the unknown values A^a form a vector ξ, such that

$$f = F\xi \tag{7}$$

where f and F represent the terms in (5) and (6), respectively. The matrix is inverted to solve for ξ, and thus we obtain the reflection and transmission coefficients.

3 Modelling the weld

To represent the weld microstructure, we have used a simplified weld model, proposed by Ogilvy [12]. This model describes a region of continuously varying orientation of elastic constants. The orientation θ of the crystal z-axis relative to the global y-axis is given by the expression:

$$\tan\theta = \begin{cases} -\dfrac{T(D + y\tan\alpha)}{x^n}, & x \geq 0 \\ \dfrac{T(D + y\tan\alpha)}{(-x)^n}, & x < 0 \end{cases} \tag{8}$$

where x and y are coordinates in a system whose origin is at the bottom of the weld centreline (not necessarily a line of symmetry), T and n are parameters associated with the formation of the orientation structure, D is the distance from the weld centreline to the bottom corner, and α the angle that the boundary between the weld and the surrounding material makes with the centreline. These parameters are shown in fig. 2. The orientations produced from this formula will take the form illustrated in fig. 3. This paper uses a transversely isotropic weld material whose elastic constants are given by Roberts [13], such that all anisotropy is confined to the xy plane. Scattering effects are ignored by the model.

To propagate a ray, we define a starting position and a phase vector. The methods outlined in section 2 are used to find its group velocity that will determine its travel course and speed. The ray will continue along its path until it reaches a boundary or the edge of the model, whereupon it is arrested and treated as an incident ray to a single interface as described in section 2, and the appropriate choice of reflected or transmitted rays completes the ray evolution process. However, when the ray passes through an inhomogeneous material, a nonphysical boundary must be applied after each time step to account for the variation in local material properties. These boundaries are oriented such that they trace a line connecting points of constant orientation of elastic constants at the location of the arrested ray.

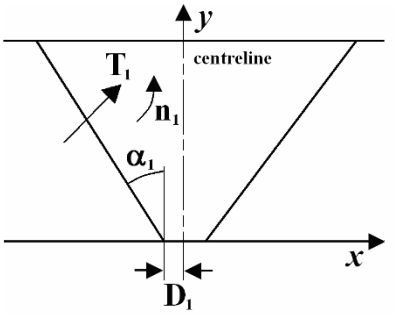

Fig. 2 Parameters associated with the grain structure in material l; T is a constant proportional to the grain tangent at the boundary and n is a constant proportional to the sharpness at which the orientations change with *x* position. The other side may take different parameters.

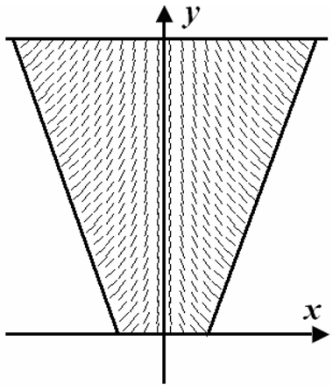

Fig. 3 Orientations of the elastic constants in the weld region as modelled by the ray tracing function.

Alternative simulations have been carried out using the finite element (FE) software package ABAQUS [14] to validate the predictions of ray interaction at a single boundary. The verification methods have been briefly described in [15]. Close agreement of ray properties with the theory has been observed across a variety of cases, including at a boundary between an isotropic material and an anisotropic material, and between two anisotropic materials of the same elastic constants but different orientation.

4 Computation of imaging delay laws

The imaging space is divided into a grid of horizontal and vertical lines. At each intersection is a node, and the following process is applied to each node in turn. According to conventional imaging procedure, delay laws are used to focus the received signals on each node and the image is constructed from the discrete intensities. Computation of these laws essentially requires the repeated solution of the path taking, in our case, a local minimum amount of time for a ray to travel from one point to another; this route is known as the Fermat path.

To select the ray that hits the target, a trial-and-error approach is used, similar to that proposed in section 3.11 of Červený [16], and is illustrated in fig. 4. A target line is constructed within the structure, perpendicularly to the vector joining the ray source to the ray target. Rays propagate from the source and will terminate somewhere along the target line. The distance along this target line between the ray intercept and the target is used to select the phase angle at which the next ray is launched. For example, in fig. 4, the first ray terminates above the ray target and the second ray terminates below. Linear interpolation will be used to select a phase angle in between the angles of a pair of the closest two attempts

that were either side of the target. This is repeated until the ray locates the target point within a particular margin of error.

When each required ray is found, we record four important properties:

1. The change in ray energy due to interaction with physical boundaries (H_B): the weld boundary and the backwall. These may be calculated from the theory in section 2.
2. The change in ray energy due to divergence (H_D). Two rays are propagated at a small angle (in the order of a few minutes of arc) to either side of the Fermat ray for a length of time given by H_T. The final positions of these two rays, along with the final position of the central Fermat ray, are used to define an arc; the length of which will be called l_D. The change in energy is then given by the following expression:

$$\frac{\theta d_0}{l_D} \tag{9}$$

where θ is the angular spread and d_0 is a short reference distance, usually in the order of a micrometre, from the starting position of the ray.

The product of H_B and H_D yields the total energy change, a value that we shall call H_E.

3. The time taken for the ray to reach the target; let us call this quantity H_T.
4. The change in phase (H_P) due to interaction with physical boundaries, given by theory in section 2.

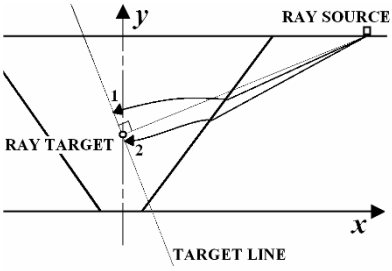

Fig. 4 Trial-and-error method applied to the problem of joining the ray source to the ray target via a Fermat path.

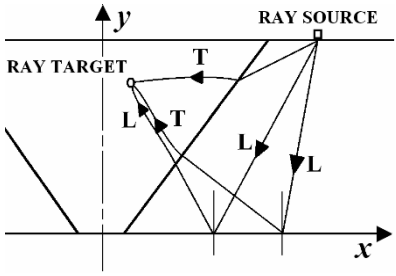

Fig. 5 Different ray paths to the target, phase angle anticlockwise: a transverse direct wave, reflection off the backwall with no mode conversion, reflection off the backwall with mode conversion. Half-skip inspection requires reflection of only the outgoing wave and full-skip inspection requires reflection of both the outgoing and the returning wave.

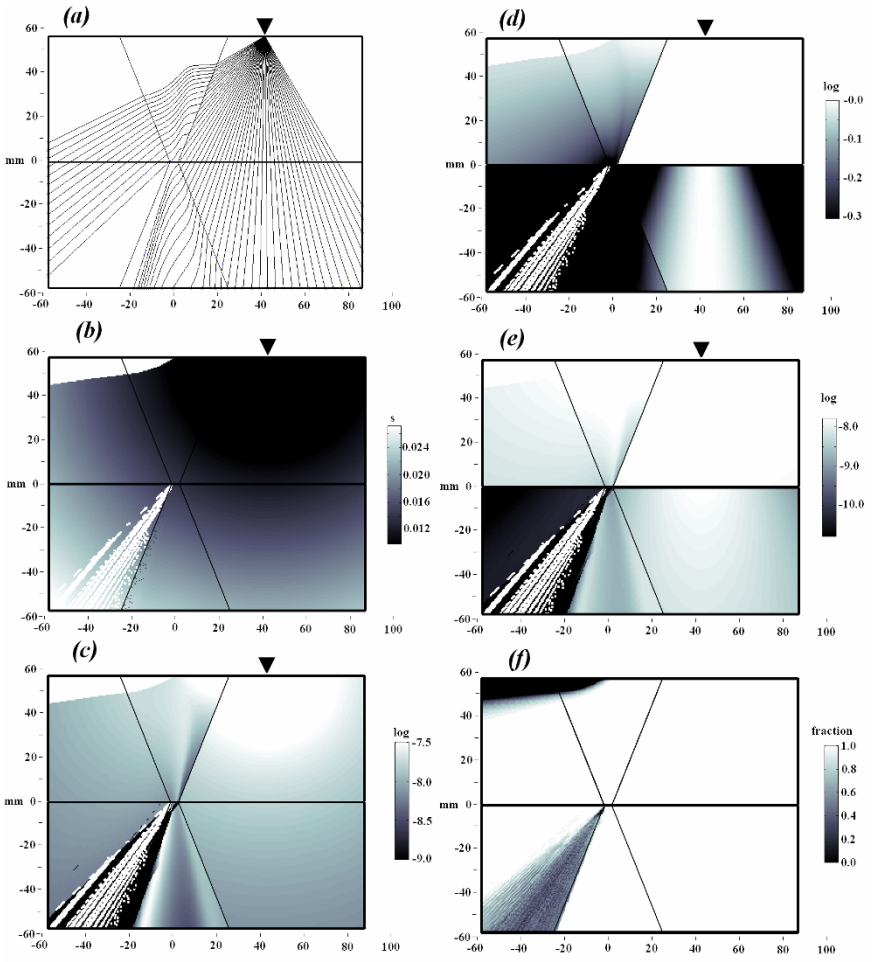

Fig. 6 Properties of a ray starting at the tip of the marker as a function of ray termination position, showing (a) original ray-tracing diagram from the transducer element at (x,y) = (42,58)mm, (b) time delay or time of flight in seconds, (c) logarithmic plot of the energy fraction due to ray divergence, (d) logarithmic plot of the energy fraction due to boundary interaction, (e) logarithmic plot of the total energy fraction and (f) overall coverage fraction for all the elements in the transducer array e.g. 0.5 means that half of the elements in the entire array can access that position. Quantities are given by the shade indicated in the scale to the right of the diagram; for (b) to (e), the white areas at the top left are entirely inaccessible to the relevant transducer element and for (c) to (e), the scale is logarithmic and relative to a reference value of 1.0 at the origin of the ray. All diagrams are for a longitudinal ray that does not convert mode upon reflection. The reflected area is shown in the negative y region for convenience.

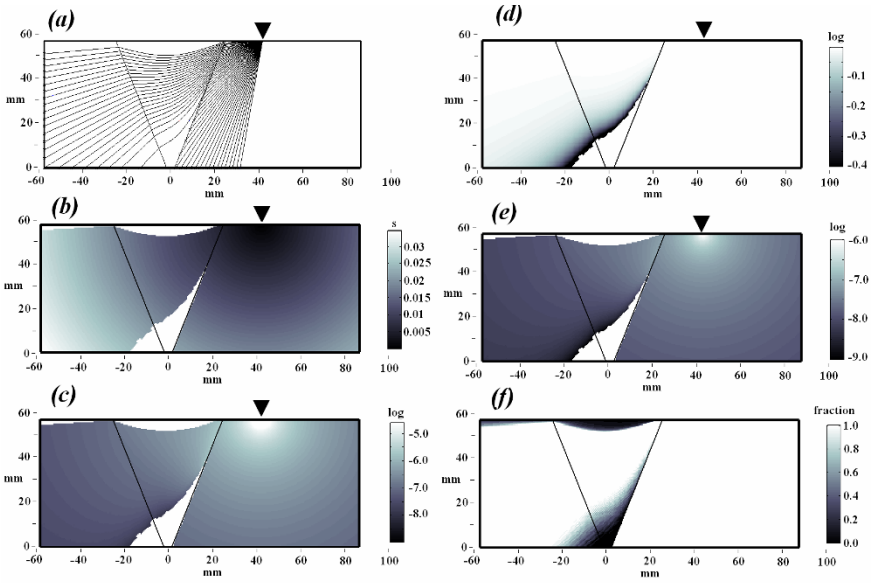

Fig. 7 Properties of a ray starting at the tip of the marker as a function of ray termination position. The significance of the letters within parentheses is as for fig. 6. All diagrams correspond to an SH ray without reflection.

The method that produces delay laws is also used to generate artificial signal data, and can also be applied with or without reflection from the backwall. If a reflection is required, then an option is given to change the wave mode upon reflection. It is in this manner that delay laws and signal data for half-skip and full-skip inspection types (see fig. 5) can be computed.

In figs 6 and 7, a 16-element simulated transducer array is situated such that its ends are at (x,y) = (28,58) and (58,58). Examples of the graphical representation of the variation of four of the properties listed above across the weld model are shown in figs 6 (P ray reflecting from backwall) and 7 (SH ray without reflection) as a function of ray target position. In (a) to (e) of both these figures, the ray has originated from the eighth transducer element from the left, at (x,y) = (42,58)mm.

In fig. 6, data points below the line at x = 0mm correspond to those rays that have been reflected at the backwall. The anomalies at the bottom-left are due to the temporal discretisation of the algorithm and the sparsity of rays (see particularly fig. 6(a)). In addition, fig. 6(f) shows that this region is difficult to access and fig. 6(e) indicates that the energy concentration is low in this area, thus any defect located here would be extremely difficult to detect.

5 Imaging algorithms

An active imaging system consists of an array of transducers, acting both as receivers and transmitters, to access an area of material. One or more of the transducers, acting as a transmitter, emits a pulse, whose reflections are received by various combinations of transducer elements acting as receivers. The Synthetic Aperture Focusing Technique (SAFT) processes a series of time traces that are sent and received by the same element in the array. Another method known as the Total Focusing Method (TFM) requires the recording of all possible transmitter and receiver combinations. The former method compromises completeness of data acquisition for a more rapid computation process; SAFT requires n summations where n is the number of elements in the array. In contrast, TFM requires $\frac{1}{2}n(n\text{-}1)$ summations.

All calculations here are performed in the frequency domain. A toneburst modified by a Hanning window is applied to simulate reflected signals, whose function $T(k)$, in its discrete form, is given by:

$$T(k) = \frac{1}{2}\left[1 - \cos\left(\frac{2\pi(k-1)}{n_k}\right)\right]\sin\left(\frac{2\pi(k-1)n_c}{n_k}\right) \tag{10}$$

for $1 \le k \le n_k$, where n_k is the number of time samples and n_c is the number of cycles. This toneburst is transformed to a function of frequency:

$$F(k) = \left(\frac{(n_f+1)(n_c-2)-4k}{(n_f+1)n_c}\right)f_c \tag{11}$$

for $1 \le k \le n_f$, where n_f is the number of frequency samples and f_c is the centre frequency. In practice, delay laws are computed in two stages: once for the journey towards the defect and once for the journey away from the defect. In this model, we assume perfect reflectivity at the defect, no change in phase for an SH wave and a change of π for SV and P waves.

From this point let us assign the superscripts + and - to denote rays travelling towards and away from a defect, and the superscripts s and d to denote signal data and delay law data, respectively. Signal data are shifted in time by a factor Φ_T, in phase by Φ_P and are modulated in energy by Φ_E. If these data were generated according to the methods of section 4, then the factors would be defined thus:

$$\begin{cases} \Phi_T = & \mathrm{H}_T^{s+} + \mathrm{H}_T^{s-} - \mathrm{H}_T^{d+} - \mathrm{H}_T^{d-} \\ \Phi_E = & \dfrac{\mathrm{H}_B^{s+}\mathrm{H}_B^{s-}}{\mathrm{H}_B^{d+}\mathrm{H}_B^{d-}} \sqrt{\dfrac{\dfrac{1}{(\mathrm{H}_D^{d+})^2} + \dfrac{1}{(\mathrm{H}_D^{d-})^2}}{\dfrac{1}{(\mathrm{H}_D^{s+})^2} + \dfrac{1}{(\mathrm{H}_D^{s-})^2}}} \\ \Phi_P = & \mathrm{H}_P^{s+} + \mathrm{H}_P^{s-} - \mathrm{H}_P^{d+} - \mathrm{H}_P^{d-} \end{cases} \tag{12}$$

The amplitude of the image intensity I at a particular point is a function of these factors, given by:

$$I(x,y) = \left\| \sum_{tx} \sum_{rx} \Phi_E \exp\left(i\omega_c \Phi_T + \Phi_P\right) \right\| \tag{13}$$

$$I(x,y) = \left\| \sum_{k=1}^{n_f} \sum_{tx} \sum_{rx} \Phi_E \exp\left(2\pi i F(k) \Phi_T + \Phi_P\right) \right\| \tag{14}$$

where *tx* indicates the transmitting element and *rx* the receiving element and (14) is the broadband variant of (13), operating over the full range of frequencies according to the function $F(k)$.

6 Simulated images

In this section, we will use materials defined in tables I and II for the weld and the parent sections respectively. The weld will also take the parameters defined in table III. A simulated array of 32 elements is positioned 27mm from the centerline of the symmetrical weld, where the elemental separation is 1.0mm. Directivity of individual elements is ignored by this model.

Figs 8 and 9 show imaging examples of a crack-like defect, modelled as a series of 24 point defects in accordance with the Huygens principle. In fig. 8, a simulated inspection is carried out using direct SH waves with both the SAFT and TFM imaging algorithms at a frequency of 1.5MHz. The crack is 8.6mm long and is located on the far weld boundary.

We see that the energy has localised on both ends of the crack, and that in cases (b) and (d), where the correct delay laws have been used, we are able to accurately locate and size the defect. Delay laws pertaining to a weld composed of the material described in table III were used to produce the images of cases (a) and (c). In these images, the peaks are not aligned with either end of the crack and so the defect will be mislocated and possibly missized, due to the erroneous assumption of weld isotropy. In all images, responses from the bottom end of the crack are rather weak since it falls within a partial blind area (also see fig. 7(f)).

In fig. 9, a full-skip inspection is employed on a crack 8.0mm in length situated along the centerline of the weld. The transverse waves are emitted by the array, mode convert to longitudinal upon reflection from the backwall. The return path is the reverse of the outgoing path. We see again that attempts to

apply homogeneous isotropic delay laws to the simulated signal data will result in mislocation of the defect within an inhomogeneous weld but use of the inhomogeneous delays show a substantial improvement in location. In both figs, it is also seen that SAFT images show tighter concentration of energy about the crack tips but TFM shows better rejection of unwanted image features.

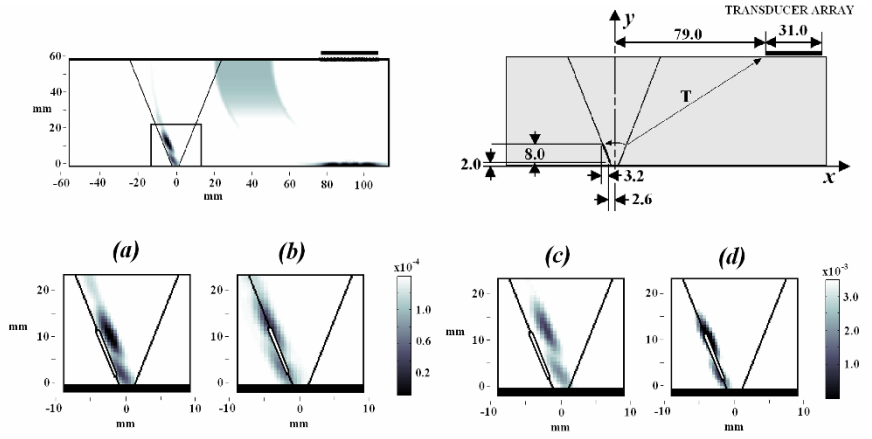

Fig. 8 Imaging of a crack using direct SH inspection. A typical simulated SAFT image and the weld geometry and the crack location are shown, along with: (a) SAFT image using incorrect delay laws (i.e. assuming weld isotropy), (b) SAFT image using correct delay laws, (c) TFM image using incorrect delay laws and (d) TFM image using correct delay laws.

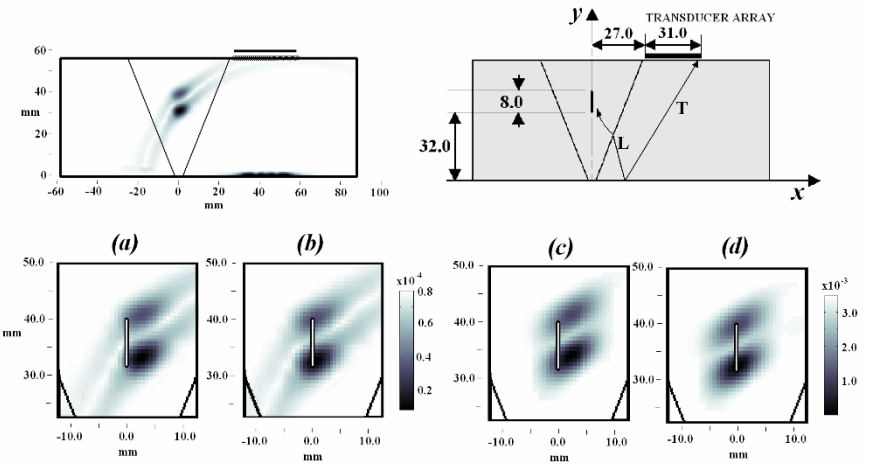

Fig. 9 Imaging of a crack using full-skip TLLT inspection. A typical simulated SAFT image and the weld geometry and the crack location are shown, along with: (a) SAFT image using incorrect delay laws, (b) SAFT image using correct delay laws, (c) TFM image using incorrect delay laws and (d) TFM image using correct delay laws.

Table I Elastic constants for the transversely isotropic stainless steel[a]. Voigt notation applies

$C_{11} = C_{22} = 249.0$
$C_{12} = C_{21} = 124.0$
$C_{13} = C_{31} = C_{23} = C_{32} = 133$
$C_{33} = 205$
$C_{44} = C_{55} = 125$
$C_{66} = 62.5$

[a]Units $\times 10^9 \mathrm{Nm}^{-2}$, with $\rho = 7.85 \times 10^3 \mathrm{kgm}^{-3}$

Table II Elastic constants for isotropic mild steel[b]. Voigt notation applies

$C_{11} = C_{22} = C_{33} = 282.7$
$C_{12} = C_{21} = C_{23} = C_{32} = 122.2$
$C_{44} = C_{55} = C_{66} = 80.7$

[b]Units $\times 10^9 \mathrm{Nm}^{-2}$, constants computed using $E = 2.10 \times 10^{11} \mathrm{Nm}^{-2}$, $\nu = 0.30$, with $\rho = 7.90 \times 10^3 \mathrm{kgm}^{-3}$

Table III Parameters for the weld material

$\alpha = \arctan(0.4)$
D = 1.8mm
n = 1.0
T = 1.0

7 Conclusion and discussion

This paper has presented an overview of ray-tracing principles through strongly inhomogeneous and complex anisotropic materials. A technique to compute delay laws applicable to a simulated transducer array has been proposed and implemented. This software tool is able to predict the Fermat path to reach a particular point, the energy carried by the ray, and the coverage of a weld region for a given array location. Examples of such plots have been shown, to include ray reflection from the backwall. Images using the SAFT and the TFM techniques have been produced by focusing simulated broadband signals to locate simple crack-like defects, where responses have been detected from both ends of the crack.

The importance of using delay laws corresponding to the correct material and using laws that represent the inhomogeneous properties of the weld has been underlined. It has been demonstrated that mislocation may occur if the inhomogeneity and the anisotropy are ignored.

There is much scope for extension of this model. It is possible to include directivity of array elements, such that sent and received signals are given a particular weighting as a function of the wavevector. The potential to make fuller use of the information listed in section 4 should be explored. The results shown here have paved the way for the possible application of another weighting of received signals to compensate for poor transducer coverage in certain areas.

8 Acknowledgements

This research was undertaken as part of the core research program of the UK Research Centre in NDE (RCNDE) with support from Rolls Royce Plc and EPSRC. Please refer to www.rcnde.ac.uk.

References

1. P. Bovik and A. Bostrom *Model of ultrasonic nondestructive testing for internal and sub-surface cracks* J. Acoust. Soc. Am. **102** 2723-2733 (1997)
2. C. Prada, E. Kerbrat, D. Cassereau and M. Fink *Time reversal techniques in ultrasonic testing of scattering media* Inverse Problems **18** 1761-1773 (2002)
3. M.G. Silk *Ultrasonic techniques for inspecting austenitic welds* Research Techniques in NDT **4** 393-449 (1980)
4. R. Halmshaw *Non-destructive Testing* Arnold, London UK (1991)
5. J. Moysan, A. Apfel, G. Corneloup and B. Chassignole *Modelling the grain orientation of austenitic stainless steel multipass welds to improve ultrasonic assessment of structural integrity* Int. J. Press. Ves. Pip. **$*** 77-85 (2003)
6. J.A. Ogilvy *An iterative ray tracing model for ultrasonic nondestructive testing* NDT&E Int. **25** 3-10 (1992)
7. A.H. Harker *Elastic waves in solids with applications to nondestructive testing of pipelines* Grosvenor Press, Portsmouth UK (1988)
8. D.N. Cheeke *Fundamentals and applications of ultrasonic waves* CRC Press, Boca Raton FL (2002)
9. S. Russel *Report on waves* Br. Assoc. Rep. 369 (1844)
10. B.A. Auld *Acoustic Fields and Waves in Solids, Volume II* Robert Krieger Publishing Company, Malabar FL (1973)
11. S.I. Rokhlin, T.K. Bolland and L. Adler *Reflection and refraction of elastic waves on a plane interface between two generally anisotropic media* J. Accoust. Soc. Am. **79** 906-918 (1996)
12. J.A. Ogilvy *Ultrasonic beam profiles and beam propagation in an austenitic weld using a theoretical ray tracing model* Ultrasonics **24** 337-347 (1986)
13. R.A. Roberts *Ultrasonic beam transmission at the interface between an isotropic and a transversely isotropic solid half-space* Ultrasonics **26** 139-147 (1988)
14. Anon *ABAQUS version 6.7 user manual* www.simulia.com Providence RI (2008)
15. G.D. Connolly, M.J.S. Lowe, S.I. Rokhlin, J.A.G. Temple *Modelling the propagation of elastic waves in generally anisotropic media and austenitic steel welds* Rev. Qnt. NDE **27** 1026-1033 (2007)
16. V. Červený *Seismic ray theory* Cambridge University Press, Cambridge UK (2001)

Materials and mechanical aspects of bonded joints

M.E.R. Shanahan

Abstract The use of adhesive bonding in transport is, to some extent, limited due to insufficiently reliable NDT techniques. We discuss various advantages and disadvantages of adhesive structures and highlight where NDT, and particularly acoustics, could alleviate the present, common, suspicion of glued structures.

1 Introduction

Bonded joints are becoming widespread in industrial applications, particularly in transport, for a variety of reasons. In general, bonded overlap joints present reduced stress concentrations when compared with their bolted, riveted, or otherwise mechanically assembled counterparts. In addition, adhesive structures are lighter, and in particular, *specific* mechanical properties are increased (e.g. E/ρ, or σ_r/ρ, where E, σ_r, and ρ are respectively Young's modulus, failure stress and density). Bonded joints are generally intrinsically fluid-tight, at least on a short time scale (over a longer time scale, diffusion of the surrounding medium may occur: see below), and adhesives may be used to bond different and/or thin materials. A schematic example of the reduced stress concentration behaviour is given in Figure 1, in which a bolted joint is compared to an adhesive joint.

Composite materials combine advantages of relative lightness, high strength and rigidity, and may be rendered anisotropic, when required, with different rigidities in different directions. As a result, there is a significant increase in quantities of composites used in aircraft structures (e.g. the Airbus A380 is purported to contain *ca.* 25% composites by weight, and therefore considerably more by volume!).

Martin E.R. Shanahan
Université Bordeaux 1, Laboratoire de Mécanique Physique -UMR CNRS 5469,
351 Cours de la Libération, 33405 Talence Cedex, France,
e-mail : m.shanahan@lmp.u-bordeaux1.fr

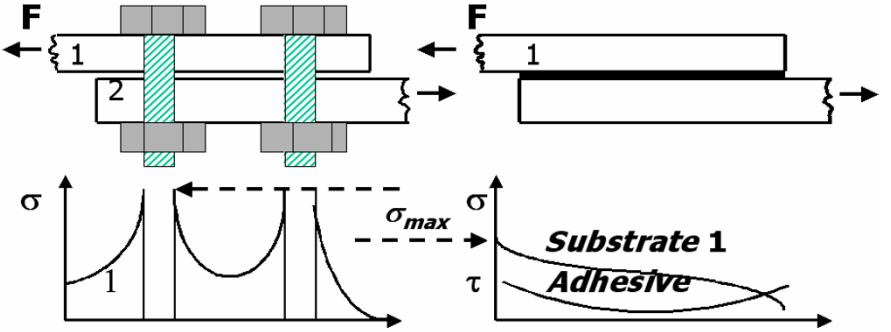

Figure 1: Schematic comparison of stress concentrations in bolted (on left) and bonded joints. σ represents tensile stress in substrate 1, and τ, shear stress in the adhesive layer.

However, it is very difficult to use classical assembly techniques when using composites materials, especially those employing an organic matrix, since the materials to be joined must be drilled. This is often not easy to do, and in addition, drilling disrupts the continuity of long fibre composites, which in turn adversely affects the performance of the material. Thus, in addition to the advantages of adhesive bonding already enumerated, its use is virtually essential in the construction of composite assemblies.

2 NDT and Adhesive Bonds

2.1 Strength versus Contact

Despite several advantages manifest with bonded joints, certain problems remain. Since adhesives are generally polymeric materials, typically with a glass transition temperature, T_g, in the range of 120 to 180°C, high temperature service conditions are precluded. Modern structural adhesives (e.g. polyimides) may have a T_g of *ca.* 300°C and withstand short periods at 600°C, but this is still not "hot", compared to the temperatures that metals and ceramics can take. Ageing in deleterious fluids, particularly water and aviation fuel, can lead to medium or long-term degradation. Bonding is generally an irreversible process, which may hinder repair work. However, perhaps the most important problem is the poor coherence between the physically observed strength of bonded joints and non-destructive testing (NDT) predictions.

In fact, NDT was probably first used to probe the reliability of adhesive assemblies during the 1st World War, when aircraft were often string and cloth attached to a wooden frame, which was glued by an organic adhesive made of casein, or milk protein. If an aeronautical engineer did the rounds in a hangar only to detect a strong whiff of camembert cheese, he would have a good idea that some of his adhesive bonding was losing its strength due to humidity! (an early form of "glue-sniffing"?) This was, of course, also a technique requiring no direct contact! However, many more modern, advanced techniques are now being developed including ultrasonics, acoustic emission, radiography, thermography, NMR spectroscopy, eddy-current testing, holography, electronic speckle pattern interferometry (ESPI).

One aim of research in our laboratory is to improve the coherence between measured, mechanical performance and NDT observations, thus developing acoustic techniques to be a reliable test of *physical strength* of a bonded joint, and not just a check on *good contact* between adhesive and adherend. Contiguity of substrate and adhesive phases is a necessary but insufficient condition for good adhesion, and assuring contact alone is not always a good gauge of potential bond strength. A typical example of such a situation is shown schematically in Figure 2.

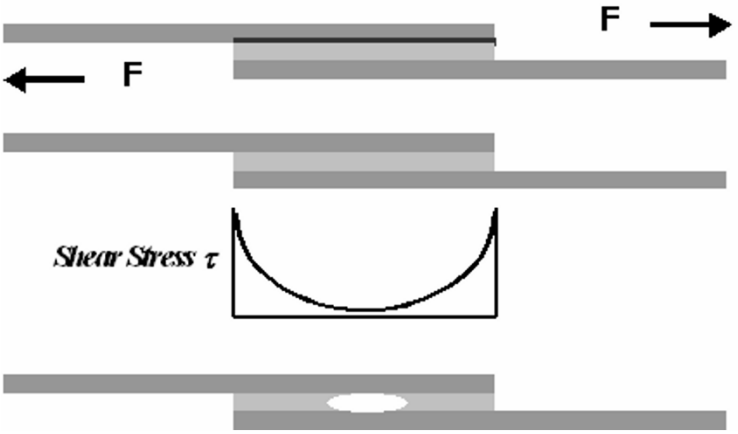

Figure 2: Sketch of (above) lap-joint with good contact, but which is weak due to oil film between adhesive and upper substrate (black line). Below are two lap-joints of similar strength because, although the lower one contains a hole, this is in a zone of low stress, τ.

Figure 2 represents three lap-joints of substrates (darker shading) bonded with an adhesive (lighter). However, in the top lap-joint, a thin layer of oil (black line) is present between the adhesive and the substrate. As a result, contact is good (even if not strictly between adhesive and substrate), especially given the high propensity of oils to spread on high energy solids [1], but clearly strength is

considerably reduced by the presence of a contaminant. Many classic forms of NDT will detect such good contact, but not the poor strength.
The central joint in Figure 2 should have a shear stress, τ, distribution within the adhesive layer something like that shown. Many analyses have been made (dating back to 1938!), e.g. [2-6], but all show the same essential features demonstrated here, *viz.* high shear stresses at (actually, *near*) the ends of the overlap, but lower loading near the joint centre. (In fact, despite its experimental facility and ubiquity in industrial uses, the lap-joint is complex from the point of view of stress analysis; see e.g. [7]) As a consequence, the central part is lightly stressed. The joint at the bottom of Figure 2, which contains a void due to, say, the inclusion of an air bubble during manufacture, will have a similar strength to the intact joint! The presence of a hole has little effect on overall strength. Thus, contact and strength must not be confused.

2.2 Diffusion, Effects on Strength and Detection

Whilst discussing lap-joints, NDT should prove useful for providing information about water ingress into a structure ageing in a humid environment. Figure 3 is a sketch of a lap-joint and of modifications to stress distribution subsequent to water diffusion and resulting plasticisation of the adhesive near the joint ends. As pointed out above, although adhesive joints are fluid-tight initially, polymeric materials are prone to liquid diffusion and absorption, e.g. [8-10]. Consider the (2D) lap-joint in Figure 3 which has been exposed to a liquid environment. Assuming the substrates to be impermeable, liquid will seep into the joint from both exposed adhesive ends, generally following kinetics governed by Fickian, e.g. [11-13] or Langmuirian, e.g. [14-16] diffusion. As may be expected with this geometry, there will be a gradient of water content, decreasing from saturation at the exposed joint ends towards a minimum in the middle where the transit time is maximal. Of course, if exposure time is sufficient, then a homogeneous saturation is obtained. However, it is the kinetics that is of most interest in bond ageing. Despite a gradual decrease in liquid concentration towards the centre, schematically, we represent the joint as consisting of a “dry” section towards the centre and “wet” sections at the two extremities, as shown. As indicated in Figure 2, a homogeneous adhesive layer will have peak shear stresses near the ends, when under load. This is related to the elastic shear modulus of the adhesive. After the absorption of liquid, the modulus greatly decreases due to plasticisation, leading to lower load-bearing capacity. A significant result of this is that the *effective* overlap of the joint, corresponding to the “dry” part, is reduced. The extremities bear little load and so the new, shorter, “dry” adhesive joint takes the essential of the load and thus the new peak shear stresses migrate towards the joint centre and, more importantly, *increase* in magnitude. This is thus an unusual case in which (partial) plasticisation can actually lead to *higher*, rather than lower, stress concentrations! This is a domain in which acoustic techniques of NDT could be of great utility. Since the diffusion of water (or other liquids) leads to variations

in adhesive modulus, presumably ultrasonics techniques could be readily developed to follow absorption and therefore joint associated degradation.

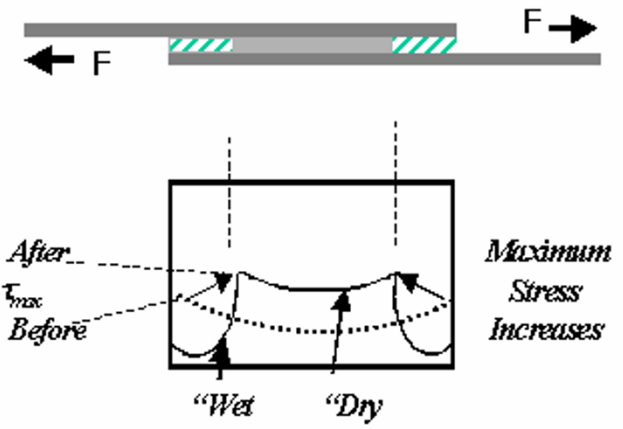

Figure 3: Liquid ingress into a lap-joint and consequent modification of stress distribution.

3. ESPI in Adhesion Research

3.1 The "Wedge" Adhesion Test

A good method for evaluating the fracture strength of structural bonding applications is the so-called "wedge-test", sometimes known as the "Boeing wedge test", due to early use of a form of the technique by the aircraft company. The principle is to bond two rectangular plates (sheets), or adherends, along their length and width, b, leaving however one extremity free of adhesive (by a separator or anti-stick coating) in order to be able to insert a wedge of thickness Δ between them, over a short length of their overlap.

This is shown in Figure 4, for the asymmetrical case where the lower solid is much more rigid than the upper. The distance between the wedge and the separation, or crack front, is denoted a. Wedge insertion leads to bending of one (in the case shown) or both adherends down stream of the separation front. We consider the case of *one* bent adherend below.

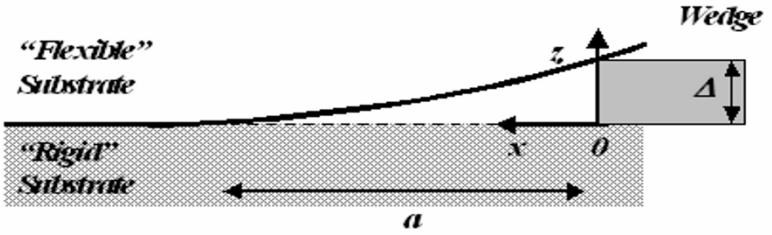

Figure 4: Schematic representation of asymmetric wedge test. Lower adherend is considered rigid, whilst bent upper adherend supplies strain energy for crack propagation.

Associated with the bending is strain energy, U:

$$U = \int_0^a \frac{M}{2R} dr = \frac{EI}{2} \int_0^a \left(z_{xx}\right)^2 dx = \frac{3EI\Delta^2}{2a^3} \quad (1),$$

where M and R are local bending moment and radius of curvature, and E and I are Young's modulus and moment of inertia of the beam section. The latter is given by $bh^3/12$, where h is beam thickness. The expression for U is obtained from simple beam theory. The strain energy release rate, G (Jm^{-2}), is simply given by:

$$G + \frac{1}{b}\frac{\partial U}{\partial a} = 0 \quad (2),$$

and at bond failure, G equals the fracture, or adhesion energy, G_c, leading to:

$$G_c = \frac{3E\Delta^2 h^3}{8a^4} \quad (3),$$

where in this elementary treatment no attention is paid to failure mode (essentially mode I). Crack length a, is a function of time, t, and G_c is a function of crack growth rate.

Note that G_c is independent of b! However, examination of fractured joints show a curved crack front [17, 18], concave towards the intact joint, and so the effect cannot be attributed to effects of diffusion!

3.2 Application of ESPI

The solution: this simple analysis neglects anticlastic curvature. This was observed by (amongst other techniques) Electronic Speckle Pattern Interferometry (ESPI). This technique is related to holography [19] and is particularly sensitive to small displacements. In *subjective speckle*, a coherent light beam is shone onto an optically rough surface and the impinging light is diffracted to give a *speckle*

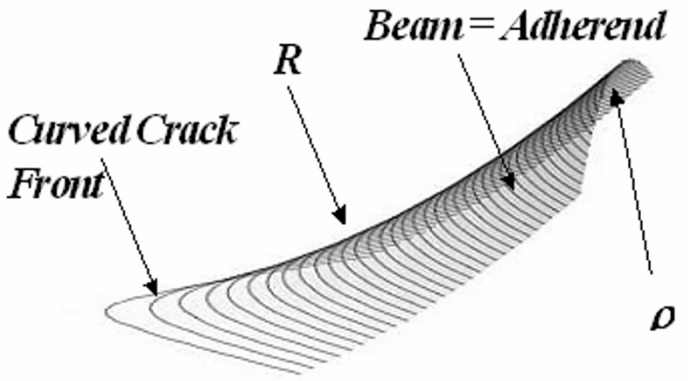

Figure 5: Sketch of anticlastic effect. R is principal radius of curvature produced by beam bending. ρ is the associated anticlastic bending, and the combination leads to a curved crack front.

distribution. After very slight movement of the rough solid, a second speckle image rough solid, a second speckle image is obtained, and it is the interference of the two diffraction patterns that is processed to give a speckle picture of the relative displacements in the optical field.

The technique was applied to asymmetric wedge tests, the more flexible adherend corresponding to the rough optical surface [17]. Indeed, it was observed that the principal curvature of the flexed beam was associated with an orthogonal reverse curvature due to anticlastic bending. This, in turn, led to a curved crack front. Figure 5 [20] demonstrates the basic mechanics, assuming no adhesion strength. In fact, effects of adhesion strength moderate crack front curvature.

The interest of this anticlastic bending effect is not purely academic. As shown in Equation (3) above, the fracture energy depends on a^{-4}. As such, any error on a is magnified fourfold in G_c. Since, in general, crack lengths tend to be measured on the sides of a wedge test, and crack fronts are concave, values of fracture energy can be easily overestimated.
The above is an application of ESPI as non-destructive testing, but it is clear that other techniques of NDT, such as ultrasonics could equally well be developed for this type of application.

4. Conclusion

In this short review, we have considered a few problems in adhesive bonding that have so far proved difficult to resolve, basically because the process is largely irreversible. However, progress is being made towards "de-bondable adhesives". The combination of irreversibility and the difficulty to find out what is occurring at the interface/interphase hinders the use of structural adhesives in several industrial fields, up to present. Despite the manifest advantages of bonding, particularly in the aerospace industry (joining different materials, stress concentration reduction, weight loss, etc.), the difficulty to predict strength without actually breaking the joint is a considerable drawback. The same is true of welding, but this process seems to be more widely accepted industrially, at present. This problem exists for freshly made structures, but is exacerbated by ageing. Ingress of water or other liquids, such as aviation fuels and solvents, generally leads to reduced strength but, again, it is difficult to monitor this reduction and whether or not it is acceptable, by present methods, without actually breaking the assembly. Contact between adhesive and substrate is readily verified, but actual mechanical strength is another story. We "adhesionists" hope that useful collaboration with "acousticians" will develop, both to improve the reliability of NDT in bonded systems, but also because there is some very interesting science in adhesive joints, and acoustics techniques should prove very powerful for a better understanding of this aspect.

References

1. Starov, V.M., Zhdanov, S.A., Kosvintsev, S.R., Sobolev, V.D., Velarde, M.G.: Adv. Coll. Interf. Sci. 104, 123 (2003)
2. Volkersen, O.: Fuftfahrtforsch. 15, 41 (1938)
3. Goland, M., Reissner, E.: J.Appl.Mech.,Trans.ASME 66, A17 (1944)
4. Adams, R.D. , Peppiatt, N.A.: J.Strain Anal. 8, 134 (1973)
5. Renton, W.J., Vinson, J.R. : J. Adhesion 7, 175 (1975)
6. Adams, R.D. , Mallick, V.: J.Adhesion 38,199 (1992)

7. Adams, R.D., Comyn, J., Wake, W.C.: Structural Adhesive Joints in Engineering, 2nd Ed., ch.2. Chapman & Hall, London (1997)
8. Gledhill, R.A., Kinloch, A.J.: J.Adhesion 6, 315 (1974)
9. Carfagna, C., Apicella, A., Nicolais, L. : J.Appl. Polym. Sci. 27, 105 (1982)
10. De Nève, B., Shanahan, M.E.R. : Polymer 34, 5099 (1993)
11. Crank, J: Mathematics of Diffusion, 1st Ed., Oxford University Press (1956)
12. Brewis, D.M., Comyn, J., Tegg J.L.: Polymer 21, 134 (1980)
13 Peyser, P., Bascom, W.D.: J. Mater. Sci. 16, 75 (1981)
14 Carter, H.G., Kibler, K.G. : J. Compos. Mat. 12, 118 (1978)
15 Bonniau, P., Bunsell, A.R.: J. Compos. Mat. 15, 272 (1981)
16 Popineau, S., Rondeau-Mouro, C., Sulpice-Gaillet, C., Shanahan, M.E.R. : Polymer 46,10733 (2005)
17. Popineau, S., Gautier, B., Slangen, P., Shanahan, M.E.R. : J. Adhesion 80 (12), 1173 (2004)
18. Qi J., Dillard D.A.: J. Adhesion 79, 559 (2003)
19. Goodman, J.W. In : Dainty, J.C. (ed.) Laser Speckle and Related Phenomena, p.9. Springer-Verlag, Berlin (1984)
20. Popineau, S : PhD Thesis, Ecole des Mines de Paris (2005)

The causal differential scattering approach to calculating the effective properties of random composite materials with a particle size distribution

A. Young and A. J. Mulholland and R.L. O'Leary

Abstract An implementation of the Causal Differential Method (CDM) for modelling the effective properties of a random two-phase composite material is presented. Such materials are commonly used as ultrasonic transducer matching layers or backing layers. The method is extended to incorporate a particle size distribution in the inclusion phase. Numerical issues regarding the implementation and convergence of the method are discussed. It is found that, for a given frequency of excitation, the calculated velocity for the composite has a distribution whose variance increases as the volume fraction of inclusions increases. The model predictions would suggest that to reliably and repeatedly manufacture these composites, with a desired mechanical impedance, a low volume fraction of inclusions should be used.

1 Introduction

The transmission and detection of ultrasonic energy forms the basis for imaging and non-destructive testing systems in a broad range of applications such as biomedical therapy and diagnosis, underwater sonar, non-destructive testing, structural condition monitoring, industrial processing and control, and materials characterisation [4]. The requirement for efficient generation and detection over a desired frequency band is paramount and very often the limiting component of the entire system relates to the front end transducer design [7]. These devices normally consist of an active piezoelectric layer sandwiched between a backing material for damping

A. Young
University of Strathclyde, Department of Mathematics, Glasgow, UK

A. J. Mulholland
University of Strathclyde, Department of Mathematics, Glasgow, UK, e-mail: ajm@maths.strath.ac.uk

R.L. O'Leary
University of Strathclyde, Department of Electrical and Electronic Engineering, Glasgow

and bandwidth control and some form of matching layer for interfacing to the mechanical load medium. Piezoelectric ceramics are mechanically stiff and do not interface well to media with low mechanical impedance such as water and air. Matching layers are therefore used to bridge this large impedance mismatch [5]. In many cases however these matching layers have to be manufactured by mixing two different materials in order to achieve the desired effective mechanical impedance [8]. A large variability in these effective properties can often be found for a given base and inclusion material, and volume fraction of inclusions. This is thought to be due to the random agglomeration of the inclusion particles to form percolation paths in the base material. This paper investigates this experimentally observed phenomenon by using the Causal Differential Method [3] with the addition of a particle size distribution to mimic the particle aggregation process. The model can be configured to assess the longitudinal and shear wave properties of the composite. This will allow for full characterisation of the material's elastic character. Such data is routinely employed in advanced two and three dimensional finite element analysis of these types of composite materials within transducer structures and as such a complete description of the elastic character is required. For example, matching layers are typically designed to a specific acoustic impedance in order to match the transducer to some load. However, in a transducer array configuration the matching layer is capable of supporting guided waves which will compromise the beam directivity and degrade imaging performance. Hence it is desirable to implement a methodology that will facilitate a more complete characterisation of these materials.

In the next section therefore, the model equations for a shear wave travelling in a two-dimensional plane containing randomly dispersed disc-like inclusions are presented. A dimensional rescaling is introduced to alleviate the numerical instabilities inherent to the model. A discussion on the convergence of the method and the effect that the properties of the two constituent materials have on the model's output is then given. Finally, the effect that the particle size distribution has on the variance of the model's output is presented.

2 The Causal Differential Method

By adding inclusions into a homogeneous material, the acoustic properties of the original material are modified by those of the inclusions [6]. In the regime where the particle size is commensurate with the wavelength of the insonifying wave there are a range of scattering theory methods for calculating the speed of propagation of the ultrasound wave [1]. The differential (or incremental) methods start by calculating the effective properties of a composite material containing a very small volume fraction of isolated particles (single particle scattering). The effective properties of this material are then used as the base material when adding another small volume fraction of inclusions. In this way the desired volume fraction of inclusions is obtained in a step by step manner and the final effective material properties are given by the final iteration. One such approach is the Causal Differential Method (CDM) [3].

The method considers the single scattering effect of adding small amounts of the inclusion, $\Delta\phi$, into a homogeneous matrix. By homogenising this new matrix, and repeating the process, the prescribed volume fraction of the inclusion, ϕ, can be met. The predictions therefore lie between those given by a single-scattering approach and those given by a multiple-scattering method. The initial inclusion volume fraction is set at $\phi_0 = \Delta\phi$ with ρ_0 (and μ_0) set at the density (and shear modulus) of the pure base material. A subscript I will be used to denote the corresponding properties of the inclusion material. The volume fraction is updated using

$$\phi_{n+1} = \phi_n + \Delta\phi \qquad n = 0, 1, 2, \ldots, N-1, \tag{1}$$

where N is the number of steps in the iteration given by

$$N = \frac{\phi}{\Delta\phi}. \tag{2}$$

The homogenised properties are then given by [2]

$$\rho_{n+1} = \rho_n(1-\phi_n) + \rho_I\,\phi_n, \tag{3}$$

and

$$\mu_{n+1} = \frac{\mu_I(1+\phi_n) + \mu_n(1-\phi_n)}{\mu_I(1-\phi_n) + \mu_n(1+\phi_n)}\,\mu_n. \tag{4}$$

The attenuation is calculated at each step using the additive law associated with acoustic attenuation given below by

$$\alpha_{n+1}(\omega) = \alpha_n(\omega) + \Delta\phi\ \frac{\gamma_n^{ex}(\omega)}{2\pi a^2}, \tag{5}$$

where πa^2 is the area of the inclusion. The extinction cross-section γ_n^{ex} can be shown to simplify to the scattering cross-section of a single disc. This is given by the solution to the diffraction of elastic simple harmonic waves by an elastic embedded cylinder [3]. The incident wave is given by

$$u_z^{in} = e^{i(k_n x - \omega t)}, \tag{6}$$

and the scattered wave by

$$u_z^{sc} = \sum_{m=0}^{\infty} A_m H_m^{(1)}(k_n r)\cos(m\theta)e^{-i\omega t}, \tag{7}$$

where $H_m^{(1)}$ is a Hankel function of the first kind of the m^{th} order and the wave number k_n of the current homogenised 'base' material is given by

$$k_n = \frac{\omega}{c_n(\omega)} + i\alpha_n(\omega). \tag{8}$$

The extinction cross-section γ_n^{ex} is a function of $\omega, \rho_n, \rho_I, \mu_n, \mu_I$ and a and is given by

$$\gamma_n^{ex} = 2\left(2|A_0|^2 + \sum_{m=1}^{\infty} |A_m|^2\right)(k_n)^{-1}, \tag{9}$$

with

$$A_m = -i^m \varepsilon_m \begin{pmatrix} \mu_I k_I J_m(ak_n) J_m'(ak_I) \\ -\mu_n k_n J_m'(ak_n) J_m(ak_I) \end{pmatrix} \Big/ \begin{pmatrix} \mu_I k_I H_m^{(1)}(ak_n) J_m'(ak_I) \\ -\mu_n k_n H_m^{(1)'}(ak_n) J_m(ak_I) \end{pmatrix} \tag{10}$$

where

$$\varepsilon_m = \begin{cases} 1 & m = 0 \\ 2 & m \geq 1 \end{cases}, \tag{11}$$

and $J_m(z), J_m'(z), H_m^{(1)}(z)$ and $H_m^{(1)'}(z)$ denote the the m^{th} order Bessel and Hankel functions of the first kind and their derivatives with respect to z, respectively, and the wave number in the inclusion material k_I is given by

$$k_I = \omega\sqrt{\frac{\rho_I}{\mu_I}}. \tag{12}$$

The phase velocity ignoring attenuation is given by

$$v_n = \sqrt{\frac{\mu_n}{\rho_n}}. \tag{13}$$

This value is then used to calculate the model's phase velocity adjusted for attenuation given by the Kramers-Kronig relationship

$$c_{n+1}(\omega) = v_{n+1}\left(1 + \frac{2\omega^2}{\pi} v_{n+1} \not\int_0^{\infty} \frac{\alpha_{n+1}(\Omega)}{\Omega^2(\Omega^2 - \omega^2)} d\Omega\right)^{-1}. \tag{14}$$

where the slash in the integral sign denotes Cauchy's principal value.

The algorithm is initialised by setting values for $\mu_I, \rho_I, \mu_0, \rho_0, a, \Delta\phi, \phi$, setting $\alpha_0 = 0$, setting $c_0 = v_0$ using equation (13), and by setting k_I using equation (12). The algorithm steadily updates the volume fraction using equation (1) until the desired volume fraction is achieved. At each step k_n is calculated using equation (8), A_m from equation (10), γ_n^{ex} from equation (9), α_{n+1} from equation (5), v_{n+1} from equations (4), (3) and (13), and finally c_{n+1} from equation (14). The number of steps N is given by equation (2) and so the phase velocity is given by

$$c(\omega) = v_N\left(1 + \frac{2\omega^2}{\pi} v_N \not\int_0^{\infty} \frac{\alpha_N(\Omega)}{\Omega^2(\Omega^2 - \omega^2)} d\Omega\right)^{-1}. \tag{15}$$

3 Numerical Implementation

Four implementation issues present themselves:

- the inaccuracies and numerical instabilities associated with the very large and very small parameter values
- the singularity in the integrand of equation (14) and the associated Cauchy principal value
- the infinite integral in equation (14)
- the infinite summation in equation (9)

To improve the accuracy and efficiency of the computations a re-scaling of the dimensions was implemented. This allowed the program to compute with numbers of $O(1)$ instead of the extremely large and small values that exist. The fundamental units of mass (M), length (L) and time (T) were scaled by $\widehat{M} = \gamma M$, $\widehat{L} = \beta L$ and $\widehat{T} = \delta T$ with the scaling factors chosen to make each of the parameters as close as possible to $O(1)$. For the particular example considered here this was achieved by setting $\gamma = 10^6$, $\beta = 10^3$ and $\delta = 10^6$ (see Table 1).

Parameter	Dimensions	Scaling
μ	$ML^{-1}T^{-2}$	$\gamma\beta^{-1}\delta^{-2}$
ρ	ML^{-3}	$\gamma\beta^{-3}$
a	L	β
ω	T^{-1}	δ^{-1}
c, v	LT^{-1}	$\beta\delta^{-1}$
k	L^{-1}	β^{-1}
γ	L	β
α	L^{-1}	β^{-1}

Table 1 Dimensional Analysis of the Model Parameters

In equation (15) the integrand has a singularity at $\Omega = \omega$ and Cauchy's principal value takes the finite limit of the integral as Ω tends towards this singular point. This was numerically implemented by introducing a neighbourhood $\Delta\omega$ around this singularity. Additionally, a finite (but large) parameter ω^u was introduced to replace the infinite upper limit in this integral. A series of numerical experiments were then conducted to determine appropriate values for $\Delta\omega$ and ω^u that ensured reasonable convergence. A balance between the accuracy of the result with the computational time is then desired. A further numerical issue arose in the calculation of γ_n^{ex} in equation (9) since the upper limit in the summation is infinite. This was replaced by a finite sum to M terms. In order to apply the model there are therefore four implementation parameters that need to be set: $M, \Delta\phi, \Delta\omega$ and ω^u. Convergence was assessed by considering the summed difference in the phase velocity over a suitable angular frequency range defined as

$$F(M,\Delta\phi,\Delta\omega,\omega^u)=\sum_i\left|c^{j+1}(\omega_i)-c^j(\omega_i)\right|^2, \tag{16}$$

where j represents the j^{th} value of the particular parameter being examined. For this analysis three of the parameters were fixed, and the decay in F examined whilst the fourth parameter was varied. When varying ω^u, the phase velocity had a range $\omega\in\left[1.7\times10^3,2.5\times10^5\right]$ Hz with the remaining numerical parameters fixed at $M=3,\Delta\phi=4.625\times10^{-2}$ $(N=4)$ and $\Delta\omega=15$ Hz. The physical parameters were chosen similar to those in [3]: $\phi=0.185,\mu_I=0.1\,\text{GPa},\mu_0=0.0155\,\text{GPa},\rho_I=1\times10^3\,\text{Kg}\,\text{m}^{-3},\rho_0=1.075\times10^3\,\text{Kg}\,\text{m}^{-3}$ and $a=2.3$ mm. The results were compared for $(\omega^u)^j=\{0.2,0.8,1.7,10,18\}\times10^5$ Hz respectively. The results showed that F converged to a reasonable level for $\omega^u\geq0.8\times10^5$ Hz with a linear relation between the computational time and $(\omega^u)^j$. This procedure was repeated in order to determine the effect of increasing M. All parameters were identical with the exception of fixing $\omega^u=0.8\times10^5$ Hz and running the model with $(M)^j=\{1,3,5,7,10,15,20\}$. Again F converged as M increased, a linear increase in computational time was observed and reasonable convergence was observed for $M\geq5$. A similar analysis was conducted for $\Delta\omega$ however, unlike ω^u and M, there was no linear relationship between the computational time and $\Delta\omega$. The effect of increasing N (decreasing $\Delta\phi$) was analysed over different volume fractions ϕ for the same angular frequency range with $M=9$ and ω^u as above. The volume fractions considered were $\phi^j=\{0,0.25,0.5,0.75,1\}$ with $N^j=\{2,4,6,\ldots,18,20\}$. It was observed that there was a linear increase in the computational time as N increased, as expected. There was also evidence of a linear increase in the computational time as the angular frequency increased. Additionally, the phase velocity tended to a limit as N increased and if too large a value for $\Delta\phi$ was chosen then the method became unstable.

4 Analysis of Relationships of Physical Properties in Model

In this section the model was applied to a material commonly used to produce transducer matching layers and backing blocks (epoxy resin and tungsten particles). The appropriate data are summarised in Table 2.

Material	μ (G Pa)	ρ (Kgm^{-3})
Epoxy	1.48	1140
Tungsten	161.2	19300

Table 2 Physical properties of epoxy and tungsten

The effect that the various physical parameters of the two constituents have on the model's prediction of the phase velocity was then examined. For example, it

was found that the phase velocity increased as the square root of the effective shear modulus and as the square root of the effective density. The radius of the inclusions has a marked influence on the final phase velocity. The typical mean particle size used for the tungsten inclusions was $4-6\mu$m with a range of other commercially available mean particle sizes being $a=\{1,10,25,100,250\}\ \mu$m.

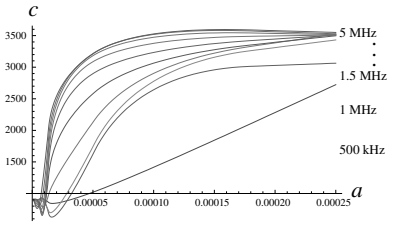

Fig. 1 Phase velocity $c(\mathrm{ms}^{-1})$ versus particle size a(m) for frequencies 500 kHz to 5 MHz, with inclusion volume fraction $\phi=0.3$. The velocity profiles move upwards monotonically as the frequency increases.

Figure 1 shows that the velocity changes as the particle size increases and that it does so in a nonlinear fashion. In addition, at these values of the particle size, this velocity depends on the frequency of the ultrasound wave. In this region the particle size is commensurate with the wavelength of the ultrasound wave. As the frequency increases the velocity profile increases monotonically until once again the velocity curves converge for very high frequencies.

5 Comparison between the theoretical predictions and experimental measurements

In order to carry out an experimental validation of this model a number of samples of epoxy resin, filled with tungsten particles, were prepared and their acoustic properties measured by a through transmission method [9]. The epoxy resin, CY1303/HY1300, was supplied by Huntsman, Cambridge, UK and the tungsten particles with a mean particle size of 5 μm were supplied by Ultimate Metals, Chingford, UK. The epoxy resin was mixed by hand in accordance with the manufacturer's instructions and degassed in a vacuum chamber to remove any entrained air bubbles. The epoxy and tungsten, in the required volume ratio, were placed in a pestle and mortar and the mixture carefully ground together. For each sample sufficient material was prepared in excess to produce a sample with the dimensions 49mm diameter with a 10mm thickness. Once thoroughly mixed the material were transferred to a mould with a close fitting lid. The mould was designed to allow the excess material to escape prior to sealing the mould, once sealed the tungsten-epoxy composite was allowed to cure for 18 hours at room temperature prior to being re-

moved from the mould. Once removed from the mould the major faces were then machined to ensure parallelism for the measurement of acoustic properties.

In samples with low volume fraction, in the current context $\phi \leq 0.4$, the density of the tungsten particles will mean that settlement will occur during the cure cycle. To limit the settlement, the cylindrical mould is mounted axially into a rotation fixture and rotated about the axis during the cure cycle. In the case of samples where $\phi \geq 0.4$, the tungsten-epoxy composite must be cured under pressure in order to obtain a uniform fully cured composite. To apply pressure to the curing material a reusable cylindrical mould manufactured from PTFE was used, a simple plunger mechanism was incorporated into the mould design such that the material could be compressed using a hydraulic press attached to the plunger. For each sample having a volume fraction greater than 0.4, the mould was subject to 1000 psi pressure during the cure cycle.

The acoustic velocities were measured using a through transmission time of flight method. Since the samples were acoustically matched to water, oil having a velocity of 680 m/s was employed as the coupling medium in order to refract a shear wave into the sample. Figure 2 shows the measured acoustic velocities and these compare well with those obtained using the theoretical approach detailed in Section 2.

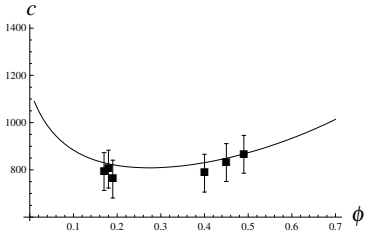

Fig. 2 Phase velocity c (ms^{-1}) versus the volume fraction of the tungsten inclusions ϕ at frequency 500 KHz. The model results (full line) are compared with experimentally measured values (filled squares), with a particle size of 5 μm.

6 A Particle Size Distribution

In a practical situation it is impossible to add inclusions of identical size. In fact, most commercially available materials follow a normal distribution with a specified mean particle size. It is also of interest to investigate the root cause for the experimentally observed variations in the measured mechanical impedance of epoxy-tungsten samples at a fixed volume fraction of inclusions. The CDM algorithm was adapted by replacing the fixed particle size at each step with a random value drawn from a normal distribution of known mean and standard deviation. The phase velocity was plotted as a function of the final volume fraction of inclusions with the

physical parameters set at those for epoxy and tungsten (see Table 2), with $\bar{a} = 5\mu$m, and the implementation parameters set as $M = 9, \Delta\phi = 0.05$ and $\Delta\omega = 0.8 \times 10^3$ Hz. The process was conducted for a standard deviation of $\sigma_1 = 0.1\bar{a}$ to determine the effect that a spread of particle sizes in a sample of tungsten powder would have. The algorithm was run several times and the variation in the results was then compared with those from a fixed particle size simulation.

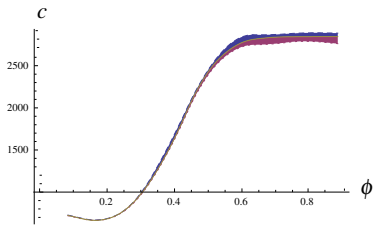

Fig. 3 Phase velocity $c(\text{ms}^{-1})$ versus inclusion volume fraction ϕ at frequency $f = 1$ MHz for random particle size selection from a normal distribution with $\bar{a} = 5\mu$m and a 10% standard deviation. The shaded regions denote the variance in the model's output lying above and below the fixed particle size simulation.

Figures 3 shows an increase in the difference between the maximum and the minimum values from the phase velocity for constant particle size as the volume fraction increases.

An alternative view can be taken of these results by fixing the volume fraction ($\phi = 0.2$ and $\Delta\phi = 0.04$) and calculating the phase velocity as the frequency of the insonifying wave is varied.

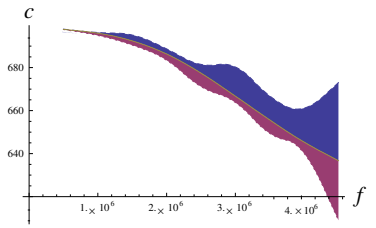

Fig. 4 Phase velocity $c(\text{ms}^{-1})$ versus frequency f (Hz) at an inclusion volume fraction of $\phi = 0.2$, for a random particle size selection from a normal distribution with $\bar{a} = 5\mu$m and a 10%standard deviation. The shaded regions denote the variance in the model's output lying above and below the fixed particle size simulation.

As the frequency increases, the variance in phase velocity due to the random particle size increases, highlighting the fact that the higher the frequency the more the variations in particle size affect the velocity. In order to produce a composite for a transducer matching layer, capable of working over a broad-bandwidth, it is important to have a sample of inclusions with as low a variance as possible in a size regime

that is outwith the effects of scattering. This will allow a greater predictability of the phase velocity, and as a result be able to produce a desired composite material with greater control.

7 Conclusion

Ultrasonic transducer designs typically consist of an active piezoelectric layer sandwiched between a backing material for damping and bandwidth control and some form of matching layer for interfacing to the mechanical load medium. These materials are very often manufactured by mixing two different materials in order to achieve a desired mechanical impedance. A large variability in these effective properties can often be found for a given base and inclusion material, and a fixed volume fraction of inclusions. This is thought to be due to the random agglomeration of the inclusion particles to form percolation paths in the base material. In this paper an implementation of the Causal Differential Method (CDM) has been presented and, by incorporating a particle size distribution in the inclusion phase, the root cause of this variability in the effective composite properties is examined. Numerical issues regarding the implementation and convergence of the method were also discussed. Reasonable convergence and computational times for the method were found as functions of the implementation parameters in the model. A dimensional rescaling was also introduced to alleviate the numerical instabilities inherent to the model. It was found that, for a given frequency of excitation, the calculated velocity for the composite has a distribution whose variance increases as the volume fraction of inclusions increases. This would suggest that to reliably and repeatedly manufacture composites with a desired mechanical impedance, a low volume fraction of inclusions should be used.

References

1. Anson, L.W., Chivers, R.C.: Ultrasonic Velocity in Suspensions of Solids in Solids - A Comparison of Theory and Experiment. J. Physics D: Appl. Phys. **26**, 1566–1575 (1993)
2. Beltzer, A.I.: Acoustics of Solids. Springer-Verlag, Berlin (1988)
3. Beltzer, A.I., Brauner, N.: The Dynamic Response of Random Composites by a Causal Differential Method. Mech. of Mats. **6**, 337–345 (1987)
4. Beyer, R.T., Letcher, S.V.: Physical Ultrasonics. Academic Press, New York (1969)
5. Desilets, C.S., Fraser, J.D., King, G.S.: The design of efficient broad-band piezoelectric transducers. IEEE Trans. Sonics. Ultrasonics **SU-25(3)**, 115–125 (1978)
6. Grewe, M.G., Gururaja, T.R., Shrout, T.R., Newnham, R.E.: Acoustic Properties of Particle/Polymer Composites for Transducer Backing Applications. IEEE Trans. UFFC. **37(6)**, 506–514 (1990)
7. Hayward, G.: The influence of pulser parameters on the transmission response of piezoelectric transducers. Ultrasonics **23(3)**, 103–112 (1985)

8. Mulholland, A.J., Ramadas, N., O'Leary, R.L., Parr, A., Troge, A., Pethrick, R.A., Hayward, G.: Enhancing the Performance of Piezoelectric Ultrasound Transducers by the use of Multiple Matching Layers. IMA J. Appl. Maths. (Accepted), (2008)
9. O'Leary, R.L.: An investigation into the passive materials utilized in the construction of piezoelectric composite transducers. Ph.D. thesis, University of Strathclyde, Glasgow, (2003)

Modelling of scattering of ultrasounds by flaws for NDT

M. Darmon, N. Leymarie, S. Chatillon and S. Mahaut

Abstract The CIVA software platform is developed at CEA-LIST and partners in the aim of simulating non-destructive evaluation. Most of the developed models are based on semi-analytical methods since they aren't heavy on computation time. The ultrasonic simulation tools in CIVA allow to fully predict a real ultrasonic inspection in a various range of applications which requires the computation of the beam propagated, as well as its interaction with flaws. The purpose of this communication is to describe the methods used to model the beam to flaw interaction. Three kinds of models for the scattering of ultrasound by flaws have been integrated in CIVA: approached analytical solutions, exact analytical solutions and numerical modelling methods. Numerous experimental validations of all the developed models are provided including comparisons between different simulation methods. Perspectives of new developments are finally emphasized.

1 Introduction: CIVA simulation approach

Simulation codes developed at CEA [1] and gathered in the expertise software platform CIVA aim at providing cost-effective tools to predict the results of inspection techniques carried out in realistic configurations, in order to conceive or to optimize inspection characteristics', probes, as well as to qualify inspection procedures or to allow interpretation of results.

Such tools have been continuously extended through the development of simulation models, from the early nineties, to account for realistic testing configurations in terms of probes (monolithic, phased arrays…), flaws and arbitrary component shapes (canonical shapes, parametrically defined or 2D/3D Computer Aided Design i.e. CAD defined).

M. Darmon, N. Leymarie, S. Chatillon and S. Mahaut

CEA, LIST, Laboratoire de Simulation et de Modélisation, F-91191 Gif-sur-Yvette, France.

e-mail: michel.darmon@cea.fr

The beam propagation model is based upon a semi-analytical method which calculates the impulse response of the probe inside the component, assuming individual source points distributed over the radiating surface of the probe. Each elementary source point contribution of the probe toward the computation point is therefore evaluated using a so-called pencil method applied to elastodynamics [2]. This model allows to compute the ultrasonic field in the component for wedge coupled or immersed probes of arbitrary shapes, for monolithic or phased-array transducers. Firstly developed for homogeneous and isotropic materials, it has been extended to deal with anisotropic and heterogeneous cases [3].

The CIVA tools are also dedicated to the prediction of flaw responses. We report here the main general assumptions applied to deal with the application of the semi-analytical models used:

1. A separation of variables is operated on the radiated field which has been computed in CIVA. Indeed the ultrasonic field radiated by the transducer is approached by the product of a spatial function $q(x, y, z)$ describing the amplitude distribution in the beam and a time-dependent function describing the wave propagation $\Phi_0(t - \Delta t)$. We assume that the wave fronts in the beam are locally plane in the vicinity of the flaw. In the case of plane fronts, a separation of variables can be operated so that the incident field at point M can be expressed as:

$$\Phi(M, t) = q(x, y, z)\, \Phi_0(t - \Delta t) \tag{1}$$

in which (x, y, z) are the cartesian coordinates of the point M of the flaw and Δt the time of flight from the probe to point M. The functions $q(x, y, z)$, Δt and $\Phi_0(t)$ are model inputs extracted from the CIVA field calculation.

2. The flaw scattering model is based upon various approximations depending on the inspection technique and the nature of flaw (void, solid inclusion). These approximations will be detailed in part 2.

3. Finally, the signal received by the probe is obtained by summing up all the scattered contributions. The amplitude of one contribution is proportional to the probe sensitivity at the location of the source. The model assumes the transmission-reception reciprocity for the transducers so that this sensibility is directly deduced from the transmitted field computation.

The aim of this article is to give an overview of all the methods used in CIVA to solve the scattering problem. First, we will focus on analytical methods since Part 2 will be dedicated to approached analytical solutions and then exact analytical solutions are studied in Part 3. In addition to analytical methods, an hybrid method coupling numerical and semi-analytical models which is integrated in CIVA is detailed in Part 4.

2 Approached analytical solutions

To deal with the wave scattering, the different classical approximations are applied [4] depending of the scatterer. In the case of specimen boundaries, calibration reflectors (side drilled hole, flat bottom hole, etc…) or large voids, the high frequency Kirchhoff approximation is used. In the case of cracks, the Kirchhoff approximation or GTD (Geometrical Theory of Diffraction) can be used depending on the considered echo mechanism (tip diffraction; specular reflection). At last, to predict the response of solid inclusions a slightly modified form of the low-frequency Born approximation has been proposed and implemented.

2.1 Kirchhoff approximation

The application of Kirchhoff approximation, used to simulate most inspection techniques, assumes that the flaw is a scattering surface discretized as a set of elementary surfaces, for which one calculates the interaction of the incident field (L or T mode) with the flaw (reflection with or without mode conversions).

Kirchhoff approximation considers an incident plane wave on a stress-free crack or a void and is characterized by the following hypotheses:

- on the shadow crack face: the total displacement vanishes.
- the insonified face is replaced by an infinite plane free surface: the total displacement is there the sum of the incident field and the reflected fields.

Then the scattered field is expressed by means of Green Theorem in terms of jumps of displacement across the surface of the flaw. Finally, the scattered field at an observation point is obtained as a spherical wave associated to a directivity coefficient depending on the incident and scattered directions [5].

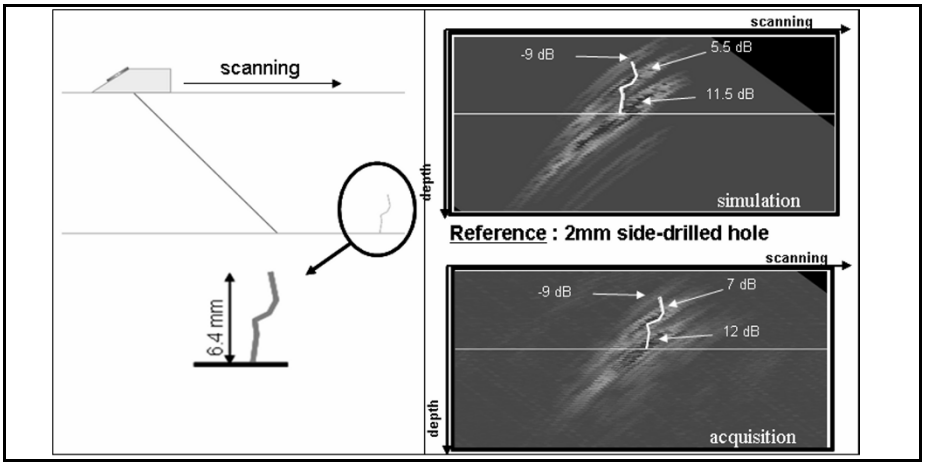

figure 1: Inspection of a complex (multi-facetted) flaw with a contact SW45.

The application of Kirchhoff approximation is commonly used in NDT modelling since it is an efficient way to model specular effects (corner echo or specular reflection). The Kirchhoff model integrated in CIVA is able to predict the responses of planar flaws (rectangular or CAD contour) or multi-facetted defects and also "void" flaws, as volumetric flaws (side drilled holes). The figure 1 concerns an example of experimental validation dealing with the inspection of a complex (multi-facetted) flaw. A multi-facetted flaw is made of several parts (segments) which can be extruded in the perpendicular direction to form a "2.5D" CAD flaw, or extruded with a more complex polyline to form a 3D multi-facetted flaw. The figure (a True B-Scan) shows the comparison between simulation and experiment for such a flaw, inspected with a 45° shear waves probe. One can observe the corner echo, diffraction echo, as well as a "local" specular echo resulting from the complex shape of the flaw, both for experimental and simulated image. The amplitude of these echoes are reported, with respect to a side drilled hole used as a reference, which exhibits a good agreement between simulation and experiments, in terms of flaw response and overall amplitudes.

Nevertheless Kirchhoff model owns several limitations. Indeed, since it is an high frequency approximation, experimental validations have shown that it is valid when the flaw height is in the same order or more than the wave length. Moreover the Kirchhoff approximation is less accurate for angles of observation away from the specular direction. We have to be aware that the Kirchhoff approximation gives rise to quantitative errors in predicting diffraction echoes from edges and that, besides it can't be used to model diffraction echoes in a TOFDT (Time of Flight Diffraction Technique) configuration (see Figure 2).

2.2 Geometrical theory of diffraction

Kirchhoff approximation lies in the fact that the field scattered by a crack is approached by the reflected field and consequently is not perfectly adapted to describe diffraction phenomena (for instance due to flaw edges). In that goal, the Geometrical Theory of Diffraction (GTD) is an alternative model which relies on ray theory (analogy with geometrical optics) [6].

Two different strategies have been investigated in CIVA concerning the calculation of the GTD coefficients: a so-called "projected 2D" option, which is based onto the projection of the incoming and scattered wave vectors over the plane which is perpendicular to the flaw edge, and a "pure" 3D GTD code, using developments carried out by Larissa Fradkin and co-workers at London South Bank University [7]. The complete modelling of the flaw response therefore lies upon the contour meshing of the flaw, the computation of the incident field over this mesh, and the estimation of the GTD coefficient according to local curvature of the edge.

GTD is not valid for specular reflection (corner echo), forward transmission and near a critical angle or a caustics (intersection of scattered rays). It's also a

high frequency approximation: the distance between two different flaw edges is supposed to be around or more than the wave length.

GTD is notably used to predict TOFD (Time Of Flight Diffraction) inspection performance in realistic configurations. TOFD (Figure 2) is an inspection technique, which relies on an arrangement of two probes of opposite beam directions. The simulation can account for arbitrarily oriented flaws (tilt, skew…) and realistic flaws (CAD contour planar flaws. The application of the TOFD technique over a planar component containing a tilted mid-wall notch is shown on Figure 2. The maximal amplitudes obtained in edge scattering simulation with the Kirchhoff and projected 2D GTD models are compared for various flaw tilts ($0° < \alpha < 180°$). We can observe that Kirchhoff approximation can't be applied in the shadow area bounded by the flaw plane so that no simulated results are given for about $0° < \alpha < 40°$ and $140° < \alpha < 180°$. GTD coefficients leads to a divergence around the specular reflection ($\alpha = 90°$) and consequently GTD models can't be used for tilts corresponding to about $75° < \alpha < 105°$. The Kirchhoff and GTD models provide similar results when these two methods are both valid. This comparison suggests that Kirchhoff and GTD models correspond to complementary approaches. In order to deal with all configurations, the development of a generic model for the scattering from cracks derived from the two previous approximations could be a perspective of future work.

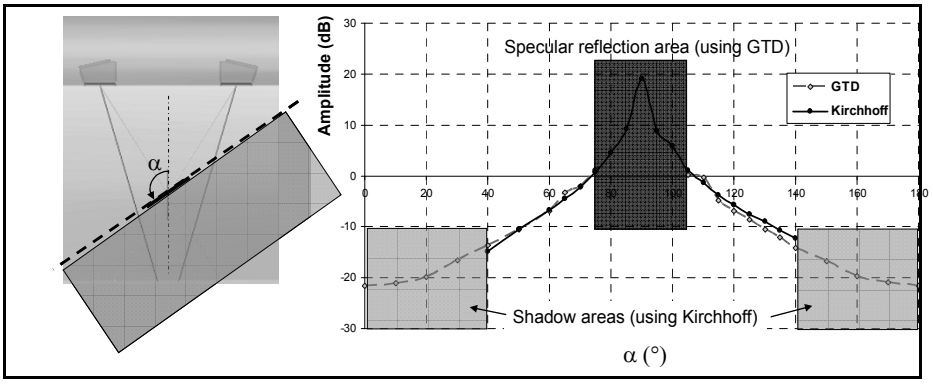

figure 2: Comparison of simulated amplitudes obtained with both Kirchhoff and projected 2D GTD models in the case of the TOFD inspection of a tilted mid-wall notch (3 MHz frequency, 30° L-waves).

2.3 Born approximation

The Born approximation applied to elastodynamics [8] has been shown to be effective to model weak scattering from solid inclusions. This low frequency ($ka<1$) model consists in approximating fields inside the scatterer by the incident fields. This assumes small variations of the structural parameters between the host me-

dium and the inclusion (density and elastic stiffness tensor). This approach has been modified in order to improve its accuracy domain. The modification leads to describe the wave propagation in the flaw by taking into account both density and wave velocity differences between the host medium and the inclusion [9].

The model is available for canonical shapes: spheres; cylinders and ellipsoids along the transmitted focal axis (L or T). The attenuation inside the inclusion can be taken into account (direct modes). The limitations of this Born modified model are the following:

- Low contrast for density and velocities between the host medium and the inclusion medium.
- The flaws are supposed to be small with respect to the wavelength.

Strongly laminated stainless steel products containing natural alumina inclusions have been investigated in the aim of validation of the model. The sample acquisitions were performed at 50 MHz. The results presented on Figure 3 a) concern an alignment of inclusions detected by ultrasonics and by X-rays measurements. The figure shows the superimposition of the ultrasonic C-scan and the corresponding X-rays view. From X-rays view have been deduced the sizes of inclusions assumed to be ellipsoidal which have been inputted in the model. We can see on Figure above b) and c) the good agreement between the simulated and experimental C-scan; the amplitude discrepancy being less than 1 dB. These excellent results have to be confirmed by additional measurements on other defects.

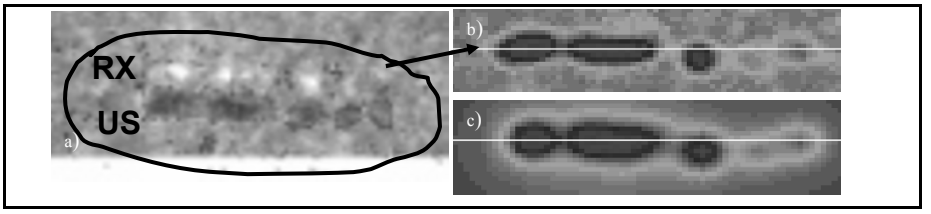

figure 3: a) Superimposed experimental C-Scan and X radiography b) experimental C-Scan c) simulated C-Scan.

3 Exact analytical solutions

The semi-analytical Kirchhoff approximation, in a wide range of situations, leads to satisfactory quantitative predictions with a low computation time. Nonetheless, this model may cause some discrepancies in the prediction of small flaws responses, since it is an high frequency approximation. Particularly, experimental validations carried out in a pulse-echo configuration on small side drilled holes highlighted some differences between Kirchhoff simulation and measure for shear waves. These discrepancies could be explained by the theoretical principle of Kirchhoff approximation: it takes into account specular reflection on a cavity but

not the creeping waves. These waves (called Franz waves [10]) propagate around the cavity circumference and may have a significant influence especially at low frequency or for small defect radii. They are the analogues on curved surfaces of Stoneley waves (surface waves excited by grazing incidence) on flat surfaces. The creeping waves differ from Stoneley waves in two respects: they are attenuated because energy is radiated tangentially away from the cylinder; they are many circumferential modes n of different speeds but the damping increases with n.

Therefore, the development of the exact analytical model for the scattering from a cavity has been integrated in CIVA for the moment for the cylindrical geometry. This model will be available in the next version of CIVA.

This exact model relies on the separation of variables (SOV) method [11]. We consider a plane wave propagating along x direction and incident on a cylindrical cavity embedded in an elastic isotropic solid. Only a 2D configuration can be treated: the incident and scattered waves vectors are included in the plane normal to the cylinder axis $\vec{z}$. The observation point of the scattered field is defined in a cylindrical coordinate system (r, θ, z) whose origin is the flaw centre and where θ is the angle between the incident and scattered wave vectors.

The SOV method enables to obtain series developments of the scattered waves. Terms of these series expressed here for the scalar velocity potentials (respectively longitudinal and transverse) are products of Hankel and complex exponential functions of separate variables (r, θ):

$$\varphi^{diff} = \sum_{n=0}^{\infty} A_n H_n^{(1)}(k_L r).\cos(n\theta).e^{-i\omega t} \tag{2}$$

$$\psi^{diff} = \sum_{n=0}^{\infty} B_n H_n^{(1)}(k_T r).\sin(n\theta).e^{-i\omega t} \tag{3}$$

Then the expression of boundary conditions allows to determinate the series coefficients A_n and B_n : the surface tractions on the cavity are set to zero. Under a far field hypothesis, the Hankel functions associated to the scattered waves can finally be approached by cylindrical waves. Finally, the application of Huygens' Principle enables us to replace each cylindrical scattered wave by a collection of spherical waves, which makes possible the use of the reciprocity theorem (mentioned in Part 1) for the echo synthesis. The developed SOV model in CIVA is developed for a cylinder for the moment and valid without flaw disorientation.

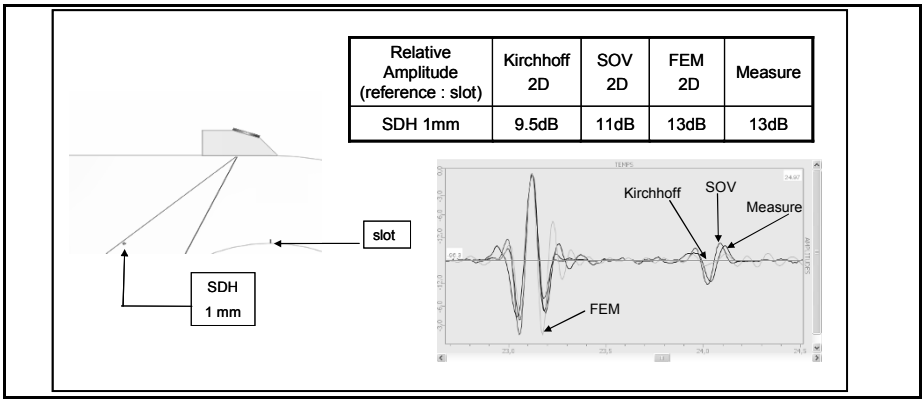

Figure 4: Inspection of a 1mm diameter side drilled hole (SDH) with a SW45° contact transducer at 5MHz (ka = 5).

An example of experimental validation is presented in the figure 5 below: it deals with control at 5MHz of a 1mm diameter side drilled hole (SDH) with a SW45° contact transducer. The corner echo measured on a slot is taken as the amplitude reference. Are given in the figure comparisons of both maximum amplitudes and A-Scans corresponding to echoes obtained with several 2D simulations (Kirchhoff, exact SOV and finite element method FEM detailed in Part 4) and with measure. Kirchhoff model is unable to predict the creeping circumferential wave (chronologically the second and less intense observed echo) and leads to discrepancy compared to measurement because the creeping wave affects the maximum amplitude of the first echo (specular reflection on the cylinder). SOV and FEM give rise to a good agreement in amplitude with experience and SOV is the model which predicts better the relative amplitude of the creeping wave.

4 Numerical modelling methods

The choice of a semi-analytical approximation, in a wide range of situations, provides quantitative predictions with a low computation time. However, these approximations may fail at predicting results in some complex configurations (particularly when defects of complex geometry are considered). In numerical schemes, the numerical resolution of the wave propagation equation could be quantitatively well defined ensuring the accuracy of the model. However, numerical schemes are computer intensive (computation time, memory).

To combine the advantages of both methods while minimizing their inconveniences, a hybrid model has been developed. The pencil method used for beam calculations in CIVA is applied to deal with most of the propagation, while intricate phenomena located in a small region surrounding the defects are computed nu-

merically by the FEM code ATHENA developed by EDF [12]. To synthesize the echo-response from the defect, an integral formulation extending Auld's reciprocity principle has been derived coupling computed results from both codes [13].

Indeed, Auld establishes a relationship between two typical NDT configurations. The first one, called state 1, involves a component without defect, whereas the second one, called state 2, takes the flaws into account (see Fig. 5). The extracted signal is computed from an integral over the surface *S* of a volume containing all flaws, using particle velocity and stress tensor quantities. The idea is that CIVA and ATHENA will be devoted to the computation of state 1 (without defects) and state 2 (with defects), respectively.

For practical reasons, the region in which the FEM computation is done must be as small as possible to avoid intensive computation. Then, state 2 is only considered inside the surface *S* surrounding the defect, called FEM box. This box is a rectangle for 2D computation and a parallelepiped for 3D computation.

The coupling computation is composed of 3 steps. (1) First, on the face of the box first crossed by the incident beam, the incident field is computed using the pencil method. (2) This field is then used as an input into ATHENA computation. The boundary conditions applied on the faces of the box are absorbing conditions (Perfectly Matched Layer), so no artificial reflection comes back from these faces. During a limited number of time steps, the calculation is done by modelling both the complex propagation and the interaction with defects. (3) Finally, the field corresponding to state 1 is computed using the pencil method in terms of impulse responses, for particle velocities and stresses. The coupling integral can then be calculated giving the signal due to the presence of defects contained in the box.

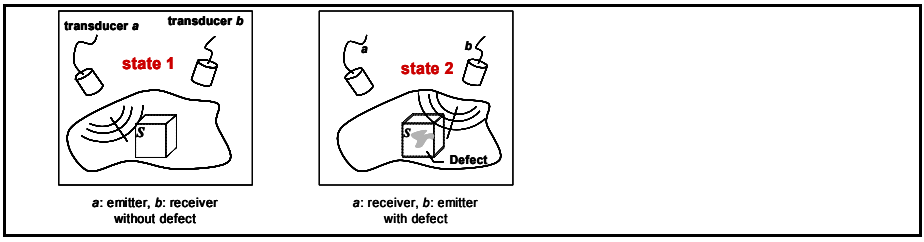

figure 5: Definition of state 1 and state 2 used for Auld's reciprocity principle.

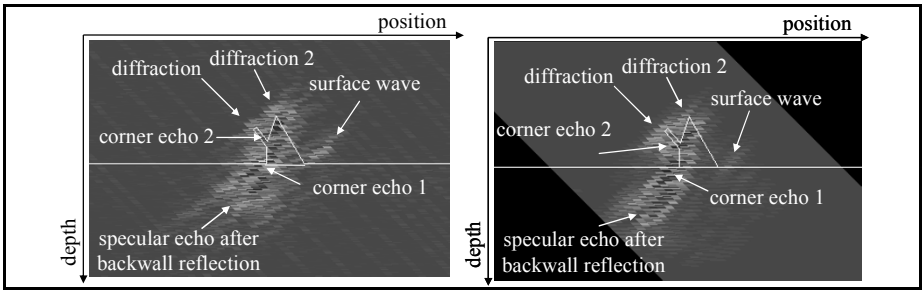

figure 6: B-scan images provided experimentally (at left) and from computing (at right) for a 45°-SW control of a surface-breaking crack with a branched geometry.

An experimental validation dealing with the inspection of a surface-breaking crack with a branched geometry is given in Figure 7 below. The experimental image (true B-Scan) presents multiple echoes due to the complex shape of the defect. At the base of the crack, the classical corner echo is generated but another one is observed on the top of the crack coming from reflections between 2 contiguous faces. A specular echo after a backwall reflection is observed arising from one branching of the crack. At last, 3 echoes with lower amplitudes are distinguished. Two of them are located on the tips of the crack and correspond to diffraction echoes. The other should be due to a surface wave propagating on the crack boundary. By comparing simulated result with the experimental one, all of these phenomena are recovered. The relative amplitudes between echoes are in general well evaluated except for the surface wave. Once more, this example demonstrates the ability of the coupling model to simulate complex beam/defect interactions, notably the wave interaction between faces of a same crack.

5 Conclusion

Ultrasonic simulation tools gathered in the CIVA software have been briefly presented. Those models, based on semi-analytical formulations kernels and numerical integration to deal with generic applications, include beam modelling and field-to-flaw interactions. The response of the flaw is calculated using specific algorithms, depending on the type of the flaw and of the inspection technique, which is an efficient and rather classical way to proceed. The Kirchhoff approximation stands for “void” flaws, as volumetric flaws (side drilled holes SDHs) and planar or multifaceted cracks, which assumes that the wave does not propagate into the defect. For planar or multifaceted cracks, the edges diffraction are simulated thanks to GTD (Geometrical Theory of Diffraction), either in pulse echo or TOFDT inspection. A modified version of Born approximation is used to deal with solid inclusions. In addition to these approached analytical solutions, an exact analytical solution can be used to improve the simulation response of small SDHs and a hybrid method coupling semi-analytical beam model and finite elements interaction model has been developed to simulate defects in complex configurations.

Perspectives of new developments have to be quoted: for instance, the need of a generic model for cracks valid for all configurations, the interaction of a flaw with either a Rayleigh surface wave, either an head or creeping wave [14], or a guided wave, the use of 3D FEM computation...

At last, we point out the plat-form approach adopted in CIVA which allows, in the framework of collaborative projects, the connection of modelling and data processing tools developed by other R&D laboratories.

References

1. CIVA software website, http://www-civa.cea.fr
2. N. Gengembre, "Pencil method for ultrasonic beam computation", Proc. of the 5th World Congress on Ultrasonics, Paris, 2003.
3. Gengembre N. and Lhémery A., "Calculation of wideband ultrasonic fields radiated by water-coupled transducers into heterogeneous and anisotropic media", in Review of progress in QNDE, 19, (2000) 977
4. R. Raillon and I. Lecœur-Taïbi, "Transient elastodynamic model for beam defect interaction. Application to nondestructive testing", *Ultrasonics*, 38 (2000), pp. 527-530
5. R.K. Chapman, *Ultrasonic scattering from smooth flat cracks: An elastodynamic Kirchhoff diffraction theory*, CEGB Report, North Western Region NDT Applications Centre, NWR/SSD/82/0059/R (1982).
6. Achenbach J D and Gautesen A K, Edge Diffraction in Acoustics and Elastodynamics, in *Low and High Frequency Asymptotics*, 1986 Vol 2, edited by V K and VV Karadan, Elsevier, 335-401.
7. M. Darmon, S. Chatillon, S. Mahaut, L. J. Fradkin and Art Gautesen, "Simulation of disoriented flaws in a TOFD technique configuration using GTD approach", Review of Progress in QNDE, ed. by D. O. Thompson and D. E. Chimenti 27, (2008), pp. 155-162.
8. Gubernatis J.E., E. Domany, *J. Appl. Phys.* 48, 2812 (1977).
9. M. Darmon, P. Calmon, B. Bele, "An integrated model to simulate the scattering of ultrasounds by inclusions in steels" in *Ultrasonics* ***42*** 237-241 (2004)
10. Uberall H. in *Physical Acoustics*, Volume 10, edited by W.P. Mason and R.N Thrston, Academic Press, 1973.
11. Achenbach J.D., Brind R.J., Gubernatis J.E. (1984),"High-frequency scattering of elastic waves from cylindrical cavities", Wave Motion 6. 12. Bécache E., Joly P., Tsogka C., "Application of the fictitious domain method to 2D linear elastodynamic problems", *J Comput Acoust*, 9, pp. 1175-1202, 2001.
13. N. Leymarie, P. Calmon, T. Fouquet, A. Schumm, « A Semi-analytical FEM Hybrid Model for Ultrasonic Simulation of Complicated Wave Defect Interaction », *International Conference on NDE in relation to structural Integrity for Nuclear and Pressurised Component 2006*
14. G. Huet and M. Darmon, « Modelling of corner echo ultrasonic inspection with bulk and creeping waves », in the present series.

Finite element computation of leaky modes in stratified waveguides

A. S. Bonnet-Ben Dhia, B. Goursaud, C. Hazard and A. Prieto

Abstract Using guided waves can greatly facilitate the inspection of large structures such as pipes or plates. One can wonder if it remains possible for waveguides which are embedded in an elastic matrix. For NDT, guided modes could be replaced by the so-called "leaky modes": these modes are attenuated in the axial direction while they increase exponentially in the transverse ones. We are interested here in the finite element computation of leaky modes. The difficulty comes precisely from this exponential behaviour, which prevents us from simply truncating the infinite medium. This is the reason why we use Perfectly Matched layers (PMLs) in order to bound the domain of calculation. We checked this approach in the simple case of SH waves in a stratified waveguide, where the analytic dispersion relation is available. Numerical experiments show that the main parameter is the distance between the PML and the guide. Finally, we illustrate in this simple case a numerical application using leaky modes: the Green function of the embedded waveguide is given by modal expansion.

1 Introduction

Using ultrasonic guided waves for the non-destructive testing of elastic waveguides like pipelines, rails or aircraft plate-like parts is becoming quite popular. Com-

A. S. Bonnet-Ben Dhia (e-mail: anne-sophie.bonnet-bendhia@ensta.fr),
B. Goursaud (e-mail: benjamin.goursaud@ensta.fr),
C. Hazard (e-mail: christophe.hazard@ensta.fr)
POEMS, CNRS-INRIA-ENSTA UMR 2706, 32 Boulevard Victor, 75015 Paris, France

A. Prieto (e-mail: maprieto@usc.es)
Departamento de Matemática Aplicada, Universidade de Santiago de Compostela, Santiago de Compostela, C.P. 15782, Spain

This work was supported by the French ANR (SIM NANO PHOT project) as well as the Xunta de Galicia project PGIDIT07PXIB105257PR and Ángeles Alvariño grant AA07-76.

pared to classical inspection techniques, guided waves provide a way to control non-accessible parts of the waveguide and allow an efficient evaluation of large structures.

In several applications, the elastic waveguide is embedded in water or in another elastic medium (concrete, ground...): it is for instance the case of concrete reinforcing tendons. A main consequence is that the modes of the elastic waveguide become *leaky*, the leakage resulting from radiations in the outside medium. Let us mention that leaky modes have been already extensively studied in electromagnetism since the 50's (see for example Vassalo [9]).

An accurate determination of leaky modes (and the corresponding damping) arises to be a necessary preliminary step for who wants to use these modes for non-destructive evaluation of the embedded waveguide. Unfortunately, the computation of leaky modes is far from straightforward. The difficulty comes from a unusual behavior of these modes : indeed, leaky waves which are exponentially decreasing in the longitudinal direction of the guide are also exponentially growing in the transverse directions.

A classical approach for a numerical determination of elastic modes relies on a finite element discretization of the eigenvalue problem set in the transverse section (the so-called SAFE method, see Hayashi et al [7]). For a waveguide embedded in an infinite medium, this cannot be performed directly since the transverse section is unbounded. This feature needs a particular care: for instance, a rough truncation of this transverse section with a free surface condition on the artificial boundary will produce a high concentration of modes due to the reflections on the artificial boundary but will not allow to determine the discrete spectrum of leaky modes. A solution has been proposed by Castaing and Lowe [4] which consists in surrounding the domain of interest by a viscoelastic layer; as mentioned by the authors, an alternative approach is to use the now popular Perfectly Matched Layers (PMLs).

The object of the present paper is precisely to investigate the potentiality of PMLs for computing leaky modes of an embedded waveguide. In order to get a quantitative evaluation of the method, we have chosen a very simple configuration for which an analytical expression of the dispersion relations, with and without PMLs, is available (see Zhu and Lu [10]). We consider the propagation of SH waves in a stratified waveguide (a steel plate embedded in concrete for example) which leads to a one-dimensional modal problem.

The outline of the paper is the following. In section 2, the modes of the embedded waveguide are described, including leaky modes, and compared to those of the isolated waveguide. Section 3 is devoted to the computation of leaky modes using PMLs. A particular attention is devoted to the influence of the parameters of the PMLs on the accuracy of the results. The main conclusion is that the absorbing layer should be placed as close as possible to the waveguide to avoid spectral pollution. Finally, we show in section 4 that some phenomena can be simulated very efficiently using leaky modes: for instance, an accurate expression of the Green function of the embedded waveguide is derived by using a small number of leaky modes.

2 From guided modes to leaky modes

2.1 Propagation of SH waves in a stratified medium

The considered domain of propagation is $\mathbb{R} \times (a,b)$ where $x \in \mathbb{R}$ defines the longitudinal direction, and $y \in (a,b)$ is the transverse coordinate, where a and b can either be finite or infinite. We deal with time-harmonic SH waves, for a fixed circular frequency ω, which are solutions to

$$\frac{\partial}{\partial y}\left(\mu \frac{\partial u}{\partial y}\right) + \frac{\partial}{\partial x}\left(\mu \frac{\partial u}{\partial x}\right) + \omega^2 \rho u = 0 \text{ in } \mathbb{R} \times (a,b), \tag{1}$$

where $u = u(x,y)$ is the component of the displacement in the z direction, which is orthogonal to the considered planar domain, and where $\mu = \mu(y)$, the shear modulus, and $\rho = \rho(y)$, the density, are functions of the transverse coordinate y. We denote by $C(y) = \sqrt{\mu(y)/\rho(y)}$ the speed of shear waves, and $C_{\min} = \inf_{y\in(a,b)} C(y)$. These functions may be discontinuous at some points in (a,b) : in (1), it is implicitly understood that both u and $\mu\, \partial u/\partial y$ are continuous at these points.

In addition to this equation, a free boundary condition is imposed whenever a or b is finite:

$$\text{if } c \in \{a,b\} \text{ is finite}, \frac{\partial u}{\partial y}(x,c) = 0, \forall x \in \mathbb{R}. \tag{2}$$

The *modes* of the medium are solutions to the above equations for which the spatial variables x and y are separated, that is, of the form:

$$u(x,y) = \phi(y) \mathrm{e}^{i\beta x},$$

where $\beta \in \mathbb{C}$ is the longitudinal wavenumber. This leads to a one-dimensional eigenvalue problem: we have to find $\lambda = -\beta^2 \in \mathbb{C}$ and a non-vanishing function ϕ such that

$$\frac{-1}{\mu}\left\{\frac{d}{dy}\left(\mu \frac{d\phi}{dy}\right) + \omega^2 \rho\, \phi\right\} = \lambda\ \phi \text{ in } (a,b), \tag{3}$$

$$\frac{d\phi}{dy}(c) = 0 \text{ if } c \in \{a,b\} \text{ is finite}. \tag{4}$$

In the two following paragraphs, we recall some general results (which essentially follow from spectral theory of selfadjoint operators) about the solutions to this eigenvalue problem in two particular situations. In the first one, we consider the case when the domain is bounded in the transverse direction, so that the stratified medium plays the role of a waveguide. In the second case, this waveguide is embedded in a homogeneous infinite medium. To illustrate these general results, we then show some numerical results in both situations when the waveguide is homogeneous.

2.2 Modes of an isolated waveguide

First assume that (a,b) is a bounded interval. In this case, the solutions to problem (3)–(4) occur for a discrete set of eigenvalues which consists in a real sequence $\{\lambda_n\}_{n\in\mathbb{N}}$ contained in the interval $[-\omega^2/C_{\min}^2,+\infty)$, with $\lim_{n\to\infty}\lambda_n=+\infty$. The corresponding modes ϕ_n are *guided* in the sense that their transverse energy is finite, which can be written in the form

$$\int_a^b \mu(y)\,|\phi_n(y)|^2 dy<\infty. \tag{5}$$

We can distinguish between two kinds of modes:

- A finite number of *propagative modes* associated with negative eigenvalues λ_n, or equivalently, real longitudinal wavenumbers β_n: these modes have a sinusoidal behavior in the longitudinal direction.
- An infinite number of *non propagative modes* associated with positive eigenvalues λ_n, or equivalently, imaginary β_n: these modes have an exponential behavior along x. When considering only one of both directions $x\to\pm\infty$, the exponentially decreasing mode is called *evanescent*.

2.3 Modes of an embedded waveguide

Suppose now that the previous waveguide is embedded in a homogeneous infinite matrix. In other words, a or b (or both of them) is infinite, and outside a bounded interval contained in (a,b), the physical characteristics of the medium are constant:

$$\mu(y)=\mu_\infty,\ \rho(y)=\rho_\infty \text{ and } C(y)=C_\infty=\sqrt{\frac{\mu_\infty}{\rho_\infty}},$$

so that in the matrix, Eq. (3) simplifies as

$$-\phi''-\frac{\omega^2}{C_\infty^2}\phi=\lambda\ \phi. \tag{6}$$

Although this situation could be considered as a (possibly slight) perturbation of the previous one, the structure of the solutions to the eigenvalue problem (3)–(4) is radically modified.

- On one hand, a finite number of *guided propagative modes* may occur. They correspond to real negative eigenvalues λ_n which are necessarily contained in the interval $[-\omega^2/C_{\min}^2,-\omega^2/C_\infty^2)$. Note that this interval is empty if $C_{\min}=C_\infty^2$: there is no such modes if the speed is greater in the guide than in the matrix. The modes associated with these possible eigenvalues are called *guided*, because as for the isolated waveguide, their transverse energy remains finite, in the sense

of (5) (indeed, Eq. (6) admits exponentially decreasing solutions, of the form $A\ \exp(-\sqrt{-\omega^2/C_\infty^2-\lambda}\,|y|)$). These modes have again a sinusoidal longitudinal behavior.

- On the other hand, a continuum of *radiation modes* always occurs. For every λ in the interval $[-\omega^2/C_\infty^2,+\infty)$, one can find a bounded non-zero solution to (3)–(4), which is no more *guided* ((5) is no more satisfied) since the solutions to (6) are linear combinations of $\exp(\pm i\sqrt{\omega^2/C_\infty^2+\lambda}\,|y|)$. As for the isolated waveguide, in the longitudinal direction, the modes can either be propagative (if $\lambda<0$), or non propagative (if $\lambda>0$).

In addition to these two categories, one can find other modes, called *leaky modes*, which are not, strictly speaking, spectral objects, since they result from a more involved process of analytic continuation. Indeed, these modes appear for complex values of λ when searching for solutions to (3)–(4) which are *outgoing* in the sense that they are proportional to $\exp(i\sqrt{\omega^2/C_\infty^2+\lambda}\,|y|)$ in the matrix (instead of a linear combination of outgoing and incoming waves as for the radiation modes). When this behavior is decreasing as $|y|\to\infty$, we get the above mentioned guided modes. But if we allow an exponentially increasing behavior, we find the discrete set of leaky modes, for which $\lambda\in\mathbb{C}$. The computation of these leaky modes is the object of the present paper.

2.4 A simple example

The simplest situation is the homogeneous waveguide: $\mu(y)=\mu_0$, $\rho(y)=\rho_0$, and $C(y)=C_0=\sqrt{\mu_0/\rho_0}$, for $y\in(0,h)$. We set $a=0$ and $b=h$ for the isolated guide, $b=\infty$ for the embedded guide. The geometry of both the isolated guide and the embedded guide are summarized on Fig. 1.

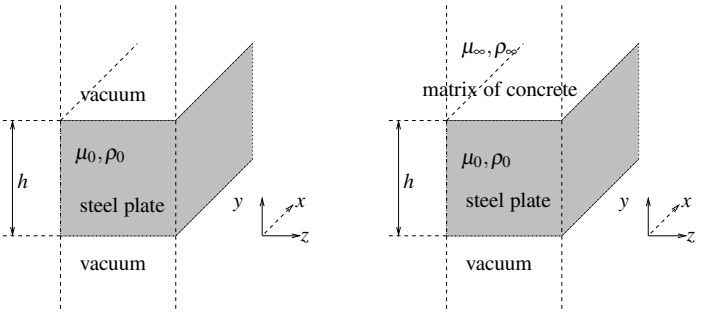

Fig. 1 Geometry of the isolated waveguide (left) and of the embedded waveguide (right).

- For the isolated waveguide, the solution of the eigenvalue problem (3)-(4) is very simple and the eigenvalues are given by:

$$\lambda_n = -\frac{\omega^2}{C_0^2} + \frac{n^2\pi^2}{h^2}, n \in \mathbb{N}.$$

- For the embedded waveguide, both guided and leaky modes verify the following dispersion relation:

$$i\mu_\infty \sqrt{\frac{\omega^2}{C_\infty^2} + \lambda} = -\mu_0 \sqrt{\frac{\omega^2}{C_0^2} + \lambda} \tan\left(\sqrt{\frac{\omega^2}{C_0^2} + \lambda}\, h\right). \tag{7}$$

For numerical applications, we use the following parameters: $\rho_0 = 7.932\,\mathrm{g/cm^3}$, $\rho_\infty = 2.3\,\mathrm{g/cm^3}$, $C_0 = 3.260\,\mathrm{km/s}$, $C_\infty = 2.6375\,\mathrm{km/s}$. The height h of the waveguide is 5 mm. The frequency is fixed at 1 MHz. This corresponds to steel plate in an infinite matrix of concrete. Note that, in this case, there is no guided mode for the embedded waveguide, since $C_0 > C_\infty$.

Fig. 2 shows the spectral values and the longitudinal wavenumbers of the isolated guide and of the embedded guide. There are four propagative modes for the isolated guide (for wich $\lambda < 0$ or equivalently $\beta \in \mathbb{R}$). The matrix perturbs these modes by essentially introducing a slight imaginary part to the longitudinal wavenumbers. The consequence is the creation of a damping in the longitudinal direction, but also, as explained in the previous paragraph, a growing behavior in the transverse direction. Fig. 3 illustrates both effects on a propagative mode. For the non propagative modes, the impact of the matrix is mainly the introduction of a small real part. This does not change fundamentally the behavior of these modes in the longitudinal direction. But, like in the previous situation, they are exponentially growing in the transverse direction.

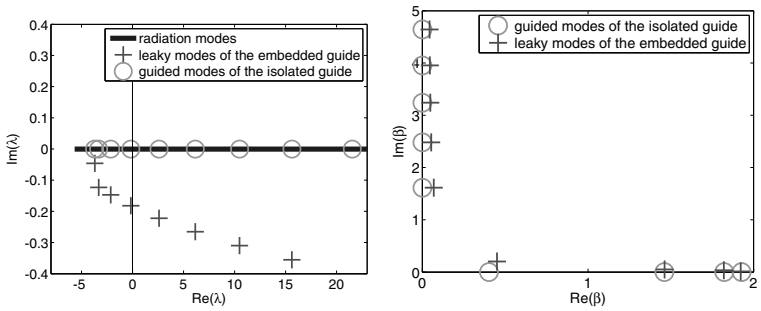

Fig. 2 Spectral values λ (left) and longitudinal wavenumbers β (right) of the isolated and embedded guides.

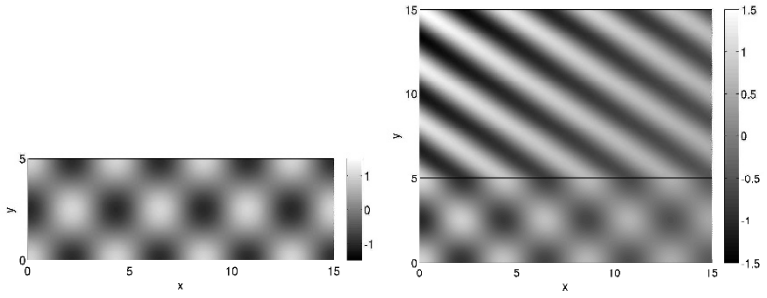

Fig. 3 Real part of a propagative mode of the isolated guide (left) and corresponding leaky mode of the embedded guide (right).

3 Finite element computation of leaky modes

With the aim of computing the leaky modes in complex configurations where the dispersion relation is unknown in a closed form, we need to introduce a numerical method which will discretize the system of equations of the model and will be accurate for computing the solution of eigenvalue problems stated in unbounded domains. In fact, the main drawback that arises in this kind of computations is related to the unbounded domain where wave propagation problems are stated.

There are different computational techniques to treat this problem numerically: absorbing boundary conditions (see, for instance, Givoli and Neta [6]), damping layers (see Castaing and Lowe [4]) or Perfectly Matched Layers (see Bérenger [2]), among others. In the last years, the Perfectly Matched Layer (PML) technique has become a standard efficient tool to numerical simulation of problems stated in unbounded domains in a wide range of problems. For instance, it has been applied to acoustic wave propagation at rest, in elasticity (see Collino and Tsogka [5]) or wave propagation under an uniform flow in ducts (see Bécache et al [1]). Moreover, the PML technique have demonstrated a high accuracy in standard finite element implementations (see Bermúdez et al [3]).

Let us describe briefly which is the basic procedure for introducing the PML technique in the problem stated in an embedded waveguide. Since the domain where the matrix of concrete is situated is unbounded in the transversal direction, we need to truncate it at a finite distance of the steel plate, and then we surround the physical domain of interest by an absorbing PML. In spite of the unbounded domain has been truncated, the original solution inside the physical domain of interest remains with minor perturbations, since the solution inside the PML "matches perfectly" with the physical solution in the sense that there does not exist spurious reflections on the interface between the PML and the physical domain.

3.1 Coupled physical-PML model

Let us recall roughly the description of the system of equations which govern the coupled physical-PML problem for an embedded waveguide. In the sequel, the PML is placed in the interval (d,e) of the transversal direction of the waveguide.

One of the most extended ideas to understand the PML technique uses the complex stretching of variable. Basically, given a complex constant, $\alpha \in \mathbb{C}$, if we introduce a complex change of variable

$$y \in (d,e) \rightarrow \tilde{y} = d + \frac{y-d}{\alpha} \in \mathbb{C} \tag{8}$$

then the equation governing the propagation inside the PML is given by the original equation (3) written formally in the new complex coordinates $\tilde{y}$ as follows:

$$\begin{aligned} -\frac{1}{\mu}\left\{\frac{d}{d\tilde{y}}\left(\mu\frac{d\tilde{\phi}}{d\tilde{y}}\right)+\omega^2\rho\tilde{\phi}\right\}-\lambda\tilde{\phi} = \\ -\frac{1}{\mu}\left\{\alpha\frac{d}{dy}\left(\mu\alpha\frac{d\tilde{\phi}}{dy}\right)+\omega^2\rho\tilde{\phi}\right\}-\lambda\tilde{\phi}=0 \qquad \text{in } (d,e). \end{aligned} \tag{9}$$

This equation must be completed with the boundary condition $d\tilde{\phi}/dy = 0$ at point $y = e$.

However, through the rest of the paper, we extend the definition of the complex change of variable (8) to the whole computational domain (a,d), where α is a non null complex function defined by

$$\alpha(y) = \begin{cases} 1 & \text{if } y \in (a,d), \\ \mathrm{e}^{-i\theta} & \text{if } y \in (d,e). \end{cases} \tag{10}$$

In this case, since $\tilde{y} = y$ in (a,d), (9) is equivalent to (3) in (a,d), and hence, the PML equation (9) can be used as the governing equation of the displacement field in both the physical and PML domains. Let us remark that since α is discontinuous at $y = d$, implicitly it is assumed that $\tilde{\phi}$ and $\mu\alpha d\tilde{\phi}/dy$ are continuous at the interface point between the physical and PML domain, $y = d$.

We are not going to detail such choice for the absorbing function of the PML. However, notice that due to the independency of the absorbing layer α with respect to the eigenvalue λ, the coupled physical-PML remains a linear eigenvalue problem with respect to λ.

Following standard arguments for deriving a variational formulation of the coupled physical-PML problem, if we multiply (9) by the complex function $1/\alpha$ and by the conjugate of a virtual displacement field φ, and integrate by parts in $(0,e)$, then we obtain the following variational problem:

Find $\tilde{\phi}$ and λ such that

$$\int_0^e \left(\mu\alpha \frac{d\tilde{\phi}}{dy}\frac{d\bar{\varphi}}{dy} - \frac{\omega^2\rho}{\alpha}\tilde{\phi}\bar{\varphi} \right) dy - \lambda \int_0^e \frac{\mu}{\alpha}\tilde{\phi}\bar{\varphi}\, dy = 0, \tag{11}$$

for all virtual displacement φ.

Finally, a discretization procedure is used by applying a standard finite element method. Piecewise linear polynomials are used to implement a Lagrange finite element on an one-dimensional uniform grid with $N+1$ nodes. It yields to the matricial problem

$$A_h\tilde{\phi}_h - \lambda B_h\tilde{\phi}_h = 0,$$

where $\tilde{\phi}_h$ is the nodal-value vector associated to $\tilde{\phi}$, i.e., $\tilde{\phi}_h = (\tilde{\phi}_h(x_0), \ldots, \tilde{\phi}_h(x_N))^t$. If we denote by $\xi_{h,j}(y)$ the canonical finite element basis associated to the j-th node, A_h and B_h are tridiagonal matrices defined by the expressions

$$(A_h)_{ij} = \int_0^e \left(\mu\alpha \frac{d\xi_{h,i}}{dy}\frac{d\xi_{h,j}}{dy} - \frac{\omega^2\rho}{\alpha}\xi_{h,i}\xi_{h,j} \right) dy,$$
$$(B_h)_{ij} = \int_0^e \frac{\mu}{\alpha}\xi_{h,i}\xi_{h,j}\, dy.$$

Notice that, as a consequence of the introduction of the PML in the model, the matrices associated to the finite dimensional eigenvalue problem become complex-symmetric and, in particular, B_h is not hermitian.

3.2 Transformation of the spectrum by the PML technique

One of the differences between the spectrum of the original problem and the coupled physical-PML problem consists in the position of the continuum of radiation modes. Before introducing the PML in the model, the continuum of radiation modes was lying in the real axis, more precisely, they were in the interval $[-\omega^2/C_\infty^2, +\infty)$.

However, the inclusion of PMLs in the problem introduces a modification in the position of the continuum of the oscillating modes, which arise in the negative imaginary half-space. More precisely, due to the complex stretching of variable, all the possible solutions of the original problem which are proportional to $\exp(i\sqrt{\omega^2/C_\infty^2 + \lambda}y)$, become proportional to

$$\exp\left(i\sqrt{\frac{\omega^2}{C_\infty^2} + \lambda}\,\frac{y}{\alpha} \right)$$

in the PML domain, i.e., they are damped (exponentially) inside the PML. In fact, since we have defined $\alpha = \mathrm{e}^{-i\theta}$ in the PML domain, for any $\lambda \in \mathbb{C}$ such that $\arg(\sqrt{\omega^2/C_\infty^2 + \lambda}) \in (-\theta, 0]$, the solutions which are bounded or exponential increasing functions in the unbounded domain become exponential decreasing inside

the PML domain. In the case $\arg(\sqrt{\omega^2/C_\infty^2+\lambda}) = -\theta$, the behavior in the PML remains oscillating.

Due to the effect of the complex change of variable, in spite of the leaky modes are exponential increasing in the physical domain, the PML technique allows to compute them since they become exponentially decreasing in the PML domain. Moreover, only the leaky modes which are exponential decreasing inside the PML, i.e., which satisfy $\arg(\sqrt{\omega^2/C_\infty^2+\lambda}) \in (\arg\alpha, 0)$, are recovered in the numerical simulations.

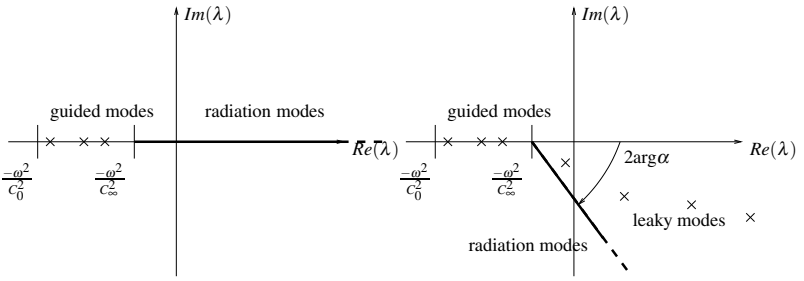

Fig. 4 Computed spectrum for the original unbounded problem (left) and for the coupled physical-PML problem (right).

The introduction of the PML in the problem can be interpreted as a rotation of the spectrum in the λ-complex plane: the continuum of the radiation modes are modified by a rotation, whose center is $-\omega^2/C_\infty^2$ and angle is -2θ. Moreover, following the same interpretation, this rotation allows to discover part of the leaky modes hidden in the original problem (see Fig. 4).

For the theoretical point of view, if the thickness of the PML is large enough, then the value of the leaky modes are independent of the parameters of the PML (i.e. independent of the absorbing function α or the position of the layer). In the sequel, since we focus our attention on all the leaky modes with positive real part and negative imaginary part, we will consider $\alpha = \mathrm{e}^{-i\theta}$ with $\pi/4 < \theta \leq \pi/2$.

3.3 An unusual requirement for the position of the PML

There are a wide range of works about the PML technique, the most of them used PMLs to compute the scattering field generated in a source problem. However, few works deal with an eigenvalue problem. At the first glance, the adequate configuration of the PML parameters for the eigenvalue problem can be considered similar to those used in the source problem, i.e., take the PML position far from the source and the PML thickness large enough to avoid spurious reflections that come from the truncated artificial boundary.

However, at the contrary of the intuition for the source problem, the optimal PML parameters are far from those fixed in the source problem. For the computation of leaky modes, the PML thickness must remain large enough to obtain an accurate eigenfunction without spurious reflections. But the PML position must be as close as it is possible to the interface between the matrix and the steel waveguide (see Kim and Pasciak [8]). This unusual requirement for the position of the PML is related to the exponential growth of the leaky modes in the physical domain and the non-hermitian character of the matrices involved in discretized eigenvalue problem.

Let us show an example where two different configurations have been used. We have considered the same physical parameters used in section 2.4 and the geometry is defined by $a = 0$mm and $h = 5$mm. In all the numerical simulations, the grid size has been kept constant and equal to 0.1mm.

On one hand, we have solved numerically the eigenvalue problem with some adequate PML parameters, $d = 6$mm, $e = 16$mm, and $\theta = \pi/3$. The numerical spectrum is shown on the left-hand side of Fig. 5. One can see on the plot a discretization of the continuum of radiation modes and four leaky modes. We have obtained an accurate result for the leaky modes, close to the exact eigenvalues of the problem which verify the dispersion relation.

On the other hand, we have used a set of parameters: $d = 20$mm, $e = 30$mm, and again $\theta = \pi/3$, analogously to those used in a source problem. We have obtained a perturbed result for the leaky modes and for the radiation modes. In addition, spurious modes, which are mixed with the leaky modes, have arisen in the spectrum. Notice that they are difficult to discard in the numerical simulations (see plot on the right-hand side of Fig. 5).

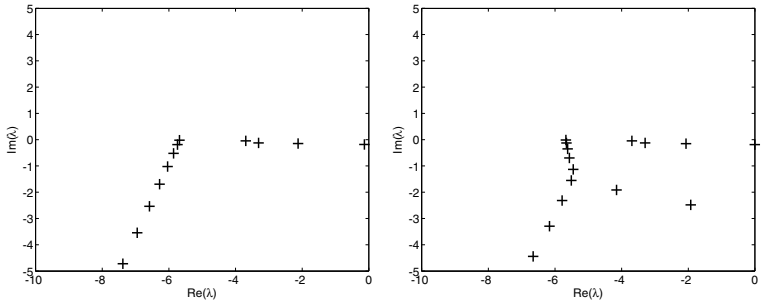

Fig. 5 Computed spectrum for a non-adequate settling (right) and an adequate one (left).

4 An application : an efficient evaluation of the Green function

We have seen how the guided modes of an isolated plate are transformed into leaky modes when the guide becomes embedded in an infinite matrix. We have also seen that the PML allows to compute these modes easily. As an application, we will use the modes in order to evaluate efficiently the Green function.

4.1 Modal representation of the Green function

We denote by $G = G_{x_0,y_0}$ the Green function whose point source is (x_0, y_0). It verifies the equation:

$$\frac{\partial}{\partial y}\left(\mu\frac{\partial G}{\partial y}\right)+\frac{\partial}{\partial x}\left(\mu\frac{\partial G}{\partial x}\right)-\omega^2\rho G=\delta_{x_0}\delta_{y_0} \text{ in } \mathbb{R}\times(a,b) \tag{12}$$

with the free boundary condition whenever a or b is finite (Eq. (2)).

For the isolated waveguide, it is well known that the Green function admits the decomposition:

$$G(x,y)=\sum_n \frac{e_n(y_0)}{2i\beta_n c_n}e_n(y)\exp(i\beta_n|x-x_0|), \tag{13}$$

with $c_n = \int_a^b \mu e_n^2$ and e_n the guided modes.

We would like to extend this representation for the embedded guide, using leaky modes instead of guided modes. Indeed, we have seen that each guided mode of the isolated guide is close to a leaky mode of the embedded guide. To achieve this aim, we use the expression of the leaky modes found in the previous section in the domain of calculation $(a,d)\cup(d,e)$, (d,e) being the PML. However, the orthogonal relation that holds for the isolated guide: $\int_a^b \mu e_m e_n = 0$ if $m \neq n$ is changed for the embedded guide by: $\int_a^e \mu/\alpha\, e_m e_n = 0$ if $m \neq n$. Hence, we replace the previous definition of c_n by $c_n = \int_a^e \mu/\alpha (e_n)^2$ and Eq. (2) gives the decomposition of the Green function for the embedded guide.

4.2 Numerical results of the decompostion

We use all the parameters described in section 2.4. Numerically, we have to truncate the series in Eq. (13). In the example of a steel plate in a matrix of concrete, there are four propagative modes. We choose to use all these modes and the first non propagative mode (β with the smallest imaginary part) in the decomposition of the Green function. Thus, these five leaky modes calculated, the decomposition (13) allows to represent the Green function very rapidly.

We place the point source at $x_0 = 0, y_0 = 0$. So as to compare the results, we also calculate the Green function of the embedded guide with a two-dimensional Finite Element method. Results are shown on Fig. 6. One can see that the difference between the modal representation with only five leaky modes and the solution with Finite Elements, which is numerically slower, is tight and concentrated above the point source. This error is less than 5% except above the point source. The modal representation is hence very efficient and accurate off the vertical of the point source.

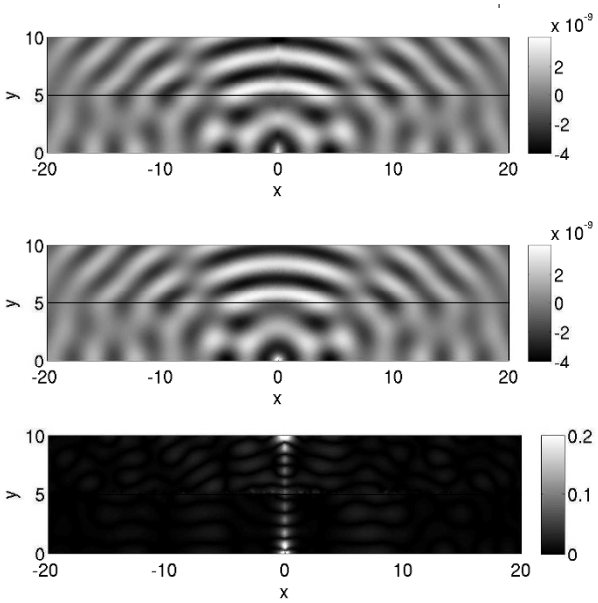

Fig. 6 Real part of the decomposition of the Green function with 5 leaky modes (top), real part of the Finite Element representation of the Green function (middle) and error between the two representations (bottom).

References

1. E. Bécache, A.-S. Bonnet-Ben Dhia, and G. Legendre, Perfectly matched layers for time-harmonic acoustics in the presence of a uniform flow. SIAM J. Numer. Anal., 44(3), pp. 1191-1217, 2006.
2. J. P. Bérenger, A perfectly matched layer for the absortion of electromagnetics waves, J. Comp. Phys., 114(1), pp. 185-200, 1994.
3. A. Bermúdez, L. Hervella-Nieto, A. Prieto, R. Rodríguez, Optimal perfectly matched layers with unbounded decay functions for time-harmonic acoustic scattering problems. J. Comp. Phys., 223, pp. 469-488, 2007.

4. M. Castaing and M. Lowe, Finite element model for waves guided along solid systems of arbitrary section coupled to infinite solid media, J. Acoust. Soc. Am., 123(2), pp. 696-708, 2008.
5. F. Collino and C. Tsogka, Application of the PML absorbing layer model to the linear elastodynamic problem in anisotropic heterogeneous media. Geophysics, 66(1), pp. 294-307, 2001.
6. D. Givoli and B. Neta, High-order non-reflecting boundary conditions for dispersive waves, Wave Motion 37, pp. 257-271, 2003.
7. T. Hayashi, W.-J. Song and J. L. Rose, Guided wave dispersion curves for a bar with an arbitrary cross-section, a rod and rail example, Ultrasonics 41, pp. 175-183, 2003.
8. S. Kim and J. E. Pasciak, The computation of resonances in open systems using a perfectly matched layer. Technical report, 2007. Preprint of the Department of Mathematics, Texas A&M University.
9. C. Vassalo, Optical Waveguide Concepts, Elsevier, 1991.
10. J. Zhu and Y. Y. Lu, Asymptotic solutions of the leaky modes and PML modes in a Pekeris waveguide , Wave Motion, 45(3), pp. 207-216, 2008.

Ultrasonic bulk wave propagation in concentrated heterogeneous slurries.

R E Challis, A K Holmes and V Pinfield

Abstract Many products in many sectors of industry exist in colloidal form and there is a requirement to measure the dispersed phase particle size distribution (PSD) non-invasively for the purposes of product and process quality assurance. Ultrasonic compression wave attenuation is sensitive to, *inter alia*, PSD, and could be applied on-line in a process plant. The ultrasonic method is based on adaptively fitting models of wave propagation to measured data. These models break down at high colloidal solids loading. This paper discusses the physical phenomena behind this failing and identifies a requirement for new formulations of local colloidal viscosity in the vicinity of suspended colloidal particles. Ultrasonic attenuation when calculated on the basis of a number of different viscosity models is compared to measured data and the model failings are thus illustrated. Empirical studies are presented which show possible forms of the viscosity - particle concentration - frequency relationship.

1 Introduction

Colloidal materials consist of small particles suspended in a liquid continuum, the size of the particles ranging from a few nm to 100s of microns. A colloid can exist in *monodisperse* form, in which all of the particles are the same size, or in *polydisperse* form in which there is a *particle size distribution* (PSD). If the

Applied Ultrasonics Laboratory, School of Electrical and Electronic Engineering, University of Nottingham, University Park, Nottingham, NG7 2RD, UK. E-mail: Richard.challis@nottingham.ac.uk

particles are liquid droplets the mixture is termed an *emulsion*, and if the particles are solid the mixture is termed a *slurry*. A vast range of products either exist in colloidal form or will have passed through the colloidal state during manufacture – examples are food, pharmaceuticals, cosmetics, paints and pigments, fuels and lubricants, grinding and polishing materials, and hazardous nuclear waste. Colloidal mixtures are not unconditionally stable and can change their state with time, temperature, light or other radiation, or with mechanical disturbance such as stirring, pumping, or vibration. There are many ways in which a colloid can change its state: particles can 'ripen' or undergo diminution by the exchange of material with the solution that forms the continuous phase; crystallisation is one but not the only process in this category. Particles can aggregate into floccules (flocs) which may themselves be either stable or unstable. In many products colloidal instability may be designed-in, and a good example here is emulsion paint which is required to remain stable and semi-solid when on a brush or on its destination surface, but is required to flow as a liquid during brushing – in response to a small input of mechanical energy. The growth of colloidal particles, by whatever process, can bring them to a size at which gravitational effects begin to dominate over Brownian phenomena and surface forces, and this leads to separation of the disperse phase from the continuous phase; common examples here are old milk and old paint. More generally, the functionality and fitness-for-purpose of a colloidal mixture depends strongly on the PSD. This leads to a requirement to measure PSD as the principal means to guarantee function, and such measurements may be required during manufacture, on the finished product, or in the context of longer term shelf-life studies. This latter is particularly important in the case of agrochemicals and pharmaceuticals in which uneven concentrations of bio-active ingredients are to be avoided for safety reasons.

There are many ways in which PSD and other aspects of colloidal structure can be assessed. These include visible and IR microscopy, SAXS, WAXS, SANS, NMR, ESR, electrical impedance, optical scattering and ultrasound, see [1]. Many of these techniques are only suited to a laboratory, as distinct from a process, environment, and many only apply to relatively dilute mixtures. Ultrasound has the potential to be used as the basis for PSD estimation in all operating environments but it, too, suffers from limitations when the concentration of particles is high. The problem is particularly acute in the case of slurries but less so for emulsions. This paper will give an outline of the basic technique for PSD estimation using ultrasound, the physics that underlies the method, and how the theory breaks down at high solids loading. Some experimental results will be presented which both illustrate these effects and pose new challenges for theoretical developments.

2 The Estimation of PSD Using Ultrasound

The basis of all ultrasonic PSD estimations is a theoretical model which predicts compression wave attenuation as a function of frequency with particle size(s) as input parameters. The model output is compared with *measured* attenuation, and the difference between the simulated and measured attenuation is identified as a mean squares error across the frequency range. The model prediction is then adapted by varying the input PSD in a manner that minimises this error. At the point where the error is minimised the particle sizes input to the model are taken as the true values which were required to be measured. The mathematical formulation to the propagation model is core to the technique.

An important consideration for the success of the method is the way in which the PSD is input to the propagation model. It would be attractive to input particle sizes in a completely free format, in the form of a histogram of fractional volume versus particle size, for example. However, such an approach leads to many degrees of freedom in the adaptation procedure, whilst typical ultrasonic attenuation spectra are relatively featureless and can be approximated by a polynomial of order three or less. Scott *et al* [2, 3] have investigated this problem for a mineral slurry and have shown that the majority of particle sizes are ignored by the model inversion procedure - only two or three size classes were needed to determine the ultrasonic attenuation. It is thus necessary to model the PSD with an analytic function with the minimum number of parameters. There are many possibilities here but the most common is the log-normal distribution in which the number of particles in the size range r to $r + \mathrm{d}r$ in a mixture containing N particles is

$$dN = Np(r)dr\,, \tag{1}$$

where

$$p(r) = \frac{1}{2\pi\sigma}\exp\left[-\frac{1}{2}\left(\frac{\ln r - \mu}{\sigma}\right)^2\right] \tag{2}$$

and μ is the logarithmic mean and σ is the logarithmic deviation. The PSD is then expressed as the volume fraction $\varphi(r)$ of particles in the range r to $r + \mathrm{d}r$. For input to the wave propagation model this distribution is then sampled to extract between three and around eleven discrete particle sizes arranged logarithmically and symmetrically about the central size μ.

3 Wave Propagation Models

Theoretical treatments of the interactions between acoustic waves with obstacles suspended in a continuum have a very long history – extending back to the work of Rayleigh in the 19th century, and for a comprehensive review the reader is referred to [1]. For the purposes of particle sizing the most commonly used model is the scattering formulation due to Epstein and Carhart [4] and Allegra and Hawley [5], now known as the ECAH model. For the examination of solid-in-liquid suspensions, slurries, it may also be possible to use coupled phase theories such as Harker and Temple [6] and Evans and Attenborough [7]. Both classes of model yield a complex compression wavenumber

$$\beta = \frac{\omega}{c(\omega)} - i\alpha(\omega), \tag{3}$$

where $c(\omega)$ is the phase speed and $\alpha(\omega)$ is the attenuation coefficient, both as functions of frequency ω. The ECAH model is a spherical wave formulation which leads to the following expression for β

$$\left(\frac{\beta}{k_c}\right)^2 = 1 + \sum_{j=1}^{J} \left[\begin{array}{l} \dfrac{3\phi_j}{ik_c^3 R_j^3}\left(A_{0j} + 3A_{1j} + 5A_{2j}\right) \\ -\dfrac{27\phi_j^2}{k_c^6 R_j^6}\left(A_{0j}A_{1j} + 5A_{1j}A_{2j}\right) \\ -\dfrac{54\phi_j^2}{k_c^6 R_j^6}\left(A_{ij}^2 + \dfrac{5}{3}\right)A_{0j}A_{ij} + 5A_{ij}A_{2j} + \dfrac{115}{21}A_{2j}^2 \end{array} \right] \tag{4}$$

Here k_c is the wavenumber for the continuous phase, typically water. φ_j is the volume concentration of particles of radius R_j, and the partial coefficients A_{nj} represent various diffraction effects that contribute to the wavenumber for particles of the jth size. A_{0j} incorporates the effects of material substitution, the difference in compressibility between the phases of the mixture, and heat transfer between the phases; they dominate in the solution for emulsions and low density polymer colloids. A_{2j} incorporate resonances in the particles and are not significant at the frequencies generally used for particle sizing, typically less that 60 MHz. A_{1j}

dominate in the case of slurries and incorporate losses from the wave due to viscous drag between the particles and the continuous phase.

In the ECAH formulation the viscous loss mechanism is described by a non-propagating transverse (shear) wave emanating away from the suspended particle with bipole symmetry and a wavelength

$$\lambda_v = 2\pi(2\eta/\rho\omega)^{1/2} \qquad (5)$$

Here η is the viscosity of the continuous phase and ρ is the density. The equation applies to the dilute limit in which λ_v is very much less than the distance between the particles, Fig. 1. Now the shear wavelength at 10 MHz in water is 1060 nm and if we consider a suspension of particles of 400 nm diameter and assume simple cubic packing this wavelength corresponds to the mean inter-particle distance for a particle concentration of only 2.8% v/v.

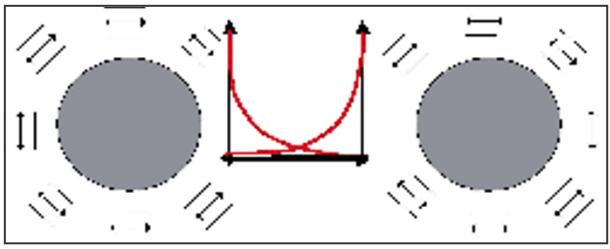

Fig. 1. Diagramatic representation of two suspended particles both diffracting non-propagating shear waves. As the particles come closer together the waves will interact.

This is the concentration limit above which the ECAH model begins to fail and predicts attenuations greater than those actually measured. Thus the ECAH model in its present form cannot be used for PSD estimation in realistic industrial slurries which can have solids concentrations up to, typically, 40% v/v. In order to develop the model for higher concentrations it will be necessary to research new theory for the effective viscosity in the vicinity of the suspended particles.

An alternative and useful model on which to base studies of the effects of viscosity on wave propagation in slurries is the coupled phase treatment of Harker and Temple [6]. With a little reworking their expression for complex wavenumber becomes

$$k^2 = \omega^2 \rho^* \beta^* . \frac{\phi(1-\phi)(\rho_f \rho_s / \rho^*) - i(\gamma/\omega)}{\phi(1-\phi)\rho' - i(\gamma/\omega)}, \tag{6}$$

where

$$\rho' = \phi\rho_f + (1-\phi)\rho_s , \tag{7}$$

$$\rho^* = \phi\rho_s + (1-\phi)\rho_f , \tag{8}$$

and

$$\beta^* = \phi\beta_s + (1-\phi)\beta_f . \tag{9}$$

The subscripts *f* and *s* refer to fluid (continuous phase) and solid (dispersed phase) respectively. γ is the drag coefficient which in its simplest form reduces to the Stokes force on *N* particles in a unit volume

$$\gamma = 6\pi R\eta \tag{10}$$

In principle, this expression can be extended to include more complex expressions for the effective viscosity η_{eff} through the use of a hydrodynamic correction factor *Q*

$$\eta_{eff} = Q\eta \tag{11}$$

We have used this expression with various forms for *Q* to benchmark the predictions of the ECAH coupled phase models against experimental data.

4 Viscosity Models

There is a vast literature associated with the viscosity of particulate suspensions which includes both formal theoretical approaches and empirical studies – indeed, there are so many different approaches that it is difficult to find a unifying theme. In the current study we have so far considered a small but nevertheless representative group of formulations. The simplest is due to Einstein [8], in which

$$\eta_{eff} = \eta(1 + k\phi) , \tag{12}$$

Where k is 2.5 for rigid spheres. The more complex models considered were: Vand [9-11], in which

$$Q = 1 + 2.5\phi + 7.349\phi^2 + ... \tag{13}$$

Hasimoto [12], in which

$$Q = \frac{1}{1 - 1.791\phi^{1/2} + \phi - 0.329\phi^2}, \tag{14}$$

Kuwabara [13], in which

$$Q = \frac{5}{5 - 9\phi^{1/2} + 5\phi - \phi^2}, \tag{15}$$

and Happel [14], in which

$$Q = \frac{2 + \frac{4}{3}\phi^{5/3}}{2 - 3\phi^{1/3} + 3\phi^{5/3} - 2\phi^2}. \tag{16}$$

We have also included the complex correction factor implied in Harker and Temple's paper [6] in which

$$\gamma = i\omega\phi\rho_f S, \tag{17}$$

where

$$S = \frac{1}{2}\left(\frac{1 + 2\phi}{1 - \phi}\right) + \frac{9}{4}\frac{\delta_v}{R} + i\frac{9}{4}\left(\frac{\delta_v}{R} + \frac{\delta_v^2}{R^2}\right)., \tag{18}$$

and the effective hydrodynamic correction factor is

$$Q = \frac{i\omega\phi\rho_f S}{6\pi R\eta_0}. \tag{19}$$

Due to limitations of space, we do not detail the physics underlying these models here – they have been reviewed by us in [1].

5 Experiments

The ultrasonic spectrometer instrument used to measure attenuation was built in-house some years ago [15]. The test colloid was monodisperse and consisted of 30 nm diameter silica spheres (Ludox) in an aqueous continuous phase. The suspension had a maximum concentration of approximately 35% solids v/v, and this was successively diluted to provide 12 samples with concentrations in the range 1% and 35% v/v. The attenuation spectrum was measured for all 12 samples in the frequency range up to 50 MHz and the attenuation value at 30 MHz was identified for comparison with the model predictions for various concentrations.

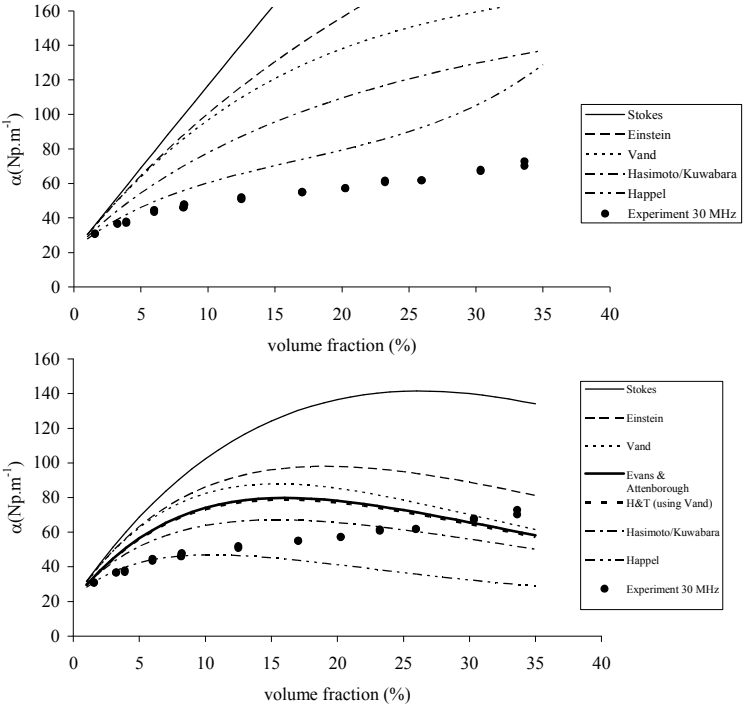

Fig. 2. Measured attenuation (Npm^{-1}) at 30 MHz versus concentration (volume fraction) for the 30 nm diameter silica suspensions (dots) compared to the predictions of the ECAH model (top) and the coupled phase model (bottom), with various viscosity functions included through the hydrodynamic correction factor *Q*.

The values of the attenuation at 30 MHz expected from the ECAH (Eq. 4) and coupled phase models (Eq. 6) with various hydrodynamic correction factors Q, based on Eqs. 11-17, were calculated as functions of volume concentration φ. The experimental data is compared to these calculations on Fig. 2 from which it will be seen that only the Happel model matches the experimental data but only up to a low concentration limit. All of the other models predict significantly different attenuations across the concentration range. It will be clear from these results that there is a requirement for new theoretical formulations for viscosity in the context of wave propagation in slurries.

Whilst the viscosity models cited above are functions of φ alone, we have explored the possibility that they may also be functions of frequency due, for example, to a dependence on shearing rate. For both the coupled phase and the ECAH models we have fitted viscosity functions in a least squared error sense to get the best match to experimental data – within error bounds of better than 1%. In the fitting procedure we have allowed the viscosity to be a complex function ($\eta = \eta_R + i\eta_I$) so as to include physical phenomena such as induced mass, at least notionally. The resulting viscosity functions are shown on Fig. 3, and the corresponding attenuations are shown on Fig 4. It will be clear from Fig. 4 that fitting of empirical functions to represent viscosity results in excellent agreement between measured and modelled attenuation data. For the ECAH model the best fits were obtained when the real part of the viscosity took the value for water (approximately 0.9 x 10^{-3} Pas) and a small negative imaginary component was added (value up to 6 x 10^{-6} Pas).

The implications of this are difficult to assess on the basis of current knowledge, but most probably have their origin in phenomena such as induced mass. This imaginary component was a fairly uniform function of frequency over the range up to 40 MHz. In contrast, for the coupled phase model good fits were obtained when the viscosity was wholly real and a function of both volume concentration and frequency. The 'required' viscosity showed a maximum value somewhere close to the middle of the concentration range, between 15% and 20% v/v. The fall-off at higher concentrations is to be expected, given the over-prediction in that range on Fig. 2. We note also that the fitted viscosity is a rising function of frequency up to around 30 MHz, above which the frequency dependence is negligible.

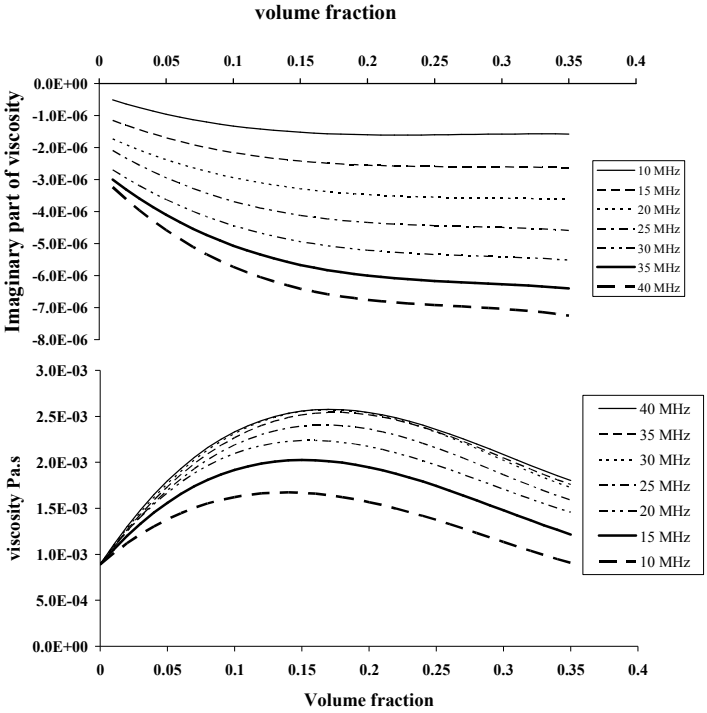

Fig. 3. Real viscosity versus volume concentration for the silica suspension – results from fitting to the ECAH model (top) and the coupled phase model (bottom).

6 Discussion and Conclusions

Ultrasonic compression wave attenuation, when measured as a function of frequency, can be used as the basis for techniques to measure PSD in slurries. It is known that the method works well for low solids loadings but tends to fail at higher concentrations – due to the shortcomings of the theoretical propagation models that are used in the analysis. It is believed that the origin of this failure can be found in the formulation of viscosity functions that are part of the models. This failure can be thought of as originating in overlaps between non-propagating viscosity waves diffracted from adjacent particles. The implication of this is that concepts of viscosity require further consideration in the context of wave propagation. Most literature on the subject of viscosity has as its basis problems in rheology in the context of chemical engineering. These approaches do not necessarily match the requirements for theoretical treatments of wave propagation

in slurries. It is likely that new research will arrive at formulations for viscosity that are functions of both concentration and frequency.

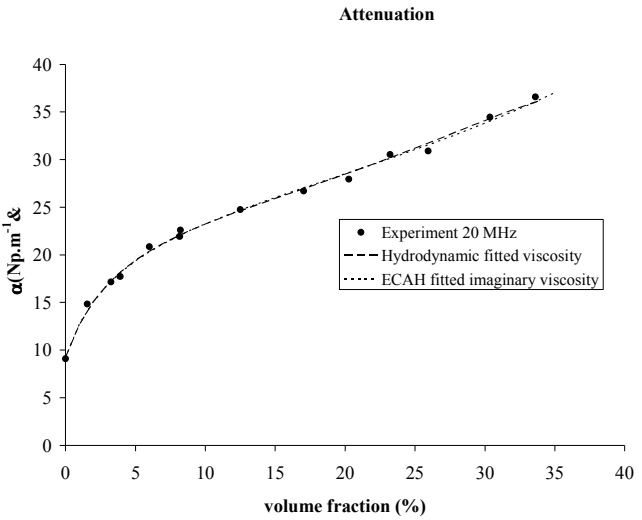

Fig. 4. Measured attenuation (dots) compared to the coupled phase (hydrodynamic) and ECAH models after fitting of empirical viscosity functions.

They will be further complicated by the requirement to include a wide range of particle sizes in the propagation medium – a problem that has not yet been solved satisfactorily in the context of rheology. It is also likely that any new viscosity functions will have imaginary parts in order to account for implicit dynamic phenomena apart from friction alone. We have also found that the empirical viscosity functions required to simulate wave attenuation data are different for the scattering (ECAH) and coupled phase approaches. This clearly unsatisfactory situation will require further understanding and resolution. We conclude that the mathematical formulation for viscosity in the context of wave propagation in slurries represents an exciting challenge for theoreticians, experimentalists, and ultimately, the designers of process instruments.

References

[1] Challis, R. E, Povey, M. J. W, Mather, M. L, and Holmes, A. K. (2005). "Ultrasound techniques for characterising colloidal dispersions." Reports on Progress in Physics, 68: 1541-1637.

[2] Scott, D. M., Boxman, A. and Jochen C. E. (1995). "Ultrasonic measurement of sub-micron particles." Part. Part. Syst. Charact. 12: 269-273.

[3] Scott, D. M., Boxman A., and Jochen, C. E. (1998). "In-line particle characterization." Part. Part. Syst. Charact. 15: 47-50.

[4] Epstein, P. S. and Carhart, R. R. (1953). "The absorption of sound in suspensions and emulsions. I. Water fog in air." J. Acoust. Soc. Am. 25: 553-565.

[5] Allegra, J. R. and Hawley, S. A. (1972). "Attenuation of sound in suspensions and emulsions: Theory and experiments." J. Acoust. Soc. Am. 51: 1545-1564.

[6] Harker, A. H. and Temple, J. A. G. (1988). "Velocity and attenuation of ultrasound in suspensions of particles in fluid." J. Phys. D: Appl. Phys. 21: 1576-1588.

[7] Evans, J. M. and Attenborough, K. (1997). "Coupled phase theory for sound propagation in emulsions." J. Acoust. Soc. Am. 102: 278-282.

[8] Einstein, A. (1906). "Eine neue Bestimmung der Molekul-dimensionen." Ann. Phys. 4: 289-306.

[9] Vand, V. (1948a). "Viscosity of solutions and suspensions. I. Theory." J. Phys. Colloid Chem. 52: 277-299.

[10] Vand, V. (1948b). "Viscosity of solutions and suspensions. II. Experimental determination of the viscosity-concentration function of spherical suspensions." J. Phys. Colloid Chem. 52: 300-314.

[11] Vand, V. (1948c). "Viscosity of solutions and suspensions. III. Theoretical interpretation of viscosity of sucrose solutions." J. Phys. Colloid Chem. 52: 314-321.

[12] Hasimoto, H. (1959). "On the periodic fundamental solutions of the Stokes equations and their application to viscous flow past a cubic array of spheres." J. Fluid Mech. 5: 317-328.

[13] Kuwabara, S. (1959). "The forces experienced by randomly distributed parallel circular cylinders or spheres in a viscous flow at small Reynolds numbers." J. Phys. Soc. Jap. 14(4): 527-532.

[14] Happel, J. (1957). "Viscosity of suspensions of uniform spheres." J. App. Phys. 28(11): 1288-1292.

[15] Challis R. E, Harrison, J.A, Holmes, A.K. and Cocker, R.P. (1991). “A wide bandwidth spectrometer for rapid ultrasonic absorption measurements in liquids”. J. Acoust. Soc. Am. 90(2): 730-740.

Dynamics of elastic bodies connected by a thin adhesive layer

C. Licht, F. Lebon and A. Léger

Abstract We study a problem of wave propagation in a structure made of two tridimensional elastic bodies connected by a thin adhesive layer. We recall that, after several heuristic models, the bonding problem, which basically amounts to study how does the thin layer can be replaced by a simpler model without thickness, has been carried out in the case of equilibrium problems. The present work deals with the dynamical problem. We obtain that the problem of elastodynamics with a thin adhesive layer can be approximated, with a convergence result, by another problem in which the layer is changed into a mechanical constraint, which is precisely the same as the one of the equilibrium case.

1 Introduction

We study the effect of a thin adhesive layer in a problem of elastodynamics. We recall that the problem of the modelling of bonded solids goes back to ancient studies in the field of physics and acoustics (see e.g. [12, 6]) and has essentially given rheological models consisting in changing the layer of the adhesive into an areal distribution of springs. This kind of models was used in many fields of wave propagation analyses such as for instance seismology [5]. But it was observed that the range of applicability of these rheological models has not been clearly established and lots of studies tried to back up the models either by comparisons with experiments or, up to very recently, by comparison with finite elements calculations in which a mesh of a thin layer was used to take the behavior of the adhesive into ac-

C. Licht
CNRS, Laboratoire de Mécanique et Génie Civil, Place Eugene Bataillon, 34095 Montpellier, France e-mail: licht@lmgc.univ-montp2.fr

F. Lebon and A. Léger
CNRS, Laboratoire de Mécanique et d'Acoustique, 31, chemin Joseph Aiguier, 13402 Marseille Cedex 20, France e-mail: lebon, leger@lma.cnrs-mrs.fr

count [14].

The purpose of the present work is to make a contribution to the way of modelling a system made of two elastic bodies connected by an adhesive joint, and in particular to give a mathematical justification of rheological models. We shall get that the models given by the physicists years ago can be justified rigorously, which will settle the problem of the range of applicability of a given model, but we shall also get that these models may fail in some physical situations.

Let us now outline the main steps of the paper.
A first section recalls the problem of justifying the effect of a thin adhesive layer in equilibrium problems. This section only stands for a motivation since the equilibrium case has now widely been treated. The main idea of the justication deals with taking the thinness of the adhesive layer into account by an asymptotic analysis. We state the problem for a given thickness of the layer and we look for a limit, this means that we look at the changes of the problem or at the behavior of its solution, as the layer is thinner and thinner. Among different methods using tools of asymptotic analyses, we recall very briefly the basic notions of variational convergence.
The next sections of the paper concerns the dynamical problem. The classical statement of the elastodynamical problem is transformed into a first order problem for the pair (displacement, velocity) which gives the form of a so-called semi-group depending on the set of the mechanical parameters of the problem. Then the last parts show that, as the parameters tend to zero, this semi-group converges, in a sense which will be given, towards a limit which gives the convenient model.

2 The equilibrium problem

The mechanical analysis of soft thin adhesive bonded joints between two deformable bodies involves problems with several parameters. At least two of them are essential: the thickness of the joint, which is small with respect to those of the deformable bodies and the stiffness of the joint, which is usually lower than that of the bodies. In previous studies (see e.g. [2, 4, 7, 8, 11]), the bonding of two three-dimensional solids by an adhesive layer, within linear elasticity, small strains or finite strains, or viscoelasticity, has been handled by performing asymptotic analyses, i.e. by assuming that the thickness and the stiffness of the layer tend to zero.

Within this approach, the layer is replaced by a mechanical constraint. The layer no longer exists from the geometrical point of view, but is replaced by a jump condition taking the asymptotic behaviour of the parameters into account. When the adhesive is linearly elastic, the limit problem involves a transmission condition linking the stress vector to the jump of the displacement which occurs at the interface $\sigma.n = \mathbb{K}[u]$. The structure of this interface law is similar in this case to that of the original constitutive equation, but the strain tensor is replaced by the symmetrized

tensorial product of the displacement jump by the unit normal vector. The coefficients of the tensor $\mathbb{K}$ keeps the memory of the stiffness parameters of the original material. For example, for two-dimensional domains made of isotropic elastic material, the stiffness $\mathbb{K}$ is a diagonal tensor which can be shared into normal and tangential parts:

$$\mathbb{K}_N = \lim_{s\to 0} \frac{\lambda + 2\mu}{\varepsilon},\ \mathbb{K}_T = \lim_{s\to 0} \frac{\mu}{\varepsilon}.$$

ε is the thickness of the adhesive, λ and μ are the Lamé coefficients of the adhesive, and parameter s stands for the triplet $(\lambda, \mu, \varepsilon)$. This result can be proved rigorously using variational convergence arguments [10]. Variational convergence is a notion of convergence of sequences of functions introduced during the 70's (see e.g. [3]). Let $\mathscr{F}^s$ be an energy functional and let u_s be a minimum of this functional (i.e. an equilibrium state in equilibrium problems). The idea of the variational convergence is to define the "lowest" notion of convergence of $\mathscr{F}^s$ to some functional $\mathscr{F}$ when s tends to zero, which implies the convergence of both the minima and the minimizers of $\mathscr{F}^s$ to those of $\mathscr{F}$.

In the case of the thin layer, the sequence $\{\mathscr{F}^s\}$ corresponds to the total energy in the adherents and in the adhesive. The variational limit is a sum of the total energy of the adherents together with an areal energy on a surface S which is the geometrical limit of the part of the domain made of the adhesive as its tickness tends to zero. The latter areal energy is given by:

$$\int_S \frac{1}{2}\mathbb{K}[u]^2 ds.$$

The rigorous proof of this result is obtained using a regularization operator R^ε which gives a good approximation of the solution u_s in the adhesive. For example, if the adhesive layer of thickness ε lies along a plane orthogonal to the third direction, the regularization can be taken as:

$$R^\varepsilon u(.,x_3) = \frac{1}{2}\left\{u(.,\frac{\varepsilon}{2}) + u(.,-\frac{\varepsilon}{2}) + \min(1,\frac{|x_3|}{\varepsilon})(u(.,\frac{\varepsilon}{2}) - u(.,-\frac{\varepsilon}{2}))\right\}.$$

We now just recall the results in the form of the set of possible behaviors of the rheological model which can be used to replace the thin layer and to understand the equilibrium of the system adherent-adhesive under external loads. This is given in Table 1. It is worth seeing that some cases give exactly a rheological behavior with the explicit stiffness of the springs in the normal and tangential direction, but some other cases do not.

$\mu/\varepsilon \to 0$	$\sigma_N = 0,$ $\sigma_T = 0.$	$\sigma_N = \bar{\lambda}\,[u_N]\,,$ $\sigma_T = 0.$	$[u_N] = 0,$ $\sigma_T = 0.$
$\mu/\varepsilon \to \bar{\mu}$	$\sigma_N = 2\bar{\mu}\,[u_N]\,,$ $\sigma_T = \bar{\mu}\,[u_T]\,.$	$\sigma_N = (\bar{\lambda} + 2\bar{\mu})\,[u_N]\,,$ $\sigma_T = \bar{\mu}\,[u_T]\,.$	$[u_N] = 0,$ $\sigma_T = \bar{\mu}\,[u_T].$
$\mu/\varepsilon \to \infty$	$[u_N] = 0,$ $[u_T] = 0.$	$[u_N] = 0,$ $[u_T] = 0.$	$[u_N] = 0,$ $[u_T] = 0.$
	$\lambda/\varepsilon \to 0$	$\lambda/\varepsilon \to \bar{\lambda}$	$\lambda/\varepsilon \to \infty$

Table 1 Transmission conditions

3 Statement of the dynamical problem

Let Ω be a tridimensional domain with a Lipschitz continuous boundary having an intersection with the plane $\{x_3 = 0\}$ of non zero measure denote by S. Let this domain be divided into $\Omega^\varepsilon := \{x \in \Omega, |x_3| > \varepsilon\}$ and $B^\varepsilon := \{x \in \Omega, |x_3| < \varepsilon\}$. The parts Ω^ε will be referred to as the bodies, and the layer B^ε as the adhesive. The equations of the dynamics are the following:

$$(\mathscr{P}_s) \quad \begin{cases} \gamma \dfrac{\partial^2 \mathrm{u_s}}{\partial t^2} - \mathrm{div}\sigma_\mathrm{s} = \mathrm{f} \quad \text{in } \Omega \times [0,\mathrm{T}] \\ \\ \sigma_s = \begin{cases} a\mathrm{e}(\mathrm{u_s}) \ \text{ in } \Omega^\varepsilon \times [0,\mathrm{T}] \\ \lambda \mathrm{tr}(\mathrm{e}(\mathrm{u_s}))\mathbb{I}\mathrm{d} + 2\mu \mathrm{e}(\mathrm{u_s}) \ \text{ in } \mathrm{B}^\varepsilon \times [0,\mathrm{T}] \end{cases} \\ \sigma_s n = g \ \ on\ \Gamma_1, \ \ \mathrm{u_s} = 0 \ \text{ on } \Gamma_0, \\ \mathrm{u_s}(\mathrm{x},0) = \mathrm{u_s^0}(\mathrm{x}), \ \ \mathrm{v_s^0} = \dfrac{\partial \mathrm{u_s}(\mathrm{x},0)}{\partial \mathrm{t}} \quad \forall \mathrm{x} \in \Omega. \end{cases} \tag{1}$$

(λ, μ) in B^ε and a in Ω^ε are the elasticity coefficients which are assumed to satisfy:
i) $a \in \mathbb{L}^\infty\left(\Omega; \mathscr{L}in(\mathbb{S}^3)\right)$; $\exists \alpha > 0$ such that $a(x)\xi.\xi \geq \alpha |\xi|^2_{\mathbb{S}^3}$ a. e. in $\Omega \ \ \forall \xi \in \mathbb{S}^3$, $\mathscr{L}(\mathbb{S}^3)$ denotes the space of linear operators from the set $\mathbb{S}^3$ of symmetrical 3×3 matrixes onto itself;
ii) λ and μ are positive real numbers which will tend to zero.
The voluminal mass γ is such that:
i) $\exists \bar{\rho} \in \mathbb{L}^\infty(\Omega)$ such that $\bar{\rho}(x) \geq \rho_m > 0$ a. e. in Ω
ii) $\gamma(x) = \bar{\rho}(x)$ a. e. in Ω^ε, $\gamma(x) = \rho$ a. e. in B^ε, where ρ is a positive real number assumed to have a limit $\rho_L \geq 0$.
u_s is the displacement field, v_s the velocity field, σ_s the stress field and n the outer normal, (f, g) are the given external loads for which we assume that $\exists \varepsilon_0$ such that $supp(g) \cap B^\varepsilon \neq \emptyset$

The index s means that this problem depends on a quadruplet of parameters $s := (\lambda, \mu, \varepsilon, \rho)$. It is well known that for smooth enough data f and g, this problem possesses a single solution u_s.
We now aim at studying the behavior of problem $(\mathscr{P}_s)$ as the parameter s tends to zero. This is more easily carried out if we first put problem $(\mathscr{P}_s)$ in the form of an evolution equation in a convenient function space which will be the set of admissible states of finite energy.

4 Changing the formulation of the problem

In order to study problem $(\mathscr{P}_s)$ we first introduce the classical function space (see e.g. [1]) $\mathbb{H}^1_{\Gamma_0}(\Omega)^3 = \left\{\mathrm{u} \in \mathbb{H}^1(\Omega)^3; \mathrm{u} = 0 \text{ on } \Gamma_0\right\}$ and the following notations so that we shall go on with simple formula:

$$\begin{aligned} &\text{for } \phi, \psi \in \mathbb{H}^1_{\Gamma_0}(\Omega)^3, \\ &a_s(\phi, \psi) = \int_{\Omega^\varepsilon} a\mathrm{e}(\phi).\mathrm{e}(\psi)dx \ + \ \int_{B^\varepsilon} \lambda \mathrm{tr}(\mathrm{e}(\phi))\mathrm{tr}(\mathrm{e}(\psi)) + 2\mu \mathrm{e}(\phi)\mathrm{e}(\psi)\mathrm{dx}. \end{aligned} \tag{2}$$

We then make the following regularity assumption on the surface loads:

Assumption $\mathbb{H}_1$
$g \in \mathbb{C}^{2,1}([0,T]; \mathbb{L}^2(\Omega)^3)$.

Assumption $\mathbb{H}_1$ implies

$$\exists!\ \mathrm{u}^{\mathrm{e}}_{\mathrm{s}} \in \mathbb{C}^{0,1}([0,\mathrm{T}]; \mathbb{H}^1_{\Gamma_0}(\Omega)^3); \quad \mathrm{a_s}(\mathrm{u}^{\mathrm{e}}_{\mathrm{s}}, \phi) = \int_{\Gamma_1} \mathrm{g}\phi \mathrm{ds}, \ \ \forall \phi \in \mathbb{H}^1_{\Gamma_0}(\Omega)^3).$$

The phase space is then $\mathbb{H}_s = \left\{\mathrm{U} = (\mathrm{u}, \mathrm{v}) \in \mathbb{H}^1_{\Gamma_0}(\Omega)^3 \times \mathbb{L}^2(\Omega)^3\right\}$ endowed with the hilbertian norm and scalar product:

$$|\mathrm{U}|^2_{\mathbb{H}_\mathrm{s}} = |(\mathrm{u}, \mathrm{v})|^2_{\mathbb{H}_\mathrm{s}} := \mathrm{a_s}(\mathrm{u}, \mathrm{u}) + \int_\Omega \gamma \mathrm{v}\mathrm{v}\mathrm{dx}; \ \ (\mathrm{U}, \mathrm{U}') = \mathrm{a_s}(\mathrm{u}, \mathrm{u}') + \int_\Omega \gamma \mathrm{v}\mathrm{v}'\mathrm{dx}.$$

Let us now define in $\mathbb{H}_s$ an unbounded operator $\mathbb{A}_s$ with a domain $\mathbb{D}(\mathbb{A}_s)$ as:

$$\begin{cases} \mathbb{D}(\mathbb{A}_s) = & \{\mathrm{U} = (\mathrm{u}, \mathrm{v}) \in \mathbb{H}_\mathrm{s}; \mathrm{v} \in \mathbb{H}^1_{\Gamma_0}(\Omega)^3) \text{ and } \exists!\ \mathrm{w} \in \mathbb{L}^2(\Omega)^3 \ \text{ such that} \\ & \int_\Omega \gamma w.\phi dx \ + \ \mathrm{a_s}(\mathrm{u}, \phi) \ = \ 0, \ \forall \phi \in \mathbb{H}^1_{\Gamma_0}(\Omega)^3\} \\ \mathbb{A}_s \mathrm{U} = \mathbb{A}_\mathrm{s}(\mathrm{u}, \mathrm{v}) = (\mathrm{v}, \mathrm{w}), \end{cases} \tag{3}$$

in such a way that, if

$$\mathrm{U_s^r} = (\mathrm{u_s^r}, \mathrm{v_s^r}) := (\mathrm{u_s} - \mathrm{u_s^e}, \mathrm{v_s} - \mathrm{v_s^e}) \text{ and } \mathrm{F_s} = (0, \frac{\mathrm{f}}{\gamma} - \frac{\mathrm{dv_s^e}}{\mathrm{dt}}),$$

then problem $(\mathscr{P}_s)$ is formally equivalent to the evolution equation in $\mathbb{H}_s$:

$$\frac{\mathrm{dU_s^r}}{\mathrm{dt}} = \mathbb{A}_s \mathrm{U_s^r} + \mathrm{F_s}, \;\; \mathrm{U_s^r}(0) = (\mathrm{u_s^0} - \mathrm{u_e}(0), \mathrm{v_s^0} - \dot{\mathrm{v}}_\mathrm{e}(0)). \tag{4}$$

Theorem 1. *Let assumption* $\mathbb{H}_1$ *be satisfied and assume* $\mathrm{f} \in \mathbb{C}^{0,1}([0,T];\mathbb{L}^2(\Omega)^3)$ *and* $\mathrm{U}^s \in \mathbb{D}(\mathbb{A}_s)$*, then problem* $(\mathscr{P}_s)$ *possesses a unique solution in* $\mathbb{C}^1([0,T];\mathbb{H}_s) \cap \mathbb{C}^0([0,T];\mathbb{D}(\mathbb{A}_s))$.

Due to Stone's theorem, the proof of theorem 1 just requires to show that operator $\mathbb{A}_s$ is skew-adjoint. First, from the definition of operator $\mathbb{A}_s$ we have $\forall\ \mathrm{U} = (\mathrm{u}, \mathrm{v}) \in \mathbb{D}(\mathbb{A}_\mathrm{s})$, $(\mathbb{A}_\mathrm{s}\mathrm{U}, \mathrm{U})_{\mathbb{H}_\mathrm{s}} = \int_\Omega \gamma \mathrm{w}.\mathrm{v}\,\mathrm{dx} + \mathrm{a_s}(\mathrm{u}, \mathrm{v}) = 0$. Secondly, given an arbitrary $\boldsymbol{\Phi} = (\boldsymbol{\Phi}^1, \boldsymbol{\Phi}^2)$ in $\mathbb{H}_s$, it is clear that for U such that $\mathrm{U} - \mathbb{A}_\mathrm{s}\mathrm{U} = \boldsymbol{\Phi}$ we have:

$$\mathrm{u} \in \mathbb{H}^1_{\Gamma_0}(\Omega)^3, \;\; \int_\Omega \gamma(\mathrm{u}, \boldsymbol{\Phi}^1 - \boldsymbol{\Phi}^2)\phi\,\mathrm{dx} + \mathrm{a_s}(\mathrm{u}, \phi) = 0 \;\; \forall \phi \in \mathbb{H}^1_{\Gamma_0}(\Omega)^3. \tag{5}$$

The existence and uniqueness of u follows from Lax-Milgram lemma, and then:

$$\mathrm{U} := (\mathrm{u}, \mathrm{u} - \boldsymbol{\Phi}^1) \in \mathbb{D}(\mathbb{A}_\mathrm{s}),\ \mathrm{U} - \mathbb{A}_\mathrm{s}\mathrm{U} = \boldsymbol{\Phi}. \tag{6}$$

5 The asymptotic behavior as the parameters tend to zero

We shall now make use of Trotter's theory about the convergence of semi-groups of operators acting on variable Hilbert spaces. Let us first recall a brief definition of a semigroup. The notion of semi-groups follows from that of groups by removing the requirement of a symmetrical element. In the case of sets of operators this notion can be understood by the following example which can be seen as a basic introduction to the flows in the theory of ordinary differential equations. Let us assume that an ordinary differential equation of the following form is given:

$$\frac{du}{dt} = \mathbb{T}u,$$

the latter being associated with some initial data $u(0)$ and $\mathbb{T}$ being some operator whose domain and properties will be given explicitly in the particular case we shall deal with. The solution is then formally $u^t := g^t u(0)$ and satisfies:
i) for any positive real numbers t_1 and t_2, $g^{t_1+t_2} = g^{t_1}.g^{t_2}$,
ii) $g(0) = \mathbb{I}$.
The set $\{g^t\}$ for $0 < t < \infty$ is called a one parameter semi-group generated by $\mathbb{T}$.

Let us now come back to problem $(\mathscr{P}_s)$ and to its transformation into equa-

tion (4). Assume that the elasticity coefficients are such that the ratio λ/ε and μ/ε have finite limits as the thichness tends to zero: $\lambda/\varepsilon \longrightarrow \bar{\lambda} \in (0,+\infty)$ and $\mu/\varepsilon \longrightarrow \bar{\mu} \in (0,+\infty)$. This can be seen as a nondegeneracy assumption, but the cases $\bar{\lambda},\bar{\mu} \in \{0,+\infty\}$ could be more or less studied in the same way.

Let $\mathbb{H}^1_{\Gamma_0}(\Omega\backslash S)^3 = \left\{ \mathrm{u} \in \mathbb{H}^1(\Omega\backslash \mathrm{S})^3;\ \mathrm{u} = 0 \text{ on } \Gamma_0 \right\}$. For any $\mathrm{u} \in \mathbb{H}^1_{\Gamma_0}(\Omega\backslash \mathrm{S})^3$ let us now define two functions u^+ and u^- as elements of $\mathbb{H}^1(\Omega^\pm)$ which are the restrictions of functions u to $\Omega^\pm = \{x \in \Omega;\ \pm x_3 > 0\}$. In this way we can define a jump $[\mathrm{u}] \in \mathbb{L}^2(\mathrm{S})$ as the difference between the traces on S of u^+ and u^-. Let n be the third axis of the frame of $\mathbb{R}^3$ that is the normal vector to S oriented from Ω^- to Ω^+, and for any vector ξ of $\mathbb{R}^3$ let us denote $\xi_N = \xi.n$ and $\xi \otimes_s \eta = \frac{1}{2}(\xi \otimes \eta + \eta \otimes \xi);\ \xi,\eta \in \mathbb{R}^3$.
We can now define a continuous $\mathbb{H}^1_{\Gamma_0}(\Omega\backslash S)^3 -$elliptical bilinear form on $\mathbb{H}^1_{\Gamma_0}(\Omega\backslash S)^3$ as:

$$\begin{aligned} &\text{for } \phi,\psi \in \mathbb{H}^1_{\Gamma_0}(\Omega)^3, \\ &a(\phi,\psi) = \int_{\Omega\backslash S} a\mathrm{e}(\phi).\mathrm{e}(\psi)dx \ + \ \int_S \bar{\lambda}[\phi]_N[\psi]_N + 2\bar{\mu}[\phi] \otimes_s n.[\psi] \otimes_s n d\hat{x}, \end{aligned} \tag{7}$$

where $\hat{x}$ denotes (x_1,x_2) if x is (x_1,x_2,x_3).
The space $\mathbb{H}$ of finite energy states in which the problem governing the asymptotic behavior of $\mathrm{u_s}$ will be formulated is then:

$$\mathbb{H} = \left\{ \mathrm{U} = (\mathrm{u},\mathrm{v}) \in \mathbb{H}^1_{\Gamma_0}(\Omega\backslash \mathrm{S})^3 \times \mathbb{L}^2(\Omega)^3 \right\} \tag{8}$$

endowed with the following norm and scalar product:

$$|\mathrm{U}|^2_{\mathbb{H}} = |(\mathrm{u},\mathrm{v})|^2_{\mathbb{H}} := \mathrm{a}(\mathrm{u},\mathrm{u}) + \int_\Omega \bar{\rho}|\mathrm{v}|^2 \mathrm{dx};\ \ (\mathrm{U},\mathrm{U}')_{\mathbb{H}} = \mathrm{a}(\mathrm{u},\mathrm{u}') + \int_\Omega \bar{\rho}\mathrm{v}.\mathrm{v}'\mathrm{dx}.$$

Since the space $\mathbb{H}$ of states of finite energy is different from the natural phase space $\mathbb{H}_s$, we introduce a family of linear operators from $\mathbb{H}$ to $\mathbb{H}_s$, $\mathbb{P}_s \in \mathscr{L}(\mathbb{H},\mathbb{H}_s)$, which aim at "comparing" an element of $\mathbb{H}$ with an element of $\mathbb{H}_s$:

$$\begin{aligned} &\mathrm{U} = (\mathrm{u},\mathrm{v}) \in \mathbb{H} \longrightarrow \mathbb{P}_\mathrm{s}\mathrm{U} = (\mathrm{u_s},\mathrm{v_s}) \in \mathbb{H}_\mathrm{s}, \\ &\mathrm{u_s}(\mathrm{x}) = \mathbb{R}_\varepsilon \mathrm{u}(\mathrm{x}) := \tfrac{1}{2}\left\{ \mathrm{u}(\hat{\mathrm{x}},\mathrm{x_3}) + \mathrm{u}(\hat{\mathrm{x}},-\mathrm{x_3}) \ + \ \min(\tfrac{|\mathrm{x_3}|}{\varepsilon},1)(\mathrm{u}(\hat{\mathrm{x}},\mathrm{x_3}) - \mathrm{u}(\hat{\mathrm{x}},-\mathrm{x_3}))\right\}, \\ &\mathrm{v_s}(\mathrm{x}) = \mathrm{v}(\mathrm{x}) \text{ if } \mathrm{x} \in \Omega^\varepsilon,\ \ \mathrm{v_s}(\mathrm{x}) = \mathrm{v}(\mathrm{x}).\left(\tfrac{\bar{\rho}(\mathrm{x})}{\rho}\right)^{1/2} \text{ if } \mathrm{x} \in \mathrm{B}^\varepsilon. \end{aligned} \tag{9}$$

It is fundamental to observe that:

$$\begin{aligned} &i)\ \exists\, C > 0, |\mathbb{P}_s\mathrm{U}|_{\mathbb{H}_\mathrm{s}} \leq \mathrm{C}|\mathrm{U}|_{\mathbb{H}},\ \forall \mathrm{U} \in \mathbb{H},\ \ \forall \mathrm{s} \neq 0, \\ &ii)\ \lim_{s\to 0} |\mathbb{P}_s\mathrm{U}|_{\mathbb{H}_\mathrm{s}} = |\mathrm{U}|_{\mathbb{H}}. \end{aligned} \tag{10}$$

In the same way, for $s \neq 0$, it is clear that:

$$\exists!\ u^e \in \mathbb{C}^{0,1}([0,T];\mathbb{H}^1_{\Gamma_0}(\Omega\backslash S)^3);\ \text{such that}\ a_s(u^e,\phi) = \int_{\Gamma_1} g\phi ds,\ \ \forall \phi \in \mathbb{H}^1_{\Gamma_0}(\Omega\backslash S)^3),$$

and we define the operator $\mathbb{A}$ as:

$$\begin{cases} \mathbb{D}(\mathbb{A}) = \begin{array}{l} \{U=(u,v)\in\mathbb{H}; v\in\mathbb{H}^1_{\Gamma_0}(\Omega\backslash S)^3) \text{ and } \exists!\ w\in\mathbb{L}^2(\Omega)^3 \text{ such that} \\ \displaystyle\int_\Omega \bar{\rho} w.\phi dx \ +\ a(u,\phi)\ =\ 0,\ \forall \phi\in\mathbb{H}^1_{\Gamma_0}(\Omega\backslash S)^3\} \end{array} \\ \mathbb{A}U = \mathbb{A}(u,v) = (u,v), \end{cases} \tag{11}$$

Let us now introduce $F = (0, \dfrac{f}{\bar{\rho}} - \dfrac{du^e}{dt})$ and consider the following evolution equation in $\mathbb{H}$:

$$\frac{dU^r}{dt} = \mathbb{A}U^r + F,\ \ U^r(0) = U^r_0. \tag{12}$$

In the same way as for operator $\mathbb{A}_s$, it is clear that operator $\mathbb{A}$ is skew-adjoint in $\mathbb{H}$, so that we have:

Theorem 2. *Let assumption $\mathbb{H}_1$ be satisfied and assume $f \in \mathbb{C}^{0,1}([0,T];\mathbb{L}^2(\Omega)^3)$ and $U^r_0 \in \mathbb{D}(\mathbb{A})$, then equation (12) possesses a unique solution in $\mathbb{C}^1([0,T];\mathbb{H}) \cap \mathbb{C}^0([0,T];\mathbb{D}(\mathbb{A}))$.*

It is easily shown that $u := u^r + u^e$ satisfies formally the following problem $(\mathscr{P})$

$$(\mathscr{P})\ \begin{cases} \bar{\rho}\dfrac{\partial^2 u}{\partial t^2} - \mathrm{div}\sigma = f \ \ \text{in}\ \Omega\backslash S\times[0,T] \\ \\ \sigma_s = ae(u)\ \ \text{in}\ \Omega\backslash S\times[0,T] \\ \sigma n = g\ \ \textit{on}\ \Gamma_1,\ \ u_s = 0\ \ \textit{on}\ \Gamma_0, \\ \\ \begin{cases} u(x,0) = u^r_0(x) + u^e(x,0) = u^O(x), \\ \partial_t u(x,0) = v^r_0(x) + \partial_t u^e(x,0) := v^O(x) \end{cases} \quad \forall x\in\Omega \\ \textbf{and} \\ [\sigma n] = 0,\ \ \sigma n + \lambda [u]_n n + 2\mu [u]\otimes_s n = 0\ \ \text{on S}. \end{cases} \tag{13}$$

It remains to show that u_s converges to u when $s \longrightarrow 0$. Let us recall the following result which has been established in the static case [10].

Proposition 1. *If $s \longrightarrow 0$, then $u^e_s \longrightarrow u^e$ in $\mathbb{L}^2(\Omega)^3$, $u_s \longrightarrow u$ in $\mathbb{H}^1(\Omega^\eta)^3$, $\forall\ \eta > 0$, $a_s(u^e_s, u^e_s) \longrightarrow a(u^e,u^e)$ and $u^e_s|_{x_3=\varepsilon} - u^e_s|_{x_3=-\varepsilon} \longrightarrow [u^e]$ in $\mathbb{L}^2(S)$.*

This gives the convergence of U^e_s towards U^e. The convergence of U^r_s towards U^r will be given by Trotter's theory of approximation of semi-groups which roughly says that "if the stationary problems are converging, then the dynamical problems will also converge". More precisely (see [13])

Theorem 3. *Assume operators* $\mathbb{A}_s$ *and* $\mathbb{A}$ *are anti-adjoint in the Hilbert spaces* $\mathbb{H}_s$ *and* $\mathbb{H}$ *and satisfy (9) and (10). Assume in addition:*
i) $\lim_{s\to 0} |\mathbb{P}_s(\mathbb{I}-\mathbb{A})^{-1}f-(\mathbb{I}-\mathbb{A}_s)^{-1}\mathbb{P}_s f|_{\mathbb{H}_s}=0 \ \forall f\in\mathbb{H}$,
ii) $\lim_{s\to 0} |\mathbb{P}_s U^0-U_s^0|_{\mathbb{H}_s}$, ,
iii) $\lim_{s\to 0}\int_0^T |\mathbb{P}_s\mathscr{F}_s(t)-\mathscr{F}_s(t)|_{\mathbb{H}_s}dt=0$,
If U_s *and* U *are respectively the solutions to equations* $\dfrac{dU_s}{dt}=\mathbb{A}_s U_s+\mathscr{F}_s,\ U_s(0)=U_s^0$ *and* $\dfrac{dU}{dt}=\mathbb{A}U+\mathscr{F},\ U(0)=U^0$,
then $\lim_{s\to 0}\mathrm{Sup}\left\{|\mathbb{P}_s U(t)-U_s(t)|_{\mathbb{H}_s},\ t\in[0,T]\right\}=0$.

This abstract result allows us to establish:

Theorem 4. *Let assumption* $\mathbb{H}_1$ *be satisfied and assume* $f\in\mathbb{C}^{0,1}([0,T];\mathbb{L}^2(\Omega)^3)$. *Assume in addition that*

$$\begin{array}{l}\lim_{s\to 0}|\mathbb{P}_s U^0-U_s^0|_{\mathbb{H}_s}=0,\ U^0-U^e(0)\in\mathbb{D}(\mathbb{A}),\ U_s^0-U_s^e(0)\in\mathbb{D}(\mathbb{A}_s)\\ (\text{conpatibility/convergence assumption}),\end{array}\tag{14}$$

then the solutions U_s^r *and* U^r *of problems (4) and (12) satisfy:*
$\lim_{s\to 0}\mathrm{Sup}\left\{|\mathbb{P}_s U^r(t)-U_s^r(t)|_{\mathbb{H}_s},\ t\in[0,T]\right\}=0$.

Remark 1. This Trotter's convergence (that is $\lim_{s\to 0}|\mathbb{P}_s U^0-U_s^0|_{\mathbb{H}_s}=0$) is very natural and seems well suited from a mechanical point of view since it deals with a gap of energy, but it may be reassuring to compare this convergence with more usual points of view. This is the purpose of the next proposition.

Proposition 2. *i) if* $\lim_{s\to 0}|\mathbb{P}_s U-U_s|_{\mathbb{H}_s}$, *then* $u_s\longrightarrow u$ *in* $\mathbb{L}^2(\Omega)^3$ *and* $u_s\longrightarrow u$ *in* $\mathbb{H}^1(\Omega^\eta)^3,\ \forall\,\eta>0$,
ii) if $a_s(u_s,u_s)\longrightarrow a(u,u)$ *and* $a_s(R_\varepsilon u,u_s)\longrightarrow a(u,u)$ *then* $\lim_{s\to 0}a_s(R_\varepsilon u-u_s,R_\varepsilon u-u_s)=0$.
Proof:
The assumption of point i) implies that $a_s[u_s,u_s)$ is bounded, so that the result is established in [9] or [10].
Point ii) follows immediately from the already noticed fact that $a_s(R_\varepsilon u,R_\varepsilon u)\longrightarrow a(u,u)$.

We can now prove theorem 4.
The proof simply consists in showing that assumptions i), ii) and iii) of Trotter's theorem are satisfied.
Points ii) and iii) are immediate consequences of assumption $\mathbb{H}_1$ together with propositions 1 and 2.

Remark 2. There exists many initial data satisfying (14):

$$U_s^0-U_s^e(0):=(\mathbb{I}-\lambda\mathbb{A})^{-1}\mathbb{P}_s(\mathbb{I}-\lambda\mathbb{A})(U^0-U^e(0))\ \ \forall\lambda\in\mathbb{R}\backslash\{0\},$$

since one has Trotter's convergence of the resolvants of operators $\mathbb{A}$ and $\mathbb{A}_s$.

Let's now focuss on point i). Let $U = (u, v)$ and $U_s = (u_s, v_s)$ satisfying respectively $U - \mathbb{A}U = \Phi$ and $U_s - \mathbb{A}_s U_s = \mathbb{P}_s \Phi$. From equations (5) and (6) we have:

$$\begin{cases} u_s \in I\!H^1_{\Gamma_0}(\Omega)^3, \\ \displaystyle\int_\Omega \gamma u_s . \phi \, dx + a_s(u_s, \phi) \;=\; \int_\Omega \gamma(\Phi_s^1 + \Phi_s^2)\phi \, dx \;\; \forall \phi \in I\!H^1_{\Gamma_0}(\Omega)^3. \\ v_s = u_s - \Phi_s^1, \end{cases} \tag{15}$$

$$\begin{cases} u \in I\!H^1_{\Gamma_0}(\Omega)^3, \\ \displaystyle\int_\Omega \gamma u . \phi \, dx + a(u, \phi) \;=\; \int_\Omega \gamma(\Phi^1 + \Phi^2)\phi \, dx \;\; \forall \phi \in I\!H^1_{\Gamma_0}(\Omega)^3. \\ v = u - \Phi^1. \end{cases} \tag{16}$$

This means that u and u_s are solutions to a perturbation of equilibrium bonding problems, so that we only have to establish the convergence of the equilibrium problems, which has been carried out in [10]. Using the same tools we get that conditions ii) of proposition 2 are satisfied, which in turn establishes point i) of Trotter's theorem.

6 Concluding remarks

Starting from the physical problem $(\mathscr{P}_s)$ of the wave propagation in two linearly elastic solids connected by a layer of thickness ε we have obtained a limit problem $(\mathscr{P})$ when the parameter s tends to zero, i.e. when the thickness ε of the layer tends to zero together with assumptions on the voluminal mass and on the elasticity coefficients. The mathematical meaning of this convergence result is that the dynamical behavior of two solids connected by a thin soft layer is asymptotically equivalent to the one of two solids connected by the following mechanical constraint:

$$\sigma n = \bar{\lambda}[u]_n \mathbb{I}d + 2\bar{\mu}[u] \otimes_s n = 0 \quad \text{with } \bar{\lambda}, \bar{\mu} = \lim(\lambda, \mu)/\varepsilon \tag{17}$$

The main worth seeing point is that condition (17) is the stationary condition which is obtained at the limit of the equilibrium bonding problem, which has been recalled in the first section. This has been explicitely carried out here in the case when the limits $\bar{\lambda}$ and $\bar{\mu}$ are finite and different from zero. The remaining cases $\bar{\lambda}, \bar{\mu} \in \{0, \infty\}$ could be handled with very slight changes so that it is not useful to write down this cases again here. Only the case where the voluminal mass ρ tends to infinity may be more difficult but this case is probably less interesting from a physical point of view.

Now it seems interesting to close this paper by some comments on the mechanical meaning of the result. According to the different cases of the limit behavior of the parameters, the set of results is given in Table 1. Let us describe the result in some particular cases.

- The case where $\lambda/\varepsilon \longrightarrow \bar{\lambda}$ and $\mu/\varepsilon \longrightarrow \bar{\mu}$ corresponds to the physical situation where the thickness of the layer is small with respect to the diameter of the whole domain and the stiffness of the layer is also small, "at the same order" with respect to the one of both other parts of domain. This could be seen as the generic case. The meaning of the result is that the thin layer will behave as a line of springs both in the normal and in the tangential directions. In a numerical model, say by a finite element method, the thin layer could be replaced by a set of linear elastic relations between the opposite nodes, with stiffnesses given by the limit problem.
- But when the thickness and the stiffness of the layer are both small but in such a way that the ratio of the thickness of the layer with respect to the diameter of the whole domain is much smaller than the ratio of the stiffnesses, the result is very different. This situation will correspond to the case where $\lambda/\varepsilon \longrightarrow \infty$ and $\mu/\varepsilon \longrightarrow \infty$ and the body will globally behave as two half bodies perfectly stuck.
- On the contrary if the physical problem is such that the thickness and the stiffness of the layer and both small but in such a way that the ratio of the thickness of the layer with respect to the diameter of the whole domain is much larger than the ratio of the stiffnesses then the body will behave as two completely separated parts.
- In intermediate cases which will for instance be modelized by the fact that $\lambda/\varepsilon \longrightarrow (\infty \text{ or } \bar{\lambda})$ and $\mu/\varepsilon \longrightarrow 0$, we may get a rigid or an elastic connection between the two parts in the normal direction but a free sliding in the tangential direction.

Now it remains to put the above results in correlation with previous analyses of bonded solids, and in particular with the occurence of guided waves along the thin layer. As a first step, this guided waves analysis could be performed in the case of two half spaces connected by an infinite layer. Another point is that, from a physical point of view, bonding layers usually involve viscoelastic properties. Viscoelasticity in thin layers has already been taken into account in equilibrium problems, so that it can probably be introduced in the previous analysis in some cases. But the kind of viscoelastic behaviors encountered in physics seems to be precisely those for which important difficulties remain.

References

1. Adams R.A., Sobolev spaces, Academic Press, New York (1975)
2. Ait Moussa A., Modélisation et étude des singularités d'un joint collé, PhD thesis, Montpellier II University (1989)
3. Attouch H., Variational convergence for functions and operators, Pitman Advanced Publishing Program, Boston-London-Melbourne (1984)
4. Geymonat G. and Krasucki F., Analyse asymptotique du comportement en flexion de deux plaques collées, C. R. Acad. Sci., I, 325, 307-314 ((1997)
5. Gupta R.N., Reflection of elastic waves from a linear transition layer, Bull. Seism. Soc. Am., 701-717 (1966)

6. Jones J.P. and Whittier J.S., Waves at flexibility bonded interface, J. Appl. Mech. 905-908 (1967)
7. Klarbring A., Derivation of the adhesively bonded joints by the asymptotic expansion method, Int. J. Engineering Sci., 29, 493-512 (1991)
8. Lebon F., Ould-Kaoua A. and Licht C., Numerical study of soft adhesively bonded joints in finite elasticity, Computational Mechanics, 21, 134-140 (1997)
9. Licht C. and Michaille G., Une modélisation du comportement d'un joint collé, C. R. Acad. Sci., I, 322, 295-300 (1996)
10. Licht C. and Michaille G., A Modeling of elastic adhesive bonded joints, Advances in Mathematical Sciences and Applications, 7, 711-740 (1997)
11. Suquet P., Discontinuities and Plasticity, in Nonsmooth mechanics and applications, CISM Courses and Lectures 302, Springer, Berlin (1998)
12. Thompson W.T., Transmission of elastic waves through a stratified solid medium, J. Appl. Physics, 21, 89-93 (1950)
13. Trotter H.F., Approximation of semi-groups of operators, Pacific J. Maths., 28, 897-919 (1958)
14. Vlassie V. and Rousseau M., Acoustical validation of the rheological models for a structural bond, Wave Motion, 37, 333-349 (2003)

Acoustic wave attenuation in a rough-walled waveguide filled with a dissipative fluid

T. Valier-Brasier, C. Potel, M. Bruneau, C. Depollier

Abstract The aim of this work is to analyze the behaviour of the acoustic pressure field in fluid-filled waveguides having small irregularities on the walls. In a previous publication [J. Sound Vib. (2008), doi 10.1016/j.jsv.2007.12.001], an analytic solution was presented for a non dissipative fluid. This solution emphasizes the acoustic coupling of modes which are the solution of the Neumann boundary problem in the regularly shaped waveguide which encloses the real waveguide. The model makes use of the integral formulation with an appropriate Green function which illustrates two mechanisms of energy exchange between modes, namely bulk coupling and surface coupling, the first one depending on the depth of the roughness and the second one depending in addition on the local slope. It provides interpretation of the attenuation phenomena of the propagating modes due to the irregularities. In the work presented here, a model in which viscosity and heat conduction of the fluid are considered allows us to take into account the dissipative phenomena (which take place in the boundary layers) in order to interpret better the attenuation phenomena.

1 Introduction

The study of waveguides having small irregularities on the walls has an industrial interest in terms of ultrasonic non destructive testing: improvement of the wetting of the glue between two bonded structures [1, 3], corrosion, etc.

Laboratoire d'Acoustique de l'Université du Maine (LAUM, UMR CNRS 6613)
Avenue Olivier Messiaen, 72 085 LE MANS Cedex 9 - FRANCE
tony.valier-brasier.etu@univ-lemans.fr, catherine.potel@univ-lemans.fr,
michel.bruneau@univ-lemans.fr, claude.depollier@univ-lemans.fr

The irregularities are considered to be secondary sources which redistribute the energy of the acoustic incident field by scattering. In a previous publication [4], an analytic solution was presented for a non dissipative fluid. This solution emphasizes the acoustic coupling of modes which are the solution of the Neumann boundary problem in the regularly shaped waveguide which encloses the real waveguide. The model makes use of the integral formulation with an appropriate Green function which illustrates two mechanisms of energy exchange between modes, namely bulk coupling and surface coupling, the first one depending on the depth of the roughness and the second one depending in addition on the local slope.
The aim of the present study is to account for the dissipative phenomena which take place in the thermo-viscous boundary layers in order to interpret better the attenuation phenomena. These thermo-viscous effects are introduced through appropriate mixed boundary conditions.

2 The fundamental problem

The considered waveguide is limited by two parallel rigid walls having small irregularities, the dimensions of which are small in comparison with the transversal dimension of the waveguide. The fluid plate with rigid, regularly shaped surfaces $z=0$ and $z=\delta$, which encloses the real waveguide, is characterized by its thickness δ, the inner plate surrounded by the real waveguide is characterized by its thickness d (see Fig .1). The depth of the small shape deviations are respectively denoted $h_1(x,y)$ and $h_2(x,y)$ at $z_1=h_1$ and $z_2=\delta-h_2$.

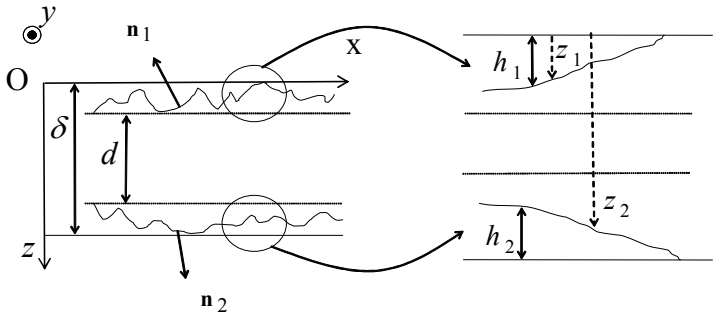

Fig. 1: Geometry of the fluid-filled waveguide

The fluid is characterized by its density ρ_0, the adiabatic speed of sound c_0, its shear viscosity coefficient μ_0, its thermal conductivity coefficient λ_0, its specific

heat ratio γ, and its heat capacity at constant pressure per unit mass C_P (see Appendix for numerical values).
The motion is supposed harmonic with ω the angular frequency (the time dependence being $\exp(i\omega t)$).

3 Boundary conditions

In the situations that we are interested in here, the viscous and thermal effects on the acoustic fields are predominant inside the so-called "viscous and thermal boundary layers".
As the thickness of these boundary layers is much smaller than the thicknesses of the fluid plates considered (d or δ), the localisation of these viscous and thermal phenomena at the immediate vicinity of the rigid walls leads to introduction of an "equivalent wall acoustic admittance"

$$\hat{Y} = \frac{(1+i)}{\sqrt{2}}\sqrt{k_0}\left[\sqrt{\frac{\mu_0}{\rho_0 c_0}} + (\gamma - 1)\sqrt{\frac{\lambda_0}{\rho_0 c_0 C_P}}\right], \tag{1}$$

where k_0 is the adiabatic wavenumber, defined by $k_0 = \omega / c_0$ [5].
This equivalent wall admittance accounts for the dissipative and reactive properties on the acoustic field, of the energy exchanges between the acoustic field itself, and both the vortical and the entropic (thermal) fields which are created on the rigid walls and which exist inside the boundary layer only (there are diffusion processes).
Outside the boundary layers, the entropic and vortical fields vanish; the only field of interest is therefore the acoustic field which behaves near the walls as if the admittance of the wall would be the equivalent admittance given by Eq. (1).
As far as resonances near cut off frequencies are concerned, taking into account these dissipative effects will limit the amplitudes of the modes generated by the source and created by scattering on the roughness.
The boundary conditions satisfied by the acoustic field on the perturbed surface of the waveguide are given by mixed boundary conditions which involve the equivalent admittance given above [Eq. (1)]. Denoting $\mathbf{n}_1$ and $\mathbf{n}_2$ the local unit vectors normal to the real surface of the waveguide at the points $z_1 = h_1$ and $z_2 = \delta - h_2$ and pointing outside the fluid, the normal derivatives take the classical form

$$\begin{cases} \partial_{n_1} = \dfrac{1}{N_1}\left[(\partial_x h_1)\partial_x + (\partial_y h_1)\partial_y - \partial_z \right], \\ \partial_{n_2} = \dfrac{1}{N_2}\left[(\partial_x h_2)\partial_x + (\partial_y h_2)\partial_y + \partial_z \right], \end{cases} \tag{2}$$

with

$$\begin{cases} N_1 = \sqrt{(\partial_x h_1)^2 + (\partial_y h_1)^2 + 1}, \\ N_2 = \sqrt{(\partial_x h_2)^2 + (\partial_y h_2)^2 + 1}. \end{cases} \tag{3}$$

Thus, the normal derivative of the acoustic pressure field $\hat{p}$ on the boundaries can be written in the form

$$\partial_{n_q}\,\hat{p} = \frac{1}{N_q}\left[(\partial_x h_q)\partial_x + (\partial_y h_q)\partial_y - (-1)^{q+1}\partial_z \right]\,\hat{p}\,,\ q = 1,2\,. \tag{4}$$

Therefore, combining conditions (1) and (4) permit to write the mixed boundary conditions as follows:

$$\begin{cases} \left(\partial_{n_1} + ik_0\hat{Y}\right)\hat{p}(x,y,z) = 0, \forall (x,y), z = z_1\,, \\ \left(\partial_{n_2} + ik_0\hat{Y}\right)\hat{p}(x,y,z) = 0, \forall (x,y), z = z_2\,, \end{cases} \tag{5}$$

or

$$\partial_z \hat{p}(x,y,z) = O(x,y,z)\,\hat{p}(x,y,z), \forall (x,y), z = z_q\,, q = 1,2, \tag{6}$$

where O is an operator defined by

$$\begin{aligned} O(x,y,z) = (-1)^{q+1}\Big\{ & ik_0 N_q \hat{Y} + \Big[(\partial_x h_q)\partial_x \\ & + (\partial_y h_q)\partial_y \Big] \Big\}, \forall (x,y), z = z_q\,, q = 1,2, \end{aligned} \tag{7}$$

which involves both the thermo-viscous effects and the slope of the profile.

4 Eigenfunctions of outward waveguide

In order to highlight the mechanisms of coupling between modes, the acoustic pressure $\hat{p}$ is expressed as an expansion on the (normalised and orthogonal) eigenfunctions $\hat{\psi}_m$, $m \in \mathbb{N}$

$$\hat{p}(x,y,z) = \sum_m \hat{A}_m(x,y)\hat{\psi}_m(z), \tag{8}$$

where the eigenfunctions $\hat{\psi}_m$ are solutions to the (1-D transverse) eigenvalue problem, including the mixed boundary conditions, namely

$$\begin{cases} \left(\partial_{zz}^2 + \hat{\chi}_m^2\right)\hat{\psi}_m(z) = 0, \quad z \in [0,\delta], \\ \left(\partial_z - ik_0\hat{Y}\right)\hat{\psi}_m(z) = 0, \quad \text{at } z = 0, \\ \left(\partial_z + ik_0\hat{Y}\right)\hat{\psi}_m(z) = 0, \quad \text{at } z = \delta. \end{cases} \tag{9}$$

The eigenvalues $\hat{\chi}_m$ are given by

$$\begin{cases} \hat{\chi}_0 \approx \sqrt{\dfrac{2ik_0\hat{Y}}{\delta}}, \ \textit{if } m = 0, \\ \hat{\chi}_m \approx k_m + \dfrac{2ik_0\hat{Y}}{k_m\delta} = 0, \ \textit{if } m \neq 0, \end{cases} \tag{10}$$

$k_m = m\pi/\delta$ being the eigenvalues for the problem with Neumann condition at the boundaries, and the eigenfunctions $\hat{\psi}_m$ take the form [6]

$$\hat{\psi}_m(z) = \frac{1}{\hat{C}_m}\left[\ \hat{\chi}_m \cos(\hat{\chi}_m z) + ik_0\hat{Y}\sin(\hat{\chi}_m z)\ \right], \tag{11}$$

with

$$\begin{cases} \hat{C}_0 \approx \sqrt{2ik_0\hat{Y}}, \ \text{if } m = 0, \\ \hat{C}_m \approx \hat{\chi}_m\sqrt{\delta/2}, \ \text{if } m \neq 0. \end{cases} \tag{12}$$

5 Modal formulation

The acoustic pressure field is governed by the set of equations, including the propagation equation and the boundary conditions, which is written as

$$\begin{cases} \left(\partial_{xx}^2 + \partial_{yy}^2 + \partial_{zz}^2 + k_0^2\right)\hat{p}(x,y,z) = -\hat{f}(x,y,z), \forall(x,y),\ z \in [z_1, z_2], \\ \partial_z \hat{p}(x,y,z) = O(x,y,z)\,\hat{p}(x,y,z), \forall(x,y), z = z_q\ , q = 1,2, \end{cases} \tag{13}$$

where $\hat{f}$ represents the bulk source factor.

Expanding the pressure field $\hat{p}$ on the eigenfunctions $\hat{\psi}_m$ given by Eq. (11), the expression of this problem takes the following form, with the help of the orthogonal properties of the eigenfunctions,

$$\begin{aligned} \left(\Delta_{//} + \hat{k}_{x_m}^2\right)\hat{A}_m(x,y) &= -\hat{S}_m(x,y) \\ &\quad + \sum_{\mu} \hat{\gamma}_{\mu m}(x,y)\,\hat{A}_\mu(x,y) \\ &\quad + \sum_{\mu} \hat{b}_{\mu m}(x,y)\left(\Delta_{//} + \hat{k}_{x_m}^2\right)\hat{A}_\mu(x,y), \end{aligned} \tag{14}$$

with

$$\hat{k}_{x_m}^2 = k_0^2 - \hat{\chi}_m^2\,, \tag{15}$$

where the source term takes the form

$$\hat{S}_m(x,y) = \int_{z_1}^{z_2} \hat{\psi}_m(z)\,\hat{f}(x,y,z)\,\mathrm{d}z\,, \tag{16}$$

and where the coupling factors are given by

$$\hat{\gamma}_{\mu m}(x,y)=\left[\hat{\psi}_m(z)\hat{\psi}_\mu(z)O(x,y,z)-\hat{\psi}_\mu(z)\partial_z\hat{\psi}_m(z)\right]_{z_1}^{z_2}, \tag{17}$$

and $$\hat{b}_{\mu m}(x,y) = \int_0^{z_1}\hat{\psi}_m(z)\hat{\psi}_\mu(z)\mathrm{d}z + \int_{z_2}^{\delta}\hat{\psi}_m(z)\hat{\psi}_\mu(z)\mathrm{d}z. \tag{18}$$

Two coupling mechanisms can be identified, namely the "bulk" or "global" modal coupling and the "boundary" or "local" modal coupling [4]. The term $\hat{b}_{\mu m}$, is related to the coupling of modes throughout the section of the guide (arising from the non orthogonality of the modes in the perturbed lateral dimensions of the guide due to the depth of the surface perturbation), while the operator $\hat{\gamma}_{\mu m}$, is related to the coupling through the slope and the depth of the surface perturbation itself. The behaviour of the acoustic pressure field is determined by these two mechanisms when propagating along the axis of the waveguide, the continuously distributed modes coupling along the distributed slight geometrical perturbation being accounted for in using a method relying on integral formulation.

6 Small perturbation method

The coefficients $\hat{A}_m$ are determined using methods relying on integral formulation and modal analysis, and using the appropriate Green function G_m [5]. When the waveguide is infinite and bounded by surfaces with one dimensional corrugations (two-dimensional problem $z\in[z_1,z_2]$ and $x\in[0,+\infty[$) the appropriate one-dimensional Green's function corresponding to a point source located at a point in the waveguide is given by

$$G_m(x;x')=\frac{e^{-ik_{x_m}|x-x'|}}{2ik_{x_m}}. \tag{19}$$

Using an iterative method to express the amplitude of each mode $\hat{A}_m$, which assumes that the coupling functions in the right hand side of Eq. (14) are small

quantities of the dimensionless parameters h_1/δ and h_2/δ, of their derivatives with respect to the coordinate x, thus the n[th]-order solution of Eq. (14) for $\hat{A}_m$ is written as follows:

$$\hat{A}_m^{[N]}(x) = \hat{A}_m^{(0)}(x) + \hat{A}_m^{(1)}(x) + \ldots + \hat{A}_m^{(N-1)}(x) + \hat{A}_m^{(N)}(x), \tag{20}$$

where $\hat{A}_m^{[N]}$ denotes the N th-order perturbation expansion for $\hat{A}_m$, $\hat{A}_m^{(0)}$ the zero order approximation, $\hat{A}_m^{(1)}$ the first order correction term, and so on. The zero order approximation takes the form

$$\hat{A}_m^{(0)}(x) = \hat{Q}_m G_m(x;x'), \tag{21}$$

where $\hat{Q}_m$ is the strength of a monochromatic source which is assumed to be flush-mounted at $x = 0$, related to the m-th mode. In fact, it represents the energy transfer between the external source and the eigenmode m.
The first-order perturbation expansion $\hat{A}_m^{(1)}$ is then given by

$$\begin{aligned}\hat{A}_m^{(1)}(x) = &-\sum_{\mu}\int_{-\infty}^{+\infty} G_m(x;x')\hat{\gamma}_{\mu m}(x')\hat{A}_\mu^{(0)}(x')\mathrm{d}x' \\ &+\sum_{\mu}\hat{Q}_\mu\int_{-\infty}^{+\infty} G_m(x;x')\hat{b}_{\mu m}(x')\mathrm{d}x' \\ &-\sum_{\mu}\left(\hat{k}_{x_m}^2 - \hat{k}_{x_\mu}^2\right)\int_{-\infty}^{+\infty} G_m(x;x')\hat{b}_{\mu m}(x')\hat{A}_\mu^{(0)}(x')\mathrm{d}x'.\end{aligned} \tag{22}$$

7 Results

This section aims at providing results illustrating the inter-modal model using periodically one dimensional corrugated surfaces (two-dimensional problem). The particular case chose here is that of a periodically sawtooth profile (see Fig. 2, spatial period denoted Λ) assumed to be of infinite extent.

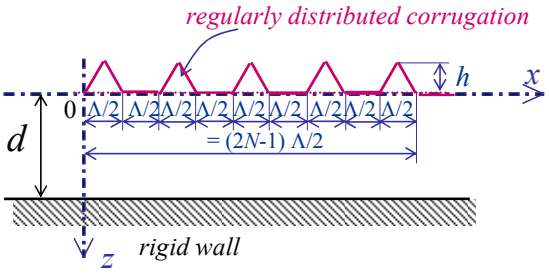

Fig. 2: Periodically sawtooth profile (height of the teeth denoted h)

When the roughness is periodic, the phonon relations [4, 7] which involve the wavenumbers of the modes and the spatial period Λ of the roughness, allow to know for all the frequencies the mode coupling (see Fig. 3).

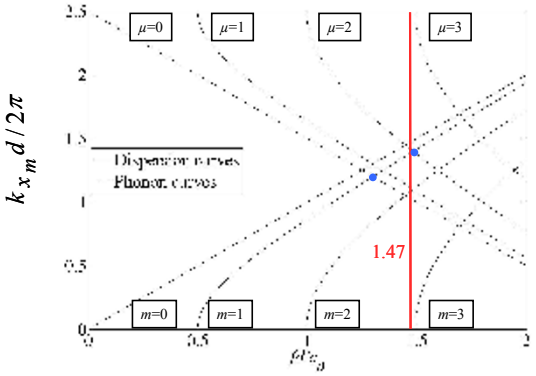

Fig. 3: Dispersion curves and curves from the phonon relations

The intersection of the dispersion curve of a mode m and the phonon curve of a mode μ shows the frequency for which the coupling between both modes m and μ is strongest. The green point represents the intersection of the dispersion curve of the mode $m=1$ and the phonon curve of the mode $\mu=0$ and the blue point represents the intersection of the dispersion curve of the mode $m=1$ and the phonon curve of the mode $\mu=2$.

The acoustic source is assumed to create only the mode $m=1$ (incoming wave), at the forcing frequency f. Four modes are considered in the solution: for the chosen frequency ($f\,d/c_0=1.47$ with $d/\Lambda=2.5$), the first three modes ($\mu=0,1,2$) are propagative and the last one ($\mu=3$) is evanescent. The chosen frequency is in the vicinity of the value given by a phonon relation, thus both a strong coupling between the mode $m=1$ created by the source and the coupled

modes $\mu = 0$ and $\mu = 2$, and a quite strong "self-coupling" of the mode $m = 1$ occur, as can be seen on Figs 4-a, b and c, which present the modulus of the normalised amplitudes of the modes 0, 1 and 2 as a function of the dimensionless parameter $k_0 x$ (evanescent mode $\mu = 3$ is not represented: its amplitude vanishes because its coupling with the other modes is very weak).
The decreasing of the amplitude of the mode $m = 1$ generated by the source (see Fig. 4-b) when the abscissa of the observation point ($k_0 x$) corresponds to a loss of energy of the mode generated by the source, through energy transfers between modes. This decrease has an approximate exponential shape, with an attenuation factor equal to approximately the same order of magnitude as that experimentally found in solid media for roughness profile (shot blasted glass plate) [8-10].

8 Conclusion

A method for calculating the modal behaviour of a fluid plate with rough walls, when the dissipative (thermo-viscous) effects are accounted for, has been presented. The major result, in comparison with the previous one [4], is that the effects of the viscous and thermal phenomena, which are predominant inside the thermo-viscous boundary layers, are quite small in comparison with the effect of the modal coupling due to the wall roughness, in the situations considered here.
Owing to the large range of sizes and shapes of the roughnesses that can be modelled, the method appears to be quite general for describing the modal coupling and the modal attenuation for the propagative modes. Therefore, this method can be directly used for several applications concerning fluid-filled wave guides. It also paves the way for modelling the effects of the wall roughness on the Lamb modes in homogeneous solid plates (having in mind applications in the domain of non destructing testing).

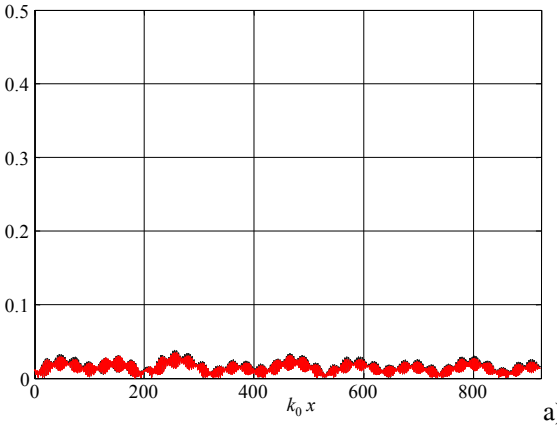

a)

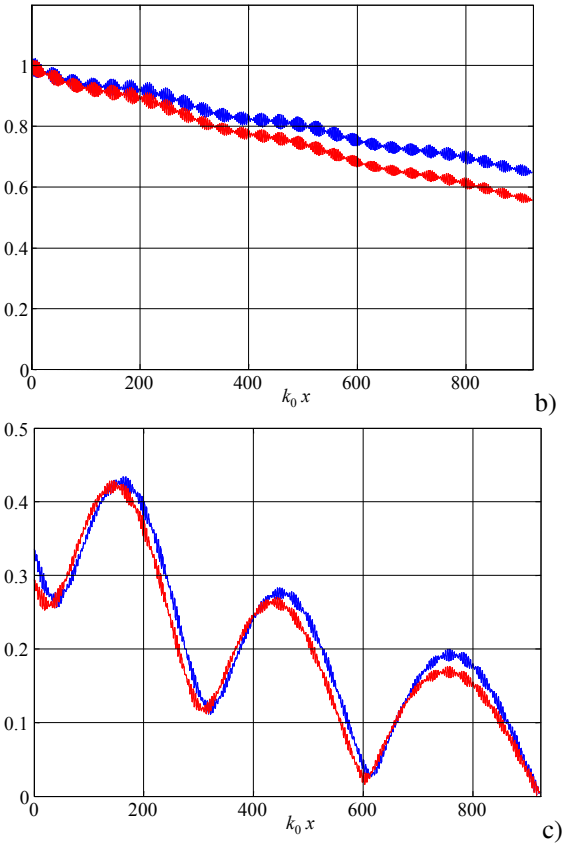

Fig. 4: Modulus of the normalized amplitude of the pressure variation (3rd order) for a sawtooth profile (see Fig. 3). -a) $\hat{A}^{[3]}_{\mu=0}\left(x_1\right) \big/ A^0_m$ for the mode $\mu = 0$, -b) $\hat{A}^{[3]}_{m=1}\left(x_1\right) \big/ A^0_m$ of the mode $m = 1$ (the only mode generated by the source), -c) $\hat{A}^{[3]}_{\mu=2}\left(x_1\right) \big/ A^0_m$ for the mode $\mu = 2$, when $f\, d / c_0 = 1.47$ with $d/\Lambda = 2.5$. The heights of the teeth are such as $\zeta = \tilde{h} / d = 0.005$; the interface $x_3 = d$ is smooth. The red lower and blue higher curves correspond respectively to a dissipative and a non dissipative fluid.

Appendix: characteristics of the dissipative fluid

The fluid is characterized by its density ρ_0, the adiabatic speed of sound c_0, its shear viscosity coefficient μ_0, its thermal conductivity coefficient λ_0, its specific heat ratio γ, and its heat capacity at constant pressure per unit mass C_P. The numerical values used above are those of the air at standart conditions:

$\rho_0 = 1.2\ kg.m^{-3}$, $c_0 = 343\ ms^{-1}$, $\mu_0 = 1.94 \cdot 10^6\ Pa.s$, $\gamma = 1.4$,
$\lambda_0 = 2.62 \times 10^{-3}\ W.m^{-1}.K^{-1}$, $C_p = 1.07 \times 10^3\ J.kg^{-1}.K^{-1}$.

References

1. Chimenti, D.E. , Lobkis, O.I.: The effect of rough surfaces on guided waves in plates. Ultrasonics **36**, 155-162 (1998)
2. Ogilvy J.A.: Theory of wave scattering from random rough surface, Institute of Publishing Bristol (1992)
3. Maradudin, A.A., Mills, D.L.: The attenuation of Rayleigh surface waves by surface roughness, Annals of Physics **100**, 262-309 (1976)
4. Potel, C., Bruneau, M.: Modes coupling due to non homogeneously-shaped walls in duct acoustics, J. Sound Vib. **313**, 738-759 (2008)
5. Bruneau, M., Scelo, T., (translator and contributor): Fundamentals of Acoustics, ISTE, UK and USA (2006)
6. M. Necati Ozizik, Heat conduction, John Wiley and sons, Inc. (2d edition) (1993)
7. Leduc, D., Hladky-Hennion, A.C., Morvan, B., Izbicki, J.L., Pareige, P.: Propagation of Lamb waves in a plate with a periodic grating: interpretation by phonon, J. Acoust. Soc. Am. **118** (4), 2234-2239 (2005)
8. Leduc, D., Morvan, B., Pareige, P., Izbicki, J.L.: Measurement of the effects of rough surfaces on Lamb waves propagation, NDT&E International **37** (3), 207-211 (2004)
9. Potel, C., Leduc, D., Morvan, B., Pareige, P., Depollier, C., Izbicki, J.L.: Propagation of Lamb waves in anisotropic rough plates: a perturbation method", 7th Congrès Français d'Acoustique joint with 30th Deutsche Jahrestagung für Akustik, Collected papers on CD-ROM ISBN 2-9521105-3-0, Strasbourg, 147-148, 22-25 mars 2004
10. Potel, C., Leduc, D., Morvan, B., Depollier, C., Hladky-Hennion, A.C., Izbicki, J.L., Pareige, P., Bruneau, M.: Lamb wave attenuation in a rough plate. I. Analytical and experimental results in an anistropic plate", J. Appl. Phys. **104** (7), 074909 (2008).

Some advances towards a better understanding of wave propagation in civil engineering multi-wire strands

L. Laguerre and F. Treyssede

Abstract Steel members of civil engineering structures undergo degradations mainly due to corrosion and mechanical fatigue. In this context, non-destructive inspection techniques using mechanical guided waves have potential to monitor these structures. Even if wave propagation is not yet fully understood in these structures, useful results can be derived for inspection methodology by using wave modeling in cylindrical waveguide, embedded or not. However, further improvement can be expected from the development of wave propagation simulation tools for real-life structures. Indeed, several difficulties arise in the understanding of guided ultrasonic waves in such structures, partly due to the helical geometry and the inter-wire coupling effects. Moreover, these structures are pre-stressed and can be free or embedded in solid material. This paper shows some recent research results at LCPC. A first part deals with experimental results on the guided wave propagation in a commonly used steel member, the seven wire strand (*i.e* one straight single cylindrical wire surrounded by six helical wires). The second part aims at numerically investigating the propagation of elastic waves in free helical waveguides. A numerical method is chosen based on a semi-analytical finite element technique that relies on a specific non-orthogonal curvilinear coordinate system. This system is shown to be translationally invariant along the helix centerline so that a spatial Fourier transform can be explicitly performed along the axis to re-

L. Laguerre

Laboratoire Central des Ponts et Chaussées (LCPC), Centre de Nantes, Division Reconnaissance et Géophysique, Route de Bouaye - BP 4129, 44341 Bouguenais, France, email :Laurent.Laguerre@lcpc.fr

F. Treyssede

LCPC, Centre de Nantes, Division Métrologie et Instrumentation, Route de Bouaye - BP 4129, 44341 Bouguenais, France, e-mail :Fabien.Treyssede@lcpc.fr

duce the problem to two dimensions. The method can thus readily be used for the analysis of helical structures by considering the special case of no curvature. Results for single straight and helical wires are first computed. A dispersion analysis for a seven wire strand with simplified contact conditions is then performed.

1 Introduction

Multi-wire strands are commonly used as structural members in the field of civil engineering, in bridges constructions (suspended, cable-stayed and prestressed ones) as well as in geotechnics for retaining walls applications. These civil engineering structures suffer from ageing and degradation due to corrosion and fatigue of structural steel members. Guided ultrasonic waves are potentially attractive tools for non destructive assessment of their integrity. They generally combine the ability to inspect, in a single measurement, the whole width of the structure over an appreciable length along the guiding direction. Moreover, they provide a mean to access hidden parts of the structure, such as sections of strand partially or totally grouted in grease or cement. Guided wave non-destructive methodologies of inspection using magnetostrictive or piezoelectric devices are generally proposed, depending on the desired applications.

The goal of this paper is to show some recent advances performed at LCPC dealing with the development of a numerical model for the guided wave propagation in a free seven-wire strand. This common strand configuration is composed of a straight cylindrical wire of 5.4 mm in diameter surrounded by six helical wires of 5.22 mm in diameter. These works come within the scope of developing tools to provide a better insight in the interpretation of guided wave propagation in such complicated waveguides for further optimised inspection strategy.

The simplest and classical way to approach the wave propagation in the seven-wire strand is to use the approximation of the infinite cylinder. In particular, experimental studies have been performed in the literature for both a cylindrical bar and a seven wire strand, trying to find analogies between both behaviours that could be interpreted from Pochhammer-Chree solutions, for the bare waveguide case (Kwun et al. 1998, Laguerre et al. 2002, 2003, Lanza di Scalea et al. 2003 and Rizzo and Lanza di Scalea 2004) or the embedded one (Pavlakovic et al. 1999, 2001 and Beard et al. 2003). Even if the non-destructive inspection strategy of a seven-wire strand with guided ultrasonic waves has gained from this approach, the authors point out the limits of Pochhammer-Chree solution for the accurate interpretation of experimental data for the seven wire strand. The theoretical understanding of guided ultrasonic waves in multi-wire strands is still challenging because of the complexity of this structure, i.e. the helical geometry of

peripheral wires surrounding the straight inner wire, the inter-wire coupling and contact effects, and the presence of applied loads.
In order to deal with complex geometry, some of the most popular and efficient numerical techniques are based on finite element (FE) methods. The so-called semi-analytical finite element (SAFE) method is a first approach that has been used to study uniform waveguides of arbitrary cross-section – see for instance, (Gavric 1995, Hayashi et al. 2003, Damljanovic and Weaver 2004). (Demma et al. 2005) and (Finnveden and Fraggstedt 2008) investigated toroidal waveguides. (Onipede and Dong 1996) extended SAFE methods to study uniformly pretwisted waveguides along a straight axis.
A second approach is based on the theory of wave propagation in periodic structures from Floquet's principle. A review on the topic can be found in Mead 1996. Based on a general theory presented by Mead 1973, some periodic FE approaches and procedures have then been developed – see for instance (Gry and Gontier 1997, Mace et al. 2005).
For modelling a single helical wire, which is a uniform waveguide, both SAFE or periodic FE approaches can be applied. (Treyssede 2007) has proposed a numerical procedure based on a periodic FE approach combined with a specific helical mapping in order to arbitrarily reduce the periodic cell length. (Treyssede 2008) has also recently developed a SAFE method extended to helical waveguides. The weak variational formulation is written in terms of a non-orthogonal curvilinear coordinate system that is translationally invariant along the helix centreline, so that a Fourier transform can be explicitly performed. In this paper, it is shown how this SAFE method can also be readily used to study some more general helical structures, made of both straight and helical wires such as multi-wire strands.
The first part of this paper is devoted to show, from experimental data, the analogy and discrepancies existing between the guided ultrasonic wave propagation into a cylindrical bar and the seven-wire strand in the low frequency regime. This is done through spectrogram analyses of time history signals generated and detected using a longitudinally polarized non-contact magnetostrictive device.
In the second part, one proposes a numerical method allowing the study of elastic guided waves inside helical multi-wire strands. Inter-wire coupling effects are included in the analysis through simplified contact conditions. Prestress and embedment are not considered.

2 Experimental results

Magnetostrictive transducers were used herein for the generation and detection of guided ultrasonic waves into steel cylindrical bars and seven-wire strands. The major advantage of non-contact electromagnetic magnetic transducers (EMAT) such as magnetostrictive transducer is in the greater transduction efficiency at low bias fields contrary to Lorentz force based EMATS. Conversely, magnetostrictive

EMATS are rather low-frequency transducers (typically <500kHz). These transducers uses the property of ferromagnetic materials to mechanically strain under a variation of their magnetic state (magnetostrictive Joule's effect). The magnetic excitation is though produced by a dynamic electrical current feeding a driving coil. This in turn generated the mechanical wave. The mechanical wave while propagating produces magnetic field variation (magnetostrictive Villari's effet) that can be detected using and inducting coil. Bias magnetic fields are superimposed at the generation and detection to linearize and enhance the transduction. The selected bias field longitudinal orientation makes the generation and detection predominantly sensitive to longitudinal guided waves.

In this study, various through-transmissions experimentations were performed for free cylindrical bars and a free seven-wire strand or under applied tensile loads. Time excitation is a gaussian-shaped low radiofrequency burst of bandwidth Δf centered at f_0, and such that $\Delta f / f_0 = 1$ at -20 dB. Detected guided ultrasonic time waveforms are then studied using a short time Fourier transform (STFT). According to the positioning of transducers (the transmitter and detector locations are at $L/4$ from the left-end side of the specimen and $L/2$ respectively, with L the specimen length, see for instance Laguerre et al. 2003), the first wave arrival is the incident wave propagating to the right, the second arrival is the incident wave propagating to the left after one reflection, and the third one is the incident wave propagating to the right after one reflection (and so on for the next arrivals). According to their intrinsic dispersive behaviours in this frequency range, the wavepacket arrivals (Fig. 1) can be identified from Pochhammer-Chree theory as the first and second longitudinal modes $L(0,1)$ and $L(0,2)$ respectively. Similar measurements performed in the same frequency range for a lower diameter show that the waveguide behaviour is limited to the fundamental $L(0,1)$ longitudinal mode, in its weak dispersive region as a consequence of the frequency-to-diameter conservation.

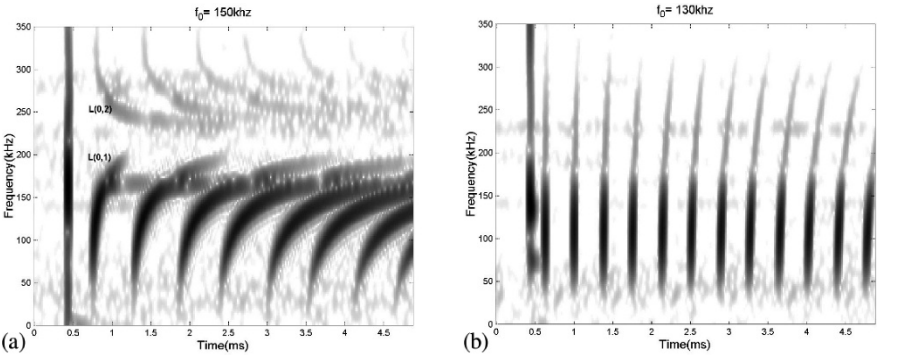

Fig. 1 Fourier spectrograms of magnetostrictive time history signals for (a) a steel cylindrical bar of 6-m length and 15.5mm in diameter, and (b) a single central cylindrical wire of 4-m and 5.22 mm in diameter excited at f_0=150 kHz and 130 kHz respectively.

These expected above-mentioned results are only quoted here to point out the discrepancies existing between a cylindrical bar and a free seven-wire strand. The Fourier spectrograms associated to the free seven-wire strand are shown in Fig. 2. In the low-frequency region (lower than 50 kHz), the pulse propagates without significant dispersion, at the bar celerity, while the higher frequency trends cannot be explained at all by the Pochhammer-Chree theory, neither by considering a bar of the same diameter as the strand nor by considering a bar of the same diameter as the single central wire. One of the major differences between the cylinder and the strand arises mainly from a frequency band from 60 to 80 kHz, electrically excited, but which disappears from the Fourier spectrogram for all wave arrivals.

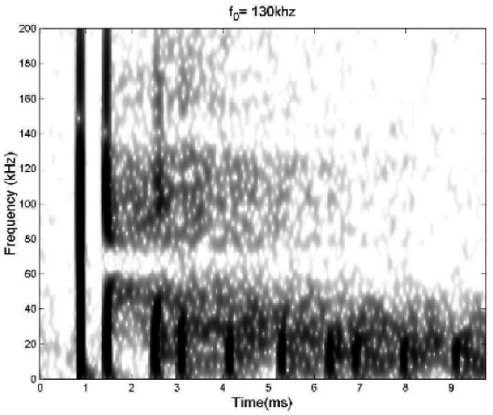

Fig. 2 Fourier spectrograms of magnetostrictive time-history signals for a free seven-wire strand of 10-m length and 15.9 mm in diameter excited at f_0=130kHz.

This phenomenon which was first observed by (Kwun et al. 1998) who called it "missing notch-frequency" seems to exhibit a similar pattern as the one of a cut-off frequency. It was confirmed later by (Laguerre et al. 2003, Rizzo and Lanza di Scalea 2004) but still remains unexplained. The "missing notch-frequency" reveals the influence of the seven-wire geometrical structure on the guided wave propagation. Indeed, the origin of this missing notch-frequency can solely be understood, as will be shown in Sect. 3.3, by considering the whole assembling of helical wires around the central cylindrical straight with inter-wire coupling conditions. So this missing notch-frequency phenomenon will be retrieved from the seven-wire strand theoretical propagation model derived in the following section.
Moreover, the influence of prestress and inter-wire contacts on the wave propagation is confirmed by the results obtained for a seven wire strand under different tensile loading strengths varying from 2% (5.8kN) to 60% (141kN) of the breaking load. The non-contact magnetostrictive transducers are particularly well-suited for this loaded strand experimental arrangement since they allow to work on the first wave arrival whose propagation path did not interact with the clamped ends, by positioning them between the anchorages. The Fourier spectrograms Fig. 3

clearly show the modification in the missing notch frequency with load, *i.e.* an increase in the loading strength leads to the increase in the missing notch frequency (from 60-to-80 kHz at 2% to 80-to-100 kHz at 60% of the breaking load). This demonstrates the influence of prestress and inter-wire contact conditions on guided wave propagation in a seven-wire strand.

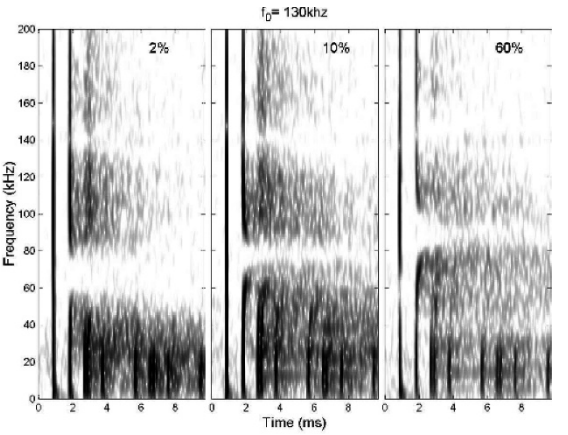

Fig. 3 Fourier spectrograms of magnetostrictive time-history signals for a seven-wire strand of 10-m length and 15.9 mm in diameter excited at f_0=130kHz at different tensile load strengths.

3 Numerical model

3.1 The SAFE method

One assumes a linearly elastic material, small strains and displacements and a time harmonic dependence. There is no external force. The 3D variational formulation governing elastodynamics is given by:

$$\int_{\Omega} \delta\boldsymbol{\varepsilon}^T \mathbf{C}\boldsymbol{\varepsilon} dV - \omega^2 \int_{\Omega} \rho \delta\mathbf{u}^T \mathbf{u} dV = 0 \tag{3.1}$$

for any kinematically admissible trial displacement field $\delta\mathbf{u}$. $\delta\boldsymbol{\varepsilon}$ denotes the virtual strain vector $\left[\delta\varepsilon_{11} \quad \delta\varepsilon_{22} \quad \delta\varepsilon_{33} \quad 2\delta\varepsilon_{12} \quad 2\delta\varepsilon_{13} \quad 2\delta\varepsilon_{23}\right]^T$. The superscript T denotes the matrix transpose. Subscripts $i = 1,2,3$ are the respective components in the considered coordinate system, denoted (x, y, s) – which might be different from the Cartesian coordinate system denoted (X, Y, Z). $\mathbf{C}$ is the matrix of mate-

rial properties. ρ is the material density and Ω is the structural volume. In the remainder of this paper, s will denote the waveguide axis (not necessarily straight).

The strain-displacement relation can be written as follows:

$$\boldsymbol{\varepsilon} = \left(\mathbf{L}_{xy} + \mathbf{L}_s\, \partial/\partial s\right)\mathbf{u} \tag{3.2}$$

where $\mathbf{L}_{xy}$ is the operator containing all terms that do not contain derivatives with respect to the axis s. Now we further assume a e^{iks} dependence, k being the axial wavenumber. The problem is hence reduced from three to two dimensions (from the volume Ω to the cross-section S of the waveguide). Then, the FE discretisation of Eq.(3.1) finally leads to the following eigenvalue problem:

$$\left\{\mathbf{K}_1 - \omega^2\mathbf{M} + ik\left(\mathbf{K}_2 - \mathbf{K}_2^T\right) + k^2\mathbf{K}_3\right\}\mathbf{u} = \mathbf{0} \tag{3.3}$$

with the following elementary matrices:

$$\begin{aligned} \mathbf{K}_1^e &= \int_{S^e} \mathbf{N}^{eT}\mathbf{L}_{xy}^T\mathbf{C}\mathbf{L}_{xy}\mathbf{N}^e dS, \quad \mathbf{K}_2^e = \int_{S^e} \mathbf{N}^{eT}\mathbf{L}_{xy}^T\mathbf{C}\mathbf{L}_s\mathbf{N}^e dS \\ \mathbf{K}_3^e &= \int_{S^e} \mathbf{N}^{eT}\mathbf{L}_s^T\mathbf{C}\mathbf{L}_s\mathbf{N}^e dS, \quad \mathbf{M}^e = \int_{S^e} \rho\mathbf{N}^{eT}\mathbf{N}^e dS \end{aligned} \tag{3.4}$$

where $\mathbf{N}^e$ is a matrix containing nodal interpolating functions of the element. The solution of Eq. (3) yields the propagation modes. At fixed real k, the eigenproblem Eq. (3.3) is linear for finding ω^2. This simpler approach is useful only if interest is restricted to propagating modes in undamped systems. Given ω and finding k, the eigenproblem is quadratic. It can be recast into a generalized linear eigensystem written for $\left[\mathbf{u} \quad k\mathbf{u}\right]^T$ in order to be solved by standard numerical solvers – see (Tisseur and Meerbergen 2001) for instance.

3.2 Helical coordinate system

In the previous section, we have assumed a e^{iks} dependence. This is equivalent to perform a spatial Fourier analysis in the s direction. This dependence indeed implies the following assumptions:

- the cross-section of the waveguide does not vary along s (condition 1);
- the material properties do not vary along s (condition 2, which is assumed to be satisfied throughout this work);
- the (x, y, s) coordinate system is so that s does not appear explicitly in the coefficients of the equilibrium equations (condition 3)

Verifying this last condition (condition 3) is somewhat more technical than the first two.

First, the helix centerline curve must be described by the following position vector in the Cartesian orthonormal basis:

$$\mathbf{R}(s) = R\cos\left(\frac{2\pi}{l}s\right)\mathbf{e}_X + R\sin\left(\frac{2\pi}{l}s\right)\mathbf{e}_Y + \frac{L}{l}s\mathbf{e}_Z \tag{3.5}$$

where $l = \sqrt{L^2 + 4\pi^2 R^2}$. R and L are respectively the radius of the centreline in the (X,Y) Cartesian plane and the helix step along the Z axis. The unit tangent, normal and binormal vectors to the centreline are respectively obtained from $\mathbf{T} = d\mathbf{R}/ds$ and the Serret-Frenet formulae, $d\mathbf{T}/ds = \kappa\mathbf{N}$ and $d\mathbf{N}/ds = \tau\mathbf{B} - \kappa\mathbf{T}$. Both curvature $\kappa = 4\pi^2 R/l^2$ and tortuosity $\tau = 2\pi L/l^2$ are constant. For clarity, Fig.4 exhibits one helix step and its Serret-Frenet basis.

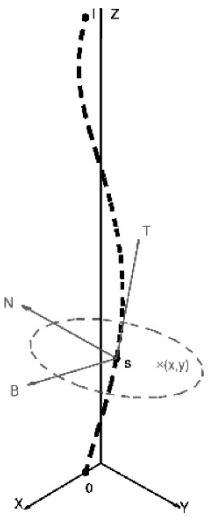

Fig. 4. Helix step and its Serret-Frenet basis with (x, y) the helical cross-section coordinates.

Now, a new coordinate system is constructed from the orthonormal basis $(\mathbf{N},\mathbf{B},\mathbf{T})$ as follows:

$$\mathbf{X}(x, y, s) = \mathbf{R}(s) + x\mathbf{N}(s) + y\mathbf{B}(s) \tag{3.6}$$

yielding the covariant basis $(\mathbf{g}_1,\mathbf{g}_2,\mathbf{g}_3) = (\partial\mathbf{X}/\partial x, \partial\mathbf{X}/\partial y, \partial\mathbf{X}/\partial s)$ (non-orthogonal). It could be checked that the metric tensor, defined by $(\mathbf{g})_{ij} = \mathbf{g}_i \cdot \mathbf{g}_j$, does not depend on the third curvilinear coordinate s. One consequence is that the coefficients of the partial differential equilibrium equations are not dependent upon s either (condition 3 is satisfied).

In Eqs. (3.3) and (3.4), covariant components have been chosen for $\boldsymbol{\varepsilon}$ while components with respect to $(\mathbf{N},\mathbf{B},\mathbf{T})$ have been preferred for $\mathbf{u}$. Also, the components of $\mathbf{C}$ should be understood as contravariant. Assuming an isotropic material, $\mathbf{C}$ can be obtained from the following tensor expression:

$$C^{ijkl} = \frac{\nu E}{(1+\nu)(1-2\nu)} g^{ij} g^{kl} + \frac{E}{2(1+\nu)} \left(g^{ik} g^{jl} + g^{il} g^{jk} \right) \tag{3.7}$$

where g^{ij} is the contravariant metric tensor, ν and E denotes Poisson coefficient and Young modulus – for more details, see (Treyssede 2008).

Now, consider a single helical wire of circular cross-section. The cross-section obviously does not change along the helical axis s (condition 1 is fulfilled) so that the proposed approach is valid. The analysis of a straight wire can also be readily performed, the cylinder corresponding to the special case $\kappa = \tau = 0$.

However, a question arises about the choice of the invariant coordinate system to be used when considering helical structures made of both straight and helical wires. Of course, the choice $\kappa = \tau = 0$ (resp. $\kappa \neq 0, \tau \neq 0$) cannot be applied because condition 1 would not be satisfied for helical (resp. straight) wires.

The adequate system is indeed given by $\kappa = 0$, $\tau = 2\pi/L$ (R=0), corresponding to a rotating coordinate system around the Z axis ($s \equiv Z$). With this system, a central straight wire (cylinder) has an invariant circular cross-section along Z ("a rotating circle remains a circle"). Furthermore, the cross-sections of peripheral helical wires do not change either along Z (but their shape in the (x, y) plane is not circular any more).

3.3 Numerical results

The material is assumed to be isotropic, with no material damping. For a steel wire, a typical value of 0.30 will be chosen for the Poisson coefficient. We consider waveguides with a circular cross-section of radius a. The adimensionalized angular frequency is given by $\omega a/c_s$, with c_s the shear velocity. Six-node triangles meshes will be used. FE computations are held at fixed real wavenumbers k.

As a preliminary result, one single wire is first considered. Both cylindrical ($\kappa = \tau = 0$) and helical geometries ($\kappa \neq 0, \tau \neq 0$) are analysed. For the helical waveguide, a small lay angle of $\phi = \tan^{-1}(2\pi R/L) = 7.5°$ with $R = 2a$ has been chosen (typical values for civil engineering seven wire strands). Figure 5 exhibits the dispersion curves for both cases. Few differences are observed. For the helical waveguide, flexural modes do not occur in pairs of equal wavenumbers, while wavenumbers of compressional and torsional modes remain nearly unchanged (Treyssede 2007). It could be checked that the rotating system $(\kappa = 0, \tau = 2\pi/L)$ yields some physically equivalent results, thus demonstrating its adequacy (not shown in this paper for conciseness).

The wave modes propagating inside a typical seven-wire strand are now studied. Stick contact conditions are assumed for simplicity (no slip, no separation and no friction are considered). a denotes the central wire radius (a=2.7mm). Peripheral

wires radii are chosen as $0.97a$, with the same lay angle as before. The coordinate system to be used is $(\kappa a = 0, \tau a = 0.0668)$.

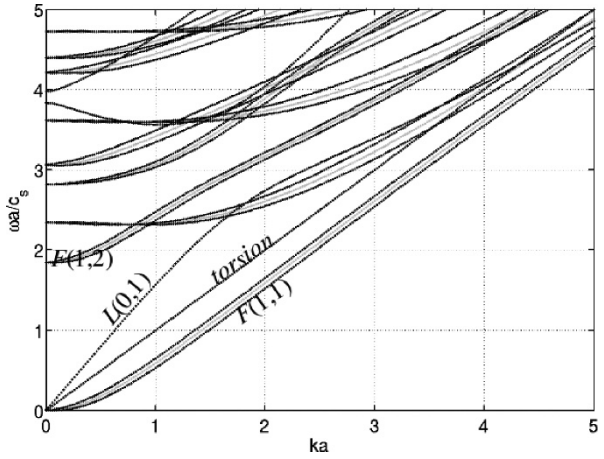

Fig. 5 Plot of frequency versus wavenumber. Black: helical, gray: cylindrical waveguides

The FE mesh, corresponding to a (X,Y) plane cut, is given in Fig. 6.

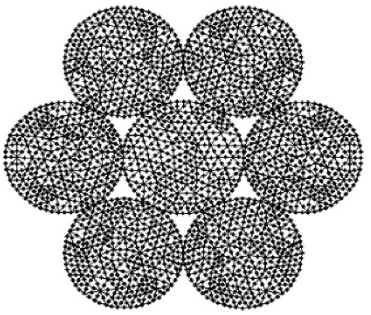

Fig. 6 (X,Y) plane cross-section FE mesh used for the seven-wire strand ($\phi = 7.5°$)

Figure 7 exhibits the energy velocity curves for the adimensional frequency range [0;2]. Single wire curves are also given for comparison (for both central and peripheral wires). Due to a strong inter-wire coupling, a far more complex behaviour is observed for the seven wire strand. The most striking phenomenon is a seemingly cut-off of the fastest mode (compressional-like $L(0,1)$ mode) around $\omega a/c_s = 0.4$, corresponding to about 75kHz, which is in agreement with experiments where a mean frequency of 70 kHz is deduced from the spectrogram (and associated to group velocities). In fact, this apparent cut-off is due to some strong bifurcations occurring near 0.4 as clearly shown by Fig.8.

The upper curve of Fig.7 is composed of two distinct branches, describing the behaviour of two distinct wave modes.

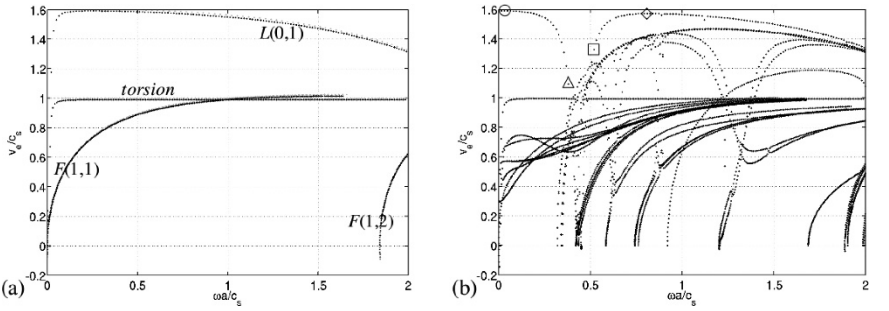

Fig. 7 Plot of energy velocity (a) single wire (black: peripheral, gray: central, (b) seven-wire strand ($\phi = 7.5°$)

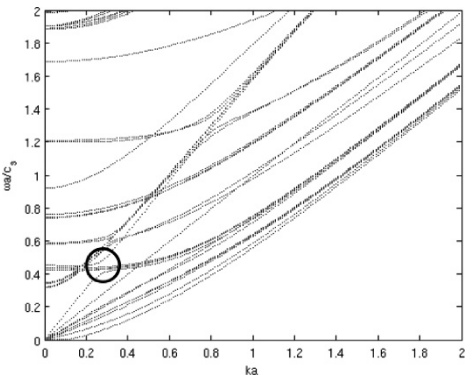

Fig. 8 Plot of frequency vs wavenumber for the seven-wire strand. Circle: bifurcation zone

Finally, Fig. 9 shows modeshapes computed for $\omega a/c_s = 0.03$ and 0.38 (left branch), $\omega a/c_s = 0.52$ and 0.81 (right branch).

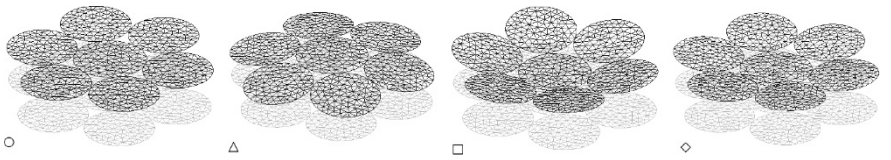

Fig. 9 Modeshapes computed for: ○ $\omega a/c_s = 0.03$, △ 0.38, □ 0.52, ◇ 081 (symbols of Fig. 7)

4. Conclusions

Elastic wave propagation inside helical wires has been analysed through a SAFE method based on a translationally invariant helical coordinate system. The special case of no curvature yields an adequate coordinate system to be used for the analysis of helical structures made of a straight core and peripheral helical wires. Dispersion inside a typical 6+1 strand has been investigated by assuming stick contact conditions. A far more complex behaviour than for single wires has been observed. However, it is worth noting, that the fastest compressional-like mode of the seven-wire strand dispersion behaviour looks like the $L(0,1)$ one for a single wire, excepted in a frequency region typically around 75kHz where an apparent band-cut zone is observed. This intrinsic seven-wire strand low-frequency dispersion behaviour agrees well the experimental results obtained with encircling longitudinally-polarized magnetostrictive transducers on a seven-wire strand. Thus, the proposed seven-wire propagation model allows a novel interpretation, through the strong bifurcation between two distinct modes, of the missing notch frequency experimentally observed here and in the literature. Future works will be devoted to the numerical modelling of the loading effect.

References

Beard M. D., Lowe M. J. S., Cawley P.: Ultrasonic guided waves for inspection of grouted tendons and bolts. J. Mater. Civil Eng. **212**, 212–218 (2003)

Damljanovic V., Weaver R. L.: Propagating and evanescent elastic waves in cylindrical waveguides of arbitrary cross-section. J. Acoust. Soc. Am. **115**, 1572–1581 (2004)

Demma A., Cawley P., Lowe M.: The effect of bends on the propagation of guided waves in pipes. J. Press Vess.-T ASME **127**, 328–335 (2005)

Finneveden S., Fraggstedt M.: Waveguide finite element for curved structures. J. Sound Vib. **312**, 644–671 (2008)

Gavric L.: Computation of propagative waves in free rail using a finite element technique. J. Sound Vib. **185**, 531–543 (1995)

Gry L., Gontier C.: Dynamic modeling of railway track: a periodic model based on a generalized beam formulation. J. Sound Vib. **199**, 531–558 (1997)

Hayashi T., Song W.-J., Rose J. L.: Guided wave dispersion curves for a bar with an arbitrary cross-section, a rod and rail example. Ultrasonics **41**, 175–183 (2003)

Kwun H., Bartels K. A., Hanley J. J.: Effects of tensile loading on the properties of elastic-wave propagation in a strand. J. Acoust. Soc. Am. **103**, 3370–3375 (1998)

Laguerre L., Brissaud M., Aime J.-C.: Magnetostrictive pulse-echo device for non-destructive evaluation of steel cylindrical materials using guide waves. Ultrasonics **39**, 503–514 (2002)
Laguerre L., Brissaud M., Aime J.-C. : Low frequency ultrasound reflectometry device based on magnetoelastic transducers for the non-destructive evaluation of steel rods and cables. Bull. Lab. Ponts et Chaussées **239**, 7–27 (2003)
Lanza di Scalea F., Rizzo P., Seible F.: Stress measurement and defect detection in steel strands by guided stress waves. J. Mater Civil Eng. **15**, 219–227 (2003)
Mace B. R., Duhamel D., Brennan M. J.: Finite element prediction of wave motion in structural waveguides. J. Acoust Soc. Am. **117**, 2835–2843 (2005)
Mead D. J.: A general theory of harmonic wave propagation in linear periodic systems with multiple coupling. J. Sound Vib. **27**, 235–260 (1973)
Mead D. J.: Wave propagation in continuous periodic structures: research contributions from Southampton, 1964–1995. J. Sound Vib. **190**, 495–524 (1996)
Onipede O., Dong S. B.: Propagating waves and end modes in pretwisted beams. . J. Sound Vib. **195**, 313–330 (1996)
Pavlakovic B., Lowe M. J. S., Cawley P.: Inspection of tendons in post-tensioned concrete using guided ultrasonic waves. Insight **41**, 446-452 (1999)
Pavlakovic B., Lowe M. J. S., Cawley P.: High-frequency low-loss modes in imbedded bars. J. App. Mech. **68**, 67-75 (2001)
Rizzo P., Lanza di Scalea F.: Wave propagation in multi-wire strands by wavelet-based laser ultrasound. Exp. Mech. **44**, 407–415 (2004)
Tisseur F., Meerbergen K.: The quadratic eigenvalue problem. SIAM Rev. **43**, 235–286 (2001)
Treyssede F.: Numerical investigation of elastic modes of propagation in helical waveguides. *J. Acoust. Soc. Am.* **121**, 3398–3408 (2007)
Treyssede F.: Elastic waves in helical waveguides. *Wave Motion* **45**, 457–470 (2008)

A numerical method for the simulation of NDT experiments in an elastic waveguide

V. Baronian, A. S. Bonnet-Ben Dhia, A. Lhémery and E. Lunéville

Abstract This work concerns the numerical simulation of a non destructive testing experiment in an elastic waveguide. The transient wave which is produced by the transducer is represented, in the frequency domain, as a superposition of modes. As a consequence of Auld's reciprocity principle, the echo measured by the receiver can be expressed by a formula combining the modal amplitudes and the scattering matrix of the defect. An original and efficient finite element formulation has been developed for the computation of this matrix, which applies to arbitrary flaws: the unknowns are the displacement field in a small portion of the waveguide containing the defect and the normal component of the normal stresses on the artificial boundaries. Numerical results are presented in the two-dimensional case.

1 Introduction

The ability to inspect large structures from a single probe position makes inspection by elastic guided waves a very attractive solution for many industrial applications

V. Baronian
POEMS, CNRS-INRIA-ENSTA UMR 2706, 32 Boulevard Victor, 75015 Paris, France, and Commissariat à l'Energie Atomique, LIST, CEA-Saclay, 91191, Gif-sur-Yvette Cedex, France, e-mail: vahan.baronian@ensta.fr

A. S. Bonnet-Ben Dhia
POEMS, CNRS-INRIA-ENSTA UMR 2706, 32 Boulevard Victor, 75015 Paris, France, e-mail: anne-sophie.bonnet-bendhia@ensta.fr

A. Lhémery
Commissariat à l'Energie Atomique, LIST, CEA-Saclay, 91191, Gif-sur-Yvette Cedex, France, e-mail: Alain.LHEMERY@cea.fr

E. Lunéville
POEMS, CNRS-INRIA-ENSTA UMR 2706, 32 Boulevard Victor, 75015 Paris, France, e-mail: eric.luneville@ensta.fr

[4] (aircraft parts, rails, pipes...). However, guided waves are dispersive and multimodal by nature [11]; as a consequence, interpreting experimental data, conceiving optimal testing configurations are more than often difficult tasks. This calls for the development of efficient and comprehensive simulation tools. The simulation of a complete inspection by guided waves requires specific models to describe the radiation and reception of guided waves by a transducer, their propagation in the waveguide and their interaction with a hypothetical flaw.

In order to develop such a simulation tool, a theoretical formulation has been proposed co-authored by one of the present authors [6] allowing these phenomena to be computed separately. The formulation, in the frequency domain, results from Auld's reciprocity principle [1] written by using modal descriptions of the wave in the safe part of the waveguide and the scattering matrix of the defect. Actually, two formulations were derived (readers interested in their detailed derivation are referred to [6]): a first one deals with inspection configurations where a single transducer is used to both radiate guided waves and receive them, the other with configurations where two separate transducers are used for radiation and reception (cf. Fig. 1). In

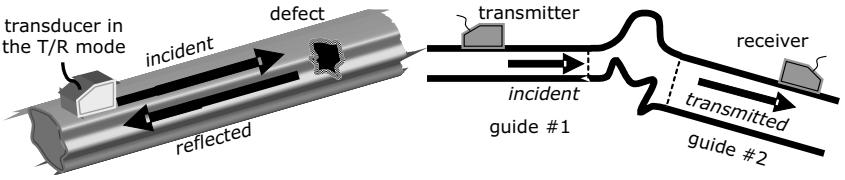

Fig. 1 Two configurations to deal with. Left: scattering by an arbitrary defect in a guide of arbitray section in the pulse-echo mode. Right: scattering by the complex junction of two different guides in the T/R mode.

Ref. [6], the method has been applied to general waveguides (with arbitrary cross section) but only for particular defects, i.e. a crack normal to the guide axis. The semi-analytical finite element (SAFE) method (see [5] for example for a description of this method) was used to predict the modal solution over the frequency spectrum of interest (standard Fourier synthesis is made to consider time-dependent waveforms). Using similar discretization of the guide section, other systems of equations were derived to compute the amplitude of modes radiated by a given transmitter, the sensitivity of a receiver to the various modes and the scattering matrix of the crack.

The object of the present work is to extend the previous method to flaws of more complex shape and in an arbitrary position in the guide. The difficulty concerns the computation of the scattering matrix of the defect. The method should be flexible and provide with a good accuracy the coefficients linking reflected or transmitted modes to the incident modes. An original finite element formulation has been proposed in [3]; transparent boundary conditions based on modal expansions are used on each side of the defect. This leads to zones of numerical computation which can be of very small extent, all the smaller since the number of evanescent modes taken

into account is large. The method can also be used for guides inhomogeneities like local variations of the guide thickness, junction of two guides etc...

The paper is organized as follows. First, some results concerning guided modes are briefly recalled. The main point is the biorthogonality relation which is extensively used in the sequel. Then the overall modal formulation based on Auld's reciprocity principle [6] is described. The new model for computing the scattering of guided waves by an arbitrary scatterer is presented in section 4. Examples are given to demonstrate the efficiency of this method to limit to a minimum the size of the FE computation zone. Finally, an illustration of interest for NDT applications is shown in section 5.

2 Guided modes of the elastic waveguide

2.1 The elastodynamic system

We consider an isotropic elastic waveguide of section S in $\mathbf{x_S} = (x_1, x_2)$ plane (S is a bounded domain of $\mathbb{R}^2$) and of axis x_3 with a stress-free boundary. The density ρ and Lamé's coefficients λ and μ may depend on $\mathbf{x_S}$. The propagation in Ω ($\Omega = S \times \mathbb{R}$) is modeled by the following classical equations ($\omega > 0$ denotes the pulsation and $\mathbf{u} = (u_1, u_2, u_3)^T$ the displacement field):

$$\begin{cases} -\mathrm{div}\sigma(\mathbf{u}) - \omega^2 \rho \mathbf{u} = 0 \text{ in } \Omega, \\ \sigma(\mathbf{u})\nu = 0 \qquad\qquad\qquad \text{on } \partial\Omega, \end{cases} \tag{1}$$

where $\sigma(\mathbf{u})$, the stress tensor, is related to the strain tensor $\varepsilon(\mathbf{u}) = 1/2(\nabla\mathbf{u} + \nabla^T\mathbf{u})$ by Hooke's law and ν denotes the outward unitary normal to $\partial\Omega$.
Because of the cylindrical geometry of the waveguide it is convenient to introduce new notations. So we denote by $\mathbf{u_S}$, $\mathbf{t_S}$, σ_S and ε_S the transverse part of the displacement field $\mathbf{u}$, of the normal stress $\sigma(\mathbf{u})\mathbf{e_3}$, of the stress tensor and of the strain tensor:

$$\mathbf{u_S} = \begin{pmatrix} u_1 \\ u_2 \end{pmatrix}, \quad \mathbf{t_S} = \begin{pmatrix} \sigma_{31} \\ \sigma_{32} \end{pmatrix}, \quad \sigma_S = \begin{pmatrix} \sigma_{11} & \sigma_{12} \\ \sigma_{21} & \sigma_{22} \end{pmatrix} \text{ and } \quad \varepsilon_S = \begin{pmatrix} \varepsilon_{11} & \varepsilon_{12} \\ \varepsilon_{21} & \varepsilon_{22} \end{pmatrix}.$$

Finally we set $t_3 = -\sigma_{33}$, and we define the two hybrid vectors

$$\mathbf{X} = \begin{pmatrix} \mathbf{t_S} \\ u_3 \end{pmatrix} \quad \text{and} \quad \mathbf{Y} = \begin{pmatrix} \mathbf{u_S} \\ t_3 \end{pmatrix}. \tag{2}$$

Then it is possible to write the elastodynamic system as an evolution problem (with respect to the coordinate x_3 of the waveguide) on $\mathbf{X}$ and $\mathbf{Y}$ (which extends to the general 3D case the formulation of [9, 10]):

$$\frac{\partial}{\partial x_3} \begin{pmatrix} \mathbf{X} \\ \mathbf{Y} \end{pmatrix} = \begin{pmatrix} 0 & F \\ G & 0 \end{pmatrix} \begin{pmatrix} \mathbf{X} \\ \mathbf{Y} \end{pmatrix} \tag{3}$$

where the operators F and G are defined by

$$F\mathbf{Y} = \begin{pmatrix} -\mathrm{div}_S \sigma_S(\mathbf{Y}) - \omega^2 \rho \mathbf{u_S} \\ -\alpha \, \mathrm{div}_S \, \mathbf{u_S} - \dfrac{\alpha}{\lambda} t_3 \end{pmatrix} \text{ and } G\mathbf{X} = \begin{pmatrix} \dfrac{\mathbf{t_S}}{\mu} - \nabla_S u_3 \\ \mathrm{div}_S \mathbf{t_S} + \omega^2 \rho u_3 \end{pmatrix} \tag{4}$$

with ∇_S and div_S the surfacic gradient and divergence operators, and

$$\sigma_S(\mathbf{Y}) = (\delta \, \mathrm{div}_S \mathbf{u_S} - \alpha t_3) Id + 2\mu \varepsilon_S(\mathbf{u_S}) \tag{5}$$

with $\delta = \dfrac{2\lambda\mu}{\lambda + 2\mu}$ and $\alpha = \dfrac{\lambda}{\lambda + 2\mu}$.

The boundary condition can be written equivalently in terms of two uncoupled boundary conditions on $\mathbf{X}$ and $\mathbf{Y}$:

$$\sigma(\mathbf{u})\nu = 0 \quad \text{on} \quad \partial\Omega \Longleftrightarrow \begin{cases} \sigma_S(\mathbf{Y})\mathbf{n_S} = 0 \\ \mathbf{t_S}\mathbf{n_S} = X_1 n_1 + X_2 n_2 = 0 \end{cases} \quad \text{on} \quad \partial S \tag{6}$$

Operators F and G are defined in a more precise mathematical setting in [3] (as unbounded operators in L^2 with domains $D(F)$ and $D(G)$ taking into account the boundary conditions): they are proved to be selfadjoint, which will be useful in the sequel.

2.2 Elastic modes and biorthogonality

The modes are the solutions of (1) of the form: $\mathbf{u}(\mathbf{x_S}) e^{i\beta x_3}, \beta \in \mathbb{C}$, or equivalently, the solutions of (3) of the form:

$$\begin{pmatrix} \mathbf{X}(\mathbf{x_S}) \\ \mathbf{Y}(\mathbf{x_S}) \end{pmatrix} e^{i\beta x_3}, \quad \beta \in \mathbb{C}.$$

This leads to solve the following eigenvalue problem,

$$i\beta \begin{pmatrix} \mathbf{X} \\ \mathbf{Y} \end{pmatrix} = \begin{pmatrix} 0 & F \\ G & 0 \end{pmatrix} \begin{pmatrix} \mathbf{X} \\ \mathbf{Y} \end{pmatrix} \tag{7}$$

with $\mathbf{X} \in D(F)$ and $\mathbf{Y} \in D(G)$.

Let us point out that spectral problem (7) is not selfadjoint although F and G are. However, using the selfadjointness of F and G, we can derive a biorthogonality relation between two eigensolutions $(\beta, \mathbf{X}, \mathbf{Y})$ and $\left(\tilde{\beta}, \tilde{\mathbf{X}}, \tilde{\mathbf{Y}}\right)$:

$$\left(FG\mathbf{X}|\tilde{\mathbf{Y}}\right)_S = \left(\mathbf{X}|GF\tilde{\mathbf{Y}}\right)_S \Leftrightarrow (\tilde{\beta}^2 - \beta^2)\left(\mathbf{X}|\tilde{\mathbf{Y}}\right)_S = 0 \tag{8}$$

This relation implies that the eigensolution $(\beta, \mathbf{X}, \mathbf{Y})$ is "orthogonal" to any other mode $\left(\tilde{\beta}, \tilde{\mathbf{X}}, \tilde{\mathbf{Y}}\right)$, except if $\tilde{\beta} = \pm\beta$.

We assume in the following that the pulsation ω is such that the group velocity of propagative modes does not vanish. As a consequence, for a propagative mode $(\beta, \mathbf{X}, \mathbf{Y})$, the following identity:

$$\frac{d\beta}{d\omega}(\mathbf{X}|\mathbf{Y}) = i\omega \int_S \rho \, (|\mathbf{u_S}|^2 + |u_3|^2) dS.$$

proves that $(\mathbf{X}|\mathbf{Y})$ does not vanish.

Then we can split the modes in two families corresponding respectively to the rightgoing and leftgoing modes:

- An evanescent mode is rightgoing (resp. leftgoing) if $\Im m\, \beta > 0$ (resp. $\Im m\, \beta < 0$).
- A propagative mode is rightgoing (resp. leftgoing) if its group velocity $\partial\omega/\partial\beta$ is positive (resp. negative).

Let us denote by $(\beta_n, \mathbf{X_n}, \mathbf{Y_n})$ for $n \in \mathbb{N}$ the eigenelements corresponding to rightgoing modes (so that $(\beta_{-n}, \mathbf{X_{-n}}, \mathbf{Y_{-n}}) = (-\beta_n, -\mathbf{X_n}, \mathbf{Y_n})$, for $n \in \mathbb{N}$, is the family of leftgoing modes) (according to Auld's labeling convention [2]). Then after a suitable normalization:

$$(\mathbf{X_n}|\mathbf{Y_m})_S = \delta_{nm}. \tag{9}$$

By setting $\int_S f\, g\, dS = (f,g)_S$, this can be written:

$$(\mathbf{t_S^n}, \mathbf{u_S^m})_S + (u_3^n, t_3^m)_S = \delta_{nm}. \tag{10}$$

3 A reciprocity formula for ultrasonic inspection in a waveguide

We assume that ultrasonic fields $\mathbf{u}$ (displacement) and σ (stress) at coordinates $(\mathbf{x_S}, x_3)$ and at a given frequency ω in a safe waveguide can be expressed as a linear combination of the eigenmodes. Then the overall problem of radiation, propagation, scattering by a defect and reception of guided waves can be handled using reciprocity relations. In 1979, Auld introduced a formulation [1] that relates the difference between the electrical signal received by a transducer in absence (state 1) and in presence of a flaw (state 2) to the elastodynamic field taken in both states integrated on a surface surrounding a flaw. A similar approach can be applied to guided waves. For the sake of simplification, we assume in what follows a pulse-echo configuration with stress free boundary conditions on the guiding surface (Figure 2).

Auld's formula writes:

$$\delta\Gamma = \frac{-i\omega}{4P} \int_{S_F} (\mathbf{u_{(1)}} \cdot \sigma_{(2)} - \mathbf{u_{(2)}} \cdot \sigma_{(1)}) \nu \, dS \tag{11}$$

where

Fig. 2 Definition of states 1 and 2 in the formulation of Auld's reciprocity theorem applied to pulse echo configuration.

- $\delta\Gamma$ is the difference between the electrical transmission coefficient of the transducer in state 2 and in state 1. This coefficient is defined as the ratio of the amplitude of the electromagnetic wave transmitted into the coaxial line in reception to the amplitude of the electromagnetic wave incident in the coaxial line in emission
- $\mathbf{u}_{(\mathbf{j})}$ and $\sigma_{(j)} = \sigma(\mathbf{u}_{(\mathbf{j})})$ are the particle displacement and stress fields in state j in response to an incident electrical signal carrying power P in the coaxial line of the transducer.
- ν is the unit vector normal to the boundary S_F surrounding the flaw.

In state 1, that is, in the absence of the defect, the field radiated by the transducer is decomposed over the modal solutions with amplitude coefficients denoted by A_n^r:

$$\mathbf{u}_{(\mathbf{1})} = \sum_{n\in\mathbb{N}} A_n^r \mathbf{u}^{\mathbf{n}}(\mathbf{x_S}) e^{i\beta_n x_3^{\pm}} \quad \text{on } \Sigma^{\pm} \tag{12}$$

where $x_3^{\pm}$ are the axial coordinates of the left (-) and right (+) boundaries, assuming that the transducer is located at $x_3 = 0$.

In state 2, the incident field is decomposed over the modal solutions with amplitude coefficients denoted by A_n^e. To take into account the defect, we introduce the scattering coefficients which are defined as follows:

- R_{mn} is the amplitude of the reflected mode m on Σ^- for an incident mode n of unit amplitude on Σ^-.
- T_{mn} is the amplitude of the transmitted mode m taken on Σ^+ for an incident mode n of unit amplitude on Σ^-.

On Σ^-, the field writes as a superposition of incident and reflected contributions; on Σ^+, it writes as the expression of transmitted contributions:

$$\begin{aligned} \mathbf{u}_{(\mathbf{2})} &= \sum_{n\in\mathbb{N}} A_n^e \mathbf{u}^{\mathbf{n}}(\mathbf{x_S}) e^{i\beta_n x_3^-} + \sum_{n\in\mathbb{N}}\sum_{m\in\mathbb{N}} A_n^e R_{mn} \mathbf{u}^{-\mathbf{m}}(\mathbf{x_S}) e^{i\beta_n x_3^-} \quad \text{on } \Sigma^- \\ \mathbf{u}_{(\mathbf{2})} &= \sum_{n\in\mathbb{N}}\sum_{m\in\mathbb{N}} A_n^e T_{mn} \mathbf{u}^{\mathbf{m}}(\mathbf{x_S}) e^{i\beta_n x_3^-} \quad \text{on } \Sigma^+ \end{aligned} \tag{13}$$

Introducing Eqs. (12) and (13) in (11), most of the terms vanish due to the bi-orthogonality of eigenmodes. Indeed:

$$\int_{\Sigma^{\pm}} (\mathbf{u^n}\sigma(\mathbf{u^m}) - \sigma(\mathbf{u^n})\mathbf{u^m}) \cdot \nu \, dS = (\mathbf{X_n}|\mathbf{Y_m})_S - (\mathbf{X_m}|\mathbf{Y_n})_S$$

so that using (9):

$$\frac{1}{2}\int_{\Sigma^{\pm}} (\mathbf{u^n}\sigma(\mathbf{u^m}) - \mathbf{u^m}\sigma(\mathbf{u^n})) \cdot \nu \, dS = \delta_{n,-m} \quad \text{for } n \in \mathbb{N} \text{ and } m \in \mathbb{Z}. \tag{14}$$

This leads finally to the following formula:

$$\delta\Gamma = \frac{-i\omega}{P} \sum_{n\in\mathbb{N}} \sum_{m\in\mathbb{N}} A_n^r A_m^e R_{nm} e^{i(\beta_n+\beta_m)x_3^-} \tag{15}$$

The various terms can be calculated independently and then combined in (15) to get the received electrical signal in the presence of the flaw. A similar derivation can be made to get a formula equivalent to (15) for configurations where two separate transducers are used. The formula for this case writes

$$\delta\Gamma = \frac{-i\omega}{P} \sum_{n\in\mathbb{N}} \sum_{m\in\mathbb{N}} A_n^r A_m^e T_{nm} e^{i\beta_m x_3^-} e^{i\beta_n(L-x_3^+)} \tag{16}$$

where the transmitter is located at $x_3 = 0$ and the receiver at $x_3 = L$.

Since these formulations were derived assuming a time harmonic excitation, standard Fourier synthesis can be further applied to predict time-dependent waveforms typical of those measured in practice.

4 A finite element formulation for the scattering matrix of the defect

4.1 Description of the method

Let us now present a numerical method which allows to compute the scattering matrix of the defect, or more precisely with the previous notations the matrices R_{nm} and T_{nm}. To fix ideas, we consider without loss of generality the case of a crack $\Gamma \subset \Omega$, with $\Gamma \subset \{x_3^- < x_3 < x_3^+\}$. Our purpose is the computation of the wave diffracted by the crack, when the incident wave is supposed to be any rightgoing mode $\mathbf{u^{inc}}(\mathbf{x}) = \mathbf{u^m}(\mathbf{x_S})e^{i\beta_m(x_3-x_3^-)}$. The total displacement field $\mathbf{u}$ then satisfies:

$$\begin{cases} -\mathbf{div}\sigma(\mathbf{u}) - \omega^2\rho\mathbf{u} = 0 \text{ in } \Omega\backslash\Gamma, \\ \sigma(\mathbf{u})\nu = 0 \qquad\qquad\qquad\quad \text{on } \partial\Omega \cup \partial\Gamma, \end{cases} \tag{17}$$

where the diffracted wave defined as $\mathbf{u^{dif}} = \mathbf{u} - \mathbf{u^{inc}}$ has to be a superposition of outgoing modes:

$$\mathbf{u^{dif}} = \sum_{n\in\mathbb{N}} A_n^{\pm}\mathbf{u^{\pm n}}(\mathbf{x_S})e^{\pm i\beta_n(x_3-x_3^{\pm})}$$

respectively for $x_3 \geq x_3^+$ and $x_3 \leq x_3^-$. Let us emphasize that the amplitudes $A_n^\pm$ (which are a unknown and will be obtained as a result of the computation) are directly related to the scattering matrices since:

$$A_n^+ = T_{nm} \text{ and } A_n^- = R_{nm}.$$

We aim to build a variational formulation for the displacement field in the computational domain $\Omega_B = S \times \{x_3^- < x_3 < x_3^+\}$ and the difficulty is to exhibit transparent conditions on the artificial boundaries $\Sigma^\pm = S \times \{x_3 = x_3^\pm\}$. The idea is to introduce additional unknowns t_3, defined on $\Sigma^\pm$ (remember that $t_3 = -\sigma_{33}$). Then the amplitudes of the scattered field $A_n^\pm$ are given as functions of $\mathbf{u}$ and t_3 by using the biorthogonality relation (9):

$$A_n^\pm = \left(\mathbf{t}_\mathbf{S}^{\pm\mathbf{n}}, u_S\right)_{\Sigma^\pm} + \left(u_3^{\pm n}, t_3\right)_{\Sigma^\pm}.$$

Next the transverse components of the normal stess on the artificial boundaries can be recovered by the following formula:

$$t_{S|\Sigma^\pm} = \sum_{n\in\mathbb{N}} A_n^\pm \mathbf{t}_\mathbf{S}^{\pm\mathbf{n}}.$$

Finally the complete normal stress (t_S, t_3) on $\Sigma^\pm$ can be introduced in a classical manner in the variational formulation for the displacement field.

As we have introduced an additional unknown, we add an additional equation which expresses the compatibility between the longitudinal component of the displacement u_3 given by the finite element representation and its modal representation (on the artificial boundaries):

$$u_{3|\Sigma^\pm} = \sum_{n\in\mathbb{N}} A_n^\pm u_3^{\pm n}.$$

In practice, the series expansions are truncated, keeping at least all propagative modes.

4.2 Numerical validation

The method has been implemented in the 2D case using the code MELINA [7]. All the numerical results concern a steel plate for which the velocities of longitudinal and transversal waves are given by $c_L = 5960ms^{-1}$ and $c_T = 3260ms^{-1}$. We use P2 Lagrange finite elements for both unknowns $\mathbf{u}$ and t_3.

For the validation, we considered the case of a vertical planar crack of length 10 mm in a steel plate of thickness 20 mm. The computations are made for a frequency $f = 0.25$ MHz. At this frequency, it can be shown that exactly 6 Lamb modes can propagate in the plate: the three symmetric S0, S1 and S2 and the three skew-symmetric A0, A1 and A2 modes. As an illustration we show in figure 4.2 the

modulus of the reflection coefficients R_{nn} for $1 \leq n \leq 6$ versus the distance between the artificial boundaries and the crack. The dashed (resp. continuous) lines correspond to the case where 41 (resp. 6) modes are used in the modal expansions of the artificial boundary conditions. As expected, the values obtained with 41 modes (dashed lines) are independent of the position of the artificial boundaries, which confirm the efficiency of the transparent boundary conditions. Accurate results can also be obtained by using only propagative modes if the artificial boundaries are no too close to the defect.

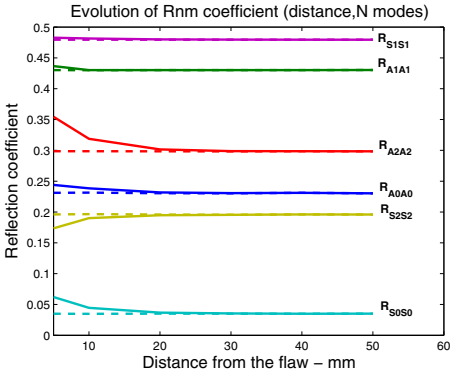

Fig. 3 Validation of the method for a vertical crack

5 Time synthesis

Combining the reciprocity formulas established in section 3 and the finite element approach presented in the previous section, we are now able to simulate a non destructive testing experiment for an arbitrary flaw. We consider as an example the following configuration: a steel plate of height 20 mm and length 500 mm including an oblique crack (45 $^\circ$) located at 250 mm of the edges of the plate. A normal stress $t_3(\mathbf{x_S}, t)$ is imposed by the transducer at one extremity of the plate, uniform in space and time modulated:

$$t_3(\mathbf{x_S}, t) = e^{-(t-tc)^2/2\theta} \sin(\omega_c t)$$

where the central frequency $f_c = \omega_c/2\pi$ is equal to 0.85 MHz and the frequency bandwidth is $[0.81, 0.88]$ (with $t_c = 70.5\ \mu s$ and $\theta = 216$). Our aim is to simulate the signal measured by the receiver located at the other extremity.

In practice, the frequency bandwidth is sampled ($\Delta f = 1000$ Hz). For each frequency:

1. The modes of the plate are computed (SAFE method).

2. The amplitude coefficients $A_n^e = A_n^r$ are determined (following [6]).
3. The transmission matrix T is computed by the above finite element method (in the computational domain represented in figure 5).

The third step is the most expensive part of the computations, but it is independent of the NDT configuration (location and spatial behavior of the transducers). The

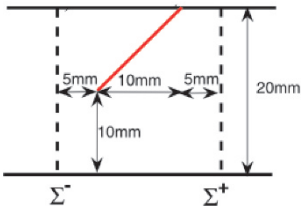

Fig. 4 The oblique crack and the finite element domain

received time signal is finally recomposed by using expression (16) and applying a Fast Fourier Transform. Let us emphasize one of the advantages of this approach:

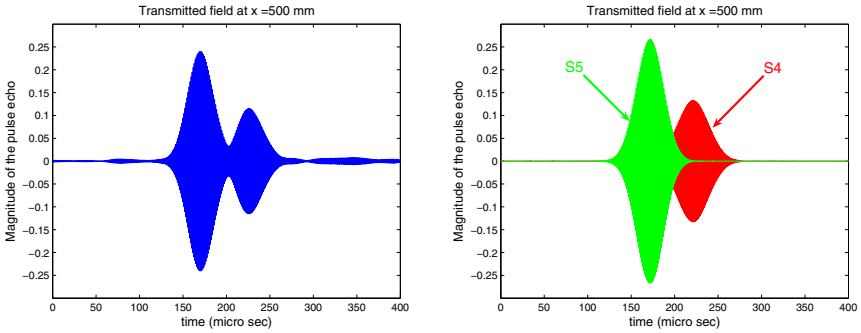

Fig. 5 Time signal at the receiver: total field (left) and main modal contributions (right)

compared to full time domain simulations, the time response of each modal contribution is available. In the present example, the main contributions are due to modes S4 and S5 (see figure 5).

Summary

A numerical method has been developed for simulating NDT experiments based on elastic guided waves. This method relies on a modal formulation [6] to deal with

the radiation by an ultrasonic transducer, the guided propagation, the scattering by a defect and the reception by the same transducer (pulse-echo configurations) or another one (transmission configurations), each stage being computed separately. The modal formalism is particularly interesting to easily interpret typical complicated waveforms observed in experiments; furthermore, number of interesting new results can be obtained by means of simple post-processing, thus limiting computational efforts in multi-parametric studies. In practice, eigenmodes are computed by means of the Semi-Analytical Finite Element method for numerical efficiency.

The main novelty described in the present paper is the possibility to compute in the smallest possible zone the scattering of an incident field by an arbitrary defect or generally speaking a non-uniformity of the guide. For this, a new Finite Element scheme has been developed combining exact transparent boundary conditions and the account of the modal decomposition of an arbitrary field thanks to biorthogonality relations: the higher the number of evanescent modes accounted for in the computation, the smaller the discrete FE computation zone surrounding the guide non-uniformity. These developments result in a versatile and numerically efficient method that can address complicated configurations typical of those encountered in practice. At present, the numerical tool developed is used to deal with various configurations of interest for NDT applications.

References

1. B. A. Auld, *Wave Motion 1*, 3 (1979).
2. B. A. Auld, *Acoustic fields and waves in solids - Vol. II*, Krieger Publishing Company, Malabar, Florida, 1990, Chapter 10.
3. V. Baronian, A.-S. Bonnet-Ben Dhia and E. Lunéville, *Transparent boundary conditions for the harmonic diffraction problem in an elastic waveguide*, to appear in JCAM.
4. P. Cawley, *Practical long range guided wave inspection - Managing complexity*, Review of Progress in QNDE 22A, ed. by D. O. Thompson and D. E. Chimenti, AIP Conference Proceedings vol. 657, American Institute of Physics, Melville, NY, (2003), pp. 22-37.
5. J. M. Galàn and R. Abascal, *Numerical simulation of Lamb wave scattering in semi-infinite plates*, Int. J. Numer. Meth. Engng. 53, 1145 (2002).
6. K. Jezzine and A. Lhémery, *Simulation of guided wave inspection based on the reciprocity principle and the semi-analytical finite element method*, Review of Progress in QNDE 26, ed. by D. O. Thompson and D. E. Chimenti, AIP Conference Proceedings vol. 894, American Institute of Physics, Melville, NY, (2007), pp. 39-46.
7. D. Martin, *On line documentation of mélina*, http://perso.univ-rennes1.fr/daniel.martin/melina.
8. V. Pagneux and A. Maurel, *Lamb wave propagation in inhomogeneous elastic waveguides*, Proc. R. Soc. Lond. A, 458 (2002), pp. 1913–1930.
9. V. Pagneux and A. Maurel, *Scattering matrix properties with evanescent modes for waveguides in fluids and solids*, J. Acoust. Soc. Am. , 116 (2004), pp. 1913–1920.
10. V. Pagneux and A. Maurel, *Lamb wave propagation in elastic waveguides with variable thickness*, Proc. R. Soc. A (2006) 462, pp. 1315—1339.
11. J. L. Rose, *Ultrasonic waves in solid media*, Cambridge University Press, Cambridge, (1999), Chap. 8-16.

Finite elements for a beam system with nonlinear contact under periodic excitation

H. Hazim, B. Rousselet

Abstract Solar arrays are structures which are connected to satellites; during launch, they are in a folded position and submitted to high vibrations. In order to save mass, the flexibility of the panels is not negligible and they may strike each other; this may damage the structure. To prevent this, rubber snubbers are mounted at well chosen points of the structure; a prestress is applied to the snubber; but it is quite difficult to check the amount of prestress and the snubber may act only on one side; they will be modeled as one sided springs (see figure 2).
In this article, some analysis for responses (displacements) in both time and frequency domains for a clamped-clamped Euler-Bernoulli beam model with a spring are presented. This spring can be unilateral or bilateral fixed at a point. The mounting (beam +spring) is fixed on a rigid support which has a sinusoidal motion of constant frequency.
The system is also studied in the frequency domain by sweeping frequencies between two fixed values, in order to save the maximum of displacements corresponding to each frequency. Numerical results are compared with exact solutions in particular cases which already exist in the literature.
On the other hand, a numerical and theoretical investigation of nonlinear normal mode (NNM) can be a new method to describe nonlinear behaviors, this work is in progress.

H.Hazim
Université de Nice Sophia-Antipolis, Laboratoire J.A. Dieudonné U.M.R. C.N.R.S. 6621, Parc Valrose, F 06108 Nice, Cedex 2 e-mail: hamad.hazim@unice.fr

B. Rousselet
Université de Nice Sophia-Antipolis, Laboratoire J.A. Dieudonné U.M.R. C.N.R.S. 6621, Parc Valrose, F 06108 Nice, Cedex 2 e-mail: br@math.unice.fr

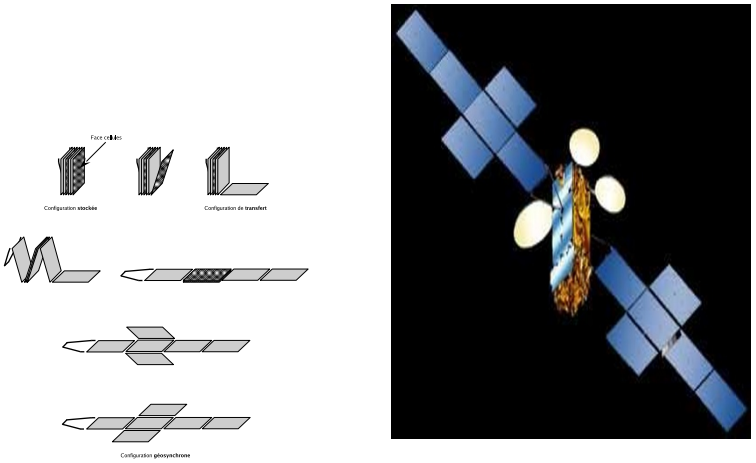

Fig. 1 At left: solar arrays from folded to final position, at right: picture for the satellite AMC12 from Thales Alenia Space company

1 Introduction

1.1 Previous Works

In articles [BFN], [FWW], [FL] et [VHCKF], proposed by Thales Alenia Space research team, the dynamic of a beam sytem with a nonlinear contact force, under a periodic excitation given as an imposed acceleration form is studied both numerically and experimentally. When sweeping frequencies in an interval which contains eigen frequencies of the beam, resonance phenomena appear as well as new frequencies caused by the unilateral contact.
Finite element method in space domain is used, followed by numerical integration of the ordinary differential systems using specific software like 'STRDYN' of the finite element package DIANA.
The frequency sweeping is done in different ways, one of these way is such as the frequency f changes as a function of the time t according to :$f(t) = f_0 2^{st/60}$ where s is the sweep rate in octaves/min and f_0 is the start frequency of the sweep. Results prove differences between sweep-down and sweep-up around eigen frequencies of the system where solutions are unstable.
At each value of the time t, computation is done and the maximum of displacement and acceleration are saved.
Finally, comparison is made in time and frequency domains, between linear and nonlinear cases.

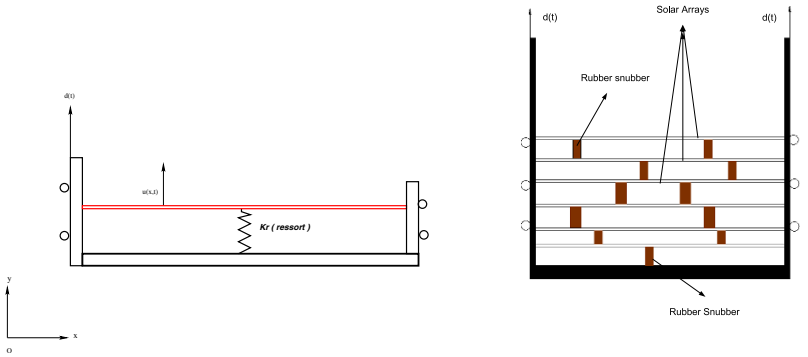

Fig. 2 left: Simplified Mechanical Model, right: folded solar arrays with snubbers

1.2 Present Work

This work is part of the phd work of the author under the guidance of B. Rousselet with the support of Thales Alenia Space, France.
Some analysis for responses (displacements) in both time and frequency domain for a clamped-clamped Euler-Bernoulli beam model with a linear spring are presented, the spring can be unilateral or bilateral fixed at a point. The mounting (beam +spring) is fixed on a rigid support which has a sinusoidal motion of constant frequency.
The system is also studied in the frequency domain by sweeping frequencies between two fixed values, such as saving the maximum of displacements corresponding to each frequency.

Numerical results are compared with exact solutions in particular cases which already exist in the literature.
On the other hand, a numerical and theoretical investigation of nonlinear normal mode (NNM) can be a new method to distinguish linear from nonlinear cases.

2 Simplified Mechanical Model

The study of the total dynamic behavior of solar arrays in a folded position with snubbers are so complicated, that to simplify, a solar array is modeled by a clamped-clamped Bernoulli beam with one-sided linear spring. This system is fixed on a shaker which has a vibratory motion $d(t)$ see figure (2).

The motion of this beam system is modeled by the following PDEs with boundary conditions : $u(0,t) = u(L,t) = d(t)$ and $\partial_x u(0,t) = \partial_x u(L,t) = 0$:

$$\textbf{Bilateral spring: } \rho S\ddot{u}(x,t) + EIu^{(iv)}(x,t) = k_r(d(t) - u(x_0,t))\delta_{x_0} \quad (1)$$

$$\textbf{Unilateral spring: } \rho S\ddot{u}(x,t) + EIu^{(iv)}(x,t) = k_r(d(t) - u(x_0,t))_+ \delta_{x_0} \quad (2)$$

u_+ is the function defined by $u_+ = \frac{u+|u|}{2}$ L= 0.485 m beam length.
k_r = spring stiffness. $d(t) = -\frac{a}{(2\pi f)^2}\sin(2\pi ft)$ is the shaker motion.
$\rho = 2700\, kg/m^3$ beam density. $S = 7,5.10^{-4}\ m^2$ cross sectional area.
$E = 7.10^{10}\ N/m^2$ Young's modulus. $I = 1,41.10^{-8}\ m^4$ second moment of area.
This data are taken from [FWW]. The classical Hermite cubic finite element approximation is used here to find an approximate solution for equations (1) and (2), we find then two ordinary differential systems in the form :

$$M\ddot{q} + Kq = k_r(d(t) - q_{x_0})\overrightarrow{e_{x_0}} \quad (3)$$

$$M\ddot{q} + Kq = k_r(d(t) - q_{x_0})_+\overrightarrow{e_{x_0}} \quad (4)$$

M et K are respectively the mass and the stiffness assembled matrices, q is the vector of degree of freedom of the beam, $q_i = (u_i, \partial_x u_i)$, $i = 1,2,...,n$. To each node are associated two degrees of freedom, the displacement and its derivative.

To integrate numerically systems (3) and (4), we use the Scilab routines "ODE's" followed by the FFT (Fast Fourier Transformation) to find frequencies of solutions, there is no special treatment for "ODE" routine to deal with the local non-differentiable nonlinearity $(d(t) - u(x_0,t))_+$.

3 Numerical Results

3.1 Highlights on the linearized system and the nonlinear effects

There are two linear cases, the first one when there is no spring attached to the beam, and the second case is such as a linear spring is always attached to the beam (bilateral spring). The system becomes nonlinear when the spring becomes one-sided when the prestress is not well tuned. The nonlinearity has a special form, it is locally not differentiable but it is lipchitz.
Without spring, the motion has the following linear system of equation :

$$M\ddot{q} + Kq = 0 \quad (5)$$

The eigen frequencies of the motion are easily calculated by computing the generalized eigen values of M and K, this calculus can be done using software like Scilab

[S]. We are interested by the first three eigen frequencies of the system, we note that the precision depends on the number of the finite elements used for the modeling of the system. We verify that ten finite elements give a good approximation for the first three eigen frequencies and their values are respectively :334.21622Hz, 921.48815Hz and 1807.7966Hz. As known, the eigen-frequencies of a Bernoulli beam could be calculated using this formula:
$f_i = \frac{1}{2\pi}\sqrt{\mu_i^4 \frac{EI}{Ml^4}}$, μ_i $i = 1,2,3,...n$ are given in [G]. $\mu_1 = 4.73$, $\mu_2 = 7.853$ and $\mu_3 = 10.996$ give $f_1 = 334.19889Hz$, $f_2 = 921.19996Hz$ and $f_3 = 1806.1432Hz$. The nonlinearity on the system modifies the motion by adding new frequencies, subharmonics and superharmonics, besides the eigen frequencies. When the system is under periodic excitation, new frequencies appear also, there are many combinations of the excitation frequency with the system frequencies. These new frequencies appears in FFT of the system and also in the sweep test. There are many ways to calculate these frequencies, harmonic balance method and nonlinear normal mode (MNN) and asymptotic expansions methods ([JB]) .

3.2 One Node Finite Element Model Without Periodic Excitation

In this case, the beam is modeled by two finite elements without periodic excitation. Equations of displacement and its derivative are independent here because of the structure of the mass and stiffness matrices:

$$M = \begin{pmatrix} 0.3647893 & 0 \\ 0 & 0.0005500 \end{pmatrix} \text{ and } K = \begin{pmatrix} 1661090 & 0 \\ 0 & 32560.825 \end{pmatrix}.$$

To find eigen frequencies of the system in the linear case (system without contact), we juste have to calculate the generalized eigen values of M and K.
The motion is divided into two phases: the first one when the beam touches the spring and another one when the beam does not touch the spring. The spring mass is negligible beside the beam mass, the equations of displacement of these two phases are respectively :

$$M(1,1)\ddot{u} + (K(1,1) + k_r)u = 0$$

$$M(1,1)\ddot{u} + K(1,1)u = 0$$

The boundary conditions are :$u(0,t) = u(L,t) = 0$ and $\partial_x u(0,t) = \partial_x u(L,t) = 0$. The period of the solution will be the sum of the half period of the first phase and the second phase :

$$T = \frac{\pi}{\sqrt{\frac{K_{11}(1,1)}{M_{11}(1,1)}}} + \frac{\pi}{\sqrt{\frac{K_{11}(1,1)+k_r}{M_{11}(1,1)}}}$$

the numerical value of the motion frequency $\frac{1}{T}$ is 384.74186Hz this is in agreement with the numerical calculus. In figure (3), The Fast Fourier Transformation shows frequencies of the system, the first peak correspond to the analytical value. The motion in the phase plane shows a periodic conservative solution.

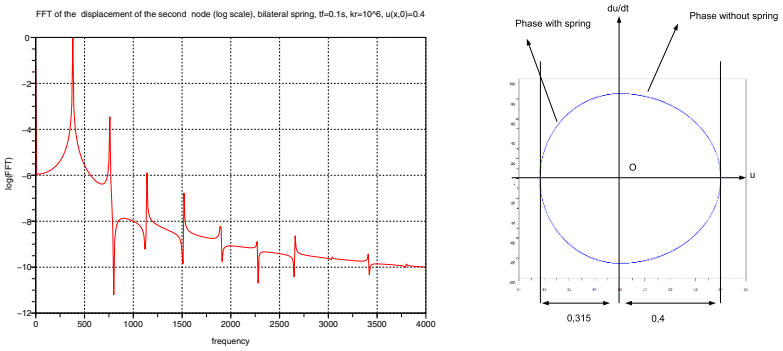

Fig. 3 Left: FFT of the displacement of the second node with unilateral spring contact with initial conditions $u(x,0) = 0.4$, $\dot{u}(x,0) = 0$. Right: solution in the phase space.

3.3 One Node Finite Element Model, Beam Under Periodic Excitation

The beam is modeled by two finite elements under periodic prescribed displacement $d(t)$. The spring is always fixed in the middle of the beam on a node, it can be unilateral or bilateral.

Figure (4) shows the displacement of the second node (in the middle) of the beam with bilateral and unilateral spring, the period of the motion changes with unilateral spring. Figure (5) shows frequencies of the beam with bilateral and unilateral cases; In the bilateral case, there are two frequencies, the eigen frequency (430 Hz) and the frequency of the shaker (500 Hz); In the unilateral case, there are the system frequency, the shaker frequency and many other superharmonics and subharmonics frequencies due to the contact.

3.4 Ten Finite Elements

In this section, the beam is modeled with ten finite elements, this approximation is quite good if we are interested by the first two eigen frequencies of the system.
The spring is always fixed in the middle of the beam on a node, and can be unilateral or bilateral, the whole system is fixed on a shaker which has periodic prescribed displacement $d(t)$, we compare the linear with the nonlinear case for the same value of parameters.
Figure (6) shows the displacement in the time domain for bilateral and unilateral

case and their corresponding frequencies using FFT. In the linear case (bilateral spring), the first and the third eigen frequencies are shown, the shaker frequency also(500 Hz); The middle of the beam is node of the second mode. In the nonlinear case (unilateral spring), frequencies corresponding to the first and the third eigen frequencies of the linear case and also the shaker frequency are shown; Many other superharmonics, subharmonics and combination with the shaker frequency appear also due to the non linear contact.

4 Frequency Sweep Excitation

Frequency sweep excitation is usually used in the experiments to check the dynamic behavior of mechanical systems. As mentioned before, the beam is under periodic excitation given as a displacement form
$d(t) = -\frac{a}{(2\pi f)^2}\sin(2\pi ft)$, that means that the beam is under an effort (acceleration) $\ddot{d}(t) = a\sin(2\pi ft)$, a in m/s^2 is the amplitude of the acceleration and f in Hz is the frequency of excitation.

We are just interested by a sweep-up test, for a initial given frequency f_0 and a fixed value of a. We compute the solution of differential systems, then we save the maximum of the acceleration and the displacement. In a second time, we add a fixed value to f_0, the frequency step df. We compute again for $f_0 + df$ and we save the same quantities for this iteration, the initial conditions are fixed on zero again. We continue our test to reach a fixed frequency f_1 chosen such as to cover the first and the second eigen frequency of the system.

Finally, we plot the maximum saved in each sweep test, then we compare linear with nonlinear cases, we study also the effect of the amplitude a and the frequency step on the system.

We remark that obtained curves are similar to curves of FFT, it is an another method to find frequencies for mechanical systems.

4.1 Two Finite Elements

The beam is modeled by two finite elements, the spring is fixed in the middle, the Bernoulli beam is clamped in its both extremities, we just have a free node of two degrees of freedom, the first is the displacement, the second is the derivative of the displacement. The eigen frequency of the linearized system in this case is around $339Hz$, the sweep-up begin from $100Hz$ to $1000Hz$, the frequency step $df = 5Hz$ and the amplitude of excitation $a = 50m/s^2$.

In each iteration, the integration time is $tf = 0.1s$, the initial conditions are always fixed at $0 : q(x,0) = \dot{q}(x,0) = 0$, $k_r = 10^6 N/m$.

In figure (7), the peak in the bilateral case corresponds to the eigen frequency of the system, its abscissa is $430Hz$. In the unilateral case, the peak corresponds to the eigen frequency too, its abscissa is $384Hz$. Other peaks appear; they are due to the unilateral contact. These results conform well with the FFT in figure (5).

4.2 Ten finite elements

The beam is modeled by ten finite elements, the spring always in the middle, the other parameters are the same defined in section 4.1.
In figure (8), the peak in the bilateral case corresponds to the first eigen frequency of the system, the second eigen frequency does not appear because the imposed displacement is not enough to excite it ($d(t) = -\frac{a}{(2\pi f)^2}\sin(2\pi f t)$ very small when f become so high). Peaks in the unilateral case show the system frequencies corresponding to the eigen frequency of the linear system and other frequencies due to the contact. These results conform with the FFT in figure (6) in the interval $[100, 1000]$ Hz.

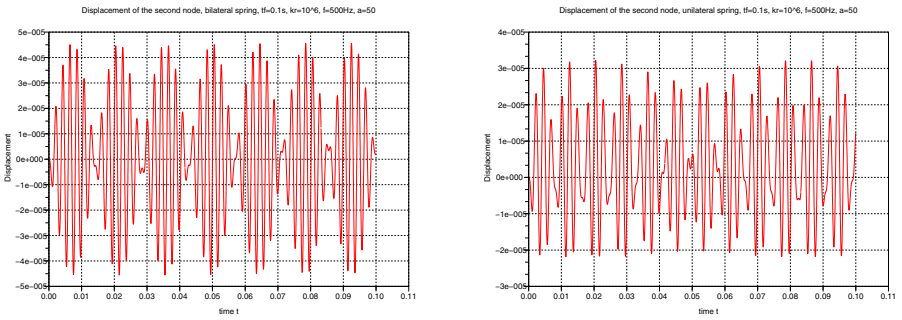

Fig. 4 Displacement of the second node with **bilateral and unilateral** spring contact under periodic excitation of 500 Hz (Two finite element model)

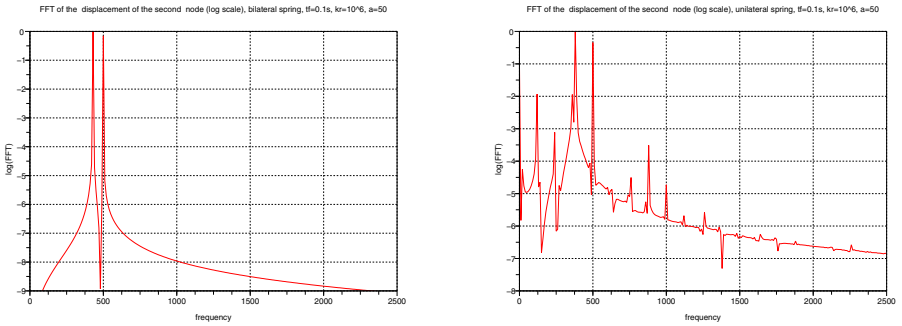

Fig. 5 FFT of the displacement of the second node with **bilateral and unilateral** spring contact under periodic excitation of 500 Hz (Two finite element model)

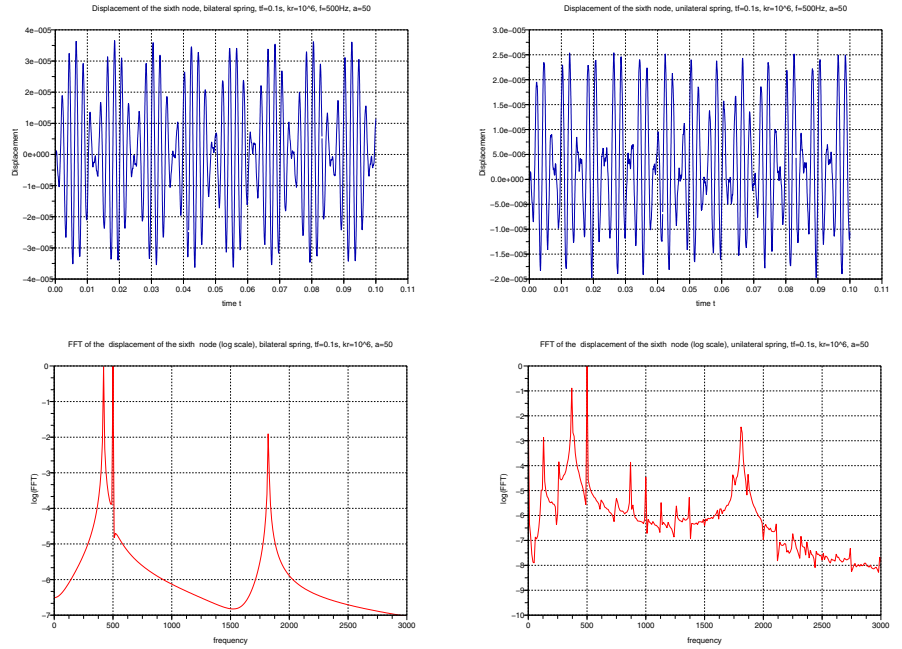

Fig. 6 Displacement and their FFT of the sixth node with **bilateral and unilateral** spring contact under periodic excitation of 500 Hz (Ten finite element model)

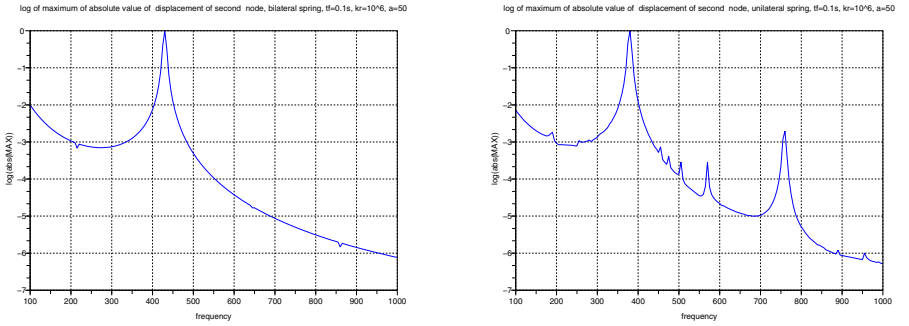

Fig. 7 Maximum of absolute value of the displacement for both **bilateral and unilateral spring**, two finite element model, $kr = 10^6 N/m$, $a = 50m/s^2$, $tf = 0.1s$ (Sweep-up test)

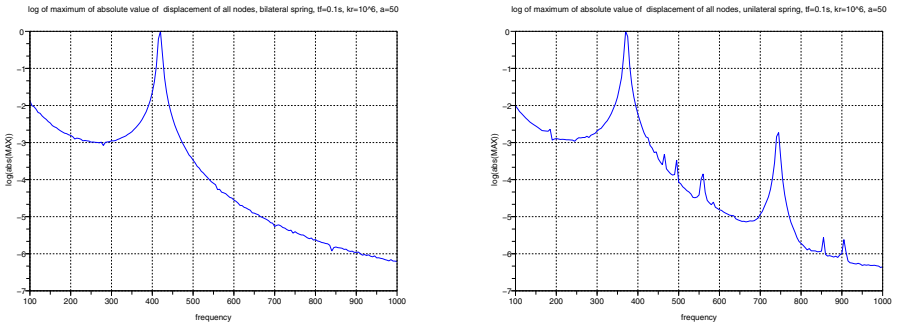

Fig. 8 Maximum of absolute value of the displacement of all nodes(log scale) for both **bilateral and unilateral spring**, ten finite element model $k_r = 10^6$, $tf = 0.1s$, $a = 50m/s^2$ (sweep-up test)

5 Conclusion

We have presented some preliminary numerical results to compare the vibrations of a beam equipped with a bilateral or a unilateral spring. Asymptotic expansions using some results of S. Junca ([JB]) are in project and compared with numerical results in order to asses the quality of both approaches. In particular accurate computations of non linear normal modes (see [DPS]) will be considered.

References

[BFN] J. H. Bonsel, R. H. B. Fey. and H. Nijmeirjer: Application of a Dynamic Vibration Absorber to a Piecewise Linear Beam System. *Nonlinear Dynamics* 37: 227-243, 2004.

[BB] Sergio Bellizzi, Robert Bouc : A new formulation for the existence and calculation of nonlinear normal modes. *Journal of sound and vibration* 287 (2005) 545-569 .

[DPS] D.Jiang,C.Pierre, S.W. Shaw: Large-amplitude non-linéar normal modes of piecewise linear systems. *Journal of sound and vibration* 272 (2004) 869-891

[FWW] Rob H.B. Fey and Berend Winter, Jaap J. Wijker
Sine sweep and steady - state response of a simplified solar array model with nonlinear support. DETC99/VIB-8027, 1999 ASME Design Engineering Technical Conferences, Las Vegas, Nevada, USA.

[FL] R.H.B. Fey and F.P.H. van Liempt :
Sine sweep and steady-state response of a simplified solar array model with nonlinear elements. International conference on Structural Dynamics Modelling, 3-5 june 2002, pp.201-210.

[G] M Géradin Théorie des vibrations: applications la dynamique des structures. Masson Paris 2eme edition 1996

[JB] Stéphane Junca et Bernard Rousselet: Asymptotic Expansions of Vibrations with Unilateral Contact, proceeding of the GDR 2501- Anglet 2-6 Juin 2008.

[R] Richard H. Rand:Lecture Notes on Nonlinear Vibrations, Dept. Theoretical Applied Mechanics Cornell University Ithaca NY 14853

[S] Scilab [www.scilab.org]

[VHCKF] E.L.B. Van De Vorst, M.F.Heertjes D.H. Van Campen and A. De Kraker and R.H. B. Fey: Experimental and numerical analysis of the steady state begavior of a beam system with impact. *Journal of Sound and Vibration* 1998 212(2), 210-225

Nonlinear acoustic fast and slow dynamics of damaged composite materials: correlation with acoustic emission

M. Bentahar, A. Marec, R. El Guerjouma and J.H. Thomas

Abstract Slow and fast dynamics in the elastic response of damaged materials to external excitations show evidence of an anomalous hysteretic elastic behavior. Experimental observations may be used to detect and eventually characterize damage existing in structural components. Here we analyze the evolution of nonlinear dynamic behavior of a polymer-based composite (SMC) and concrete. More particularly, nonlinear slow dynamics parameters have been found to be very sensitive to damage evolution for both materials. Besides, acoustic emission monitoring is used to calculate the elastic energy released by SMC during a gradual increasing damage procedure. Interesting logarithm-like evolution of the followed nonlinear parameters as a function of the calculated energy is found. A classification of the calculated acoustic emission signal is proposed to understand the contribution of the different damage mechanisms to the evolution of the nonlinear behavior of SMC.

M. Bentahar
LAUM, CNRS, Université du Maine, Av. O. Messiaen, 72085 Le Mans, France
e-mail: mourad.bentahar@univ-lemans.fr
A. Marec
LAUM, CNRS, Université du Maine, Av. O. Messiaen, 72085 Le Mans, France
e-mail: anne.marec.etu@univ-lemans.fr
R. El Guerjouma
LAUM, CNRS, Université du Maine, Av. O. Messiaen, 72085 Le Mans, France
e-mail: rachid.elguerjouma@univ-lemans.fr
J.-H. Thomas
LAUM, CNRS, Université du Maine, Av. O. Messiaen, 72085 Le Mans, France
e-mail: jean-hugh.thomas@univ-lemans.fr

1 Introduction

Heterogeneous materials (concrete, rocks, composites, etc.) are the place of creation and propagation of microcracks even at stress levels well below their rupture strength. The characterization of damage in these materials by linear acoustical methods, based on the measurement of ultrasonic waves' velocities and/or attenuation, does not generally give the expected sensitivity to damage in particular during the first loading stages, where weak damage is involved. As such, acoustical nonlinear methods appear like an interesting alternative capable to detect diffused or localized damage through the application of very weak strains [1-7]. Classical nonlinear theory for atomic elasticity uses the expansion of the elastic strain energy in powers of strain, where the expansion coefficients designate the second and third order elastic constants [4]. The interaction of an ultrasonic wave with strain (stress), also called acoustoelastic effect, leads to the effective elastic constants, which are revealed to be very sensitive to damage [4]. Nonlinear effects can also be observed through the distortion of an ultrasonic sine wave when propagating in a medium. In that case, higher harmonics (multiples of the initial frequency) are created with the following specific relations as function of the micro-strain ε: the amplitudes of the second and third harmonics scale as ε^2 and ε^3, respectively. As the acoustoelastic and harmonic approaches are strongly dependent on the ultrasonic path and hence mainly used to detect and characterize local damages, resonance method is more suitable for both global as well as local damage characterization. In that case, classical nonlinearity predicts that the resonance frequency of the fundamental resonance mode (Young's mode) changes as ε^2. Predictions of classical elastic theory (Landau theory) are well respected in many materials (intact and damaged materials: metals, rocks, concrete, composites, etc.) as long as the involved strains remain small (order of $\sim 10^{-7}$ and lower, depending on materials). However, at higher strains classical nonlinear elasticity predictions do not correspond to experimental observations. Indeed, in that case the resonance frequency shift and the second harmonic amplitude depend linearly on the stain, and the third harmonic displays quadratic strain dependence [1].

Different theoretical approaches attempting to understand the origin of these "non-classical" observations have been proposed [6-9]. However, despite these theoretical attempts, the non-classical fascinating observations made on materials of different constituents and structures are still poorly understood in terms of their underlying causes and the conditions under which they occur [10]. In this contribution we present results using Nonlinear Resonance Spectroscopy (NRS) approach to characterize damage in concrete and polymer-based composite SMC (Sheet Molding Compound). Materials are characterized at intact and damaged states. Besides, damage was monitored using Acoustic Emission system. A classification of the calculated acoustic emission signal is proposed to understand the contribution of the different damage mechanisms to the evolution of the nonlinear behavior of SMC.

2 Materials and experimental device

Samples as well as the experimental device are presented in figure 1. The gain-phase analyzer generates a continuous sinusoidal excitation whose frequency is swept through a frequency range encompassing one of the resonant frequencies of concrete bars and SMC plates. This signal is amplified at 52 dB using a power amplifier tailored for frequency range of 10 kHz to 200 MHz. Vibrations of SMC are generated and detected through two PZT ceramics bonded with epoxy at both SMC extremities. For concrete samples vibrations are detected using a *Polytech* laser vibrometer.

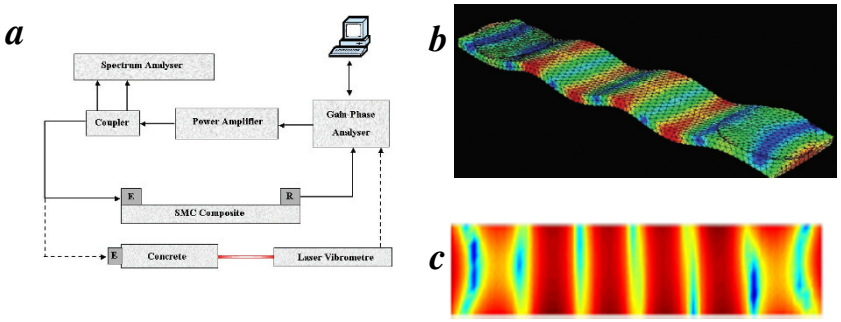

Fig. 1. (*a*) Experimental device used for nonlinear damage characterization of concrete bars and SMC plates: the use of a coupler and a spectrum analyzer allowed a good characterization of nonlinear threshold; (b) sixth flexural resonance mode identified with simulations using Abaqus^{TM} ; (c) sixth flexural resonance mode identified with the help of c-scan imaging system (*f = 16685Hz*)

A reliable nonlinear characterization is highly dependent on the linearity of the experimental device i.e. no electronic nonlinearity is generated. To make this possible, we used a reference material (intact aluminium bar), whose nonlinear properties are of the atomic order, on which we applied the same excitations needed to characterize concrete and SMC at resonance. The aluminium sample was excited around its fundamental Young's mode with a PZT bonded on one of its extremities. On the other extremity we registered its resonance response using a laser vibrometer. For an accuracy corresponding to 0.1Hz, the response has proved to be linear until an excitation corresponding to $\varepsilon = 10^{-5}$ beyond which a frequency shift is registered due to the influence of the electronic chain on the measurements. This threshold corresponds to the electronic nonlinear limit of the experimental device and will consequently not be encompassed.

3 Nonlinear characterization of concrete

For the rod-shaped concrete samples, frequency is swept through the first longitudinal resonance mode of the specimen and the amplitude of the output strain (or the root mean square output velocity) is recorded in stationary conditions. This resonance characterization was made at intact and damaged states, where damage is created using quasi-static compression tests. As discussed in several theoretical and experimental papers [2, 3, 9, 10], the first signature of the presence of nonclassical (hysteretic) elasticity is given by the downward shift of the specimen resonance frequency with increasing driving amplitude. This shift has been shown to be a linear function of the driving amplitude. Such phenomenon, known as fast dynamics, has been analysed in Fig. 2. First, resonance curves for different vibration velocities are reported for an intact concrete specimen. As known, depending on manufacturing processes, concrete is in fact slightly hysteretic already in the intact case, as confirmed by the downward shift observed in the reported plot. The sensitivity of fast dynamics to the damaged state of the specimen is analysed in the same Fig. 2 using the same excitation levels. Here we can see that the resonance frequency shift for the damaged concrete sample is much higher than the one corresponding to the intact state. Indeed, when we plot the resonance frequency shift $\Delta f/f$ vs. the output amplitude A (i.e. the amplitude of the resonance curve in correspondence of the resonance frequency) we find a slope at the damaged state 400 times higher than in the intact state.

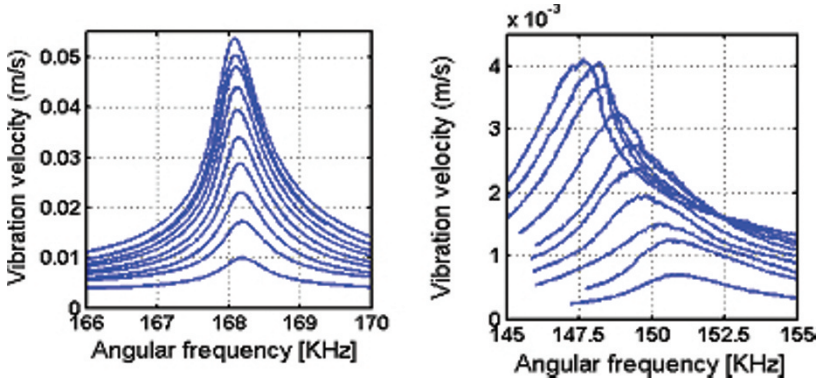

Fig. 2. Resonance curves at different excitation amplitudes (fast dynamics) for intact (left) and damaged (right) concrete samples.

A second set of results is reported here to evidentiate sensitivity of slow dynamics to the presence of damage. In a slow dynamic experiment, the specimen is probed at constant driving amplitude, after a large excitation (conditioning) has been applied. As well known, after perturbation, the specimen is temporarily softened, which means its resonance frequency is shifted to lower values. Nevertheless, by tracking the resonance frequency at successive times, it can be shown that it slowly recovers to its value before conditioning. Ex-

periments performed on a wide variety of materials have pointed out that recovery is logarithmic with time. Slow dynamics in concrete is illustrated in Fig. 3, where resonance frequencies at successive times are reported for the concrete sample mentioned above at intact and damaged states. Here, we can see that for the same conditioning, frequency relaxation time is more important at the damaged state. Furthermore, the frequency drop due to conditioning is also more important at the damaged state, showing the sensitivity of this approach to the presence of damage. The same characterization method (fast and slow dynamics) is applied in the next section on a gradually damaged polymer-based composite.

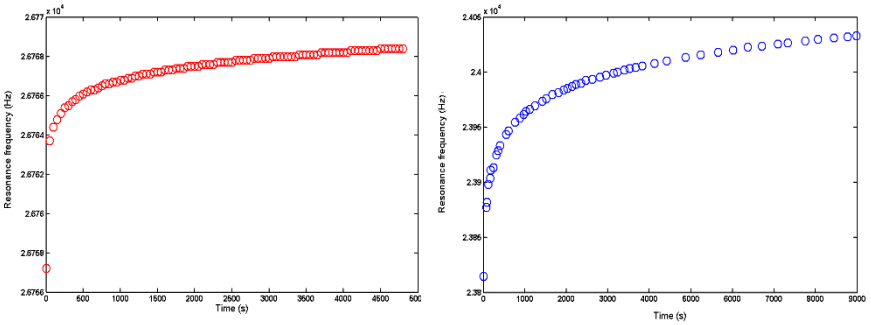

Fig. 3. Resonance frequency relaxation when probed with a weak drive amplitude vs. time of both intact (left) and damaged (right) concrete samples submitted to the same conditioning.

4. Damage characterization of instrumented SMC plates

4.1 What resonance mode to chose: identification and sensitivity to damage

For the rod-shaped concrete samples we have used the first longitudinal resonance mode in the intact and damaged states where the amplitude of the output strain (or the root mean square output velocity) is recorded in stationary conditions. However, sometimes damage areas are not well excited by fundamental modes on one hand, and experimental devices are not able to generate these modes due to their frequency limitations, on the other hand. Indeed, in the case of the instrumented SMC plates it was experimentally not possible to follow the first resonance flexural mode since the amplifier does a poor job below 10 kHz. In that

case, we had to explore higher resonance modes, identify each of them using simulations and/or an experimental imaging procedure, and study their sensitivity to an increasing damage. Resonance modes determination was performed using a Finite Element Modeling (FEM) with the help of ABAQUS™, which allowed us to identify the eigenmodes of the instrumented SMC plates. The model was fed with the mechanical properties of both SMC sample and PZT sensors shown in table 1. Simulations were compared to C-Scan images made with the help of a laser interferometer when SMC was excited at each of its different resonance frequencies. Agreement between simulations and experiments could be observed in Fig. 1.

Table 1. Mechanical properties of the materials used as input for the FEM modal analysis

Material	**Density (kg/m^3)**	**Stiffness tensor components (GPa)**								
		C_{11}	C_{12}	C_{22}	C_{13}	C_{23}	C_{33}	C_{66}	C_{55}	C_{44}
SMC	**1926**	**21.3**	**7.1**	**21.3**	**6.5**	**6.5**	**16.2**	**7.1**	**4.3**	**4.3**
PZT	**7650**	**121.0**	**75.4**	**121.0**	**75.2**	**75.2**	**111.0**	**21.1**	**22.6**	**22.6**

The choice of the most suitable vibrating mode to characterize damage is a crucial point that deserves a particular attention [4, 5]. To know the way the excited modes are affected by damage, we have induced a localised damage by increasing the flexural displacement from 0mm to 3mm using a step of 0.5mm. At each damage step, we have followed the changes in resonance frequency and amplitude and have drawn the curve shown in figure 4-a, which is normalized with respect to the sixth flexural vibrating mode of the SMC. This curve represents frequency variations for the aforementioned damage states while coding the amplitude of resonance curves in a grey scale going from white for the highest amplitudes to black for the weakest ones. We notice that the flexural vibrating mode is not the only one that is affected by damage. Indeed, with the help of figure 4-b, which is a continuation of figure 4-a, we can confirm that the frequency shift and the decrease of the amplitude affect other vibrating modes as well, though differently. This proves that exploring other resonance modes of different orders is an interesting issue that may give more information about the induced damage. However, one should be aware about the fact that experimentally we are limited by attenuation whose effect increases with damage and makes the access to higher order resonance modes difficult and sometimes impossible.

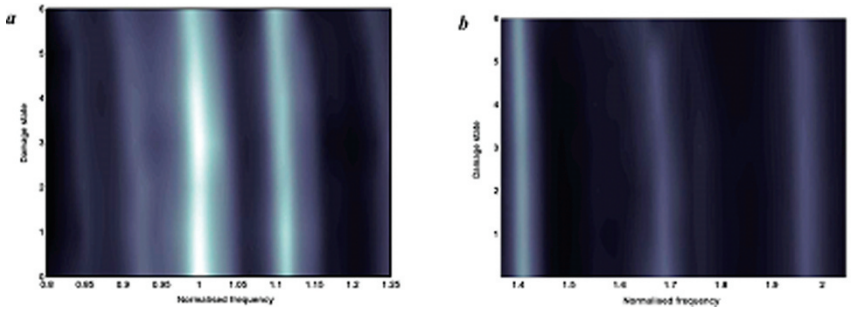

Fig. 4. (*a*) Amplitude and frequency variations around the flexural mode normalised for the identified flexural mode; (*b*) Amplitude and frequency variations for higher vibrating modes normalized for the same flexural mode

4.2 Damage quantification and characterization using Acoustic Emission (AE)

SMC specimens (100x20x3 mm3) were gradually damaged with three points bending tests [4, 5]. Four damage steps going from 0.4 mm to 1.6 mm were realised using a flexural machine (Instron with 5 kN cell). Simultaneously, elastic waves generated by the created micro-cracks were recorded using AE system (MISTRAS-2001). Acoustic emission (AE) could be used to identify the different damage mechanisms in SMC using an analysis of the recorded ultrasonic waves [10]. A classification of AE hits based on their corresponding amplitudes shows the possibility to separate the different damage mechanisms as shown in Fig. 5. However, the amplitude-based classification is not sufficient to separate and identify the different mechanisms existing in SMC: another classification procedure is needed. Indeed, the detected AE signals are characterized by different characteristics such as amplitude, duration, energy, rise time and counts. These parameters are used to build patterns. In the considered feature space, the patterns can be divided into clusters by using multivariable data analysis based on similarity measurements. In this work, unsupervised pattern recognition analyses (Fuzzy Cmeans Clustering) associated with a principal component analysis are used for the classification of the monitored AE events [12]. A cluster analysis of AE data is made where the resulting clusters are correlated to damage mechanisms existing in SMC. Identified mechanisms for SMC are [12]: matrix cracking, interfacial debonding and fiber failure (Fig. 6).

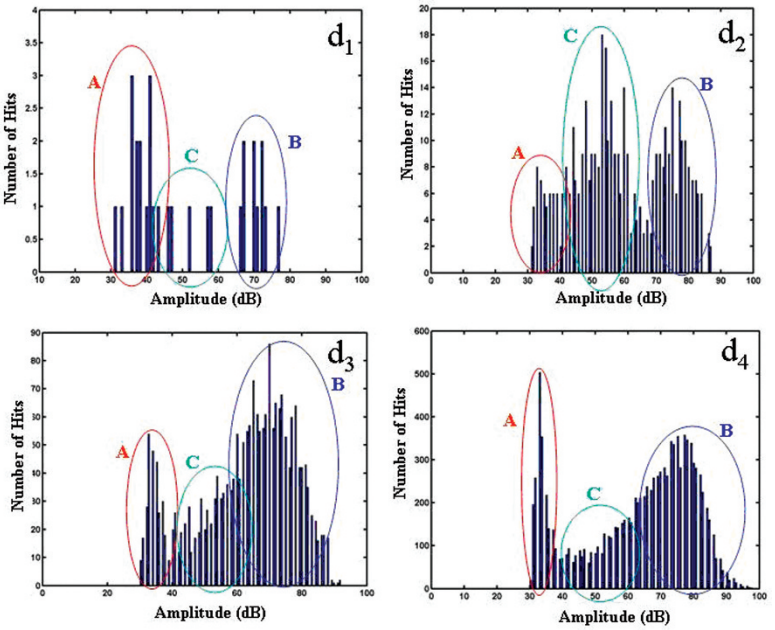

Fig. 5. Amplitude-based classification of AE hits : appearance of groups called here A, C and B which correspond to the three main damage mechanisms : matrix micro-cracking, fibre/matrix debonding and fibres cracking respectively.

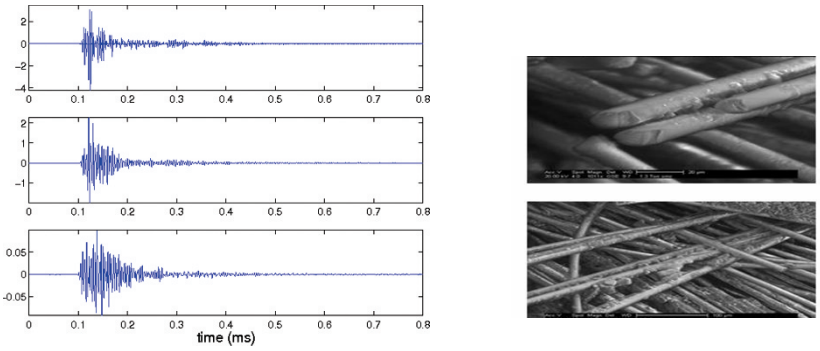

Fig. 6. (Right) Signals of the three main damage mechanisms. Form top to bottom: fibres cracking, fibre/matrix debonding and matrix micro-cracking. (Left) Damage mechanisms created in SMC.

Furthermore, the proposed clustering method allows to monitor the evolution of the different mechanisms in time. Cumulated Number of hits of hits during SMC damaging, which corresponds to the three identified damage types is shown in Fig. 7 for the four damaged stages (noted d_1 to d_4, where d_4 corresponds to the

appearance of a macrocrack on the surface). Fig. 7 allows to see that no fiber failure is detected during the first damage stage. In addition, energy differences can be readily appreciated, where fiber failure (when exists) is ten times more important than matrix cracking.

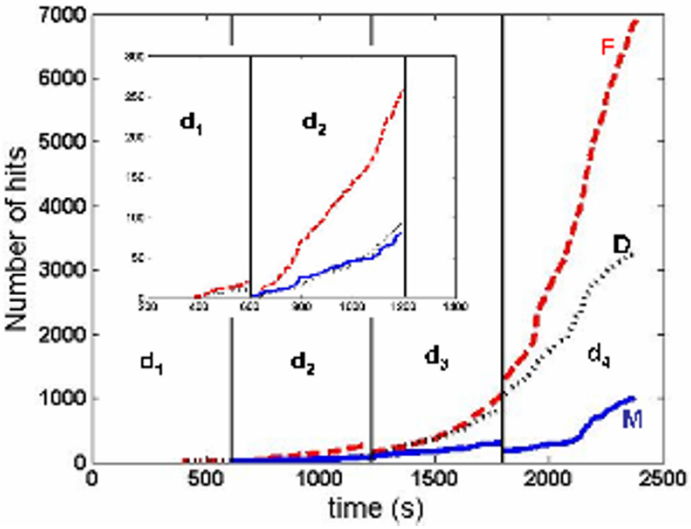

Fig. 7. Cumulated Number of hits of the three damage mechanisms (matrix cracking, interfacial debonding, fiber failure) in the SMC composite material under static three-point bending test. The four damaged stages are noted d1 to d4

5 Nonlinear Acoustic Slow Dynamics : Correlation with Acoustic Emission

To make a reliable "SNLD / AE" correlation for damage characterization, we need to check the irreversibility of phenomena at the origin of AE hits, commonly called Kaiser Effect (KE). If KE exists, little or no acoustic emission will be recorded before any previous maximum stress level is achieved. Furthermore, the presence of KE in a material allows to verify if it has been damaged between two consecutive loads. For SMC damaged with three points bending tests, the existence of KE was verified. In that case, all changes observed in HNL behaviour of SMC are due to the gradual damage. Therefore, the cumulated energy content of AE hits represents well the elastic energy of the different events that happen in SMC.

As detailed above, in these measurements we were mainly interested in following SMC relaxation in time. Qualitatively, SMC relaxation behaves the same way for undamaged and damaged states due to its highly heterogeneous structure, with

a logarithm-like recovery as found in SNLD experiments on several other materials [1-3]. Furthermore, the increase of damage makes relaxation time longer for the same conditioning. Quantitatively, relaxation time goes from 108% to 250% in comparison with the intact state. Without AE classification we can only follow variations of relaxation time as function of the cumulated energy of all damages created in SMC as shown in Fig.8.a. The latter seems to confirm the following intuitive and basic statement: A perfect material (intact) submitted to a conditioning would have an instantaneous relaxation ($t \rightarrow 0$). However, if the same conditioning is applied to a highly damaged material, the relaxation time would be very important ($t \rightarrow \infty$). Furthermore, SMC relaxation time seems to change as the logarithm of the elastic energy.

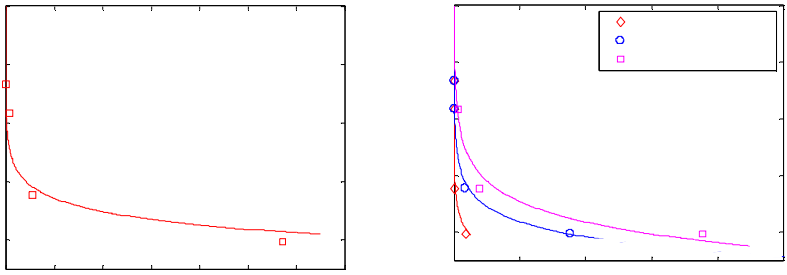

Fig. 8. Cumulated energy of the three damage mechanisms (matrix cracking, interfacial debonding, fiber failure) in the SMC composite material under static three-point bending test. The four damaged stages are noted d1 to d4.

When the different mechanisms at the origin of AE hits are well separated, it is possible to know how SMC relaxation time depends on the cumulated energy freed by every damage mechanism (Fig. 8.b). The latter shows the same logarithm dependence on the elastic energy for all damage mechanisms as for the aforementioned global response. However, the main characteristic of Fig. 8.b is that it helps to appreciate the slowness of relaxation for each mechanism. Indeed, we could see that the matrix cracking relaxation is much slower compared to fibers failure. This is mainly due to the fact that glass fibres are less viscoelastic than the polymer matrix. These two viscoelastic limits give intermediate relaxation to the interfacial debonding. These original results validate our AE classification method and offer new possibilities to investigate HNL behaviour of numerous materials of academic as well as industrial interests.

References

1. P. A. Johnson, A. Sutin, J. Acoust. Soc. Am., vol. 117(1), pp. 124-130 (2005)
2. M. Bentahar, H. Elaqra, M. Griffa,, R. El Guerjouma, M. Scalerandi, Phys. Rev. B, vol.73 (2006)
3. R. A. Guyer, P.A Johnson, Physics Today, April 1999, pp. 30-36.
4. M. Bentahar, R. El Guerjouma, T. Monnier and L. Deville, Journal of Advanced Science 17, 70-75 (2005)
5. M. Bentahar, R. El Guerjouma, J. Acoust. Soc. Am. (2008), Accepted
6. O. O. Vakhnenko, V. O. Vakhnenko, T. J. Shankland, and J. A. TenCate. Strain-induced kinetics of intergrain defects as the mechanism of slow dynamics in the nonlinear resonant response of humid sandstone bars. *Physical Review E.* Vol. 70. (2004)
7. McCall, K.R., and R. A. Guyer, "Hysteresis, discrete memory and nonlinear elastic wave propagation in rock: a new theoretical paradigm," *Nonlinear Geophysics*, 1996.
8. M. Scalerandi, P. P. Delsanto, V. Agostini, K.Van Den Abeele, P.A.Johnson. Local Interaction Simulation Approach to Modeling Nonclassical, Nonlinear Elastic Behavior in Solids, *Journ. Ac. Soc. Am.* 113, (2003) 3049-3059
9. V. Zaitsev, V. Gusev, and B. Castagnede, Thermoelastic mechanism for logarithmic slow dynamics and memory in elastic wave interaction with individual cracks, Phys. Rev. Lett. 90, 075501 (2003)
10. TenCate, J. N., D. E. Smith, and R. Guyer, Universal Slow Dynamics in Granular Solids, Phys Rev. Lett Vol. 85, No. 5 1020-1023, 2000
11. K. Ono, Acoustic emission, Encyclopedia of acoustics, Wiley, (1997)
12. A. Marec, J.-H. Thomas, R. El Guerjouma, Mechanical Systems and Signal Processing, Volume 22, Issue 6, 1441-1464 (2008)

Asymptotic expansions of vibrations with small unilateral contact

S. Junca and B. Rousselet

Abstract We study some spring mass models for a structure having a small unilateral contact with a small parameter ε. We valid an asymptotic expansion with the method of strained coordinates with new tools to handle such defects, including a non negligible cumulative effect over a long time: $T_\varepsilon \sim \varepsilon^{-1}$ as usual; or, for a new critical case, we can only expect: $T_\varepsilon \sim \varepsilon^{-1/2}$.

1 Introduction

For spring mass models, the presence of a small piecewise linear rigidity can model a small defect which implies unilateral reactions of the structure. For nondestructive testing we study a such singular nonlinear effect for large time by asymptotic expansion of the vibrations. New features and comparisons with classical cases of smooth perturbations are given, for instance for the Duffing equations: $\ddot{u} + u + \varepsilon u^3 = 0$. Indeed, piecewise non linearity is singular, lipschitz but not differentiable. We give some new results to validate such asymptotic expansions. Furthermore, these tools are also valid for a more general piecewise non linearity.

For short time, a linearization procedure is enough to compute a good approximation. But for large time, nonlinear cumulative effects drastically alter the nature of the solution. We will consider the classical method of strained coordinates to compute asymptotic expansions. The idea goes further back to Stokes, who in 1847 calculated periodic solutions for a weakly nonlinear wave

Stéphane Junca
Université de Nice, IUFM, 89 avenue George V, 06046 Nice, France
e-mail: junca@unice.fr

Bernard Rousselet
Université de Nice, Parc Valrose, 06108 Nice, France
e-mail: br@unice.fr

propagation problem. Subsequent authors have generally referred to this as the method of Poincaré or the Lindstedt's method. It is a simple and efficient method which gives us approximate nonlinear normal modes with 1 or more degrees of freedom.
In section 2 we present the method on an explicit case with lipschitz force. We focus on an equation with one degree of freedom with expansions valid for time of order ε^{-1} or, more surprisingly, $\varepsilon^{-1/2}$. Section 3 contains a tool to expand $(u+\varepsilon v)_+$ and some accurate estimate for the remainder. This is a new key point to validate the method of strained coordinates with unilateral contact. In Section 4, we extend previous results for systems with N degrees of freedom, first, with the same accuracy for approximate nonlinear normal modes, second, with less accuracy with all modes. Section 5 is an appendix containing some technical proofs and results.

2 One degree of freedom

2.1 Explicit pulsation

We replace in the Duffing equation u^3 by the piecewise linear term $u_+ = \max(0,u)$.

$$\ddot{u} + \omega_0^2 u + \varepsilon u_+ = 0, \tag{1}$$

where ω_0 a positive constant. This case has got a conserved energy E: $\dot{E} = 0$,

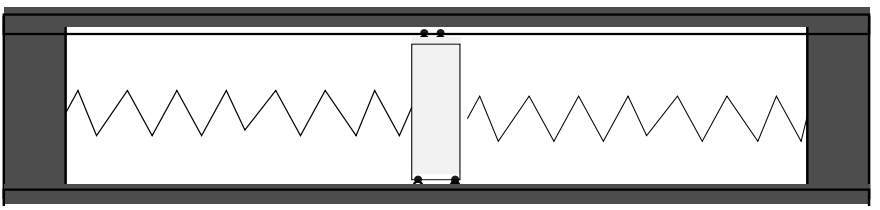

Fig. 1 Two springs, one on the right with an unilateral contact.

where $2E = \dot{u}^2 + \omega_0^2 u^2 + \varepsilon (u_+)^2$. Therefore, the level sets of $E(u,\dot{u})$ will be made of two half ellipses. Indeed, for $u < 0$ the level set is an half ellipse, and for $u > 0$ is another half ellipse. Any solution $u(t)$ is confined to a closed level curve of $E(u,\dot{u})$ and is necessarily a periodic functions of t.
More precisely, a non trivial solution ($E > 0$) is on the half ellipse: $\dot{u}^2 + \omega_0^2 u = 2E$, in the phase plane during the time $T_C = \pi/\omega_0$, and on the half ellipse $\dot{u}^2 + (\omega_0^2 + \varepsilon)u = 2E$ during the time $T_E = \pi/\sqrt{\omega_0^2 + \varepsilon}$. The period $P(\varepsilon)$ is

then
$P(\varepsilon) = (1 + \left(1 + \varepsilon/\omega_0^2\right)^{-1/2})\pi/\omega_0$, and the exact pulsation is:

$$\omega(\varepsilon) = 2\omega_0(1 + \left(1 + \varepsilon/\omega_0^2\right)^{-1/2})^{-1} = \omega_0 + \frac{\varepsilon}{(4\omega_0)} - \frac{\varepsilon^2}{(8\omega_0^3)} + \mathcal{O}(\varepsilon^3). \quad (2)$$

Let us compare with the pulsation for Duffing equation which depends on the amplitude a_0 of the solution: $\omega_D(\varepsilon) = \omega_0 + \frac{3}{8\omega_0^2}a_0^2\varepsilon - \frac{15}{256\omega_0^4}a_0^4\varepsilon^2 + \mathcal{O}(\varepsilon^3)$.

2.2 The method of strained coordinates

Now, we compute, with the method of strained coordinates, ω_ε, *an approximation* of the exact pulsation $\omega(\varepsilon)$. We expose completely this case to use the same method further when we will not have such explicit pulsation.
Let us define the new time $s = \omega_\varepsilon t$ and the following notations:

$$\omega_\varepsilon = \omega_0 + \varepsilon\omega_1 + \varepsilon^2\omega_2, \quad \omega_\varepsilon^2 = \alpha_0 + \varepsilon\alpha_1 + \varepsilon^2\alpha_2 + \mathcal{O}(\varepsilon^3) \quad (3)$$

$$\alpha_0 = \omega_0^2,\ \alpha_1 = 2\omega_0\omega_1, \quad \alpha_2 = \omega_1^2 + 2\omega_0\omega_2. \quad (4)$$

The unknowns are ω_1, ω_2 or α_1, α_2. Replacing the solution of (1) by the following anzatz with the following initial data to simplify the exposition:

$$\begin{aligned} u_\varepsilon(t) &= v_\varepsilon(\omega_\varepsilon t) + \varepsilon^2 r_\varepsilon(\omega_\varepsilon t), \\ v_\varepsilon(s) &= v_0(s) + \varepsilon v_1(s), \quad \text{where } s = \omega_\varepsilon t, \\ u_\varepsilon(0) &= a_0 > 0, \qquad \dot{u}_\varepsilon(0) = 0, \end{aligned}$$

then, we obtain initial data and next differential equations for v_0, v_1, r_ε:

$$v_0(0) = a_0\, \dot{v}_0(0) = 0, \quad 0 = v_1(0) = \dot{v}_1'(0), \quad 0 = r_\varepsilon(0) = \dot{r}_\varepsilon(0).$$

We use the natural expansion: $(u + \varepsilon v)_+ = u_+ + \varepsilon H(u)v + \cdots$, where H is the Heaviside function, equal to 1 if $u > 0$ and else 0, (see Lemma 3.1 below).

$$\ddot{v}_0 + v_0 = 0, \quad (5)$$

$$-\alpha_0(\ddot{v}_1 + v_1) = (v_0)_+ + \alpha_1\ddot{v}_0, \quad (6)$$

$$-\alpha_0(\ddot{r}_\varepsilon + r_\varepsilon) = H(v_0)v_1 + \alpha_2\ddot{v}_0 + \alpha_1\ddot{v}_1 + R_\varepsilon(s). \quad (7)$$

We now compute, α_1, v_1 and then α_2. We have $v_0(s) = a_0\cos(s)$. A key point in the method of strained coordinates is to keep bounded v_1 and r_ε for large time by a choice of α_1 for u_1 and α_2 for r_ε. For this purpose, we avoid resonant or **secular** term in the right-hand-side of equations (6), (7). Let us first focus on α_1. Notice that, $u_+ = \dfrac{u}{2} + \dfrac{|u|}{2}$. $|\cos(s)|$ has no term

with frequencies ± 1, since there are only even frequencies. Thus $-\alpha_0((v_0)_+ - \alpha_1 v_0) = a_0\cos(s)(1/2-\alpha_1) + a_0|\cos(s)|/2$ has no secular term if and only if $\alpha_1 = 1/2$, $\omega_1 = 1/(4\omega_0)$. Now, v_1 satisfies:

$$-\omega_0^2(\ddot{v}_1 + v_1) = |v_0|/2, \qquad v_1(0) = 0, \quad \dot{v}_1(0) = 0.$$

To remove secular term in the equation (7) we have to obtain the Fourier expansion for $H(v_0)$ and v_1. Some computations give us:

$$\begin{aligned}
|\cos(s)| &= \frac{2}{\pi} - \frac{4}{\pi}\sum_{k=1}^{+\infty} \frac{(-1)^k}{4k^2-1}\cos(2ks),\\
v_1(s) &= \frac{-a_0}{\omega_0^2}\left(\frac{1}{\pi} - \frac{2}{\pi}\sum_{k=1}^{+\infty}\frac{(-1)^k}{(4k^2-1)^2}\cos(2ks)\right),\\
H(v_0) &= \frac{1}{2} + \frac{2}{\pi}\sum_{k=1}^{+\infty}\frac{(-1)^j}{2j+1}\cos((2j+1)s)
\end{aligned}$$

To remove secular term of order one in (7), it suffices to take α_2 such that:

$$0 = \int_0^{2\pi} \left[H(v_0(s))v_1(s) + \alpha_2 \ddot{v}_0(s) + \alpha_1 \ddot{v}_1(s)\right] \cdot v_0 ds. \tag{8}$$

For Duffing equation, see [6, 7, 8], the source term involve only few complex exponentials and the calculus of α_2 is explicit. For general smooth source term, Fourier coefficients decay very fast. Here, we have an infinite set of frequencies for v_1 and $H(v_0)$, with only a small algebraic rate of decay for Fourier coefficients. So, numerical computations need to compute more Fourier coefficients. For our first simple example, we can compute explicitly α_2. After lengthy and tedious computations involving numerical series, we obtain $\alpha_2 = -3(4\omega_0)^{-2}$, thus $\omega_2 = -(2\omega_0)^{-3}$ as we have yet obtained in (2). More generally, we have:

Proposition 2.1. *Let u_ε be the solution of (1) with $u_\varepsilon(0) = a_0 + \varepsilon a_1$, $\dot{u}_\varepsilon(0) = 0$, then, there exists $\gamma > 0$, such that, for all $t < T_\varepsilon = \gamma\varepsilon^{-1}$:*

$$u_\varepsilon(t) = v_0(\omega_\varepsilon t) + \varepsilon v_1(\omega_\varepsilon t) + \mathcal{O}(\varepsilon^2), \qquad \omega_\varepsilon = \omega_0 + \varepsilon\omega_1 + \varepsilon^2\omega_2,$$

where $v_0(s) = a_0\cos(s)$, $\ddot{v}_1 + v_1 = -\frac{|v_0|}{2\omega_0^2}$, $\quad v_1(0) = a_1$, $\dot{v}_1(0) = 0$.
$\omega_1 = 1/4\omega_0$ and ω_2 is given by α_2 thanks equations (8), (3).

Remarks:
a new critical case: we give another simple example, with an asymptotic expansion only valid for time of order $\frac{1}{\sqrt{\varepsilon}}$. Consider, the solution u_ε of:

$$\ddot{u} + u + \varepsilon(u-1)_+ = 0, \;\; u_\varepsilon(0) = 1+\varepsilon, \;\; \dot{u}_\varepsilon(0) = 0. \tag{9}$$

The method of strained coordinates gives us the following approximation for $u_\varepsilon(t)$: $v_\varepsilon(t) = (1+\varepsilon)\cos(t)$ for $t \leq T_\varepsilon$. This system has got an energy: $2E_\varepsilon = \dot{u}^2 + u^2 + \varepsilon[(u-1)_+]^2$. Since, 1 is the maximum of $v_0(t) = \cos(t)$, a new phenomenon appears, during each period, $u_\varepsilon > 1$ for interval of time of order $\sqrt{\varepsilon}$ instead of ε, and then T_ε is smaller and of order $\frac{1}{\sqrt{\varepsilon}}$. To explain this new phenomenon, we give precise estimates of the remainder when we expand $(v_0 + \varepsilon v_1 + \varepsilon^2 r_\varepsilon)_+$ in the next section.

Nonlinear dependence of pulsation with respect to the amplitude : Previous examples have pulsation independent of the amplitude. It is not always the case, as we can see on following case. Let b be a real number and consider, the solution u_ε of:

$$\ddot{u} + u + \varepsilon(u-b)_+ = 0, \;\; u_\varepsilon(0) = a_0 > |b|, \;\; \dot{u}_\varepsilon(0) = 0. \tag{10}$$

At the first order, the method of strained coordinates gives us following equations:

$$\ddot{v}_0 + v_0 = 0, \qquad -\alpha_0(\ddot{v}_1 + v_1) = (v_0 - b)_+ + \alpha_1 \ddot{v}_0 + O(\varepsilon).$$

Then $v_0(s) = a_0\cos(s)$ and α_1 satisfies following equation:

$$\alpha_1 = \frac{1}{\pi}\int_0^{2\pi} (a_0\cos(s) - b)_+ \cos(s) ds = \frac{a_0}{2\pi}\left(2\beta + \sin(2\beta) - 4b\sin(\beta)\right),$$
$$\beta = \beta(b, a_0) = \arccos\left(\frac{b}{a_0}\right) \in [0, \pi].$$

Notice the nonlinear dependence of $\omega_1 = \alpha_1/2$ with respect to b and a_0. Furthermore, at the first order, and for time of the order ε^{-1}, we have: $u_\varepsilon(t) = a_0\cos((1+\varepsilon\alpha_1/2)t) + \mathcal{O}(\varepsilon)$.

3 Expansion of $(u + \varepsilon v)_+$

We give some useful lemmas to make asymptotic expansions and to estimate precisely the remainder for the basic piecewise linear map $u \to u_+ = \max(0, u)$.

Lemma 3.1. [Asymptotic expansion for $(u+\varepsilon v)_+$] *Let be $T > 0$, $M > 0$, u, v two real valued functions defined on $I = [0, T]$, $J_\varepsilon = \{t \in I, |u(t)| \leq \varepsilon M\}$, $\mu_\varepsilon(T)$ the measure of the set J_ε and H is the Heaviside step function, then*

$$(u+\varepsilon v)_+ = (u)_+ + \varepsilon H(u)v + \varepsilon\chi_\varepsilon(u, v), \;\; \textit{with} \;\; H(u) = \begin{cases} 1 & \textit{if } u > 0 \\ 0 & \textit{else} \end{cases},$$

where $\chi_\varepsilon(u,v)$ is a non negative piecewise linear function and 1-Lipschitz with respect to v, which satisfies for all ε, If $|v(t)| \leq M$ for any $t \in I$,:

$$|\chi_\varepsilon(u,v)| \leq |v| \leq M, \ \int_0^T |\chi_\varepsilon(u(t),v(t))|\,dt \leq M\mu_\varepsilon(T). \tag{11}$$

The point in inequality (11) is the remainder $\varepsilon\chi_\varepsilon$ is only of order ε in L^∞ but of order $\varepsilon\mu_\varepsilon$ in L^1. In general, μ_ε is not better than a constant, take for instance $u \equiv 0$. Fortunately, it is proved below that μ_ε is often of order ε, and for some critical cases of order $\sqrt{\varepsilon}$.

Proof : Equality (11) defines χ_ε and can be rewritten as follow:

$$\chi_\varepsilon(u,v) = \frac{(u+\varepsilon v)_+ - u_+ - \varepsilon H(u)v}{\varepsilon}. \tag{12}$$

So, χ_ε is non negative since $u \to u_+$ is a convex function. We also easily see that the map $(u,v) \to \chi_\varepsilon(u,v)$ is piecewise linear, continuous except on the line $u = 0$ where χ_ε has a jump $-v$. This jump comes from the Heaviside step function. An explicit computations gives us the simple and useful formula: $0 \leq \varepsilon\chi_\varepsilon(u,v) = \begin{cases} |u+\varepsilon v| & \text{if } |u+\varepsilon v| < |\varepsilon v| \\ 0 & \text{else} \end{cases}$.We then have immediately $0 \leq \chi_\varepsilon(u,v) \leq |v|$. Let u be fixed, then $v \to \chi_\varepsilon(u,v)$ is one Lipschitz with respect to v. Furthermore, the support of χ_ε is included in J_ε, which concludes the proof. □

Now, we investigate the size of $\mu_\varepsilon(T)$ with notations of Lemma 3.1.

Lemma 3.2 (Order of $\mu_\varepsilon(T)$). *Let u be a smooth periodic function. If u has only simple roots on $I = [0,T]$, then , for some positive C: $\mu_\varepsilon(T) \leq C\varepsilon T$. More generally, if u has also double roots then $\mu_\varepsilon(T) \leq C\sqrt{\varepsilon}T$.*

Notice that any non zero solution of any linear homogeneous second order ordinary differential equation has always simple zeros.

Proof : First assume u only has simple roots on a period $[0,P]$, and let $Z = \{t_0 \in [0,P], u(t_0) = 0\}$. A well known result state that Z is a discret set since u has only simple roots. Thus Z is a finite subset of $[0,P]$: $Z = \{t_1, t_2, \cdots, t_N\}$. We can choose an open neighborhood V_j of each t_j such that u is a diffeomorphism on V_j with derivative $|\dot{u}| > |\dot{u}(t_j)|/2$. On the compact set $K = [0,P] - \cup V_j$, u never vanishes, then $\min_{t\in K} |u(t)| = \varepsilon_0 > 0$. Thus, we have for all $\varepsilon M < \varepsilon_0$, the length of J_ε in V_j is $|V_j \cap J_\varepsilon| \leq \dfrac{4\varepsilon M}{|\dot{u}(t_j)|}$. μ_ε is additive: $\mu_\varepsilon(P+t) = \mu_\varepsilon(P) + \mu_\varepsilon(t)$ which give the linear growth of $\mu_\varepsilon(T) = \mathcal{O}(\varepsilon T)$ for the case with simple roots.

For the general case, on each small neighborhood of t_j: V_j, we have with a Taylor expansion, $|u(t_j+s)| \geq d_j|s|^l$, with $1 \leq l \leq 2$, $d_j > 0$, so, $|V_j \cap J_\varepsilon| \leq 2(\varepsilon M/d_j)^{1/l}$, then $\mu_\varepsilon(P) = \mathcal{O}(\sqrt{\varepsilon})$,which is enough to conclude the proof. □

4 N degrees of freedom

$M\ddot{U} + KU + \varepsilon(AU - B)_+ = 0$, where $[(AU - B)_k]_+ = \left(\sum_{j=1}^{N} a_{kj}u_j - b_k\right)_+$,
M is the diagonal mass matrix with positive term on the diagonal, K is the stiffness matrix which is symmetric definite positive. For the term $\varepsilon(AU - B)_+$, modeling small defect, it is possible to add many of such terms. For a such system, endowed with a natural energy for the linearized part, we control the ε-Lipschitz last term, and the solutions remain bounded for all time. Without loosing generality, with a change of variables, we deal with following diagonalized system for the linear part, keeping the same notation, except for the positive diagonal matrix Λ:

$$\ddot{U} + \Lambda^2 U + \varepsilon(AU - B)_+ = 0, \tag{13}$$

4.1 Nonlinear normal mode, second order approximation

For the system (13) with an initial condition on an eigenmode of the linearized system: $u_1^\varepsilon(0) = a_0 + \varepsilon a_1$, $\dot{u}_1^\varepsilon(0) = 0$ and, for $k \neq 1$: $u_k^\varepsilon(0) = 0$, $\dot{u}_k^\varepsilon(0) = 0$. Using the same time $s = \omega_\varepsilon t$ for each component and following notations:

$$\omega_\varepsilon = \omega_0 + \varepsilon\omega_1 + \varepsilon^2\omega_2, \qquad \omega_0 = \lambda_1, \qquad (\omega_\varepsilon)^2 = \alpha_0 + \varepsilon\alpha_1 + \varepsilon^2\alpha_2 + \mathrm{O}(\varepsilon^3),$$
$$u_j^\varepsilon(t) = v_j^\varepsilon(s), \qquad v_j^\varepsilon(s) = v_j^0 + \varepsilon v_j^1 + \varepsilon^2 r_j^\varepsilon, \qquad j = 1, \cdots, N.$$

Replacing, this anzatz in the System (13) we have in variable s:

$$(\omega_\varepsilon)^2\ddot{v}_k^\varepsilon + \lambda_k^2 v_k^\varepsilon = -\varepsilon\left(\sum_{j=1}^{N} a_{kj}v_j^\varepsilon(s) - b_k\right)_+,$$
$$L_k v_k^0 = \alpha_0\ddot{v}_k^0 + \lambda_k^2 v_k^0 = 0, \quad -L_k v_k^1 = \left(\sum_{j=1}^{N} a_{kj}v_j^0 - b_k\right)_+ + \alpha_1\ddot{v}_k^0 = S_k^1,$$
$$-L_k r_k^\varepsilon = H\left(\sum_{j=1}^{N} a_{kj}v_j^0 - b_k\right)\left(\sum_{j=1}^{N} a_{kj}v_j^1\right) + \alpha_2\ddot{v}_k^0 + \alpha_1\ddot{v}_k^1 + \varepsilon\cdots = S_k^2 + \varepsilon\cdots$$

Equations for v_k^0, for all $k \neq 1$, with zero initial data give us $v_k^0 = 0$. In equation for v_1^1, we remove the secular term for the right hand side. If $b_1 = 0$ we have $\omega_1 = \dfrac{a_{11}}{4\lambda_1}$. Then, for $k \neq 1$, we can compute v_k^1 since: $\alpha_0\ddot{v}_k^1 + \lambda_k^2 v_k^1 = -\left(a_{k1}v_1^0 - b_k\right)_+$. v_k^1 is a 2π-periodic bounded function since $\lambda_k \neq \lambda_1$.

Simplifying equation for r_1^ε we can compute numerically α_2 and then ω_2 as in the Propoposition 2.1. Then we check, for all $k \neq 1$ that r_k^ε stay bounded for large time since there is no resonance of order one. We have obtained following results with previous notations:

Theorem 4.1. *The following expansion of the nonlinear normal mode is valid on $(0, T_\varepsilon)$, under assumption $\lambda_1 \neq \lambda_k$ for all $k \neq 1$:*

$$u_1^\varepsilon(t) = v_1^0(\omega_\varepsilon t) + \varepsilon v_1^1(\omega_\varepsilon t) + \mathcal{O}(\varepsilon^2),\ \ u_k^\varepsilon(t) = 0 + \varepsilon v_k^1(\omega_\varepsilon t) + \mathcal{O}(\varepsilon^2),$$

where $v_1^0(s) = a_0 \cos(s)$, and ω_1, v_1^1, v_k^1, ω_2 are given by following equations, in the sense that we compute successively α_1, ω_1, v_1^1, v_k^1, α_2, ω_2:

$$\begin{aligned}
&0 = \int_0^{2\pi} S_1^1 \cdot v_1^0 ds, \qquad \text{where } S_1^1 = (a_{11} v_1^0 - b_1)_+ + \alpha_{\mathbf{1}} \ddot{v}_1^0,\\
&-L_1 v_1^1 = \left(a_{11} v_1^0 - b_1\right)_+ + \alpha_1 \ddot{v}_1^0 = S_1^1, \quad v_1^1(0) = a_1,\ \dot{v}_1^1(0) = 0,\\
&-L_k v_k^1 = \left(a_{k1} v_1^0 - b_k\right)_+ = S_k^1, \quad v_k^1(0) = 0,\ \dot{v}_k^1(0) = 0,\ \text{for } k \neq 1,\\
&0 = \int_0^{2\pi} S_1^2 \cdot v_1^0 ds \qquad \text{where } S_1^2 = H(a_{11} v_1^0 - b_1) \left(\sum_{j=1}^N a_{1j} v_j^1\right) + \alpha_{\mathbf{2}} \ddot{v}_1^0 + \alpha_1 \ddot{v}_1^0.
\end{aligned}$$

Furthermore, if $(a_{j1} v_1^0 - b_j)$ has got only simple roots for all $j = 1, \cdots, N$, then T^ε is of order ε^{-1}, else T^ε is of order $\varepsilon^{-1/2}$.

4.2 First order asymptotic expansion

The method of strained coordinates is used for each normal component, with general initial data $u_k^\varepsilon(0) = a_k$, $\dot{u}_k^\varepsilon(0) = 0$ and, with following anzatz:

$$\lambda_k^\varepsilon = \lambda_k^0 + \varepsilon \lambda_k^1, \quad \lambda_k^0 = \lambda_k, \quad u_k^\varepsilon(t) = v_k^\varepsilon(s_k) \text{ where } s_k = \lambda_k^\varepsilon t, v_k^\varepsilon(s) = v_k^0 + \varepsilon r_k^\varepsilon.$$

Replacing, this anzatz in the system (13) we have:

$$\begin{aligned}
(\lambda_k^\varepsilon)^2 \ddot{v}_k^\varepsilon(s_k) + \lambda_k^2 v_k(s_k) &= -\varepsilon \left(\sum_{j=1}^N a_{kj} v_j^\varepsilon \left(\frac{\lambda_j^\varepsilon}{\lambda_k^\varepsilon} s_k\right) - b_k\right)_+,\\
L_k v_k^0 = (\lambda_k^0)^2 \ddot{v}_k^0(s_k) + \lambda_k^2 v_k^0(s_k) &= 0,\\
-L_k r_k^\varepsilon(s_k) = \left(\sum_{j=1}^N a_{kj} v_j^0 \left(\frac{\lambda_j^0}{\lambda_k^0} s_k\right) - b_k\right)_+ &+ 2\lambda_k \lambda_k^1 \ddot{v}_k^0 + \varepsilon(\cdots) \equiv S_k^1 + \varepsilon(\cdots).
\end{aligned}$$

If $b_k = 0$, we identify the secular term with the Lemma 5.4 since $S_+ = S/2 + |S|/2$. Then, we remove the resonant term in the source term for the remainder r_k^ε, which gives us $\lambda_k^1 = \dfrac{a_{kk}}{4\lambda_k}$. If $b_k \neq 0$, we compute λ_k^1 numerically.

Noting that, replacing $v_j^\varepsilon(s_j)$ by $v_j^0\left(\frac{\lambda_j^0}{\lambda_k^0}s_k\right)$ implies a secular term of order εt. Since the map $S \to S_+$ is one-Lipschitz, the error goes to the right-hand side of equation (14). Furthermore, $r_k^\varepsilon = r_k^\varepsilon(s_1, \cdots, s_N)$, and the method of strained coordinates is not valid to get u_k^1 and λ_k^2. Nevertheless, we obtain:

Theorem 4.2. *If $\lambda_1, \cdots, \lambda_N$ are $\mathbb{Z}$ independent, then, for all k, for $t < T_\varepsilon \sim \varepsilon^{-1}$:*

$$u_k^\varepsilon(t) = v_k^0\left(\lambda_k^\varepsilon\, t\right) + \mathcal{O}(\varepsilon) \qquad \text{where } \lambda_k^\varepsilon = \lambda_k + \varepsilon\lambda_k^1,$$

where $v_k^0(s) = a_k\cos(s)$, and λ_k^1 is defined by the equation:

$$0 = \int_0^{2\pi}\left[\left(\sum_{j=1}^N a_{kj}v_j^0\left(\frac{\lambda_j^0}{\lambda_k^0}s_k\right) - b_k\right)_+ + 2\lambda_k\lambda_{\mathbf{k}}^{\mathbf{1}}\ddot{v}_k^0\right]\cdot v_k^0 ds$$

Furthermore, if $b_k = 0$ we have: $\lambda_k^1 = \dfrac{a_{kk}}{4\lambda_k}$.

5 Appendix: technical proofs

We briefly give some results used before. Complete proofs are avaible in [4]. The following Lemma is useful to prove an expansion for large time. There is a similar version for system.

Lemma 5.3. [Bounds for large time] *Let w_ε be a solution of*

$$w_\varepsilon{}'' + w_\varepsilon = S_\varepsilon(s) + f_\varepsilon(s) + \varepsilon g_\varepsilon(s, w_\varepsilon),\ w_\varepsilon'(0) = 0, w_\varepsilon'(0) = 0. \qquad (14)$$

If source terms satisfy the following conditions with $M > 0$:

1. S_ε are periodic functions orthogonal to $e^{\pm it}$, and $|S_\varepsilon(t)| \le M$

2. $|f_\varepsilon| \le M$ and for all T, $\displaystyle\int_0^T |f_\varepsilon(s)|ds \le C\varepsilon T$ or $C\sqrt{\varepsilon}T$,

3. there exists $R > 0$ such that: $M_R = \sup_{\varepsilon\in(0,1), s>0, R>u^2} |g_\varepsilon(s,u)| < \infty$,

then, w_ε is uniformly bounded in $L^\infty(0, T_\varepsilon)$, where $T_\varepsilon = \dfrac{\gamma}{\varepsilon}$ or $\dfrac{\gamma}{\sqrt{\varepsilon}}$ and $\gamma > 0$.

For system we have to work with linear combination of periodic functions with different periods and nonlinear function of such sum. So we work with the adherence in $L^\infty(\mathbb{R},\mathbb{R})$ of span$\{e^{i\lambda t},\ \lambda \in \mathbb{R}\}$, namely the set of almost periodic functions $C_{ap}^0(\mathbb{R},\mathbb{R})$, see [1]. We first give an useful Lemma about the spectrum of $|w|$ for $u \in C_{ap}^0(\mathbb{R},\mathbb{R})$. Let us recall definitions for the Fourier coefficient of u associated to frequency λ: $c_\lambda[u]$ and its spectrum: $Sp[u]$,

$$c_\lambda[u] = \lim_{T\to+\infty} \frac{1}{T}\int_0^T u(t)e^{-i\lambda t}dt, \qquad Sp[u] = \{\lambda \in \mathbb{R},\, c_\lambda[u] \neq 0\}.$$

Lemma 5.4. [About spectrum of $|u|$] *If $u \in C^0_{ap}(\mathbb{R},\mathbb{R})$, u has got a finite spectrum: $Sp[u] \subset \{\pm\lambda_1, \cdots, \pm\lambda_N\}$, $(\lambda_1, \cdots, \lambda_N)$ are $\mathbb{Z}$-independent, $0 \notin Sp[u]$, then $\lambda_k \notin Sp[\,|u|\,]$ for all k.*

References

1. Corduneanu, *Almost periodic functions,* Interscience, New York, 1968.
2. H. Hazim, B. Rousselet, *Finite Elements for a Beam System with Nonlinear Contact Under Periodic Excitation,* preprint 2008.
3. D. Jiang, C. Pierre, S.W. Shaw, *Large-amplitude non-linear normal mode of piecewise linear systems.* Journal of Sound and Vibration, 272, p. 869-891, 2004.
4. S. Junca, B. Rousselet, *The Method of Strained Coordinates for Discrete Models with Small Unilateral Contacts,* preprint 2008.
5. J.B. Keller & S. Kogelman, *Asypmtotic solutions of initial value problems for nonlinear partail differential equations*, S.I.A.M. J. Appl. Math. 18, p. 748-758, 1970.
6. Kevorkian, J.; Cole, Julian D., *Perturbation methods in applied mathematics.* Applied Mathematical Sciences, 34. Springer-Verlag, New York-Berlin, 1981.
7. J. Kevorkian and J. Cole, *Multiple Scale and Singular Perturbations Problems,* Applied Mathematical Sciences, volume 114, Springer, Berlin, 1996.
8. Peter D. Miller, *Applied Asymptotic Analysis*, American Mathematical Society, Providence, Rhode Island, volume 75, ch 9-10, 2006.
9. Nayfeh, Ali Hasan, *Introduction to perturbation techniques.* Wiley-Interscience [John Wiley & Sons], New York, 1981.
10. M. Roseau, *Vibrations des systèmes mécaniques. Méthodes analytiques et applications.* Masson, Paris, 489 pp, 1984.
11. B. Rousselet, G. Vanderborck, *Non destructive control of cables: O.D.E. models of non linear vibrations.* Variational Formulations in Mechanics : Theory and Applications - A Workshop dedicated to the 60th Birthday of Professor Raùl A. Feijoo; 3-5/9/2006, 2006.
12. G. Vanderborck, B. Rousselet, *Structural damage detection and localization by nonlinear acoustic spectroscopy* , Saviac, 76th Shock and Vibration Symposium, October 31 - November 3, 2005, Destin (Florida / USA), 2005.

Propagation of compressional elastic waves through a 1-D medium with contact nonlinearities

B. Lombard, and J. Piraux

Abstract Propagation of monochromatic elastic waves across cracks is investigated in 1D, both theoretically and numerically. Cracks are modeled by nonlinear jump conditions. The mean dilatation of a single crack and the generation of harmonics are estimated by a perturbation analysis, and computed by the harmonic balance method. With a periodic and finite network of cracks, direct numerical simulations are performed and compared with Bloch-Floquet's analysis.

1 Introduction

Failure processes resulting in a crack generally produce rough crack faces. Once crack opening has taken place, and the crack faces have undergone slight relative sliding displacement, the crack will never completely close again due to the non-conforming surfaces in partial contact. A complicated interaction between crack faces is expected, depending strongly on the magnitudes of the tractions transmitted across the rough surfaces in contact [9].

The interaction of ultrasonic waves with cracks has been investigated by many authors, assuming that the wavelength is much larger than a characteristic length of the roughness of the contacting surfaces. Linear slip-displacement models of crack-face interaction have been widely used [12, 10]. However, a non-physical penetration of contacting surfaces may occur in linear models. Moreover, laboratory experiments have shown that methods of non-destructive evaluation based on linear models may fail to detect partially closed cracks [13].

Here, we study wave propagation with a nonlinear model of contact proposed in [1, 2]. A monochromatic compressional wave propagates normally to a plane flaw surface, leading to a 1D problem detailed in section 2. Analysis of scattered fields is performed in section 3. With a single crack, the generation of harmonics and the

B. Lombard and J. Piraux
LMA - CNRS, 31 chemin Joseph Aiguier - 13402 Marseille, France.

mean dilatation of the crack are addressed analytically and numerically. Propagation through periodic networks of contact nonlinearities is studied by Bloch-Floquet's analysis [8] and simulations. Numerical experiments are proposed in section 4. Conclusions are drawn and future perspectives are suggested in section 5.

2 Problem statement

2.1 Configuration

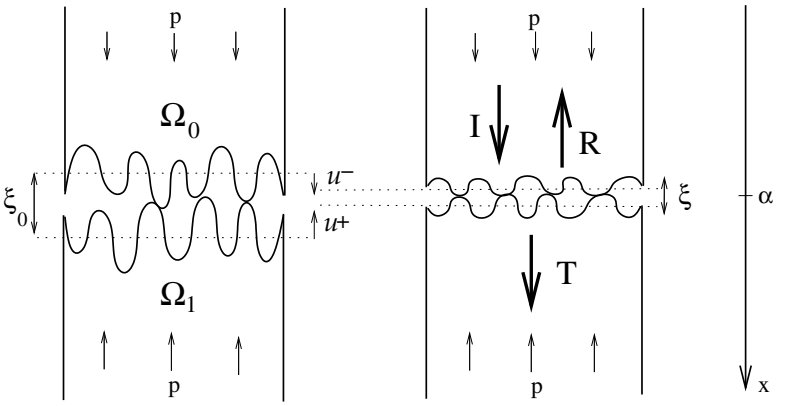

Fig. 1 Elastic media Ω_0 and Ω_1 separated by vacuum, with rough contact surfaces. Static (left) and dynamic (right) case, with incident (I), reflected (R) and transmitted (T) waves.

We consider a single crack with rough faces separating two media Ω_0 and Ω_1 linearly elastic and isotropic, with density ρ and elastic speed of the compressional waves c. These parameters are piecewise constant and may be discontinuous around the crack: (ρ_0, c_0) if $x \in \Omega_0$, (ρ_1, c_1) if $x \in \Omega_1$. The media are subject to a constant static stress p. At rest, the distance between planes of average height is $\xi_0(p) > 0$ (figure 1, left). An incident monochromatic wave, emitted by a ponctual stress source at $x = x_s$ in Ω_0, gives rise to reflected (in Ω_0) and transmitted (in Ω_1) compressional waves. These perturbations in Ω_0 and Ω_1 are described by the 1D elastodynamic equations

$$\rho \frac{\partial v}{\partial t} = \frac{\partial \sigma}{\partial x}, \qquad \frac{\partial \sigma}{\partial t} = \rho c^2 \frac{\partial v}{\partial x} + 2\rho_0 c_0^2 v_0 \delta(x - x_s) \sin \omega t, \tag{1}$$

where v_0 is the amplitude of the incident elastic velocity, and $\omega = 2\pi f$ is the angular frequency of the source. The elastic velocity $v = \frac{\partial u}{\partial t}$, the elastic displacement u, and the elastic stress perturbation σ around p, are averaged fields per unit area in crack's

plane. The dynamic stresses induced by the elastic waves affect the thickness $\xi(t)$ of the crack (figure 1, right). The constraint

$$\xi = \xi_0 + [u] \geq \xi_0 - \delta > 0 \tag{2}$$

must be satisfied, where $[u] = u^+ - u^-$ is the difference between the elastic displacements on the two sides of the crack, and $\delta(p) > 0$ is the *maximum allowable closure* [2]. We also assume that the wavelengths are much larger than ξ, neglecting the propagation time through the crack, and replacing it by a zero-thickness *interface* at $x = \alpha$: $[u] = [u(\alpha, t)] = u(\alpha^+, t) - u(\alpha^-, t)$.

2.2 Contact law

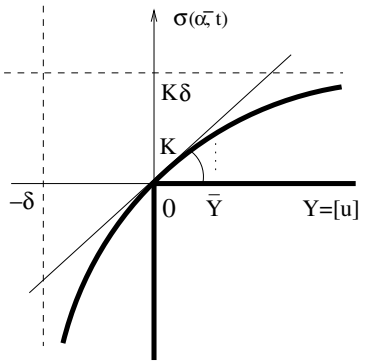

Fig. 2 Nonlinear relation between stress and slip displacement.

Cracks are classically modeled by linear jump conditions [12] with *stiffness* K:

$$[\sigma(\alpha, t)] = 0, \qquad [u(\alpha, t)] = \frac{1}{K}\,\sigma(\alpha^{\pm}, t). \tag{3}$$

If $K \to +\infty$, welded conditions are recovered. Conditions (3) violate (2) under large compression loadings: $\sigma(\alpha^{\pm}, t) < -K\,\delta \Rightarrow \xi < \xi_0 - \delta$. Hence, the linear regime induced by (3) is realistic only with very small perturbations. With larger ones, nonlinear jump conditions are required.

Compression loading increases the number and the surface of contacting faces. Consequently, a smaller stress is needed to open than to close a crack of a given displacement; an infinite stress is even required to close the crack faces completely. This behavior can be modeled by the global jump conditions proposed in [1, 2]

$$[\sigma(\alpha,t)]=0, \qquad [u(\alpha,t)]=\frac{1}{K}\,\frac{\sigma(\alpha^{\pm},t)}{1-\sigma(\alpha^{\pm},t)/(K\,\delta)}, \tag{4}$$

satisfying (2) and implying $\sigma(\alpha^{\pm},t)<K\,\delta$. The second relation in (4) is sketched in figure 2. The straight line with a slope K tangential to the hyperbola at the origin amounts to the linear jump conditions (3); as deduced from (4), the linear regime is valid only if $|\sigma(\alpha^{\pm},t)|\ll K\,\delta$. A second limit-case not investigated here is obtained if $\delta\to 0$ and K bounded: the hyperbola tends towards the nondifferentiable graph of the unilateral contact, denoted by bold straight segments in figure 2.

3 Analysis of scattered fields

3.1 Single crack

Analytical approach. The scattered fields can be expressed in terms of $Y(t)=[u(\alpha,t)]$. Following [11, 4] gives the nonlinear ordinary differential equation (ODE)

$$\frac{dY}{dt}+\beta\,\frac{Y}{1+Y/\delta}=2\,v_0\,\sin\omega t, \tag{5}$$

satisfied by Y, with $\beta=K((\rho_0\,c_0)^{-1}+(\rho_1\,c_1)^{-1})$. Inspection of (5) and dimensional analysis show that Y is δ times a function of $\frac{v_0}{\beta\,\delta}$, $\frac{\omega}{\beta}$ and ωt. To solve (5), we assume $|Y|/\delta<1$, which leads to the series

$$\frac{dY}{dt}+\beta\sum_{n=0}^{\infty}\frac{(-1)^n}{\delta^n}\,Y^{n+1}=2\,v_0\,\sin\omega t. \tag{6}$$

An approximate solution of (6) is sought by a *perturbation approximation* (PA) [3]

$$Y(t)=\sum_{n=0}^{\infty}Y_n(t)=\sum_{n=0}^{\infty}\frac{1}{\delta^n}\,y_n(t). \tag{7}$$

Nothing ensures that (7) converges: $|Y|/\delta<1$ is always satisfied when $Y<0$, but it is true when $Y>0$ only if $\frac{v_0}{\beta\,\delta}$ is sufficiently small. Plugging (7) into (6) and identifying the terms with identical power of δ leads to an infinite series

$$\begin{aligned}
&\frac{dy_0}{dt}+\beta\,y_0=2\,v_0\,\sin\omega t,\\
&\frac{dy_1}{dt}+\beta\,y_1=\beta\,y_0^2,\\
&\frac{dy_2}{dt}+\beta\,y_2=\beta\,y_0\left(2y_1-y_0^2\right),
\end{aligned} \tag{8}$$

and so on. There is no influence of the truncation order N on the accuracy of the solution Y_n with $n < N$. The recursive and linear ODE are much simpler to solve than the nonlinear ODE (5), even if computing Y_n with $n \geq 2$ is cumbersome. This computation has been automatized with computer algebra tools. Since the number of terms in Y_n is roughly 2^{2n+1}, very high orders are currently out of reach. Computing Y_n up to $N = 8$ takes 20 mn on a Pentium 3 GHz. We detail the case $N = 1$. Setting $\varphi_0 = \arctan \frac{\omega}{\beta}$, the zero-th order periodic solution of (7)-(8) is

$$Y_0(t) = 2\,\frac{v_0}{\beta}\,\frac{1}{\sqrt{1+(\omega/\beta)^2}}\,\sin(\omega t - \varphi_0). \tag{9}$$

Setting $\varphi_1 = \arctan \frac{\beta}{2\omega}$, the first-order periodic solution of (7)-(8) is

$$Y_1(t) = 2\,\frac{v_0^2}{\beta^2\,\delta}\,\frac{1}{1+(\omega/\beta)^2}\left(1 - \frac{1}{\sqrt{1+(2\,\omega/\beta)^2}}\,\sin(2\,\omega t - 2\,\varphi_0 + \varphi_1)\right). \tag{10}$$

Two properties are deduced from (10). First, the mean value of Y_1 is non-null

$$\overline{Y}_1 = 2\,\frac{v_0^2}{\beta^2\,\delta}\,\frac{1}{1+(\omega/\beta)^2} > 0. \tag{11}$$

More generally, the mean value $\overline{Y}_{2n+1}$ of Y_{2n+1} is proportional to $\delta\left(\frac{v_0}{\beta\,\delta}\right)^{2n+2}$, and $\overline{Y}_{2n} = 0$. The mean thickness of the crack $\overline{\xi}$ deduced from (2) satisfies $\overline{\xi} = \xi_0 + \overline{Y} > \xi_0$, with $\overline{Y} = \sum \overline{Y}_n$. The dilatation predicted here is similar to the *DC* signal measured by [6] with glass-piezoceramic interface. The second property deduced from (10) concerns the term with angular frequency $2\,\omega$. Its importance is quantified by the ratio of amplitudes between sinusoidal terms in (10) and (9)

$$\gamma_2 = \frac{v_0}{\beta\,\delta}\,\frac{1}{\sqrt{1+(\omega/\beta)^2}\sqrt{1+(2\,\omega/\beta)^2}}. \tag{12}$$

Consequently, nonlinear effects increase with $\frac{v_0}{\beta\,\delta}$ and decrease with $\frac{\omega}{\beta}$.

Numerical approach. To compute the scattered fields with high accuracy and no limitation about the range of validity, one implements the numerical *harmonic balance method* (HBM). The periodic elastic displacements are written ($k_0 = \omega/c_0$, $k_1 = \omega/c_1$)

$$
\begin{aligned}
u_I(x,t) &= \frac{v_0}{\omega}\left\{\cos(\omega t - k_0 x) - 1\right\},\\
u_R(x,t) &= R_0^a + \sum_{n=1}^{\infty}\left\{R_n^a \sin n(\omega t + k_0 x) + R_n^b \cos n(\omega t + k_0 x)\right\},\\
u_T(x,t) &= T_0^a + \sum_{n=1}^{\infty}\left\{T_n^a \sin n(\omega t - k_1 x) + T_n^b \cos n(\omega t - k_1 x)\right\}.
\end{aligned}
\tag{13}
$$

The elastic stresses are deduced from (13). Fields are truncated at N and injected in (4). The truncation implies that $R_n^{a,b}$ and $T_n^{a,b}$ depend on N. The terms with identical trigonometric arguments are put together, and the terms with a trigonometric argument greater than $N\omega t$ are removed. The first condition (4) implies $2N$ linear equations, without R_0^a and T_0^a. The second condition (4) implies $2N+1$ nonlinear equations, including $T_0^a - R_0^a + v_0/\omega$. Finally, we get a $(4N+1)\times(4N+1)$ nonlinear system with first-order or second-order polynomial entries

$$
F(X) = 0, \qquad X = \left(\overline{Y}, R_1^a, T_1^a, R_1^b, T_1^b, ..., R_N^b, T_N^b\right)^T, \qquad \overline{Y} = T_0^a - R_0^a + \frac{v_0}{\omega}. \tag{14}
$$

To solve (14), three cases may be considered:

- *linear regime, for all N*: (14) becomes a linear system whose solution is easy to compute analytically. In this limit-case, $\overline{Y} = 0$ and $R_n^{a,b} = T_n^{a,b} = 0$ if $n \geq 2$;
- *nonlinear case,* $N = 1$: (14) can be solved analytically. A detailed study shows that the solution may not be unique: if v_0 is lower than a critical value $\tilde{v}_0$, there exists only one real root; if $v_0 > \tilde{v}_0$, there are three real roots. Moreover, $\overline{Y} > 0$; an approximation of this jump recovers the value $\overline{Y}_1$ deduced from the PA (11);
- *nonlinear case,* $N > 1$: (14) is solved numerically by the Newton-Raphson method. The determination of F and of its jacobian J has been automatized with computer algebra tools: computing F and J with $N = 100$ roughly takes 1 second on a Pentium 3 GHz. The root of (14) may be not unique, like with $N = 1$ and $v_0 > \tilde{v}_0$. The initialization must therefore be done carefully, e.g. using the exact values of the first 5 components of X at $N = 1$, and setting the other components to zero. This simple initialization works up to $v_0 \approx \tilde{v}_0$. With stronger nonlinearities, this approach is coupled with a basic continuation.

3.2 Network of cracks

Analytical approach. A Bloch-Floquet's analysis [8] is applied to an infinite and periodic network in linear regime. With constant parameters, the dispersion relation is

$$
\cos \hat{k}h = \cos kh - \frac{\rho\, c\, \omega}{2K} \sin kh, \tag{15}
$$

where $\hat{k}$ is the effective wavenumber and h is the spacing between cracks. If

$$-\left|\frac{1-\theta}{1+\theta}\right| \leq \cos kh \leq \left|\frac{1-\theta}{1+\theta}\right|, \qquad \theta = \left(\frac{\rho\, c\, \omega}{2K}\right)^2, \tag{16}$$

the waves are not attenuated. Otherwise, the waves are evanescent with decay

$$\Im \mathrm{m}\, \hat{k} = -\frac{1}{h} \cosh^{-1}\left(\cos kh - \frac{\rho\, c\, \omega}{2K} \sin kh\right). \tag{17}$$

Numerical approach. The analysis is much harder in nonlinear regime, since successive harmonics generated across cracks may not belong to the same pass-band structure. Consequently, nonlinear regime as well as non-periodic configurations are investigated by *direct numerical simulations* (DNS). A fourth-order ADER scheme solves (1) in the time domain. The jump conditions (4) are enforced numerically by an interface method [7]. With high nonlinearities, space-time mesh refinement is implemented around the cracks to discretize correctly the stiff fronts. Obviously, this approach also works with a single crack, hence it will be used to get reference solutions in each experiment.

4 Numerical experiments

A crack at $\alpha = 0.5$ m in aluminium is studied: $\rho_0 = \rho_1 = 2600$ kg/m^3, $c_0 = c_1 = 6400$ m/s, $K = 10^{13}$ Pa/m, $\delta = 3\,10^{-7}$ m. Three amplitudes v_0 are considered: 0.01 m/s, 0.13 m/s, and 0.6 m/s. The source is at $x_s = 0.25$ m, and $f = 100$ kHz.

First, the elastic stress transmitted across the crack is shown in figure 3. In the left column, σ_T computed by HBM ($\circ$) is compared with the DNS (-). In the right column, the normalized harmonics Γ_i ($i = 1, ..., 5$) are shown. The amplitude $v_0 = 0.01$ m/s (a-b) is too small to mobilize the nonlinearity of the crack, and $N = 2$ harmonics are sufficient. We measure $\Gamma_2 = 0.017$, to compare with $\gamma_2 = 0.016$: the approximation (12) is good. With $v_0 = 0.13$ m/s (c-d), $N = 10$ harmonics are used, and $\Gamma_2 = 0.24$ is measured, to compare with $\gamma_2 = 0.25$. Lastly, with $v_0 = 0.6$ m/s, $N = 50$ harmonics are required (e). We measure $\Gamma_2 = 0.60$, to compare with $\gamma_2 = 1.02$: the approximation (12) becomes poor. In the three cases and as deduced from the PA (section 3.1), the nonlinearity increases with v_0. At a given v_0, the Γ_i's decrease strictly with i.

Second, the influence of v_0 on the jump $\overline{Y}$ is illustrated in figure 4. The left column shows snapshots of u computed by DNS. The jump between mean values of u yields $\overline{Y}$. In the right column, the time history of $Y(t) = [u(\alpha, t)]$ is computed by fourth-order Runge-Kutta integration of (5) (-) and by PA ($\circ$). At small t, PA differs from RK 4 because it does not compute transients. With $v_0 = 0.01$ m/s, $\overline{Y} = 5.42\,10^{-11}$ m/s (to compare with the approximation $\overline{Y}_1 = 5.026\,10^{-11}$ m/s) is not visible (a), and $N = 2$ in the PA (b). With $v_0 = 0.13$ m/s, $\overline{Y} = 5.84\,10^{-8}$ m/s is measured (c), to compare with $\overline{Y}_1 = 5.60\,10^{-8}$ m/s, and $N = 6$ is required (d). In that case, the maximum value of $Y(t)$ is roughly $0.99\,\delta$: with greater values of v_0, then $\max|Y|/\delta > 1$, and the PA may not converge. It is what happens with $v_0 = 0.6$

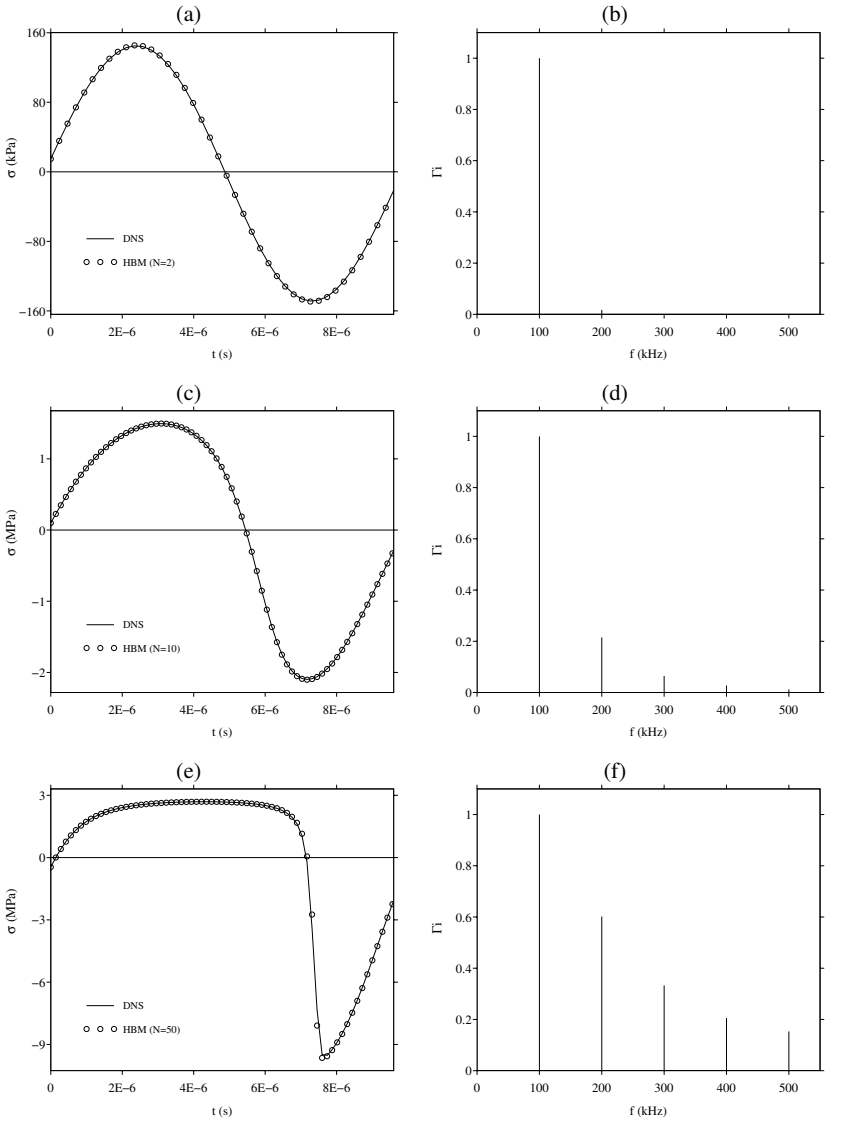

Fig. 3 Transmitted stress, with $v_0 = 0.01$ m/s (a-b), $v_0 = 0.13$ m/s (c-d), $v_0 = 0.6$ m/s (e-f). Left column: values of σ_T on a period; right column: normalized harmonics Γ_i ($i = 1, ..., 5$).

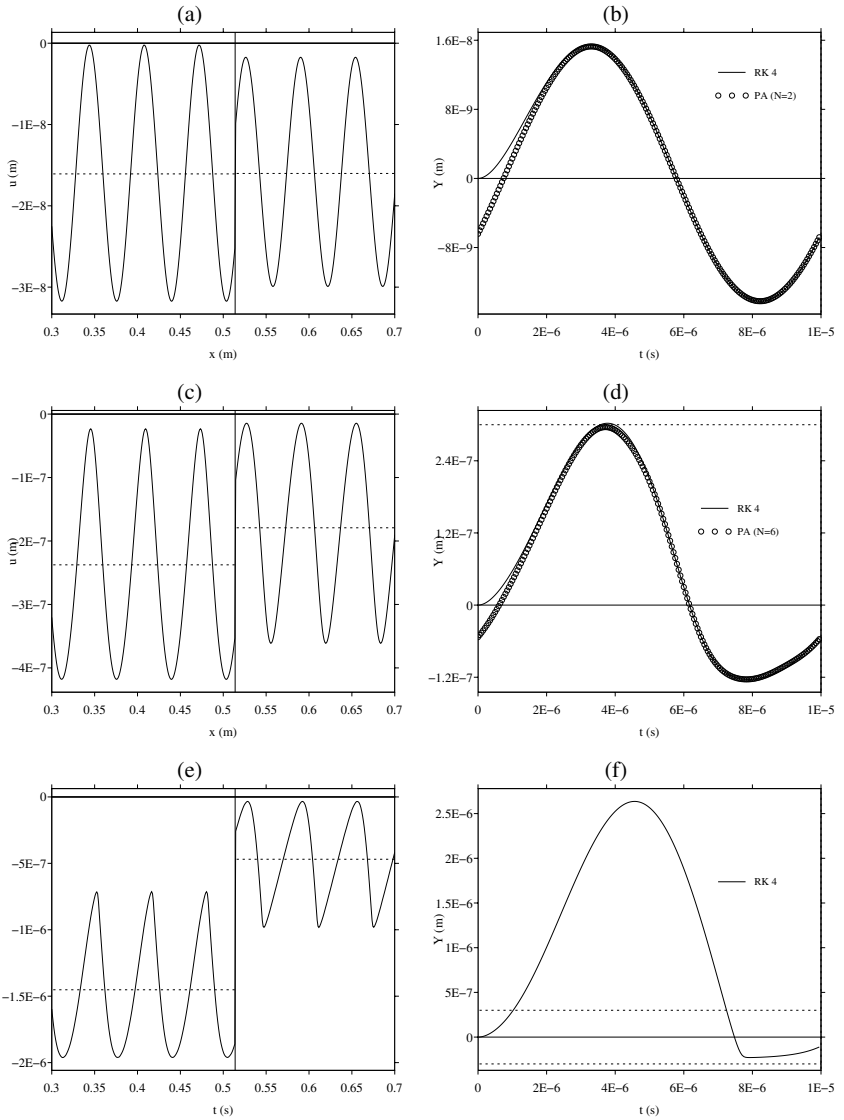

Fig. 4 Left column: snapshots of u around α (the dotted horizontal lines denote the mean value of u, on both sides of α). Right column: time history of $Y = [u(\alpha, t)]$ (the horizontal dotted lines denote $\pm\delta$). (a-b): $v_0 = 0.01$ m/s, (c-d): $v_0 = 0.13$ m/s, (e-f): $v_0 = 0.6$ m/s.

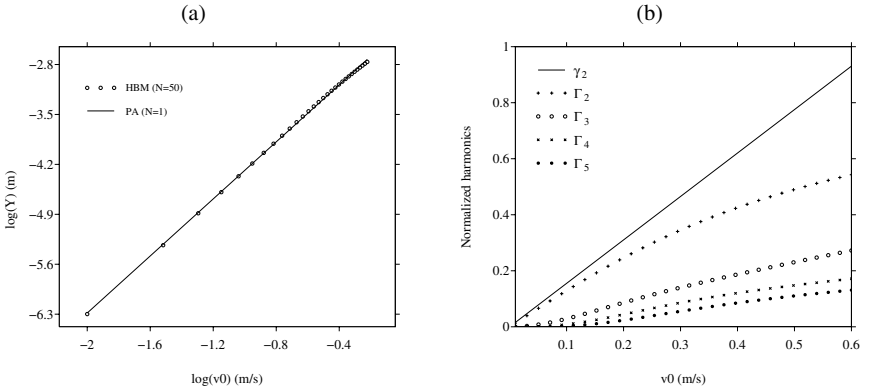

Fig. 5 Parametric studies in terms of v_0: $\overline{Y}$ (a), normalized harmonics Γ_i ($i = 2, ..., 5$) (b).

m/s: only RK 4 is shown (f), and $\overline{Y} = 9.82\,10^{-7}$ m/s is measured, to be compared with $\overline{Y}_1 = 1.02\,10^{-7}$ m/s.

Parametric studies performed by the HBM ($N = 50$) are proposed in figure 5. A log-log scale shows that $\overline{Y}$ is very close to the line with slope 2 deduced from (11), even at high v_0 (a). The amplitude of Γ_i increases strictly with v_0, and Γ_2 tends towards γ_2 at small v_0 (b).

Lastly, propagation across a periodic and finite network of cracks is simulated in figure 6. Two spacings are considered: $h = 1.72\,10^{-2}$ m and $h = 5.17\,10^{-2}$ m. In linear regime and with an infinite network, the Bloch-Floquet's analysis predicts respectively a pass-band and a stop-band behavior, observed with small amplitudes (a-b). The attenuation measured in (a) is in good agreement with the theoretical attenuation (17). With higher amplitudes (c to f), the behaviors are maintained.

5 Conclusion

The main results of this work are as follows:

1. with one crack, two phenomena are induced by the nonlinearity: mean dilatation of the crack, generation of harmonics, that both increase with $\frac{v_0}{\beta\,\delta}$ and $\frac{\beta}{\omega}$;
2. with many cracks, simulations show that properties of infinite linear networks are valid in nonlinear regime with finite networks much greater than wavelength.

Three directions are distinguished for further investigation:

1. investigation of shear effects, coupled or not with compressional efforts [1, 9];
2. analysis of the periodic solution of (5), to prove $\overline{Y} > 0$ and $\partial\,\overline{Y}/\partial\,\frac{v_0}{\beta\,\delta} > 0$;
3. effective properties of a random linear and nonlinear networks [5].

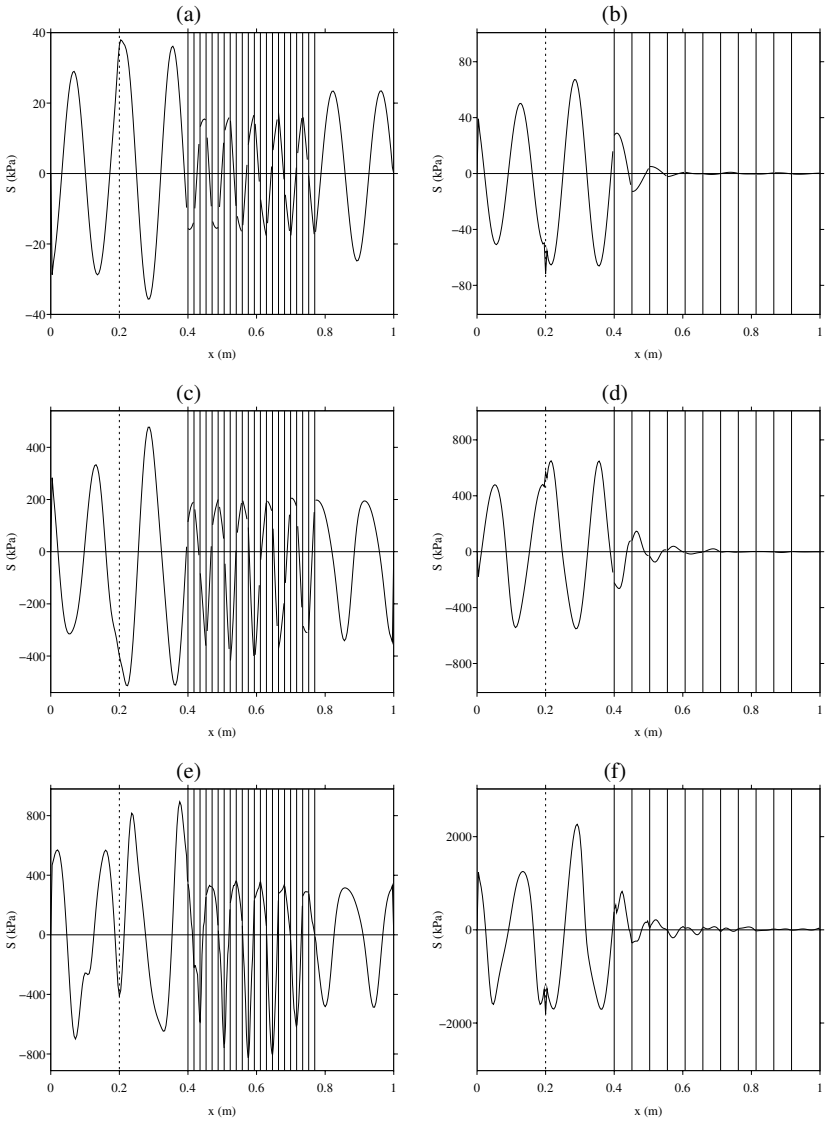

Fig. 6 Snapshots of σ, with $v_0 = 0.01$ m/s (a-b), $v_0 = 0.13$ m/s (c-d), $v_0 = 0.6$ m/s (e-f). The single vertical dashed line on the left denotes the source. The vertical solid lines denote the cracks.

References

1. J. D. Achenbach, A. N. Norris, *Loss of specular reflection due to nonlinear crack-face interaction*, J. NonDest. Eval., 3-4 (1982), pp. 229–239.
2. S. C. Bandis, A. C. Lumsden, N. R. Barton, *Fundamentals of rock fracture deformation*, Int. J. Rock Mech. Min. Sci. Geomech. Abstr., 20-6 (1983), pp. 249–268.
3. C. M. Bender, S. A. Orzag, *Advanced mathematical methods for scientists and engineers 1*, Springer, New-York, 1999.
4. S. Biwa, S. Nakajima, N. Ohno, *On the acoustic nonlinearity of solid-solid contact with pressure dependent interface stiffness*, ASME J. Appl. Mech., 71 (2004), pp. 508–515.
5. C. E. Bradley, *Time-harmonic acoustic Bloch wave propagation in periodic waveguides. Part III. Nonlinear effects*, J. Acoust. Soc. Am., 98-5 (1994), pp. 2735–2744.
6. B. A. Korshak, I. Y. Solodov, E. M. Ballad, *DC effects, sub-harmonics, stochasticity and "memory" for contact acoustic non-linearity*, Ultrasonics, 40 (2002), pp. 707–713.
7. B. Lombard, J. Piraux, *Modeling 1-D elastic P-waves in a fractured rock with hyperbolic jump conditions*, J. Comput. App. Math., 204 (2007), pp. 292-305.
8. S. Nakagawa, K. Nihei, and R. Myer, *Stop-pass behavior of acoustic waves in a 1D fractured system*, J. Acoust. Soc. Am., 107-1 (2000), pp. 40–50.
9. C. Pecorari, *Nonlinear interaction of plane ultrasonic waves with an interface between rough surfaces in contact*, J. Acoust. Soc. Am., 113-6 (2003), pp. 3065–3072.
10. L. Pyrak-Nolte, L. Myer, N. Cook, *Transmission of seismic waves across single natural fractures*, J. Geophys. Res., 95-B6 (1990), pp. 8617–8638.
11. J. M. Richardson, *Harmonic generation at an unbonded interface: I. Planar interface between semi-infinite elastic media*, Int. J. Eng. Sci., 17 (1979), pp. 73–85.
12. M. Schoenberg, *Elastic wave behavior across linear slip interfaces*, J. Acoust. Soc. Am., 68-5 (1980), pp. 1516–1521.
13. I. Y. Solodov, *Ultrasonics of non-linear contacts: propagation, reflection and NDE-applications*, Ultrasonics, 36 (1998), pp. 383–390.

3D Finite Element simulations of an air-coupled ultrasonic NDT system

W. Ke, M. Castaings, C. Bacon

Abstract A single-sided, air-coupled ultrasonic NDT system based on the generation and reception of the A_0 Lamb mode is used for detecting defects in plates. Transmitting and receiving transducers, being oriented at the appropriate coincidence angle for the generation and detection of the mode, are scanned along a line from one side to the other over the surface of the sample, passing the area with the defect. This contact-less NDT system is modelled in three dimensions with a Finite Element -based method. The air-coupled transmitter is modelled by the normal pressure that it locally applies on the surface of the plate, and the air-coupled receiver by integrating normal displacements over a finite area of appropriate position on the surface of the plate. In this way, beam spreading of both incident and scattered fields is considered. Numerical predictions have successfully been compared with experimental data for a through-thickness hole in an Aluminium plate and also for an impact damage in a composite sample.

1 Introduction

Lamb modes are widely used in non-destructive testing (NDT) for detecting invisible flaws in plate-like structures [1-4], as they can explore the entire thickness of the plate while propagating along large distances with reasonable attenuation.

W. Ke
Université de Bordeaux, Laboratoire de Mécanique Physique, UMR CNRS 5469, 351 cours de la Libération, 33400 Talence, France, and Tongji University, Institute of Acoustics, 1239 Siping Road, 200092, Shanghai, China, e-mail: w.ke@lmp.u-bordeaux1.fr

M. Castaing
Université de Bordeaux, Laboratoire de Mécanique Physique, UMR CNRS 5469, 351 cours de la Libération, 33400 Talence, France, e-mail: m.castaings@lmp.u-bordeaux1.fr

C. Bacon
Université de Bordeaux, Laboratoire de Mécanique Physique, UMR CNRS 5469, 351 cours de la Libération, 33400 Talence, France, e-mail: c.bacon@lmp.u-bordeaux1.fr

Generally speaking, there are two different ways to perform ultrasonic testing, i.e. direct or indirect techniques depending on the type of transducers used for the generation and detection of the ultrasonic waves. Air-coupled ultrasonic transducers, known as one of the typical indirect non-contact techniques, are very convenient to perform rapid non-destructive inspections compared with directly coupled transducers or with laser technique [4-7].

In this paper, the inspection is based on the scattering of a single incident Lamb wave by a defect in a plate. The first-order antisymmetric Lamb mode A_0 is chosen as the incident mode for its high coupling level at the solid-air interfaces, thus making easy its generation/detection using air-coupled elements. Two cases are investigated: the diffraction by either a through-thickness hole in an Aluminium plate or by an impact damage in a glass-polyster composite plate. The frequency of the excitation producing the incident mode is chosen equal to 250 kHz, which is close to the centre frequency of the air-coupled transducers used in the study. This frequency is below and above the cut-off frequency of A_1 for the Aluminium and composite cases, respectively. Both experiments and numerical simulations are made with one transmitting and one receiving transducers, which are oriented at appropriate coincidence angles for the generation and detection of the A_0 mode. These elements are moved together along a line from one side of the sample to the other, passing the area with the defect, for scanning the samples. Changes in the amplitudes of the mode detected by the receiver are monitored and plotted versus the positions as an indicator of the damage. In the experiments, the amplitudes are picked-up at the appropriate frequency in the frequency spectrum of each measured temporal waveform. In the numerical predictions, 3D models [8, 9] are used because they offer better representation of real phenomena than 2D models [10]. Indeed, they allow ultrasonic beam angular aperture, scattering in all directions around the defect as well as complicated shapes of defects to be fully simulated [11]. The model is based on the Finite Element method using a commercially available code [12] and solving the equations of dynamic equilibrium in the frequency domain. Different techniques are used to reduce the numbers of degrees of freedom, which usually are huge in 3D models. One is an improved definition of absorbing regions (AR), such regions being known to suppress unwanted reflections coming from the edges of the meshed domain [13]. Another consists in simply applying standard symmetrical or anti-symmetrical boundary conditions when possible. Finally, similar to what has been done in Ref. [6] to avoid modelling the air domain supposed to be surrounding the plate samples, two elliptic-shaped zones are modelled at one surface of the plate to simulate the excitation produced by an air-coupled transmitter and the detection by an air-coupled receiver.

2 Experiments

A Samples

The tested Aluminium plate used in this study is 4 mm thick and square with 700 mm long sides. It has a 5 mm in diameter through-thickness hole machined in its centre. The composite plate is 4.5 mm thick, 460 mm long and 325 mm wide. It is made of unidirectional glass fibres impregnated in a polyester matrix, which makes the sample quite transparent. This plate has an impact damage in its centre (*Fig. 2b*), which has not a circular but elliptical shape running parallel to the plate surfaces, due to the strong anisotropy of the material. Through the thickness, this damage has a conical shape due to the shock wave effect produced by the impact. Visually, this region seems to be made of cracks and delaminated structures with a decaying concentration from the centre to the edges.

The mechanical properties of these two materials are measured using an immersion, ultrasonic and through-transmission technique described in [14]. Namely, stiffness moduli, C_{ij}, defined in the coordinate axis shown in *Fig. 1*, are measured and supplied in Table 1.

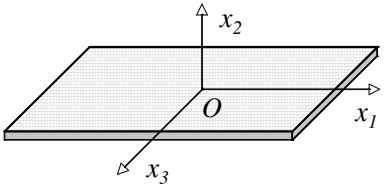

Fig. 1. Composite plate sample with coordinate-system defining the viscoelastic moduli.

Real elastic moduli are obtained for the Aluminium, while complex viscoelastic moduli are measured for the composite material: $C_{ij} = C'_{ij}+iC''_{ij} = C'_{ij}(1+i2.8\%)$, where the real part represents the material stiffness, and the imaginary part its viscoelasticity. For the composite plate, seven complex moduli have been identified using the immersion technique, while C_{44} and C_{23} were deduced from the hexagonal symmetry of this unidirectional fibre medium.

Table 1 Measured thickness (h in mm), density (ρ) and viscoelastic moduli (in GPa) for Aluminium and glass-polyster plates.

Material	h	r	C_{11}	C_{22}	C_{33}	C_{44}	C_{55}	C_{66}	C_{12}	C_{13}	C_{23}
Aluminium	4	2.78	112	112	112	27	27	27	58	58	58
Glass-polyster	4.5	1.8	40.3	14.1	15.9	3.9	3.9	3.9	6.3	6.3	2.2

B Experimental set-up

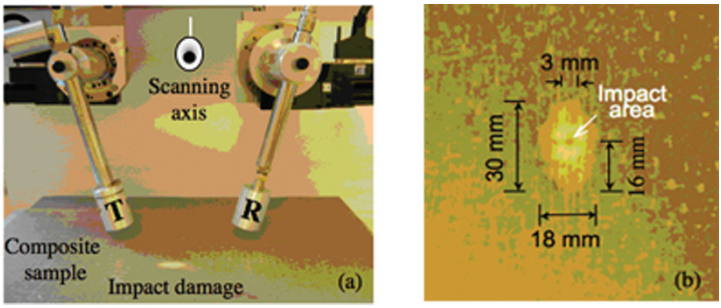

Fig. 2 Photos of (a) experimental set-up (b)impact damage of composite plate.

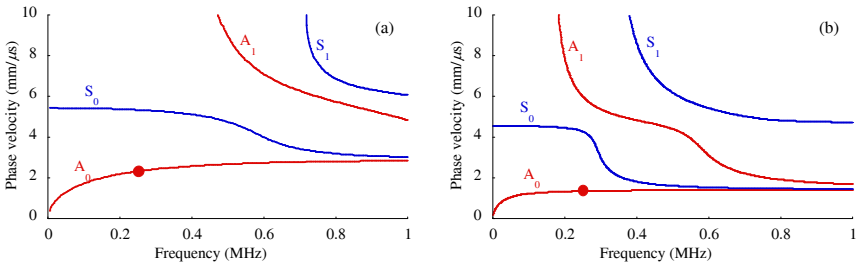

Fig. 3 Lamb waves dispersion curves and operating points for the A0 mode for (a)Aluminium plate (b)along fibres of glass-polyster plate.

Two air-coupled transducers, with 50 kHz to 400 kHz frequency bandwidth, down to -15 dB, are used for generating and detecting guided modes. As shown in *Fig. 2a*, the distance between the transducers is fixed during each scanning, while these are oriented at opposite angles. These angles are deduced from the phase velocity dispersion curves presented in *Fig. 3*, using the Snell-Descartes' law [15]. These curves are predicted using the mechanical properties shown in Table 1 as input data to a guided wave propagation model described in Ref. [17]. During the whole scanning, both emitter and receiver are moved together from one side of the sample to the other, passing the area with the defect. Both plates are large enough to avoid receiving reflections from the edges, so only signals corresponding to waves directly scattered from the defects are selected in the time domain. Changes in the amplitudes of the detected signals are monitored and plotted versus the positions as an indicator of the damage. For further comparison with the simulations, these amplitudes are picked-up at the appropriate frequency (250 kHz) in the frequency spectrum of each measured temporal waveform.

3 3D model for anisotropic materials

A commercially available numerical analysis package [12] based on the Finite Element (FE) method is used to simulate the dynamic responses of viscoelastic, anisotropic plates. Two external routines are also developed. One is for simulating the pressure field produced by the ultrasonic air-coupled transmitter, used in turn as the excitation to the FE meshed plate. The other one is for simulating the response of the ultrasonic air-coupled receiver supposed to be placed over the surface of the plate. In fact, the purpose is to model as well as possible the experimental conditions shown in *Fig. 2a*.

A FE model for propagation and scattering in plates

The equation of dynamic equilibrium for orthotropic viscoelastic material (nine complex moduli) is written and solved in the Fourier domain according to previous developments made for 2D problems:

$$\sum_{j,k,l=1}^{3} C_{ikjl}\left[\frac{\partial^2 u_j}{\partial x_k \partial x_l}\right] + \rho\omega^2 u_i = 0, \qquad i = 1,2,3 \tag{1}$$

where u_i are the displacement components of the displacement vector $\boldsymbol{u}$, with $i = 1,2,3$ representing the direction of the coordinate axis, x_1 being the main direction of propagation, x_2 being the normal to the plate and x_3 being along the plate and normal to x_1, as shown in *Fig. 1*. ρ is the material density and ω is the angular frequency. The above partial differential equation (PDE), Eq. (1), must be written in the following form imposed by the commercial software used in the study:

$$\nabla \cdot (c\nabla \boldsymbol{u}) - a\boldsymbol{u} = 0, \tag{2}$$

where c is a 3*3 matrix composed of nine sub-matrices such that

$$c_{11} = \begin{pmatrix} C_{11} & 0 & 0 \\ 0 & C_{66} & 0 \\ 0 & 0 & C_{55} \end{pmatrix}, \; c_{12} = \begin{pmatrix} 0 & C_{12} & 0 \\ C_{66} & 0 & 0 \\ 0 & 0 & 0 \end{pmatrix}, \; c_{13} = \begin{pmatrix} 0 & 0 & C_{13} \\ 0 & 0 & 0 \\ C_{55} & 0 & 0 \end{pmatrix},$$

$$c_{21} = \begin{pmatrix} 0 & C_{66} & 0 \\ C_{21} & 0 & 0 \\ 0 & 0 & 0 \end{pmatrix}, \; c_{22} = \begin{pmatrix} C_{66} & 0 & 0 \\ 0 & C_{22} & 0 \\ 0 & 0 & C_{44} \end{pmatrix}, \; c_{23} = \begin{pmatrix} 0 & 0 & 0 \\ 0 & 0 & C_{23} \\ 0 & C_{44} & 0 \end{pmatrix},$$

$$c_{31} = \begin{pmatrix} 0 & 0 & C_{55} \\ 0 & 0 & 0 \\ C_{31} & 0 & 0 \end{pmatrix}, \; c_{32} = \begin{pmatrix} 0 & 0 & 0 \\ 0 & 0 & C_{44} \\ 0 & C_{32} & 0 \end{pmatrix}, \; c_{33} = \begin{pmatrix} C_{55} & 0 & 0 \\ 0 & C_{44} & 0 \\ 0 & 0 & C_{33} \end{pmatrix},$$

and a is a 3*3 matrix given by $a = \begin{pmatrix} -\rho\omega^2 & 0 & 0 \\ 0 & -\rho\omega^2 & 0 \\ 0 & 0 & -\rho\omega^2 \end{pmatrix}$.

When modelling the propagation in the frequency domain, absorbing regions (AR) must be used all around the plate to avoid unwanted reflections that would exist due to the permanent established regime. The definition of these 3D AR is based on that previously established for 2D AR made from gradual increase of damping properties, as explained in Ref. [16]. However, they include some recent improvements that allow the size of the AR to be reduced from about $3\lambda_{MAX}$ to $1\lambda_{MAX}$, where λ_{MAX} is the maximum wavelength for all modes existing in the plate at the frequency of investigation. This new definition is given below:

$$\begin{aligned} C_{ij}^{AR} &= C'_{ij}\left(1 - D(r) + I * D(r)\right) + I * C''_{ij} \\ \rho^{AR} &= \frac{\rho}{\left(1 - D(r) + I * D(r)\right)} \\ D(r) &= A * \left(\frac{r}{L_{abs}}\right)^3, \qquad C_{ij} = C'_{ij} + I * C''_{ij} \end{aligned} \tag{3}$$

where $C_{ij} = C'_{ij} + I * C''_{ij}$ represents the material properties in the domain of propagation (DP), i.e. the domain of interest for the generation, propagation, diffraction and detection. r represents the distance away from the interface separating the DP and the AR, and A is a coefficient that may be adjusted to minimize the acoustic impedance mismatch between the domain of propagation and the AR.

Localised defects of finite size and of various 3D shapes are modelled by locally varying the mechanical properties of the material. For instance, to model a cylindrical through-thickness hole in the plate, a function of space with values very close to zero in the domain of the defect and equal to 1 elsewhere is defined and used to multiply the density and mechanical stiffness of the material. In this way, the properties of the domain are unchanged except in the cylindrical domain where they tend towards those of an empty cavity. This makes very easy changing the location, shape and dimensions of the defect, which may be very convenient for parametric studies or for further solving of inverse problems. It has been checked that if the mesh is correctly defined in the region of strongly varied properties, then this approach supplies simulated results very close to those obtained if the hole is modelled by removing from the mesh the cylindrical domain, as more

classically done. This technique will also be used to model the impact damage as explained in section 4.B.

B Transducers modelling

In the model, both the air-coupled transmitter and the receiver used in the experiments are considered by modelling the ultrasonic fields that they send on or receive from the plate, respectively, as illustrated in *Fig. 4a*. The air domain surrounding the plate-transducers system is not modelled in order to reduce the number of degrees of freedom of the FE model, so vacuum is considered all around the plate, which may be an acceptable approximation if one considers that the acoustic impedance of the air is negligible in comparison to that of the solid plates. Specific routines are developed to properly model the ultrasonic beams supposed to be travelling from the transmitter to the plate and from the plate to the receiver.

The acoustic pressure produced at the top surface of the plate by the finite-size transmitter inclined at the appropriate angle is simulated and used as the input excitation applied to the plate. This excitation is considered to be produced by a collimated beam radiated by a circular air-coupled transducer placed above the plate and inclined at an optimized incident angle θ chosen for selecting the A_0 guided mode of the plate. Dispersion curves (*Fig. 3*) are used together with the Snell-Descartes Law [15] to set this angle. Due to this angle, the length of the propagation path from various points of the transducer surface to positions on the top of the plate change, thus producing changes in phase between the various rays forming the collimated incident beam in the air. This effect is taken into account in the model by using the wave-number in the air and the different lengths of propagation paths in the air, as in Ref. [6], in which this was done in 2D. As a result for this actual 3D model, the contour of the projected incident circular beam has an elliptical shape. A Gaussian window is used to define the pressure distribution on the surface of the transducer. The resulting simulated excitation applied on top of the plate is shown in *Fig. 4b*. This excitation is applied via the boundary conditions as a normal stress locally applied on one surface of the plate.

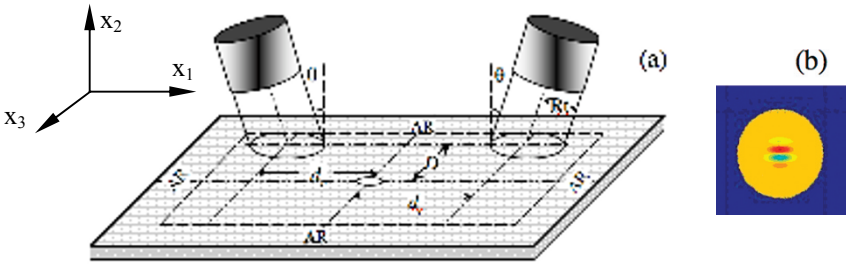

Fig. 4 (a) Schematic of simulation model, (b) Example of simulated excitation on top of plate

Normal displacements are monitored at the surface of the plate in a localized region supposed to be in the field of view of the receiver. Since this element is inclined at an angle opposite to that of the transmitter, for detecting the A_0 mode propagating along the plate, the monitoring region on the plate has an elliptical shape too. Normal displacements monitored over this region are shifted in phase to take into account the differences in path of propagation in the air to the receiver (as those existing between the transmitter and the plate) and then integrated over the surface of the receiver. A Gaussian window is also used to model the distribution of the sensitivity over the receiver's surface. This process is also similar to that proposed in Ref. [6], but in 3D this time.

Besides, for investigating the propagation of the anti-symmetry mode A_0, and its scattering by defects being symmetric with respect to the mid-plane of the plate (cases of the hole in the Aluminium sample and of the impact damage in the composite sample), anti-symmetry boundary conditions are applied at the middle plane to divide the size of the model by two. In this way, only the top half-plates need to be simulated, and a two-sided excitation of the A_0 mode is simulated while one-sided excitation is produced in the experiments. However, since all predicted or measured scattered amplitudes are normalized so that they have the same maximum value, the double or single side excitation has no importance.

4 Results

Measurements and numerical simulations of changes in the amplitudes of the A_0 mode generated-detected using air-coupled transducers, at a frequency equal to 250 kHz, are presented both for the Aluminium and the composite plates. Both transducers are moved together over the samples from one extreme position to another, these being -50 mm and +50 mm away from the defect. The scanning step is equal to 2.5 mm and along direction x_3 as shown in *Fig. 4a*. Both measured and predicted amplitudes of signals delivered by the receiver, at 250 kHz, are plotted versus the x_3 position to produce the ultrasonic image of the plate including the defect.

A Scanning through-thickness hole in Aluminium plate

The incident and receiving angles for A_0 in this 4mm thick Aluminium plate are equal to ±8.3°. The distance, d_e, from the hole centre to the line the emitter is moved along, is set equal to 40mm. The distance, d_r, from the hole centre to the line the receiver is moved along, is set equal either to 40 mm and 60 mm, respectively. These positioning parameters are shown in *Fig. 4a*. These configurations

lead to two sets of measurements and predictions presented in *Fig. 5*. In this case, no normalization was needed.

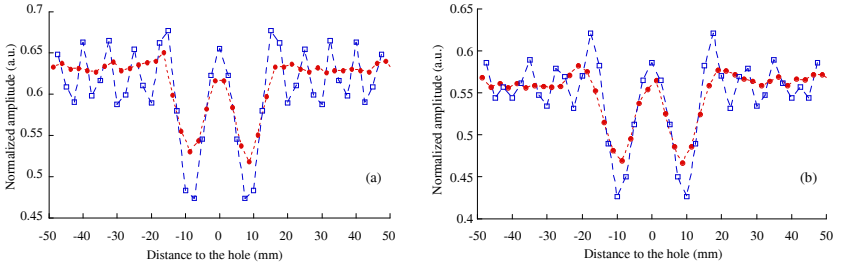

Fig. 5 Results of scanning Aluminium plate for the hole, changing the position of the receiver (a)minimum distance equal to 40mm (b) minimum distance equal to 60mm; (●) measurements and (□) numerical predictions

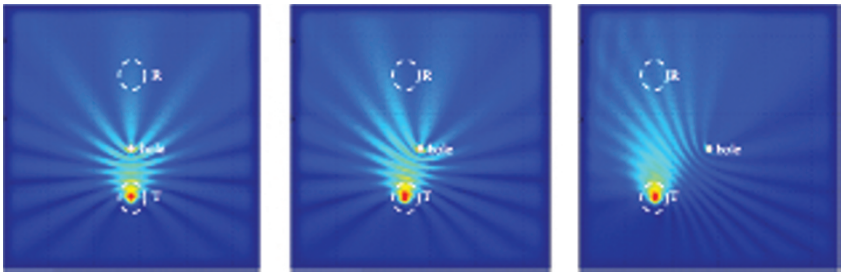

Fig. 6 FE predictions of scattered v displacements on top of Aluminium plate for various values of distance D shown in Fig. 4a, (a) D=0 mm , (b)D=-10 mm and (c) D=-35 mm.

There is a clear peak of amplitudes obtained both in the measurements and predictions when both transducers are well aligned with the centre of the hole in the Aluminium plate, probably due to straight propagating paths on each side of the hole with constructive interference past the hole. Then, the amplitudes decrease significantly as the transducers get misaligned with the hole, probably due to a strong scattering effect producing normal displacements distribution with a shadow where the receiver is. When slightly increasing the misalignment between the transducers and the hole, the amplitude increases to a value very close to that at perfect alignment. Then, as the transducers are further moved away from the defect, the amplitudes oscillate around an average value close to 90% of the maxima reached during previous positions. Obviously the predicted curves are perfectly symmetric with respect to the position of perfect alignment. This is not exactly the case for the measurements due to various experimental noises. Comparing the graphs obtained for both distances d_r between the hole and receiver, it is observed that the first one (*Fig. 5*a), corresponding to the shorter distance d_r, has globally bigger amplitudes and more pronounced lateral oscillations. These are likely to be due to the angular beam aperture of the guided A_0 mode travelling both directly from the transmitter to the receiver and also being scattered by the hole, and to the interferences between these two parts that are alternatively constructive or destructive depending on the position on the surface of the plate, and also on the distance

between the transducers lines and the hole. Snapshots of the normal displacements predicted with the FE model are presented in *Fig. 6*. These help understanding the scattering phenomena and analysing scanning curves as those presented in *Fig. 5*.

B Scanning impact damage in composite plate

To simulate the impact damage of the composite plate, the material stiffness is decreased according to a spatial function defined to represent the distribution of cracks and delaminated structures supposed to be existing through the thickness of the sample, in the region below the impact point. Since the glass-polyester constituting this sample is slightly transparent, then it is possible to roughly evaluate the geometry of the damage. This defect has a nearly-3mm-in-diameter cylindrical zone in the middle running all through the thickness of the plate, which seems to correspond to very high level of damaging. In the model, the material stiffness is decreased by 90% in this region. Around this cylinder, damages are distributed in ellipsoidal-shaped zones running parallel to the plate surfaces, and having different sizes depending on their position through the plate thickness. The ellipsoid shape is due to the strong anisotropy of the material in the plane of the plate, and the varying size through the thickness is usually due to the shock wave produced by the impact, which creates defects of larger sizes as it propagates through the medium with a given angular aperture, and defects of smaller sizes as it gets damped after a certain penetration depth. Ellipses close to the plate surfaces seem to have the same size together, and to be roughly half size that located close to the mid-plane of the sample. A function of space with variables x_1, x_2 and x_3 is created to represent this particular distribution, and then used to locally multiply the material stiffness by a factor equal to 10% in the region of the central cylinder of very high damaging, and to 50% all around this central cylinder to the edges of the damage. Moreover, a large delamination located at the mid-plane of the sample was modelled to represent all the cracks and delaminated structures by setting this factor very close to 0% within a 0.5 mm thick (in fact 0.25 mm with antisymmetry conditions) ellipse of 30 mm long and 18 mm wide (*Fig. 2b*).

The parameters d_e and d_r defined in previous section and shown in *Fig. 4a*, that indicate the positions of the transmitter and receiver, are equal to 20 mm and 35 mm, respectively. The air-coupled transducers are oriented at angles equal to $\pm 15.2^{\circ}$, and positioned so that the A_0 mode is generated-detected in the direction parallel to the glass fibres. The obtained scanning image is shown in *Fig. 7*. The experimental results are in good agreement with the numerical predictions, especially the width and relative depth of the U-shaped part of the curve that indicates the defect. It is noticeable that the peak down in the centre of the U-shaped part of the curve is much less pronounced than that for the Aluminium plate. This may come from the extent of the damage, which is larger than the diameter of the hole

in the Aluminium sample, thus preventing direct propagation paths at the sides of the defect, which have been identified in previous section as causing the strong peak in the middle of the U-shaped curve (*Fig. 5*). Moreover, the gradually changing stiffness within the damage may cause some attenuation of the incoming ultrasounds. However there are some differences between the measured and simulated results when the distance between the line running from transmitter to receiver and the defect, i.e. D defined in *Fig. 4a*, is ether close to -40 mm or greater than 25 mm. The non-uniformity in the measured curve out of the impact damage area is likely to be indicating some invisible defects inside the plate, which are not considered in the model.

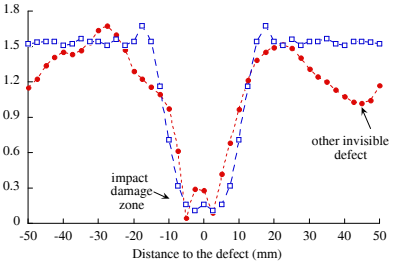

Fig. 7 Results of scanning composite plate with an impact damage; (●) measurements and (□) numerical predictions normalized to the maximum experimental amplitude

5 Conclusions

A three-dimensional FE-based model has been developed to simulate the propagation of ultrasonic guided beams along plates made of anisotropic, viscoelastic materials, and their scattering by defects of complex shape. Specific interfaces have been developed to model in 3D circular air-coupled transducers used in alternate experiments as a transmitter and a receiver to generate and detect the A_0 Lamb wave, and to scan samples with defects. Ultrasonic C-scan curves have been measured and predicted for an isotropic Aluminium plate with a through-thickness hole in the centre, and for a glass-polyester composite plate with an impact damage. Numerical predictions are in good agreement with the measured data, especially concerning the positions and magnitudes of changes in the signals delivered by the receiver. Plots of predicted normal displacement snapshots allow understanding some 3D wave scattering phenomena, and explaining the shapes of the measured C-scan curves. In this study, the importance of considering 3D effects in the FE models has been demonstrated. Works in progress are focussing on using this numerical tool for modelling several permanently attached transducers alternatively working as transmitters or receivers, for SHM applications.

6 References

1. P. Cawley, The rapid non-destructive inspection of large composite structures. Compos. 25, 351-357, 1994.
2. K. S. Tan, N. Guo, B. S. Wong, C. G. Tui, Experimental evaluation of delaminations in composite plates by the use of Lamb waves. Composite Science and Technology **53**, 77-84, 1995.
3. K. Diamanti, J. M. Hodgkinson, C. Soutis, Detection of Low-velocity Impact Damage in Composite Plates using Lamb Waves. Structural Health Monitoring **3**(1), 33-41, 2004.
4. M. Castaings, B. Hosten, Ultrasonic guided waves for health monitoring of high-pressure composite tanks. In press for NDT&E Intern.
5. D. W. Schindel, D. A. Hutchins, Applications of micromachined capacitance transducers in air-coupled ultrasonics and non-destructive evaluation, IEEE UFFC, 42(1), 51-58, 1995.
6. M. Castaings, P. Cawley, R. Farlow, G. Hayward, Single sided inspection of composite materials using air-coupled ultrasound, NDE, 17(1), 37-45, 1998.
7. A. Safaeinili, O. I. Lobkis, D. E. Chimenti, Air-coupled ultrasonic estimation of viscoelastic stiffness in plates, IEEE UFFC, 43(6), 1171-1180, 1996.
8. L. Moreau, M. Castaings, The use of an orthogonality relation for reducing the size of finite element models for 3D guided waves scattering problems, In press for Ultrasonics.
9. T. Grahn, Lamb wave scattering from a circular partly through-thickness hole in a plate. Wave Motion 37, 63–80, 2003.
10. J. Mackerle, Coatings and surface modification technologies: a finite element bibliography (1995–2005), Modelling Simul. Mater. Sci. Eng., 13, 935–979, 2005.
11. R. Kazys, L. Mazeika, R. Barauskas, R. Raisutis, V. Cicenas, A. Demcenko, 3D Analysis of interaction of Lamb waves with defects in loaded steel plates, Ultrasonics, 44, e1127–e1130, 2006.
12. COMSOL, User's Guide and Introduction. Version 3.2 by – COMSOL AB 2005 http://www.comsol.com/, most recently viewed 6th May 2008.
13. M. Drozdz, Efficient Finite Element modelling of ultrasound waves in elastic media. PhD theses, Mechanical Engineering, Imperial College London, 2008.
14. M. Castaings, B. Hosten, T. Kundu, Inversion of ultrasonic, plane-wave transmission data in composite plates to infer viscoelastic material properties. NDT & E International, 33 (6), 377-392, 2000.
15. B. A. Auld, Acoustic Fields and Waves in Solids, Wiley, New York, 1973.
16. M. Drozdz, M. Lowe, P. Cawley, L. Moreau, M. Castaings, Efficient numerical modeling of absorbing regions for boundaries of guided waves problems. Review of Progress in Quantitative Non Destructive Evaluation, Ed Thompson D.O. and Chimenti D.E., AIP Conf. Proc., New York, 25A, 126-133, 2006.
17. B. Hosten, M. Castaings, Surface impedance matrices to model the propagation in multilayered media. Ultrasonics, 41, 501-507, 2003.

The reverse time migration technique coupled with finite element methods

C. Baldassari, H. Barucq, H. Calandra, B. Denel, J. Diaz

Abstract The Reverse Time Migration (RTM) is a technique for imaging the subsurface based on successive solutions of the full wave equation which must be computed by fast numerical methods to perform well in three-dimensional domains. In this framework, we propose to solve the full wave equation by the Interior Penalty Discontinuous Galerkin method (IPDG). We analyse the performances of IPDG by comparing it to classical spectral element method and we show that IPDG is more adapted to the RTM. We present 2D migration results to illustrate the ability of the new method to recover the location of the interfaces of stratified media.

1 Introduction

Seismic imaging is based on the seismic reflection method which produces an image of the subsurface from reflected waves recordings by using a tomography process and seismic migration is the industrial standard to improve the quality of the images. The migration process consists in replacing the recorded wavefields at their actual place by using various mathematical and numerical methods. Among them, the Kirchhoff migration algorithm is the most popular. It is based on ray tracing and provides an intuitive representation of wave propagation. One of its significant computational advantage is to be quite efficient for target-oriented migration in which only a subset of the whole image cube is imaged. The computational cost of Kirchhoff migration is then reduced in proportion to the reduction in image size. Howe-

C. Baldassari, H. Barucq, J. Diaz
INRIA Bordeaux Research Center Team Project Magique3D, LMA, CNRS UMR 5142 University of Pau 64013 PAU e-mail: caroline.baldassari@inria.fr, helene.barucq@inria.fr, julien.diaz@inria.fr

H. Calandra, B. Denel
TOTAL, Avenue Larribau, 64000 PAU e-mail: henri.calandra@total.com, bertrand.denel@total.com

ver, since Kirchhoff methods are based on a high-frequency ray approximation of the wave equation, they are not accurate for imaging complex geological structures where multipathing occurs. Migration methods based on the numerical propagation of the recorded wavefield (the so-called wavefield-continuation methods) can overcome some of the limitations of Kirchhoff migration methods. There exist different wavefield-continuation methods which differ in particular from the numerical method applied for computing the propagated fields but each of them follows the same schedule, according to the pioneering idea of Claerbout [2, 3]: numerical propagation of the source function (propagation) and of the recorded wavefields (retropropagation) and next, construction of the image by applying an imaging condition. Thus, the relation between data and the produced image is indirect, as compared to the Kirchhoff imaging method which involves multi-convolutional operators whose kernels lead to a direct insight into the relation between the recorded data and the migrated image. The retropropagation step can be realized accouting for the time reversibility of the wave equation and the resulting algorithm is currently called Reverse Time Migration (RTM). During the propagation and retropropagation steps, seismograms are generated and are correlated through a scalar product whose value is attributed to the respective subsurface location, according to the fact that a reflection is associated to a strong correlation coefficient which corresponds to the case where a down-going wave field is generated by the source and an up-going wave field propagates towards the receivers at the same time. This procedure is valid under the assumption that only first-order reflections are present in the seismograms and justifies both the direct wave and head waves are muted in the records before feeding them into the reverse modeling. The wave equation can be solved by considering one-way propagators which provides a fast numerical solution. However the full-wave RTM method does not have the angle limitation of one-way propagators and can be used to image complex structures where turning waves are involved. During a long time, the full-wave RTM was considered as a too much expensive tool and there was not really an interest to image very complex media. Today, since the hydrocarbons resources have decrease dramatically, it is necessary to image more and more heterogeneous regions and broken grounds. Besides, the impressive improvement of scientific computing relaunches the RTM as an efficient method for seismic imaging. It is nevertheless obvious that an efficient RTM is based on a good compromise between accuracy and computational cost. One of the most accurate numerical solution of the wave equation involves finite element methods but the resulting seismic imaging procedure thus requires a very large amount of computational power, especially as far as the memory storage is concerned. Even if finite element methods lead to the solution of huge systems with several millions of degrees of freedom, they are considered as the most accurate discretization methods since they use meshes adapted to the topography of the domain and the boundary conditions are naturally taken into account in the variational formulation. Among the different finite element families, the spectral element method (SEM)[4, 5, 6, 9] is very interesting because it is compatible with the use of a Gauss Lobatto quadrature rule which leads to a diagonal mass matrix and does not hamper the order of convergence of the finite element method. However, this method requires to mesh

the domain with quadrangles in 2D ou hexaedra in 3D that are difficult to compute and not always suitable to complex topographies. Recently, Grote et al. [8] applied the Interior Penalty Discontinuous Galerkin (IPDG) [7] method to the wave equation. This new approach is based on meshes made of triangles in 2D or tetrahedra in 3D, which implies the topography of the computational domain is discretized accurately. Furthermore, the mass matrix is block-diagonal without any approximation of its entries by a quadrature rule which means the discretization scheme is quasi-explicit. The convergence order is then preserved as for the spectral element method. Moreover this method seems to be well-adapted for the handling of polynomial velocities inside each element. In this work, we intend to show the effects of coupling the full-wave RTM with the IPDG finite element method. Most of the papers dealing with full-wave RTM consider finite difference which are not efficient enough to consider general complex propagation media. The most popular finite elements for seismic imaging are the spectral elements which provide an accurate approximation of the solution to the wave equation in complex media and to the best of our knowledge, the IPDG method has never been applied to the RTM. The paper is organized as follows: section 2 deals with the general setting of the IPDG method, section 3 is devoted to the analysis of performance of the IPDG approach and a comparison with the SEM in 1D and the last section illustrates how the IPDG method performs well for RTM in 2D.

2 Interior Penalty Discontinuous Galerkin method

In this section we recall the formulation proposed by Grote, Schneebeli and Schtzau [8].

2.1 General setting

We consider the problem of acoustic waves propagation:

$$\begin{cases} \dfrac{1}{\mu(x)}\dfrac{\partial^2 u}{\partial t^2} - \nabla.\left(\dfrac{1}{\rho(x)}\nabla u\right) = f \quad \text{in} \quad I\times\Omega \\ \dfrac{1}{\sqrt{\mu(x)}}\dfrac{\partial u}{\partial t} + \dfrac{1}{\sqrt{\rho(x)}}\nabla u\cdot\mathbf{n} = 0 \quad \text{on} \quad \partial\Omega \end{cases} \tag{1}$$

where $I =]0,T[$ is a bounded time interval and Ω is a bounded domain of $\mathbb{R}^2$. The condition imposed on $\partial\Omega$ is a first order absorbing boundary condition. The vector $\mathbf{n}$ is the unitary outward normal to Ω, ρ is the density of the medium, μ is the compressibility modulus and $c = \sqrt{\mu/\rho}$ is the propagation velocity of the waves in Ω. The initial conditions are supposed to be zero.

In the following, $\mathscr{T}_h$ is a partition of Ω composed of triangles K such that $\overline{\Omega} = \bigcup_{K\in\mathscr{T}_h} \overline{K}$. We denote by h_K the diameter of the element K and by $h = \min_{K\in\mathscr{T}_h} h_K$; E_i is an internal edge defined by two elements K^+ et K^- (i.e $E_i = \partial K^+ \cap \partial K^-$); $\mathbf{n}^\pm$ are the outward normal vectors to $K^\pm$; $v^\pm$ are the traces of a function v on $K^\pm$; $\mathscr{E}_i$ is the set of internal edges; E_e is an edge lying on the boundary $\partial\Omega$; $\mathscr{E}_e$ is the set of all the edges lying on $\partial\Omega$.

We also define the jump and the mean-value of a function v on an internal edge E_i by: $[[\, v\,]] = v^+\mathbf{n}^+ + v^-\mathbf{n}^-$ and $\{\{v\}\} := \left(v^+ + v^-\right)/2$ and we define similarly the jump and the mean-value of a vectorial function $\mathbf{q}$ by:
$[[\mathbf{q}]] := \mathbf{q}^+\cdot\mathbf{n}^+ + \mathbf{q}^-\cdot\mathbf{n}^-$ and $\{\{\,\mathbf{q}\,\}\} := \left(\mathbf{q}^+ + \mathbf{q}^-\right)/2$ on E_i.

2.2 The approximate problem

We seek an approximation of $u(t,.)$, solution to (1) in the finite element space:

$$V_l^h := \left\{ v \in L^2(\Omega) : v_{|K} \in P_l(K)\ \forall K \in \mathscr{T}_h \right\}, \tag{2}$$

where $P_l(K)$ is the set of polynomials on K whose total degree is less or equal to l.

Then we consider the semi-discretized problem, arising from a variational formulation of (1):
Find $u_h : \bar{I} \times V_l^h \to I\!R$ such that:

$$\left(\frac{1}{\mu}\frac{\partial^2 u_h}{\partial t^2}, v_h\right) + b_h\left(\frac{\partial u_h}{\partial t}, v_h\right) + a_h(u_h, v_h) = (f, v_h) \quad \forall v_h \in V_l^h, \quad t \in I \tag{3}$$

with zero initial conditions.

The bilinear form b_h on $V_l^h \times V_l^h$ is given by:

$$b_h(u_h, v_h) := \sum_{E_e\in\mathscr{E}_e} \int_{E_e} \frac{1}{\sqrt{\mu\rho}} u_h v_h \, dE \tag{4}$$

and the bilinear form a_h on $V_l^h \times V_l^h$ is given by:

$$\begin{aligned} a_h(u_h, v_h) := & \sum_{K\in\mathscr{T}_h} \int_K \frac{1}{\rho}\nabla u_h \cdot \nabla v_h \, dx - \sum_{E_i\in\mathscr{E}_i} \int_{E_i} [[\, u_h\,]] \cdot \{\{\, \frac{1}{\rho}\nabla v_h \,\}\}\, dE \\ & - \sum_{E_i\in\mathscr{E}_i} \int_{E_i} [[\, v_h\,]] \cdot \{\{\, \frac{1}{\rho}\nabla u_h \,\}\}\, dE + \sum_{E_i\in\mathscr{E}_i} \int_{E_i} \gamma [[\, u_h\,]] \cdot [[\, v_h\,]]\, dE. \end{aligned}$$

The three last terms correspond to the jumps and the fluxes of u_h through the edges of the elements. They obviously vanish when u_h and v_h belong to $H_0^1(\Omega)$. In this

case, problem (3) is the one we would have obtained with classical finite elements. The function γ, which penalizes the jump of u_h and v_h through the edges of $\mathscr{T}_h$ is the so-called interior penalty function. It is defined on each edge $E \in \mathscr{E}_i$ by: $\gamma_{|E} := \alpha\, c_{max} h_{min}^{-1}$ where α is a positive parameter independent of the mesh, c_{max} and h_{min} are defined by:

$$c_{max} = \max\left(c_{|K^+}, c_{|K^-}\right), \text{ on } E \in \mathscr{E}_i \text{ and } h_{min} = \min\left(h_K, h_{K'}\right), \text{ on } E \in \mathscr{E}_i.$$

Let us recall that, in order to ensure the coercivity of a_h, we need $\alpha > \frac{1}{2} l\,(l+1)$ (see [7]).

As for a classical finite element method, we consider a basis $(v_k)_{1 \le k \le N}$ of V_l^h, where N is the dimension of V_l^h, to obtain the linear system:

$$\mathscr{M} \frac{d^2 U_h}{dt^2} + \mathscr{B} \frac{dU_h}{dt} + \mathscr{K} U_h = F_h \tag{5}$$

where

- U_h is the vector whose components are the coefficients of u_h in the basis (v_k);
- the matrix $\mathscr{M}$ is the mass matrix, whose entries are defined by $\mathscr{M}_{ij} = \sum_{K \in \mathscr{T}_h} \int_K \frac{1}{\mu} v_i v_j$. This matrix is **block-diagonal**;
- the coefficients of matrix $\mathscr{B}$ are defined by $\mathscr{B}_{ij} = b_h(v_i, v_j)$. Most of them vanish, but the ones associated to degrees of freedom lying on the boundary $\partial\Omega$. This matrix is also **block-diagonal**.
- the matrix $\mathscr{K}$ is the stiffness matrix, whose coefficients are defined by $\mathscr{K}_{ij} = a_h(v_i, v_j)$
- F_h is the source vector defined by $F_i = \sum_{K \in \mathscr{T}_h} \int_K f v_i$.

Let us recall that the approximate solution converges to the exact one with an order $l+1$ [8].

For the time discretization we use a classical second order centered scheme:

$$\mathscr{M} \frac{U_h^{n+1} - 2U_h^n + U_h^{n-1}}{\Delta t^2} + \mathscr{B} \frac{U_h^{n+1} - U_h^{n-1}}{2\Delta t} = -\mathscr{K} U_h^n + F_h \tag{6}$$

This scheme is semi-explicit, since $\mathscr{M}$ and $\mathscr{B}$ are block-diagonal.

3 Performance analysis

In this section, we compare the accuracy of the IPDG method to the one of the SEM. We present here the results we obtained for the one-dimensional case. The 2D

comparison is in progress but the first experiments we performed seem to confirm the 1D results.

We simulate the propagation of a sinusoid on a 9m axis discretized by a regular grid of space step dx during 60s. The period of the sinusoid is 9/8s, and the medium velocity is $c = 1\mathrm{m/s}$. Morevoer, in order to avoid any spurious phenomena due to the discretization of the boundary conditions, we impose periodic boundary conditions. In Tab. 1, we present the $L^2(\Omega \times [0,t])$ error (err) for various space steps and orders of approximation. Actually, the space step does not really indicate the cost of the methods which depends essentially on the size of matrix $\mathscr{K}$ and the number of multiplications by U. The size of $\mathscr{K}$ is directly given by the number of degrees of freedom (N) and the number of multiplications (or iterations) is related to the time-step (dt) which is constrained by the so-called CFL (Courant-Friedriech-Levy) relation : the higher this time step, the less the number of iterations.

Order 2		Order 3		Order 4	
IPDG	SEM	IPDG	SEM	IPDG	SEM
N=180	N=181	N=180	N=181	N=180	N=180
dx=0.100	dx=0.0500	dx=0.1500	dx=0.100	dx=0.200	dx=0.1500
dt=0.0404	dt=0.0495	dt=0.0347	dt=0.0400	dt=0.0307	dt=0.0348
err=11.0781	err=0.0676	err=1.2187	err=1.5961	err=0.4865	err=0.6263
N=360	N=361	N=360	N=361	N=360	N=360
dx=0.0500	dx=0.0250	dx=0.0750	dx=0.0500	dx=0.100	dx=0.0750
dt=0.0202	dt=0.0247	dt=0.0174	dt=0.0200	dt=0.0153	dt=0.0174
err=2.9120	err=0.0169	err=0.3040	err=0.4018	err=0.1215	err=0.1565
N=720	N=721	N=720	N=721	N=720	N=720
dx=0.0250	dx=0.0125	dx=0.0375	dx=0.0250	dx=0.0500	dx=0.0375
dt=0.0101	dt=0.0124	dt=0.0087	dt=0.0100	dt=0.0077	dt=0.0087
err=0.7325	err=0.0042	err=0.0760	err=0.1007	err=0.0304	err=0.0391
N=1440	N=1441	N=1440	N=1441	N=1440	N=1440
dx=0.0125	dx=0.00625	dx=0.0187	dx=0.0125	dx=0.0250	dx=0.0187
dt=0.00677	dt=0.00625	dt=0.0043	dt=0.0050	dt=0.0038	dt=0.0044
err=0.204	err=0.00105	err=0.0190	err=0.0252	err=0.0076	err=0.0098

Table 1 Comparison between IPDG and SEM.

Let us first remark that all the methods converge with the expected order. For the second order case, the SEM is much more accurate than IPDG for a given number of degrees of freedom and the number of required iterations is lower. For higher order the IPDG is more accurate than the spectral element method, while the number of iterations is quite the same for both approaches.

We have repeated the same experiments on irregular meshes and we have obtained similar results [1].

As a conclusion, the IPDG method and the SEM present equivalent performances for high-order accuracy. The first results we obtained in 2D seem to confirm this conclusion [1]. The choice of the IPDG method for the RTM is then justified by the fact that, it can be applied on meshes made of triangles or tetraedra which are easier to handle.

4 Application to depth imaging

In this section, we intend to show some 2D migration results involving the IPDG method. For the first numerical experiment, the velocity model is very simple and we only want to verify the capability of the IPDG method to accurately represent a two-layered medium. For the second experiment, the velocity model consists of four layers with a step-shaped interface. For both experiments we consider the fourth order IPDG method.

4.1 Two-layered medium

We consider a two-layered medium of size 800m×800m. The velocity in the upper layer 800m×400m is $c_1 = 1500\text{m/s}$. The velocity in the bottom layer 800m×400m is $c_2 = 3000\text{m/s}$ (cf. Fig.1). We use ponctual sources in space at point $(25 * j, 0), j = 1, ..., 31$, the time sources are first derivatives of a Gaussian with a central frequency 20Hz. Moreover, we impose an absorbing boundary condition on the whole boundary in such a way that the top of the model does not produce reflections into the propagation domain.

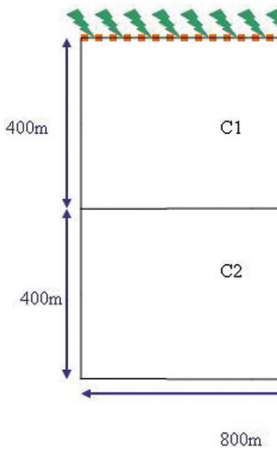

Fig. 1 Two-layered medium

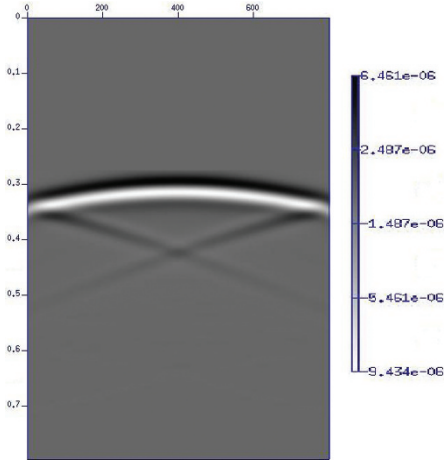

Fig. 2 Seismogram obtained for the two-layered medium with the source at x=400m

Figure 2 represents the seismogram obtained when the source is located in the middle of the surface. The vertical axis represents the time (in seconds) whereas the horizontal axis represents the position of the receivers in the x-direction (in meters). From this seismogram we can deduce the arrival times of the waves. We can then

validate our results by checking that the travel time source/interface/receiver for a velocity c_1 corresponds to the time indicated by the seismogram. We note spurious reflections due to the absorbing boundaries whose modelling is not very accurate.

On Fig. 3 we present the final image obtained by the RTM method. It is constructed by summing all the partial images obtained for each shooting point. We can observe that we recover the interface at depth 400m. On both sides of the figure, the interface is not perfectly straight. This is due to the absence of shooting points at the two extremities of the free surface x=0 and x=800m.

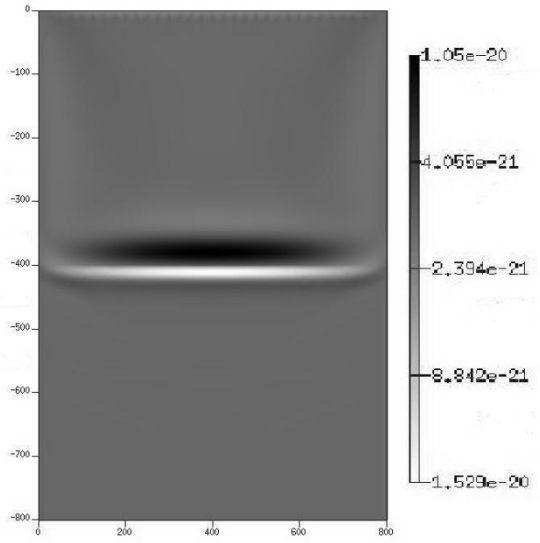

Fig. 3 Final image of the two-layered medium

4.2 Four-layered medium

We consider a four-layered medium of size 2000m$\times$1200m as shown in Fig.4. The velocity in the upper layer of size 2000m$\times$300m is $c_1 = 4500$m/s. The second and third layers with respective velocities $c_2 = 1500$m/s and $c_3 = 3000$m/s are separated by a step-shaped boundary. The bottom of the step is located at 700m depth and the top at 500m. At last, in the layer 2000m$\times$300m, $c_4 = 6000$m/s. We use ponctual sources in space at point $(25 * j, 0), j = 1, ..., 79$, the time sources are first derivatives of a Gaussian with central frequency 20Hz. Moreover, we impose absorbing boundary conditions on the whole boundary as in the previous case.

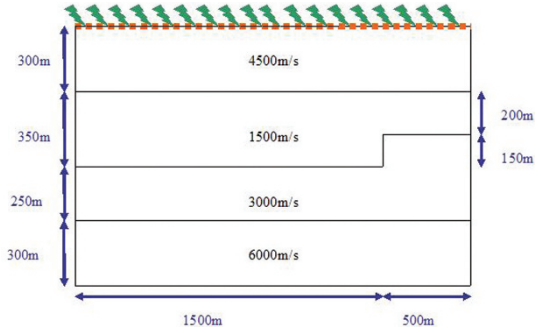

Fig. 4 Four-layered medium

On Fig. 5 we depict the final image obtained by the RTM method on a mesh with approximatively 12 points per wavelength on the second layer. The three interfaces are well localized at their actual depth.

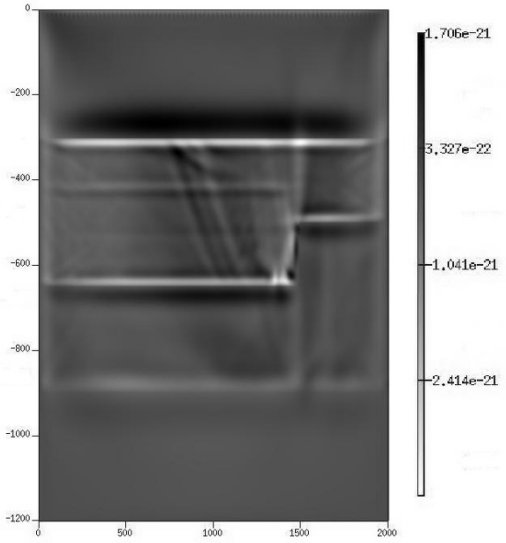

Fig. 5 Final image of the four-layered medium

5 Conclusion

The results we have present are very promising but further improvements have still to be done. First of all, we intend to tackle the optimization of the computational costs by addressing the issue of adapting both the space steps and the order of convergence in the various layers of the domain. Concerning the time discretization we shall use a local time-stepping strategy to avoid the numerical dispersion. Then, we also aim at studying more accurate absorbing boundary conditions to avoid spurious reflections at the boundary of the domain. After all these improvements we shall compare the RTM-results obtained by the IPDG to the ones obtained by SEM and finite difference schemes and finally, we shall extend our code to 3D problems.

References

1. C. Baldassari, H. Barucq, and J. Diaz. Comparison of the performances of interior penalty discontinous galerkin and spectral element methods. in preparation.
2. B.L. Biondi. *3D Seismic Imaging*. SEG, 2006.
3. J.F. Claerbout. *Imaging the Earth's Interior*. Blackwell Scientific Publications, 1985.
4. J. Tromp D. Komatitsch. Introduction to the spectral element method for three-dimensional seismic wave propagation. *Geophys. J. Int.*, 139:806–822, 1999.
5. R. Vai J.M. Castillo-Covarrubias F.J. Sanchez-Sesma D. Komatitsch, J-P. Vilotte. Higher-order finite elements with mass-lumping for the 1d wave equation. *International Journal for numerical methods in engineering*, 45:1139–1164, 1999.
6. N. Tordjman G. Cohen, P. Joly. Higher-order finite elements with mass-lumping for the 1d wave equation. *Finite Elements in analysis and Design*, 16:329–336, 1994.
7. W. Muniz M. Ainsworth, P. Monk. Dispersive and dissipative properties of discontinuous gakerkin finite element methods for the second-order wave equation. *Journal of Scientific Computing*, 27(1-3), 2006.
8. D. Schtzau M. J. Grote, A. Schneebeli. Discontinuous galerkin finite element for the wave equation. *SIAM J. Numer. Anal.*, 44(6):2408–2431.
9. J. Lions P. Ciarlet. *Handbook of numerical analysis*, 2, 1991.

Modelling of corner echo ultrasonic inspection with bulk and creeping waves

Guillaume Huet, Michel Darmon, Alain Lhémery and Steve Mahaut

Abstract The creeping wave is a well-known phenomenon in seismology and in non-destructive evaluation. This wave which is generated at the interface between two media radiates during its propagation as a head wave. The amplitude of creeping wave is usually small compared to the compressional and shear waves. However, in some configurations, especially near critical angle (at backwall reflection, for instance), its contribution to the echo response may be significant. Such a case is discussed in this communication, both theoretically and experimentally. Computation of echo response of this wave, based on ray theory has been developed. The resulting model combined with bulk wave modelling is compared to experimental measurements.

1 Context

In some configurations, contribution of creeping wave to the echo response may be significant. This point is highlighted by an experimental validation of corner echo prediction. In this study a stainless steel component composed of two different bottom slopes of 0° and 10° is considered. For each slope, the specimen contains a 10 mm height by 20 mm length rectangular backwall breaking flaw. The pulse-echo response of these defects is measured by a 45° refracted SV-wave planar contact transducer of 2 MHz center frequency. Simulation of the interaction between incident wave and flaw is performed with Civa software [1]. In this simulation, wave interactions with the flaw are only considered for bulk waves. To make a comparison between experimental and simulation results, they are normalized with the maximum amplitude of response obtained with a side drilled hole.

CEA, LIST, Laboratoire de Simulation et de Modélisation, F-91191 Gif-sur-Yvette, France.
e-mail: guillaume.huet@cea.fr; michel.darmon@cea.fr

The figure 1 presents geometry of the problem and the ray path of SV-mode corner echo for 0° slope configuration.

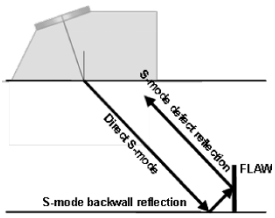

Fig. 1 Geometry of problem and ray path for the 0° slope.

The figure 2 gives the measured (a), computed (b) B-scans, and measured (black line) and computed (dashed grey line) spatial distributions (c) of the corner echo for the 0° slope configuration. We observe for this configuration a good agreement for the both in amplitude and in spatial distribution corner echo.

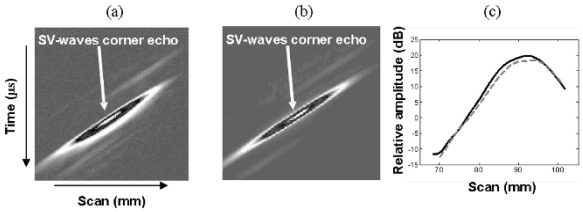

Fig. 2 Measured (a) and calculated (b) B-scans, and measured (black line) and computed (dashed grey line) spatial distributions (c), of the corner echo SV-mode reflection according to the 0° slope bottom of the specimen.

The figure 3 presents the measured (a), computed (b), and measured (black line) and computed (dashed grey line) spatial distributions (c) of the corner echo for the 10° slope configuration (see figure 4). We see important differences of amplitude between these two results. The simulation describes only interactions of bulk waves with the flaw. Then for this configuration it is necessary to take into account other types of interactions for a description of corner echo response.

It can be noticed that for 10° slope bottom configuration, incident 45° SV wave impacts the backwall with 35° angle which is close to the critical angle (32.8°). Hence, a creeping wave appears along the bottom of specimen. The contributions related to interactions of this wave with the flaw are not taken into account in the simulation. Then this may explain differences observed between experimental and simulated results. A time of flight analysis based on geometrical ray has highlighted two potential interactions between a creeping wave and the flaw to explain these differences. Geometrical paths of these contributions are presented in figure 4.

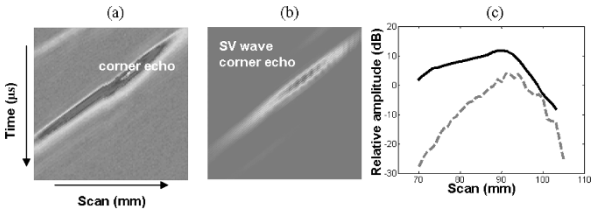

Fig. 3 Measured (a) and calculated (b) B-scans, and measured (black line) and computed (dashed grey line) spatial distributions, of the corner echo SV-mode reflection according to the 10° slope bottom of the specimen.

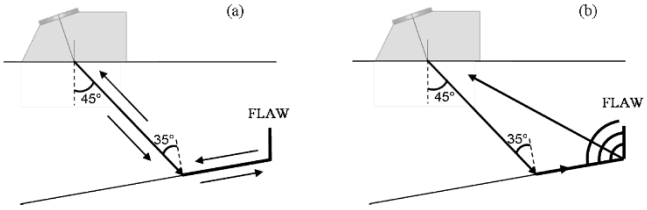

Fig. 4 Geometrical paths of creeping wave interaction with flaw: (a) reflection on flaw bottom, (b) diffraction on flaw bottom.

The first interaction (a) corresponds to the reflection of the creeping wave on the flaw bottom. After reflection, the creeping wave propagates along interface in the opposite direction and radiates a head wave in the specimen. The second one (b) is diffraction of the creeping wave on the flaw bottom. The diffraction phenomenon implies important dispersion of energy during propagation. Then this second interaction is likely to have a low amplitude contribution in the corner echo response. In this paper only the first interaction is treated and a method to calculate its contribution is presented in next part.

2 Modelling of head wave contribution

Modeling of the head wave contribution radiated by reflected creeping wave on the flaw bottom is presented. This problem is based on the configuration presented in figure 4 (a). To calculate this contribution the transducer's surface is discretized as a collection of source points. For each point source, elementary contributions of the head wave are calculated applying ray theory. Before giving the method to calculate the head wave contribution, classical results of ray theory are introduced.

2.1 Geometrical path and amplitude of head wave

The ray path of the head wave is presented here in the simplest case of two semi-infinite homogeneous media. We consider propagation in the first medium with longitudinal and shear wave velocities noted respectively V_L and V_S. We assume that a point source of a spherical shear wave lies at point M_0 and we consider the ray which impacts the interface at point A_0 with critical angle θ^* defined by $\theta^* = asin(V_S/V_L)$ (see figure 5).

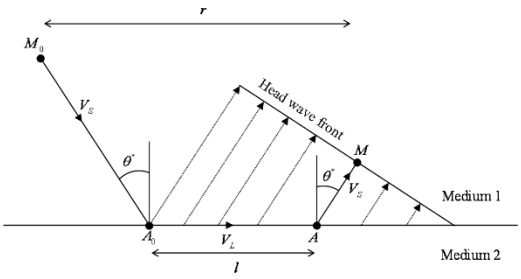

Fig. 5 Geometrical path of head wave from point source M_0 to point receiver M.

Critical incidence implies that the longitudinal reflected wave in the first medium propagates along the interface with velocity V_L. During its propagation, according to Huygens' principle, points of the interface reached by this wave become centers of disturbances propagating back into the first medium with velocity V_S. All contributions radiated from interface with direction corresponding to angle θ^* produce the head wave front. In the following, amplitude related to the contribution radiated from point A of the interface to point M is introduced.

This classical result is presented here for the case of elastic waves in an homogeneous, perfectly elastic and isotropic medium [2]. It is important to note that it is not valid in the close neighbourhood of coupling zone between head wave and reflected bulk wave [2,3]. In such cases, it is necessary to use another method. We consider displacement vector $\mathbf{u}$ at point A_0 emanating from a point source M_0 represented at figure 5:

$$\mathbf{u}(A_0, \omega) = \frac{e^{i\omega(t-R_0/V_S)}}{R_0}\mathbf{n}_S, \tag{1}$$

where $\mathbf{n}_S$ is the direction of polarization of shear wave and R_0 is the distance between point A_0 and the source. The displacement of the head wave at point M is given by:

$$\mathbf{u}(M, \omega) = -\frac{1}{i\omega}e^{i\omega(t-\tau(M))}V_L\frac{R^*_{SL}R^*_{LS}tan(\theta^*)}{r^{1/2}l^{3/2}}\mathbf{n}_S(M). \tag{2}$$

The distances r and l are represented in figure 5. The vector $\mathbf{n}_S(M)$ gives direction of shear head wave polarization. The coefficients R^*_{SL} and R^*_{LS} are respectively reflection coefficient from shear wave to longitudinal wave and from

longi-tudinal wave to shear wave at critical angle θ^*. Time of flight is given by $\tau(M) = M_0A_0/V_S + A_0A/V_L + AM/V_S$.

The previous result corresponds to a harmonic source. The temporal dependence of displacement due to a source of spectrum $S(\omega)$ is obtained by applying the inverse Fourier transform:

$$\mathbf{U}(M,t) = \frac{1}{2\pi}\int_{-\infty}^{\infty} S(\omega)\mathbf{u}(M,\omega)d\omega. \tag{3}$$

Results of ray theory presented here are now applied to calculate contribution of the head wave in the echo response.

2.2 Calculation of displacement amplitude

In this part a method to calculate the displacement amplitude of the head wave radiated by the creeping wave after its reflection on the flaw is presented. We consider a planar contact transducer with incident angle θ_W. We assume that this transducer radiates in the component shear wave beam with incidence on backwall close to the critical angle.

To calculate the head wave contribution, the surface of the transducer is discretized as a collection of point sources. For each point source, elementary contributions of the head wave are calculated and finally summed to obtain the complete contribution. In order to apply ray theory, elementary contributions of the head wave are calculated through the path which is incident on backwall at critical angle θ^*. We call this path critical path and its related ray has an incident angle in the wedge noted θ_W^* (figure 6). In the general case, this angle is different from the real incident angle θ_W. This point implies a shift between times of flight of the different head wave paths. At emission, maximum shift is given by:

$$\Delta t = d\ sin(\theta_W - \theta_W^*)/V_W, \tag{4}$$

with V_W the velocity in the wedge and d the length of the probe. The time Δt describes the non correlation of the incident plane with the critical phase plane of the head wave.

Now the head wave elementary contribution due to a point source S of the surface transducer is calculated. At point M_0 on the critical path, the displacement due to the source is given by Rayleigh-Sommerfeld integral [4]:

$$\mathbf{u}_S(M_0,\omega) = -T_{W\to C}\frac{1}{V_W}\frac{v_0(t-\tau)}{2\pi L}\Delta S_{em}\mathbf{n}_S, \tag{5}$$

with ΔS_{em} the surface which surrounds the point source, v_0 the particular velocity normal to probe surface, $T_{W\to C}$ the coefficient of transmission from wedge to component and L the spreading function which describes amplitude divergence of the spherical wave on a plane interface.

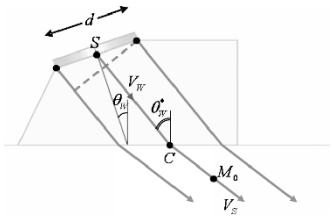

Fig. 6 Discretization of the surface transducer as a collection of point source. The ray corresponding to elementary contribution of head wave is chosen to be critical on backwall component and has an incident angle in wedge noted θ_W^*.

Propagation of the head wave in the component from point M_0 is presented. The ray we consider has been chosen to impact the backwall at the critical angle. Then at point A_0 of backwall (figure 7) a creeping wave is generated. This wave propagates along the interface, reflects on flaw, and goes back along interface in the opposite sense. To take into account interaction with the flaw, the amplitude of creeping wave has to be multiplied by a coefficient noted R_F. During its propagation, the reflected creeping wave radiates from any point of the interface head wave in component. All these points must be taken into account for the final contribution. To illustrate the case of partial contribution, radiation from point A is chosen. According to symmetry of the problem before and after reflection, the path M_0A_0FAM is analogous to path M_0A_0AM presented in the previous part. Then we can apply expression 2 with consideration of incident wave displacement at point M_0 (expression 5) and consideration of the reflection on the flaw. Finally, the amplitude of the head wave received on the probe at point R is:

$$\mathbf{u}_S(R,\omega) = -T_{C\to W} R_F T_{W\to C} \frac{v_0(t-\tau)}{2\pi V_W} \frac{1}{i\omega} \frac{R^*_{SL} R^*_{LS} V_L \, tan(\theta^*)}{r^{1/2} l^{3/2}} \Delta S_{em} \Delta S_{re} \mathbf{n}_W. \quad (6)$$

$T_{C\to W}$ is coefficient of transmission from component to wedge at point C, ΔS_{re} is the surface which surrounds receiver point and $\mathbf{n}_W$ is direction of polari-zation of the wave propagating in the wedge. Expressions of distances r and l are:

$$r = (SC_0 + RC) sin(\theta_W) + (C_0A_0 + CA) sin(\theta^*) + l \text{ and } l = A_0F + AF, \quad (7)$$

and time of flight is given by:

$$\tau = (SC_0 + RC)/V_W + (C_0A_0 + CA)/V_T + (A_0F + AF)/V_L \quad (8)$$

Total contribution is obtained by summation of all partial contributions. It corresponds to summation of the displacements given at expression 6 for all source points and all reception points.

Two points have to be developed to evaluate expression 6. The first point concerns ray theory formalism of the head wave which has to be modified in the interference zone. The second point is related to the evaluation of the reflection coefficient on the flaw, as no theoretical formulation exists for a creeping wave.

2.3 Amplitude of head wave in the critical region

In the previous part we have investigated only a non-interfering pure head wave. However in some cases this wave may interfere with another one. The question whether any given waves interfere or not depends on their travel times and phase shifts, and on the length of the pulse of the incident wave. There is, however, a region called the critical region in which the head wave will always interfere with a reflected bulk wave. This region begins with emergence of a critical ray presented in figure 8. For this particular ray, at observation point P_1, the reflected wave and the head wave are not distinguished. The critical region ends at point P_2 where the difference of time of flight of the reflected wave and the head wave are equal to the duration of the pulse.

In the critical region the formula for the head wave amplitude given by ray theory is not quite exact. The most exact formula to describe interference of reflected and head waves are obtained under an uniform asymptotics form [2,5,6]. The problem with this expression is that contribution of reflected and head waves can't be dissociated. Then this method is not applicable to the model used in the Civa inspection simulation [1] where all contributions are evaluated separately.

The region, in which the formulae for the individual waves is imprecise is usually smaller than the region of interference of the waves. Only in very narrow regions close to the critical ray, ray formulae are quite inapplicable. In this case, the distance l defined in figure 8 tends to zero, implying an infinite value of head wave amplitude (expression 2). To avoid this divergence, when distance l tends to zero, a maximum

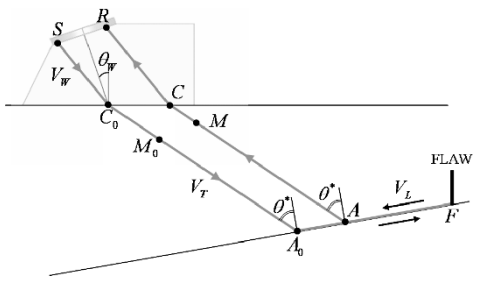

Fig. 7 Geometrical path of head wave radiated by creeping wave after reflection on flaw bottom.

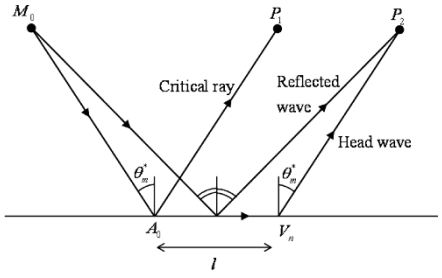

Fig. 8 Representation of the critical region in which the reflected wave and the head wave interfere.

value is imposed. This value noted l_{max} is the solution of coupling condition equation which verifies:

$$\tau_{BW} - \tau_{HW}(l_{max}) = \delta\tau, \tag{9}$$

where $\delta\tau$ is the duration of the signal. The effect of this process on head wave amplitude is presented in figure 9. We see that initial head wave amplitude calculated with ray theory (solid line) diverges in the critical region. On the contrary, calculation of head wave amplitude with the introduction of the maximum value l_{max} (dashed line) gives in the critical region amplitudes which are in the same order of amplitudes calculated in the non critical region.

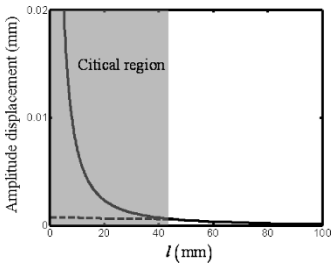

Fig. 9 Initial (solid line) and modified (dashed line) amplitude of head wave calculated with ray theory versus distance l.

2.4 Reflection coefficient of creeping wave on flaw

This part details the determination of the reflection coefficient of the creeping wave on the flaw used in expression 6. Interaction of an incident wave on a wedge has been studied for different incident waves as a Rayleigh wave [7] or plane and cylindrical waves [8]. Nevertheless it seems that no study on creeping wave interaction has been made. Then a result based on the Kirchhoff approximation which is commonly used to model specular effects (corner echo or specular reflection) is used [9, 10]. The Kirchhoff approximation applies to the case of an incident plane wave on a stress-free flaw. The result of the scattered field at an observation point is a spherical wave associated to a directivity coefficient depending on the incident and scattered directions. This result, adapted to the case of a diffracted plane wave can be presented as follows: for a given incident wave of amplitude u^{inc} impacting an interface with an incident angle β, the diffracted wave is plane with direction of angle θ and its amplitude is:

$$u^{refl} = u^{inc}\frac{B(\beta,\theta)}{i}, \tag{10}$$

where $B(\beta,\theta)$ is the Chapman coefficient which depends on directivity. To use this result for a creeping wave, we assume that the creeping wave is a plane wave. The

incident wave is the creeping wave propagating along the interface. The diffracted wave is the creeping wave that propagates along the interface in the opposite sense. Then relation between angles β and θ is: $\theta = -\beta$.

2.5 Results

Modelling of the head wave contribution is now applied to simulate the echo response corresponding to the configuration with a 10° slope bottom component presented in the first part. To the initial simulation which models only the interactions of bulk wave with flaw is added the contribution of the head wave radiated by the reflected creeping wave on the flaw bottom. The B-scan and the spatial distribution obtained with simulation is presented and compared to experiment in figure 10.

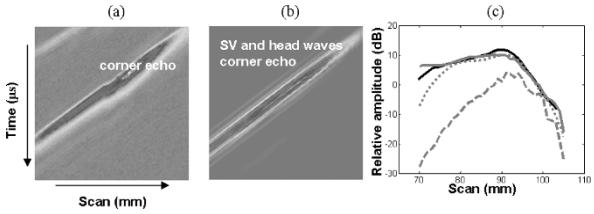

Fig. 10 Measured (a) and calculated with add of head wave (b) B-scans of corner echo, and spatial distribuiton of corner echo (c) obtained with experiment (black line), finite element calculation (dotted grey line), Civa calculation (dashed grey line) and Civa calculation with add of head wave (grey line), according to the 10 degrees slope bottom of the specimen.

We can see comparing figures (a) and (b) a good agreement between experimental and calculated B-scans. On figure (c) is shown first the initial calculation (dashed grey line) which models only bulk wave interactions. We observe then that the amplitude calculated with the inclusion of the head wave (grey line) improves modeling compared to experimental results (black line). On this figure the result obtained with an hybrid method [11] coupling semi-analytical beam model and finite elements interaction model is presented (dotted grey line). We notice that it also provides a good prediction of experimental results.

3 Conclusion

In most cases, dominant contributions to corner echo response result from the interactions of bulk waves with a flaw. But, in some configurations, consideration of these waves is not sufficient and it is necessary to take into account other contributions.

In the problem considered in this paper, one contribution implying interaction of creeping wave with flaw is dominant in echo response. This contribution is due to the reflection on the flaw bottom of the creeping wave which then radiates a head wave in the component. A method to model it, is presented. It is based on discretization of the transducer's surface as a collection of source points. For each point source, an elementary contribution is calculated using ray theory. In the model a specific treatment of the head wave amplitude in the critical region and of the reflection coefficient of the creeping wave on the flaw bottom is developed.

The modelling of the head wave is added to the initial simulation which described the interaction of bulk waves with the flaw. Simulated results obtained in the configuration under consideration are in good agreement with experiment. The inclusion of the head wave contribution in the simulation improves modelling of the corner echo response.

The integration in Civa software of the model presented in this paper is in progress. Other interactions with the flaw have to be investigated to complete the description of the corner echo. For example, the head wave reflection on the flaw may have, in other configurations, an important effect on corner echo amplitude.

References

1. CIVA software website, http://www-civa.cea.fr
2. Cerveny, V., Ravindra, R.: Theory of seismic head waves. University of Toronto Press (1971)
3. Fradkin, L., Kiselev, A.: The two-component representation of time-harmonic elastic body waves in the high- and intermediate-frequency regimes. J. Acoust. Soc. Am **101** (1), (1997)
4. Goodman, J.W.: Introduction to Fourier optics. McGraw-Hill, New-York, (1968)
5. Gridin, D.: High-frequency asymptotic description of head waves and boundary layers surrounding the critical ray in an elastic half-space. J. Acoust. Soc. Am **104** (3), (1998)
6. Gridin, D., Fradkin, L.: The high-frequency asymptotic description of pulses radiated by a circular normal transducer into an elastic half-space. J. Acoust. Soc. Am **104** (3), (1998)
7. Budaev, B., Bogy, D.: Rayleigh wave scattering by two adhering elastic wedges. Proc. R. Soc. Lond. A, 454, pp. 2949-2996, (1998)
8. Kamotski, V., Lebeau, G.: Diffraction by an elastic wedge with stress-free boundary: existence and uniqueness. Proc. R. Soc. A, 462, pp. 289-317, (2006)
9. Chapman, R.K.: Ultrasonic scattering from smooth flat cracks : An elastodynamic Kirchhoff diffraction theory. CEGB Report, North Western Region NDT Applications Centre, NWR/SSD/82/0059/R, (1982)
10. Calmon, P., Lhémery, A., Lecoeur-Taibi, I. and Raillon, R.: Integrated models of ultrasonic examination for NDT expertise. Review of progress in QNDE, Vol. 16B, Plenum Press, New-York, pp. 1861-1868, (1997)
11. Darmon, M., Leymarie, N., Chatillon, S. and Mahaut, S.: Modelling of scattering of ultrasouns by flaws for NDT, in the present series.

Attenuation of Lamb waves in the vicinity of a forbidden band in a phononic crystal

M Bavencoffe, A-C Hladky-Hennion, B Morvan and J-L Izbicki

Abstract When a Lamb wave propagates on a plate engraved by a periodic grating, it may exhibit attenuation. This attenuation is related to a coupling of this incident mode with other propagating modes. As the propagation takes place in a periodic medium, the dispersion curves of the modes are of interest because they exhibit pass bands and stop bands related to the geometry of the waveguide. The goal of this work is to quantitatively establish the relation between the value of the attenuation of the propagating waves and the width of the forbidden bands appearing inside the Brillouin zone. This study is performed by using a finite element method (ATILA® code).

1 Introduction

Guided ultrasonic waves in plates (Lamb waves) are very sensitive to the surface state. If the surface is slightly rough, the amplitude of the propagating waves is attenuated. The particular case of periodic rough surface is quite different. For certain frequencies the incident wave gives rise to converted backward modes. In a previous paper [1] Morvan *et al.* show that the conversion/reflection phenomenon is a consequence related to the opening of forbidden frequency bands. A forbidden band corresponds to the interaction of one (at the limit of BZ) or two given modes (inside the BZ) and does not affect the other propagating modes [2-4].

J-L Izbicki, B Morvan and M Bavencoffe

Laboratoire Ondes et Milieux Complexes, FRE-3102 CNRS, Groupe Ondes Acoustiques, Université du Havre, Place Robert Schuman, BP 4006, 76610 Le Havre, France

A-C Hladky-Hennion and M Bavencoffe

Institut d'Electronique, de Microélectronique et de Nanotechnologie, UMR-8520 CNRS, 41 boulevard Vauban, 59046 Lille, France

What are the parameters involved in the coupling of Lamb waves ? Is it possible to establish more clearly than previously a link between the characteristic of the mini-stop-band (forbidden band inside the BZ) and the attenuation of the waves ? Thus, the goal of this paper is to establish a bridge between mesoscopic aspects (attenuation of Lamb waves) and the band structure (mini-stop-band).

With a view to giving an answer to the previous questions, the case of an aluminium plate with a one dimensional sinusoidal grating is studied. Firstly, the dispersion curves in the first Brillouin zone is presented. Secondly, the relation between a mini-stop-band and the attenuation is exhibited. Finally, the influence of the depth of the grooves on the attenuation is considered.

2 Dispersion curves in the first Brillouin zone

2.1 Dispersion relation and first Brillouin zone

In this part, an infinite plate with a one-dimensional periodic corrugation is considered. The waveguide is considered as a repetition along the (Ox) direction of one elementary pattern.

Because the waveguide is supposed to be infinite and periodic in the (Ox) direction, the study is restricted to only one unit cell [5; 6]. Bloch-Floquet relation is written and defines boundary conditions between adjacent cells. Then the wavenumber k is deduced and vibration frequencies ω are determined for propagating waves leading to dispersion curves $\omega(k)$. The solutions of the dispersion relation are $2\pi/\Lambda$ periodic with respect to the wavenumber k : $\omega(\mathrm{k}) = \omega\left(\mathrm{k} + 2\pi/\Lambda\right)$, where Λ is the spatial period of the grating. This property implies that the study can be limited to wavenumber values in the first Brillouin zone. This zone is defined in a wavenumber range $-\pi/\Lambda \leq \mathrm{k} \leq \pi/\Lambda$.

Therefore the study of an infinite periodic waveguide can be reduced to a study of one unit cell.

2.2 Dispersion curves for a sinusoidal grating

A modal analysis is performed with a finite element method (ATILA® code [7]). In order to consider only one spatial periodicity, the numerical study deals with

the case of a sinusoidal grating with a spatial periodicity Λ [8]. This periodicity must be in the same range of values as the wavelength of the Lamb wave λ_{Lamb} excited, which is about 20 mm length. In addition, with a view to being in accordance with the hypothesis of small perturbations of the surface, the depth of the grooves must be much smaller than the thickness of the plate, which is 5 mm thick. Then, the computed sinusoidal grating has a periodicity of 7 mm and is 200 µm depth. The plate is made of aluminium (ρ = 2700 kg/m^3, c_L = 6432 m/s, c_T = 3136m/s).

Only one unit cell is meshed and then the Bloch-Floquet theorem is fulfilled on each boundary of the pattern at x = 0 and x = Λ (Figure 1).

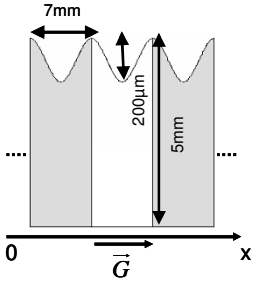

Fig. 1 Elementary periodic cell.

The dispersion curves are plotted by varying the wavenumber in a half Brillouin zone [0 ; π/Λ], and then the other half zone [-π/Λ ; 0] is plotted symmetrically. In Figure 2 the dispersion curves for the sinusoidal grating are plotted in the Brillouin zone. The periodicity of the guide implies that the Lamb waves dispersion curves fold back for k = ±π/Λ and k = 0.

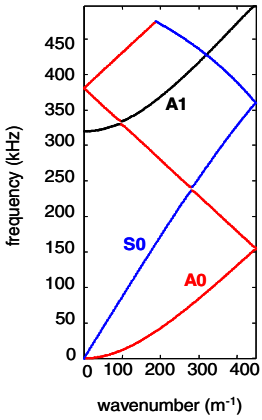

Fig. 2 Detail of the dispersion curves in the first Brillouin zone for a sinusoidal grating.

These dispersion curves clearly exhibit gaps also called forbidden bands. Two different kinds of gaps are noticed : the stop-bands at the limit of the Brillouin zone, and the “mini-stop-bands” inside the Brillouin zone [9].

Mini-stop-bands are due to the opening of gaps at the crossing of two Lamb mode dispersion curves. This leads to anti-crossing behavior of the dispersion curves. This case corresponds to mode coupling. Indeed, near the edge of the stop-band, the group velocity vanishes and allows a possible conversion between two different modes. For the sinusoidal grating, in Figure 2, a mini-stop-band appears at crossing between the S0 and A0 dispersion curves near 239 kHz. Then a coupling between the A0 and S0 modes occurs. This means that if a S0 Lamb wave is propagating in such a grating, it would give rise to a retropropagating A0 mode, and vice versa.

In the following, this band gap will be studied from an energy point of view.

3 Mini-stop-band and attenuation

3.1 Description of the plate studied

In order to study more precisely this mini-stop-band S0/A0 frequency by frequency, several harmonic analysis are performed using the modelling of a finite length waveguide. The structure is divided into three main different zones : the central zone, which is 270 mm length and 5 mm thick, contains the corrugated part which is limited to 20 periods of sinusoidal grooves and flat surfaces before and after the grating (Figure 3). However, this finite structure leads to reflections at its ends. To avoid stationary waves between the grating and the extremities of the mesh, the two other zones are composed by perfectly matched layers (PML). They are designed to act as sponge layers for a maximum incident wavelength λ_{max} = 33.9 mm and to allow less than 1 % reflection [10].

The excitation consisting in a non null displacement along the (Ox) direction is imposed on the central node and give rise to a S0 wave.

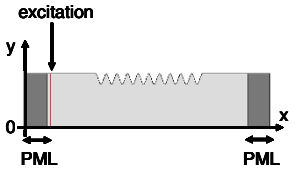

Fig. 3 The geometry of plate – schema for 10 grooves, the depth of the grooves has been volontary increased for a better reading.

3.2 Normal displacements and energy coefficients

By performing harmonic analysis at several frequencies between 160 kHz (λ_{S0} = 33.9 mm) and 400 kHz (λ_{S0} = 12 mm), normal displacements are collected under the plate before and after the grating. As expected (cf. Figure 2), a converted A0 mode is reflected and a part of the incident S0 mode is transmitted. From these results, the energy reflection and transmission coefficients are computed. Details on the computation of the energy transported by each propagating waves is given in the following.

As it is well known [11], the energy transported by a wave along the (Ox) direction is identified to the value ϕ of the flux of the Poynting vector through a 1 m thick cross section along the (Oz) direction of the plate (Figure 4).

$$\phi = \int_{-h/2}^{h/2} \int_{0}^{1} P dz dy \quad \text{with} \quad P = \Re\left(-\frac{1}{2} \underline{v}_j^* \underline{T}_{ji} \right)$$

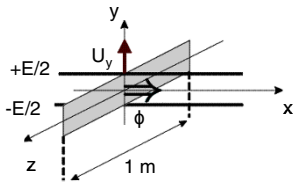

Fig. 4 The flux of the Poynting vector through a cross section of the plate.

where P is the temporal average of the flux of the Poynting vector along the (Ox) direction, $\underline{v}_j^*$ are the components of the particular conjugate velocity and $\underline{T}_{ji}$ are the components of the stress tensor. $\Re$ denotes the real part of the expression.

In order to access to the energy of the modes, two steps are needed. Firstly, on a theoretical point of view for a plate without corrugation, a coefficient ζ is defined for each mode as the ratio between the normal displacements of the surface of the plate and the energy carried by the wave [12] : $\zeta = \left|U_Z\right|_{surface}^{theory} \Big/ \sqrt{\phi_{theory}}$. Secondly, from the values of the normal displacements of the propagating Lamb waves obtained by the finite element method and using the ζ coefficient, the values of the energies of the incident wave ϕ_{inc}, the transmitted wave ϕ_{trans} and the reflected/converted wave ϕ_{conv} can be estimated : $\phi_{FEM} = \left(\left|U_Z\right|_{surface}^{FEM} \Big/ \zeta \right)^2$.

The conversion coefficient in the A0 mode is defined by $R_{A0} = \phi_{conv}^{A0} \Big/ \phi_{inc}^{S0}$. In the same way, the transmission coefficient in the S0 mode is denoted by $T_{S0} = \phi_{trans}^{S0} \Big/ \phi_{inc}^{S0}$. Figure 5.a reproduces a zoom of the dispersion curves and in

parallel with Figure 5.b, the curves of T_{S0} and R_{A0} for the sinusoidal grating are plotted.

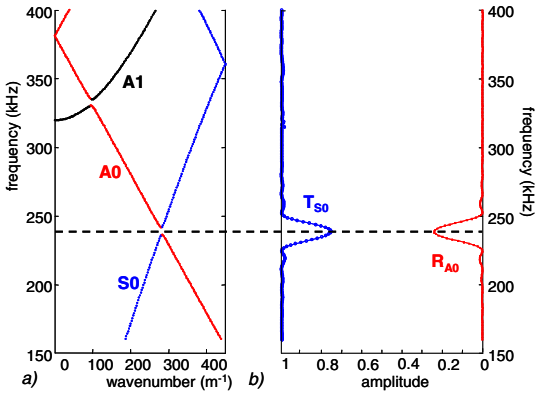

Fig. 5 a) Dispersion curves in the first Brillouin zone for the sinusoidal grating. b) Curves of the reflection and transmission coefficients.

These curves exhibit two different kinds of extrema at the same frequency f = 239 kHz. In fact, at this frequency, the T_{S0} curve presents a minimum as the R_{A0} one presents a maximum. So, there is a coupling between the S0 mode and the A0 mode in the gap. Thus, there is an energy transfer between the two modes. Moreover, the maximum of conversion occurs at the same frequency as the minimum of transmission which is the central frequency of the gap f_{gap}.

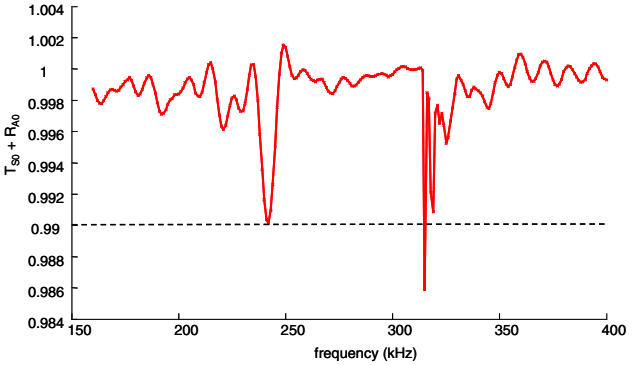

Fig. 6 Assessment of the conservation of the energy of the A0 and S0 modes.

In Figure 6, the assessment of the conservation of the energy is checked with an error lower than 1 %. Between f = 314 kHz and f = 321 kHz, one observes an uneven zone which corresponds to the A1 mode cut-off frequency. This fact is explained by a coupling between the A0 and A1 mode near 330 kHz (see Figure

5.a). In the vicinity of the cut-off frequency, large wavelengths could disturb the performances of the PML.

3.3 Influence of the limited size of the grating

The dispersion curves are obtained by modal analysis for an infinite structure whereas the T_{S0} and R_{A0} curves are the results of harmonic analysis for which a structure of finite length was modelled. The presence of secondary peaks on those curves (see Figure 5.b) reveals the finite aspect of the structure [11]. Moreover, the width of the peaks of the T_{S0} and R_{A0} curves is wider than the width of the gap. Indeed, the coupling between the modes is not strictly limited to the frequency range of the band gap ([236 kHz ; 241 kHz]). This is also a consequence of the use of a limited periodic structure.

4 Influence of the depth of the grooves

The hypothesis of the weakness of the corrugation of the surface may introduce the question of the influence of the depth of the grooves on the results of the modal and harmonic analysis. In other words, one may wonder what the influence of the depth of the grooves is on the mini-stop-band S0/A0 and on the attenuation/conversion of the S0 mode. To this end, modal and harmonic analysis were performed with the corrugation depth varying from 50 µm to 500 µm.

In Figure 7, the influence of the depth of the grooves on the width of the gap is exhibited. At least for the depths investigated a linear relation, with a reliability factor $Rf = 0.9995$, rules the variation of the width of the mini-stop-band S0/A0.

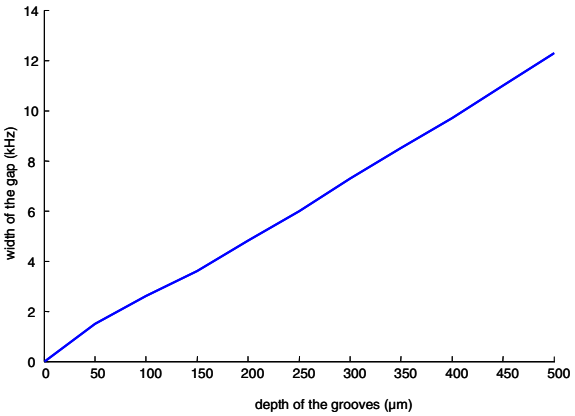

Fig. 7 Variation of the width of the gap as a function of the depth of the grooves.

For each value of the depth of the grooves and at $f = f_{gap}$, the values of the T_{S0} and R_{A0} coefficients are calculated and plotted on Figure 8 : as expected the deeper the grooves, the higher the value of R_{A0} and the lower the value of T_{S0}. These curves could be used as master curves to estimate the depth of the grooves.

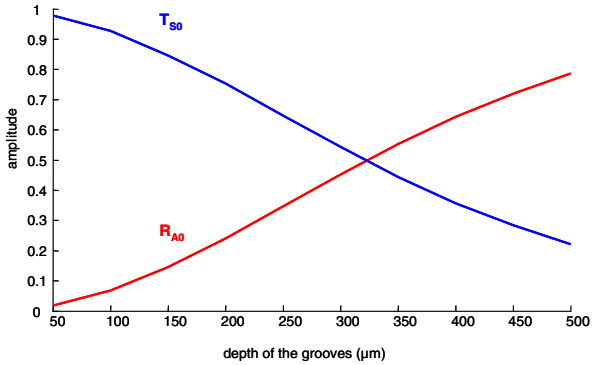

Fig. 8 Variation of the depth of the grooves on the transmission and reflection coefficients at the central frequency of the gap.

For each value of depth of the grooves considered, the sum $T_{S0} + R_{A0}$ is globally equal to 1 with less than 1 % of error while the hypothesis of the small perturbations is still verified (Figure 9). So, except the S0 and A0 modes, there is no other mode carrying energy through the waveguide at $f = f_{gap}$.

For the values of the depth greater than 400 µm, the sum $T_{S0} + R_{A0}$ increases beyond the numerical error. The physical nature of the problem is then quite different : the Lamb wave propagates no more in a slightly corrugated plate but in a structure with flaws. The coupling between the Lamb wave and the flaws has to be computed with another meshing and another PML in order to take into account the presence of evanescent modes.

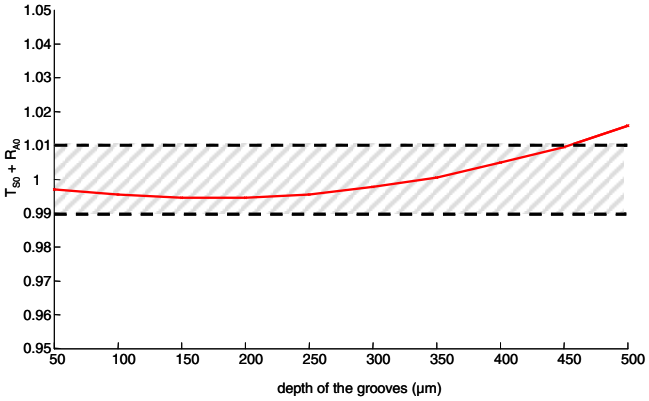

Fig. 9 Assessment of the conservation of the energy of the A0 and S0 modes.

5 Conclusion

The presence of a mini-stop band is related to a coupling between two modes. This coupling implies an energy transfer from the incident mode to the converted one. Then, the incident mode is attenuated when propagating through the grating. As this attenuation is related to the depth of the grooves, a relation with the width of the gap can be deduced. It has been quantitatively verified that the width of the gap is related to the depth of the grooves : the deeper the grooves, the larger the gap. However, even if the maximum of attenuation appears at the central frequency of the gap, the coupling is not strictly limited to the frequency range of the band gap.

Two perspectives can be envisaged for this study. Firstly, with the help of the shape of the attenuation curve, it might be possible to evaluate the parameters of the grating (groove number, depth, shape). Secondly, a theoretical coupling factor between two coupled modes has to be properly defined. This might be an alternative way to obtain the dispersion curves.

6 References

[1] Morvan B, Hladky-Hennion AC, Leduc D, Izbicki JL : Ultrasonic guided waves on a periodical grating : coupled modes in the first brillouin zone. J. Appl. Phys. **101**, 114906-114912 (2007)
[2] Kundu T, Banerjee S : An experimental investigation of guided wave propagation in corrugated plates showing stop bands and pass bands. J. Acoust. Soc. Am. **120**, 1217-1226 (2006)
[3] Sandström SE : Stopbands in a corrugated parallel plate waveguide. J. Acoust. Soc. Am. **79**, 1293-1298 (1986)
[4] El-Bahrawy A : Stopbands and passbands for symmetric Rayleigh-Lamb modes in a plate with corrugated surfaces. J. Sound Vib. **170**, 145-160 (1994)
[5] Kittel C : Introduction to solid state physics. Wiley Ed (1998)
[6] Brillouin L : Wave propagation in periodic structures. Dover Publications (1953)
[7] Atila finite element code for piezoelectric and magnetostrictive transducer modeling, version 6.0.2, user's manual. ISEN, Acoustics Laboratory, Lille (France) (2002).
[8] Banerjee S, Kundu T : Symmetric and anti-symmetric Rayleigh-Lamb modes in sinusoidally corrugated waveguides : an analytical approach. Int. J. Solids Struct. **43**, 6551-6567 (2006)
[9] Lourtioz J : Photonic crystals : towards nanoscale photonic devices. Springer (2005)
[10] Bou Matar O, Preobrazhenski V , Pernod P : 2d axisymmetric numerical simulation of supercritical phase conjugation of ultrasound in active solid media. J. Acoust. Soc. Am. **118**, 2880-2890 (2005)
[11] Royer D, Dieulesaint E : Elastic waves in solids 1. Springer (2000)
[12] Morvan B, Wilkie-Chancellier N, Duflo H, Tinel A, Duclos J : Lamb wave reflection at the free edge of a plate. J. Acoust. Soc. Am. **113**, 1417-1425 (2003)

3D orthogonality relations for the surface waves and the far field evaluation in viscoelastic layered solids with or without fluid loading

D.D. Zakharov

Abstract The 3D surface waves in the linearly viscoelastic layered plates and cylinders are considered either under any of the homogeneous boundary conditions providing energy reflection back into the solid, or in the case of fluid loading. A fundamental property of waves in such structures is their generalized orthogonality, which is deduced and discussed. The eigenmodes of discrete spectrum are orthogonal to each other and to the waves of continuous spectrum (if they exist). A method for the exact calculation of the far field caused by an acoustic source of finite size is suggested. The obtained results can be used for evaluating the fields radiated by ultrasonic transducers of arbitrary aperture and by other realistic sources in the layered plate, cylinder, space or half-space using modal analysis. The results are also applicable to the post processing of the FEM calculations.

1 Introduction

Broad use of composite materials causes a steady attention to the guided waves in layered plates and cylinders, which are described in monographs, reviews and numerous papers. As known, such guided waves are not orthogonal like trigonometrical Fourier series but they possess the orthogonality relations (OR) with respect to the power flow. These OR were deduced in the 70's for elastic strips [1-7] and cylinders [8, 9] with various homogeneous boundary conditions on their faces. The relations for 3D guided waves are presented below. Such OR can be used to construct linear algebraic system of equations with respect to unknown mode co-

D.D. Zakharov
LMP, UMR CNRS 5469, Université Bordeaux 1, 351 Cours de la Liberation, 33405 Talence, France, e-mail : dmitrii.zakharov@gmail.com

efficients when using modal decomposition for various problems, e.g., such as diffraction by crack or wave reflection by the edge of a plate or cylinder. In this paper, the 3D guided waves are considered in a laminate with homogeneous boundary conditions on its faces (HBCF). For a cylinder, HBCF are set on the lateral surfaces. The linear viscoelasticity is taken into account in the form of the Kelvin-Voigt model or of the Maxwell model. The main motivation for this study is to generalise the results obtained earlier for one layer and pure elasticity [10-13], to elucidate the physics, and to work out a method for exact calculation of the field radiated by a realistic acoustic source into viscoelastic laminates and cylinders.

Since the numerical methods for 3D problems are time consuming the analytical and semi-analytical methods remain of substantial interest for NDT needs.

2 Background

Consider a laminated solid composed of N isotropic plies subjected to the time-harmonic load $e^{-i\omega t}$ (this factor is omitted in what follows). The displacements u_α^j, stresses $\sigma_{\alpha\beta}^j$ and strains $\varepsilon_{\alpha\beta}^j$ in each j th layer satisfy the equations of motion and the relations of linear viscoelasticity in the form of Kelvin-Voigt or of Maxwell. Thus, the Lamé constants λ_j, μ_j; wave numbers $k_{P,S}^j$ and wave speeds $c_{P,S}^j$ are complex-valued $\left\{c_P^j\right\}^2 = \left(\lambda_j + 2\mu_j\right)\rho_j^{-1}$, $\left\{c_S^j\right\}^2 = \mu_j \rho_j^{-1}$, $k_{P,S}^j = \omega / c_{P,S}^j$ (ρ_j are mass densities). The body forces f_α^j are specified later. Let us proceed to the cylindrical coordinates r, θ, z: $x_1 = r\cos\theta$, $x_2 = r\sin\theta$, $x_3 = z$. The geometry of solid may be flat, so that j th ply occupies a region $0 < r < \infty$, $z_j \le z \le z_{j+1}$ (case (a)), or it may occupy a cylindrical region $R_j \le r \le R_{j+1}$, $-\infty < z < \infty$ (case (b)) as shown in Fig. 1. On the interfaces $x_3 = z_j$ (or $r = R_j$), $j = 2,3,\ldots,N$ the conditions of the full contact are assumed. In addition, the field may satisfy some boundary conditions on the faces, i.e., for the case (a) either the stresses $\sigma_{\alpha 3}^{\mp}$, or displacements $u_\alpha^{\mp}$ or their combinations may be prescribed at $z^- = z_1$ and $z^+ = z_{N+1}$. For the case (b) the same is given at the radii $R^- = R_1$ and $R^+ = R_{N+1}$. First let us describe the modes satisfying HBCF accordingly to the cases (a) and (b).

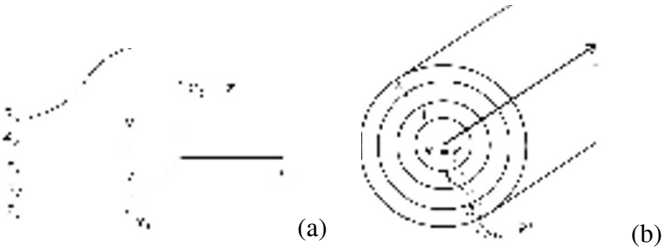

Fig. 1. (a) Laminate geometry; (b) layered cylinder.

3 Field representation

a) Using Lamé potentials and separation of variables, the waves propagating in r-direction in j th layer in the absence of body forces are as follows

$$u_r^j = \left[-u^j B_n' + w^j \frac{n}{sr} B_n\right]\begin{Bmatrix}\cos n\theta\\ -\sin n\theta\end{Bmatrix},\ u_\theta^j = \left[u^j \frac{n}{sr} B_n - w^j B_n'\right]\begin{Bmatrix}\sin n\theta\\ \cos n\theta\end{Bmatrix}, \tag{1}$$

$$u_z^j = v^j B_n \begin{Bmatrix}\cos n\theta\\ -\sin n\theta\end{Bmatrix}.$$

Here $B_n \equiv B_n(sr)$ are any of the appropriate Bessel function J_n or Neumann function N_n, or Hankel functions of the first or second kind $H_n^{(1,2)}$, $B_n' \equiv dB_n/d\{sr\}$ and s is a wave number. Functions $u^j(z)$, $v^j(z)$ and $w^j(z)$ acquire the form

$$\begin{bmatrix}u^j\\ v^j\end{bmatrix} = A_P^{+j}\begin{bmatrix}\cos q_P^j z\\ \dfrac{q_P^j}{s}\sin q_P^j z\end{bmatrix} + A_P^{-j}\begin{bmatrix}\sin q_P^j z\\ -\dfrac{q_P^j}{s}\cos q_P^j z\end{bmatrix} + \\ + A_S^{+j}\begin{bmatrix}-\dfrac{q_S^j}{s}\cos q_S^j z\\ \sin q_S^j z\end{bmatrix} + A_S^{-j}\begin{bmatrix}\dfrac{q_S^j}{s}\sin q_S^j z\\ \cos q_S^j z\end{bmatrix}, \tag{2}$$

$$w^j = B_S^{+j}\cos q_s^j z + B_S^{-j}\sin q_s^j z, \tag{3}$$

where $A_{P,S}^{\pm j}, B_S^{\pm j} = const$ and $\{q_{P,S}^j\}^2 \equiv \{k_{P,S}^j\}^2 - s^2$. The stresses are

$$\sigma_{rr}^j = \mu_j\left\{\chi^j B_n - \frac{u^j}{r}\left[(n+1)B_{n+1} + (n-1)B_{n-1}\right] - \frac{sw^j}{2}\left[B_{n+2} - B_{n-2}\right]\right\}\begin{Bmatrix}\cos n\theta\\ -\sin n\theta\end{Bmatrix},$$

$$\sigma_{r\theta}^j = \mu_j\left\{\frac{su^j}{2}\left[B_{n-2} - B_{n+2}\right] - \frac{sw^j}{2}\left[B_{n+2} + B_{n-2}\right]\right\}\begin{Bmatrix}\sin n\theta\\ \cos n\theta\end{Bmatrix},$$

$$\sigma_{rz}^j = \mu_j\left\{-\tau^j B_n' + \frac{dw^j}{dz}\frac{n}{sr}B_n\right\}\begin{Bmatrix}\cos n\theta\\ -\sin n\theta\end{Bmatrix},$$

$$\sigma_{\theta\theta}^j = \mu_j \left\{ p^j B_n + \frac{su^j}{2}\left[B_{n-2} + B_{n+2}\right] + \frac{sw^j}{2}\left[B_{n+2} - B_{n-2}\right] \right\} \begin{Bmatrix} \cos n\theta \\ -\sin n\theta \end{Bmatrix},$$

$$\sigma_{\theta z}^j = \mu_j \left\{ \tau^j \frac{n}{sr} B_n - \frac{dw^j}{dz} B_n' \right\} \begin{Bmatrix} \sin n\theta \\ \cos n\theta \end{Bmatrix}, \quad \sigma_{zz}^j = \mu_j \sigma^j B_n \begin{Bmatrix} \cos n\theta \\ -\sin n\theta \end{Bmatrix},$$

$$\chi^j \equiv \beta_j \, dv^j/dz + \alpha_j s u^j, \; \tau^j \equiv du^j/dz - s v^j,$$

$$p^j \equiv \beta_j \, dv^j/dz + \gamma_j s u^j, \; \sigma^j \equiv \alpha_j \, dv^j/dz + \beta_j s u^j,$$

where $\alpha_j \equiv 2 + \beta_j$, $\beta_j \equiv \lambda_j/\mu_j$, $\gamma_j \equiv \beta_j + 1$. The continuity equations at the interface $z = z_j$ are rewritten in the form

$$u^{j-1} = u^j, \quad v^{j-1} = v^j, \quad w^{j-1} = w^j, \tag{4}$$

$$\mu_{j-1}\sigma^{j-1} = \mu_j \sigma^j, \quad \mu_{j-1}\tau^{j-1} = \mu_j \tau^j, \quad \mu_{j-1} dw^{j-1}/dz = \mu_j dw^j/dz. \tag{5}$$

Hereafter the HBCF on the face $z^- = z_1$ imply one of the conditions:

$\sigma^1 = \tau^1 = dw^1/dz = 0$ (stress free), $v^1 = \tau^1 = dw^1/dz = 0$ (mixed 1),

$u^1 = v^1 = w^1 = 0$ (clamped), $\sigma^1 = u^1 = v^1 = 0$ (mixed 2).

The similar formulations are used for $z^+ = z_{N+1}$. Any combination of HBCF at $z = z^{\mp}$ and Eqs.(4), (5) gives us a linear system of algebraic equations with respect to $A_{P,S}^{\pm j}, B_S^{\pm j}$ whose $6N \times 6N$ matrix $\mathbf{L}$ yields two dispersion equations

$$\det \mathbf{L}_{PSV} = 0, \qquad \det \mathbf{L}_{SH} = 0, \qquad \mathbf{L} = \begin{bmatrix} \mathbf{L}_{PSV} & 0 \\ 0 & \mathbf{L}_{SH} \end{bmatrix}. \tag{6}$$

The equations (6) are independent of number n and coincide with the equations of the respective in-plane and out-of-plane problems with the same matrix blocks $\mathbf{L}_{PSV}$ and $\mathbf{L}_{SH}$. Assume that Eqns.(6) have simple roots. Then these roots can be subdivided into two subsets $s_l \in S_{PSV} \cup S_{SH}$ due to the wave polarization:

$$s \in S_{PSV}: \quad w^j = 0; \quad u^j, v^j \neq 0, \tag{7}$$

$$s \in S_{SH}: \quad u^j = v^j = 0; \; w^j \neq 0. \tag{8}$$

In addition, the frequency equations are symmetrical for s and $-s$, and in the case of pure elasticity the symmetry also holds for s and $\bar{s}$. Setting $M_n^l = A_S^{+1}$ or $M_n^l = B_S^{+1}$, other $A_{P,S}^{\pm j}, B_S^{\pm j}$ are expressed from the equations

$$\mathbf{L}_{PSV} \times \left[A_{P,S}^{\pm j}\right]^T = 0, \qquad \mathbf{L}_{SH} \times \left[B_S^{\pm j}\right]^T = 0.$$

b) For a layered cylinder the similar techniques of the variable separation leads to the following representation of homogeneous waves propagating along z -axis in j the curvilinear layer:

$$u_r^j = u^j(r)e^{isz}\begin{Bmatrix}\cos n\theta\\ -\sin n\theta\end{Bmatrix},\quad u_\theta^j = v^j(r)e^{isz}\begin{Bmatrix}\sin n\theta\\ \cos n\theta\end{Bmatrix},\quad u_z^j = w^j(r)e^{isz}\begin{Bmatrix}\cos n\theta\\ -\sin n\theta\end{Bmatrix},$$

$$u^j(r) \equiv f'_{1n}\left(q_P^j r\right) + f'_{1n}\left(q_S^j r\right) + \frac{n}{q_S^j r} f_{3n}\left(q_S^j r\right),\quad w^j(r) \equiv \frac{is}{q_P^j} f_{1n}\left(q_P^j r\right) - \frac{is}{q_S^j} f_{2n}\left(q_S^j r\right),$$

$$v^j(r) \equiv -\frac{n}{q_P^j r} f_{1n}\left(q_P^j r\right) - \frac{n}{q_S^j r} f_{2n}\left(q_S^j r\right) - f_{3n}\left(q_S^j r\right),$$

$$\sigma_{\alpha\beta}^j = \mu_j \tau_{\alpha\beta}^j(r)e^{isz}\begin{Bmatrix}\cos n\theta\\ -\sin n\theta\end{Bmatrix}\quad (\alpha\beta = rr, rz, \theta\theta, zz),$$

$$\sigma_{\alpha\beta}^j = \mu_j \tau_{\alpha\beta}^j(r)e^{isz}\begin{Bmatrix}\sin n\theta\\ \cos n\theta\end{Bmatrix}\quad (\alpha\beta = r\theta, \theta z),$$

$$\tau_{rr}^j = \left[\alpha_j \partial_r + \beta_j r^{-1}\right]u^j + \beta_j n r^{-1} v^j + is\beta_j w^j,\quad \tau_{r\theta}^j = -n r^{-1} u^j + \left[\partial_r - r^{-1}\right]v^j,$$

$$\tau_{rz}^j = isu^j + \partial_r w^j,\quad \tau_{\theta\theta}^j = \left[\beta_j \partial_r + \alpha_j r^{-1}\right]u^j + \alpha_j n r^{-1} v^j + isw^j,$$

$$\tau_{\theta z}^j = isv^j - n r^{-1} w^j,\quad \tau_{zz}^j = \beta_j\left[\partial_r + r^{-1}\right]u^j + \beta_j n r^{-1} v^j + is\alpha_j w^j,$$

where functions $f_{mn}(\xi) \equiv A_{mj}^J J_n(\xi) + A_{mj}^Y Y_n(\xi)$, $f'_{mn}(\xi) \equiv df_{mn}/d\xi$ are determined up to constants $A_{mj}^{J,Y}$. The conditions on the interface $r = R_j$ acquire the form

$$u^{j-1} = u^j,\quad v^{j-1} = v^j,\quad w^{j-1} = w^j, \tag{9}$$

$$\mu_{j-1}\tau_{rr}^{j-1} = \mu_j \tau_{rr}^j,\quad \mu_{j-1}\tau_{r\theta}^{j-1} = \mu_j \tau_{r\theta}^j,\quad \mu_{j-1}\tau_{rz}^{j-1} = \mu_j \tau_{rz}^j. \tag{10}$$

Similarly to the previous case, HBCF on the face $r = R^-$ are as follows

$$\tau_{rr}^1 = \tau_{r\theta}^1 = \tau_{rz}^1 = 0 \quad \text{(stress free)},\qquad u^1 = \tau_{r\theta}^1 = \tau_{rz}^1 = 0 \quad \text{(mixed 1)},$$

$$u^1 = v^1 = w^1 = 0 \quad \text{(clamped)},\qquad v^1 = w^1 = \tau_{rr}^1 = 0 \quad \text{(mixed 2)}.$$

At the lateral surface $r = R^+$, we assume any of these combinations. Any HBCF at $r = R^\mp$ and Eqs.(9), (10) result in a linear system of algebraic equations for $A_{mj}^{J,Y}$ whose $6N \times 6N$ matrix $\mathbf{L}$ yields the frequency equation $\det \mathbf{L} = 0$. In contrast to the case (a), the decoupling of waves with SH- and PSV- polarization takes place only for $n = 0$ (torsional waves and Pochhammer-Chree waves). For $n \geq 1$,

we deal with the flexural modes. The symmetry of the frequency equation is as above. Again, for simple roots s_l we may express $A_{mj}^{J,Y}$ via basic coefficient A_{1N}^{J}.

4 Orthogonality relations

a) Let us introduce a standard scalar product across j th layer for any two functions related to the wave numbers s_l and s_m and compose the following quantities

$$W_{lm}^{*} \equiv \sum_j \mu_j \left\{ \left(\chi_l^j , v_m^j \right) - \left(\tau_m^j , v_l^j \right) \right\} \quad (s_l , s_m \in S_{PSV}), \qquad \left(f_l^j , g_m^j \right) \equiv \int_{z_j}^{z_{j+1}} f_l^j g_m^j dz ,$$

$$G_{lm}^{*} \equiv \sum_j \mu_j \left\{ \left(p_l^j , w_m^j \right) - \left(v_l^j , dw_m^j / dz \right) + \left[s_l - s_m^2 s_l^{-1} \right] \left(u_l^j , w_m^j \right) \right\} \quad (s_l \in S_{PSV} , s_m \in S_{SH}),$$

$$T_{lm}^{*} = \sum_j \mu_j \left(w_l^j , w_m^j \right) \quad (s_l , s_m \in S_{SH}) .$$

Consider cylinders $\Omega_j = \left\{ r \le R,\ z_j \le z \le z_{j+1} \right\}$ whose lateral and top/bottom surfaces are $\Omega_R^j = \left\{ r = R,\ z_j \le z \le z_{j+1} \right\}$ and $\Omega_j^{\mp} = \left\{ r \le R,\ z = z_{j,j+1} \right\}$, respectively. Denote the integrals over Ω_R^j by angle brackets. After some manipulations, the following set of identities for the homogeneous waves can be obtained ($\xi_n \equiv 1 + \delta_n^0$, δ_β^α is a Kronecker delta)

$$\left\langle \sigma_{rr}^l , \mathbf{u}_r^m \right\rangle + \left\langle \sigma_{r\theta}^l , \mathbf{u}_\theta^m \right\rangle + \left\langle \sigma_{rz}^l , \mathbf{u}_z^m \right\rangle - \left\langle \sigma_{rr}^m , \mathbf{u}_r^l \right\rangle - \left\langle \sigma_{r\theta}^m , \mathbf{u}_\theta^l \right\rangle - \left\langle \sigma_{rz}^m , \mathbf{u}_z^l \right\rangle =$$
$$= \pi R \xi_n \left\{ W_{ml}^{*} B_n(s_m R) B_n'(s_l R) - W_{lm}^{*} B_n'(s_m R) B_n(s_l R) \right\}, \tag{11}$$

$$\left\langle \sigma_{rr}^l , \mathbf{u}_r^m \right\rangle + \left\langle \sigma_{r\theta}^l , \mathbf{u}_\theta^m \right\rangle + \left\langle \sigma_{rz}^l , \mathbf{u}_z^m \right\rangle - \left\langle \sigma_{rr}^m , \mathbf{u}_r^l \right\rangle - \left\langle \sigma_{r\theta}^m , \mathbf{u}_\theta^l \right\rangle - \left\langle \sigma_{rz}^m , \mathbf{u}_z^l \right\rangle =$$
$$= \pi \xi_n G_{lm}^{*} n s_m^{-1} B_n(s_m R) B_n(s_l R), \tag{12}$$

$$\left\langle \sigma_{rr}^l , \mathbf{u}_r^m \right\rangle + \left\langle \sigma_{r\theta}^l , \mathbf{u}_\theta^m \right\rangle + \left\langle \sigma_{rz}^l , \mathbf{u}_z^m \right\rangle - \left\langle \sigma_{rr}^m , \mathbf{u}_r^l \right\rangle - \left\langle \sigma_{r\theta}^m , \mathbf{u}_\theta^l \right\rangle - \left\langle \sigma_{rz}^m , \mathbf{u}_z^l \right\rangle =$$
$$= \pi R \xi_n T_{lm}^{*} \left(E_{lm} - E_{ml} \right), \tag{13}$$

$$E_{lm} = \tfrac{s_l}{2} \left\{ B_{n-1}(s_m R) B_{n-2}(s_l R) - B_{n+1}(s_m R) B_{n+2}(s_l R) \right\}, \left\langle \mathbf{f}^l , \mathbf{g}^m \right\rangle \equiv \sum_j \iint_{\Omega_R^j} f_l^j g_m^j dA . \tag{14}$$

The factors with cylindrical functions B_n are mutually independent and we obtain

$$W_{lm}^{*} = 0 , \qquad G_{lm}^{*} = 0 , \qquad T_{lm}^{*} = 0 \quad \text{for} \quad s_l^2 \ne s_m^2 . \tag{15}$$

Equations (15) are the sought OR between modes with the 3D "in-plane" and/or "out-of-plane" polarization. Their physical meaning is the power flow addittivity. Indeed, substituting $\mathrm{Re}\left\{ u_{\alpha l}^j e^{-i\omega t} \right\}$ instead of $u_{\alpha l}^j$ into the averaged power flow, we arrive at the expressions

$$P_{rl}^{*} \equiv \frac{\omega}{2\pi}\int_{0}^{2\pi/\omega}\sum_{j}\iint_{\Omega_R^j} P_{rl}^{j}\,dAdt \quad \left(P_{rl}^{j} \equiv P_{1l}^{j}\cos\theta + P_{2l}^{j}\sin\theta,\ P_{\alpha l}^{j} = -\sigma_{\alpha\beta l}^{j}\dot{u}_{\beta l}^{j}\right), \tag{16}$$

$$P_{rl}^{*} = \frac{\pi\xi_n R}{2}\,\mathrm{Re}\left\{\sum_j \mu_j\left[\left(\chi_1^{j},\overline{u}_1^{j}\right) - \left(\overline{\tau}_1^{j}, v_1^{j}\right)\right] i\omega\overline{B}_n'(s_l R)B_n(s_l R)\right\} \quad (s_l \in S_{PSV}), \tag{17}$$

$$P_{rl}^{*} = \frac{\pi\xi_n}{2}\,\mathrm{Re}\left\{\sum_j \mu_j\left(w_1^{j},\overline{w}_1^{j}\right) i\omega\overline{s}_l\left[B_{n-1}(s_l R)\overline{B}_{n-2}(s_l R) - \overline{B}_{n+2}(s_l R)B_{n+1}(s_l R)\right]\right\} \quad (s_l \in S_{SH}). \tag{18}$$

The choice of $B_n = H_n^{(1,2)}$ for the propagating mode $s_l > 0$ in case of pure elasticity yields

$$P_{rl}^{*} = \pm\xi_n c_l W_{ll}^{*},\ c_l = \omega/s_l \quad (s_l \in S_{PSV}), \qquad P_{rl}^{*} = \pm\xi_n \omega T_{ll}^{*} \quad (s_l \in S_{SH}). \tag{19}$$

$$P_{rl}^{*} \sim \pm c_g^{l}\left\{K_l + E_l\right\}^{*},\ R \to +\infty,\ c_g^{l} \equiv d\omega/ds\big|_{s=s_l},\ (s_l \in S_{PSV} \text{ or } s_l \in S_{SH}) \tag{20}$$

where K_l, E_l are integrals of the positive kinetic and elastic energy densities across the cylindrical surface. The sign $\pm$ is chosen accordingly to the first or second kind of Hankel's function, respectively. Thus, we may select the real s_l upon the radiation conditions (19) and (20).

b) The corresponding combinations of scalar products in the cross section of a cylinder look as follows

$$\left\langle \boldsymbol{\sigma}_{zz}^{m}, \mathbf{u}_z^{l}\right\rangle - \left\langle \boldsymbol{\sigma}_{rz}^{l}, \mathbf{u}_r^{m}\right\rangle - \left\langle \boldsymbol{\sigma}_{z\theta}^{l}, \mathbf{u}_\theta^{m}\right\rangle = \pi\varepsilon_n W_{lm}^{*},$$

$$W_{lm}^{*} \equiv \sum_j \mu_j\left\{\left(\tau_{zzm}^{j}, w_l^{j}\right) - \left(\tau_{rzl}^{j}, u_m^{j}\right) - \left(\tau_{\theta zl}^{j}, v_m^{j}\right)\right\},$$

$$\left\langle \mathbf{f}^{l}, \mathbf{g}^{m}\right\rangle \equiv \sum_j \iint_{\Omega_z^j} f_l^{j} g_m^{j}\,dA = \sum_j \int_{R_j}^{R_{j+1}}\int_0^{2\pi} f_l^{j} g_m^{j}\,rd\theta dr, \qquad \left(\mathbf{f}^{l}, \mathbf{g}^{m}\right) \equiv \sum_j \int_{R_j}^{R_{j+1}} f_l^{j} g_m^{j}\,rdr,$$

with the familiar form of the orthogonality relations: $W_{lm}^{*} = 0$ $\left(s_l^2 \neq s_m^2\right)$. The averaged power flow of the propagating mode across the cylinder cross section is simpler then for the case (a), namely,

$$P_{zl}^{*} = \tfrac{1}{2}\pi\xi_n i\omega W_{ll}^{*} \in \mathrm{R},\ \ P_{zl}^{*} = c_g^{l}\left\{K_l + E_l\right\}^{*},\ \ P_{zl}^{*} \equiv \frac{\omega}{2\pi}\int_0^{2\pi/\omega}\sum_j\iint_{\Omega_{\pm z}^j} P_{zl}^{j}\,dAdt \quad \left(s_l > 0\right).$$

5 Far field of a finite acoustic source

a) Assume that the laminate motion is caused by the body forces f_α^j distributed in a finite volume embedded into cylinder $\Omega = \cup\Omega_j$, or by surface load distributed over a finite region on Ω_1^- or Ω_N^+ (see Fig. 2a). Remaining part of the faces satisfies HBCF. Let us represent the laminate response as function of r, θ, z and de-

compose it into Fourier series of the angle θ. Accordingly the general theory of partial differential equations the field inside Ω $(r < R)$ has two components: a particular solution caused by the acoustic source and a general *homogeneous* solution. At $r > R$ the particular solution vanishes and the field equals the series of modes (1) with $B_n = H_n^{(1)}$ (or $H_n^{(2)}$) due to the energy radiation. On the surfaces Ω_R^j $(r = R)$ the inner and outer solutions satisfy the continuity of u_α^j and $\sigma_{r\alpha}^j$ $(\alpha = r, \theta, z)$. For each wave number s_m, we introduce a standing wave with $B_n(s_m r) \equiv J_n(s_m r)$ and with the same components u_m^j, v_m^j and w_m^j in formulae (1). Then, integrating the total field $\sigma_{\alpha\beta}^j$, u_α^j over cylinder a Ω with this standing wave as a dummy solution, we obtain

$$\sum_j \iint\limits_{\Omega_R^j} \left\{ \sigma_{\alpha\beta}^j u_{\alpha m}^j - \sigma_{\alpha\beta m}^j u_\alpha^j \right\} n_\beta dA = \Gamma_{mn}, \tag{21}$$

$$\Gamma_{mn} \equiv -\sum_j \iiint\limits_{\Omega^j} \left\{ f_\alpha^j u_{\alpha m}^j \right\} dV + \left\{ \iint\limits_{\Omega_1^-} + \iint\limits_{\Omega_N^+} \right\} \left\{ \sigma_{\alpha\beta m} u_\alpha - \sigma_{\alpha\beta} u_{\alpha m} \right\} n_\beta dA, \tag{22}$$

in a similar form for the combination of trigonometrical functions $\cos n\theta$, $\sin n\theta$ or $-\sin n\theta$, $\cos n\theta$ in formulae (1). By this reason we do not introduce different notations, but the value Γ_{mn} (and the mode coefficient) depends on the choice of these functions. However Γ_{mn} does not contain any unknowns. For example, if the source is given by stresses $\sigma_{\alpha z}^-$ on Ω_1^- and $\sigma_{\alpha z}^+$ on Ω_N^+ this expression yields

$$\Gamma_{mn} = -\iint\limits_{\Omega_N^+} \left\{ \sigma_{zz}^+ u_{zm}^N + \sigma_{zr}^+ u_{rm}^N + \sigma_{z\theta}^+ u_{\theta m}^N \right\} dA - \iint\limits_{\Omega_1^-} \left\{ \sigma_{zz}^- u_{zm}^1 + \sigma_{zr}^- u_{rm}^1 + \sigma_{z\theta}^- u_{\theta m}^1 \right\} dA.$$

Then the following procedure applies: replace the field on the lateral surfaces Ω_R^j by the mode series for the outer zones with Hankel's functions $H_n^{(1)} = J_n + iN_n$ (or $H_n^{(2)}$); annihilate in the left hand side of Eq.(21) all waves except $s = s_m$ using OR (11)-(15) and simplify the left hand sides in (21) using the basic property of cylindrical function: $J_{n+1}(s_m R) N_n(s_m R) - J_n(s_m R) N_{n+1}(s_m R) = 2/\pi R s_m$.

Finally it yields the exact formulae for the mode coefficients

$$\begin{cases} M_n^m = -i s_m \Gamma_{mn} \Big/ \left\{ 2\xi_n W_{mm}^* \right\}, & s_m \in S_{PSV}, \\ M_n^m = -i \Gamma_{mn} \Big/ \left\{ 2\xi_n T_{mm}^* \right\}, & s_m \in S_{SH}. \end{cases} \tag{23}$$

Hence, we suggest a general method to evaluate the "far" field – but in fact the total field at the distance $r > R$, where $2R$ is the longitudinal size of an acoustic source. The method requires the calculation of spectra S_{PSV} and S_{SH}, modes (1)-(3) and coefficients (23) in the double series wrt n and s_m. In the case of pure

elasticity the classical far field as waves propagating to infinity is expressed by ordinary series of n with a finite set of real wave numbers s_m at each frequency.

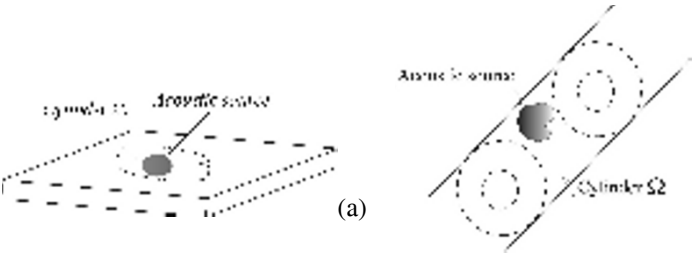

Fig. 2. Acoustic source.

(a) (b)

b) For an acoustic source, shown in Fig. 2b inside a finite cylinder Ω $\left(R^- \le r \le R^+, z^- \le z \le z^+\right)$ we obtain similarly $M_n^{\pm l} = -\Gamma_{\mp ln} / 2\pi W_{ll}^*(n)$,

$$\Gamma_{\mp ln} = \left[\sum_j \int_{\Omega_j} \left\{ f_\alpha^j u_{\alpha l}^j - f_{\alpha l}^j u_\alpha^j \right\} dV + \iint_{\Omega_{+R}^N} \left\{ \sigma_{\alpha r}^N u_{\alpha l}^N - \sigma_{\alpha r l}^N u_\alpha^N \right\} dA - \iint_{\Omega_{-R}^1} \left\{ \sigma_{\alpha r}^1 u_{\alpha l}^1 - \sigma_{\alpha r l}^1 u_\alpha^1 \right\} dA \right]_{s_l \to \mp s_l},$$

where $\Gamma_{\mp ln}$ and $M_n^{\pm l}$ depend on the choice of functions $\cos n\theta$, $\sin n\theta$ or $-\sin n\theta$, $\cos n\theta$, and the sign $\pm$ corresponds to zone $z > z^+$ or $z < z^-$, respectively.

6 Some exact solutions

a) Consider a few examples of calculating Γ_{mn}. Assume that the load is distributed over a circular region Ω_N^+ and the surface stresses $\sigma_{zz}^+(r,\theta)$, $\sigma_{rz}^+(r,\theta)$ and $\sigma_{\theta z}^+(r,\theta)$ are expanded into the Fourier series of θ. In accordance with the representations (1), let us for a moment denote coefficients of $\cos n\theta$ (or $-\sin n\theta$) for σ_{zz}^+ and σ_{rz}^+ by $\tau_{zn}^+(r)$ and $\tau_{rn}^+(r)$, respectively. For $\sigma_{\theta z}^+$ the coefficient of $\sin n\theta$ (or $\cos n\theta$) is denoted by $\tau_{\theta n}^+(r)$. The substitution into (22) yields

$$\Gamma_{mn} = -\pi\xi_n \left\{ u_m^N(z^+) T_r^+ + w_m^N(z^+) T_\theta^+ + v_m^N(z^+) T_z^+ \right\}, \quad T_z^+ = \int_0^R \tau_{zn}^+(r) J_n(s_m r) r dr,$$

$$T_{r,\theta}^+ = \frac{1}{2} \int_0^R \left\{ \left[\tau_{rn}^+(r) + \tau_{\theta n}^+(r) \right] J_{n+1}(s_m r) \pm \left[\tau_{rn}^+(r) - \tau_{\theta n}^+(r) \right] J_{n-1}(s_m r) \right\} r dr \cdot$$

In particular, for a constant normal load $\tau_{z0}^+/2$ and constant tangent load τ_{10}^+ in the direction x_1 we obtain the following

$$\Gamma_{m0} = -\frac{\pi}{s_m} R J_1(s_m R) \tau_{z0}^+ \times \begin{Bmatrix} v_m^N(z^+), & s_m \in S_{PSV} \\ 0, & s_m \in S_{SH} \end{Bmatrix},$$

$$\Gamma_{m1} = \frac{\pi}{s_m} R J_1(s_m R) \tau_{10}^+ \times \begin{Bmatrix} u_m^N(z^+), & s_m \in S_{PSV} \\ -w_m^N(z^+), & s_m \in S_{SH} \end{Bmatrix},$$

with $\Gamma_{mn} = 0$ for $n \geq 2$. It is also easy to obtain the laminate response to a concentrated load. For the concentrated body forces $f_\alpha^j = T_0 \delta_\alpha^\beta \delta(x_1, x_2, x_3 - z_0)$ ($z_j \leq z_0 \leq z_{j+1}$) at any HBCF we obtain

$$\Gamma_{mn} = -\sum_j \iiint_{\Omega^j} \{ f_\alpha^j u_{\alpha m}^j \} dV = -T_0 u_{\beta m}^j \Big|_{r=0, z=z_0},$$

with a similar result for the concentrated surface load $\sigma_{\alpha z}^+ = \tau_0^+ \delta_\alpha^\beta \delta(x_1, x_2)$: $\Gamma_{mn} = -\tau_0^+ u_{\beta m}^N \Big|_{r=0, z=z^+}$. Note that these formulae are non singular since the dummy displacements $u_{\beta m}^j(r, \theta, z_0)$ with $B_n = J_n$ is regular at the origin. However, the mode series may have singularity at the origin due to the Hankel functions involved.

b) In the similar notations, the Green function for $f_\alpha^j = T_0 \delta_\alpha^\beta \delta(x_1 - x_{10}, x_2, x_3)$, $R_j \leq x_{10} \leq R_{j+1}$ is given by modal coefficients $M_n^{\pm l}$ with the quantities $\Gamma_{\mp ln} = T_0 u_{\beta l}^j \Big|_{s=\mp s_l, x_1 = x_{10}, x_2 = 0, z=0}$ or $\Gamma_{mn} = \tau_0^+ u_{\beta l}^N \Big|_{s=\mp s_l, x_1 = R^+, x_2 = 0, z=0}$ in the case of the surface load $\sigma_{\alpha t}^+ = \tau_0^+ \delta_\alpha^\beta \delta(x_1 - R^+, x_2, x_3)$. Modelling the transducer contact area by the surface load distributed on the curvilinear rectangle Ω_N^+ ($r = R^+, -L \leq z \leq L, -\theta_0 \leq \theta \leq \theta_0$) the modal coefficients $M_n^{\pm l}$ can be easily expressed via the load components of Fourier series of θ: $\tau_{rn}^+(z)$, $\tau_{zn}^+(z)$ and $\tau_{\theta n}^+(z)$. The quantities $\Gamma_{\mp ln}$ are equal to

$$\Gamma_{\mp ln} = u_{\mp l}^N(R^+) T_{\mp lr}^+ + v_{\mp l}^N(R^+) T_{\mp l\theta}^+ + w_{\mp l}^N(R^+) T_{\mp lz}^+, \quad T_{\mp l\alpha}^+ = \int_{-L}^{+L} \tau_{\alpha n}^+(z) e^{\mp s_l z} dz.$$

7 Some generalizations

a) *First* natural generalization is for a fluid loaded laminate. Assume that some layers (specified by an additional superscript 0) are not solids but are the ideal compressible (or incompressible) fluids. Thus, in each k th fluid ply we must satisfy the equation of motion and the conditions on the fluid-solid interface: the continuity of the normal displacement and the balance of normal stress and the

fluid pressure $P^{0k} = -\lambda_{0k}\nabla\mathbf{u}^{0k}$. The analogue of HBCF in the case of the fluid face is the absence of pressure or of the normal displacement. The displacement vector in fluid is determined similarly to (1)-(3) with $w^k = 0$ and with the pressure

$$P^{0k} = \lambda_{0k} p^{0k}(z) B_n(sr) \begin{Bmatrix} \cos n\theta \\ -\sin n\theta \end{Bmatrix} \quad \left(p^{0k} \equiv -k_0^2 s^{-1} u^{0k}, k_0 \equiv \omega / c_{0k}, c_{0k} \equiv \sqrt{\lambda_{0k}/\rho_{0k}}\right).$$

The waves with the "out-of-plane" polarization in the laminate remain unperturbed, but the "in-plane" waves have some corrections. The identities (11)-(14) and orthogonality relations (15) remain in force. The formulae (15) and (23) now include W_{lm}^* modified as follows

$$W_{lm}^* \equiv \sum_j \mu_j \left\{ \left(\chi_l^j, v_m^j\right) - \left(\tau_m^j, v_l^j\right) \right\} - \sum_k \lambda_{0k} \left(p_l^{0k}, u_m^{0k}\right) \quad (s_l, s_m \in S_\Delta). \tag{24}$$

The term Γ_{mn} in Eqn.(23) should contain the additional volume integrals and modified facial integrals (if these faces are of fluid ply)

$$-\sum_k \iiint_{\Omega_k^0} \left\{ f_\alpha^{0k} u_{\alpha m}^{0k} \right\} dV, \quad \iint_{\Omega_+^{N_0}} P^+ u_{zm}^{N_0} dA, \quad \iint_{\Omega_-^{1_0}} P^- u_{zm}^{1_0} dA.$$

The *second* generalization concerns the layers of infinite thicknesses (half spaces). Now the spectrum of the corresponding boundary value problem is subdivided into discrete part $S_{PSV} \cup S_{SH}$, whose homogeneous waves are described similarly to (2), (3) (with $\exp\left(\pm q_P^j z\right)$, $\exp\left(\pm q_S^j z\right)$ for infinite thickness), and by continuous part $\eta = \eta_{PSV} \cup \eta_{SH}$ for which we obtain

$$\begin{bmatrix} u_r^j \\ u_\theta^j \\ u_z^j \end{bmatrix} = \sum_{n=0}^{+\infty} \int_\eta \begin{bmatrix} \left(-u^j B_n' + w^j n B_n / sr\right)\left(M_n^c \cos n\theta - M_n^s \sin n\theta\right) \\ \left(u^j n B_n / sr - w^j B_n'\right)\left(M_n^c \sin n\theta + M_n^s \cos n\theta\right) \\ v^j B_n \left(M_n^c \cos n\theta - M_n^s \sin n\theta\right) \end{bmatrix} ds,$$

with $M_n^{c,s} = M_n^{c,s}(s)$. The continuous part consists of the cut-offs for radicals $q_{P,S}$ in each half space. For the case of finite source it is important that the field of continuous part satisfies the homogenous equations and HBCF at $r > R$. For this reason, the identities (11)-(14) hold not only for a discrete part of spectrum but also when $s_l \in S_{PSV,SH}$, $s_m \in \eta$ $\left(s_l^2 \neq s_m^2\right)$ and vice versa. The right hand side in (11)-(14) must be integrated over η. Thus, the relations (25)-(27) are valid and:

- different homogeneous waves of discrete spectrum are orthogonal to each other;
- homogenous waves of discrete spectrum are orthogonal to the waves of continuous spectrum.

This readily results in the mode coefficients (23) for $s_m \in S_{PSV} \cup S_{SH}$ without considering the direct and inverse Fourier transform. The required wave numbers are easily obtained from the frequency equation for the plane wave problem of

laminate. However, for the continuous part of spectrum there is no simplification in the consideration of the cut-offs in the inverse Fourier transforms.

b) A hollow cylinder filled in by a compressible fluid can be described by passing to a physical limit (absence of shear modulii in fluid layers). The orthogonality relations involve the fluid pressure and remain in force with a simple modification

$$W^*_{lm} \equiv \sum_j \mu_j \left\{ \left(\tau^j_{zzm}, w^j_l \right) - \left(\tau^j_{rzl}, u^j_m \right) - \left(\tau^j_{\theta zl}, v^j_m \right) \right\} - \sum_k \lambda_{0k} \left(p^{0k}_{zm}, w^{0k}_l \right),$$

$$P^{0k} = \lambda_{0k} p^{0k}(r) e^{isz} \begin{Bmatrix} \cos n\theta \\ -\sin n\theta \end{Bmatrix}, \qquad p^{0k} = \frac{k_0^2}{q_{0k}^2} f_{0n}(q_{0k} r) \quad \left(q_{0k} \equiv \sqrt{k_0^2 - s^2} \right).$$

The modal coefficients caused by an acoustic source are sought as previously. The same concerns the waves of discrete spectrum in the case of a cylinder embedded into a fluid or into a viscoelastic space.

8 Conclusion

The obtained results can be naturally subdivided into *three* groups. *First* group includes orthogonality relations for the cylindrical guided waves in laminates and in cylinders satisfying HBCF. They correlate with known results for an elastic layer and cylinder and possess all the necessarily limit properties. The explicit expressions for reciprocity relations are obtained for both elastic and linearly viscoelastic media. The *second* group describes solving methods for one important problem of evaluating the far field from an acoustic source - surface loads or body forces localised in a finite region. The obtained Green functions can be applied to represent the field caused by an arbitrary aperture using convolution integrals. The solution for a circular region is of interest for modelling circular transducers. In particular, one may also evaluate a pulse train using harmonic synthesis. The *third* group generalizes the above mentioned for the case of fluid loaded laminate and cylinder, and/or in case of layers with infinite thicknesses. For the latter we obtain the closed form of 3D Rayleigh, Love, Stoneley or Scholte waves. As far as the guided wave completeness is concerned, we may refer to the more general result. Normally, the total set of eigenfunctions of the polynomial operator pencil has multiple completeness (accordingly to its degree) in the functional Sobolev's space on a cross-section of the geometrical region considered (see [13-18]). The same property is expected for 3D guided waves. The ordinary completeness is obtained by reducing this set, e.g., in the case of laminate (a) the subset $\operatorname{Im} s_l < 0$ for basic functions $B_n = H_n^{(1)} \ (r > 0)$ is excluded from the consideration. Another application is for the post processing of FEM calculation, performed in a finite area of laminate with defects, inclusions, etc., with the interpretation of the obtained results in terms of outgoing waves [19].

References

1. Auld, G.S. Kino, “Normal mode theory for acoustic waves and its application to interdigital transducer”, IEEE Transactions on Electron Devices ED-18 (10), 898-908 (1971).
2. Y.I. Bobrovnitskii, “Orthogonality relations for Lamb waves”, Soviet Acoust. Physics 18 (4), 432-433 (1973).
3. M.V. Fedoryuk, “Orthogonality-type relations in solid waveguides”, Soviet Acoust. Physics 20(2), 188-190 (1974).
4. W.B. Fraser, “Orthogonality relations for Rayleigh-Lamb modes of vibration of a plate”, J. Acoust. Soc. Am. 59, 215-216 (1976).
5. B.G. Prakash, “Generalized orthogonality relations for rectangular strips in elastodynamics”, Mech. Research Comm. 5 (4), 251-255 (1978).
6. A.S. Zilbergleit, B.M. Nuller, “Generalized orthogonality of the homogeneous solutions to the dynamic problems of elasticity”, Doklady–Physics 234 (2), 333-335 (1977).
7. L.I. Slepyan, “Betti theorem and orthogonality relations for eigenfunctions”, Mech. of Solids 1, 83-87 (1979).
8. M. E. D. Fama, “Radial eigenfunctions for the elastic circular cylinder”, Q. J. Mech. Appl. Math. 15, 479-496 (1972).
9. W.B. Fraser, ”An orthogonality relations for the modes of wave propagation in an elastic cylinder”, J. Sound and Vibration 43(3), 568-571 (1975).
10. D.D. Zakharov, “Generalised orthogonality relations for eigenfunctions in three dimensional dynamic problem for an elastic layer”, Mech. of Solids 6, 62-68 (1988).
11. J.D. Achenbach, Y. Xu, “Wave motion in an isotropic elastic layer generated by time-harmonic load of arbitrary direction”, J. Acoust. Soc. Am. 106, 83-90 (1999).
12. J.D. Achenbach, “Calculation of wave fields using elastodinamic reciprocity”, Int. J. of Solids and Structures 37, 7043-7053 (2000).
13. M.V. Keldysh, “On the completeness of eigenfunctions of some classes of non self-adjoint linear operators”, Russian Math. Surveys 26(4), 15–44 (1971).
14. A.G. Kostyuchenko, M.B. Orazov, “Certain properties of roots of a self-adjoint quadratic bundles”, Funct. Analysis and its Applications 9(4), 295–305 (1975).
15. M.B. Orazov, “The completeness of eigenvectors and associated vectors of a self-adjoint quadratic bundles”, Funct. Analysis and its Applications 10(2), 153–155 (1976).
16. A.G. Kostyuchenko, M.B. Orazov, “The completeness of root vectors in certain self-adjoint quadratic bundles”, Funct. Analysis and its Applications 11(4), 317–319 (1977).
17. A.G. Kostyuchenko, M.B. Orazov, “Problem of oscillations of an elastic half-cylinder and related self-adjoint quadratic pencil”, Journal of Math. Sciences 33(3), 1025–1065 (1986).
18. P. Kirrmann, “On the completeness of Lamb modes”, J. of Elasticity 37, 39–69 (1995).
19. B. Hosten, L. Moreau, M. Castaings, “Reflection and transmission coefficients of guided waves by defects in viscoelastic material plates”, J. of Acoust. Society of Am., 121(6), 3409-3417 (2007).

Damage detection in foam core sandwich structures using guided waves

N. Terrien and D. Osmont

Abstract Sandwich structures, consisting of two face sheets and an intermediate foam core, have a high potential in aerospace applications. However, they are rarely used because it is difficult to inspect them by the conventional non-destructive techniques. Indeed, non visible damage of the sandwich face sheets can in fact be accompanied by a large skin/foam core delamination. This paper describes a new approach to detect sub-interface damage in such structures by using ultrasonic guided waves. These waves are excited with a PZT disc permanently bonded on the structure and their interaction with foam core damages is detected by scanning the structure with an air-coupled transducer. To carry out this monitoring technique, the first step was to analyse the propagation of waves guided in such sandwiches with both numerical and experimental tools. This allowed selecting the specific waves and their frequency which will be the most sensitive to skin/foam core delaminations and to make easier the interpretation of the measured waveforms. Finally, an adapted signal processing was implemented in order to localize and to characterize delaminations in sandwich panels.

1 Introduction

For high performance composite structure airframe design, sandwich structures own many advantages compared to monolithic stiffened structures. Indeed, they offer higher bending stiffness and strength at lower weight and thus contribute to reduce fuel consumption. They also make easier the structural integration and take part in

Terrien
ONERA, DMSC/CS2, 29 avenue de la Division Leclerc, 92322 Châtillon cedex, France, e-mail: Nicolas.Terrien@onera.fr

Osmont
ONERA, DMSC/CS2, 29 avenue de la Division Leclerc, 92322 Châtillon cedex, France, e-mail: Daniel.Osmont@onera.fr

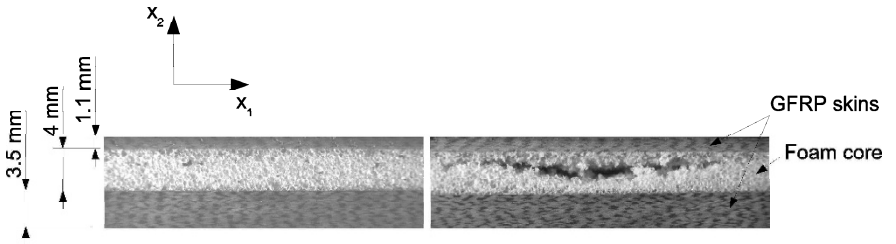

Fig. 1 Cross sections of an undamaged and of a damaged sandwich structure.

the acoustic and thermal insulation. However, low velocity/energy impacts leave only non- (or barely) visible damage in the face sheet but can be accompanied by large sub-interface damage: skin/foam core delaminations or foam core crushing (Fig. 1). This kind of impact damage may arise due to accidental tool drops during maintenance or due to runway debris, hail and bird strikes in-service [1] and reduces drastically the load-bearing capacity of the structure.

Many nondestructive techniques have already been investigated for detecting delaminations in monolithic composite structures as for example ultrasonic pulse-echo C-scans, radiography, thermography [2] or the use of Lamb waves [3]. These methods can be also used to detect delaminations or cracks in the skins of such sandwich structures but are still not well adapted to detect foam core damages [1, 4]. So this paper describes a new inspection method to detect skin/foam core delaminations or foam core crushing in sandwich structures by using ultrasonic guided waves. These waves are generated in the structure with a PZT disc while their interaction with a sub-interface damage is detected by scanning the structure with an air-coupled transducer. The emitter is permanently integrated on the sandwich panel while the air-coupled transducer is used only during the maintenance stage. To set up this monitoring method, the first step is to analyze the propagation of waves guided by the sandwich structure. This allows the selection of two different monitoring configurations: the first one for detecting the foam core damage and the second one to localize it and to evaluate it size. The last method has already been exploited to detect such damage in sandwich structures using the A_0 Lamb mode at low frequency [5] and for testing damage in metallic structures below a composite repair [6]. In both configurations, the measured waveforms are interpreted with experimental and numerical tools.

2 Guided Waves In Sandwich Structures

In this section, the waves guided by the sandwich structure are analyzed in order to select the most sensitive ones to foam core damages. The sandwich structure (Fig. 1) is composed of three layers: a thin glass-fiber epoxy skin, a foam core and a thick glass-fiber epoxy skin. To characterize the propagation of Lamb waves in this struc-

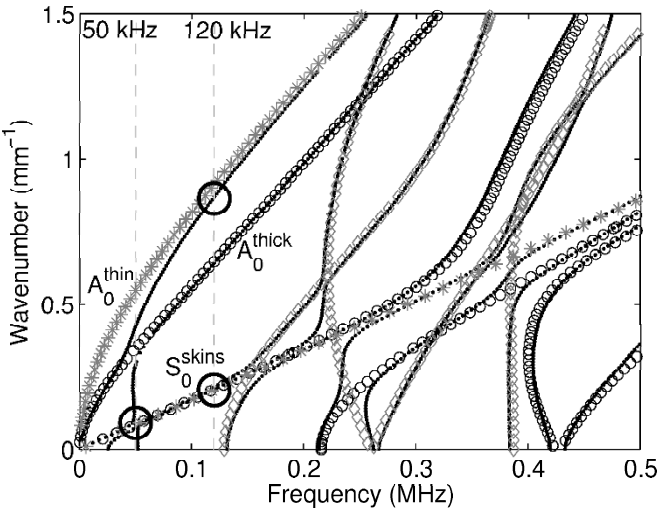

Fig. 2 Dispersion curves of the sandwich structure (•••), of the thin glass fiber skin (∗∗∗), of the thick glass fiber skin (○○○) and of the foam core with surface displacements blocked (◇◇◇). ◯ highlight the excitation/detection areas of the waves exploited in this study.

ture, the dispersion curves are computed using a global matrix method [7] for the sandwich structure but also for the glass-fiber epoxy skins and for the foam core (Fig. 2). As one can see on this figure, the dispersion curves of the sandwich structure can be associated either with the dispersion curves of the face sheets or with the curves of the foam core. This means that some waves guided by the sandwich are mainly skin waves while others are mainly guided by the foam. Fig. 3 shows the displacement components of two waves generated around 120 kHz and guided by the sandwich structure. The first one (Fig. 3a) owns large in-plane displacements and is mainly guided by the face sheets (S_0^{skins} Lamb modes). Indeed, 38 percent of the elastic energy is held by the thin skin, 17 percent by the foam core and 45 percent by the thick skin. The second wave (Fig. 3b) is mainly conducted by the thin face sheet (A_0^{thin} Lamb wave). Indeed, in this case 89 percent of the elastic energy is contained in the thin skin. These waves will be exploited in the following section in order to detect a skin/foam core delamination in such structures. On the contrary, Fig. 4 illustrates the displacements of a wave excited around 50 kHz and for which the elastic energy is mainly contained in the foam core (60 percent in the foam against 20 percent in each face sheet). This wave will be exploited in the second step of this NDI method to localize and to evaluate the size of the sub-interface damage.

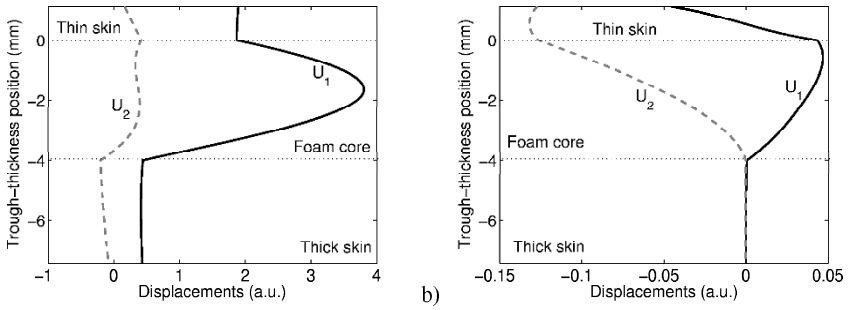

Fig. 3 Displacements calculated through the thickness of the sandwich structure for a wave launched at 132 kHz and owning a wavenumber of a) $k = 0.241\ mm^{-1}$ (S_0^{skins}) and b) $k = 0.930\ mm^{-1}$ (A_0^{thin}).

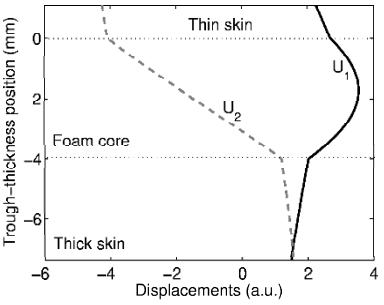

Fig. 4 Displacements calculated through the thickness of the sandwich structure for a wave launched at 47 kHz and owning a wavenumber of $0.091\ mm^{-1}$.

3 Delamination Detection

In this part, experimental investigations are carried out in order to detect skin/foam core delaminations in sandwich structures. These sub-interface damages were made in the structure during the manufacturing process by removing foam cylinders of various diameters without producing damages of the face sheets. The experimental setup is described in Fig. 5. Guided waves are generated in the sandwich structure with a 20 mm diameter PZT disc permanently bonded on the thick face sheet. The emitter is driven by a 3-cycle tone burst at 120 kHz. The waves guided by the structure are detected with a focalized air-coupled transducer. According to the Snell's law and the sandwich structure dispersion curves (Fig. 2), at oblique incidence the receiver is mainly sensitive to A_0^{thin}, whereas at normal incidence, it is S_0^{skins} modes which are the most efficiently detected waves. In Fig. 6, one can see that no wave is detected on an undamaged area for the inclined receiver while there is a meaningful ultrasonic signal measured at normal incidence. This means that some waves are launched in the undamaged structure by the PZT disc but that the air-coupled transducer is not sensitive to them at oblique incidence. A B-scan of the signal measured at oblique incidence is performed in the direction of the 17 mm diameter skin/core

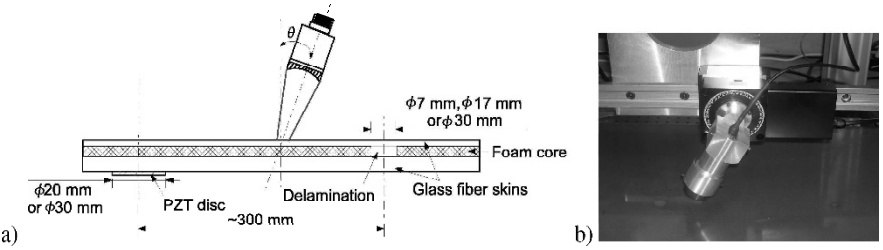

Fig. 5 a) Shematic drawing and b) picture of the experimental setup.

delamination (Fig. 7). One can notice that no wave is detected in the undamaged area (from 200 to 275 mm) while a wave packet appears from the location of the delamination and propagates after passing the damage. Fig. 8 shows the 2D-FFT of the waveform measured before the damage at normal incidence and after the damage at oblique incidence. This demonstrates that the PZT disc generates S_0^{skins} modes in the sandwich structure which are not detected at oblique incidence (Fig. 8a). These waves are sensitive to sub-interface damages and are converted into an A_0^{thin} mode when they interact with a skin/foam core delamination (Fig. 8b). So, this particular wave produced by mode conversion at the damage location is the only one detected by the inclined receiver and indicates the presence of sub-interface damage. Fig. 9 shows the C-scan of the interaction of these S_0^{skins} waves with delaminations. One can note the apparition of the A_0^{thin} wave packet produced by the sub-interface damages and its propagation far away from the damages. So, this mode conversion can be detected far away from delaminations and can be used to space the monitoring lines for improving the maintenance productivity. When a sub-interface damage is detected during this first monitoring stage, a finer scan of the suspicious area could be performed to localize and to characterize the damage. This second step will be investigated in the following section.

4 Delamination Localization And Characterization

In this section, the second stage of this NDI method is carried out in order to localize and to characterize the foam core damage detected using the previous configuration. The experimental setup is the same as previously except for the excitation frequency and the PZT disc diameter which are respectively equal to 50 kHz and 30 mm. A 2D-FFT of the waveform measured on the thin face sheet was performed in order to identify the particular waves generated in this configuration (Fig. 10). As shown in the second section, these waves are mainly guided by the foam core. A B-scan of the ultrasonic signal measured at normal incidence with the focalized air-coupled transducer was performed in the 30 mm diameter delamination path (Fig. 11). One can note that a meaningful ultrasonic signal is measured before (from 50 to 90 mm) and after the damage (from 140 mm to 200 mm) while the measured waveform

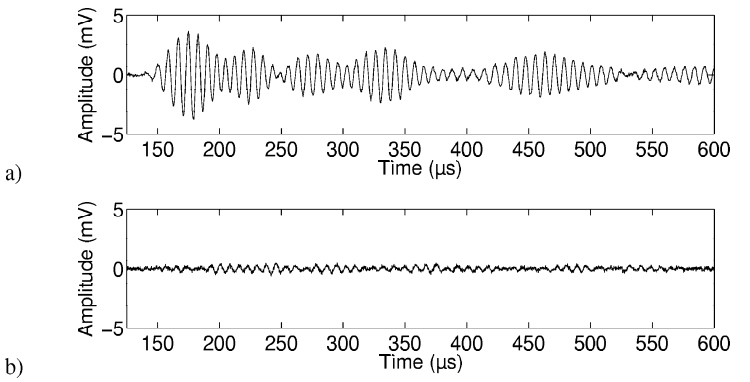

Fig. 6 Waveforms measured at the same point of an undamaged area at 200 mm propagation distance from the emitter and for the air-coupled receiver at a) normal incidence and b) oblique incidence.

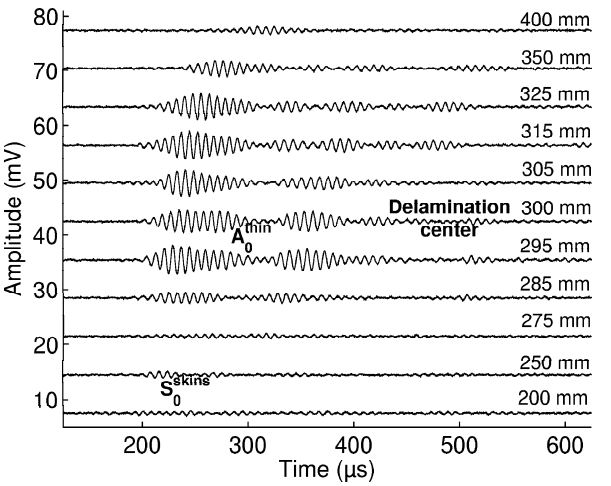

Fig. 7 B-scan of the ultrasonic signal measured at oblique incidence along the 17 mm diameter delamination path.

decreases drastically on the location of the damage. These waves generated in the sandwich structure are mainly guided by the foam core and transmit their displacements to both skins as rigid body motions. This is shown by the fact that the elastic energy contained in the face sheets is weak. That is why at the location of skin/foam core delaminations, displacements of the foam core cannot be transmitted to skins and causes the quick decrease of the waveform amplitude.

To characterize the sensitivity of this method, B-scans have also been performed along the 17 mm and 7 mm diameter delamination paths. The amplitude of the measured waveforms is corrected in order to compensate for sandwich damping and

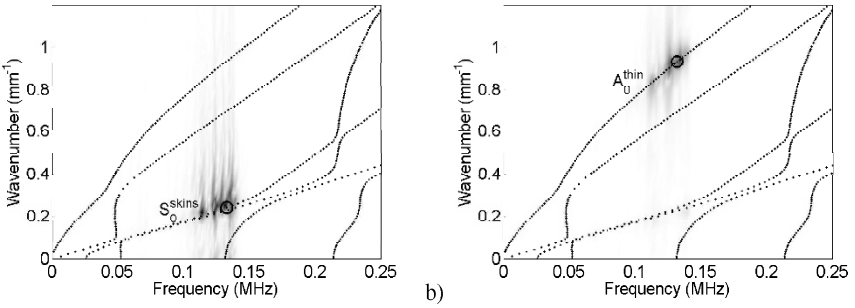

Fig. 8 2D-FFT of the waveform measured along the 17 mm diameter delamination path by the air-coupled transducer a) before the damage and b) after the damage. ◯ indicate the locations on dispersion curves for which the displacement components of the guided waves were calculated. (●●●) correspond to the sandwich structure dispersion curves.

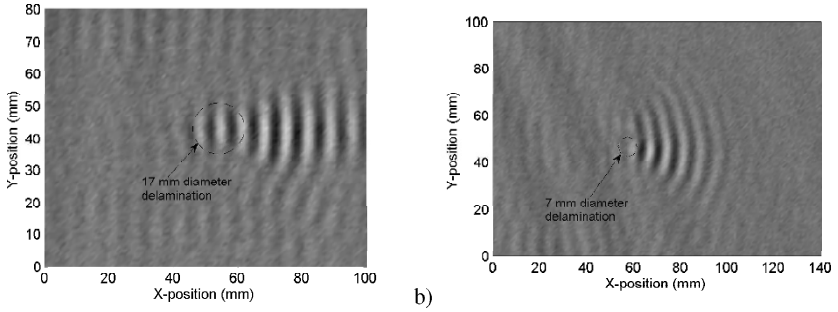

Fig. 9 C-scan images of the S_0^{skins} mode interaction with a) a 17 mm diameter delamination and b) a 7 mm diameter delamination.

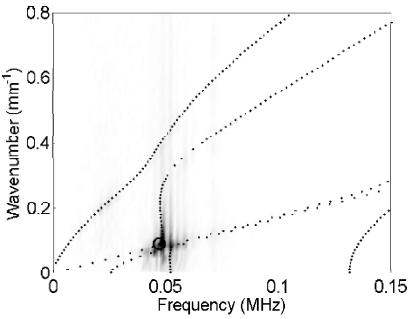

Fig. 10 2D-FFT of the waves launched at 50 kHz by the PZT disc and measured with the air-coupled transducer at normal incidence in an undamaged area.

the geometrical attenuation of the cylindrical wave front [5]. The energy of the corrected waveform measured in each position is calculated and then plotted as a function of the measurement position (Fig. 12). One can note that the waveform energy falls drastically at the location of each delamination. The larger the delamination

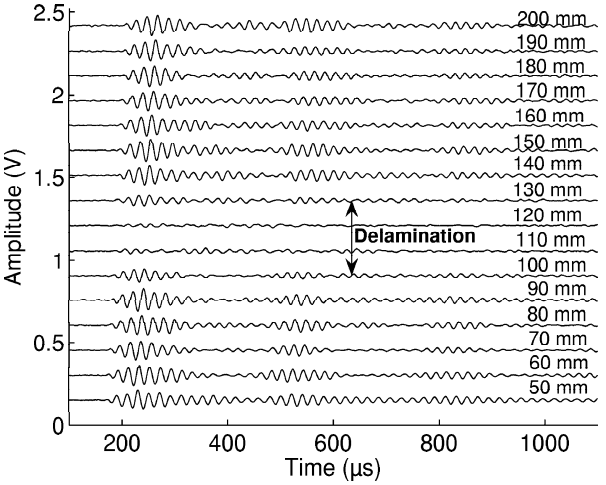

Fig. 11 B-scan of the ultrasonic signal measured at normal incidence along the 30 mm diameter delamination path.

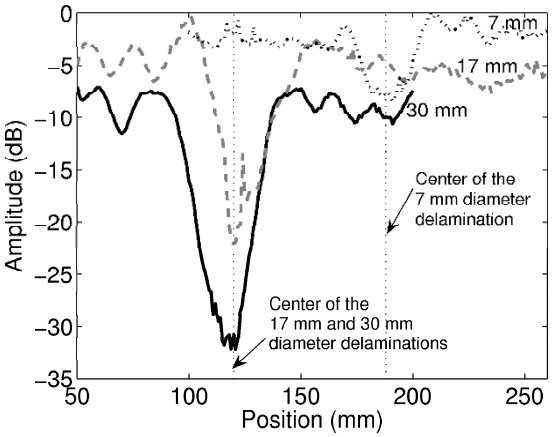

Fig. 12 Energy of the ultrasonic signal measured along the different delamination paths.

is, the more important the attenuation of the waveform energy is. Energy C-scans of guided waves were performed around both 17 mm and 7 mm diameter delaminations (Fig. 13). As can be seen, each sub-interface damage is easily detected and localized. Moreover its size can be evaluated thanks to the attenuation of the waveform energy (Fig. 12). The lack of spatial resolution of this method observed on the C-scan images is due to the wide diameter of the ultrasonic spot. However the out-of-plane displacements of the thin face sheet could also be measured with an optical probe what would improve clearly the spatial resolution of this method.

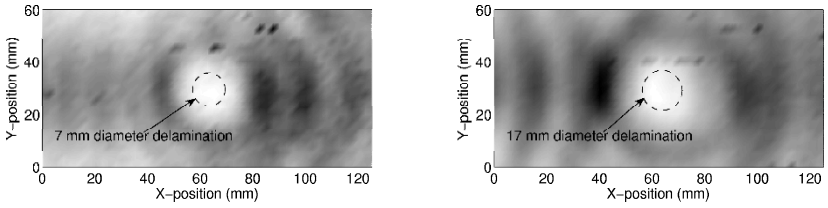

a) b)

Fig. 13 Energy C-scans of guided waves measured at normal incidence at each point of a grid of 2.5 mm steps in x and y directions and around a) a 7 mm diameter delamination and b) a 17 mm diameter delamination. The dashed circular lines indicate the true position of the delaminations.

5 Conclusion

This paper describes a new NDI approach for detecting sub-interface damages in a sandwich structure as for example skin/foam core delaminations and foam core crushing. It consists of a permanently integrated actuator on the structure and to detect the waves guided by the structure using an air-coupled transducer. This monitoring method is divided in two steps: the detection of the foam core damage using a wide step scanning for improving the NDT productivity and then the localization/characterization of the damage using a finer scan of the suspicious area. Both of these experimental methods were defined and optimized according to a theoretical analysis of the waves guided by the sandwich structure. This study allowed also explaining the physical phenomena governing the interaction of these specific waves with a sub-interface damage. Moreover the second experimental configuration can be seen as a generic technique to detect sub-interface damages in most composite structures and could have a very good spatial resolution if the air-coupled transducer was replaced by an optical probe. This last configuration seems also not to be sensitive to edge reflections. Finally, the investigation of this NDI method will be pursued by the monitoring of Non-Visible Damage produced in such sandwich structures by an impact machine.

References

1. Shipsha A (2001) Failure of sandwich structures with sub-interface damage. Report 2001-013, Department of Aeronautics, Royal Institute of Technology, Stockholm, Sweden
2. Balageas D, Krapez JC and al (1999) Industrial applications of infrared thermography. In: Scudieri F and Bertolotti M (eds) The American Institute of Physics, 10th international conference on Photoacoustic and Photothermal Phenomena, 357-361

3. Guo N and Cawley P (1993) The interaction of Lamb waves with delaminations in composite laminates. J. Acoust. Soc. Am. 94(4)
4. Aktas E, Seaver M and al (2007) Detecting Delamination and Core Crushing in a sandwich Composite Wing. In: Fu-Kuo Chang (eds) Structural Health Monitoring
5. Barnoncel D, Osmont D and al (2003) Health Monitoring of Sandwich Plates with Real Impact Damages using PZT devices. In: Fu-Kuo Chang (eds) Structural Health Monitoring
6. Osmont D, Tur M and al (2007) Smart composite material bonded repair. Final report, ONERA, Tel-Aviv University, Israel Aerospace Industries, Israeli MOD, French DGA
7. Knopoff L (1964) A matrix method for elastic wave problems. Bull. Seism. Soc. Am 54:431-438

Sensitivity of the guided waves to the adhesion of lap joints: Finite Element modeling and experimental investigations

H. Lourme, B. Hosten, P. Brassier

Abstract Despite considerable efforts in the last decades to find reliable NDT methods for the control of adhesive joints, the durability and the quality of the adhesive bonding remains troublesome to be determined by ultrasonic non-destructive methods knowing that both the cohesion and the adhesion aspects must be considered. In this paper, the adhesive lap joints between two aluminum plates are first investigated by a finite element approach to compute the transmission and reflection coefficients of Lamb modes. The cohesion is taken into account by the characteristics of the adhesive layer and the adhesion by the interfacial conditions. Two methods are used to compute the energy dissipation: one based on the orthogonality relations and the other based on a signal processing procedure that involves a 2D Fourier transform. Then they can be used to verify the sensitivity of the guided waves to the presence of a contaminant. This model is compared to experimental measurements performed on adhesive lap joints. In order to get reproducible measurements, the detection of the fundamental ultrasonic guided modes is performed with air-coupled transducers.

1 Introduction

Using adhesive joints in the industry instead of screw or rivets has many advantages: they are lighter and the concentration of stresses is reduced. The classical ultrasonic methods like pulse-echo or pitch-catch methods, permits to detect defects like lack of adhesive or porosity but not to quantify the quality of adhesive

H. Lourme, B. Hosten
Laboratoire de Mécanique Physique, Université de Bordeaux, UMR C.N.R.S. 5469, 351 cours de la Libération, 33405 Talence Cedex, France, e-mail: h.lourme@lmp.u-bordeaux1.fr

P. Brassier
ASTRIUM SPACE Transportation, BP20011, Avenue du Général Niox, 33165 Saint Médard en Jalles Cedex, France

joint at the beginning of the structure life and during its life. At the present time, there is no reliable method to control the quality of adhesive joints. There are two aspects to take into account: the quality inside the adhesive (defects, cracks…) i.e. the cohesion and the quality at the interfaces (peeling, presence of a contaminant…) i.e. the adhesion.
The methods for the control of adhesive joints are currently destructive. So an important objective of industry is to find a Non Destructive Testing (NDT) method. Find reliable NDT methods for the control of adhesive joints, the durability and the quality of the adhesive bonding remains troublesome. Indeed it's not easy to consider both the cohesion and the adhesion aspects.
The aim of this work is to try to establish a method to control the quality of adhesive joint. The classical ultrasonic investigations are not satisfactory for the adhesive bonded joint because they usually only have longitudinal effects on the joint. Since ultrasonic guided waves are loading the joint with shear effects, they are promising to investigate the adhesive bonds. In the first part of the paper a model taking into account both the adhesion and the cohesion is introduced. The model is validated by computation of the energy balance with the orthogonality relations and compared to the experimental results by a 2D Fourier Transform.

2 Modeling of the adhesive joint

2.1 The geometry of the samples

Two aluminum plates with the same dimensions, 250 mm length and 3 mm thick, as shown in Figure 1, are bonded with an overlap length of 50 mm. The thickness of the adhesive layer is 0.2 mm. The aluminum is chosen as a well-known material, isotropic and elastic, in order to focalize the study on the lap joint.
Two samples were supplied by ASTRIUM-ST. The first sample is made with an adhesive, which is usually used in industry. This sample is the reference sample. The second sample was prepared with the same adhesive but the interfaces were partly contaminated with silicon in the middle part of the overlap in order to simulate a bad adhesion. The density ρ and the viscoelastic properties C_{11}^* and C_{66}^* of the adhesive, given in Table 1, were measured with a classical transmission method [1]. It's important to note that the imaginary parts of these stiffnesses C_{11}^* and C_{66}^*, obtained by experimental investigations, which take into account the attenuation in the adhesive, play an important rule in the model and can't be ig-

nored.

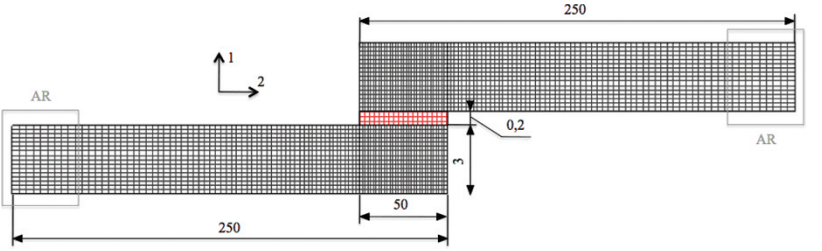

Figure 1: Dimensions (mm) and mesh of the adhesive lap joint.

	Adhesive	Aluminum
ρ (g/cm^3)	1.17	2.78
$C_{11}^* = \frac{E^*(1-\nu)}{(1+\nu)(1-2\nu)}$ (GPa)	6.7 (1 + 0.04 i)	112
$C_{66}^* = \frac{E^*}{2(1+\nu)}$ (GPa)	1.4 (1 + 0.06 i)	27

Table 1: Characteristics of the materials

2.2 The model

A criterion to design a right mesh is to verify, after the computation, that the shear stresses are equal to 0, everywhere at the free surfaces. Of course, 0 means much smaller than the amplitudes of the stresses elsewhere. On the corner of the structure, this can be not completely satisfied in a small area since it was verified that in this case, the local refinement of the mesh does not change the whole result.
So the structure is meshed with 10400 quadrilateral elements and 11271 nodes. In the thickness of the adhesive layer, a minimum of two elements is assumed (Figure 1). Two absorbing regions (AR) are added at the two extremities of the aluminum plates to make the plates semi-infinite and eliminate the undesirable reflections. The adhesive layer enables to simulate the cohesion. Indeed the characteristics of the adhesive can be modified and some defects can be added in order to simulate a decrease in the value of the cohesion. If the continuity of interfacial stresses and displacements is assumed, this model enables only the study of the cohesion. To take into account the adhesion, two surface distributions of springs with stiffnesses k_L and k_T, are added at the interfaces (Figure 2). These stiffnesses are respectively the normal and the tangential stiffness and are defined with the discontinuity of displacements [2]:

$$\sigma_{11} = k_L \left(u_1^+ - u_1^- \right)$$
$$\sigma_{12} = k_T \left(u_1^+ - u_1^- \right) \quad (1)$$

In equation (1), u_1 and u_2 are the normal and longitudinal displacements and σ_{11} and σ_{12} are the normal and the shear stress at the interface.

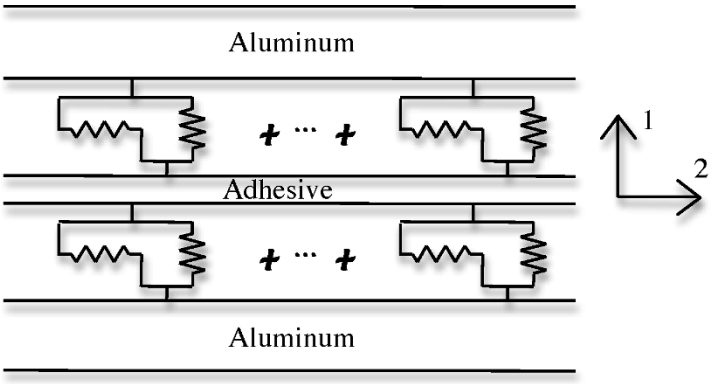

Figure 2: Model of the adhesive layer taking into account the properties of the interfaces.

It is assumed that the presence of a contaminant has essentially an influence on the shear stiffness k_T at the interface. So the longitudinal stiffness k_L is chosen to be equal to the minimum value that simulates a perfect bonding, defined in the following. The decrease of the value of k_T represents the loss of adhesion for studying the interfacial contamination. In the Finite Element program [3], the displacements discontinuities at the interfaces are introduced by using a "multiphysic" approach [4].

3 Computation of the intrinsic amplitudes

To check the model, the energy balance is computed with the reflection and transmission coefficients, which are the ratios between reflected and incident amplitudes and between transmitted and incident amplitudes (Equation 2).

$$R_m = \frac{\alpha_R^m}{\alpha_I} \qquad T_m = \frac{\alpha_T^m}{\alpha_I} \quad (2)$$

The energy balance E is the ratio between the sum of reflected and transmitted energies and the incident energy. These energies are the sums of the energies carried

by all the modes m. The energy carried by a mode is proportional to the square of the intrinsic amplitudes α^m. Then the energy balance is defined by:

$$E = \frac{\sum_m \left(\alpha_R^{m2} + \alpha_T^{m2}\right)}{\sum_m \alpha_I^{m2}} \tag{3}$$

The intrinsic amplitude of a mode m is defined by these relations:

$$\mathbf{U} = \alpha^m \begin{bmatrix} u_1(x_1) \\ u_2(x_1) \end{bmatrix} e^{-ik_m x_2}, \quad \sigma = \alpha^m \begin{bmatrix} \sigma_{11}(x_1) \\ \sigma_{22}(x_1) \\ \sigma_{12}(x_1) \end{bmatrix} e^{-ik_m x_2} \tag{4}$$

To compute the intrinsic amplitude of each mode, two methods are introduced.

4 Signal processing based on a 2D Fourier Transform.

This method can be used for the model and the experimental results. The intrinsic amplitudes of each mode are deduced from the displacements fields at the surface of the plate. The monitored zones are two regions at the surface of the plate: one before the joint and the other after the joint.

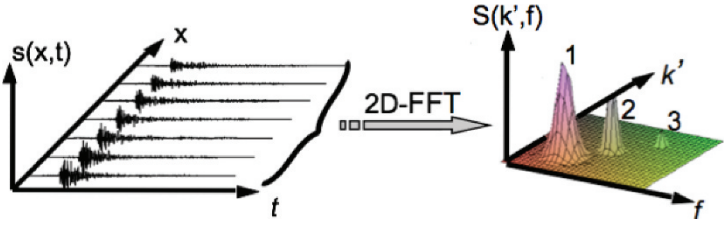

Figure 3: Space/Time to Frequency/Wave number transformation

From the data in the time/space domain, a two-dimensional Fourier Transform [7] gives results in the frequency/wave number domain taking into account the spatial window [5] as shown in Figure 3. At a given frequency the amplitude at the surface of each mode $A^m_{(x_1=0)}$ can be obtained. This amplitude is the amplitude of the normal displacement at the surface in the centre of the spatial window [5]. A power-normalized mode is defined as a mode carrying an energy equal to 1 [5-6].

Knowing the power-normalized displacements field $u^m_{1(x_1=0)}$ at the surface of the aluminum plate, given by a semi-analytical computation [8], the intrinsic amplitudes are computed by:

$$\alpha^m = \frac{A^m_{(x_1=0)}}{u^m_{1(x_1=0)}} \tag{5}$$

This signal processing needs only the normalized displacements field at the surface and the amplitudes at the surface, which are obtained with a set of signals computed or required experimentally.

4.1 The orthogonality relations

This post process computation uses the results of the FE model given along two cross sections into the aluminum plates, one before the joint for the incident and reflected modes and the other after the joint for the transmitted modes. Like in the previous section the powered-normalized fields of displacements and stresses of mode m are given by a semi analytical computation. So the intrinsic amplitude of each mode are given by the following relation:

$$\alpha_m = \frac{\int_0^h \left(\sigma^m_{12}\, u^{tot}_1 + \sigma^{tot}_{12}\, u^m_1 - \sigma^m_{22} u^{tot}_2 - \sigma^{tot}_2\, u^m_2\right) dx}{2\int_0^h \left(\sigma^m_{12}\, u^m_1 - \sigma^m_{22}\, u^m_2\right) dx}, \tag{6}$$

where h is the thickness of the aluminum plate and the symbol "*tot*" means the displacements and the stresses fields computed by the FE model that includes the contribution of all the modes. Then the reflection and transmission coefficients and the energy balance can be obtained with the relations (2) and (3). Since this method needs the displacements and the stresses fields in a cross section of the plate, it is not possible to use it for the experimental results, only for the results of the model.

5 Validation of the model with the orthogonality relations

In order to validate the model, two cases are studied. First the imaginary parts of the adhesive are suppressed to make the adhesive elastic, for which the expected energy balance is 1. In Figure 4 a), the energy balance plotted as a function of the frequency permits to verify the quality of the model. The second validation is the comparison between the model without springs and the model with springs in which the stiffnesses k_L and k_T are chosen to assume a perfect bonding. In these

models, the adhesive is viscoelastic. In Figure 4*b)*, the results of the models are very close. Because of the viscoelasticity of the adhesive, the energy balance is less than 1 and the variation of the energy balance as a function of the frequency is probably due to some resonances into the joint. To reach this result, the values of the stiffnesses k_L and k_T have been set to a minimum large value of 10^6 GPa/mm that defines the value for obtaining a perfect bonding.

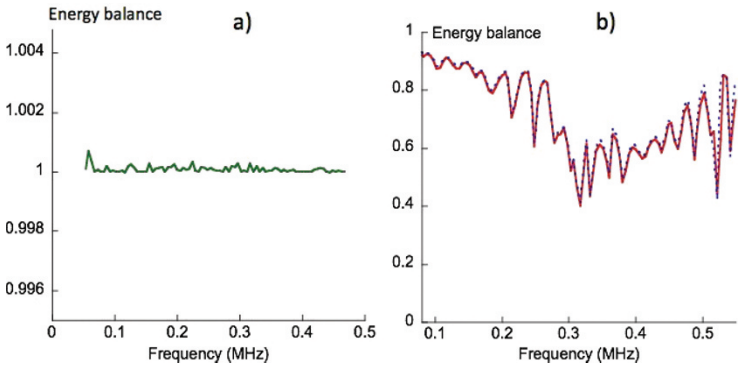

Figure 4: Validation of the model: a) Elastic case, b) Viscoelastic case (Doted line:without springs), (Continuous line : with springs).

6 Study of the adhesion - Impact of a contaminant in the model

6.1 Two cases of studies

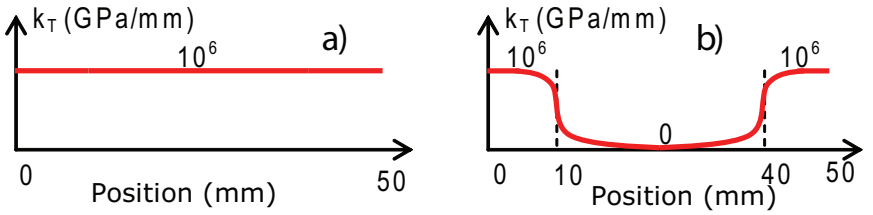

Figure 5: Values of k_T versus the position (mm) in the length of the joint: a) Perfect joint, b) Contaminated joint

Now the effect of a contaminant at the interfaces of the joint is studied with the Finite Element model. Two cases represent the experimental samples. The first sample is equivalent to a good adhesion (no contamination is present). For that,

the shear springs is chosen to be high (k_T = 10^6 GPa/mm). The second sample simulates a joint with interfaces partly contaminated. Figure 5 shows the shape of the k_T value along the joint for the two cases.

6.2 Results of the model

The A_0 mode is generated in the aluminum plate in a range of frequencies going from 0.1 kHz to 550 kHz. This mode is transmitted, reflected, converted and dissipated. Figure 6 gives the reflection and transmission coefficients of the A_0 mode. These coefficients are locally sensitive to the adhesion, but not always in the same frequency area. However around 400 kHz, the sensitivity to the contamination is important as well for the reflection as for the transmission coefficient. Then the model permits to choose the frequency domain, around 400 kHz for the experimental study.

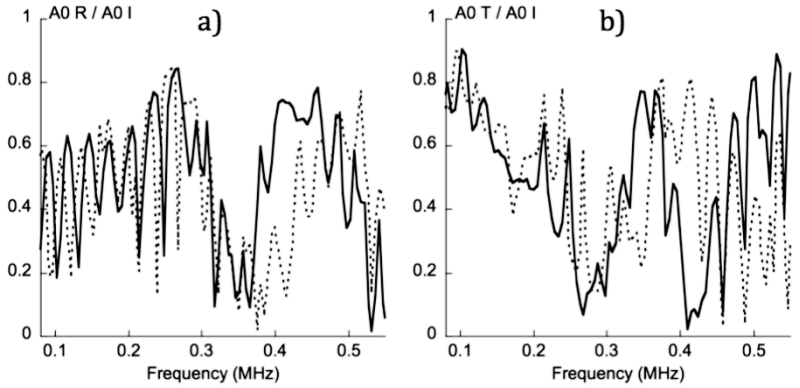

Figure 6: Results of sensitivity to a contaminant: Solid line no contaminant, Dotted line contaminant a) Reflection coefficient, b) Transmission coefficient

7 Validation with the experiments

7.1 Experimental set-up

For the generation of A_0 mode, the transmitter and the receiver are both air-coupled transducers (Figure 7). These transducers need no contact with the plates so the reproducibility of the measures is realized. The angles of the transducers must satisfy the Snell Descartes relations for transmitting or receiving a specified mode. The angle of the transmitter is fixed to the angle of A_0 and the angle of the

receiver is adjusted to the angle of A_0 (9.5°) or S_0 (3.5°) since the joint can introduce some mode conversion. So the post-processing is simplified because the modes are already almost isolated.

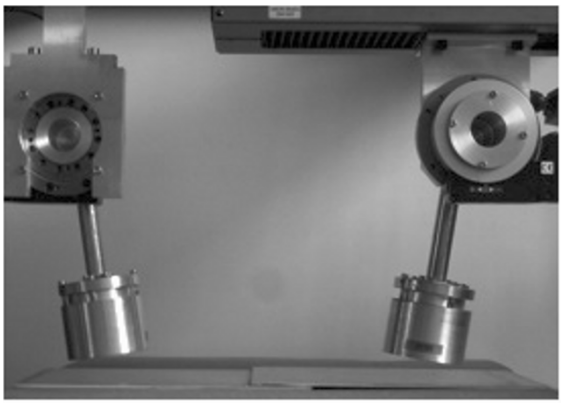

Figure 7 Experimental set-up of the generation of the A_0 model

The receiver can also be translated for scanning the plate and for obtaining a set of signals in the time/space domain. Then a double Fourier transform transforms this domain in the frequency/wave number domain to measure the amplitude of the modes [5].

7.2 Experimental results with A_0 incident

The measurements are made several times and the results given in Table 2 are the averaging of these different measures with standard deviations. A_0 mode is generated at 400 kHz, the frequency at which the model is sensitive to the contamination of the interfaces. Like the model the experiments give very different reflection and transmission coefficients in the case of presence or absence of contaminant. So this mode at this frequency seems sensitive to the contamination. The comparison with the results of FE model (given in Table 2) shows very satisfying results. Indeed the experimental coefficients are close to those for the model.

		Reference	Contaminated
Model	R/I	0.66	0.34
Experiments	R/I	0.60 ± 0.08	0.29 ± 0.03
Model	T/I	0.34	0.55
Experiments	T/I	0.27 ± 0.03	0.64 ± 0.05

Table 2: Experimental and model results for the generation of the A_0 mode in the case of the reference lap joint and contaminated lap joint

8 Conclusion

A FE model to evaluate the quality of the adhesion of a lap joint, based on a repartition of springs at the interfaces between adhesive and adherent was presented. This model was tested with two methods to compute the intrinsic amplitude of each mode: one based on a signal processing applied to the model results and the experimental results and the other based on the orthogonality relations. It was used for studying the presence of a contaminant for which it was found that the guided mode A_0 is sensitive to its presence.
The comparison between the results of the model with optimal and decreased stiffnesses permits to find the frequency domain for which the reflection and the transmission of the guided mode is the most sensitive. The good fitting between the experimental results and the model results permits to validate this sensitivity to the value of the adhesion.
In the future, some mechanical tests will be made to link the results of ultrasonic guided waves investigations to the mechanical results. Other materials like elastomer or composite will be investigated since they are more and more used in the industry.

References

1. M. Castaings, B. Hosten, and T. Kundu, “Inversion of ultrasonic, plane-wave transmission data in composite plates to infer viscoelastic material properties” NDT&E Int. 33(6), 377-392 (2000).
2. M. Schoenberg, “Elastic wave behavior across linear slip interfaces”, J.Acoust. Soc. Am. 68(5), 1516-1520 (1980).
3. COMSOL Multiphysics User's Guide, Version 3.4 by – http://www.comsol.com /(Last visited in May 2008)
4. B.Hosten and M.Castaings "Finite Elements methods for modeling the guided waves propagation in structures with weak interfaces" J.Acoust. Soc. Am. 117 (3) 1108-1113 (2005)
5. B. Hosten, L. Moreau, M. Castaings, “Reflection and transmission coefficients for guided waves reflected by defects in viscoelastic material plates”, J. Acoust. Soc. Am. 121(6) 3409-3417 (2007).
6. L. Moreau, M. Castaings, B. Hosten, “An orthogonality relation-based technique for post-processing finite element predictions of waves scattering in solid waveguides”, J.Acoust. Soc. Am. 120(2), 611-620 (2006).
7. D. Alleyne, P. Cawley, “A two dimensional Fourier transform method for the measurement of propagating multimode signals”, J.Acoust. Soc. Am. 89(3), 1159-1168 (1991).
8. B. Hosten, M. Castaings, “Surface impedance matrices to model the propagation in multilayered media”, Ultrasonics 41, 501-507 (2003).

Guided waves in empty and filled pipes with optimized magnetostrictive transduction

A. Phang and R. Challis

Abstract This paper considers the design of magnetostrictive transducers for the excitation and detection of guided waves in pipes, as part of an apparatus for monitoring pipeline contents in a chemistry laboratory. The transducer design and sensitivity were optimised on the basis of equivalent electrical circuits, the guided wave excitability function and a frequency-domain filter based on the effect of the dynamic magnetic field on the excitable spatial wavenumbers. Experiments were carried out on pipes with different contents - empty, water, and supercritical CO_2. Reassigned Spectrogram analysis of the results enabled the pipe contents to be differentiated on the basis of resolving the guided wave modes.

1 Introduction

Magnetostrictive transduction of guided wavess in rods and pipes have been reported by many workers and significant contributions are to be found in [1]-[4]. In the context of the design of the transducer and its associated electronics it is significant to note that excitation voltages and currents up to 300V and 40 A respectively have been used in order to provide adequate signal levels. The purpose of our system was to differentiate between three pipe contents – empty, when filled with water, and when filled with super-critical CO_2. The apparatus was to be used in a chemistry laboratory, and for safety reasons it was necessary to use low voltage/current excitation to the transducers, our aim being to limit the voltage and currents to no more 100 V and 1 A respectively. Therefore the transducer design requires optimisation in relation to the propagating modes and overall signal levels.

School of Electrical and Electronic Engineering, University of Nottingham, University Park, Nottingham NG7 2RD, UK.
e-mail : albert.phang@nottingham.ac.uk

This paper considers the transducer design, taking into consideration the effects of the spatial distribution of the exciting magnetic field associated with the transducers on guided wave excitation and reception, in combination with the signal transfer characteristics of the driving and receiving electronics. The sensitivity of the overall system may then be optimised, in relation to the electrical conditions and frequency bandwidths achievable. Differentiation of contents of the pipe would be based on changes to the characteristics of the propagating guided wave modes over the frequency range 0 to 500 kHz.

Guided wave modes in pipes with different contents

This work was carried out on a high-pressure, stainless steel (316L) Swagelok (Solon, OH, USA) pipe, to allow operation with different fluids including CO_2 at the supercritical state (above 304.2 K temperature and 73.8 bar pressure). The pipe diameter was 12 mm with wall thickness of 2 mm. The outer surface of the pipe was electroplated with nickel (0.1 mm thickness) to provide the required magnetostrictive properties. Longitudinal modes will be considered in this work, on account of their established feasibility for interrogation of fluid-filled pipes [4].

Figs. 1-2(left) show, respectively, the dispersions for the longitudinal modes for the pipe when empty, when filled with water, and when filled with supercritical CO_2, from 0 to 500 kHz. The dispersions were obtained using the *DISPERSE* simulation package [5]. There are clear differences between the guided wave modes, depending on the contents of the pipe. Specifically, the presence of fluids in the pipe will introduce additional modes over the given frequency and wavenumber bandwidths, i.e. L(0, 1), L(0, 2) and L(0, 3) for the water filled pipe, and L(0, 1) to L(0, 8) inclusive for the pipe filled with super-critical CO_2.

The extent to which any given mode is excitable depends on the distribution of motions across the pipe wall (the mode shape) particularly the amplitude of the motion at the pipe outer surface, where the magnetostrictive transduction will be applied. A useful quantitative measure of the excitability of a guided wave mode is $E(\omega)=A\,\omega$, where A is the displacement amplitude at the surface of the pipe and ω is radian frequency [6]. As an example, Fig. 4 shows the excitability function calculated for the L(0, 1) mode from the mode shape obtained using *DISPERSE*. The drop in excitability around 150-180 kHz is in accordance with the guided wave characteristics, which at that frequency range is most dispersive.

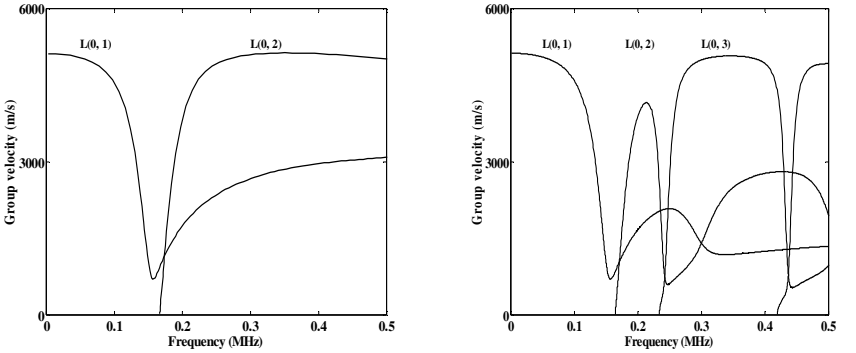

Fig. 1: Dispersion curves (group velocity versus frequency) for the Swagelok pipe when it is empty (left); and when it is filled with water (right).

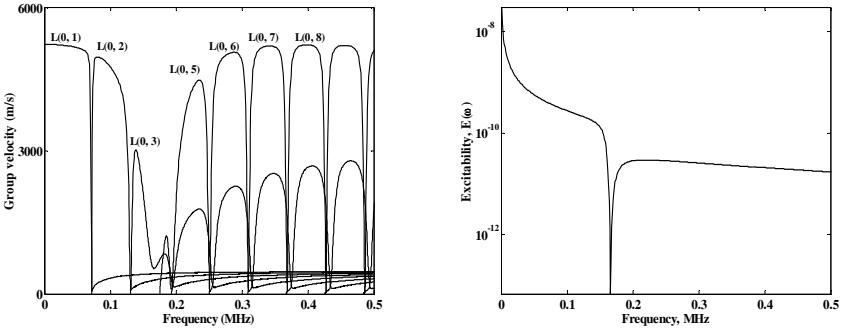

Fig. 2: (left) Dispersion curves (group velocity versus frequency) when the pipe is filled with supercritical CO_2; (right) Excitability of the L(0,1) mode versus frequency, for the empty pipe.

Magnetostrictive transduction

The magnetostrictive transducer comprised enamelled copper wire (diameter 0.762 mm) wound in a tight spiral onto a polystyrene tube with a bore diameter of 12 mm. The winding was held in place by circular side cheeks of 0.5 mm thick polystyrene sheet aligned axially on to the tube and adhered to it. Coils of 15, 30, 60 and 100 turns were prepared. Six Alcomax bar magnets (RS Components, UK, part number 297-8747) were used to provide a static biasing magnetic field. Each transducer was connected to a 50 Ω coaxial cable, which is in turn connected to the system electronics.

The basic scheme for the magnetostrictive transduction is that a static magnetic field H_s (from the magnets) is applied to bias the material (nickel layer), and an alternating field H (from the spiral coil) is superimposed in order to excite wave motion. When a sufficiently strong bias field ($H_S >> H$) is applied then the

magnetostrictive behaviour is both linear and non-hysteretic [7]-[8]. The stress σ and magnetic flux B in the material are

$$\sigma = c^H \varepsilon - e^\varepsilon H \tag{1}$$

$$B = e^H \varepsilon + \mu^\varepsilon H \tag{2}$$

where ε is mechanical strain, H is the alternating field, and c^H, e^ε, e^μ, and μ^ε are constants; the superscripts H and ε imply constant field and constant strain respectively. Given these basic relationships, the applied alternating field and the associated spatial distribution along the pipe will restrict the frequency-wavenumber range over which guided waves can be successfully excited and received. These restrictions can be expressed in terms of an overall system frequency response which applies over and above the basic excitability outlined above. The response can conveniently be expressed as

$$G(\omega) = E(\omega)G_{kT}(\omega)G_{ET}(\omega)G_{kR}(\omega)G_{ER}(\omega)Y(\omega) \tag{3}$$

where $E(\omega)$ is the excitability of the guided wave mode transmitted, $G_{kT}(\omega)$ and $G_{kR}(\omega)$ are functions which result from the spatial distribution of the applied alternating magnetic field, for the transmitting and receiving transducers, respectively. $G_{ET}(\omega)$ and $G_{ER}(\omega)$ are the respective frequency responses associated with the transmitting and receiving coils. $Y(\omega)$ is the fixed response of the transmitting and receiving electronics. Each of these frequency response functions will now be analysed.

Spatial distribution of the alternating field

The magnetostrictive transducer was based on a flat spiral coil of radius a consisting of N turns and mounted axially on a pipe of radius x. The coil generates the exciting magnetic field around the periphery of the pipe, in the direction of the pipe axis. The distribution in space of the intensity of this field then set bounds on the range of guided wavenumbers which were excitable, because the effective magnetic aperture acted as an extended acoustic source. The axial distribution of such a field in a non-magnetic medium is a classical solution [9]; calculation of the field parallel with the coil axis but at a point displaced from it by distance x (the radius of the pipe in this case) was derived on the basis of the Biot-Savart law with the following result

$$H(z) = \frac{INa}{2\pi} \int_0^\pi \frac{(a - x\cos\varphi)d\varphi}{(a^2 + x^2 + z^2 - 2ax\cos\varphi)^{3/2}} \tag{4}$$

where the integration variable ϕ corresponds to a geometrical angle on the plane of the coil, and may be integrated numerically. Fig. 3 (left) shows the distribution of the field in the axial, z-direction on the pipe surface for x = 6.1 mm. The finite dimensions of the function imply a limitation to the range of wavenumbers which are excitable. Fourier transformation of $H(z)$ gives the effective filter in wavenumber domain, and the equivalent filter in the frequency domain, $G_{kT}(\omega)$, can be obtained by reference to the dispersion curve for the guided wave mode of interest. As an example, Fig. 3 (right) shows $G_{kT}(\omega)$ for the L(0, 1) mode in the empty pipe. The same reasoning can be applied to the receiving transducer, so the transmit-receive product may be expressed as

$$G_k(\omega) = G_{kT}(\omega)G_{kR}(\omega) \tag{5}$$

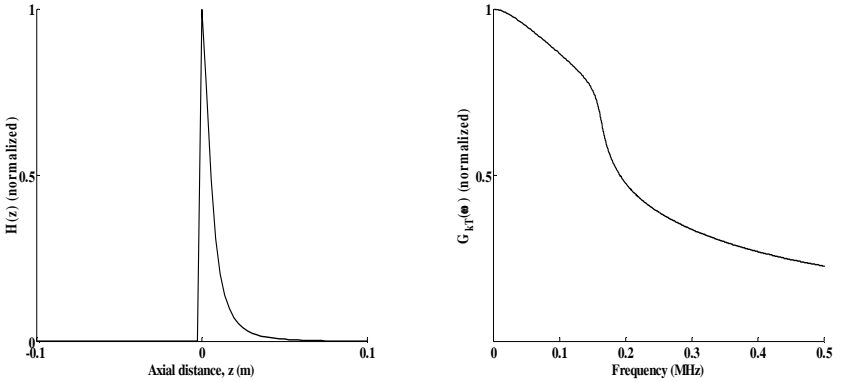

Fig. 3: (left) Spatial distribution of the alternating field in the axial direction for x = 6.1 mm; (right) The function $G_{kT}(\omega)$ for the L(0,1) mode in the empty pipe, as a function of frequency.

Equivalent electrical circuit: transmitting coil

If the transmitting coil of inductance L_T is excited by a conventional Thévenin source of output resistance R_s, the equivalent circuit is that of Fig. 4(left). The transmission sensitivity is then

$$G_{ET}(\omega) = \frac{k_{T1}N_T}{R_s + j\omega L_T} = \frac{k_{T1}N_T}{R_s + j\omega k_{T2}N_T^2} \tag{6}$$

and is therefore dependent on the source resistance R_S, operating frequency ω and the number of turns N_T. k_{T1} and k_{T2} are constants of proportionality which we do not derive theoretically; k_{T2} depends on the effective permeability of the magnetic circuit, the coil radius and axial length, and measured values were of the order of$3.5\text{x}10^{-8}$ Henries per (turns)^2. An optimization scheme is required to arrive at

working combinations of frequency, source resistance and number of turns. In real systems, the source resistance R_S will likely be restricted by the system electronics, a typical value being 50 Ω. If we take the modulus of equation 6, differentiate with respect to N_T and set the result to zero we obtain

$$R_s = \omega k_{T2} N_T^2 \tag{7}$$

For given R_s and ω the optimum number of turns is then

$$N_{opt} = \sqrt{\frac{R_s}{\omega k_{T2}}} \tag{8}$$

As a design example, Fig. 4(right) shows N_{opt} versus frequency for R_s = 50 Ω and a typical value of $k_{T2} = 3.5\text{x}10^{-8}$.

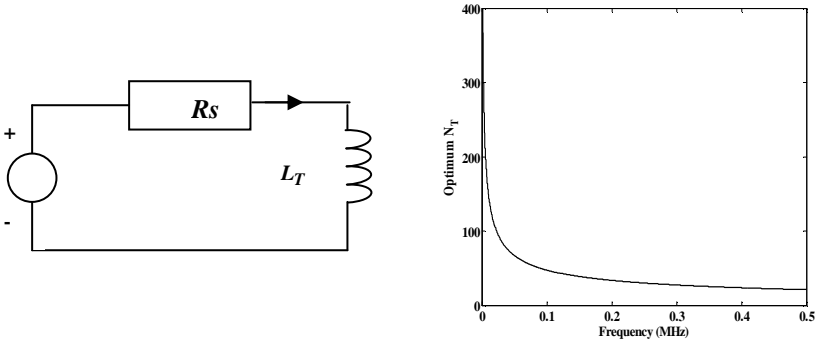

Fig. 4: (left) Equivalent circuit for the transmitting magnetostrictive transducer; (right) Optimum number of turns on the coil, N_{opt} versus frequency for R_s = 50 Ω and $k_{T2} = 3.5\text{x}10^{-8}$.

On the receiving end, the arriving guided wave results in changes to the mechanical strain and magnetic permeability – both terms in equation 1 - on the nickel layer on the pipe. These then result in changes to the magnetic flux linking the coil, which then generates a signal voltage with a rate of change which follows that of the changing flux. The equivalent circuit for the receiving transducer is shown on Fig. 5(left). Neglecting the effect of the capacitance of the cable between the transducer and the receiver amplifier, the receiver sensitivity (at the amplifier terminals) is then

$$G_{ER}(\omega) = \frac{j\omega k_{R1} N_R R_{IN}}{R_{IN} + j\omega L_R} = \frac{j\omega k_{R1} N_R R_{IN}}{R_{IN} + j\omega k_{R2} N_R^2} \tag{9}$$

As before, k_{R1} and k_{R2} are constants of proportionality, and R_{IN} will likely be constrained to 50 Ω (typical value) by the input impedance of the receiver

amplifier in a real system. The optimum value of N_R is found in the same way as for the transmitter, giving

$$N_{opt} = \sqrt{\frac{R_{IN}}{\omega k_{R2}}} \tag{10}$$

Fig. 5 (right) shows N_{opt} versus frequency for this condition, given a typical value of $k_{R2} = 3.5\text{x}10^{-8}$.

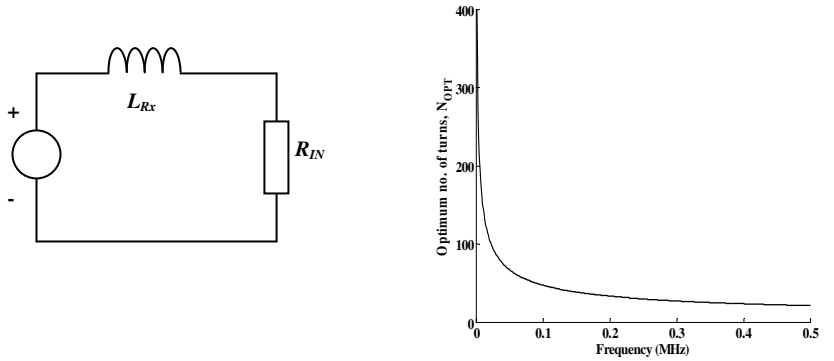

Fig. 5: (left) Equivalent circuit for the receiving magnetostrictive transducer. (right) Optimum number of turns on the coil, N_{opt} versus frequency for $R_{IN} = 50\ \Omega$ and $k_{R2} = 3.5\text{x}10^{-8}$.

Experiments: transducer sensitivities

The purpose of the experiments was to evaluate the overall transmit-receive sensitivity given by equation 3 for different transducer arrangements. The L(0, 1) mode was propagated between two magnetostrictive transducers in an empty pipe. The overall sensitivity could then be verified by fixing the receiving transducer and changing the transmitting transducer conditions, or *vice-versa*.

The transmitting transducers were driven using a *Wavemaker Duet* unit (Wavemaker, Macro Design Ltd., London, UK) which had an output resistance R_S of 50 Ω and was set to generate five-cycle Hanning windowed sine-wave bursts at 100 V amplitude in the frequency range 50 kHz (the minimum possible) to 150 kHz, which is the frequency range over which the mode L(0, 1) is non-dispersive. The receiver amplifier formed part of an *Embedded Ultrasonic Instrument* (EUI, NDT Solutions Ltd., Chesterfield, UK), and had an input resistance R_{IN} of 50 Ω and programmable gain between -20 dB and +60 dB. The amplifier output was digitised using a digital storage oscilloscope (LeCroy 9341CM, LeCroy, Chestnut Ridge, NY, USA) which was in turn connected to a personal computer for processing and analysis.

Fig. 6(left) shows the overall sensitivities as functions of frequency, for two transmitting coils with different numbers of turns (N_T = 15 and 30 turns), and a receiving coil of N_R = 100 turns. The experimental results are in reasonable agreement with the theory. A similar result may be obtained by fixing the transmitter and changing the number of turns on the receiver. In a real system however, it would be advantageous to use the same number of turns on both transducers, in addition to the 50 Ω constraints on R_s and R_{IN}. The calculated overall sensitivities for these conditions are shown versus frequency on Fig. 6(right) for four values of N – 15, 30, 60 and 100 turns respectively. The sensitivity increases as N increases but tends to saturate as N approaches 100, due to the dominance of the inductance terms (N^2) in the denominators of equations 10 and 12 at higher values of N. The frequency at which the peak sensitivity occurs reduces as N increases, due to the significance of the inductance terms in the denominators of equations 6 and 9. Whilst N should be chosen to maximise the response at any chosen frequency, a value of N around 60 turns in our case provides a close to optimum response over a range of frequencies.

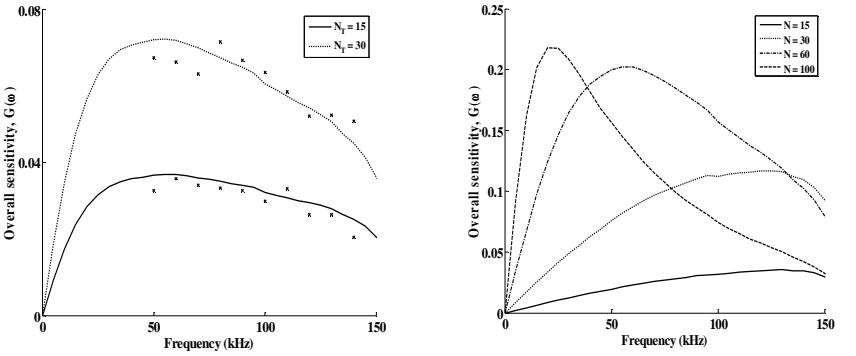

Fig. 6: (left) Overall sensitivity as functions of frequency for two transmitting coils with different numbers of turns (N_T = 15 turns – bottom; N_T = 30 turns - top), and a receiving coil of N_R = 100 turns. R_s and R_{IN} are 50 Ω. Crosses indicate experimental measurements, while solid lines represent numerical predictions from equation 3; (right) Overall sensitivity $G(\omega)$ as functions of frequency, for different numbers of turns on identical transducers (N = 15, 30, 60 and 100). Both R_s and R_{IN} are constrained to 50 Ω.

Experiments: empty and fluid filled pipes

The objective of these experiments was to differentiate between different contents in the pipe, by using the magnetostrictive transducers to excite and detect guided waves under these different conditions, and resolving changes in the guided wave dispersion curves. To excite wave modes over a broad frequency range the

transmitting transducer was driven using 100 V broadband pulses of 1 μs duration in lieu of the sinusoidal bursts used earlier. The pulses were generated by the *Embedded Ultrasonic Instrument* (see previous section) with an output resistance of 50 Ω. The received signals were processed using the Reassigned Spectrogram [10] method to provide a time-frequency representation of the signal, which then represents the arrival times of the guided wave packets. For verification, the software package *DISPERSE* was used to numerically evaluate the group velocity dispersions as functions of frequency. Division of the wave propagation distance by the group velocity dispersions then produces a time-frequency representation of the expected arrival times of the guided wave packets.

Figs. 8-9 give the experimental results showing the reassigned spectrogram data superimposed onto the transformed dispersion curves. In all three cases there is excellent agreement between the spectrograms and the expected dispersion curves. The spectrogram for the supercritical CO_2 is less well defined, due to the low density of the fluid which results in a correspondingly low coupling between the energy associated with the wave in the pipe wall and the fluid. The contrast of the processed data was enhanced by means of a logarithmic transformation with the result that the new modes could be identified clearly on the reassigned spectrogram.

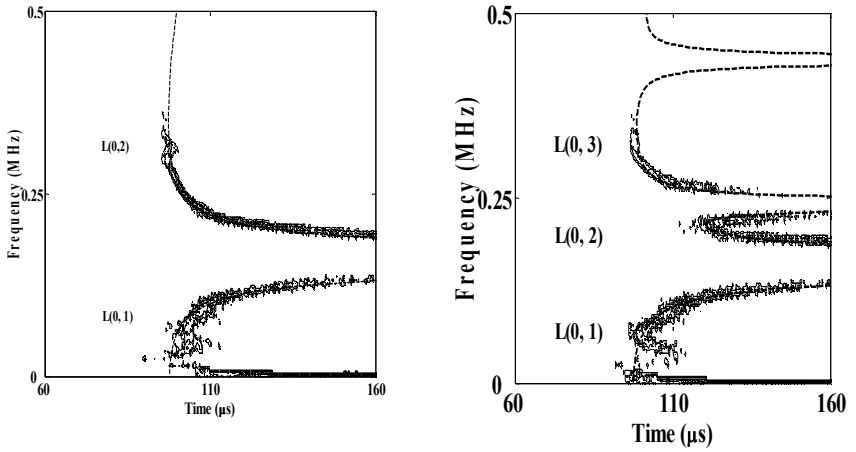

Fig. 8: (left) Reassigned spectrogram showing guided wave modes in the empty pipe, superimposed onto transformed dispersion curves. (right) Reassigned spectrogram showing guided modes in the pipe when filled with water, superimposed onto transformed dispersion curves.

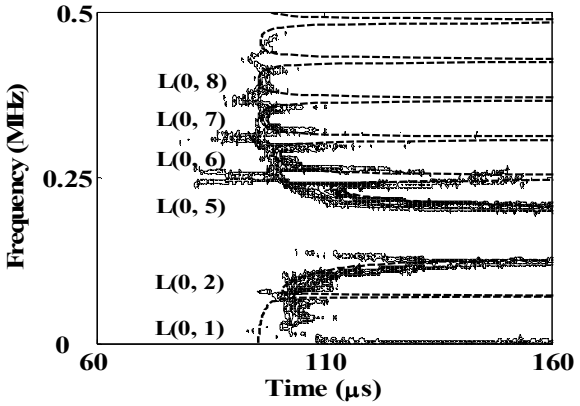

Fig. 9: Reassigned spectrogram showing guided modes in the pipe when filled with supercritical CO_2, superimposed onto transformed dispersion curves.

Concluding remarks

The principles of guided wave transduction using magnetostrictive transducers on pipes have been established by previous workers, however such systems tended to require high voltage and current excitations in order to provide adequate signal levels. Our aim was to develop a relatively simple and compact apparatus for operation in a chemistry laboratory, and this required low voltage and current excitations to the transducers due to safety concerns. Therefore it was necessary to optimise the design and sensitivity of the transducers within the frequency and wavenumber bandwidths required. This required careful consideration of the equivalent electrical circuit responses, guided wave excitability and the effects of the dynamic excitation magnetic field in the axial direction. In real applications, the system electronics will likely impose constraints on the electrical resistances of the transducers; the overall transducer sensitivities therefore depend on optimising the number of turns on the transducer coils. Experimental sensitivity results showed good agreement with expected results obtained from equations. Measurements were carried out on a thick-walled stainless steel pipe when empty, when filled with water and when filled with supercritical CO_2, and the results were processed using the Reassigned Spectrogram method. Clear differentiation of the pipe contents was achieved, and the spectrograms indicated quantitatively good agreement with expected dispersion curves calculated using *DISPERSE*.

References

[1] Kwun, H., Teller, C. M., "Magnetostrictive generation and detection of longitudinal, torsional and flexural waves in a steel rod", *J. Acoust. Soc. Am.*, **92(2)**, pp. 1202-1204, 1994.

[2] Kwun, H., Bartels, K. A., "Experimental observation of wave dispersion in cylindrical shells via time-frequency analysis", *J. Acoust. Soc. Am.*, **97(6)**, pp 3905-3907, 1995.

[3] Kwun, H., Bartels, K. A., Dynes, C., "Dispersion of longitudinal waves propagating in liquid-filled cylindrical shells", *J. Acoust. Soc. Am.*, **105(5)**, pp 2601-2611, 1999.

[4] Laguerre, L., Aime, J.-C., Brissaud, M., "Magnetostrictive pulse-echo device for non-destructive evaluation of cylindrical steel materials using longitudinal guided waves", *Ultrasonics*, **39**, pp. 503-514, 2002.

[5] Pavlakovic, B., Lowe, M. J. S., Alleyne, D. N., "*DISPERSE*: a general purpose program for creating dispersion curves," in *Review of progress in QNDE*, **16A**, pp. 185-192, 1997, ISBN: 0306455978

[6] Wilcox, P., "Modeling the excitation of Lamb and SH waves by point and line sources", *in Review of Progress in QNDE*, **23**, 2004.

[7] Seco, F., Martín, J. M., Jiménez, A. R., *5th World Congress on Ultrasonics Proceedings* (ISBN 2-9521105-0-6), Paris, September 2003.

[8] E du Tremolet de Lacheisserie, *Magnetostriction*: *Theory and Applications of Magnetoelasticity*, CRC Press, 1993.

[9] Bleaney, B. I. and Bleaney, B., Electricity and Magnetism, Oxford University Press, 3rd Edition, 1976.

[10] Auger, F., Flandrin, P., "Improving the readability of time-frequency and time-scale representations by the reassignment method", *IEEE Trans. Sig. Proc.*, **43**, pp. 1068–1089, 1995.

Piezoelectric material characterization by acoustic methods

E. Le Clézio, T. Delaunay, M. Lam, G. Feuillard

Abstract Two characterization methods of piezoelectric materials based on acoustic measurements are presented. Their main objective is to identify the entire set of electromechanical constants of piezoelectric materials from a single sample. In order to characterize new materials like single-crystals with small dimensions, the first section of the paper presents an identification protocol based on the study of the resonance spectra of parallelepipeds. The second characterization method is performed by means of the measurement of the transmission coefficients of plane waves propagating through an immersed plate. It is suitable for the determination of the properties of bulk piezoelectric ceramics.

1 Introduction

Piezoelectric material manufacturers are looking for characterization methods allowing the control of the quality, of the reliability and of the reproducibility of their production. Moreover, the complete set of constants of the constitutive materials is needed to design complex devices. Classical characterization methods are based on electrical measurements [1], and can not be applied to any kind of sample shapes and sizes. At least three samples have to be used to identify the entire electromechanical tensors [2] leading to possible inconsistencies in the identified material constants. The main objective of the methods presented in this paper is to identify the entire set of electromechanical properties of piezoelectric materials from a single sample.

E. Le Clézio, M. Lam, G. Feuillard
Université François Rabelais de Tours, CNRS FRE 2448, INSERM U930, École Nationale d'Ingénieurs du Val de Loire, rue de la Chocolaterie, BP3410, 41034 Blois, France. e-mail: emmanuel.leclezio@univ-tours.fr

T. Delaunay
IES - UMR CNRS 5214, Université Montpellier II - cc 082, Place Eugène Bataillon, 34095 Montpellier Cedex 5. e-mail: delaunay@lain.univ-montp2.fr

They were first developed for elastic materials and are here extended to piezoelectric samples. In order to characterize new materials, and especially single-crystals with small dimensions, an identification protocol based on the study of the resonance spectra of parallelepipeds is first presented [3]. The second method is based on the measurement of the transmission coefficients of plane waves propagating through an immersed plate [4]. Due to the larger dimensions of the tested samples, it is well adapted to the determination of the properties of piezoelectric plates.

2 Resonant Spectroscopy

This method was developed to characterize relaxor-based ferroelectric single crystals [3]. These materials can have excellent piezoelectric properties compared to conventional PZT ceramics commonly used in ultrasonic transducers. Their large electromechanical coefficient k_{33}, their high dielectric permittivity ε_{33}^{T} and their typical piezoelectric constant d_{33} of 2500pC/N make these materials very attractive for ultrasonic transducer applications requiring a high sensitivity and a large bandwidth [5]. However, the existing characterization methods have to be adapted to (i) the small dimensions of single crystals, (ii) their anisotropy degree, and (iii) the difficulty in obtaining homogeneous compositions [6]. The study reported in this section is based on the Resonant Ultrasound Spectroscopy method. It was first applied to elastic materials [7] and then extended to piezoelectric samples [8]. In the latter cases, mechanical excitations and detections were carried out involving pinducers or ultrasonic transducers positioned at the sample corners [9]. These methods are inherently limited by the transducer bandwidths leading to an inhomogeneous mode excitation. This section presents results from [3] where a new experimental set-up is proposed for Resonant Ultrasound Spectroscopy measurements. It is based on an electrical excitation of the piezoelectric sample and on the detection of its mechanical vibrations through a laser interferometer. The experimental set-up and the model are applied to the characterization of piezoelectric cubes and an identification protocol based on a sensitivity analysis is proposed. The identification of the entire set of properties of a $[001]_c$ PZN-12%PT single crystal in the tetragonal phase ($4mm$) is presented here.

2.1 Modeling of the resonant vibration modes of piezoelectric parallelepipeds

Consider a non metalized piezoelectric parallelepiped. The material characteristics are the density ρ and components C_{ijkl}^{E}, e_{mkl} and ε_{mn}^{S} of the elastic stiffness tensor measured at constant electrical field $\mathbf{E}$, of the piezoelectric tensor and of the dielectric tensor measured at constant strain respectively. The Lagrangian of this piezoelectric body of volume V_0 is [8, 10]:

$$L = \frac{1}{2}\iiint_{V_0} u_{i,j} C^E_{ijkl} u_{k,l} + 2\phi_{,m} e_{mkl} u_{k,l} dV - \frac{1}{2}\iiint_{V_0} \phi_{,m} \varepsilon^S_{mn} \phi_{,n} + \rho\omega^2 u_i u_i dV, \quad (1)$$

where ω is the angular frequency. A $e^{i\omega t}$ time dependence is assumed for mechanical and electrical fields. In a variational approach, any mechanical displacement $u_i \rightarrow u_i + \delta u_i$ and electrical potential variation $\phi \rightarrow \phi + \delta\phi$ yields a variation of the Lagrangian: $L \rightarrow L + \delta L$. Hamilton's principle leads to look for the Lagrangian stationary points where $\delta L = 0$. This determines a motion equation whose solutions correspond to the free vibrations of the piezoelectric body. In accordance with the Rayleigh-Ritz method [10], the mechanical displacements and the electrical potential are expressed as a linear combination of functions:

$$\mathbf{u} = \sum_{p=1}^{N} a_p \psi_p \ ; \ \phi = \sum_{r=1}^{M} b_r \varphi_r. \quad (2)$$

The $\psi_p,\ p = 1,\ldots,N$ and $\varphi_r,\ r = 1,\ldots,M$ functions are chosen to be orthonormal. To determine a_p and b_r constants, an eigenvalue problem is expressed by substituting expressions (2) into equation (1), and by the condition of the stationary Lagrangian:

$$\left(\Gamma + \Omega\Lambda^{-1}\Omega^t\right)\mathbf{a} = \rho\omega^2\mathbf{a}\,;\, \mathbf{b} = \Lambda^{-1}\Omega^t\mathbf{a}. \quad (3)$$

$\mathbf{a} = (a_1, a_2, \ldots, a_N)^t$ and $\mathbf{b} = (b_1, b_2, \ldots, b_M)^t$ are unknown vectors. Γ, Ω and Λ are respectively the elastic, piezoelectric and dielectric interaction matrices. They depend on the shape and on the electromechanical properties of the piezoelectric body, and their descriptions are given in the appendix of [8]. The determination of the eigenvalues $\rho\omega^2$ and the eigenvectors $\mathbf{a}$ and $\mathbf{b}$ allows the resonant frequency ω, the modal elastic displacements $\mathbf{u}$ and the electric potential ϕ to be identified.

As pointed out in literature, the Legendre polynomial basis is well adapted to describe the behavior of the electrical and acoustical fields inside parallelepipeds. Moreover, Mochizuki showed that the symmetry classification of the free oscillations of anisotropic parallelepipeds is useful for material characterization [11]. This principle is extended to piezoelectric materials of parallelepiped shape [3] where the free modes of vibration of a parallelepiped are classified according to eight symmetry elements. The solutions of the eigenproblem (3) are then sought in the form [8]:

$$\mathbf{u} = \sum_{\lambda\mu\nu i} \frac{a_{\lambda\mu\nu i}}{\sqrt{L_1 L_2 L_3}} \overline{P}_\lambda\left(\frac{x_1}{L_1}\right)\overline{P}_\mu\left(\frac{x_2}{L_2}\right)\overline{P}_\nu\left(\frac{x_3}{L_3}\right)\mathbf{e_i}, \quad (4)$$

$$\phi = \sum_{\xi\varsigma\eta} \frac{b_{\xi\varsigma\eta}}{\sqrt{L_1 L_2 L_3}} \overline{P}_\xi\left(\frac{x_1}{L_1}\right)\overline{P}_\varsigma\left(\frac{x_2}{L_2}\right)\overline{P}_\eta\left(\frac{x_3}{L_3}\right), \quad (5)$$

where the p^{th} and r^{th} basic functions $\psi_{\mathbf{p}}$ and φ_r are defined by the triplets (λ, μ, ν) and (ξ, ς, η), respectively $\overline{P}_\alpha(x_i)$ is the Legendre function of order α and $\mathbf{e_i}$ is the unit displacement vector in the $\mathbf{x_i}$ direction. $\frac{1}{\sqrt{L_1 L_2 L_3}}$ is a normalization term linked to L_1, L_2, L_3 dimensions of the solid. The relations between the coefficients

$a_{\lambda\mu\nu i}$ and $b_{\xi\varsigma\eta}$ and the symmetry groups are presented in [3]. Using this decomposition, the interaction matrices Γ, Ω and Λ are separated into eight independent matrices leading to eight independent eigenvalue problems yielding reduced computation times.

In order to perform poling of the piezoelectric materials, electrodes have to be laid down on two surfaces orthogonal to the desired polarization axis. To take into account any potential imposed by an electrode on the piezoelectric solid surface, the work performed by the electrical charges of the metalized surfaces has to be subtracted from the Lagrangian (1). Delaunay et al. [3] showed that no significant modification of the resonant frequencies or of the mechanical mode-shapes are induced by the electrodes. Thus, the effect of the electrodes is neglected in the following.

2.2 Experimental results and discussion

This section presents the experimental set-up developed in [3] to generate and detect the free vibrations of a piezoelectric cube. It is applied to the characterization of the electromechanical properties of a single crystal in the tetragonal phase *4mm* (PZN-12%PT).

2.2.1 Experimental set-up and materials

An electrical excitation is performed to generate the vibrations of the piezoelectric solid. It is delivered through an impedance analyzer (Agilent 4395A) also allowing the sample electrical resonances and anti-resonances to be measured (Figure 1(a)). It has a very large frequency bandwidth (10kHz - 500MHz) and the delivered electrical power is set between 0 dBm and 10 dBm depending on the excited modes. The sample is set on a plastic holder and the electrical contact is ensured by a metallic strip fixed on a spring so that the free mechanical boundary conditions at the surfaces of the cube are fulfilled.

Velocity measurements at the surface of the sample are carried out through a Laser vibrometer (Polytech OFV-505) so as to detect the resonance frequencies as well as the associated mode-shapes. The interferometer is positioned at 50 cm from the sample leading to a 20 μm focal area. The velocity decoder sensitivity is either 5 (mm$\cdot$ s^{-1})/V or 25 (mm$\cdot$ s^{-1})/V depending on the cut-off frequency, respectively 250 kHz and 1.5 MHz. The sample holder is fixed onto a two-dimensional micrometer computer controlled translation unit. 100 acquisition points are taken on the surface of the sample leading to the representation of the mode-shapes for each resonance.

To carry out the electrical excitation, the two surfaces of the sample orthogonal to the $\mathbf{x_3}$ polarization axis are metalized. In order to generate a maximum number of modes, an electrode patterning is used allowing particular mode symmetries to be highlighted. One of the metalized faces is then only partially covered by electrodes

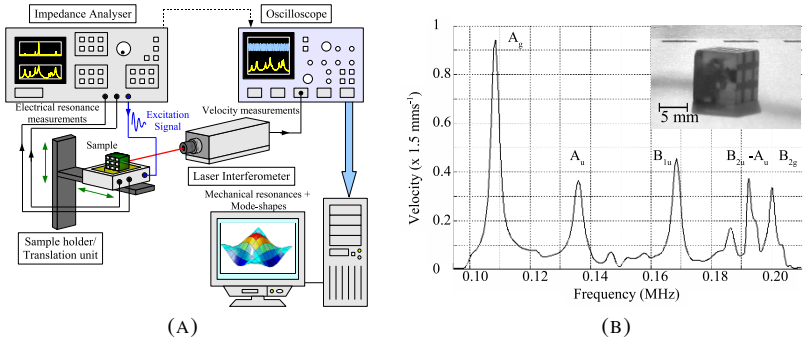

Fig. 1 (A) Experimental set-up ; (B) PZN-12%PT single crystal cube and the corresponding surface velocity spectrum measured on one of the upper corners for frequencies ranging from 94500 Hz to 210000 Hz.

(Figure 1(b)) in order to deliver enough electrical power while keeping the external electrical field close to zero. Finally, since the sample is excited by an electrical source and that mechanical velocities are measured by laser vibrometry, the detected vibrations are necessarily those of piezoelectrically coupled modes meaning that full elastic, piezoelectric and dielectric tensors are recoverable.

2.2.2 Inverse problem and PZN-12%PT single crystal characterization

To identify the material characteristics, a fit procedure has been developed. Modifying the C^E, e and ε^S tensors enables the resonant frequencies computed from (3) to be matched to the measured data. Due to symmetry considerations, eleven constants have to be identified for tetragonal (4*mm*) piezoelectric materials. An identification protocol based on a sensitivity analysis is proposed in [3]. The frequency dependence of each mode to the constants is theoretically evaluated to identify the vibration modes that were mainly sensitive to a single material constant. The modes sensitive to one or two characteristics are revealed and their resonant frequencies are used to identify the corresponding material properties.

The resonant ultrasound spectroscopy method is applied to the characterization of a $7.55 \times 7.52 \times 7.71$ mm^3 PZN-12%PT single crystal cube. The sample is poled along the $[001]_c$ direction leading to a 4*mm* symmetry. The tested sample presents internal defects that might alter its resonant behavior (figure 1(b)). However, the number of measured modes and their corresponding resonant frequencies are assumed to be sufficient in order to identify the electromechanical characteristics of the cube. Figure 1(b) also presents the spectrum of the surface velocity measured by the laser vibrometer on one of the upper corners in the $[94.5, 210]$ kHz frequency range. Six peaks are observed and identified through the measurement of their mechanical displacements. They are labelled according to the Mulliken notation [12].

No existing electromechanical tensor of a PZN-12%PT single crystal is available in the literature but some materials are expected to possess very close properties, such as PMN-x%PT single crystals with a PT ratio inducing a tetragonal symmetry. Thus, the electromechanical properties of a PMN-42%PT single crystal [13] are used as initial guess in the characterization process. To evaluate the accuracy of the results, a distance Δ_{mc} between the experimental resonance frequencies $f^{(i)}_{\text{measured}}$ and the computed ones $f^{(i)}_{\text{computed}}$ is defined by:

$$\Delta_{mc} = \frac{\sum_i \left| f^{(i)}_{\text{measured}} - f^{(i)}_{\text{computed}} \right|}{\sum_i f^{(i)}_{\text{measured}}}. \tag{6}$$

In Table 1, Δ_{mc} is equal to 0.95. Moreover, independent modifications of the constants are made and the accuracies correspond to the maximum values of these modifications inducing no significant change in Δ_{mc}. The characteristics presented in Table 1 are, to the authors' knowledge, the first complete elastic, piezoelectric and dielectric tensors of a PZN-12%PT single crystal reported in the literature. They are consistent with tensors of single crystals with similar compositions [5].

Table 1 PZN-12%PT single crystal cube properties identified by acoustic spectroscopy.

C^E_{11} (GPa)	C^E_{12} (GPa)	C^E_{13} (GPa)	C^E_{33} (GPa)	C^E_{44} (GPa)	C^E_{66} (GPa)
152 ± 2	87 ± 1	90 ± 0.5	84 ± 2	37 ± 3	22 ± 1
Density (kg/m^3)	e_{15} (C/m^2)	e_{31} (C/m^2)	e_{33} (C/m^2)	ε^S_{11} (ε_0)	ε^S_{33} (ε_0)
8380	35 ± 3	-3 ± 0.5	4 ± 1	2420 ± 150	331 ± 50

3 Transmission spectroscopy

The second characterization method is based on the generation of acoustic waves with controlled propagation paths inside plates. This method has first been implemented for the characterization of pure elastic or visco-elastic plates [14], and the model used in this paper is based of a state-vector formalism [15]. It has been extended to piezoelectric material by Kraut and Adler [16, 17] and has been fully developed by Lothe & Barnett [18, 19]. The theoretical model describing reflection-transmission of plane acoustic waves through piezoelectric anisotropic plates is based on the octet formalism of piezoacoustics and the concept of the impedance/admittance [20] matrices. Incorporating different types of electrical

boundary conditions for an immersed plate, the reflection and transmission coefficients are expressed through this admittance in explicitly the same way as in the case of a pure elastic plate [21, 22, 23]. This theoretical model is then engaged for a Ferroperm Piezoceramics high permittivity PZT-NN ceramic [24] characterization.

3.1 Theoretical background

Consider an infinite piezoelectric plate, possibly absorbing, with the density ρ and the tensors of elastic $\mathbf{C}^{\mathbf{E}}$, piezoelectric $\mathbf{e}$ and dielectric ε coefficients, referred to some crystallographic basis $\{\mathbf{x_1}, \mathbf{x_2}, \mathbf{x_3}\}$. Assume the wave train in the form

$$\begin{array}{c} \mathbf{u} = \mathbf{A}(y)\,\mathrm{e}^{\mathrm{i}k(x-vt)},\ \sigma\mathbf{n} = \mathbf{F}(y)\,\mathrm{e}^{\mathrm{i}k(x-vt)}, \\ \phi = \varphi(y)\,\mathrm{e}^{\mathrm{i}k(x-vt)},\ \mathbf{d} = \mathbf{D}(y)\,\mathrm{e}^{\mathrm{i}k(x-vt)}, \end{array} \tag{7}$$

where the axes $\mathbf{x}$ and $\mathbf{y}$ are, respectively, parallel and orthogonal to the plate faces. k is the wavenumber along the $\mathbf{x}$-axis, $v = \omega/k$ is the phase velocity. $\sigma\mathbf{n}$ is the normal component of the mechanical stress tensor σ, $\mathbf{u}$ is the elastic displacement, $\mathbf{d}$ and ϕ are the induction and potential of the electric field induced by the piezoelectric effect. The state-vector approach in piezoacoustics implies expressing the governing equations for plane waves as the first-order ordinary differential system (ODS)

$$\left[\mathrm{i}k\mathbf{N}(v) - \frac{\mathrm{d}}{\mathrm{d}y}\right]\eta(y) = \mathbf{0}, \tag{8}$$

where the eight-component state vector η is in the form

$$\eta = \begin{pmatrix} \mathbf{U} \\ \mathbf{V} \end{pmatrix},\ \mathbf{U} = \begin{pmatrix} \mathbf{A} \\ \varphi \end{pmatrix},\ \mathbf{V} = \mathrm{i}k^{-1}\begin{pmatrix} \mathbf{F} \\ D_y \end{pmatrix}. \tag{9}$$

The expression of the 8×8 matrix $\mathbf{N}(v)$ is presented in [23]. The state-vector formalism for a plate is based on the solution of (8) in the form of a matricant $\mathbf{M}$, so that $\eta(y_1) = \mathbf{M}(y_1, y_2)\,\eta(y_2)$. Through a homogeneous plate with faces at $y = \pm h$ it is given by

$$\mathbf{M}(h,-h) = \exp\left[2\mathrm{i}kh\mathbf{N}(v)\right] = \begin{pmatrix} \mathbf{M}_1 & \mathbf{M}_2 \\ \mathbf{M}_3 & \mathbf{M}_4 \end{pmatrix}. \tag{10}$$

This formalism also involves impedance/admittance matrices, representable via $\mathbf{M}$. The admittance matrix $\mathbf{Y}(h,-h)$ is defined as

$$\begin{pmatrix} \mathbf{U}(-h) \\ \mathbf{U}(h) \end{pmatrix} = \mathrm{i}\mathbf{Y}(h,-h)\begin{pmatrix} \mathbf{V}(-h) \\ -\mathbf{V}(h) \end{pmatrix}, \tag{11}$$

where $\mathbf{Y}$ can be written via the blocks of $\mathbf{M}$: $\mathbf{Y} = \mathrm{i}\begin{pmatrix} \mathbf{M}_3^{-1}\mathbf{M}_4 & \mathbf{M}_3^{-1} \\ \mathbf{M}_1\mathbf{M}_3^{-1}\mathbf{M}_4 - \mathbf{M}_2 & \mathbf{M}_1\mathbf{M}_3^{-1} \end{pmatrix}$.
The above definitions and ensuing properties are the same for the 6×6 format of

elasticity and the 8×8 format of the piezo-elasticity. However, the case of piezoelectric plates often calls for more versatile formulations of the impedance/admittance matrices [25, 26, 27]. In [23], a 6×6 version of the admittance matrix $\widetilde{\mathbf{Y}}$ including the electrical boundary conditions (BC) is presented. Once this matrix is obtained, it defines the sought coefficients of reflection and transmission via their known expressions for the purely elastic case [22]:

$$T = \frac{-2Y_3^{(\mathbf{n})}Y_f \mathrm{e}^{-2\mathrm{i}kp_f h}}{\left(Y_1^{(\mathbf{n})} - Y_f\right)\left(Y_4^{(\mathbf{n})} - Y_f\right) - Y_2^{(\mathbf{n})}Y_3^{(\mathbf{n})}}, \tag{12}$$

where $Y_f = -\mathrm{i}p_f/\rho_f v^2$, $p_f = \sqrt{v^2/c_f^2 - 1}$ and $Y_i^{(\mathbf{n})} = \mathbf{n}\cdot\widetilde{\mathbf{Y}}_i\mathbf{n}$ $(i = 1,...,4)$. $\widetilde{\mathbf{Y}}_i$ are the 3×3 blocks of the 6×6 admittance $\widetilde{\mathbf{Y}}$ of piezoelectric plate.

3.2 High permittivity PZT-NN material characterization

One of the main axes of piezoelectric material research deals currently with the elaboration of ceramics with very high properties because the size reduction of the devices usually yields smaller performances of the constitutive materials. This section presents the characterization of a high permittivity material - Pz59 - developed by Ferroperm in the framework of the MINUET European project (n°NMP2-CT-2004-505657). Of $Pb[Zr,Ti,(Ni_{1/3}Nb_{2/3})]O_3$ composition, these materials are meant to be introduced into miniature multi-element devices such as transducer networks, and possess higher piezoelectric properties than classical ceramics.

To infer the material constants, ultrasonic plane wave transmission measurements are performed. An experimental set-up has lately been applied to the characterization of carbon-polymer based composite plates [14] and is here adapted to the identification of the entire piezo-elastic tensor of piezoelectric materials. As presented in figure 2.(A), the sample is immersed into a water tank. It is fixed on a motorized rotation stage. A 0.375 inch diameter transducer (Technisonic ISL-0303-HR) with a 3.5 MHz central frequency is excited by a pulse centered between 3.5 and 4 MHz. The transmitted acoustic fields are captured for an incident angle ranging from 0° to 50° every 0.5°. The reference signal transmitted through water without the sample is also recorded. Fast Fourier Transforms are then performed and the transmitted spectra are divided by the reference one, yielding the angular spectrum of the absolute value of transmission coefficient at a given frequency.

As in §2.2, a fit procedure is then applied to compare the experimental transmission spectra to numerical simulations obtained from a program based on the formalism described in §3.1 in which the material constants $\mathbf{C}^{\mathbf{E}}$, $\mathbf{e}$ and ε are the input parameters. This method has already been validated on a Pz27 ceramic and the effect of the material metallization has been quantified [4]. It is here applied to the identification of the values of elastic, piezoelectric, and dielectric coefficients of the Pz59 plate. Figure 2.(B) presents the variation of the transmission coefficients through a

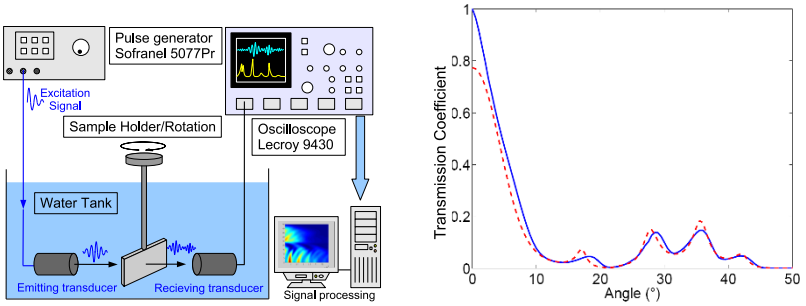

(A) (B)

Fig. 2 (A) Experimental setup ; (B) Evolution with the angle of the transmission at $f = 3.11$ MHz. Solid lines: measurements ; Dashed lines : numerical simulations.

Pz59 plate with the incidence angle. The resonance angles are accurately identified, validating the determination of the real parts of the characteristics. However, amplitude discrepancies are observed. They can be explained by diffraction losses and/or by a frequency dependance of the material damping.

Table 2 Acoustical characterization of a Pz59 plate.

Density (kg/m^3)	C_{11}^E (GPa)	C_{13}^E (GPa)	C_{55}^E (GPa)	C_{33}^E (GPa)
7850 ± 50	137.8 ± 2.2 %	78.8 ± 1.9 %	24.4 ± 7.7 %	116.6 ± 0.6 %
e_{15} (C/m^2)	e_{31} (C/m^2)	e_{33} (C/m^2)	ε_{11}^S (ε_0)	ε_{33}^S (ε_0)
19.5 ± 9.6 %	-7 ± 58 %	25.4 ± 1.6 %	4103 ± 13.9 %	2729 ± 2.9 %

Most of the characteristics presented in Table 2 are identified with an accuracy better than 3%. C_{55}, e_{15} and ε_{11}^S have accuracies of 8%, 10%, and 14% respectively, remaining in the accuracy range of the piezoelectric material characterization methods. However, e_{31} is identified at about 60% accuracy. This can be explained with the help of the Christoffel tensor calculated in the $\mathbf{x_1x_3}$ plane for a propagation angle θ given with respect to the normal of the plate surfaces. It indicates that the e_{31} angular zone of sensitivity ranges between 30°and 70°. This angular region is situated above the longitudinal wave critical angle. Only transverse waves are then transmitted through the plate and their damping is greater than that of compressional waves. The amplitudes of the resulting signals are then small and the accuracy of e_{31} is deteriorated.

4 Conclusions

Two piezoelectric material characterization methods were presented. Resonant Ultrasound Spectroscopy measurements were carried out using an experimental set-up where the electrical excitation of the parallelepiped sample and the laser detection of its mechanical displacements enabled piezo-electrically coupled vibration modes to be studied. To identify the material constants, particular attention was paid to the modes' sensitivity to independent elastic, piezoelectric or dielectric constants. The method has been applied to the identification of the full tensor of a PZN-12%PT single crystal. The tested sample was of several hundreds of mm^3 but the instrumentation, and particularly the laser interferometer, should enable the characterisation of smaller samples. The second method called Transmission Spectroscopy is based on the propagation of acoustic waves through immersed plates. It was applied to the characterization of a high permittivity ceramic developed in the framework of the MINUET European Project for high frequency medical imaging. Most of the properties are identified with very good accuracies, but a sensitivity study is currently being carried out to define a new identification protocol and improve the robustness of the characterization method.

References

1. European Standard EN 50324-2, 2002.
2. Alguero et al., *J. Am. Ceram. Soc.*, 87(2) :209-215, 2004.
3. Delaunay et al., *IEEE Trans. Ultrason., Ferroelect., Freq. Contr.*, vol. 55, pp. 476-488, 2008.
4. Le Clezio et al., *Proc. IEEE Ultrason. Symp.*, 2004, pp. 553-556.
5. Park et al., *IEEE Trans. Ultrason., Ferroelect., Freq. Contr.*, vol. 44, pp. 1140-1146, 1997.
6. Lim et al., *J. Crystal Growth*, vol. 271, pp. 435-444, 2004.
7. Leisure et al., *J. Phys.: Conden. Matt.*, vol. 9, pp. 6001-6029, 1997.
8. Ohno et al., *Phys. Chem. Minerals*, vol. 17, pp. 371-378, 1990.
9. Migliori et al., *Physica B*, vol. 183, pp. 1-24, 1993.
10. Holland et al., *J. Acoust. Soc. Amer.*, vol. 43, pp. 988-997, 1967.
11. Mochizuki et al., *J. Phys. Earth*, vol. 35, pp. 159-170, 1987.
12. Schutte et al., *Pure Appl. Chem.*, vol. 69, pp. 1641-1649, 1997.
13. Cao et al., *J. Appl. Phys.*, vol. 96, no. 1, pp. 549-554, 2004.
14. Fortineau et al., *J. Appl. Phys.*, 101 :114911-1 114911-8, 2007.
15. Stroh, *J. Math. and Physics*, vol. 41, pp. 77-103, 1962.
16. Kraut, *Phys. Rev.*, 188 :1450-1455, 1969.
17. Adler, *IEEE Trans. Ultrason., Ferroelect., Freq. Contr.*, vol. 37, pp. 485-490, 1990.
18. Lothe and Barnett, *J. Appl. Phys.*, vol. 47, pp. 1799-1807, 1976.
19. Lothe and Barnett, *Phys. Norv.* 8, 47 :239-254, 1977.
20. Honein et al., *J. Intell. Mater. Syst. Struct.*, 2 :542-557, 1991.
21. Rokhlin et al., *J. Acoust. Soc. Am.*, 112 :822-834, 2002.
22. Rokhlin et al., J. *Acoust. Soc. Am.*, vol. 112, pp. 822-834, 2002.
23. Shuvalov et al., *International Journal of Engineering Science*, vol. 46 (9), pp. 929-947, 2008.
24. *http://www.ferroperm-piezo.com/*
25. Honein et al., *J. Intell. Mater. Syst. Struct.*, vol. 2, pp. 542-557, 1991.
26. Zhang et al., *IEEE Trans. Ultrason., Ferroelect., Freq. Contr.*, vol. 48, pp. 1449-1462, 2001.
27. Zhang et al., *Acta acustica - Acustica*, vol. 88, pp. 218-230, 2002.

Ultrasound characterization of aggregated red blood cells: towards *in vivo* application

E. Franceschini, F. T. H. Yu and G. Cloutier

Abstract Ultrasonic backscattered signals from blood contain frequency-dependent information that can be used to obtain quantitative parameters reflecting the aggregation state of red blood cells (RBCs). The difficulty to use this frequency-dependent information *in vivo* is due to the attenuation caused by intervening tissue layers that distorts the spectral content of backscattering properties from blood microstructures. We propose an optimization method to simultaneously estimate tissue attenuation and blood structure factor. In an *in vitro* experiment, we obtained satisfactory estimates with relative errors below 25% for attenuations between 0.115 and 0.412 dB/cm/MHz and $D < 10$ (D the aggregate diameter expressed in number of RBCs).

1 Introduction

For the detection and characterization of tissues, quantitative ultrasound techniques using the radio frequency (rf) backscattered signals have received broad interest for the past 30 years. One approach is to use the magnitude and frequency dependence of the rf backscatter spectrum in order to quantify the tissue structures such as the size, acoustic impedance, and concentration of the scatterers. Many *in vitro* and in vivo experiments have been performed to demonstrate the utility of this approach for characterizing of the eye, liver, kidney, prostate and breast. Recently, the frequency dependence of the ultrasound backscattering coefficient (BSC) was studied to assess the level of red blood cell (RBC) aggregation. Two parameters describing RBC aggregation, the packing factor and mean aggregate diameter, were estimated from

Franceschini E., Yu F. T. H. and Cloutier G.
Laboratory of Biorheology and Medical Ultrasonics, University of Montreal Hospital Research Center, Pavillon J.A. de Sève (Room Y-1619), 2099 Alexandre de Sève, Montréal, Québec, H2L 2W5, Canada e-mail: franceschini@lma.cnrs-mrs.fr, francoisyu@videotron.ca, guy.cloutier@umontreal.ca

the Structure Factor Size Estimator (SFSE).[1] The difficulty in using the SFSE *in vivo* is that the spectral content of backscattered signals is also affected by attenuation caused by intervening tissue layers between the probe and the blood flow. More generally, ultrasound scatterer size estimation techniques for tissue characterization (such as liver, kidney, prostate or breast) has had limited success in clinical practice because of tissue attenuation effects.[2,3] Some groups[2,4,5] have developed measurement methods to evaluate the frequency-dependent attenuation in order to compensate *a posteriori* the backscattered power spectrum. Our goal is to explore another strategy for *in vivo* measures of RBC scatterer sizes. Recently, we have proposed an optimization method providing an estimate of total attenuation and blood structural parameters simultaneously, termed the Structure Factor Size and Attenuation Estimator (SFSAE).[6] This method consists in fitting the spectrum of the backscattered rf echoes from blood to an estimated spectrum by a modified SFSE model. Herein, the SFSAE is improved and *in vitro* experimental evaluation of the SFSAE is performed.

2 Background: Structure Factor Size and Attenuation Estimator

The technique allowing one to estimate simultaneously blood structural parameters and total attenuation has been described in detail in Ref. 6 and is summarized here.

Blood can be considered as a very dense suspension of particles (i.e. red cells) having strong interactions (collision, attraction, deformation, flow dependent motions). We develop a theoretical model of blood ultrasound backscattering based on the particle approach.[7,8] This approch consists of summing contributions from individual RBCs and models the RBC interaction by a particle pair-correlation function. The model proposed in Ref. 1 has been modified to predict the theoretical backscatter coefficient from blood:[6]

$$BSC_{theor}(k) = m\sigma_b(k)S(k)A(k) \tag{1}$$

where k is the wave vector, m is the number density of RBCs in blood estimated by measuring the hematocrit H by microcentrifugation ($m = H/V_s$, where V_s is the volume of a RBC), σ_b is the backscattering cross section of a single RBC, S is the structure factor describing the spatial organization of RBCs, and A is the frequency-dependent attenuation function. The backscattering cross-section σ_b of a weak scattering particle small compared to the wavelength (Rayleigh scatterer) can be determined analytically as follows: $\sigma_b(k) = 1/(4\pi^2)k^4V_s^2\gamma_z^2$, where γ_z is the variation of impedance between the RBC and its suspending medium (i.e. the plasma). The structure factor S is the Fourier transform of the pair-correlation function[8] g and is approximated by its second-order Taylor expansion[1] in k as

$$S(k) = 1 + m\int (g(r) - 1)\, e^{-2jkr} dr \approx W - \frac{12}{5}(kR)^2. \tag{2}$$

In this last equation, W is the low-frequency limit of the structure factor ($S(k)|_{k\to 0}$) called the packing factor.[8,9] R is the radius of 3D RBC aggregates assumed to be isotropic. We introduce $D = R/a$ as the isotropic diameter of an aggregate (expressed in number of RBCs) with a the radius of one RBC sphere-shaped model of volume V_s. The attenuation function A is given by: $A(k) = e^{-4\alpha_0 f}$, where f is the frequency and α_0 is the attenuation coefficient (in dB/MHz) defined by: $\alpha_0 = \sum_i \alpha_i e_i$, where α_i and e_i are respectively the intervening tissue layer attenuations (in dB/cm/MHz) and thicknesses. We thus assume that the attenuation increases linearly with the frequency: $\alpha(f) = \alpha_0 f$.

The measured backscatter coefficient was computed as

$$BSC_{meas}(k) = BSC_{ref}(k)\frac{\overline{P_{meas}(k)}}{\overline{P_{ref}(k)}}. \tag{3}$$

In Eq. (3), the mean backscattered power spectrum $\overline{P_{meas}}$ was obtained by averaging the power spectra of 20 backscattered echoes from blood. The mean power spectrum $\overline{P_{ref}}$ was obtained from a reference sample of non-aggregated RBCs at a low hematocrit of 6% (i.e. Rayleigh scatterers).[10] In this case, 20 echoes were also averaged. This reference sample was used to compensate the backscattered power spectrum $\overline{P_{meas}}$ for the electromechanical system response, and the depth-dependent diffraction and focusing effects caused by the ultrasonic beam.

The packing factor W, aggregate diameter D and total attenuation along the propagation path α_0 were determined by matching the measured BSC_{meas} given by Eq. (3) with the theoretical BSC_{theor} given by Eq. (1). For this purpose, we searched values of W, D and α_0 minimizing the cost function $F(W,D,\alpha_0)=||BSC_{meas} - BSC_{theor}||^2$. In all studied cases, the cost function seemed to have a unique global minimum, as was observed by plotting the cost function surface $F(W,D)$ with varying values of α_0 (see Fig. 1 in Ref. 6). For the optimization problem, we defined a set of lower and upper bounds on the variables (W, D, α_0) so that the solution is searched in the range: $0 \leq W \leq 100$, $0 \leq D \leq 50$ and $0 \leq \alpha_0 \leq 1$ dB/MHz. We chose to reject the solution (W, D, α_0) having an estimated diameter D very small compared to 0.1.

3 *In vitro* experiment in a Couette flow device

3.1 Blood preparation

Fresh porcine whole blood was obtained from a local slaughter house, centrifuged and the plasma and buffy coat were removed. Two blood samples were then prepared: (i) a H6 reference sample, which was a 6% hematocrit non-aggregating RBCs resuspended in saline solution; and (ii) a 40% hematocrit T40 test sample, which consisted of RBCs resuspended in plasma to promote aggregation.

3.2 Experimental set up

US measurements were performed in a Couette flow system to produce a linear blood velocity gradient at a given shear rate. The schematic configuration of the experience is shown in figure 1. The system consisted of a rotating inner cylinder with a diameter of 160 mm surrounded by a fixed concentric cylinder of diameter 164 mm. A 60 mL blood sample was sheared in the 2 mm annular space between the two coaxial cylinders. The US scanner (Vevo 770, Visualsonics, Toronto, Canada) equipped with the RMV 710 probe was used in B-mode. The single-element focused circular transducer had a center frequency of 25 MHz, a diameter of 7.1 mm and a focal depth of 15 mm. We operated at a sampling frequency of 250 MHz with 8 bits resolution (Gagescope, model 8500CS, Montreal, Canada). The probe was mounted in the side wall of the fixed outer cylinder and was positioned to have its focal zone at the center of both cylinders. To ensure ultrasonic coupling, the hole within the outer stationary cylinder (containing the probe) was filled with a liquid agar gel based mixture. When solidified, this gel was cut to match the curvature of the cylinder to avoid any flow disturbance. The gel was a mixture of distilled water, 3% (w/w) agar powder (A9799, Sigma Chemical, Saint-Louis, MO), 8% (w/w) glycerol and a specific concentration of 50 μm cellulose scattering particles (S5504 Sigmacell, Sigma Chemical, Saint-Louis, MO) that determined the attenuation coefficient. Five experiments were performed with five mixtures having Sigmacell (SC) concentrations varying from 0% to 1% (w/w). Since skin is one of the most attenuating tissue layers during *in vivo* scanning, phantoms were prepared in order to have attenuations close to skin attenuation. The 0% concentration constituted the non-attenuating gel and the four other mixtures mimicked skin attenuations.

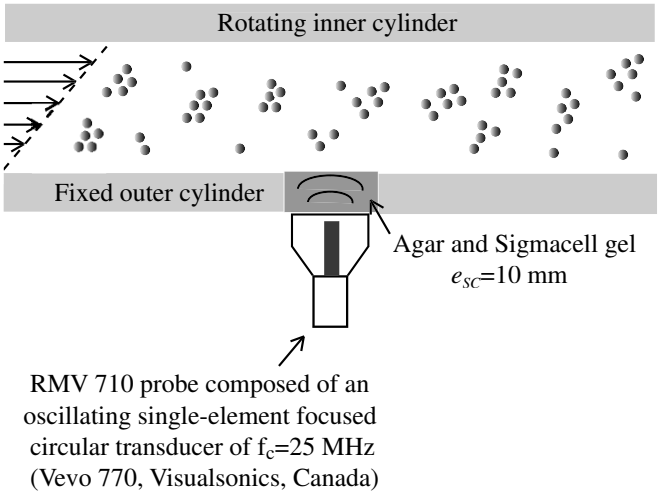

Fig. 1 The Couette flow system

3.3 Attenuation measurements

The attenuation coefficients of the reference (0% SC) and of the others skin-mimicking phantoms α_{sc} were determined by using a standard substitution method. A transducer with center frequency of 25 MHz (Vevo 770, Visualsonics, Toronto, Canada) was used in transmission/reception with a reflector on the opposite side of the phantom for reflection measurements. Reflected signals were recorded both with and without the agar gel sample in the acoustic path. The attenuation coefficient was then estimated using a log spectral difference technique. For each concentration of SC, six regions were scanned for averaging purpose. Thicknesses of skin-mimicking phantoms e_{sc} were fixed to 10 mm. As shown in the table 1 summarizing results, attenuation coefficients of skin-mimicking phantoms were in the same range as the human dermis (0.21 dB/MHz at 14 - 50 MHz considering a 1 mm dermis thickness[11]).

Attenuations of the blood α_{blood} sheared at different shear rates were also measured in the reflection mode using the same experimental configuration shown in figure 1. The gel had a 0% SC concentration and the rotating inner cylinder was used as the reflector. Table 2 summarizes results.

Table 1 Estimated values of the attenuation coefficients of the reference (0% SC) and of the others skin-mimicking phantoms (using a log spectral difference technique)

SC (%)	Sigmacell attenuation α_{sc} (dB/MHz)
0.25	0.115
0.5	0.219
0.75	0.320
1	0.412

Table 2 Estimated values of the blood attenuation sheared at different shear rates in the Couette flow device (using a log spectral difference technique)

Shear rates (s^{-1})	Blood attenuation α_{blood} (dB/MHz)
5	0.053
10	0.036
20	0.024
30	0.016
50	0.013

3.4 Measurement protocol

Prior to each measurement, the T40 blood was sheared at 200 s^{-1} during 30 s to disrupt RBC aggregates. The shear rate was then reduced to residual values of 5, 10, 20, 30 and 50 s^{-1} during 90 s to reach an equilibrium in the state of aggregation in the sheared blood sample. After that, for each shear rate, 20 B-mode images were constructed for 80 s. For each line of the B-mode images, echoes were selected with a rectangular window of length 0.4 mm at twenty depths every 0.04 mm (i.e. with 90% overlap between windows). For each depth, the power spectra of the backscattered echoes were averaged over 20 acquisitions (corresponding to the 20 acquired images) to provide P_{meas}. This protocol was repeated five times with the five agar-based phantoms. Then, the T40 blood was removed and the H6 sample was introduced in the Couette device. The H6 sample was sheared at 50 s^{-1} and coupled with the 0% SC concentration agar gel. Echoes were windowed as for the H40 sample at the same depths and their power spectra were averaged over 20 acquisitions to obtain P_{ref}.

3.5 Reference measurements with the 0% SC concentration phantom

The experiment with the 0% SC phantom was realized in order to have reference results on packing factors W_{ref} and aggregate diameters D_{ref} obtained from the classical SFSE.[1] These parameters were assumed to be true values of packing factors and aggregate diameters for all shear rates, and will be compared in the next section with packing factors and diameters estimated by the SFSAE and by the SFSE when skin-mimicking phantoms are used.

It is important to emphasize the fact that the H6 reference sample was also measured with the 0% SC phantom. The phantom attenuation, although small with no SC, therefore affected equivalently both spectra $\overline{P_{meas}}$ and $\overline{P_{ref}}$ in Eq. (3). The resulting measured backscatter coefficient BSC_{ref} was thus not biased by attenuation.

4 Results

4.1 Reference parameters with the SFSE

Figure 2 reports results on W_{ref} and D_{ref} from the SFSE with compensation for blood attenuation in the case of no gel attenuation. It can be observed that the amplitude of the backscattering coefficient as well as the estimation of the parameters on W_{ref} and D_{ref} decrease when the shear rate increases (i.e. the level of aggregation becomes smaller).

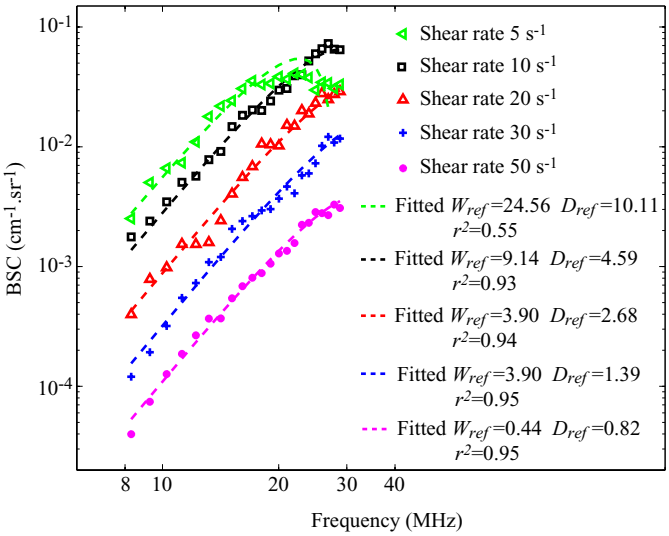

Fig. 2 Backscatter coefficients for blood sheared at different residual shear rates and measured with the 0% SC concentration phantom, and corresponding fitting with the classical SFSE with no compensation for attenuation (in dashed lines).

4.2 Parameters evaluated with the SFSAE

Typical results of the SFSAE minimization procedure for the different agar phantoms at a shear rate of 10 s^{-1} are given in Fig. 3. It can be observed that the more the total attenuation increases, the more the backscattering coefficient amplitude decreases at all frequencies and the more the frequency dependence of the backscattering coefficient changes. One can also notice that the parameters W and D from the SFSAE are very similar to the reference parameters W_{ref} and D_{ref}, as well as the total attenuation α_0 from the SFSAE similar to the reference total attenuation. The reference total attenuation α_{ref} corresponds to $\alpha_{sc}e_{sc} + \alpha_{blood}e_{blood}$ where α_{sc} and α_{blood} are the skin-mimicking phantom attenuation and the blood attenuation estimated in the reflection mode as shown in section 3.3.

For each residual shear rate, parameters W, D and α_0 were estimated by the SFSAE. Figure 4 summarizes these results. In this figure, the relative errors for each parameter correspond to: $(W - W_{ref})/W_{ref}$, $(D - D_{ref})/D_{ref}$ and $(\alpha_0 - \alpha_{ref})/\alpha_{ref}$. Except for the shear rate 5 s^{-1} with the skin-mimicking phantom having the smallest attenuation (0.25% SC), the SFSAE gave quantitatively satisfactory estimates of W and D with relative errors below 25%.

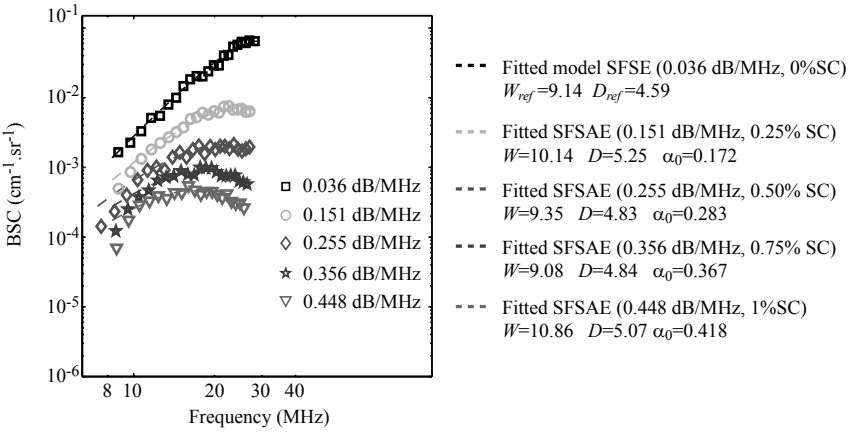

Fig. 3 Backscatter coefficients for blood sheared at 10 s^{-1} and measured with each of the five phantoms. The corresponding fitted models are the SFSE for the 0% SC phantom, and the SFSAE for the four other skin-mimicking phantoms (0.25, 0.5, 0.75 and 1% SC).

4.3 Parameters evaluated with the SFSE with compensation for blood attenuation

The packing factor W_{comp} and the diameter of the aggregates D_{comp} were also evaluated by compensating the backscatter coefficients in the SFSE with the value measured in reflection. Results are presented in Fig. 5. The relative errors are below 25% for all shear rates and all skin-mimicking phantoms.

5 Conclusions

The accuracy of the estimates obtained with the SFSAE was as satisfactory as those obtained with the SFSE with attenuation-compensation (i.e. when a priori are known about the attenuation). For both methods, relative errors for W and D were below 25%, except for one value corresponding to the shear rate 5 s^{-1} with the skin-mimicking phantom having the smallest attenuation (0.25% SC). In this last case, the SFSAE gave less accurate estimates (relative errors around 50% for W and α_0). The SFSAE seems to reach its limit of applicability for large aggregate sizes: typically D_{ref} = 10.11 (i.e. kR=2.8)

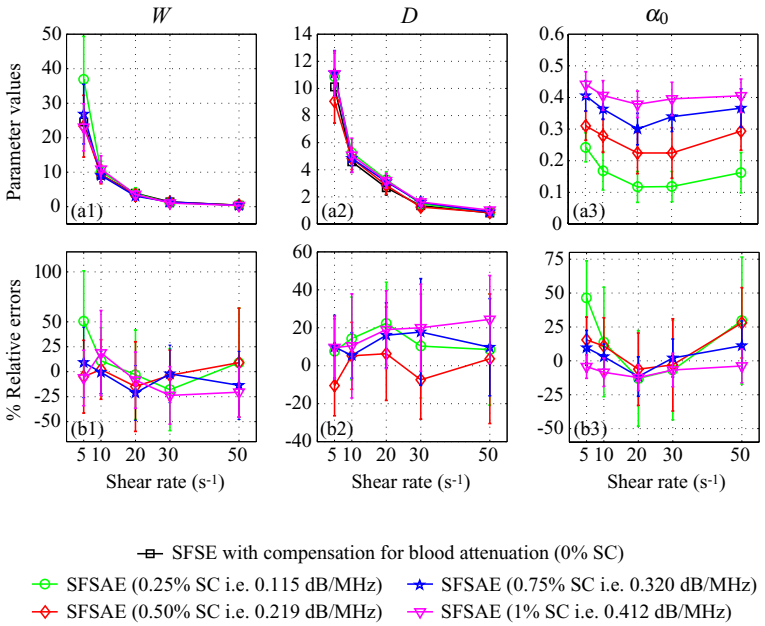

Fig. 4 (a) Values of W, D and α_0 (in dB/MHz) for different residual shear rates estimated by the classical SFSE for the 0% SC concentration and by the SFSAE for the four skin-mimicking phantoms. (b) Corresponding relative errors.

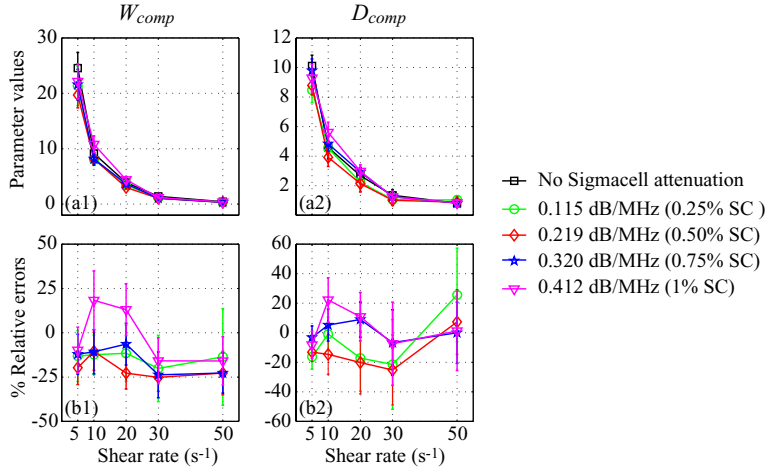

Fig. 5 (a) Values of W_{comp} and D_{comp} for the four skin-mimicking phantoms obtained with the SFSE with attenuation-compensation using the attenuation values estimated in reflection. (b) Corresponding relative errors. Parameters W_{comp} and D_{comp} are compared with W_{ref} and D_{ref}.

Nevertheless, the SFSAE has the major advantage to be easily applicable in vivo because of the simultaneous estimation of the blood structural properties and total attenuation (contrary to the SFSE attenuation-compensation method, needing the attenuation and thickness of the tissue intervening layers to be known).

Acknowledgements This work was supported by the Canadian Institutes of Health Research (grants MOP-84358 and CMI-72323), by the Heart and Stroke Foundation of Canada (grant PG-05-0313), and by the National Institutes of Health of USA (grant RO1HL078655). Dr Cloutier is recipient of a National Scientist award of the Fonds de la Recherche en Santé du Québec. We are also thankful to Dr F. Destrempes for his helpful discussion on the optimization tool.

References

1. F. T. H. Yu and G. Cloutier, "Experimental ultrasound characterization of red blood cell aggregation using the structure factor size estimator", J. Acoust. Soc. Am. **122**, 645-656 (2007).
2. V. Roberjot, S. L. Bridal, P. Laugier, and G. Berger, "Absolute backscatter coefficient over a wide range of frequencies in a tissue-mimicking phantom containing two populations of scatterers", IEEE Trans. Ultras., Ferroelect., Freq. Contr. **43**, 970-978 (1996).
3. T. A. Bigelow, M. L. Oelze, and W. D. O'Brien, "Estimation of total attenuation and scatterer size from backscatter ultrasound waveforms", J. Acoust. Soc. Am. **117**, 1431-1439 (2005).
4. P. He and J. F. Greenleaf, "Application of stochastic analysis to ultrasonic echoes - Estimation of attenuation and tissue heterogeneity from peaks of echo envelope", J. Acoust. Soc. Am. **79**, 526-534 (1986).
5. B. J. Oosterveld, J. M. Thijssen, P. C. Hartman, R. L. Romijn, and G. J. E. Rosenbusch, "Ultrasound attenuation and texture analysis of diffuse liver disease: methods and preliminary results", Phys. Med. Biol **36**, 1039-1064 (1991).
6. E. Franceschini, Y. T. H. Yu, and G. Cloutier, "Simultaneous estimation of attenuation and structure parameters of aggregated red blood cells from backscatter measurements", J. Acoust. Soc. Am. **123**, EL85-91 (2008).
7. L. Y. L. Mo and R. S. C. Cobbold, "Theoretical models of ultrasonic scattering in blood", in *Ultrasonic Scattering in Biological Tissues*, edited by K. K. Shung and G. A. Thieme (CRC, Boca Raton, FL, 1993), Chap. 5, pp. 125-170.
8. V. Twersky, "Low-frequency scattering by correlated distributions of randomly oriented particles", J. Acoust. Soc. Am. **81**, 1609-1618 (1987).
9. K. K. Shung, "On the ultrasound scattering from blood as a function of hematocrit", IEEE Trans. Ultras., Ferroelect., Freq. Contr. **SU-26**, 327-331 (1982).
10. S. H. Wang and K. K. Shung, "An approach for measuring ultrasonic backscattering from biological tissues with focused transducers", IEEE Trans. Biomed. Eng. **44**, 549-554 (1997).
11. B. I. Raju and M. A. Srinivasan, "High-frequency ultrasonic attenuation and backscatter coefficients of *in vivo* normal human dermis and subcutaneous fat", Ultrasound in Med. Biol. **27**, 1543-1556 (2001).

A 3D semi-analytical model to predict the behavior of ultrasonic bounded beam traveling in cylindrical solid bar embedded in a solid matrix.

S. Yaacoubi, L. Laguerre, E. Ducasse, M. Deschamps

Abstract A 3D semi-analytical model for predicting the behaviour of ultrasonic bounded beam travelling in cylindrical solid bar is presented. The bar is embedded in a solid matrix and the beam is emitted by an off-axis source for generating non-axisymmetric waves. Fourier series and Vector Hankel transform are combined to decompose the inside field into infinity of elementary cylindrical waves propagating into radial direction and planar waves propagating in axial direction. Global resolution method and Generalized Debye Series Expansion (GDSE) are used both to calculate the global reflection/transmission coefficients. A numerical model is implemented to demonstrate the validity of the present theoretical solution for predicting velocity signatures.

1 Introduction

In many applied fields such as civil engineering, mechanical engineering or aeronautics, ultrasonic guided waves (UGW) are applied in non-destructive evaluation (NDE) to detect defects in waveguides.

This technique is appealing among others because it can provide a rapid, accurate and inexpensive assessment in a wide range of industries. It offers also the possibility to inspecting long lengths of waveguide from a single position. But, there

S. Yaacoubi, L. Laguerre

Laboratoire Central des Ponts et Chaussées, Centre de Nantes, Route de Bouaye, BP 4129, 44341 Bouguenais Cedex, France. e-mail : slah.yaacoubi@lcpc.fr, yaacoubislah@yahoo.fr

M. Deschamps, E. Ducasse

Laboratoire de Mécanique Physique, Université de Bordeaux, UMR C.N.R.S. 5469, 351 cours de la Libération, 33405 Talence Cedex, France

are some difficulties in applying this technique. One prominent difficulty is the multimodal and dispersive nature of the waveguide [1, 2]. The presence of elastic or visco-elastic embedding medium is another [3-5]. These embeddings tend to attenuate the propagating energy. This can severely degrade the performance of guided wave test with regard to test sensitivity and the distance of propagation. Therefore, a necessary step before detecting defects is to be able to calculate and understand the propagated elasto-dynamical field in such a healthy waveguide. To do so, a number of models have been developed.

These are generally based upon source decomposition on the transverse waveguide modes. This needs to identify the wavenumber along the guiding direction versus frequency relationships (*i.e.* the dispersion curves) and associated modeshapes. This can be done for the free axisymmetric case of the infinite cylinder by solving the Pochhammer-Chree characteristic equations followed by the resolution of the eigenvalue problem. Zemanek [6] was one of the first to fully derive the dispersion curves in 3D (axisymmetric and nonaxisymmetric) using root-finding algorithms. Pavlakovic et al. [7] extends this work for the calculation of the dispersion curves and associated modehapes for multi-layered cylinder waveguides. The case of the finite cylinder including excitation, wave propagation of multiple modes and reception was considered for the 2D case by Puckett and Peterson [8] through the derivation of a normal mode expansion model.

In this paper we propose a semi-analytical alternative solution to modal technique, which is a 3D extension to the 2D model from Laguerre et al. [9] to predict and interpret the ultrasonic pulsed bounded beam propagation in solid cylinder embedded (or not) in solid matrix. The spectral response to an inside spatial limited axis-off source field can be studied from the angular spectrum decomposition and generalized reflection/transmission coefficients modeling. This can be done through global resolution of using Debye series formalism. The transient response is then expressed after inverse transform integral as the superposition of semi infinite medium contribution and longitudinal, shear (SH and SV type) and coupled longitudinal-to-transversal contributions. This avoids the time consuming task of root-findings and the difficulty to calculate complex Bessel functions for leaky systems. This formalism can help to enhanced physical interpretation since the transient response is the combination of each sidewalls interaction. Moreover, the ability of the model to consider non-axisymmetric sources can be used as a first step to study wave field from defects.

2 Problem statement

Consider an infinitely long elastic, homogeneous and isotropic bar of density ρ and circular cross-section of radius b . As shown in Fig.1. a cylindrical coor-

dinate system (r,θ,z) is chosen with the z-direction coincident with the axis of the bar. This bar is in an infinite, homogeneous, isotropic elastic medium.

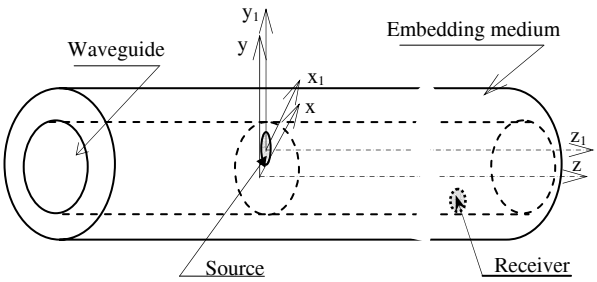

Fig. 1 Problem geometry

A source is imposed and localized off the cylinder axis of revolution. The source is assumed to be axisymmetric (with radius *a*) in its own local polar coordinate system $\left(o_1,\vec{e}_{r_1},\vec{e}_{\theta_1}\right)$. To facilitate the calculation, this function will be expressed in the global coordinate system $\left(o,\vec{e}_r,\vec{e}_\theta\right)$.

3 Theoretical development

In order to interpret accurately the elastodynamical field transiting in the bar, the field generated by the source must be first characterized. For solving this problem, there are several methods such as a normal mode expansion [10-11] and integral transform. All methods are equally rigorous and the choice is a matter of convenience for the problem at hand. The first method is not suitable when there is transmission (leakage) into embedding medium (when shear velocity is smaller than that of the waveguide). In such a case, the orthogonality relations underlying the normal mode expansion method are not directly applicable. Instead of using this method, we use here the integral transform method.

3.1 Integral transform method

The vector wave equation in cylindrical coordinates is given in space-time domain by:

$$(\lambda+\mu)\nabla\nabla\cdot\vec{v}+\mu\nabla\cdot\nabla\vec{v}+\vec{f}=\rho\dot{\vec{v}} \tag{1}$$

where λ and μ are the Lamé constants, ρ is the mass density, $\vec{f}$ and $\vec{v}$ are the vector volume force and the vector velocity respectively. Besides on the solution obtained earlier by separation of variables via the Helmholtz decomposition method, we resolve it by means of the transform integral method.

Firstly, by performing a Fourier series expansion with respect to the angular coordinate θ, any field ($\vec{v}$ and $\vec{f}$) can be written as the discrete sum of orthogonal fields, (i.e. $\int_0^{2\pi} s_1 s_2 d\theta = 0 \ \ if \ \ s_1 \neq s_2$):

$$\vec{s}(\vec{r},t)=\begin{Bmatrix} s_r^0 \\ s_\theta^0 \\ s_z^0 \end{Bmatrix}+\sum_{n=1}^{+\infty}\begin{Bmatrix} \vec{s}_r^{n,\square}\cos n\theta \\ \vec{s}_\theta^{n,\square}\sin n\theta \\ \vec{s}_z^{n,\square}\cos n\theta \end{Bmatrix}+\sum_{n=1}^{+\infty}\begin{Bmatrix} \vec{s}_r^{n,\perp}\sin n\theta \\ -\vec{s}_\theta^{n,\perp}\cos n\theta \\ \vec{s}_z^{n,\perp}\sin n\theta \end{Bmatrix} \tag{2}$$

where $\vec{r}=(r,\theta,z)$ is the displacement coordinates and t is the time. $\vec{s}_k^{\,0}$, $\vec{s}_k^{n,\square}$ and $\vec{s}_k^{n,\perp}$, $(k=r,\theta,z)$ do not depend on the azimuth coordinate θ. Injecting Eq. (2) in Eq. (1), we obtain a discrete set of three decoupled wave equations systems (corresponding to s_k^0, $\vec{s}_k^{n,\square}$ and $\vec{s}_k^{n,\perp}$), the spatial variables being r and z:

Secondly, to these systems, we apply vector Hankel transform [12-13] which is defined by:

$$\underbrace{\vec{S}_n(k_r,z,t)=\int_0^{+\infty}\Im(k_r r)\vec{s}_n(r,z,t)r dr}_{\Updownarrow}$$
$$\vec{s}_n(r,z,t)=\int_0^{+\infty}\Im(k_r r)\vec{S}_n(k_r,z,t)k_r dk_r \tag{3}$$

$\Im(k_r r)$ is 3×3 matrix which is expressed as follows:

$$\Im(k_r r)=\begin{pmatrix} \mathrm{B}_2(k_r r) & \mathrm{B}_3(k_r r) & 0 \\ \mathrm{B}_3(k_r r) & \mathrm{B}_2(k_r r) & 0 \\ 0 & 0 & \mathrm{B}_1(k_r r) \end{pmatrix} \tag{4}$$

where

$$\begin{cases} \mathrm{B}_1\left(k_r r\right) = J_n\left(k_r r\right) \\ \mathrm{B}_2\left(k_r r\right) = \dfrac{1}{2}\left[J_{n-1}\left(k_r r\right) + J_{n+1}\left(k_r r\right)\right] \\ \mathrm{B}_3\left(k_r r\right) = \dfrac{1}{2}\left[-J_{n-1}\left(k_r r\right) + J_{n+1}\left(k_r r\right)\right] \end{cases} \tag{5}$$

J_n is a cylindrical Bessel function of the first kind and order n, n is the circumferential number. The radial wavenumber k_r is related to the radial frequency by $k_r = 2\pi p$. Consequently, these systems which are already in (r, z, t) become a standard partial differential system of second order in $\left(k_r, z, t\right)$ domain:

$$\begin{cases} V_{1,t^2} = c_T^2 V_{1,z^2} & - k_r^2 c_T^2 V_1 + F_1 \\ V_{2,t^2} = c_T^2 V_{2,z^2} - k_r\left(c_L^2 - c_T^2\right) V_{3,z} & - k_r^2 c_L^2 V_2 + F_2 \\ V_{3,t^2} = c_L^2 V_{3,z^2} + k_r\left(c_L^2 - c_T^2\right) V_{2,z} & - k_r^2 c_T^2 V_3 + F_3 \end{cases} \tag{6}$$

The first equation of the above system is obviously decoupled from the two others. This system, without body force $\vec{F}$, can be solved by performing the Fourier transform with respect to the time t.

Finally, the solution is given in the frequency-radial wavenumber domain, considering the fact that the propagation is in $+z$ direction and solutions for $(z \to +\infty)$ have to vanish, by:

$$\hat{V}_1\left(k_r, f, z\right) = A_{T_1}\left(k_r, f\right) e^{-i2\pi w_T z}$$

$$\begin{Bmatrix} \hat{V}_2\left(k_r, f, z\right) \\ \hat{V}_3\left(k_r, f, z\right) \end{Bmatrix} = A_L\left(k_r, f\right) \begin{Bmatrix} \dfrac{k_r}{w_L} \\ 1 \end{Bmatrix} e^{-i2\pi w_L z} + A_{T_2}\left(k_r, f\right) \begin{Bmatrix} 1 \\ \dfrac{k_r}{w_T} \end{Bmatrix} e^{-i2\pi w_T z} \tag{7}$$

where $w_L = \sqrt{f^2 / c_L^2 - p^2}$ and $w_T = \sqrt{f^2 / c_T^2 - p^2}$ are the axial space frequencies of the longitudinal and the shear waves respectively. Their propagation velocities are $c_L = \sqrt{(\lambda + 2\mu)/\rho}$ and $c_T = \sqrt{\mu/\rho}$ respectively. A_L, A_{T_1} and A_{T_2} are the amplitudes of the cylindrical waves L, T_1 and T_2 respectively.

The function $\hat{V}_1$ is associated with horizontal polarized shear waves, while the functions $\hat{V}_2$ and $\hat{V}_3$ are associated with longitudinal and vertical polarized shear

waves. Now the source is involved in the boundary conditions at $z = 0$ and so the vector velocity $\vec{v}\ (r,\theta,t)\big|_{z=0}$ is known. Then by performing Fourier series expansions combined with vector Hankel transform and Fourier transform with respect to r and t respectively, $\vec{V}\ (k_r,f)\big|_{z=0}$ can be calculated. Hence, the amplitudes A_L, A_{T_1} and A_{T_2} can be easily deduced from Eq.(7).

To interpret the behaviour of the propagating field, solution in space-time domain is desired. For an *unbounded* medium, the general solution is obtained by means of the mathematical tools (inverse vector Hankel transform combined with inverse Fourier transform) described above. We obtain then:

$$\vec{v}\ (\vec{r},t)=\int_{-\infty}^{+\infty}\sum_{n=0}^{+\infty}\Gamma_n\int_0^{\infty}k_r\Im(k_r r)\vec{V}_n(k_r,z,f)dk_r e^{i2\pi ft}df \tag{8}$$

with $\Gamma_n = diag\left\{\begin{pmatrix}\cos n\theta\\ \sin n\theta\end{pmatrix},\begin{pmatrix}-\sin n\theta\\ cos n\theta\end{pmatrix},\begin{pmatrix}\cos n\theta\\ \sin n\theta\end{pmatrix}\right\}$

The infinity of waves constructing the incident field will propagate through the waveguide. These individual waves undergo multiple interactions with the waveguide/embedding interface. Consequently, the resulting field in such receiver point M in the waveguide (*bounded* medium) can be deduced from that in an *unbounded* medium by:

$$\vec{v}\ (\vec{r},t)=\int_{-\infty}^{+\infty}\sum_{n=0}^{+\infty}\Gamma_n\int_0^{\infty}k_r F(k_r,f)\Im(k_r r)\vec{V}_n(k_r,z,f)dk_r e^{i2\pi ft}df \tag{9}$$

$F(k_r,f)$ is the transfer function of the waveguide (By taking into account of the propagation waves conversions) or more precisely the waveguide part from the source to the point receiver M. In the following paragraph, we shall determine the transfer function. After that the total field will be determined.

3.2 Global method resolution and Debye series

The global method calculations give a global description of the scattering. The multiple reflections by waveguide/embedding interface and transmissions through it are not clear in the global formalism. The connection between the global theory and the ray acoustics is known as the Debye-series expansion. The Debye-series expansion allows for the decomposition of the global physical process in a series of local

interactions, which can bring a better physical understanding than the global resolution.

The incident wave can be longitudinal (L), vertical shear (T_1) or horizontal shear (T_2). Each engenders three waves by reflection and three waves by transmission through waveguide/embedding medium interface. Continuity conditions of velocities and stresses at this interface lead to a linear system of equations:

$$\underline{\underline{C}}^n \underline{X}_i^n = \underline{P}_i^n \quad , \left(i = L, T_1, T_2\right) \tag{10}$$

where

$$\underline{X}_i^n = \left\{ X_{iL}^{n-}, X_{iT_1}^{n-}, X_{iT_2}^{n-}, X_{iL}^{n+}, X_{iT_1}^{n+}, X_{iT_2}^{n+} \right\}^{tr} \tag{11}$$

The superscript *tr* is for vector transposition.

The first three coefficients represent the global *reflection* coefficient vector. The last three components represent the global *transmission* coefficient vector. $\underline{\underline{C}}^n$ represents the continuity matrix for each cylindrical wave. $\underline{P}_i^n$ is the velocity-stress vector of the incident field. By extending the Generalized Debye Series used in 2D study [9] for 3D study, the final explicit expression of the global *reflection* coefficient vector is:

$$\begin{Bmatrix} X_{iL}^{n-} \\ X_{iT_1}^{n-} \\ X_{iT_2}^{n-} \end{Bmatrix} = \sum_{N=1}^{\infty} \begin{bmatrix} r_{LL}^n & r_{T_1L}^n & r_{T_2L}^n \\ r_{LT_1}^n & r_{T_1T_1}^n & r_{T_2T_1}^n \\ r_{LT_2}^n & r_{T_1T_2}^n & r_{T_2T_2}^n \end{bmatrix}^{N-1} \begin{Bmatrix} r_{iL}^n \\ r_{iT_1}^n \\ r_{iT_2}^n \end{Bmatrix}, \tag{12}$$

r_{ij}^n are the local reflection coefficients of a cylindrical wave by the waveguide/embedding interface, when *i* and *j* are the incident and reflected wave respectively. *N* is the interactions number. Eq.(12) retains explicitly the multiple interactions with the interface.

3.3 Total field in the bar

In order to inspect the inner medium, it's interesting to show the velocity behaviour in this medium. So, in this section, only velocity field for $r < b$ will be expressed. The space-time velocity field at a distance *z* from the source is the combination of Vector Hankel Transform, Fourier series and the global coefficient

reflections X_{iL}^{n-}, $X_{iT_1}^{n-}$, $X_{iT_2}^{n-}$ which are determined from their respective Debye series expansions (12). The vector field can be expressed by:

$$\vec{v} = v_r\vec{e}_r + v_\theta\vec{e}_\theta + v_z\vec{e}_z \tag{13}$$

Here, for the sake of clarity, only the z-component will be shown using the following synthesized form:

$$v_z^{ij}(\vec{r},t) = \int_{-\infty}^{+\infty}\left[\sum_{n=0}^{+\infty}\Gamma_n\int_0^{\infty}2\pi p\left(\eta + X_{ij}^{n-}\right)B_1(2\pi Qr)\hat{V}_1(2\pi p,z,f)dp\right]e^{I2\pi ft}df \tag{14}$$

where I is the imaginary number, $I^2 = -1$, η is a coefficient which indicates the type of polarization (co-polarization and mode propagation conversion) and Q is the radial space frequency of the cylindrical waves propagating in the waveguide. They are expressed respectively by:

$$\eta = \begin{cases} 1 \ if \ \ i = j \\ 0 \ if \ \ i \neq j \end{cases};$$

$$Q = \begin{cases} p \ \ if \ \ i = j \ \ \ or \ \ ij = T_1T_2 \ or \ T_2T_1 \\ q_T\left(w_L\right) \ if \ \ i \neq j \ \ and \ i = L \\ q_L\left(w_T\right) \ if \ \ i \neq j \ \ and \ i = T_1, T_2 \end{cases}$$

Note that the shear waves T_1 and T_2 have the same axial space frequency ($w_{T_1} = w_{T_2} = w_T$).

The norm of the total field can be written as:

$$\|\vec{v}\| = \sqrt{v_r^2 + v_\theta^2 + v_z^2} \tag{15}$$

4 Numerical evaluation

In principle, the integral transform method is exact, but in most cases its inversion which is intractable (such Eq.(7) in this paper) must be carried out numerically. Additionally, the resolution of 6×6 matrix to determine the local coefficients reflection and the calculation then of the global coefficients reflection are complexes and should be performed numerically. Furthermore, the dispersive and multimodal

nature of the ultrasonic signals and the fact that their behaviors within the bar are desired dictate that the computations be made numerically. The interpretation of these behaviors in the time domain is complement by that in frequency domain. The mutual relation between these two domains can be described numerically by the discrete Fourier transform (DFT). For length M input vector y, the DFT is a length M vector Y, with elements

$$Y(m) = \sum_{\nu=1}^{M} y(n) e^{-I2\pi(m-1)(\nu-1)/M}, 1 \le m \le M \tag{16}$$

The inverse DFT is given by

$$y(n) = \frac{1}{M} \sum_{m=1}^{M} Y(m) e^{I2\pi(m-1)(\nu-1)/M}, 1 \le n \le M \tag{17}$$

where ν and m correspond to time and frequency respectively.

Now the discrete form of the z-component of the velocity field (Eq.(14)) can be written in the space-time domain as following:

$$v_z^{ij}(\nu) = \frac{1}{M} \sum_{m=1}^{M} \sum_{n=0}^{N_{tronc}} \Gamma_n \int_0^{P_{tronc}} 2\pi p \left(\eta + X_{ij}^n(p,m)\right) B_1(2\pi Qr) \hat{V}_1(2\pi p, z, m)\, dp \; e^{I2\pi(m-1)(\nu-1)/N}, \quad 1 \le \nu \le M \tag{18}$$

where N_{tronc} is the truncation index of the series at hand, while P_{tronc} is the truncated radial frequency of the integration over p. In the far propagation, the effects of evanescent waves are negligible compared to those of progressive waves and consequently P_{tronc} will be reduced to $P_{tronc} = m / c_L$.

The frequency dependence of the wavenumber in propagation direction (as well as the phase velocity and the group velocity) requires that the model be able to perform the velocity field in the axial wavenumber-frequency domain. To do it, we substitute the term within the square brackets of Eq. (14) into Eq.(16). The discrete form of this equation is given by:

$$V_z^{ij}(m_z, f) = \sum_{\nu_z=1}^{M_z} \left[\sum_{n=0}^{N_{tronc}} \Gamma_n \int_0^{P_{tronc}} 2\pi p \left(\eta + X_{ij}^n(p,f)\right) B_1(2\pi Qr) \hat{V}_1(2\pi p, \nu_z, f)\, dp \right] e^{-I2\pi(m_z-1)(\nu_z-1)/N}, \quad 1 \le m_z \le M_z \tag{19}$$

where the indices ν_z and m_z correspond to space coordinate z and axial frequency w_z respectively and M_z is the number of points in the DFT.

Some examples

As an application example of this model, we consider a bar embedded in a cement grout. The source can be either a transducer or a defect. For generating the non-axisymmetric waves, the source is localized in an off-axis of the bar (fig.1). A question can be asked: can we generate these waves by only an axial excitation? So, the velocity field is expressed in the source basis by:

$$\vec{v}\left(r_1,t\right)=\left\{0,\quad 0,\quad v_z\left(r_1\right)\right\}^{tr} e\left(t\right) \tag{20}$$

where, at $z=0$, v_z is a bounded Gaussian beam which is expressed as follows:

$$v_z=\begin{cases} v_0\exp\left(-\dfrac{\pi r_1^2}{\alpha^2}\right), r_1<a\,and\,\theta_1\in[0,2\pi] \\ 0\qquad\quad ,\qquad otherwise \end{cases} \tag{21}$$

By using the addition theorem [14] and the inverse vector Hankel transform, the axial velocity component can be written in the global basis after simplification as follows:

$$v_z(r,\theta)=\sum_{n=-\infty}^{n=+\infty}\int_0^{+\infty} 2\pi p\alpha^2 v_0 e^{-\pi\alpha^2p^2}B_1(2\pi pr)J_n\left(2\pi pr_0\right)e^{in(\theta-\theta_0)}dp, \tag{22}$$
$$r\in[0,b]\ and\ \theta\in[0,2\pi]$$

The propagation of the waves in the waveguide will create radial, tangential and axial motions. The velocity field in space-time domain can be expressed by:

$$v_z^{ij}(\vec{r},t)=\sum_{n=0}^{+\infty}\varepsilon\int_{-\infty}^{+\infty}\left\{\int_0^{+\infty}2\pi p\left[\eta+X_{ij}^n\right]\alpha^2v_0e^{-\pi\alpha^2p^2}B_1(2\pi Qr)\right. \tag{23}$$
$$\left. J_n(2\pi pr_0)\cos n\left(\theta-\theta_0\right)e^{-I2\pi w_i z}\,dp\right\}E(f)\,e^{-I2\pi ft}df$$

where $E\left(f\right)$ is a spectre of a modulated Gaussian input pulse.

The discrete equation (19) of the velocity z-component and those for radial and tangential velocities which can be evaluated by the same way lead to the velocity expression in $\left(r,\theta,w_z,f\right)$ domain, where w_z is the space axial frequency. For $\left(r,\theta\right)$ fixed, the velocity has a unique value for each $\left(w_z,f\right)$. The representation of the velocity amplitude $\left|V\right|$ as a function of frequencies $\left(w_z,f\right)$ defined the *dispersion diagram*.

For the sake of clarity, we represent the image of the velocity amplitude $|V|$ in the (w_z, f) plane. The result of this representation is illustrated by figures 2.a, 2.b, 2.c and 2.d. The first three simulated dispersion diagrams are superposed with

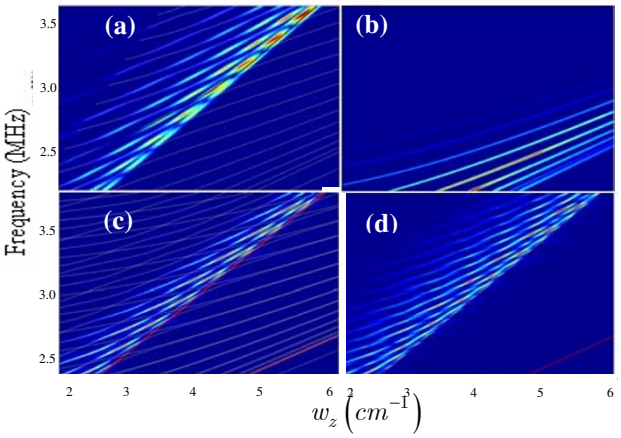

Fig. 2 Velocity dispersions diagrams (wz, f) and dispersion curves simulated by Disperse software for z0=110 mm and f0=2.5MHz: (a) longitudinal modes L(0,m), (b) Torsional modes T(0,m), (c) flexural modes F(1,m) and (d) total velocity (sum of all modes).

dispersion curves (few lines). These curves are derived from Disperse software which is based on modal solutions. We observe a very good agreement between our dispersion diagrams and dispersion curves: longitudinal L(0,m), torsional T(0,m) and flexural F(1,m). When the source is located on the cylinder axis, only the axisymmetric waves contribute to the solution. When the source is located off the cylinder axis, then the solution consists of the contributions of all waves (axisymmetric and non-axisymmetric ($n \geq 1$)). The number of these waves is determinated by means of the convergence study of the series expansion (Eq.(12)).

The dispersion diagram is a function of the source nature (piston, gaussian…), excitation type (longitudinal, shear) and evidently the bar radius and the frequency. Since the excitation is only longitudinal, the simulated signal phase velocities describe only the portion of the dispersion curves greater than the velocity of longitudinal wave in steel c_L as shown in figures 2.a, 2.c and 2.d. In spite of the axial excitation (only the v_z component is not zero), all types of modes are excited: longitudinal L(0,m), torsional T(0,m) and flexural F(n>0,m). The generation of flexural modes is due to off-axis source positioning. In addition, in some cases, the non-axisymmetric wave amplitude $(n > 0)$ is greater than that of axisymmetric wave. This is shown in Fig.3 (bottom) which plots (as histograms) the maximum of the velocity amplitude versus the circumferential number n for r_0=5mm, r=8mm. In

this case, the source and the point receiver are coplanar (they have the same circumferential angle).

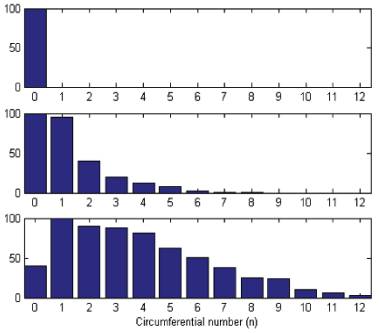

Fig. 3 Maximum of the amplitude velocity as a function of circumferential number n for $r_0 = 0$ (top), $r_0 = 2mm$ (middle) and $r_0 = 5\ mm$ (bottom). It's defined as a percentage of the greatest amplitude velocity.

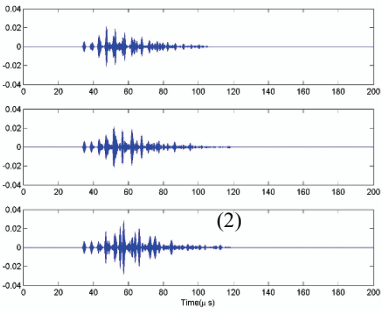

Fig. 4 Time waveforms velocity at r=8mm and z=200mm for $r_0 = 0$ (top), $r_0 = 2mm$ (middle) and $r_0 = 5\ mm$ (bottom).

Figure 4 plots time waveforms of the total velocity for the steel bar embedded in cement grout. The source is localized on the positions $r_0 = 0, 2, 5\ mm$ while θ_0 is fixed at zero for all cases. The time waveform amplitudes increase when the coordinate r_0 increase. This is due to the reduced path between source and receiver point. The interference of travel waves dictates the distortion of the signals. The first pulse is similar for the three cases while others are differents. Additionally, at $r_0 = 5\ mm$ the last trailing pulses (1, 2) are important and can not be neglected.

5 Conclusion

Because an incident field causes a non uniform energy distribution in solid cylindrical waveguide even if the transducer is on-axis cylinder, a theoretical development of a three-dimensional bounded beam traveling in a cylindrical solid waveguide embedded in an infinite medium has been presented. This development is based on a combination of Vector Hankel Transform and Fourier series for decomposing a bounded beam in partial cylindrical waves propagating in radial and axial directions. Generalized Debye series is employed for expressing global reflection coefficients with respect to local reflection coefficients. To generate nonaxially symmetric waves, an off-axis source is used. If the source is localized in the cylinder axis, only axisymmetric waves can be generated. Otherwise, non-axisymmetric are generated. For some source positioning, their amplitudes are greater than that of

the axisymmetric waves. Therefore, nonaxisymmetric waves deserve special attention when dealing with both source leading and detection characterization.

References

1. Meeker T. R. and Meitzler A. H.: Guided Wave Propagation in Elongated Cylinders and Plates, Phys. Acoust., Part A, Academic Press, New York (1964).
2. Thurston R.: Elastic waves in rods and clad rods, J. Acoust. Soc. Am. 64(1), 1-35 (1978).
3. Pavlakovic B., Lowe M., Cawley P.: High frequency low loss ultrasonic modes in embedded bars, J. Appl. Mech 68, 67-75 (2001).
4. Barshinger J., Rose J. L., Avioli M. J.: Guided wave resonance tuning for pipe inspection", J. Press. Vess. T-ASME, 124, 303-310 (2002).
5. Beard M.D, Lowe M.: Non-destructive testing of rock bolts using guided ultrasonic waves", Int. J. Rock Mech. Min. 40, 527-536 (2003).
6. Zemanek J.: An experimental and theoretical investigation of elastic-wave propagation in a cylinder, J. Acoust. Soc. Am. 51, 265-283 (1972).
7. Pavlakovic B. N., Lowe M., Alleyne D.N., Cawley P.: Disperse: a general purpose program for creating dispersion curves, QNDE Proc., 16, 185-192 (1997).
8. Puckett A., Peterson M.: A semi-analytical model for predicting multiple waveguide propagating axially symmetric modes in cylindrical waveguides, Ultrasonics 43, 197-207 (2005).
9. Laguerre L., Grimault A., Deschamps M.: Ultrasonic transient bounded-beam propagation in solid cylinder waveguide embedded in a solid medium", J. Acoust. Soc. Am. 121, 1924-1934 (2007).
10. Li J., Rose J. L.: Excitation and propagation of non-axisymmetric guided waves in a hollow cylinder, J. Acoust. Soc. Am. 109(2), 457-467 (2001).
11. Ditri J.J.: Excitation of guided wave modes in hollow cylinders by applied surface tractions, J. Appl. Phys. 72(7), 2589-2597 (1992).
12. Chew W. C, Kong J.A.: Resonance of nonaxial symmetric modes in circular microstrip disk antenna, J. Math. Phys. 21, 2590-2598 (1980).
13. Kausel E.: Fundamental Solutions in Elastodynamics. A Compendium, Cambridge University Press (2006).
14. Stratton J. A.: Electromagnetic Theory, McGraw-Hill Company, New York and London (1941).

Comparison between a multiple scattering method and direct numerical simulations for elastic wave propagation in concrete

M. Chekroun, L. Le Marrec, B. Lombard, J. Piraux and O. Abraham

Abstract Numerical simulations are performed to study the propagation of elastic waves in a 2-D random heterogeneous medium such as concrete. To reduce spurious numerical artefacts to a negligible level, a fourth-order time-domain numerical scheme and an immersed interface method are used together. Effective properties of the equivalent homogeneous medium are extracted and compared to the predictions of a multiple scattering method (ISA), to evaluate the validity of this latter.

1 Introduction

Concrete is made up of coarse aggregates embedded in a cement paste matrix (mortar). When ultrasounds propagate in this heterogeneous medium, multiple scattering is important when the wavelength and the size of scatterers are similar. In this case, the wave field is the superposition of a coherent field, obtained by averaging fields over several realizations of disorder, and of an incoherent field. The coherent field amounts to waves propagating in an equivalent homogeneous medium, with effective phase velocity and attenuation deduced from an effective wavenumber.

The goal of multiple-scattering methods, such as the Independent Scattering Approximation (ISA) [1], is to provide analytical expressions of this effective wavenumber. A basic assumption for derivation of ISA is that the concentration of scatterers is low. Since aggregates may represent 50 % in volume, the medium

Mathieu Chekroun, O. Abraham
LCPC centre de Nantes - BP4129, 44341 Bouguenais, France

L. Le Marrec
IRMAR - Université Rennes 1, Campus Beaulieu - 35042 Rennes, France

B. Lombard, J. Piraux
LMA - CNRS, 31 chemin Joseph Aiguier - 13402 Marseille, France.

cannot be considered as dilute, and a deeper analysis is required to decide whether ISA is valid in that case.

For that purpose, a purely numerical methodology is followed, based on 2D direct numerical simulations and on signal-processing tools. Doing so is much faster and less expensive than real experiments, allowing also much finer measures. In previous works, this methodology has been applied successfully to a case where ISA has been experimentally validated: steel rods immersed in water [2]. In the present paper, the host medium and the aggregates are both modeled as elastic media. Cases of different concentrations of aggregates are discussed. Since the propagation of Rayleigh waves along a free surface of concrete is the original motivation of the present study, the case of both compressional and shear incident plane wave is considered (P-SV problem).

2 Problem statement

2.1 Concrete model

Aggregates are assumed to be circular cylinders with a unique radius $a = 6$ mm, in a bidimensional geometry. The probing frequency varies from 50 kHz to 700 kHz. In that range, wavelengths vary from about 3 mm (S wave) to 90 mm (P wave), hence aggregates are considered as heterogeneities for waves. On the contrary, mortar is considered as an homogeneous medium for wave propagation, since the size of its components (water, sand and cement) is much smaller than the wavelengths. The concrete is then be considered as a two phase medium with parameters [3]

$$(\rho, c_p, c_s) = \begin{cases} (2050\,\mathrm{kg/m^3}, 3950\,\mathrm{m/s}, 2250\mathrm{m/s}) & \text{in mortar,} \\ (2610\,\mathrm{kg/m^3}, 4300\,\mathrm{m/s}, 2475\mathrm{m/s}) & \text{in aggregates,} \end{cases}$$

where ρ is the density, c_p and c_s are the celerities of P and S waves. The concentration of aggregates in concrete is described by the number n of scatterer per unit area. Three surface ratios $\phi = n\pi a^2$ are considered in the following: $\phi = 6\%$, 12%, and 18%, defining 3 concretes called C6, C12 and C18 respectively. The average distance between nearest scatterers is $l_\phi = a\sqrt{\pi/\phi}$, hence: $l_{6\%} = 43$ mm, $l_{12\%} = 32$ mm, $l_{18\%} = 25$ mm. We assume perfect contact between aggregates and mortar (continuity of tractions and of displacements at the boundaries) and no dissipative effect. These hypotheses and the low density of aggregates affect the realism of our model but allow us to focus on the validity of ISA without additional artifact.

2.2 Independent Scattering Approximation

The formulation of the *Independent Scattering Approximation* (ISA) is usually established with an fluid matrix [4], but it can be straightforwardly extended to an elastic matrix. As correlation between scatterers is not taken into account, mode conversion does not perturb the expression of effective wavenumbers. Then, the effective wavenumbers $k_{P,eff}$ and $k_{S,eff}$ obtained with incident plane P and S waves satisfy

$$k_{P,eff}^2(\omega) = k_{P,0}^2 - 4in f_{PP}(0), \qquad k_{S,eff}^2(\omega) = k_{S,0}^2 - 4in f_{SS}(0), \tag{1}$$

where $k_{P,0}$ and $k_{S,0}$ denote P and S wavenumbers of the matrix, $\omega = 2\pi f$ is the angular frequency, and $f_{PP}(0)$ is the far field pattern in P mode of the interaction between an incident plane P wave and a single scatterer in the forward direction (idem for S waves with $f_{SS}(0)$).

3 Direct numerical simulation

3.1 Elastodynamic equations

A velocity-stress formulation of 2D elastodynamics is followed. To solve the hyperbolic system so-obtained, a uniform Cartesian grid with mesh sizes $\Delta x = \Delta y$ and time step Δt is defined. An explicit fourth-order accurate finite-difference ADER scheme is used [5], with a CFL constraint of stability $\beta = c\Delta t/\Delta x \leq 0.9$. A plane wave analysis of this scheme is performed in homogeneous medium, in terms of β and of $G = \Delta x/\lambda$, $G \in]0, 0.5]$, where λ is the wavelength [6]. The maximal artifacts are obtained when the direction of propagation coincides with grid axes, that is in 1D configurations. In that case, the ratio q between exact and discrete phase velocities, and the discrete attenuation α, are

$$q(\beta, G) = 1 - \frac{2\pi^4}{15}(\beta^2 - 1)(\beta^2 - 4)G^4 + O(G^6). \tag{2}$$

$$\alpha(\beta, G, \Delta x) = \frac{4\pi^6\beta}{9\Delta x}(\beta^2 - 1)(\beta^2 - 4)G^6 + O(G^8). \tag{3}$$

In forthcoming numerical experiments, $\beta = 0.44$ and $G = 1/90$ correspond to the most penalizing situation of SV waves in mortar at $f = 250$ kHz. With these parameters, (3) gives a quality factor $Q \approx 3.2\,10^7$, hence the numerical attenuation is much smaller than the expected physical attenuation of the effective medium.

3.2 Discretization of interfaces

Three classes of drawbacks are classically induced by interfaces in finite-difference schemes on Cartesian grids. First, the geometrical description of arbitrary-shaped interfaces is poor, and generates spurious diffractions. Second, the jump conditions are not enforced numerically. Third and last, non-smoothness of the solution across interfaces decreases the accuracy, leading to spurious oscillations or even instabilities. These three drawbacks prevent from using simulations as metrological tools in highly heterogeneous media. To circumvent them, the ADER scheme is coupled with an immersed interface method [7], which accounts both for the jump conditions and for the subcell geometry at points along the interfaces. The main part of the work can be done during a preprocessing step, before numerical integration. At each time step, $O(\mathscr{L}/\Delta x)$ matrix-vector products are done, where $\mathscr{L}$ is the total perimeter of interfaces, and the matrices are small-size, typically 5×100. Then, the results are injected in the scheme.

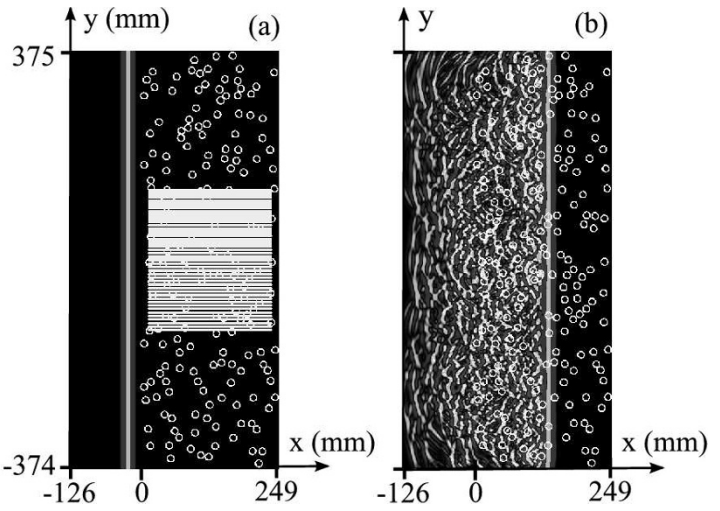

Fig. 1 Snapshot of the horizontal velocity at the initial instant (a), and after 0.04 μs of propagation (b). In (a), the regular grid denotes the location of the receivers.

3.3 Numerical setup

The size of the computational domain is 375 mm along x and 750 mm along y, with $\Delta x = 0.1$ mm and $\beta = 0.85$ in aggregates. The aggregates are randomly distributed on a 248 mm $\times$ 740 mm rectangular subdomain (figure 1). An exclusion length of $6\Delta x$ between each scatterer is ensured. The right-going incident P or SV plane

wave is a Ricker centered at 250 kHz. At the initial instant, the right part of the wave front is located at $x = 0$. At each time step, the exact plane wave solution in homogeneous medium is enforced on the edges of the domain. The simulations are stopped when the incident wave has crossed the inclusions: 3250 time steps with an incident P wave, 5300 time steps with an incident S wave.

A set of 41 horizontal lines of receivers is taken with $N = 221$ regular offsets along x, denoted by $d_i = d_0 + i\Delta x_r$, with $i = 0, ..., N-1$, $d_0 = 14$ mm and $\Delta x_r = 1$ mm. The distance between two lines is $\Delta y_r = 6.25$ mm. Each line corresponds to a realization of a random process. These parameters are discussed in section 4.2. Receivers are sufficiently far from the boundaries of the computational domain to avoid spurious reflections.

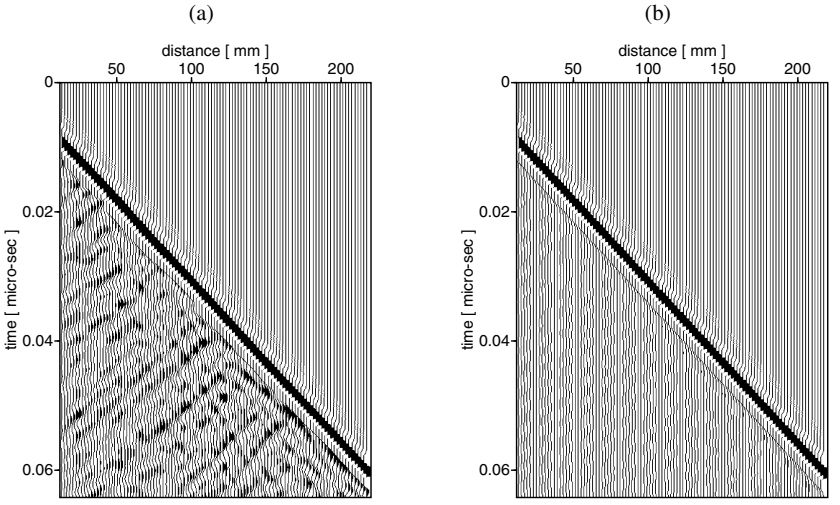

Fig. 2 Seismograms of the horizontal velocities u_x from the simulation with incident P wave in C12: one particular realization (a), coherent field obtained after averaging (b).

Three simulations provide $41 \times 3 = 123$ independent realizations of disorder, ensuring the convergence of the signal processing methods. Recorded velocities along a line of receivers can be plotted as seismograms. A particular seismogram in the case of incident P wave in C12 is presented in figure 2(a). A main wave train is clearly visible and is followed by an incoherent coda. After averaging on the 123 realizations of disorder, the coherent field is obtained and is presented in figure 2(b). The main wave train is still clearly visible and all the incoherent variations of the field have greatly decreased.

With an incident P wave (respectively S wave), the coherent field is observed through the averaging of horizontal velocities u_x (respectively vertical velocities u_y).

In such configuration, the propagation through the effective medium is equivalent to a 1D propagation in a slab, what explains that no effective S wave (respectively P wave) is observed in the case of an incident P wave (respectively S wave).

The dispersion curves and damping factor curves can now be estimated from the Fourier transform of this coherent field.

4 Signal processing

4.1 Methods

The phase velocity $c(\omega)$ is computed using the $p-\omega$ transform which represents the entire data wave field into the slowness-frequency domain ($p-\omega$), where $p = 1/c$ [8]. The method consists in a "slant stack summation" of the wave field (or $\tau-p$ transform, with τ representing a delay time) followed by a 1D Fourier transform over τ to obtain the wave field in the $p-\omega$ plane, where the dispersion curves can be directly picked. Here, we follow a formulation entirely in the frequency domain [9]. The time Fourier transform of the coherent field $s(\omega, d_i)$ at the distance d_i is

$$s(\omega, d_i) = A(\omega, d_i)\mathrm{e}^{-i\omega p_0(\omega) d_i}, \tag{4}$$

where $A(\omega, d_i)$ is the amplitude spectrum at d_i. The $p-\omega$ stack $\hat{s}(\omega, p)$ is

$$\hat{s}(\omega, p) = \sum_{i=1}^{N} A(\omega, d_i) e^{i\omega(p-p_0(\omega))d_i}. \tag{5}$$

The computation of $\hat{s}(\omega, p)$ is performed with several values of p. Given ω, the maximum of the modulus $|\hat{s}(\omega, p)|$ is reached at $p = p_0(\omega)$; the $|\hat{s}(\omega, p)|$ map is plotted as a 2D function of p and ω and the maximum locus is extracted at each frequency.

The damping factor is estimated from the decrease of the amplitude spectrum of the coherent field during propagation. In the frequency domain, the amplitude spectrum in (4)-(5) takes the following expression:

$$A(\omega, d_i) = A_0(\omega)\mathrm{e}^{-\alpha(\omega) d_i}, \tag{6}$$

where $A_0(\omega)$ is the amplitude of s at the first receiver. The damping parameter $\alpha(\omega)$ is determined by the slope of a least-square linear fit of $\ln(A(\omega, d_i))$. Since the incident wave is plane, no geometrical spreading has to be considered.

4.2 Analysis of accuracy

For evaluating the damping factor, no restriction is imposed about the number and position of receivers. For phase velocity, however, aliasing and limited resolution may be encountered [10]. The quantification of these artifacts has justified the numerical acquisition setup (number and position of the receivers). Aliasing occurs when $\Delta x_r > \lambda_{min}$, while resolution is limited by the total length of the acquisition setup $L_N = N \times \Delta x_r$. Phase velocity estimation is accurate as long as $\lambda < L_N/2$. Consequently, in the range of frequency under study, $L_N \geq 180$ mm and $\Delta x_r = 1$ mm.

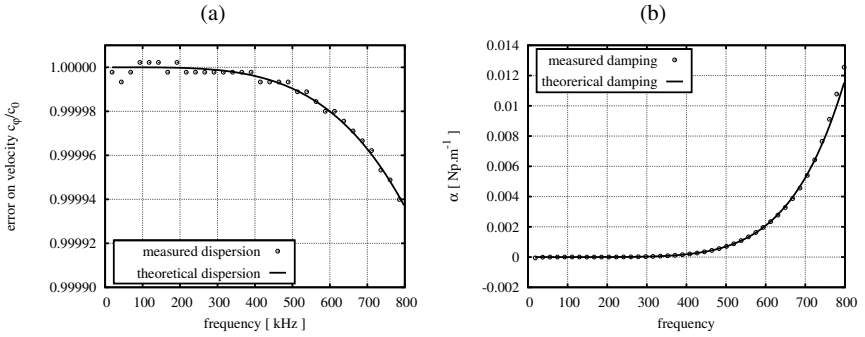

Fig. 3 1D homogeneous medium: analytical and simulated dispersion (a) and damping (b).

To evaluate how accurately the phase velocity and the damping factor are estimated, we apply the processing tools to 1-D simulation in an homogeneous medium, where numerical dispersion (2) and damping (3) are known. The numerical errors are maximum with the slowest celerity and shortest wavelength. In our case, it corresponds to the propagation of shear waves in mortar. A 1D homogeneous simulation of this case is computed, using the same numerical and acquisition parameters as used in 2D. The phase velocity and damping factor measured are compared to their theoretical counterparts in figure 3. The error between the theoretical curves and the measured ones is lower than $10^{-3}\%$. The signal processing method used and the acquisition setup chosen is then suitable to evaluate the dispersion curves and the damping factor with no significant signal processing artifacts.

5 Numerical experiments

5.1 Stabilized regime

The multiple-scattering regime requires a minimal distance of propagation to be established. The numerical tools proposed in sections 3 and 4 allow to estimate this distance l_{stab} to get a stabilized regime, frequently mentioned in the litterature [11] but rarely quantified to our knowledge. To do so, measures of α deduced from (6) are used: unlike the phase velocity, the attenuation may be estimated accurately on a distance of acquisition much smaller than the total length L_N, authorizing to test various zones of acquisition. Here, a fixed offset d_0 is considered, with a variable length of acquisition $L_M = d_0 + (M-1)\Delta x_r$ and $M \leq N$ (see section 3.3). The configuration under study is an incident S wave in a concrete C12.

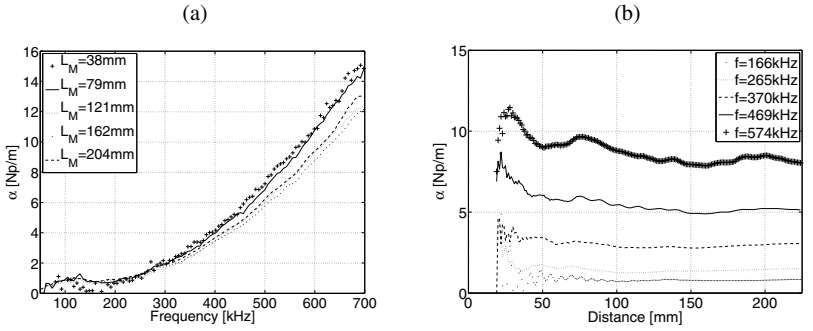

Fig. 4 Damping evaluated from the first offset d_0, at fixed length of acquisition L_M (a) and at fixed frequency (b).

Figure 4-(a) shows $\alpha(f)$ obtained with various values of the length of acquisition L_M. If $L_M < 90$ mm, the curves are noisy, especially in the low-frequency range where they do not grow monotonically, which is not realistic. In high frequency, differences up to 2 Np/m are measured between the various curves. Figure 4-(b) shows $\alpha(L_M)$ with various values of f. The attenuation is noisy up to $L_M \approx 90$ mm, independently of the frequency; with greater values of L_M, the curves are almost constant, which amounts to a stabilized regime of propagation.

This observation is confirmed with the other concentrations and with incident plane P waves. Only the approximate minimal length of acquisition L_M varies: 90 mm for C6, as seen in the previous paragraph; 70 mm for C12; and 50 mm for C18. These distances are close to $2l_\phi$ whatever the frequency range and the concentration.

Consequently, numerical simulations indicate that the minimal distance of propagation to get a stabilized scattering regime is roughly $l_{\text{stab}} \approx 2l_\phi$. Similar expressions have been proposed in the related area of band-gap creation in phonic crystals

[12]. From now on, all measures are done by excluding this zone of stabilization, i.e. from $2\,l_\phi$ to L_N.

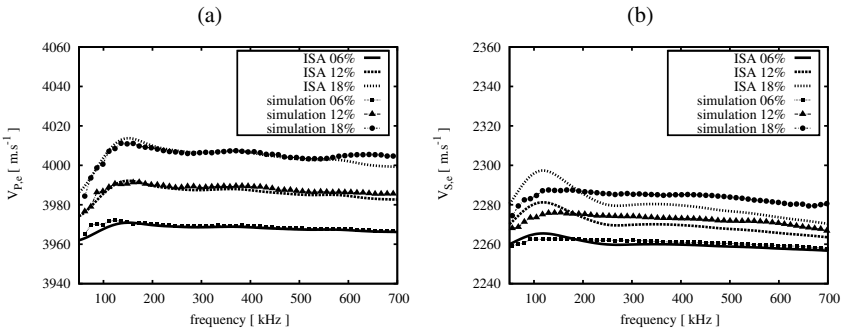

Fig. 5 Phase velocity: comparison between ISA and numerical simulations, with various concentrations of aggregates. (a): incident P wave (a); incident S wave (b).

5.2 Validity of ISA

The damping factor and phase velocity computed with ISA are compared to similar quantities measured on simulated data. The latter can be considered as the reference solutions, as shown in section 3.

First, the phase velocity is examined in figure 5. With an incident P wave (a), differences up to 1 m/s are observed between ISA and the simulated measures. Even with C18, ISA fits well the measured phase velocity. With an incident S wave (b), differences are of about 5 m/s, which remains acceptable. The slight decrease of the phase velocity at high frequencies is well described by ISA for both waves.

Second, the damping factor is examined in figure 6. With an incident P wave, the error is lower than 2 Np/m at the concentration 18 % (b). With an incident S wave, the same remark holds up to 12 %; with higher concentration, the error increases dramatically (d). In both cases, ISA gives better results with lowest concentration and low frequencies, which is consistent with the main hypotheses of a dilute medium.

6 Concluding remarks

The main results of this work are as follows:

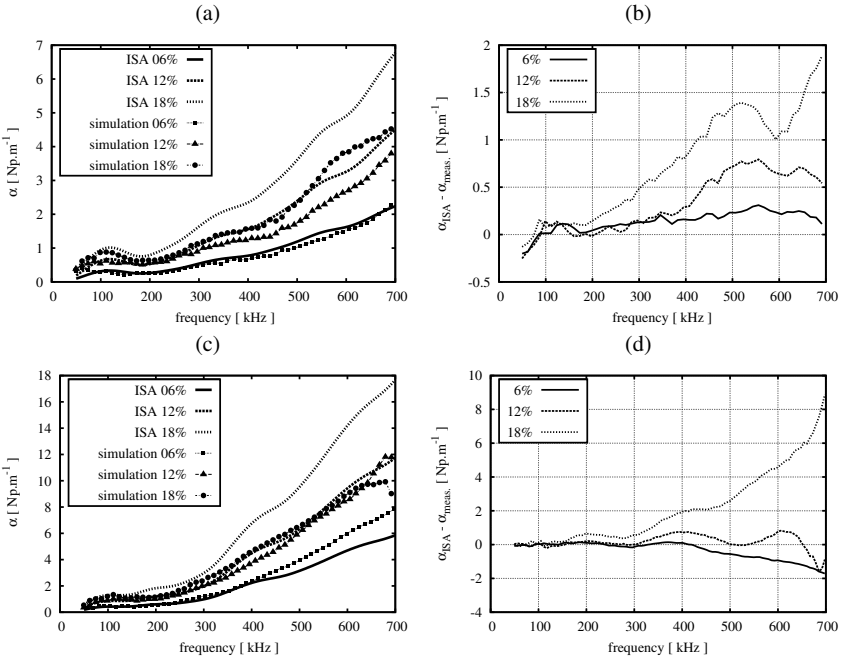

Fig. 6 Damping factor: comparison (left) and difference (right) between ISA and numerical simulations, with various concentrations of aggregates. Top: incident P wave; bottom: incident S wave.

1. the distance of propagation required to get a stabilized regime of multiple scattering is roughly $2l_\phi$, where l_ϕ is the mean distance between scatterers;
2. with an incident P wave, ISA provides good estimations of phase velocity and acceptable estimation of attenuation (lower than 2 Np/m) with a concentration nearly up to 20%; with an incident S wave, the concentration must be smaller than 10% to get the same agreement.

Three directions are distinguished for further investigation:

1. increasing the surfacic concentration of aggregates, up to 50%. Doing so requires to parallelize the algorithms used for direct numerical simulations;
2. considering continuous distribution size of aggregates, from a few mm to 20 mm. Is the aforementionned empirical formula still valid in the case of a medium where l_ϕ varies ?
3. studying higher-order multiple-scattering methods [11].

References

1. A. Derode, A. Tourin and M. Fink, *"Random multiple scattering of ultrasound. I. Coherent and ballistic waves"*, Phys. Rev. E 64, 036605, 2001.
2. M. Chekroun, L. Le Marrec, B. Lombard, J. Piraux and O. Abraham, *"Numerical methods for multiple scattering of ultrasound in random media"*, Proceedings of Waves 2007 Conference (Reading, UK), 2007, pp 492-494.
3. F. Schubert and B. Koehler, *Numerical time-domain simulation of diffusive ultrasound in concrete*, Ultrasonics **42**(1-9), 781-786 (2004).
4. A. Derode, V. Mamou and A. Tourin, *"Influence of correlations between scatterers on the attenuation of the coherent waves in random medium"*, Phys. Rev. E 74, 036606, 2006.
5. T. Schwartzkopff, M. Dumbser, C.D. Munz, *Fast high order ADER schemes for linear hyperbolic equations*, J. Comput. Phys., 197-2 (2004), 532-539.
6. J.S. Strikwerda, *Finite Difference Schemes and Partial Differential Equations*, Wadsworth-Brooks, New-York, 1989.
7. B. Lombard and J. Piraux, *Numerical treatment of two-dimensional interfaces for acoustic and elastic waves*, J. Comput. Phys., 195-1 (2004), 90-116.
8. G.A. McMechan and M.J. Yedlin, *"Analysis of dispersive waves by wave field transformation"*, Geophysics **46** (6), pp. 869-874 (1981)
9. T.A. Mokhtar, R.B. Herrmann and D.R. Russel, *"Seismic velocity and Q model for the shallow structure of the Arabian shield from short-period Rayleigh waves"*, Geophysics **53** (11), pp. 1379-1387 (1988)
10. T. Forbriger, *"Inversion of shallow-seismic wavefield: I. Wavefield transformation"*, Geoph. J. Int. **153**, 719-734 (2003)
11. C.M. Linton and P.A. Martin, *"Multiple scattering by random configurations of circular cylinders: second order corrections for the effective wavenumber"*, J. Acoust. Soc. America **117** (6), 3413-3423 (2005).
12. J-P. Groby, A. Wirgin and E. Ogam, *"Acoustic response of a periodic distribution of macroscopic inclusions within a rigid frame porous plate"*, Waves in Random and Complex Media (2008) - to be published

Investigation of a novel polymer foam material for air coupled ultrasonic transducer applications

L. Satyanarayan, J. M. Vander Weide, N. F. Declercq, Y. Berthelot

Abstract This experimental study aims at investigating the use of porous polymer foam piezoelectrets as a potential transducer material for air coupled ultrasonic applications. When a voltage is applied, these materials exhibit a phenomenon similar to the inverse piezoelectric effect. The defining features of the piezo-like polymer foam are small, elliptically shaped and electrically polarized voids located inside the polymers. The sensitivity is related to the effective piezoelectric coupling coefficient d_{33} which is much higher than in traditional piezoelectric materials. The d_{33} values of the cellular polypropylene foams were estimated using a laser vibrometer at different input voltages for a continuous wave excitation. It was observed that the effective d_{33} coefficient strongly depends on the volume fraction of electrically charged voids in the material as the material compliance decreases with increased material voids. The change in acoustic impedance across the surface of the sample was measured with a high-resolution ultrasonic scanning system. Finally, these foams were used as prototype transducers for the transmit-receive mode in air; practical limitations imposed by acoustic attenuation in air were assessed.

1 Introduction

Traditional ultrasonic inspection of components can be broadly categorized as contact and immersion based testing. In both cases however, a good coupling medium with optimum acoustic impedance and thickness is essential to transmit

Georgia Tech Lorraine – G.W. Woodruff School of Mechanical Engineering,
Georgia Tech-CNRS UMI-2958, 2 rue Marconi, 57070 Metz, France
e-mail: lsatyana@georgiatech-metz.fr

the maximum amount of ultrasonic energy into the component being inspected. An immersion testing configuration requires the component to be immersed in the couplant medium which can be difficult in case of very heavy and large size components and/or those that cannot be dismantled from their place of operation. The contact based inspection has the advantage over immersion testing by offering flexibility of "in-situ" and in many occasions "real-time" testing of components. However, transducers used in contact inspections have to be very rugged to endure rough handling in the field and subjected to wear and tear as the surface conditions of the components are seldom smooth. Also, a uniform layer of couplant cannot be ensured always during such complicated testing conditions.

As an alternative, air coupled ultrasonics (ACU) offers several advantages with respect to immersion or contact inspection. Firstly, the need for a couplant is eliminated. This means that the components need not be immersed in a couplant medium and hence *in situ* and real time testing are possible. Second, a layer to protect the transducer from rough surfaces is no longer necessary. This increases the sensitivity of the transducer considerably. Thus the domain of non-contact inspection using air-coupled ultrasonics (ACU) becomes attractive if the challenge of the acoustic impedance mismatch with air as the couplant layer can be eliminated. This is because the impedance mismatch between *transducer-air-component* is so high that very little ultrasonic energy is actually transmitted. When the issues with regard to ACU are suitably addressed, many applications open up for ACU [1, 2]. Possible applications include weld monitoring, coated textile testing, bond-integrity, and composite materials testing.

2 Transducer materials for ACU

New polymer based materials like PVDF, Teflon and cellular polypropylene have been identified as potential transducer materials for air coupled applications. Though the use of PVDF for ultrasonic applications has been reported, the piezoelectret nature and high sensitivity of the polypropylene electret foam, with experimentally measured values of d_{33} ranging from 100-200 pC/N, makes it a very good candidate for ACU applications [3, 4]. These materials are electrically charged, extremely porous polymers containing gas bubbles 10-100 microns long and a few microns thick with the charges residing on the bubble surfaces.

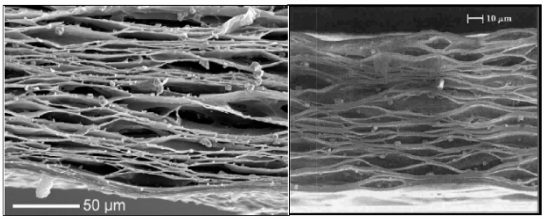

Figure 1: Typical polymer foam cross sections as imaged using SEM [5,6]

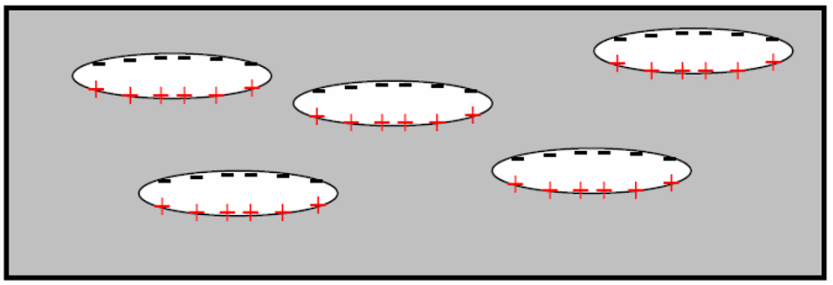

Figure 2: Charge arrangement in voids of closed cell polymer foam

Figure 1 shows the internal structure of a cellular polypropylene imaged using scanning acoustic microscopy [3]. Figure 2 shows how the charges are distributed inside the voids in a polymer foam cellular polypropylene sample specimen [7, 8]. Of particular interest is the flexibility of the foams, making possible a wide range of transducer geometries. For larger transducer sheets, the homogeneity of void distribution in the material is increasingly important. Characterization of any heterogeneity in the material response is a key step to creating large scale transducers for air coupled ultrasonics.

Table 1: Comparison of piezoelectret and other transducer material properties [6]

Material Property	Air (at 20° C)	Cellular Polypropylene Piezoelectrets	Polyvinylidene fluoride PVDF	Ceramic (PZT) polymer composite	Ceramics PZT
Quasi-static piezoelectric coefficient d_{33} (pC/N)	-	25 - 700 (100)	- 33	50 - 300	70 - 600
Acoustic Impedance Z_A (MRayl)	0.00042	0.028	3.9	6.5	25 - 37

Table 1 gives a comparison of cellular polypropylene with other common transducer materials. It can be seen from Table 1 that the acoustic impedance of the polymer foam is two orders of magnitude closer to that of air than to the PVDF and the ceramic (PZT) polymer composites. The highest impedance mismatch is shown by ceramics PZT, which is four orders of magnitude higher, even though the piezoelectric coefficient is quite high. It should be noted that both a compatible acoustic impedance with air and a very high piezoelectric (d_{33}) coefficient (and also a very small d_{13} coefficient) make the cellular polypropylene a very good transducer material with high sensitivity even in air coupled applications.

3 Experimental Setup

3.1 Laser Vibrometer based studies

A laser vibrometer based estimation of the material response and sensitivity is very convenient as an accurate, non-contact measurement. Samples of polymer foam cellular polypropylene (70 micrometers thick) with dimensions 15 mm x 15 mm were fixed on a rigid copper tape backing material attached to an ABS plastic base. The polymer foam was subject to a continuous wave excitation for different voltage-frequency combinations and the transient surface displacements were measured using the laser interferometric techniques. The schematic diagram of the experimental setup used for the study is shown in Figure 3.

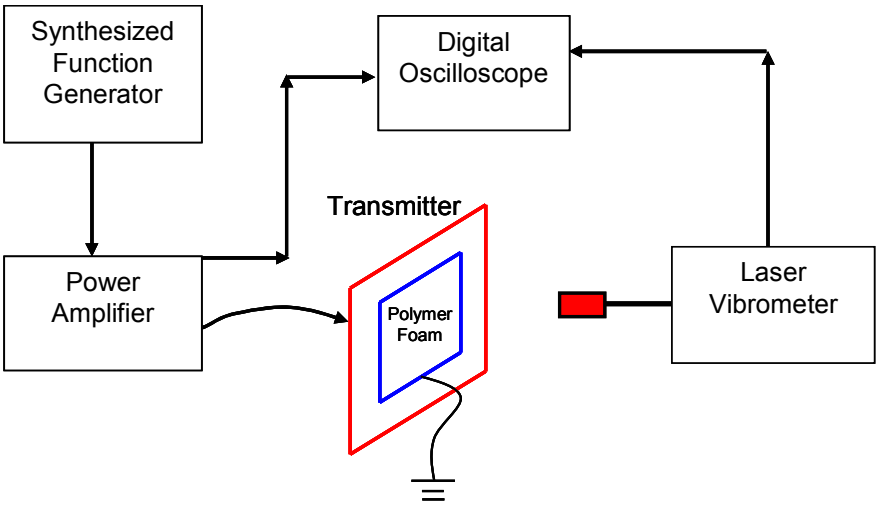

Figure 3: Schematic of the laser vibrometer setup used to measure d_{33}.

3.2 The C-scan system

The experimental setup used in the study consists of a custom built immersion testing tool using a fully automated manipulator with five degrees of freedom: three translations and two rotations. The samples under study were mounted on a suitable stand and immersed in water. The imaging was carried out using a focused immersion transducer of 10 MHz centre frequency using a pulse-echo based configuration. The experimental setup is given in Figure 4. The position of the specimen was optimally placed at the transducer focus so as to obtain a signal of maximum amplitude.

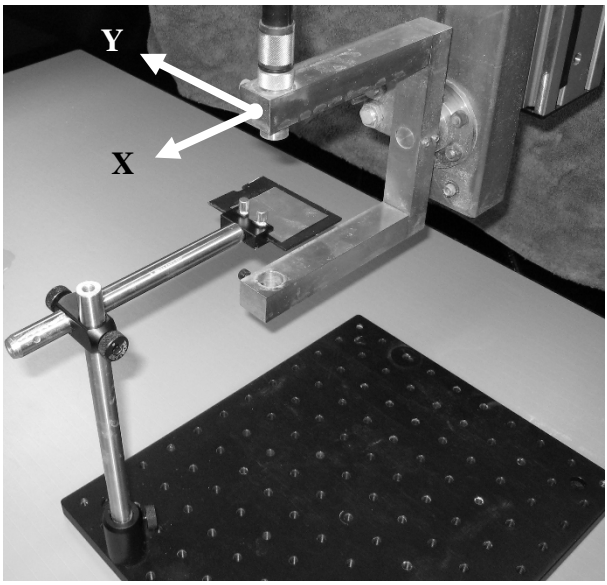

Figure 4: Experimental setup of the C-scan apparatus for imaging polymer foams

4 Results and Discussions

The experiments were divided into five parts. The first part involved the estimation of the piezoelectric coupling coefficient at randomly chosen points on the polymer foam sample. The second part of the experiments involved the C-scan imaging of the polymer foams to locate regions which might have low values of the piezoelectric coupling coefficient. Once these regions are located, the third part involved the estimation of the d_{33} in these regions and estimates the deviation from the average value. The fourth part investigated the decay in the amplitude of the signal with separation distance when using a prototype polymer foam transmit-receive transducer pair subjected to a pulsed excitation on one of the transducers. The fifth part of the study investigated the foams used as prototype ACU transducers in transmit-receive mode in air.

4.1 Estimation of the material response using a laser vibrometer

The variation of the piezoelectric coefficient with different input voltages and/or at different frequencies of excitation is of crucial interest as it is desirable to use these novel polymer foams as broadband transducers. Figure 5 shows the variation

of the d_{33} with respect to different excitation frequencies for different input voltages. Many specimen samples of the polymer foam transducer materials were investigated and the following observations were made.
The resonant frequency of the polymer foams was observed to be around 300-330 kHz.
The variation in d_{33} with respect to the frequency of excitation was also quite flat till 250 KHz after which there was a steep rise till the resonant frequency and fell rapidly after 340 kHz.
The d_{33} value was found to fluctuate between 1.0 and 2.1 Å/V in the region having nearly flat response. The average value of d_{33} in this region was estimated to be 1.22 Å /V.

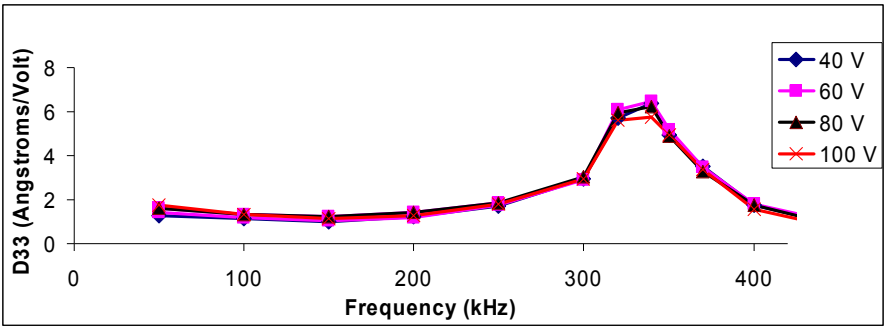

Figure 5: The variation of the material response (d_{33}) with respect to the frequency of excitation for different input voltages.

The measured values of d_{33} through laser vibrometry vary between 1.0-2.1 Angstrom/Volt (100-210 pm/V) in the frequency range of 50-250 kHz. The magnitude of the d_{33} is in the same range as 100-200 pC/N (or pm/V) as the experimentally measured values reported in the literature [3,4]. The numerical value of d_{33} will be the same for the foams either in pC/N and pm/V, from Maxwell thermodynamic relations [9]. Additionally, the small gradual drop in material response between 50 – 150 kHz is to be expected due to the frequency dependence of material visco-elasticity. After this, response increases due to the first thickness resonance at 330 kHz.

4.2 C-scan imaging

The polymer foam has many gas filled voids that are randomly distributed along the thickness. It is desirable to have as many voids as possible so as to achieve maximum piezoelectric like effect. However, the piezoelectric coupling coefficient varies along the surface as not only the distribution but also the size of

the bubbles across the foam thickness is not uniform. It is therefore essential that a quick and reliable method be used which can qualitatively estimate the distribution of the piezoelectric coupling coefficient along the polymer surface. The ultrasonic imaging technique is based on the fact that more reflection of ultrasonic energy will result from a region having higher impedance mismatch than from a region having lower impedance mismatch.

Although voids are assumed to be randomly distributed in the material, there are certain regions that have higher or lower concentration of voids. Regions having more voids have more gas entrained inside the material. The lower local material density and sound speed results in lower acoustic impedance and hence greater acoustic impedance mismatch with water. The local variation in impedance mismatch can be imaged using the ultrasonic C-scan as increased impedance mismatch at the surface corresponds to increased reflection. Thus, the regions having a low density of voids will reflect much less ultrasonic energy which are invariably the regions of relatively lower d_{33} values. C-scan imaging of two samples was carried out and regions with potentially lower d_{33} were identified. Figure 6 shows the C-scan images of the two samples along with these regions.

4.3 Estimation of the d_{33} at areas of low void concentration

After the locations of the low void density were identified in the foam samples, the positions were marked and tested using the laser vibrometer. Figure 7 shows the estimated d_{33} values at normal and low void density locations in one of the polymer foam samples. It was observed that the value of d_{33} in the normal region was significantly lower than the value in a low void density region. It was also observed that the value of the d_{33} increased steeply beyond 250 kHz as the excitation frequency approached the resonance frequency. The values of d_{33} in the range close to the resonance frequency are not a true measure of the piezoelectric coupling coefficient d_{33} but are actually the resonant response of the material. This is because the foam loses the broadband characteristic in this regime and the material response at resonance overtakes the otherwise nearly constant surface displacement characteristic. The average percentage error (calculated between 50-250 kHz) in the estimation of d_{33} between regions of normal and low void fraction was estimated to be 13%.

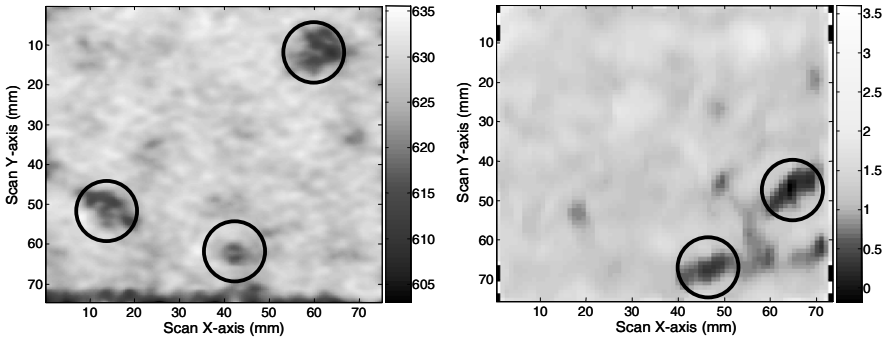

(a) Polymer foam sample 1 **(b) Polymer foam sample 2**

Figure 6(a-b): C-scan images of the three polymer foam samples along with the circled regions of low void density and potentially low d_{33} values.

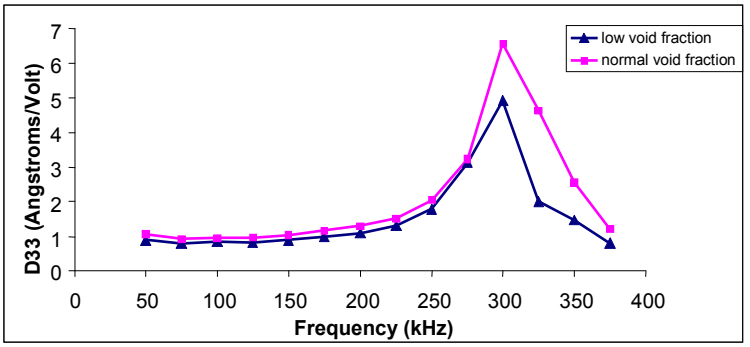

Figure 7: Estimated d_{33} values at normal and low void density locations for different excitation frequencies.

From the ultrasonic C-scan, a region of low void fraction was identified. To correlate the ultrasound data to the laser vibrometer measurement of d_{33}, the absolute amplitude plot along a single line was extracted from the ultrasonic C-scan. Laser vibrometer data was taken along the same line on the polymer foam surface. A one to one correspondence was observed between the two measurements, as seen in Figure 8. However, the variation may not be on the same scale for the two. The laser vibrometer is more sensitive and can resolve subtle surface displacements more accurately than the ultrasonic imaging as the impedance variation between low and normal void fraction regions need not be very high. Though the percent variation between low and normal void density areas on the foam was lower for ultrasonic signals, the measurement can be performed quickly, with higher spatial resolution, and without applying a voltage.

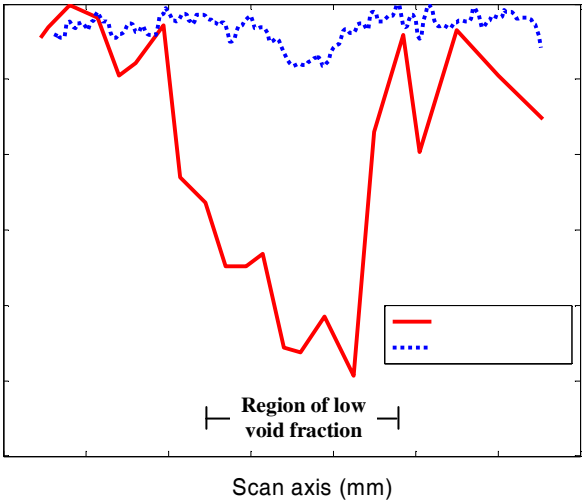

Figure 8: Comparison of a line scan of laser vibrometer measurement of d_{33} at 200 kHz and ultrasonic C-scan data showing a region of low void fraction.

In order to investigate the utility of the polymer foams for air coupled ultrasonics, prototype piezoelectret transducers were fabricated and used in the transmit-receive mode. The experimental arrangement is shown in Figure 9 above. It was observed that the transducers could pick up the signal at a separation distance of 130 mm. A typical pulsed signal obtained at a separation distance of 25 mm in the pitch catch mode is shown in Figure 10. When an obstruction was placed between the two transducers, a fall in the signal amplitude was also observed. Thus, it was inferred that the piezoelectret foam transducers can be used successfully in ACU applications. Studies are being conducted at the Laboratory for Ultrasonic NDE at Georgia Tech Lorraine on the application of the piezoelectret polymer foam transducers to image defects for mainstream applications.

4.4 Polymer foam transducers in transmit-receive mode

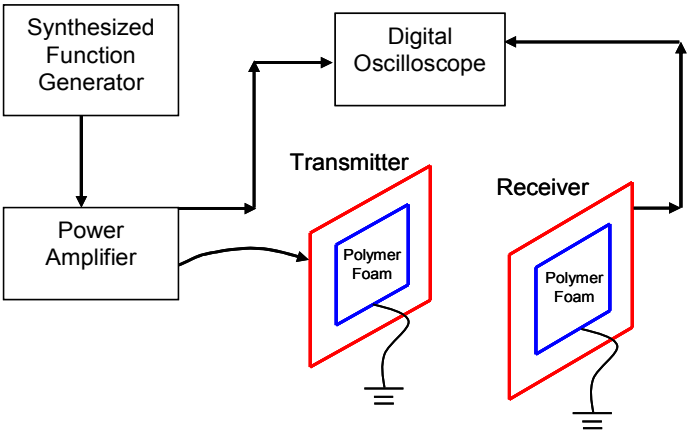

Figure 9: Experimental setup used for the prototype piezoelectret polymer foam transmitter-receiver arrangement.

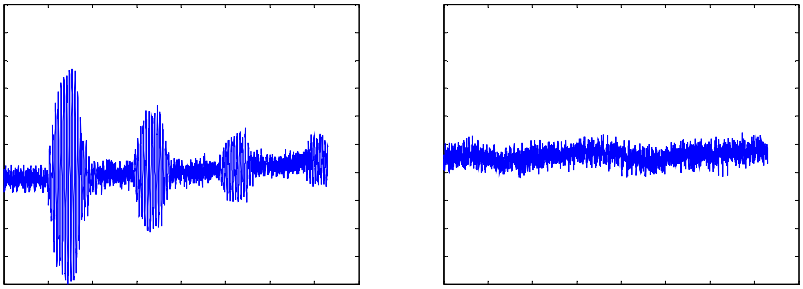

(a) No obstruction **(b) With obstruction**

Figure 10(a-b): Signal from the prototype piezoelectret polymer foam transmitter-receiver arrangement for a tone burst of 330 kHz

5.5 Decay of Signal amplitude with distance

It is important to estimate the decay of the signal amplitude with distance to obtain a signal of sufficiently high signal to noise ratio. The strength of a signal for different distances can be investigated, characterizing the attenuation in air of the acoustic field emitted from the piezoelectret polymer foam transducer. Figure 11

shows the variation of the peak amplitude of the output signal with increasing separation between the two transducers. The 330 kHz centre frequency of the 10 cycle tone burst signal was set close to the material resonance (300-330 kHz), so as to obtain the maximum signal. It is seen that a signal of sufficient amplitude can be observed even at a separation distance of 130 mm between the transducer pair.

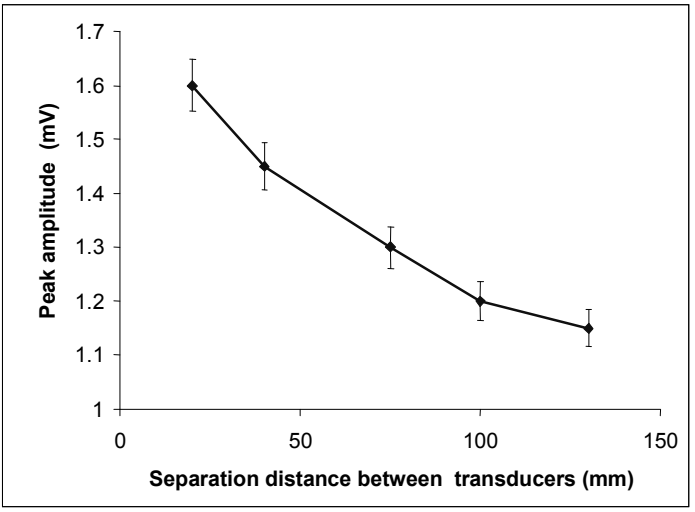

Figure 11: Variation of the peak amplitude of the received signal with distance

6 Conclusions

Experiments were carried out on novel polymer foam samples to estimate the piezoelectric coupling coefficient (d_{33}) for different input voltage-excitation frequency combinations. It was seen that the material response is nearly flat for 50-250 kHz. This makes them a potential candidate for broadband air coupled transducer or commercial acoustic applications. C-scan imaging was carried out on polymer samples to locate regions of heterogeneity which can result from manufacturing variability. These heterogeneities were carefully identified and the d_{33} values in these locations were also estimated. It was seen that the d_{33} values were significantly lower in the low void density regions when compared with the normal density regions. It can hence be concluded that the C-scan imaging can be successfully used to identify and locate regions of decreased material response in polymer foam materials which can increase the reliability of larger scale transducers. Prototype transducers were fabricated and used successfully in transmit-receive mode. The fall in the amplitude of the received signal with increase in the distance of separation between the transducers was also

investigated. The ability to measure ultrasonic signal even at a separation of 130 mm indicates the initial promise of these materials in air coupled ultrasonics.

7 Acknowledgements

The authors wish to thank the CNRS and the Conseil Regional de Lorraine for funding the investigation on these novel materials for ultrasonic transducer applications. The authors also wish to sincerely thank Dr. G. M. Sessler and Dr. J. Hillenbrand for providing insightful suggestions and also enlightening us about the corona charging process. The authors also wish to thank Dr. Abdallah Ouggazaden for his support throughout the study.

References

1. M. Castaings, B. Hosten, The use of electrostatic, ultrasonic, air-coupled transducers to generate and receive Lamb waves in anisotropic, viscoelastic plates. Journal Ultrasonics vol. 36, p. 361-365, 1998 (conf. Ultrasonics Intern. in Delft, Holland, July 1997).
2. M. Castaings, B. Hosten, Air-coupled measurement of plane-wave, ultrasonic plate transmission for characterising anisotropic, viscoelastic materials. Journal Ultrasonics vol. 38, p. 781-786, 2000 (conf. Ultrasonics Intern. In Copenhagen, Denmark, June 1999).
3. R. Gerhard-Multhaupt, "Voided polymer electrets-New materials, new challenges, new chances," IEEE 11th Int. Symp. on Electrets, 36 – 45, 2002.
4. G. M. Sessler, "Electrets: recent developments," J. of Electrostatics, 51-52, 137-145, 2001.
5. S. Bauer, R. Gerhard-Multhaupt, G. M. Sessler; "Ferroelectrets: Soft electroactive foams for transducers," Physics Today, 37-43, Feb 2004
6. X. Qiu, et. al. "Penetration of sulfur hexafluoride into cellular polypropylene films and its effect on the electric charging and electromechanical response of ferroelectrets." J. Phys D: Appl. Phys., 38, 4, 649-654, 2005.
7. J. Hillenbrand, G. M. Sessler, "Piezoelectricity in cellular electret films", IEEE Trans. on Dielectrics EI, Vol. 7(4), 537-542, August 2000.
8. Viktor Bovtun, Joachim Döring, Yuriy Yakymenko, "EMFIT Ferroelectret Film Transducers for Non-Contact Ultrasonic Testing", ECNDT - Tu.1.7.1, Nov.2006, Berlin.
9. S. Sriram, M. Bhaskaran, K. T. Short, B. A. Latella, and A. S. Holland, "Measurement of high. piezoelectric response of strontium-doped lead zirconate titanate thin films using a nanoindenter", Journal of Applied Physics Vol. 101, 2007.

Dual signal processing approach for Lamb wave analysis

J. Assaad, S. Grondel, F. El Youbi, E. Moulin and C. Delebarre.

Abstract The identification of Lamb modes is still the most difficult step in the process of damage detection. Therefore, the aim of this paper is to use a dual signal processing approach in order to better identify Lamb modes. This approach is based on the use of a relationship between the Short Time Fourier Transform (STFT) and the Two Dimensional Fourier Transform (2DFT). Indeed, one direct theoretical relationship between their amplitudes is given in the case of both monomode and multimode signals. This relationship is then numerically verified by a two dimensional finite element method. This system is suitable for defect detection and can be easily implemented for real application to structural health monitoring.

1 Introduction

Since their propagation characteristics are directly related to the microstructure and the mechanical properties of the medium, ultrasonic waves are widely used in the fields of characterisation and non-destructive testing of structures. Usually, the full characterisation of the structures requires two kinds of information: the first one is related to the material quality, the other one aims at the evaluation of the structure health, i.e. the detection of localised damage or defects. The problem of detecting and locating defects or damage in thin structures is currently of tremendous importance, due to an increasing tendency to maintain ageing structures in service much beyond their originally designed service life. Therefore,

J. Assaad, S. Grondel, F. El Youbi, E. Moulin andC. Delebarre

IEMN, UMR CNRS 8520, Département OAE, Université de Valenciennes et du Hainaut Cambrésis, Le Mont Houy, 59313 Valenciennes Cedex 9, France. jamal.assaad@univ-valenciennes.fr

many ultrasound-based techniques have been investigated to address this problem [1].

A large number of researchers have already recognised the advantages of using Lamb waves for rapid inspection of metallic and composite structures [2-6]. A good summary of guided Lamb waves for identification of damage in composite structures can be found in *ref.* 6. The damage or flaw detection is traditionally carried out by analysing the modifications in the received Lamb wave signals. However, due to the multi-mode and dispersive nature of the Lamb waves, the interpretation of the received signal is not always obvious, particularly in complex structures [7]. Indeed, the major problem in using such techniques is to find a solution to ease the signal analysis.

In this way, time-frequency analyses [8-10] have been used to solve such a problem. Indeed, time-frequency representation allows the group velocities of the Lamb modes to be obtained as functions of the frequency. This type of presentation has its own intrinsic advantages and disadvantages, but most importantly, it suffers from the Heisenberg's uncertainty principle [11], i.e. the optimum resolution cannot be achieved in both time and frequency. Consequently, it is not always possible to separate Lamb waves packets propagating in the structure even if the group velocities are well known.

Another possible digital signal processing technique that can be used to analyse Lamb waves propagation is the two Dimensional Fourier Transforms (2DFT). Indeed, by measuring the Lamb waves signal at different positions along the Lamb waves propagation, it allows to identify Lamb waves in the wave number-frequency domain. The identification of the modes is then performed either by the wave number or the phase velocity. This technique has been used by a large number of researchers [12-13] and they showed its effectiveness to identify and measure the amplitude of Lamb modes generated in metallic plates. It was also used for composite structures and adhesive bonded components [3]. Nevertheless, this technique requires a multi-element transducer at the reception and the identification of converted modes or reflected modes with such a technique is not always obvious.

In order to optimise this kind of analysis, it is essential that the propagation characteristics of the waves could be studied using both parameters, i.e. the phase velocity and the group velocity. So, the time-frequency representation could be combined with the 2DFT to better identify Lamb modes propagating within the structure. The purpose in this work is therefore to present a dual signal processing approach based on the relationship between the STFT and the 2DFT amplitudes that allows a better interpretation and identification of Lamb modes.

In the next section, the theoretical relationship between the STFT and the 2DFT in the case of a monomode Lamb wave is given and tested in the case of a simulated S_0 mode. A subsequent section is devoted to the development of the relationship in the case of a multimode Lamb wave. This relation will be experimentally verified using a healthy plate in the last section. Experimentally, a 3 mm thick aluminum plate with an emitter and a receiver are considered (see section III). The emitter consists of two piezoelectric elements with different widths in order to allow the excitation of two different frequency bands. In fact, Fromme *et al.*[14] considered that in practical applications measurements should be performed at more than a single frequency, corresponding to different wavelength-diameter ratios, in order to ensure the reliable detections of damage of unknown severity. The receiver consists of a multi-electrodes piezoelectric transducer developed especially to increase the received power. Experimental results concerning the detection of the hole through the plate can be found in *Ref. 15*. Work under progress is the detection of asymmetric hole in the plate.

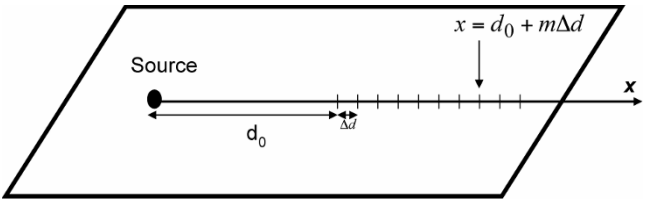

Fig. 1 Schematic description for the application of the two dimensional Fourier Transforms

2 Relationship between STFT and 2DFT in the case of a monomode Lamb wave

2.1 Problem statement

In order to find a relationship between the STFT and the 2DFT, let us consider the situation present in Fig. 1 with the following assumptions. (1), the source is a five cycle sinusoidal tone burst at center frequency f_0 windowed by a Hanning function. (2), only one non attenuating mode of wave number k_1 in the x direction is generated. Thus, the emitted signal $e(t)$ and the received signal $s_1(t,x)$ at the distance x can be written respectively as:

$$e(t) = e^{j2\pi f_0 t} w_H(t)\,, \tag{1}$$

and

$$s_1(t,x) = A_1 e\left(t - t_1\right) = A_1 e^{j\left(-k_1 x + 2\pi f_0 t\right)} w_H\left(t - t_1\right), \tag{2}$$

where t_1 corresponds to the time of flight of the signal between the source and the reception positions ($t_1 = x/V$, V is the group velocity of the considered mode), A_1 is the maximum amplitude of the signal and w_H is a Hanning window of size N_H and given by [16]:

$$\begin{cases} w_H(n) = \dfrac{1}{2}\left[1 - \cos\left(\dfrac{2\pi n}{N_H - 1}\right)\right] \text{ for } n \in [0, N_H - 1], \\ w_H(n) = 0 \text{ otherwise.} \end{cases} \tag{3}$$

In the discrete form and for $x = d_0 = m_0 \Delta d$ (m_0 being an integer), the received signal is given by:

$$s_1(n) = A_1 e^{j(-m_0 K_1 + 2\pi F_0 n)} w_H(n - \alpha_1), \tag{4}$$

with $\alpha_1 = d_0/V\Delta t$, $t = n\Delta t$ (n being an integer), $K_1 = k_1 \Delta d$ and $F_0 = f_0 \Delta t$. Δt and Δd are the temporal and spatial sampling respectively. Finally, K_1 and F_0 correspond to the normalized wave number and the normalized temporal frequency respectively.

In the following, it is assumed that around the excitation frequency, the effect of dispersion is relatively unimportant. Although this assumption is not strictly true, it is a reasonable approximation when the input signals are windowed tonebursts with a precise centre frequency and limited bandwidth and the Lamb waves are barely dispersive around the excitation frequency [17].

2.2 Development of the STFT formulation

The general equation of the numerical *N* points Short Time Fourier Transform is given by [11]:

$$S^{STFT}(b, F) = \sum_{n=0}^{N-1} w_R(n - b) s(n) e^{-j2\pi F n}, \tag{5}$$

where $w_R(n)$ is a rectangular window of length *L* which is translated in time along the temporal signal $s(n,m)$ with delay *b*. The frequency *F* is the normalized one. By introducing Eq.(4) in Eq. (5), the STFT can be written as:

$$S_1^{STFT}(b,F) = A_1 e^{-jK_1 m_0} e^{-j2\pi(F-F_0)\alpha_1} \sum_{n'=-\alpha_1}^{N-1-\alpha_1} w_R(n'+\alpha_1-b) w_H(n') \; e^{-j2\pi(F-F_0)n'} . \tag{6}$$

When $b = \alpha_1$, the above equation simply reduces to :

$$S_1^{STFT}(\alpha_1,F) = A_1 e^{-jK_1 m_0} e^{-j2\pi(F-F_0)\alpha_1} \sum_{n'=-b}^{N-1-b} w_R(n') w_H(n') e^{-j2\pi(F-F_0)n'} . \tag{7}$$

In the following study, the length of the rectangular window used for the STFT is always chosen greater than the length of the Hanning window corresponding to the transient excitation, i.e. $L \geq N_H$. The integer number N is always taken greater than $N_H + 1 + b$. Hence, when $F = F_0$, the modulus of the STFT is given by:

$$\left|S_1^{STFT}(\alpha_1,F_0)\right| = \left| A_1 \left(\frac{N_H}{2} - \frac{\sin\left[-\frac{N_H\pi}{N_H-1}\right]}{4\sin\left[-\frac{\pi}{N_H-1}\right]} - \frac{\sin\left[(\frac{N_H\pi}{N_H-1})\right]}{4\sin\left[\frac{\pi}{N_H-1}\right]} \right) \right| . \tag{8}$$

Since $N_H >> 1$, the previous modulus of the STFT can be easily approximated as:

$$\left|S_1^{STFT}(\alpha_1,F_0)\right| \cong \frac{A_1 N_H}{2} . \tag{9}$$

2.3 Development of the 2DFT formulation

The monomode Lamb wave $s_1(n,m)$ received at m equidistant spatial positions situated between $x = d_0$ and $x = d_0 + (m-1)\Delta d$ and its two Dimensional Fourier Transform are given by:

$$s_1(n,m) = A_1 e^{j(-m_0 K_1 - mK_1 + 2\pi F_0 n)} w_H\left(n - \alpha_1 - m\beta_1\right) \tag{10}$$

and

$$S_1^{2DFT}(K,F) = \sum_{n=0}^{N-1}\sum_{m=0}^{M-1} w_N(n) w_M(m) s_1(n,m)\, e^{-j(2\pi Fn - Km)}, \quad (11)$$

respectively, where w_N and w_M are two rectangular windows of sizes N and M respectively. $\beta_1 = \Delta d / V\Delta t$ is the time of flight of the considered Lamb mode corresponding to the distance Δd. Substituting Eq. (10) in Eq. (11), the 2DFT can be rewritten as:

$$S_1^{2DFT}(K,F) = A_1 e^{-j2\pi(F-F_0)\alpha_1 - jm_0 K} W_H(F-F_0) \sum_{m=0}^{M-1} w_M(m) e^{-j2\pi\left[(F-F_0)\beta_1 - (K-K_1)/2\pi\right]m} \quad (12)$$

where W_H is the Fourier Transform of the Hanning window w_H on the time dimension. The modulus of the 2DFT at the frequency $F=F_0$ is equal to:

$$\left|S_1^{2DFT}(K,F)\right| = \frac{A_1 N_H}{2} \left| \frac{\sin\left[\left(\frac{K-K_1}{2}\right)M\right]}{\sin\left(\frac{K-K_1}{2}\right)} \right| . \quad (13)$$

For $K = K_1$ the above 2DFT reaches to its maximum value which is equal to $A_1 N_H M/2$. This maximum value is related to the modulus of the STFT {see Eq. (9)} by the following relationship :

$$\left| S_1^{2DFT}(K_1, F_0) \right| = M \left| S_1^{STFT}(\alpha_1, F_0) \right| \quad (14)$$

In the following N, L and N_H are always taken equal to 1024, 180 and 160 respectively.

2.4 Application of the dual signal processing approach in the case of a simulated S_0 mode

In order to verify the validity of the above relationship in quasi-realistic conditions of Lamb wave propagation, the propagation of a S_0 Lamb mode in a 3 mm thick aluminium plate has been simulated (Fig. 2) with the help of a two-dimensional finite element (FE) model. The size of each element (quadratic interpolation) in the FE mesh was chosen to be at least smaller than $\lambda/4$, where λ is the smallest wavelength from all generated modes, to maintain a large accuracy of the FE results.

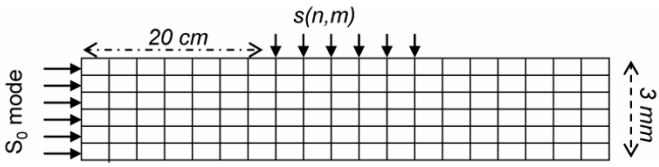

Fig. 2 Finite element mesh of the aluminium plate of thickness 3mm.

The generation of only the S_0 symmetrical Lamb mode was done by applying, at the edge of the plate, both tangential symmetrical and normal anti-symmetrical displacements, with respect to the median plane, windowed by a Hanning temporal function. The applying displacement was a 5 cycles 400 kHz sinusoidal tone burst. At this central frequency, the group velocity of this mode is about $5460\ \mathrm{m/s}$ and its wave number is about $460\ \mathrm{m^{-1}}$. In addition, the S_0 mode is not very dispersive in the vicinity of this frequency. Tangential displacements are extracted at *M=32* different spatial positions spaced by a step $\Delta d = 2\,mm$ on the surface of the plate. The initial distance between the excitation and the response is $d_0 = 20\,cm$.

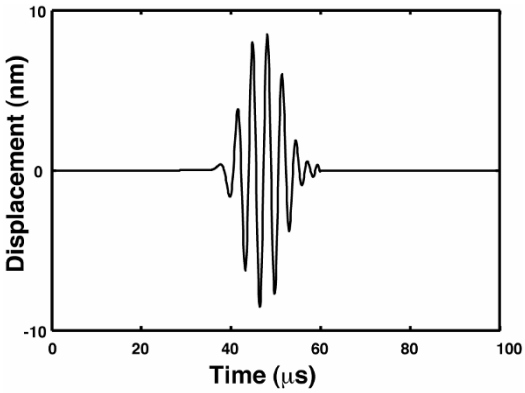

Fig. 3. Tangential surface displacement of the plate at d_0 = 20 cm.

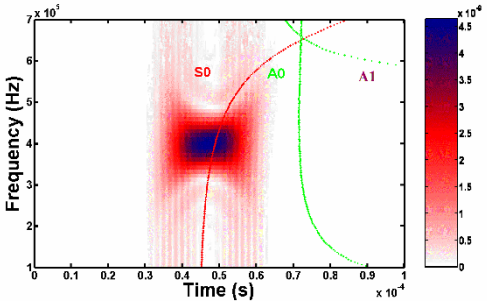

Fig. 4.STFT of the tangential surface displacement of Fig. 3.

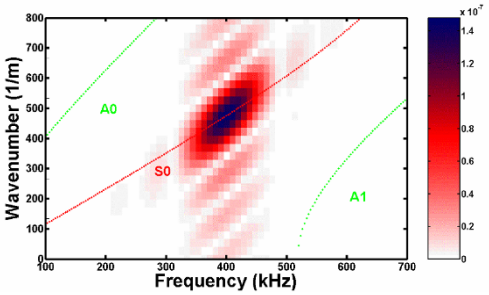

Fig. 5. 2DFT of the 32 predicted free tangential surface displacements.

The computed time history of the tangential displacement is shown in Fig. 3. The 1024 points STFT of the free tangential surface displacement given in Fig.3 is shown in Fig. 4. The presence of only one mode, i.e. the S_0 mode, is confirmed. The 2DFT application, 1024 point Fourier transforms were used in both time and spatial domains, the length of the spatial records being increased from the 32 computed points by zero padding. Fig. 5 shows the result of carrying out a 2DFT. At $F = F_0$, the amplitude reaches a maximum at a single wave number that corresponds to that of the S_0 mode, thus confirming that the incident wave is a pure S_0 mode. In Figs. 4-5 the secondary lobes due to the use of the windowed time in order to compute the two transformations can be easily seen. In fact, the continuous Fourier transform of à pure sinusoidal signal is equal to Dirac operator but the numerical Fourier transform of the same signal is given by sinus cardinal function.

Finally, the comparison of the STFT and 2DFT amplitudes computed at the frequency 400 kHz is in good agreement with the Eq. (14).

3 Application to a multimode Lamb wave

In most cases, the generation of a monomode is not possible and the response is usually composed by several Lamb modes. Therefore, the resulting Lamb wave signal $s_T(n,m)$ can be supposed as the sum of these Lamb modes:

$$s_T(n,m) = \sum_i s_i(n,m), \tag{15}$$

where $s_i(n,m)$ is given by Eq. (2) by substituting index 1 by i. So, the STFT of the Lamb wave signal s_T can be written as:

$$S_T^{STFT}(b,F) = \sum_i S_i^{STFT}(b,F). \tag{16}$$

If we assume that Lamb modes can be distinguished in the temporal signal then the i^{th} Lamb mode $(b = \alpha_i + m\beta_i)$ and at the frequency $F = F_0$, the modulus of the STFT is given by:

$$\left|S_T^{STFT}(\alpha_i + m\beta_i, F_0)\right| \cong \frac{A_i N_H}{2}. \tag{17}$$

Similarly, by using the linearity properties of the Fourier transform, the 2DFT of signals $s_T(n,m)$ can be given by:

$$S_T^{2DFT}(K,F) = \sum_i S_i^{2DFT}(K,F). \tag{18}$$

Thus, when $F = F_0$ and $|K_i - K_j| > 4\pi/M \ \forall j \neq i$, the modulus of the 2DFT of the i^{th} Lamb mode of wave number K_i can be approximated by : $A_i N_H M/2$. In theses conditions, it is interesting to note that the relation obtained in the case of a single mode {see Eq. (14)} is still valid for the case of multi modes.

4 Experimental results

The experimental setup is shown in Fig. 6. The emitter consists of two piezoelectric elements with different widths. They have the same length and thickness, which are equal to 15 mm and 1 mm respectively. Their widths are 2 and 3 mm and their transverse resonance frequencies are then equal to 600 kHz and 400 kHz respectively. These elements were stuck on the plate, keeping an arbitrary inter-element distance of 6 mm. The excitation in phase of these elements by a 5 cycles sinusoidal tone burst at their resonance frequency allowed us to work in the frequency band between 300 kHz and 650 kHz. At these frequencies the fundamental A_0 and S_0 modes are excited [14]. Moreover, the S_0 mode is less dispersive at the frequency of 400 kHz and dispersive at the frequency of 600 kHz. At the reception, a sensor using metallic multi-electrodes deposited on a piezoelectric substance [18] was especially developed to allow the temporal measurements with an inter-electrode distance of 2 mm. This receiver

has 32 electrodes, and is chosen to be 400 µm thick, 15 mm wide and 63 mm long. The initial distance between the emitter and the sensor was chosen to be 25 cm.

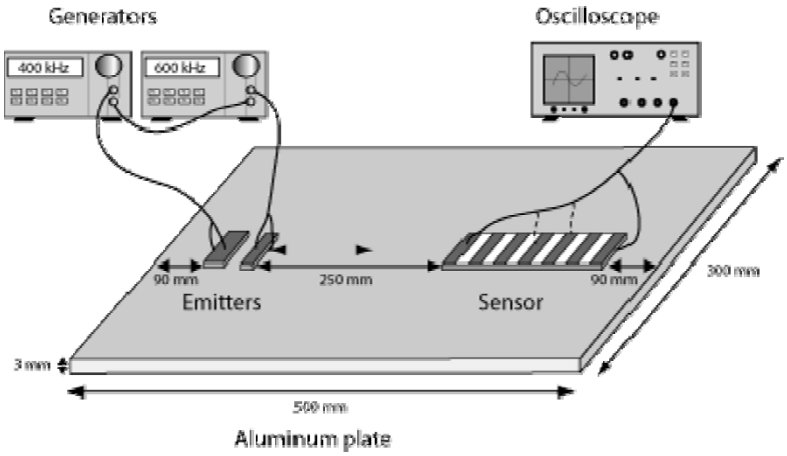

Fig. 6. Experimental measurement setup.

The Lamb waves generated by the emitter were received on the different electrodes of the sensor. All the signals were then recorded by a digital oscilloscope and transferred to a PC computer in which signal processing, i.e. STFT and 2DFT, could be applied.

Figs. 7(a) and 7(b) below show the received signal on the first electrode and its time-frequency representation respectively. Fig. 7(c) shows the result of the 2DFT of the 32 received signals. The Fourier transforms in Figs. 7(a) and (7b) have been filtered in order ton eliminate secondary lobes. It is interesting to note that the A_0 mode is stronger than S_0 mode. After comparison of the theoretical curves with the experimental results, these representations demonstrate that fundamental Lamb modes (S_0 and A_0) propagate within the structure in the frequency band between 300 and 650 kHz. Since it is difficult to make a direct comparison between amplitudes of the STFT and 2DFT using Fig. 7, table I gives a comparison between the STFT and 2DFT amplitudes of the identified Lamb modes. These amplitudes were computed from Fig. 7 for $(b = \alpha_i \; and \; F = F_i)$ and for $(K = K_i \; and \; F = F_i)$, respectively (i = 1 corresponding to the S_0 mode while i = 2 corresponding to the A_0 mode). As a result, it can be noticed that for each Lamb mode, the values obtained with both methods are close to each other. So, the theoretical and experimental results are in good agreement. Finally, the relationship as given by Eq. (14) is then verified.

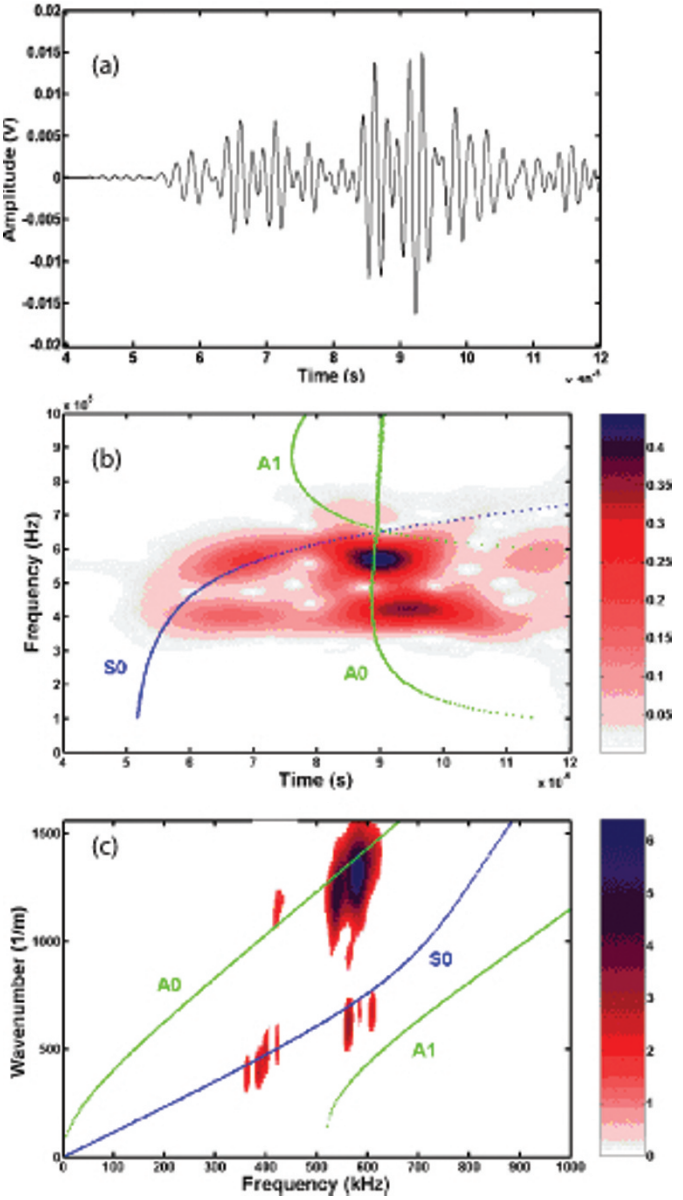

Fig. 7. (a) Time history of the received signal on the first electrode of the receiver transducer; (b) the STFT of the above received signal; (c) the 2DFT of the 32 received signals.

Tab. 1. Comparison between the 2DFT and STFT amplitudes for the identified Lamb modes.

Frequency (kHz)	Mode	Wavelength (mm)	Amplitude (TF2D)	Amplitude (STFT)
400	S_0	13	2.00	2.10
	A_0	6	1.95	2.15
600	S_0	8.5	2.66	2.74
	A_0	4.5	6.16	6.23

5 Conclusion

A dual signal processing analysis using the STFT and the 2DFT was developed to characterize Lamb wave propagation in plates. The relation between their amplitudes was first demonstrated theoretically and second validated by the finite element method. The proposed approach can be simply implemented for real application on SHM systems. In fact, the SFTD and the 2DFT must be only computed at one point.An experimental study has been done using an aluminum plate. The proposed dual signal processing has been used to detect defects in plates [15].

References

1. J. Blitz, G. Simpson, *Ultrasonic Methods of Non-Destructive Testing*, Chapman & Hall, 1996.
2. M. Z. Silva, R. Gouyon, F. Lepoutre, "Corrosion detection in aircraft aluminium structures using laser ultrasonics and wavelet transform signal analysis," Ultrasonics, **41**, 301-305 (2003).
3. R. Basri, W. K. Chiu, "Numerical analysis on the interaction of guided Lamb waves with a local stiffness reduction in quasi-isotropic composite structures," Composite structures, **66**, 87-99 (2004).
4. S. Grondel, C. Paget, C. Delebarre, J. Assaad , K. Levin, "Design of optimal configuration for generating A_0 Lamb mode in a composite plate using piezoelectric transducers," J. Acoust. Soc. Am., **112**, 84-90 (2002).
5. Y. Cho, "Estimation of ultrasonic guided wave mode conversion in a plate with thickness variation", IEEE Trans. Ultrason., Ferroelectr. Freq. Control, **47**, 591-603 (2000).
6. Z. Q. Zu, L. Ye, Y. Lu, Guided Lamb waves for identification of damage in composite structures : a review, J. Sound of Vibration, **295**, 753-780, (2006).
7. S. Grondel, C. Delebarre, J. Assaad, J. P. Dupuis, L. Reithler, "Fatigue crack monitoring of riveted aluminium strap joints by Lamb wave analysis and acoustic emission measurement techniques", NDT&E International, **25**, 137-146 (2002).
8. C. Valle, W. Jerrol, J. Littles, "Localization using the reassigned spectrogram on laser-generated and detected Lamb modes," Ultrasonics, **39**, 535-542 (2002).
9. W. H. Prosser, M. D. Seale, "Time-frequency analysis of the dispersion of Lamb modes," J. Acoust. Soc. Am., **105**, 2669-2676 (1999).

10. F. L. D. Scalea, J. Mc. Namara , “Measuring high-frequency wave propagation in railroad tracks by joint time–frequency analysis,” Journal of Sound and Vibration, **273**, 637-651 (2004).
11. L. Cohen, *Time-Frequency Analysis*, Prentice-Hall, New Jersey (1995).
12. D. Alleyne, P. Cawley, “A two Dimensional Fourier Transform for the measurement of propagation multimode signals,” J. Acoust. Soc. Am., **89**, 1159-1168 (1991).
13. F. El youbi, S. Grondel, J. Assaad, “Signal processing for damage detection using two different array transducers,” Ultrasonics, **42**, 803-806 (2004).
14. P. Fromme, M.B. Sayir, “On the scattering and mode conversion of the A0 Lamb wave mode at circular defects in plates’’, Review of Quantitative Nondestructive Evaluation, **23**, 142–149 (2004).
15. El Youbi, “Study of multi-element transducers for an Integrated Health Monitoring System using Lamb waves and development of associated signal processing tool”, PhD thesis, Report 0518, University of Valenciennes, France, (2005).
16. F. J. Harris, “On the use of windows for harmonic analysis with the discrete Fourier transform,” Proceedings of the IEEE, 66, 51-83 (1978).
17. P. Wilcox, M. Love, P. Cawley, “The effect of dispersion on long-range inspection using ultrasonic guided waves,” NDT&E International, **34**, 1-9 (2001).
18. M. Rguiti, S. Grondel, F. El youbi, C. Courtois, M. Lippert, A. Leriche, “Optimized piezoelectric for a specific application: detection of Lamb waves,” Sensors & Actuators, **126**, 362-368, (2006).

Structural health monitoring of bonded composite patches using Lamb waves

B. Chapuis, N. Terrien, D. Royer and A. Déom

Abstract Bonded composite patches are an attractive way to repair cracked or corroded airframe structures because of their several advantages compared to traditional riveted doublers. However, certification issues limit the application of this technology. We present here the first step in the development of a SHM system for detecting disbonds between the patch and the structure. This will provide important information concerning the damage state of the repair. PZT discs embedded between the patch and the metallic parent structure are used to excite and detect Lamb waves. Analytical study of the ultrasonic characteristics of both structure and actuator is essential to adjust the experimental setup. Processing of experimental signals allows us to locate the damage and shows the sensitivity of the SHM system to the size of the defect.

1 Introduction

The appearance of cracks in ageing aircraft structures is one of the main issues for maintenance operators. In order to avoid a replacement of the damaged structure, always time consuming and costly, a metallic riveted doubler is generally applied to provide a supplementary path for the load. However this solution induces stress concentrations around the fasteners leading to additional problems. An alternative and

B. Chapuis
ONERA, 29 av. Division Leclerc 92322 Châtillon, France, e-mail: bastien.chapuis@onera.fr

N. Terrien
ONERA, 29 av. Division Leclerc 92322 Châtillon, France, e-mail: nicolas.terrien@onera.fr

D. Royer
Laboratoire Ondes et Acoustique, 10 rue Vauquelin, 75231 Paris, France, e-mail: daniel.royer@espci.fr

A. Déom
ONERA, 29 av. Division Leclerc 92322 Châtillon, France, e-mail: alain.deom@onera.fr

more recent technique involves bonding a composite patch on the damaged structure with an adhesive film. Such patches have been successfully used to repair cracked but also corroded structures. They are usually composed by a stacking of several layers of carbon or boron composite reinforced polymer (CFRP or BFRP). This technology provides significant advantages compared to traditional mechanical repairs [1, 2] : there is no further damage to the structure, as the interface is sealed there is no corrosion problems, patches can be easily conformed to curved surfaces and their mechanical performances are excellent. However certification requirements limit their application to non-primary structures due to the lack of methodology for monitoring the damaged state of the repaired structure. The most promising solutions using the concept of smart structures are given by fibre optic Bragg grating sensor [3, 4] and piezoceramics [5, 6].

We present here the development of a SHM system based on piezoelectric (PZT) discs inserted between the patch and the structure (figure 1).

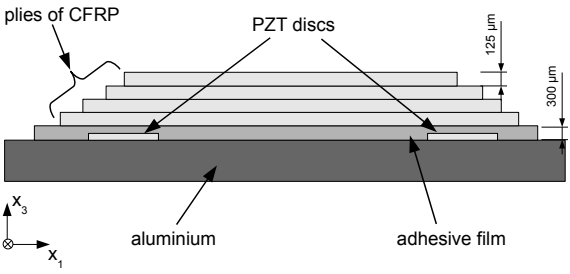

Fig. 1 Schematic section of a typical bonded patch repair and integration of PZT discs.

The discs are used both as actuators and sensors of Lamb waves and we try to monitor the defect by studying the waves reflected by it. We focus our study on the detection of disbonds between the patch and the structure. However, with the aim of separating the difficulties we have divided the work in several steps and the results presented here are the set-up of tools which will be used in the final application.

In the first part we recall the principles of Lamb wave propagation in multilayered anisotropic structures and we detail some theoretical and experimental considerations about the detection and the excitation of these Lamb waves by PZT discs. In the second part we present the experimental results of the detection of a growing hole drilled in an aluminium plate by three PZT discs bonded on the surface.

2 Identification of propagative modes in the healthy structure

2.1 Dispersion curves

The studied structure is very complex from an ultrasonic point of view due to the presence of different anisotropic materials. Each layer (one single layer of the CFRP patch, the adhesive film or the aluminium) can be considered as a monoclinic material with x_1x_2 as a plane of symmetry. The stress-strain relation in the n-th layer is therefore:

$$\begin{pmatrix} T_{11} \\ T_{22} \\ T_{33} \\ T_{23} \\ T_{13} \\ T_{12} \end{pmatrix} = \begin{pmatrix} C_{11} & C_{12} & C_{13} & 0 & 0 & C_{16} \\ C_{12} & C_{22} & C_{23} & 0 & 0 & C_{26} \\ C_{13} & C_{23} & C_{33} & 0 & 0 & C_{36} \\ 0 & 0 & 0 & C_{44} & C_{45} & 0 \\ 0 & 0 & 0 & C_{45} & C_{55} & 0 \\ C_{16} & C_{26} & C_{36} & 0 & 0 & C_{66} \end{pmatrix} \begin{pmatrix} S_{11} \\ S_{22} \\ S_{33} \\ S_{23} \\ S_{13} \\ S_{12} \end{pmatrix} \tag{1}$$

where C_{ij} $(i,j = 1,...,6)$ is the stiffness matrix of the material in the direction of propagation. The Christoffel equation allows us to determine the phase velocity in the direction x_1 and the polarisation of a plane wave ($u_l^r = U_l^r e^{i(kx_1 + q_r x_3 - \omega t)}$, $l = 1,2,3$) propagating in the plane x_1x_3 of an infinite medium of the material of the n-th layer with the phase velocity $V_\phi = \dfrac{\omega}{k}$ in the direction x_1 :

$$\begin{pmatrix} C_{11}k^2 - \rho\omega^2 + C_{55}q_r^2 & C_{16}k^2 + C_{45}q_r^2 & (C_{13} + C_{55})kq_r \\ C_{16}k^2 + C_{45}q_r^2 & C_{66}k^2 - \rho\omega^2 + C_{44}q_r^2 & (C_{36} + C_{45})kq_r \\ (C_{13} + C_{55})kq_r & (C_{36} + C_{45})kq_r & C_{55}k^2 - \rho\omega^2 + C_{33}q_r^2 \end{pmatrix} \begin{pmatrix} U_1^r \\ U_2^r \\ U_3^r \end{pmatrix} = \begin{pmatrix} 0 \\ 0 \\ 0 \end{pmatrix} \tag{2}$$

Vanishing the determinant of the $3 * 3$ matrix given in (2) yields to a third-order polynomial in q_r^2 which 6 roots can be explicitly obtained from known formulas. The general solution of the motion equation in the n-th layer is therefore a linear combination of 6 partial waves:

$$u_l = \left(\sum_{r=1}^{6} A_r U_l^r e^{iq_r x_3} e^{i(kx_1 - \omega t)} \right) \quad l = 1,2,3 \tag{3}$$

where the coefficients A_r are the amplitude of the partial waves. They are determined by the boundary conditions of each layer: displacement and stress continuity along the interfaces between the layers and traction-free boundary conditions for the top and the bottom surfaces of the laminate. A total of 6N equations if there are N layers is established and numerically solved by using the global matrix method [7].

This method is very general but necessary for the studied structure. It gives us in the simple case of an aluminium plate the dispersions curves of figure 2 which are the phase velocities of the different modes as a function of the product frequency-thickness. These curves are significant from an experimental point of view as they permit to adjust the experimental setup. They represent the modes which can

propagate in the plate, provided they are correctly excited as we will see in the next section.

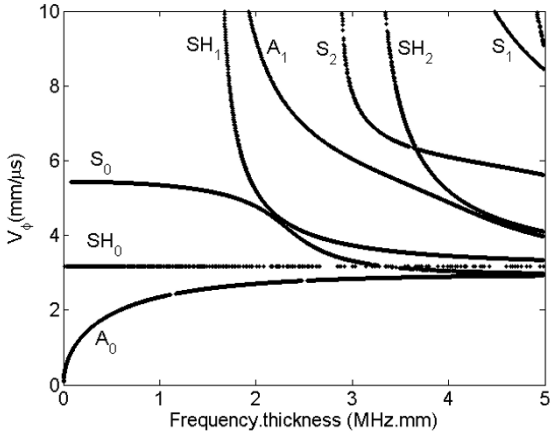

Fig. 2 Dispersion curves of Lamb waves propagating in an aluminium plate.

Another important data can also be derived from these curves: the group velocity, which represents the velocity of energy propagation and is defined by:

$$V_i^g = \left(\frac{\partial \omega}{\partial k_i}\right)_{k_j} \qquad j \neq i \tag{4}$$

In anisotropic materials this equation leads to :

$$\mathbf{V^g} = \frac{1}{\cos\psi}\left(\frac{\partial \omega}{\partial \mathbf{k}}\right)_{n_i} \tag{5}$$

were $\mathbf{n_i}$ is a unit vector parallel to the wave vector $\mathbf{k}$ and ψ is the angle between the group velocity vector and $\mathbf{k}$. In isotropic materials ψ vanishes, hence the wave front curve, which is the locus of group velocity vector for every possible choice of direction of propagation, is simply a circle. We will see in the last section how to use this wave front curve to locate a defect.

2.2 Generation and Detection of Lamb Waves by PZT Discs

In this section we investigate the behavior of a bonded thin PZT disc used to generate and detect Lamb waves. First we calculate analytically the response of the PZT to an incident plane wave. That reveals the presence of cut-off wavelengths that the disc cannot detect properly. Then FE simulations and experimental measurements

show that the PZT disc regarded as an actuator generates Lamb waves with the same cut-off wavelengths.

We consider a PZT of thickness h_{PZT} and diameter $D = 2R$ bonded on the host structure of thickness h_{plate}. According to its geometry ($h_{PZT} \ll h_{plate}$ and $R \gg h_{PZT}$) it can be considered in state of plane stresses, with $T_{33} = 0$. Considering that the electrical impedance of the measurement circuit is higher than those of the PZT, we can assume that the electric displacement $D_3 = 0$. Simplification of the constitutive equations of the piezoelectric material leads to:

$$E_3 = -\tilde{h}_{31}\,(S_{11} + S_{22}) \tag{6}$$

where E_3 is the electric field in the third direction, $\tilde{h}_{31}$ is the piezoelectric coefficient at plane stress and S_{ii} the strain [8].

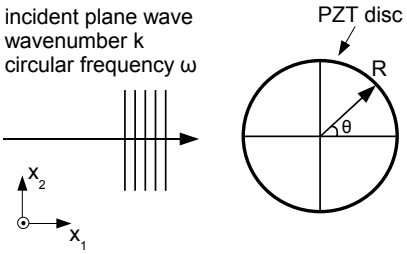

Fig. 3 Incident plane wave on a circular PZT disc.

We now consider the displacement created by an incident plane wave (figure 3):

$$u(\mathbf{x},t) = U_0 e^{j(kx_1 - \omega t)} \tag{7}$$

The measured voltage V is therefore averaged on the surface of the PZT:

$$V = -\tilde{h}_{31}\frac{h_{PZT}}{\pi R^2}\int_S (S_{11} + S_{22})\,ds \tag{8}$$

Applying Stockes theorem to the previous equation gives:

$$V = -\tilde{h}_{31}\frac{h_{PZT}}{\pi R^2}\int_S div(u)ds = -\tilde{h}_{31}\frac{h_{PZT}}{\pi R^2}\int_{\partial S} u.n\,d\Gamma \tag{9}$$

thus

$$\begin{aligned} V &= -\tilde{h}_{31}\frac{h_{PZT}}{\pi R^2}U_0 2e^{-j\omega t}\int_0^{\pi} e^{jkR\cos\theta}R\cos\theta\,d\theta \\ &= -2j\tilde{h}_{31}\frac{h_{PZT}}{R}U_0 e^{-j\omega t}J_1(kR) \end{aligned} \tag{10}$$

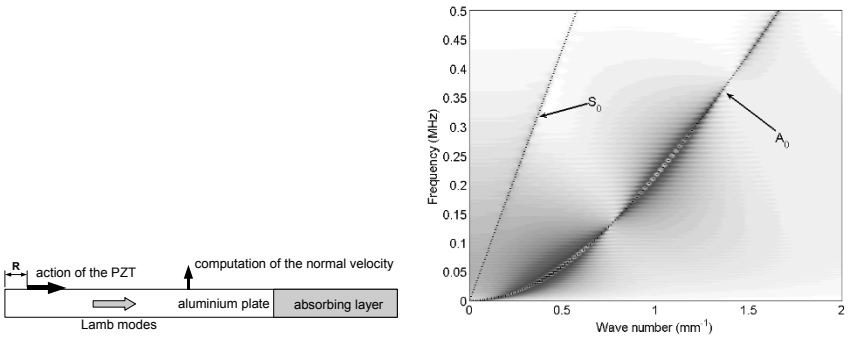

Fig. 4 (a) Geometry used in the FE simulations, (b) 2D-FFT of the normal velocity computed at the surface of a 1 mm thick aluminium plate excited by a PZT of diameter 10 mm driven by a 1-cycle toneburst at 300 kHz; dots correspond to theoretical dispersion curves.

where J_1 is the Bessel function of first kind and first order. Hence, the voltage of the PZT disc is proportional to $|J_1(kR)| = |J_1(\pi D/\lambda)|$. The plane wave is therefore optimally detected for the wavelength $\lambda = 1.7D$ (maximum of the $|J_1|$ function) and minimally detected for $\lambda = 0.8D$ (first zero of the $|J_1|$ function).

Now we will study the behavior of the PZT discs as actuators. We determine the impulse response of a PZT bonded on an aluminium plate by FE simulations and we compare them with experimental data. The FE model is a 2D axisymetric aluminium plate with an absorbing layer to minimize the reflection at the edges of the plate (figure 4(a)). As the bonded material is very thin, the shear stress is transmitted to the structure only at the periphery of the disc [9]. The action of the PZT is therefore represented as a ponctual force at the extremity of the disc.

In order to study the influence of a single mode, we consider the out of plane velocity at the surface of the aluminium plate for low frequency-thickness products. A 2D-FFT confirms that, under that hypothesis, only the A_0 mode has to be considered (figure 4(b)). In figure 5(a) we can see the amplitude of the out of plane velocity versus the wavelength of A_0 mode for different diameters of PZT discs. The simulations were computed in the frequency domain and then converted to a function of λ_{A_0} using the wavelength curve deduced from the previous dispersion curves (figure 2). We can see that there are again cut-off wavelengths which also correspond to the zeros of the function $|J_1(\pi D/\lambda)|$.

The results of the FE simulations are compared to experimental measurements of the normal velocity at the surface of the aluminium plate performed with a heterodyne interferometric probe (figure 5(b)). The positions of the cut-off wavelengths are clearly visible and correspond well with numerical results.

This study shows the necessity of adapting the diameter of the PZT disc to the wavelength of the Lamb modes we want to generate/detect in the structure.

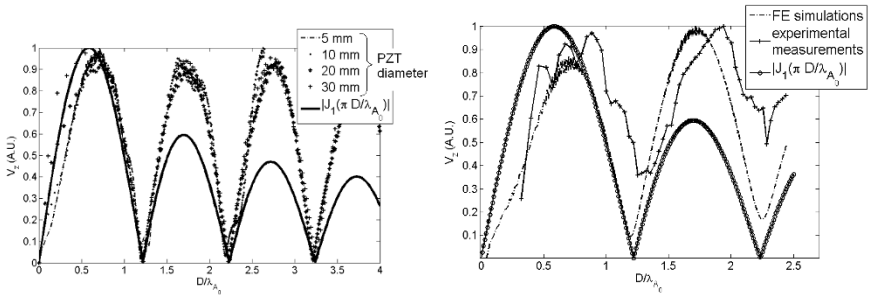

Fig. 5 (a) Normal velocity at the surface of a 1 mm thick aluminium plate for PZT discs of different diameters, (b) Normal velocity at the surface of a 2 mm thick aluminium plate excited by a 10 mm diameter PZT disc, comparison between FE simulations and measurements with a heterodyne interferometric probe.

3 Experimental study of the SHM system

Some experiments were conducted to set-up the tools necessary to locate and evaluate the size of a defect with the SHM system. To avoid facing all the difficulties directly, we have not bonded an anisotropic patch in our experiments yet. Therefore the specimen used was a 2 mm thick aluminium plate and the defect a hole well calibrated.

The SHM system was achieved with three PZT discs of 10 mm diameter and 0.15 mm thickness bonded onto the aluminium plate. The distances between the discs were respectively 15.4 mm, 15.8 mm and 18.9 mm. The instrumentation consisted of an Agilent 33220A [Santa Clara, USA] arbitrary waveform generator and a Lecroy Waverunner 44Xi [Chestnut Ridge, USA] oscilloscope. Pulse-echo method was employed, the generation consisted of a 1-cycle toneburst of centre frequency 300 kHz and an amplitude of 10 V_{pp}. We used the S_0 mode which is the fastest mode at this frequency and is therefore not perturbed by edge reflection of other modes. In order to minimize the voltage at the input of the oscilloscope during the transmit event, a limiter diode bridge placed in parallel with the receive circuitry was used. The signals were initially measured on a healthy plate and then compared to those measured after drilling a hole of increasing diameters from 2 mm to 10 mm.

Figure 6(a) shows the typical pulse-echo signal measured. After the initial excitation we observe a spurious ringing due to the diode limiter which may obstruct the visualisation of the signal due to the hole if it is too close to the PZT disc. The presence of the hole is visible due to the wave packet arriving at 24 μs, the first boundary echo occurs at 46 μs. Figure 6(b) shows the difference between the signal in the damaged structure and the healthy one. The presence of the hole is clearly observed when its diameter is larger than 2 mm. However, when the distance between the sensor and the hole is too large, it can be difficult to detect a defect smaller than 4 mm. Measuring, with the three PZT discs, the time of flight of the wave packet

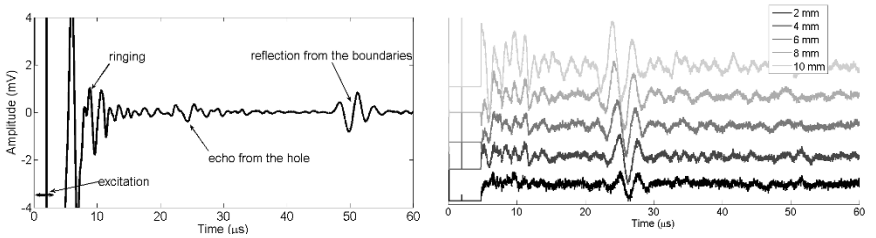

(a) (b)

Fig. 6 (a) Pulse-echo signal measured on a 10 mm diameter PZT disc bonded onto a 2 mm thick aluminium plate. The PZT disc is excited by a 1-cycle toneburst at 300 kHz and localized at 120 mm of a 8 mm diameter hole, (b) Difference between the signal measured for increasing diameters of hole and the signal obtained for an undamaged plate.

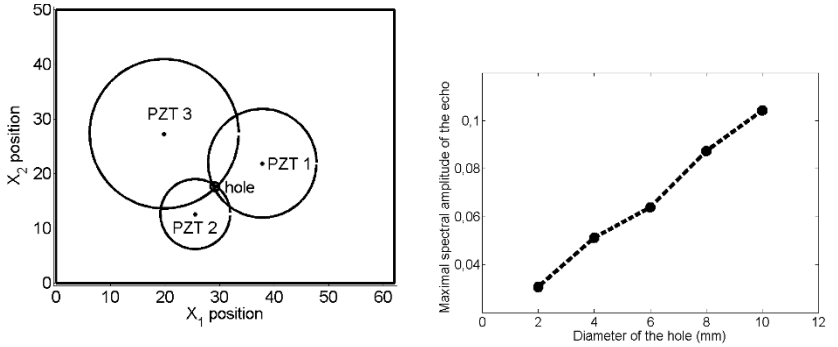

(a) (b)

Fig. 7 (a) Localization of the hole by triangulation, (b) Variation of the maximal spectral amplitude of the echo as a function of the diameter of the hole.

reflected on the hole enables us to locate the defect by triangulation as we can see in figure 7(a). The estimated position is the intersection of the three wave front curves (calculated in a previous paragraph) centered on the PZT and dilated by the corresponding time of flight. In the case of the aluminium it is simply the intersection of three circles but it will give a more complex figure in the case of anisotropic structures. However the estimated position of the hole is in a very good agreement with the real one.

Figure 7(b) shows the maximal spectral amplitude of the echo as a function of the hole diameter. The quasilinear variation of this indicator allows us to estimate the size of the defect.

4 Conclusion

A SHM system for detecting and locating a defect based on three PZT discs using propagative Lamb waves has been presented. In order to properly generate and detect the waves some considerations about the behavior of PZT discs have been detailed. In particular it has been highlighted the necessity to adapt the diameter of the PZT disc with the wavelength. Some experimental preliminary tests of the SHM system in an academic situation have also been described showing the ability of the setup to locate a defect and estimate its size.

References

1. Baker A (1999) Bonded composite repair of fatigue-cracked primary aircraft structure. Compos. Struct. 47:431–443
2. Avdelidis N, Moropoulou A et al (2003) The technology of composite patches and their structural reliability inspection using infrared imaging. Prog. Aerosp. Sci. 39:317–328
3. Li H, Dupouy O et al (2006) Health monitoring of bonded composite repairs using fibre optic sensors. In: SPIE (ed) Smart Structures and Materials, San Diego
4. Jones R and Galea S (2002) Health monitoring of composite repairs and joints using optical fibres. Compos. Struct. 58:397–403
5. Koh Y, Chiu W et al (2002) Integrity assessment of composite repair patch using propagating lamb waves. Compos. Struct. 58:363–371
6. Chiu W, Galea S et al (2000) Damage detection in bonded repairs using piezoceramics. Smart Mater. Struct. 9:466–475
7. Lowe M (1995) Matrix techniques for modeling ultrasonic waves in multilayered media. IEEE Trans. Ultrason. Ferroelectr. Freq. Control 42:525–542
8. Fribourg-Blanc E (2003) Actionneurs en couches minces pour le contrôle santé de structures aéronautiques - étude de films de PZT et de PMNT -. Ph.D. thesis. Université de Valenciennes et du Hainaut-Cambrésis
9. Giurgiutiu V (2005) Tuned lamb wave excitation and detection with piezoelectric wafer active sensors for structural health monitoring. J. Intell. Mater. Syst. Struct. 16:291–305

Simulation of structural noise and attenuation occurring in ultrasonic NDT of polycrystalline materials

V. Dorval, F. Jenson, G. Corneloup and J. Moysan

Abstract In some polycrystalline materials, ultrasonic non destructive testing is affected by structural noise and attenuation. Those phenomena can cause significant loss in detection performances, thus their prediction is of great practical interest. During previous works at CEA-LIST, noise and attenuation models have been developed and implemented into the simulation software for non destructive testing CIVA. These two models are based on distinct methods and both require reference ultrasonic measurements to reproduce the behavior of a given material. The main purpose of this work is to improve these models by linking structural noise and attenuation to the microstructural parameters. This should suppress the need for reference measurements and allow for more accurate simulations. In this communication, a method using one scattering model to compute both structural noise and attenuation is presented. This method is based on the assumption that both phenomena can be considered to depend only on the average of the energy scattered by a unit volume of the material. A model based on the Born approximation is used to relate this averaged scattered energy to second order statistical properties of the microstructure and to the elastic properties of a single crystallite. This model is valid in a frequency domain larger than the Rayleigh domain. During the simulation of the testing of a polycrystalline material, a non-attenuated ultrasonic field is firstly computed. Attenuation is applied afterwards using a time-dependant filtering. Noise is simulated by generating a random set of point-like scatterers in the medium. Mode conversions and phenomena related to anisotropic

Vincent Dorval, Frederic Jenson
CEA, LIST, F-91191 Gif sur Yvette, France,
email: vincent.dorval@cea.fr
Gilles Corneloup, Joseph Moysan
LCND, Université de la Méditerranée, IUT Aix-en-Provence, Avenue Gaston Berger, 13625 Aix en Provence, France, email: joseph.moysan@univmed.fr

scattering are accounted for. Simulation results obtained with this approach are compared to experimental results.

1 Introduction

As an ultrasonic wave propagates in a polycrystalline material, a part of its energy is scattered in all directions of space by individual crystallites. This interaction between the ultrasonic field and the microstructure of the material induces the attenuation of defect echoes and the presence of signals known as structural noise. During the ultrasonic testing of some materials, those phenomena can become significant and hide defect echoes.

The simulation software for non destructive testing CIVA includes tools for taking into account structural noise and attenuation. These two phenomena are handled separately: attenuation is computed by applying a frequency filter to signals, and structural noise is obtained using a specific "noise generator" algorithm. In the current version of the software, expressions of the attenuation coefficients as well as parameters for the noise generator have to be entered manually using the software interface. Preliminary measurements of attenuation and noise are necessary to adjust those parameters for a given material.

The work outlined in this article aims at gaining a better knowledge of the phenomena that cause attenuation and structural noise. This should enable to develop new simulation tools.

The existing CIVA tools, which will serve as a basis for new developments, are described. Then, a theoretical model relating ultrasonic scattering to properties of the microstructure is outlined. Its integration to existing algorithms, which should enable to compute structural noise and attenuation from material properties, is discussed.

2 Simulation of structural noise and attenuation in CIVA 9

The CIVA 9 software offers tools that allow taking into account structural noise and attenuation when modeling ultrasonic testing. The computation of an ultrasonic testing involving noise and attenuation can be summarized as such: an ultrasonic field is computed without noise or attenuation. A user-defined attenuation filter will be applied afterwards at any position where the value of the ultrasonic

field is needed. A set of point-like scatterers is generated to produce noise. Finally, the responses of those scatterers as well as the responses of defects are computed, using the value of the computed field and the attenuation.

Attenuation

The CIVA algorithms start by computing ultrasonic fields that are not attenuated. Then, at any position where the knowledge of the attenuated field is needed, the attenuation is accounted for by using the Beer-Lambert law:

$$u = u_0 \exp\left[-\alpha(\omega) d\right].$$

u_0 being the non-attenuated field and u the attenuated one. d is the distance traveled by the wave from its entry interface to the position where u is computed. $\alpha(\omega)$ is a parameter known as the attenuation coefficient, and reflects the attenuative properties of the medium. The expression above can be regarded as a frequency filter that depends on the distance the wave has traveled in the medium.

Several forms of attenuation functions $\alpha(\omega)$ are available to the user. In any case the parameters of the function have to be set by the user, who has to refer either to a model or to preliminary measurements.

Noise

The CIVA noise generator creates a random set of point-like scatterers. These scatterers are uniformly distributed in the medium, and each of them is characterized by a random scattering coefficient. Two parameters must be adjusted to mimic the noise reflected by a given material: ρ (the number of scatterers per volume unit) and σ (the standard deviation of the probability density function from which scattering coefficients are drawn).

The model used to compute noise is similar to the one developed by Gustafsson and Stepinski [1]. It is a single scattering model. The response of a set of scatterers to an ultrasonic pulse $S(\omega)$ is the sum of the individual contributions of each scatterer and can be expressed as:

$$V(\omega) = \sum_{k=1}^{K} A_k \omega^2 \exp\left[-\alpha(\omega) d_k\right] \exp\left(-j\omega\tau_k\right) C_k S(\omega).$$

A_k is a coefficient randomly assigned to each scatterer. It follows a normal probability distribution whose mean is zero and standard deviation is σ. d_k is the length of the emitter-scatterer-receiver path and τ_k is the corresponding time of

flight. C_k is a factor which quantifies the interaction between the emitter and the receiver at the location of the scatterer, and stems from a form of the reciprocity theorem which is used in CIVA to compute echoes. The ω^2 term in the expression describes how the amplitude of the scattered waves varies with frequency: ω^2 corresponds to the Rayleigh domain and is used here because it is assumed that structural noise is due to scatterers that are very small compared to wavelengths. $exp[-\alpha(\omega)d_k]$ is the attenuation filter expressed as a function of the time of flight.

The set of scatterers remains the same as the echoes are computed for different positions of the transducer. Consequently, a same grain is apparent for successive positions of the transducer, which ensures that a generated B-scan has the same coherent properties as the measured one.

Limitations of the method

Once correct noise and attenuation parameters have been set for one material in one configuration, they can be used for the same material in some other configurations. But this transposability of parameters has limits.

As the parameters reflect intrinsic properties of the material, they do not depend on the geometry of the inspected block, on the incidence angle, or on the divergence of the beam. They are also independent of frequency, as long as the bandwidth remains in the Rayleigh domain (grains must be small compared to wavelength). However, the noise model is only valid for a simulation involving one wave type (Longitudinal or Shear) and one scattering angle.

The integration of a scattering model should enable to refine the noise generator and to go past the transposability limits, as well as suppressing the need for reference measurements.

3 Integration of a scattering model

Principles

A model based on the approach proposed by Rose [2] was selected. This model describes a metal as a set of juxtaposed anisotropic crystallites. All the crystallites have identical properties, except for their shape, size, and orientation. The elastic

constants of crystallites being anisotropic, the variations of orientation induce the scattering.

The study presented here is limited to materials whose crystallites are only slightly anisotropic (which is the case in usual metals) and whose grains are not too big compared to wavelengths. For such materials the Born approximation, which assumes that the ultrasonic field is only slightly affected by the microstructure, is relevant. Rose [2] shows that when using the Born approximation it is possible to compute the field scattered by the microstructure as a function of the field that would propagate in an effective uniform medium. This will make it possible to use an ultrasonic field computed by CIVA in a uniform medium as a basis for structural noise computations.

In the computation method presented here, the Born approximation will only be used locally, to compute scattering coefficients. When it comes to computing the response of an entire block, it is important to take into account some perturbation of the field by the microstructure in the form of attenuation, which becomes significant at the scale of several wavelengths. Consequently, it will be considered that noise arises from the interaction between the microstructure and a beam equal to the beam propagating in an unperturbed medium, except that it has been attenuated. It will be a single scattering model, thus the interaction between the microstructure and the scattered field will not be taken into account (except for attenuation, as in the case of the incident field).

In many ways, the new algorithm will be similar to the one used in CIVA 9: an unperturbed field will be computed, attenuation will be applied afterwards, and noise will be accounted for by a random set of scatterers. The main differences are that in the new algorithm the attenuation filters and the properties of the scatterers will not be user-defined, and that the response of the scatterers will represent more accurately structural noise.

Noise

A straightforward way to generate noise based on a scattering model would be to generate a realistic polycrystalline microstructure, and to use the model to compute the ultrasonic responses of every crystallite. But the number of crystallites present in metals (typically several thousands crystallites per mm^3) would require unacceptably long computations.

As the statistical properties of structural noise are simple, a faster method can be developed. Structural noise recorded at a given moment comes from a large number of crystallites, which can be regarded as uncorrelated scatterers. Therefore

structural noise is a case of fully developed speckle, as described by Goodman [3], which is basically a colored Gaussian noise with zero mean. Such a noise can be mimicked using a smaller number of scatterers, as long as it is ensured that the generated noise will be Gaussian with zero mean and will have the same variance as the original noise.

As in the case of the CIVA 9 noise generator, random sets of scatterers will be created. Again, their scattering coefficients will be randomly assigned following a Gaussian probability with zero mean, which will ensure that even when a small number of scatterers are insonified the probability distribution of the noise will have the correct form. The standard deviation of the scattering coefficient distribution will be set in a way that will ensure that the noise has the correct variance.

It can be shown that if the scattering coefficients are set in the following way, the noise signal generated by point-like scatterers will have the same variance as the noise generated by crystallites:

$$D_k(\omega) = \beta_k \sqrt{\frac{\eta(\omega)}{N}\frac{v_{inc}}{v_{scat}}}\,.$$

D_k is the scattering coefficient of one scatterer, β_k a random factor affected to each scatterer using a standard normal distribution (with a mean of zero and a standard deviation of one), and N the number of point-like scatterers per unit volume. *inc* and *scat* refer to the types (longitudinal, shear horizontal or shear vertical) of the incident and scattered waves and v_{type} to wave speeds. η is the differential cross section as defined by Margetan et al. [4]. The noise computed by the new noise generator will be equal to:

$$V(\omega) = \sum_{k=1}^{K} \beta_k \sqrt{\frac{\eta(\omega)}{N}\frac{v_{inc}}{v_{scat}}} \exp\left[-\alpha(\omega) d_k\right] \exp\left(-j\omega\tau_k\right) C_k S(\omega)\,.$$

This new noise generator will account for mode conversions and variations of the scattering coefficient as a function of scattering angles. These phenomena are included in the computations made by Margetan et al. [4]. They write η in the following form:

$$\eta_{inc\to scat}(\theta) = \frac{\omega^4}{(4\pi\rho)^2 v_{scat}^5 v_{inc}^3} \left\langle \delta C_{ijkl} \delta C_{mnpq} \right\rangle_{Or} \pi D^3 \left[1 + \frac{\Delta k(\theta)^2 D^2}{4}\right]^{-2}\,.$$

θ is the scattering angle, ρ the material density, δC the variations of elastic constants compared to the average medium, $\Delta k(\theta)$ the difference between scattered and incident wave vectors. D is the correlation length that is used in the spatial correlation function $W(R)=exp(-2R/D)$.

This spatial correlation function is defined as the probability that two points separated by a distance R are in the same crystallite. The inverse exponential form

that leads to the expression of η above is an approximation meant to simplify calculations. In a real material, the spatial correlation function depends on the grain size distribution. It should be noted that some theoretical results obtained during this Ph.D. work suggested that, for certain grain size distributions, assuming this inverse exponential form will lead to an error of a few decibels in the computed noise.

Attenuation

Several methods can be used to compute attenuation coefficients. A method that allows for relatively flexible computations (which will permit an easier adaptation to different microstructures), and whose domain of validity is fairly large, was used in this study. It consists in relating the attenuation to the energy that the beam looses on average as it propagates. The latter quantity can be obtained through a sum of η on all directions and on all scattered wave types. In the case of longitudinal waves, it yields the following expressions for the attenuation coefficient:

$$\alpha_L = \frac{\pi}{2} \int_{\theta=0}^{2\pi} \left[\eta_{L\to L}(\theta) + \eta_{L\to SH}(\theta) + \eta_{L\to SV}(\theta) \right] \sin(\theta)\, d\theta \,.$$

SH and SV indicate respectively shear horizontal and shear vertical waves, as defined in [4].

Figure 1 compares attenuation computed with this method to attenuation computed by a reference model [7] and to its Rayleigh asymptote.

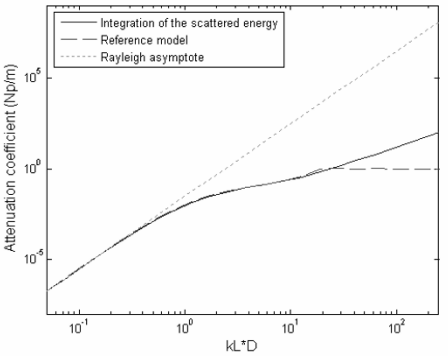

Fig. 1: Attenuation computed by different models, L wave in austenitic steel

This comparison shows that in terms of attenuation this model agrees with the reference model beyond the Rayleigh domain. Nevertheless, it should be noted that the reference model used here assumes, like the model used to compute η,

that the spatial correlation function is inverse exponential. Therefore it does not allow estimating how a particular grain-size distribution would change attenuation coefficients.

4 Comparison to experiment

Computations were run with the algorithms, and the results were compared to a set of measurements. These measurements were made on a diffusive block of austenitic steel. Computations were run using the CIVA 9 algorithm, by adjusting the entry parameters for noise and attenuation in order to obtain the best possible fit. Computations were also run using the new algorithm based on the interaction model. As no micrographs were available for this block, grain size was unknown and different likely values of the correlation lengths were tested. The one that gave the best agreement (120 μ m) between measured and simulated attenuation was chosen.

The results presented here are obtained for a configuration using shear waves with a 45° incidence angle, and a 2.25MHz central frequency. When plotted in B-scans (Figure 2), measured and computed results have a similar aspect.

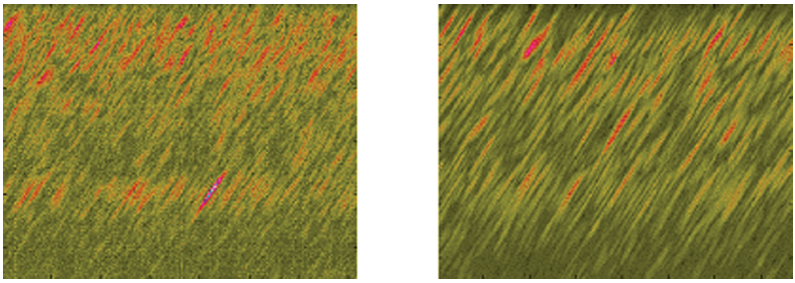

Measurement Computation based on model

Fig. 2: Measured and computed B-scans for a block of austenitic steel

Differences appear when plotting noise as a function of time, as in Figure 3 (noise is quantified as the variance of the signal at a given time, along transducer positions where only noise was present).

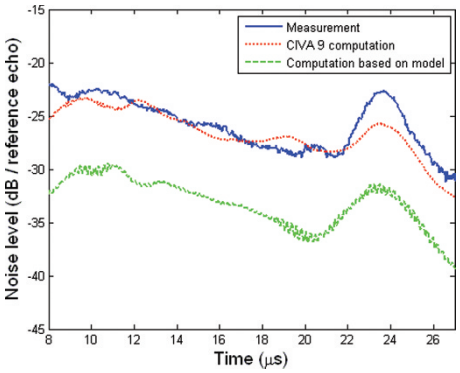

Fig. 3: Noise as a function of time (measurement and computations by the two algorithms). The echo of a defect in a reference block was used as a reference in amplitude.

The slopes of the three curves are identical, which means that attenuation is correctly predicted. Thus, in the case of the CIVA 9 computations the user-defined attenuation coefficients were correct, and in the case of the new algorithm they were correctly predicted by the model.

The two computations show different errors on noise. The CIVA 9 algorithm agrees with experiment until 20 μ s. Afterwards it underestimates the noise peak that corresponds to the bottom of the block. This underestimation can be explained by the fact that a fraction of the noise coming from the bottom of the block involves corner echoes which are scattered at an angle different from the angle of direct echoes (Figure 4). As the CIVA 9 algorithm does not account for angular variation of the scattering coefficient, it can not compute those echoes properly. The new algorithm, which takes angular variations into account, yields a better estimation of the relative height of that noise peak.

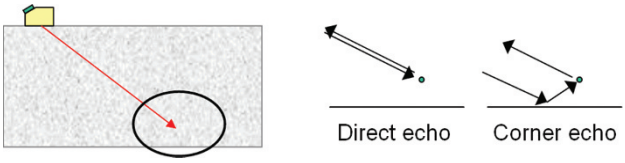

Fig. 4: Types of echoes involved in the noise coming from the bottom of the block

However, the noise computed by the new algorithm is underestimated by approximately 6 dB. There are several possible origins for that error. Some theoretical results obtained during this work suggested that the inverse exponential form assumed for the spatial correlation function could introduce an error of several decibels when applied out of the Rayleigh domain, as an accurate representation of the grain size distribution becomes necessary. The Rayleigh domain can be de-

fined as the frequencies for which $k_S D << 1$: in this example $k_S D \approx 0.5$, which could explain the error. Knowing the actual spatial correlation function of the material would allow correcting for such an error, but micrographs would be necessary. The error could also be due to an additional source of diffusion in the material (for example a high density of dislocations). It also might just be a calibration problem.

Still, it is not possible to conclude on the complete relevance of this new algorithm without testing it on a material for which the microstructure is perfectly known. Consequently, new noise measurements are currently performed on blocks for which micrographs are planned.

5 Conclusion

The algorithm used by CIVA 9 to compute ultrasonic testing involving noise and attenuation may be improved using a wave-microstructure interaction model. This new approach would suppress the need for reference measurements and account for mode conversions and angular variations of scattering.

A model which can be used to compute both noise and attenuation was selected. A method to generate noise based on this model with a limited number of calculations was developed. The predictive abilities of this new algorithm have been tested showing encouraging results. Yet, discrepancies remain between measured and simulated noise amplitude. These discrepancies are currently addressed in a study that includes both ultrasonic and micrographic measurements on a set of specimens with various mean grain sizes.

Subsequently, this work may continue with the application of the approach outlined here to materials having more complex microstructures. Other themes of research could be the improvement of the scattering model, of the noise generator algorithm, or the study of potential additional sources of noise.

References

[1] Gustafsson, M.G., Stepinski, T.: Studies of split spectrum processing, optimal detection and maximum likelihood amplitude estimation using a simple clutter model, Ultrasonics **35**, 31-52 (1997)

[2] Rose, J.H.: Ultrasonic backscatter from microstructure, Rev. of Prog. in QNDE **11**, 1677-1684 (1992)

[3] Goodman, J.W.: Statistical Properties of Laser Speckle Patterns, Top. in Appl. Phys. **9**, 9-75 (1975)

[4] Margetan, F.J., Linxiao Yu, Thompson R.B.: Computation of grain noise scattering coefficients for ultrasonic pitch/catch inspections of metals, Rev. of Prog. in QNDE **24**, 1300-1307 (2005)
[5] Gubernatis F.E., Domany, E., Krumhansi, J.A., Formal aspects of the theory of the scattering of ultrasound by flaws in elastic materials, J. of Appl. Phys. **48**, 2812-2819 (1977)
[6] Gubernatis F.E., Domany, E., Krumhansi, J.A., Huberman, M.: The Born approximation in the theory of the scattering of elastic waves by flaws, J. of Appl. Phys. **48**, 2812-2819 (1977)
[7] Stanke, F.E., Kino, G.S.: A unified theory for elastic wave propagation in polycrystalline materials, Journal of the Acoustical Society of America **75**, 665-681 (1984)

Ultrasonic array reconstruction methods for the localization and the characterization of defects in complex NDT configurations

A. Fidahoussen, P. Calmon, and M. Lambert

Abstract In this paper, we present ultrasonic array reconstruction techniques aiming at localizing and characterizing flaws in an inspected piece. The proposed algorithms derive from the synthetic focusing approach, which exploits the time-of-flight information. Theoretical forward models implemented in the CIVA software platform are able to provide this information. An advantage is that these models can deal with complex inspection configurations, in particular with complex geometries (irregular surface, for example). The algorithms can be applied to data issued from various operating modes of array inspection. We describe the different algorithms and show examples of their applications for both simulated and measured data.

1 Introduction

Ultrasonic arrays are increasingly used in NDT applications. They offer more flexibility and adaptability to complex configurations compared to conventional probes. In addition they provide a larger amount of data, which can improve diagnostics through adapted processing techniques. Classical reconstruction methods based on simple hypotheses are not always able to localize defects for non-canonical configurations, such as complex geometries.

In this paper, we study reconstruction algorithms based on an inspection modelling, which allows to deal with complex configurations. The proposed algorithms derive from the synthetic focusing approach, which consists in coherently summing the received signals to have maximum amplitude where scatterers are really located. Basically, the algorithms exploit the time of flight, which is evaluated theoretically,

A. Fidahoussen and P. Calmon
CEA-LIST, Centre de Saclay, F-91191 Gif-sur-Yvette cedex, France,

M. Lambert
L2S (CNRS-Suplec), 3 rue Joliot Curie, 91192 Gif-sur-Yvette, France, e-mail: marc.lambert@lss.supelec.fr

but the possibility of exploiting the amplitude of the signals is also studied here. These quantities (time of flight and amplitude) are determined from existing forward models implemented in CIVA platform, which allow to deal with non-canonical situations (complex geometry, heterogeneous parts, anisotropic materials, etc) [1, 2]. Moreover the adopted approach is generic and can be applied to any inspection providing a set of ultrasonic signals. So a wide range of array operating modes (electronic scanning, beam steering, transmit-receive independent functions, per channel acquisition) can be processed. This paper is organized as follows: the principle of the algorithms is first described, some examples of reconstruction using both simulated and measured data are shown in Section 3. Finally, the conclusion is given in Section 4.

2 Algorithm description

2.1 Modelling of the ultrasonic response of a point-like scatterer

To extract the quantities we need for the reconstruction algorithms, echo signal for a point-like scatterer and for every array inspection is modelled with the acoustical impulse response formalism. Under the hypothesis of scalar waves, it can be shown that the echo signal $s_{ij}^{(th)}(P,t)$ due to a point-like scatterer in P, with the transmitting element i and receiving element j, is proportional to

$$s_{ij}^{(th)}(P,t) = v(t) \otimes h_i^{tr}(P,t) \otimes h_j^{re}(P,t)\,, \tag{1}$$

where $\otimes$ stands for the temporal convolution product, $v(t)$ is the excitation signal, and $h_i^{tr}(P,t)$, $h_j^{re}(P,t)$ are respectively the acoustical impulse responses of transmitting element i and receiving element j.

Any kind of array inspection can be envisaged, we introduce two sets of elements T and R, which represent transmitting elements and receiving elements used in the acquisition. Electronic delays at transmission (τ_i^{tr}) and reception (τ_j^{re}) can also be applied. So in the general case, the echo signal can be considered proportional to

$$s^{(th)}(P,t) = v(t) \otimes \sum_{i\in T}\sum_{j\in R} h_i^{tr}(P,t-\tau_i^{tr}) \otimes h_j^{re}(P,t-\tau_j^{re})\,. \tag{2}$$

The reconstruction algorithms exploit the time and amplitude information by considering the Hilbert envelope of the signal. For a signal $s(t)$, this envelope denoted $\mathrm{env}\,[s]\,(t)$, is the modulus of its associated complex analytical signal $s_a(t) = s(t) + j\mathscr{H}\{s\}(t)$ where $\mathscr{H}\{s\}(t)$ is the Hilbert transform of $s(t)$. So, this envelope is calculated by

$$\mathrm{env}\,[s]\,(t) = \sqrt{s(t)^2 + \mathscr{H}\{s\}(t)^2}\,. \tag{3}$$

The times of flight t_P, which are the propagating times transmitters-P-receivers, and the amplitudes $s_P^{(th)}$ are calculated from the Hilbert envelope of the echo signal (2) denoted env $\left[s^{(th)}\right](P,t)$, $s_P^{(th)}$is the maximum of the echo signal envelope, t_P is the time for this amplitude:

$$t_P = \arg\max_t \left\{ \text{env}\left[s^{(th)}\right](P,t) \right\}, \tag{4a}$$

$$s_P^{(th)} = \text{env}\left[s^{(th)}\right](P,t_P). \tag{4b}$$

2.2 Imaging algorithms

The proposed algorithms aim at localizing in the part, the origin of the echoes detected during the inspection. The output of the reconstruction process is the mapping in the Region Of Interest (ROI) of an estimator $E(P)$ proportional to the presence probability of a scatterer at a point P. Let us consider that the inspection is constituted by the acquisition of N signals $s_n(t)$, n varying from 1 to N. The ROI is a grid and each node P is considered as a potential point-like scatterer. Such scatterer can be for example flaws edges, which are at the origin of diffraction echoes, or flaws with a caracteristic length smaller than the considered wavelength. The first step of the process corresponds to the computation of the times of flight t_{nP} with (4a), corresponding to all the transmit-receive operations and to all nodes P. The second step consists in computing the "localized amplitudes" s_{nP}, which are the values of the measured signals $s_n(t)$ at the time of flight t_{nP}.

The first estimator E_1 considered here corresponds to classical synthetic focusing. It is given by the summation over all the transmit-receive operations of the quantities s_{nP}

$$E_1(P) = \sum_{n=1}^{N} s_{nP}, \tag{5}$$

it consists in assuming that the signal amplitude at the time t_{nP} is likely to be due to the scattered wave from P and, the closer P to the real defect localization is, the larger s_{nP} is. This algorithm combined to a simplified model has been firstly introduced in ultrasonic NDT field in the context of mechanically scanned monolithic transducers with the well-known SAFT algorithm [3]. More recently it has been applied by different authors to process UT array data of the type "Full Matrix Capture" (see below) (for example see [4]).

The latter estimator exploits only the times-of-flight information extracted from forward modelling. We propose an other estimator which aims at taking into account the global correlation between theoretical amplitudes $s_{nP}^{(th)}$ extracted from simulation –thanks to (4b)– and the quantities $\widetilde{s}_{nP} = \text{env}\left[s_n\right](t_{nP})$ obtained from the measured data $s_n(t)$. By defining the correlation coefficient $C(P)$ as:

$$C(P) = \left(\sum_{n=1}^{N} \widetilde{s}_{nP}\, s_{nP}^{(th)} \right)^2 \Big/ \left(\sum_{n=1}^{N} \widetilde{s}_{nP}^{\,2} \sum_{n=1}^{N} s_{nP}^{(th)\,2} \right), \tag{6}$$

this second estimator E_2 is expressed by:

$$E_2(P) = C(P) \sum_{n=1}^{N} s_{nP} = C(P)\, E_1(P). \tag{7}$$

By applying this estimator, the amplitudes of the echoes measured at t_{nP} are weighted according to the correlation between the distribution of these measured amplitudes and the theoretical amplitudes corresponding to the presence of a scatterer at P.

3 Application on both simulated and measured data

In the following, our general approach is used on both simulated and experimental acquisitions obtained from three different array inspection modes: sectorial scanning, per channel data and full matrix acquisitions. Sectorial scanning is a standard acquisition for which delay laws are applied to electronically sweep the beam. The others are examples of acquisition for which we consider elementary signals corresponding to the different transmitting elements.

The array we used in the experiments is a 2-MHz linear array composed of 64 elements. The element dimensions are 25×1.2 mm and the spacing between elements is 0.2 mm. The inspected part is a steel block with an irregular surface as shown in figure 1. It contains a set of four 2-mm diameter side drilled holes located at different depths. All the measurements were performed in immersion.

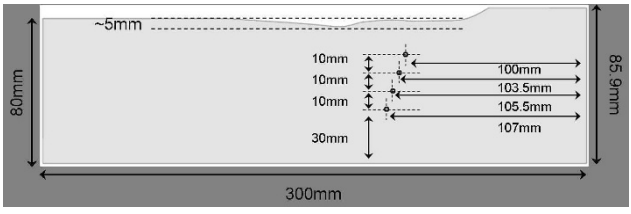

Fig. 1 Inspected piece containing a set of side drilled holes under the irregular surface.

3.1 Reconstruction with US beam: example of sectorial scanning

The first example concerns the technique of sectorial scanning, which consists in applying successively different delay laws to deflect the beam at different angles. This technique is schematized in figure 2. Delay laws are applied both at transmission and reception, and the signals are summed at reception.

Here, only the 16 elements at the center of the array are used to considere the set of side drilled holes in the far field and to have a narrow beam. The delay laws are taking into account the irregular surface to perform the sectorial scanning from 0° to 60° (1° step) with longitudinal waves.

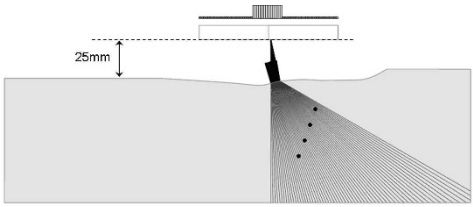

Fig. 2 Sectorial scanning inspection configuration.

In figure 3 we can see the sectorial images (S-scan) obtained with simulated and experimental data. Such an image is obtained by displaying the signals along the beam axis (represented in figure 2). This imaging technique is based implicitly on a ray model and supposes both i) that the beam is distributed around a central ray (”the beam axis”), ii) that the received echo signal is due to the presence of a scatterer somewhere along the central ray. The rays are calculated by taking into account the surface [5].

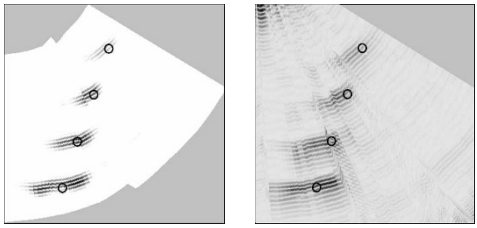

Fig. 3 S-scan imaging. Simulated (left) and measured (right) data.

In figure 3 we can see the localization of the deepest hole is inaccurate, this is due to the perturbation of the beam by the surface irregularities. Indeed, if we replace this complex surface by a plane surface, the S-scan obtain in this case shows an accurate localization of the defect as we can see in the figure 4.

Synthetic focusing algorithms are now applied. The dimensions of the ROI are 50×47 mm. In figure 5, we can see the results obtained with both simulated and measured data for each estimator E_1 and E_2. Experimental and simulated results are similar, which confirms the validity of the forward model. The maxima of the

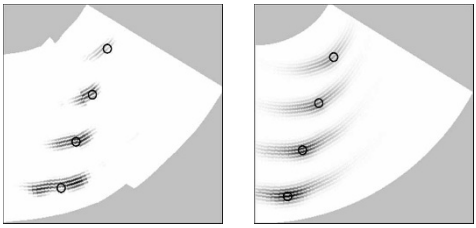

Fig. 4 S-scan imaging with simulated data. Irregular (left) and plane (right) surface.

amplitude of the two estimators are observed at the real position of the defects however the one we proposed (E_2, equation (7)) drastically reduces the artefacts and improves the precision of the localization.

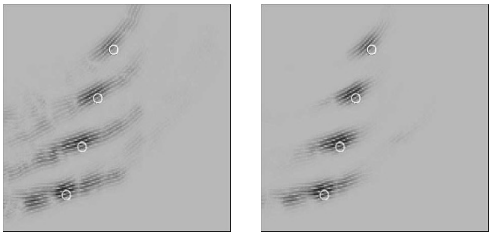

(a) Simulated data

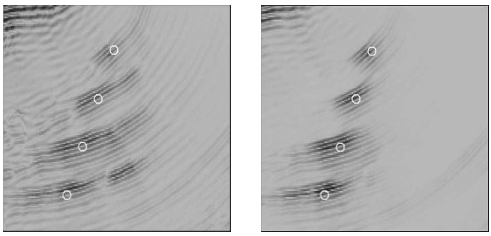

(b) Measured data

Fig. 5 Mapping of the estimators E_1 (left) and E_2 (right) in the beam steering case, with both simulated (a) and measured data (b).

3.2 Reconstruction from elementary signals

In the previous example, reconstruction was performed from phased-array data for which delay laws were applied to the various elements of the array. Now we are interested with acquisitions in which all the elementary signals are collected.

Let us first consider the technique called "Full Matrix Capture", which consists in acquiring the complete set of signals corresponding to the combination of all transmitting-receiving elements on the array. In our case we obtain 64×64 signals which can be put together in the so-called inter-element matrix transfer whose element links the response of one element of the array to the excitation of another. From this kind of acquisitions, another imaging methods based on the analysis of singular values decomposition of this matrix can be processed (for example see [6, 7]).

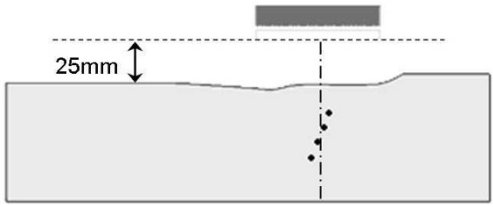

Fig. 6 inspection configuration for the "Full Matrix Capture"

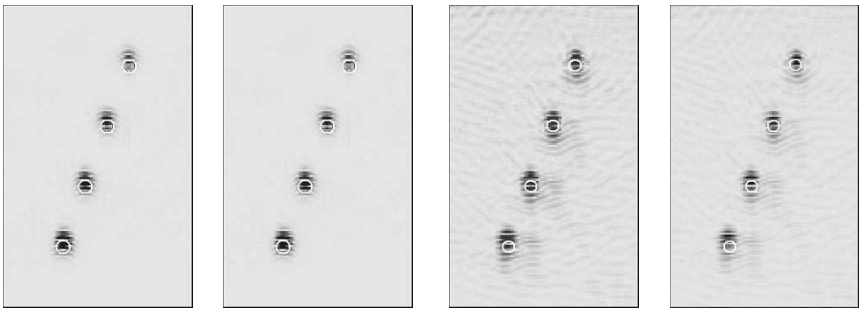

(a) Simulated data (b) Measured data

Fig. 7 Mapping of the estimators E_1 (left) and E_2 (right) in the third considered case, with both simulated (a) and measured (b) data.

The array is positioned in immersion above the irregular surface of the part as illustrated in figure 6 and the dimensions of the ROI are 30×50 mm. Defects are correctly localised with a good signal to noise ratio (SNR) (the reference is the maximum amplitude), 21 dB and 25 dB respectively, with the application of estimators E_1 and E_2, as shown in figure 7. These results show that synthetic focusing based algorithms are very well adapted to such kind of acquisition technique. Indeed, the redundancy of processed data is very important and the US field both in transmission and in reception is divergent. The defect localization is very effective by only exploiting times of flight (estimator E_1) whereas taking into account amplitudes (estimator E_2) doesn't significantly improve the results.

The last application example presented here corresponds to another per channel data acquisition technique, simpler than the previous one. Here, all the elements

emit at the same time and all the received signals are independently stored. So the number of post-processed signals is equal to the number of active elements in reception, 64 in this case. This technique aims at creating a planar wave front in the part. Well adapted for planar geometry it appears that in the case of irregular surface, the aberration effects, which are not corrected by suitable delay laws are notably perturbing the transmitted beam. This is illustrated in figure 8, which shows a cartography of the (normalized) amplitude of the elastodynamic field (for longitudinal waves) in the considered ROI, the array being also in the same position as considered in the previous example. In this image it is easy to see that the insonification of the four defects is very weak.

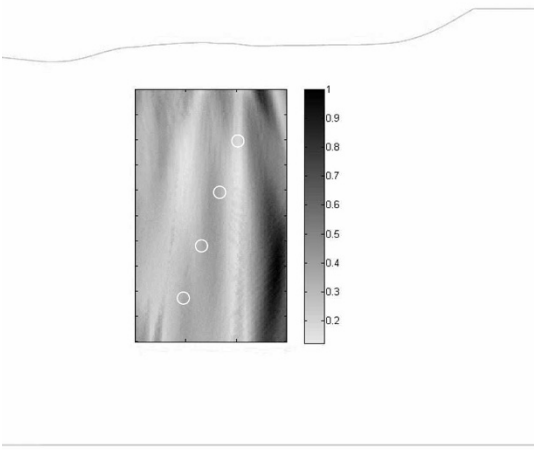

Fig. 8 Cartography of the (normalized) amplitude of the elastodynamic field inside the ROI (30×50 mm).

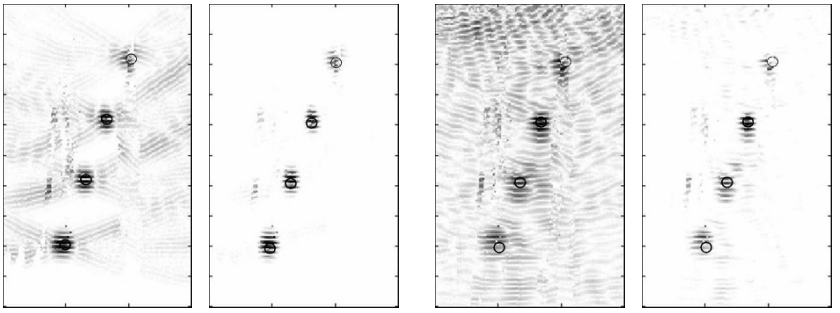

(a) Simulated data (b) Measured data

Fig. 9 Mapping of the estimators E_1 (left) and E_2 (right) in the third considered case, with both simulated (a) and measured (b) data.

The synthetic focusing algorithms have been tested in this unfavourable situation. The results obtained by reconstruction algorithms E_1 and E_2 with both simulated and measured data are reported in figure 9. The algorithms provide an accurate localization of the defects. We can also notice a SNR improvement by exploiting theoretical amplitudes (SNR = 7 dB and SNR = 17 dB respectively for E_1 and E_2). Nevertheless, some artefacts remain, which shows that with a perturbated US beam (in this case due to the complex specimen surface), the times of flight may not be efficiently evaluated in the areas where the field is the weakest.

4 Conclusion

In this paper, we describe reconstruction algorithms based on the synthetic focusing approach. Unlike the classical reconstruction techniques, the algorithms have been coupled to existing forward models, which allow to deal with complex parts. We have presented some examples of results obtained on simulated and experimental data, which show the ability of the reconstruction to localize echoes in parts presenting irregular surfaces. The algorithms can be applied on any array (or conventional) acquisition providing ultrasonic signals. Work in progress aims at accurately quantifying performances of the algorithms coupled to various operating modes of array inspection.

References

1. Calmon, P., Mahaut, S. , Chatillon, S., Raillon, R.: CIVA: an expertise platform for simulation and processing NDT data. Ultrasonics **44**, 975–979 (2006)
2. A collection of papers concerning CIVA can be found at http://www-civa.cea.fr
3. Seydel, J.A.: Ultrasonic synthetic aperture focusing techniques in NDT, Research Techniques in Nondestructive Testing, Vol. 6, R.S. Sharpe, Ed., New York Academic, 1983.
4. Holmes, C., Drinkwater, B.W., Wilcox, P.D.: Post-processing of the full matrix of ultrasonic transmit-receive array data for non-destructive evaluation. NDT&E International **38**, 701–711 (2005)
5. Porré, J., Mahaut, S., Chatillon, S., Calmon, P.: Simulation of phased array techniques and model based data reconstruction. Review of progress in QNDE **24**, 906–913 (2004)
6. Prada, C., Kerbrat, E., Cassereau, D., Fink, M.: Time reversal techniques in ultrasonic nondestructive testing of scattering media. Inverse Problems **18**, 1761–1773 (2002)
7. Lehman, S.K., Devaney, A. J.: Transmission mode time-reversal super-resolution imaging. J. Acoust. Soc. Am. **113**, 2742–2753 (2003)

Ultrasonic nonlinear parameter measurement: critical investigation of the instrumentation

L. Haumesser, J. Fortineau, D. Parenthoine, T. Goursolle, F. Vander Meulen

Abstract Identification methods of nonlinear parameters are developed to characterize solid materials and soft tissues. In the frame of classical parametric interaction methods, the parameter evaluation is based on the measurement of quantities related to the acoustic wave propagation medium. They appear at frequencies combinations and/or multiple harmonic of primary wave frequencies, and are generally weak in comparison to the amplitudes of the sources. Hence, the use of experimental devices excited at high amplitude levels is required. One problem in the identification of nonlinear parameters is that the ultrasonic device itself is not exempt of nonlinearity. Generally speaking the problem is to ensure, for each specific configuration, that the involved instrumentation (waveform generator, voltage amplifier, transducer), the coupling medium, mutual interactions between many sources…, do not perturb the evaluation of the investigated nonlinear effects.

1 Introduction

The measurement of nonlinearity by classical harmonic generation and parametric interaction methods [1-4] require to discern between nonlinearity whose craddle is the sample and spurious nonlinearity from the instrumentation. The approach has been used in nondestructive testing of soft tissues [5] and solid materials [6]. In Fig. 1, for both configurations, the influence of the nonlinearity originating from the experimental device has been calculated and compared to Second Harmonic Generation (SHG) from the primary wave at the source [7]. In the first case (Fig. 1a), the propagation medium is water, simulating tissue-like medium. The second case deals with aluminum (Fig. 1b). Pressure and velocity fields take into account

L. Haumesser, J. Fortineau, D. Parenthoine, T. Goursolle, F. Vander Meulen

Université François Rabelais de Tours, LUSSI CNRS ERL 3106 / INSERM U930, Ecole Nationale d'Ingénieurs du Val de Loire, rue de la Chocolaterie, BP3410, 41034 Blois Cedex, France
e-mail : lionel.haumesser@univ-tours.fr

attenuation effects and diffraction corrections for 0.5 and 1 inch diameter active elements, respectively. Both situations exhibit similar behaviour concerning the linear propagation of the spurious component at twice the fundamental frequency. It is different in the case of SHG which is less important in the heavy medium. It emerges from the comparison that spurious nonlinearity is a most affecting factor in the case of solid samples. Furthermore, the amount of nonlinearity from the device has to be controlled in order to obtain reliable results with regards to the sample under test.

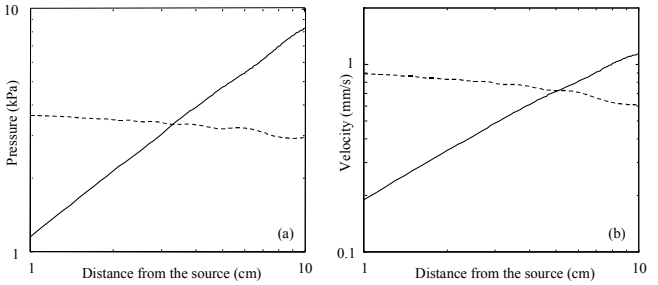

Fig. 1: (a) SHG from a 0.2 MPa field at 1 MHz in water (solid line) and linear propagation at double frequency for a 0.5% component of the primary field (dashed line), as a function of the distance from the source. (b) Similar calculations for an aluminum medium using a 0.2 m/s primary field.

Ultrasonic measurements in the linear regime, for non destructive testing, are tools which comply with industrial constraint. Dedicated devices, including transducers and electronic systems, are commercially available at typical frequencies within the 0.5MHz -10MHz range.

In the case of nonlinear acoustic methods, high excitation voltages are usually required to obtain nonlinear effects in the sample. The usual devices are no longer efficient and specific instrumentation has to be employed. It includes accessories originally manufactured for Radio Frequency (RF) (see e.g. www.arww-rfmicro.com) or amateur radio applications (see e.g. www.mfjenterprises.com) [4,8]. A main challenge is to obtain suitable characteristics, as for instance, low distortion factors. Up to now, nonlinear acoustic methods are less spread than linear ones, so that only a few high-power ultrasonic instruments are available (see e.g. www.ritecinc.com). Another difficulty to built acoustic systems with elements from other fields of application concerns the frequency range which is intermediate between the vibration field at low frequencies and the RF range which extends far beyond the ultrasonic frequency range.

Parametric interaction methods in solids have been used with bulk waves [1-4, 6, 8], and recently with Rayleigh [9] and Lamb [10,11] waves. Among the elements commonly used in the accompanying devices, the electric instruments, the transducer and coupling medium are possible sources of nonlinearity. For the harmonic generation and phase modulation setups [12,13], the main sources of spurious nonlinearity correspond to elements excited by high voltages and/or parts in the system, in which wave mixing can occur, affecting the quantity under interest

(transducers, electronics, coupling medium). Generally speaking, spurious nonlinearity from the device has many origins and is of various kinds.
In Sect. 2, the nonlinearity from the emitting part of devices is experimentally investigated. The results do not provide an exhaustive analysis of a particular setup, but rather a way to highlight and classify the effective sources of spurious harmonic signals. In support of this experimental study, a simplified analytical model of the source is presented in Sect. 3.

2 Nonlinearity in the instrumentation

2.1 Distorsion of the electric signal

A basic setup to reach a sufficient velocity field in an aluminum sample, such as to induce observable second order effects, is presented (Fig. 2a). A 1.8 MHz sinusoidal tone-burst generated by a HP 3314A waveform generator is sent into a 60dB ENI A150 power amplifier and applied to a wideband transducer (Videoscan Panametrics). Signals are obtained from an AR DC 2600A dual directional coupler inserted between a Ritec low pass filter whose cut-off frequency is 2 MHz, and the transducer. The forward signal applied to the transducer is the only one to be measured. The spectrum, measured for a 350mV excitation from the waveform generator, highlights a discrepancy of 40dB between fundamental (f) and second harmonic ($2f$) components (Fig. 2b). For amplitude levels up to 350mV, the amplification at f is constant (Fig. 2c). Fig. 2d shows that the transducer is also excited by a $2f$ component which approximately reaches 1V. The influence of this component is linked to the electromechanical conversion efficiency of the transducer at this frequency. By choosing it close to a mechanical antiresonance frequency, the second order radiation level in the sample can be minimized.

2.2 Cross modulation in a dual frequency transducer

A case of a multifrequency excitation is considered and the nonlinear component at combination of primary frequencies is investigated [14]. The dual frequency transducer (Figs. 3a-b) used is a prototype designed and made by the Dakel Czech company in the frame of the AERONEWS European FP7 project. Two piezoelectric elements, a ring and a disk with nominal frequencies of 2 MHz and 6 MHz respectively, are excited by separate electric channels in order to avoid cross interactions in the amplification stage. The transducer is loaded by a 75mm thick aluminum plate sample. The acoustic contact is ensured by a salt of phenylsalicilate (salol), which is a solid coupling medium. The displacement field at the sum frequency of the primary waves, is measured at the rear face of the sample along a line corresponding to a diameter of both emitting elements, using a Polytech OFV 505 laser interferometer (Fig. 3c).

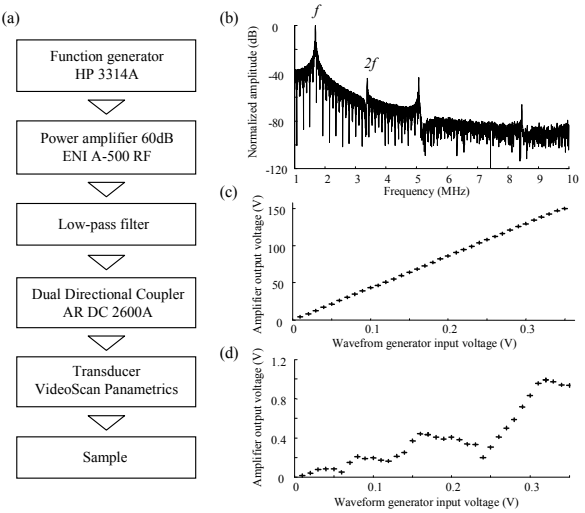

Fig. 2: Voltage applied to a loaded transducer. (a) Setup, (b) spectrum at 150V, (c) fundamental and (d) second harmonic components.

The experimental data are compared to calculations considering only cumulative nonlinear effects in the sample. The model deals with longitudinal waves and is based on the development of the radiated field from a piston like source, into a sum of Gaussian beams to depict diffraction phenomenon for both circular [15,16] and annular active elements [14]. The crucial input parameters for the model are the two averaged displacement fields at the radiating areas of the transducer. These quantities are the source terms needed for sum-frequency harmonic generation calculations; they are determined experimentally using a self-reciprocity calibration method based on measurements of the transducer input and the output voltage and current signals [4,13]. Only taking into account the sample nonlinearity, the theoretically field amplitude is found to be half of the measured one (Fig. 3c). This result shows that SHG in the sample is not sufficient to explain the measured values. Since electrical channels are separated, it highlights that a mixing between the High Frequency (HF) and the Low Frequency (LF) signals takes place in the transducer, possibly from close active elements mutual interactions, or/and in the coupling layer, the resulting component being propagated linearly across the sample.

2.3 Saturation in a commercial type transducer

Considering the classical SHG experiment [4], the wave auto-modulation during propagation in a homogeneous solid sample yields weak nonlinear effects. A highly linear device is required to ensure pure harmonic excitation at high voltage levels. It is shown in this section that the choice of a commercial type transducer is not suitable to this situation in order to evaluate the nonlinearity from the sample.

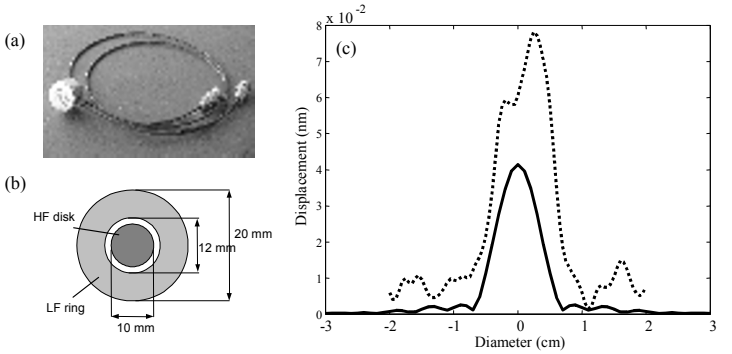

Fig. 3: (a) Dual frequency transducer (b) sketch of the PZT element dimensional characteristics (c) Sum frequency displacement field profile at the rear face of a 75mm thick aluminum plate (theoretical from the sample: solid line, experimental: doted line).

The experiment is conducted using a VideoScan Panametrics V109 broadband transducer [17]. It is excited at 5 MHz by a tone-burst with a number of periods fitted to the thickness of the sample to avoid interferences. 10, 15, 20, 30, 40, 45, 50 and 100 mm thick samples made of aluminum are used. Cross sectional areas of the plates are 200x200mm^2. The electrical signal is produced by a Ritec's RAM-5000. For each sample, the excitation amplitude is 400 Vpp. To lessen the second harmonic level produced by the excitation system, a high power low pass filter is inserted between the RAM-5000 and the transducer. All the electrical signals for the eight samples have been observed and no rate of harmonic distortion has been found above 0.5%.

Optical measurements are achieved at the rear surface of the sample. The amplitude of the particle velocity is strongly dependent on the position since the wavelength is smaller than the diameter of the radiating area. Thus, an accurate positioning of the probe is needed in order to properly evaluate the fundamental and second harmonic components on the acoustical axis.

The evolution with the distance of the amplitude of the fundamental component is reported in Fig. 4a. Source velocities are measured for each sample [4, 13] and used to obtain theoretical velocity evolutions on the acoustical axis. Since each measurement is made from a particular sample, the agreement between theory and measurements establishes a satisfying reproducibility in the manufacturing of the coupling between the transducer and the samples. The mean particle velocity corresponding to 400 Vpp at f is 0.19 m/s. It is used as input parameter in the model for the determination of the second harmonic generated in aluminum along a propagation path from 0 to 10 cm (solid line in Fig. 4b). The velocity amplitude at double frequency is equal to zero at the source. In the near field, SHG should be weak because of its cumulative nature, but a great amount of harmonic has been measured. The discrepancy observed between predicted and measured data is interpreted through the existence of a supplementary source at $2f$ coming from the apparatus and the coupling media (salol). Fitting its amplitude and summing both theoretical nonlinear contributions furnishes a curve displaying a clear correlation

with the measurements, both in near and far fields (dashed line). The double frequency component linearly propagated from the transducer enables to evaluate the velocity distortion rate at the transducer radiating area around 6%. This value is very high compared to the electrical harmonic distortion and can not be explained by the distortion within the electrical device. It is also more important than the maximum theoretical second harmonic distortion rate predicted by the model. It is therefore produced by the transducer and/or the contact. A possible reason is the presence in the transducer of an inductor to match the electric impedances of the piezoelectric disk and the coaxial cable. Standard commercially available inductors usually have ferrite cores which saturate under high power. After 10 cm of propagation through aluminum, the measured second harmonic distortion decreases to about 4.5%, and merges the value from the sample alone.

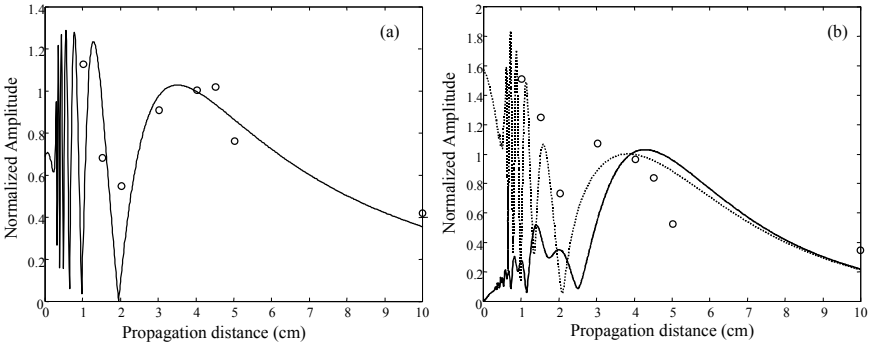

Fig. 4: On axis radiated velocity field as a function of distance from the transducer for an excitation voltage of 400 Vpp. (a) : theoretical (solid line) and experimental data (circles) at the fundamental frequency. (b) : theoretical SHG in the sample (solid line), SHG with an added component at double frequency linearly propagated (doted line) and experimental data (circles).

3 Analytical calculations

Works dealing with the modelling of the response of ultrasonic systems and electromechanical behavior of monoelement transducers have been conducted by Schmerr and Song for nondestructive testing purpose in the linear approximation [18]. Considering nonlinear effects in the system leads to a more challenging computational task since they are connected to the linear field knowledge that has to be quantified precisely [19]. Works are concerned with configurations giving possibility to measure the distorsion of PZT (Lead Zirconate Titanate) elements and depict theoretically their functionning [20].

In the following, simple calculations are proposed to support the observed experimental trend giving to spurious nonlinearity a proeminent role near the source. The 1-D model depicts the situation of a piezoelectric plate (medium 1) excited electrically and radiating in a semi infinite passive medium indexed 2. Governing

equations for the piezoelectric material along the coordinate z comprised into the interval [-a, 0], are [21-23]:

$$\rho_1 \frac{\partial^2 u_1}{\partial t^2} = \frac{\partial T_1}{\partial z}, \ \frac{\partial D}{\partial z} = 0 \tag{1.a-b}$$

and for $z > 0$, $\rho_2 \frac{\partial^2 u_2}{\partial t^2} = \frac{\partial T_2}{\partial z}$, (1.c)

where $T_1 = c_1 \frac{\partial u_1}{\partial z} + eE - \frac{q}{2} E^2 - lE \frac{\partial u_1}{\partial z} + \frac{m_1}{2} \left(\frac{\partial u_1}{\partial z} \right)^2$, (2.a)

$$D = \varepsilon E - e \frac{\partial u_1}{\partial z} + qE \frac{\partial u_1}{\partial z} + \frac{\varepsilon'}{2} E^2 + \frac{l}{2} \left(\frac{\partial u_1}{\partial z} \right)^2 \tag{2.b}$$

and $T_2 = c_2 \frac{\partial u_2}{\partial z} + \frac{m_2}{2} \left(\frac{\partial u_2}{\partial z} \right)^2$. (2.c)

In these expressions, ρ_i, T_i and u_i are respectively the density, the stress and the mechanical displacement in the medium i, E the electrical field and D the electrical displacement in medium 1. c_i and m_i are the second and third order elasticity constants, e and l the second and third order piezoelectric constants, ε and ε' the second and third order permittivity constants and q the electrostriction constant. The problem is solved by the successive approximation method for the displacement field, assuming u_i written as follow:

$u_i = u_i^0 + u_i^1$ with $u_i^1 << u_i^0$

The reader is referred to [22] for the derivation of the solution u_i^0. In our problem, the following boundary conditions are used: zero stress at $z = -a$, stress and displacement continuity at $z = 0$, time harmonic voltage V applied across the thickness a : $\int_{-a}^{0} E^0 dz = V$. The quantity u_i^0 can be used to express source terms in wave equations, thus leading to:

$$\rho_1 \frac{\partial^2 u_1^1}{\partial t^2} - c_1^D \frac{\partial^2 u_1^1}{\partial z^2} = \Gamma \frac{\partial}{\partial z}\left(\frac{\partial u_1^0}{\partial z}\right)^2 - \Lambda D^0 \frac{\partial^2 u_1^0}{\partial z^2} \tag{3.a}$$

$$\text{and } \rho_2 \frac{\partial^2 u_2^1}{\partial t^2} - c_2 \frac{\partial^2 u_2^1}{\partial z^2} = \frac{m_2}{2} \frac{\partial}{\partial z}\left(\frac{\partial u_2^0}{\partial z}\right)^2 \tag{3.b}$$

where Γ and Λ are effective third order constants of the piezoelectric plate and $c_1^D = c_1 + e^2/\varepsilon$ [23]. Superscripts 0 and 1 refer to second and third order quantities, respectively. Hence, solutions can be chosen as:

$$u_1^1(z,t) = (Az + C)e^{2j(\omega t - k_1 z)} + (Bz + X)e^{2j(\omega t + k_1 z)} + Ye^{j(2\omega t - k_1 z)} + Fe^{j(2\omega t + k_1 z)} \quad \text{for } -a < z < 0 \tag{4.a}$$

$$\text{and } u_2^1(z,t) = (Gz + H)e^{2j(\omega t - k_2 z)} \text{ for } z > 0 \tag{4.b}$$

A, *B, Y, F* and *G* are calculated from wave equations (3). *C*, *X* and *H* are found with boundary conditions similar to those used in the linear case, except for the external source which becomes: $\int_{-a}^{0} E^1 dz = 0$.

The computations are conducted for a 500Vpp excitation voltage at 5MHz applied to a plate of thickness a = 0.56 mm and a cross sectional area equal to 20 mm^2. The following non zero parameters are used in the computations: ρ_1 = 7780 kg.m^{-3}, c_1=245(1+0.003j) GPa, $\varepsilon = 247\varepsilon_0$ (ε_0 : permittivity in vacuum), e = 1.3 C.m^{-2}, m_1 = -50000 GPa, q = 86.10^{-10} F.m^{-1}, ρ_2 = 2700 kg.m^{-3}, c_2 = 107 GPa, m_2= -749 GPa. The evolution of the nonlinear velocity fields in the aluminum medium are displayed in Fig.5. At the interface (z = 0), SHG in the piezoelectric element leads to a transmitted value equal to 0.4 mm.s^{-1}. It is linearly propagated in the aluminum and its influence decreases with an increasing travel length. The source velocity amplitude at 5MHz is 50.5dB higher than this spurious component. In the sample, SHG from the source is shown to rapidly become the main origin of the nonlinear component. However, the influence of the spurious components is not negligible 10 cm away from the source.

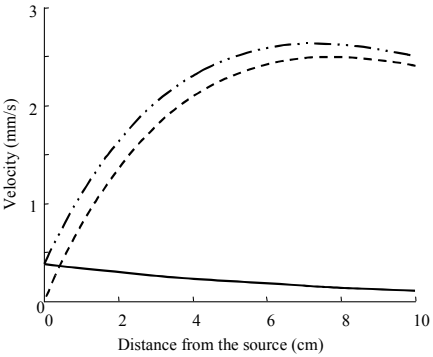

Fig. 5: 1-D calculations of the second order velocity field in an aluminum semi-infinite medium as a function of the propagation distance, for a 500Vpp excitation voltage at 5MHz. SHG in the medium (dashed line), linear propagation at double frequency (solid line) and their sum (dashed-doted line).

Finally, calculations confirm that the spurious nonlinearity induced by the behaviour of the piezoelectric element is significant close to the source. It can be noted that the level is found to be below the maximum of SHG in the sample. In the case of experimental results in Fig.4, the spurious nonlinearity is of the order of SHG in the sample. The difference indicates that the active element is not the only origin of nonlinearity in a commercial type transducer such as the one used in section 2.3.

4 Concluding remarks

The few situations presented in this work deal with the nonlinearity in parametric interaction devices. Among commonly found elements in the devices, the investigations concern the electronics and the emitting transducers. It emerges from this work that spurious nonlinearity can contribute to the measurements or even overwhelm weak nonlinear effects from the sample, especially in the near field of the source. A straight choice to minimize spurious nonlinearity is to use elements in the device, which exhibit highly linear behavior under high excitation voltages [2,4,6,8]. In this way, results can be satisfying but the choice of elements is limited due to the very specific needed instrumentation and also to the application: e.g. $LiNbO_3$ (Lithium Niobate) piezoelectric elements have on one side very low distorsion factor and on the other side long transient response not suitable for thin samples. Authors have proposed electrical and mechanical improvements to reinforce wave generation efficiency. Impedance matching networks can be used to favour power transmission between the amplifier and the electroactive element. Concerning the coupling medium between the transducer and the sample and the efficiency of the electromechanical conversion, a recent paper describes a direct

way for nonlinear Rayleigh wave excitation without the use of a polymeric wedge [24]. It offers the advantage to reduce the excitation voltages needed to reach the quadratic regime range (below 60Vpp in [24]), giving back the opportunity to use commercial PZT-based transducers.

Acknowledgments Authors thank Pr. O. Bou Matar, Pr. L. P. Tran Huu Hue and Dr. S. Dos Santos for very valuable discussions and comments about the topics developed in this paper. M. Veselsky from DAKEL is also greatly acknowledged. This work was supported by the EC Sixth Framework Program AERONEWS: Specific Targeted Research FP6-502927 (http://www.kulak.be/AERONEWS).

References

1. L. K. Zarembo, V. A. Krasilnikov 1971 Nonlinear phenomena in the propagation of elastic waves in solids. Sov. Phys. Uspekhi 13, 778-797.
2. M. A. Breazeale, J. Philip, Physical Acoustics. 1984 Principle and methods : Determination of third-order elastic constants from ultrasonic harmonic generation measurements. vol. XVIII, Academic Press, Orlando.
3. P. Li, W. P. Winfree, W. T. Yost, J. H. Cantrell. 1983 Observation of collinear beam-mixing by an amplitude modulated ultrasonic wave in a solid. IEEE Ultra. Symp. 1152-1156.
4. G.E. Dace, R.B. Thompson, and O. Buck. 1991 Measurement of the acoustic harmonic generation for materials characterization using contact transducers. Rev. Prog. QNDE 11 1685-1692.
5. M. Rielly, V. Humphrey, F. Duck. 2000 Theoretical and experimental investigation of nonlinear ultrasound propagation through tissue mimicking fluids. IEEE Ultra. Symp. 1355-1358.
6. W. T. Yost, J. H. Cantrell, J. K. Na. 2001 Nonlinear ultrasonic pulsed measurements and applications to metal processing and fatigue. Rev. Prog. QNDE 20, AIP.
7. F. Vander Meulen, L. Haumesser. 2008 Evaluation of B/A nonlinear parameter using an acoustic self-calibrated pulse-echo method. Appl. Phys. Lett. 92, 214106.
8. W. T. Yost, J. H. Cantrell. 1999 Calibration techniques for electronic-based systems used in measurement of nonlinearity parameters. Rev. Prog. QNDE 18, 2345-2351.
9. J. Herrmann, J.-Y. Kim, L. J. Jacobs, J. Qu, J. W. Littles, M. F. Savage. 2006 Assessment of material damage in a nickel-base superalloy using nonlinear Rayleigh surface waves. J. Appl. Phys. 99, 124913.
10. C. Bermes, J.-Y. Kim, J. Qu, L. J. Jacobs. 2007 Experimental characterization of material nonlinearity using Lamb waves. Appl. Phys. Lett. 90, 021901.
11. M. Deng, P. Wang, X. Lv. 2005 Experimental verification of cumulative growth effect of second harmonics of Lamb wave propagation in an elastic plate. Appl. Phys. Lett. 86, 124104.
12. X. Jacob, C. Barrière, D. Royer. 2003 Acoustic nonlinearity parameter measurements in solids using the collinear mixing of elastic waves. Appl. Phys. Lett. 82 (6), 886-888.
13. M. Vila, F. Vander Meulen, S. Dos Santos, L. Haumesser , O. Bou Matar. 2004 Contact phase modulation method for acoustic nonlinear parameter measurement in solid. Ultrasonics 42, 1061-1065.
14. J. Fortineau, F. Vander Meulen, L. Haumesser. 2007 Experimental method for the nonlinear behaviour evaluation of an ultrasonic dual frequency transducer. ICU proceedings, session S01, paper 1331, Vienna.
15. Wen J.J. and Breazeale M.A. 1988 A diffraction beam field expressed as the superposition of Gaussian beams. J. Acoust. Soc. Am. 83, 1752-1756.
16. Bou Matar O., Vila M., Vander Meulen F., Rossignol C., Lethiecq M. 2001 Experimental and Numerical Study of the Insert-Substitution Method: Application to the Measurement of the Nonlinear Parameter of Solids. IEEE Ultra. Symp. 709-713.

17. J. Fortineau, F. Vander Meulen, T. Goursolle, L. Haumesser. 2006 Experimental Study of the Non Linearity from Ultrasonic Transducers. IEEE Ultra. Symp. 1786-1789.
18. L. W. Schmerr Jr., S.-J. Song. 2007 Ultrasonic nondestructive evaluation systems: models and measurements. ed. Springer New-York.
19. G. Sebald, L. Lebrun, D. Guyomar. 2005 Modeling of elastic nonlinearties in ferroelectric materials including nonlinear losses: application to nonlinear resonance mode of relaxors single crystals. IEEE Trans. Ultra. Ferroelec. Freq. Contr., 52 (4), 596-603.
20. A. Albareda, R. Perez, J. L. Villar, E. Minguella and J. A. Gorri. 1997 Intermodulation measurement of nonlinearities in piezoelectric resonators. Rev. Sci. Instrum. 68 (8) 3143-3149.
21. M. Planat. 1984 Propagation nonlinéaire des ondes acoustiques dans les solides. Thèse de doctorat, Université de Franche-Comté.
22. D. Royer, E. Dieulesaint Ondes élastiques dans les solides. 1996 T. 2, ed. Masson, Paris.
23. W. Jiang, S. Zhou, X. Li, Y. Shui. 1994 Second harmonic generation in piezoelectric resonators. IEEE Ultra. Symp. 969-972.
24. G. Shui, J.-Y. Kim, J. Qu, Y.-S. Wang, L. Jacobs. 2008 A new technique for measuring the acoustic nonlinearity of materials using Rayleigh waves. NDT&E Int. 41 (5), 326-329.

Investigation of damage mechanisms of composite materials: Multivariable analysis based on temporal and wavelet features extracted from acoustic emission signals

A. Marec, J.H. Thomas, R. El Guerjouma, R. Berbaoui

Abstract A procedure for the investigation of damage development and time-to-failure mechanisms within composite materials based on the analysis of the signals of acoustic emission (AE) is presented. An unsupervised automatic classification is proposed for the clustering of the monitored AE events in order to identify the different damage mechanisms and the most critical damage sources in composite materials. Thus, pattern recognition analyses (fuzzy C-means clustering) associated with a principal component analysis are used for the classification. A cluster analysis of AE data is achieved and the resulting clusters are correlated to the damage mechanisms of the material under investigation. After being validated on model samples composed of unidirectional fiber-matrix composites, this method is applied to actual composites such as polymer concretes. Furthermore, AE signals generated by heterogeneous materials are not stationary. Thus, time-scale methods (continuous and discrete wavelet transforms) are used to determine new relevant descriptors to be introduced in the classification process in order to improve the characterization and the discrimination of the damage mechanisms. They provide a better discrimination of damage mechanisms of composite materials such as cross-ply composites than some time-based descriptors.

A. Marec, R. El Guerjouma

LAUM, CNRS, Université du Maine, Av. O. Messiaen, 72085 Le Mans, France, e-mail: anne.marec.etu@univ-lemans.fr

J.H. Thomas

ENSIM, CNRS, Université du Maine, Rue Aristote, 72085 Le Mans, France, e-mail: jean-hugh.thomas@univ-lemans.fr

R. Berbaoui

IUT, Université du Maine, Av. O. Messiaen, 72085 Le Mans, France, e-mail: rachid.berbaoui.etu@univ-lemans.fr

1 Introduction

Fiber/matrix and polymer concrete composite materials are extensively used in industry. However, their damage and time-to-failure mechanisms still require a better understanding. Acoustic Emission (AE), which represents the generation of transient ultrasonic waves in a material under load, is a useful tool for non destructive testing [1]. It is used in this paper to identify the most critical damage mechanisms occurring in these materials in order to estimate their remaining lifetime in a non-destructive way. One of the main issues is to discriminate the different types of source mechanisms from the detected AE signals which are characterized by multiple relevant descriptors. Most studies so far have used AE descriptors such as the amplitude and the energy of the signal to characterize the development of damage [2,3]. In order to improve these analyses, it is possible to consider all descriptors with multivariable data analyses [4]. Thus, each AE signal is associated to a pattern composed of multiple descriptors. In the feature space, the patterns can be divided into clusters representative of damage mechanisms according to their similarity by the use of pattern recognition algorithms. In order to improve the classification for complex composite materials, fuzzy C-means clustering [5] associated with a principal component analysis (PCA) [6] are proposed in this paper. The fuzzy C-means clustering method is an effective unsupervised algorithm for automatic clustering and separation of AE events based on multiple features extracted from the random AE waveforms. The PCA is first used to give an idea of the relevance of the descriptors. If the representation in the projection space shows several clusters with a minimum overlap between them, the features could lead to classify the damage mechanisms. The clustering data obtained with the fuzzy C-means are also visualized in the projection space given by the PCA. The proposed method, applied on a model unidirectional fiber/matrix composite material and a more complex material such as polymer concrete, leads to the identification of the damage mechanisms and their evolution with time till the sample failure.

However AE signals in composite materials mainly result from the energy release of failure modes and are usually not stationary. Thus, waveform processing of AE signals based on time-scale [7] or time-frequency analysis appears as a very promising signal processing technique to discriminate fracture mechanisms. Some previous works have shown that continuous and discrete wavelet transforms can provide relevant information from AE signals to discriminate the damage types [8,9]. This point has been investigated in [9] and it has been shown that it is possible to use both wavelet transforms in order to define new relevant time-scale descriptors to improve the characterization of damage mechanisms. In this paper, classification results obtained with time-scale descriptors are applied on another composite materials: cross-ply composites. A comparison with the classification results obtained with temporal descriptors on the same test confirms the improvement of the discrimination with the use of time-scale descriptors.

2 Materials and experimental procedure

The experimental work is carried out on glass fiber reinforced polymer composite materials. Model composite materials are studied: unidirectional composites with fiber reinforcement at ±45° to the loading direction. Complex composite materials are also studied: cross-ply composites noted $[\pm 90°]_8$ consist of 8 layers of unidirectional reinforcement at ±0° and ±90° to the loading direction. These composite materials samples are in parallelepiped form and have dimensions 10×150×2 mm^3. Polymer concrete samples are also studied. They consist of a combination of 30% of polymer resin, 30% of gravel and 40% of fine sand. They are in parallelepiped form with the dimensions 40×160×15 mm^3.

An external load applied to the composite materials results in several damage mechanisms occurring at a microscopic scale. Some damage mechanisms are predominant depending on the composite materials and the fibre orientation in comparison with the loading direction. In this study, fiber/matrix composite materials are damaged with static tensile tests. Concrete samples and cross-ply composites are damaged with three-point static bending tests. Experiments are performed at room temperature using a servo-hydraulic Instron universal testing machine with a 5 kN capacity. The crosshead speed of the machine is fixed at 0.05 mm/min.

Simultaneously, transient ultrasonic waves generated by damage occurrence and propagation within the materials were recorded using two channel AE data acquisition system of Euro Physical Acoustics company (EPA) (see Fig. 1). AE is used to discriminate the different damage mechanisms and permits real-time monitoring of damage growth by the analysis of these generated ultrasonic waves. AE measurements are achieved by using two piezoelectric sensors with a frequency range 100kHz - 1MHz, coupled on the faces of the specimens with silicon grease. To eliminate background noise, we included an amplitude threshold of 35dB, where 0dB corresponds to 1µV. The data acquisition system is used to record AE data such as temporal descriptors and waveforms of each AE signal with a sampling rate of 5MHz and 40dB pre-amplification.

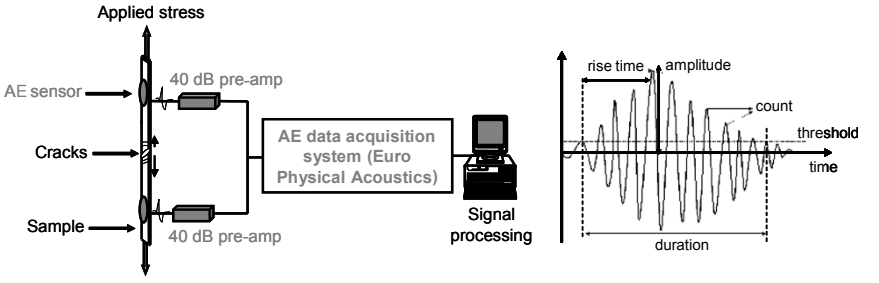

Fig. 1. Composite sample under load with AE monitoring. Typical AE waveform and its descriptors calculated by the acquisition system for each AE event.

Several time-based descriptors are calculated by the acquisition system for each AE event (see Fig. 1): maximum amplitude, energy, duration, rise time, number of peaks whose amplitudes are higher than the given amplitude threshold (called counts), etc. These collected features as well as new time-scale descriptors computed by wavelet analysis are used as input parameters in the proposed classification method.

3 Multivariable data clustering

Multivariable analyses provide a data classification. Similarities are found between data clusters in a multidimensional space with the use of several features. Applied to AE, these methods enable to identify, within multiple parameters, signal clusters with similar features and thus characterizing the same source damages in a material.

The parameters collected from AE waveforms are the components of an input pattern vector. Each component provides information from the AE signals such as the amplitude of the signal, its energy, etc. To make this study as general as possible we used an unsupervised pattern recognition analysis: the fuzzy C-means clustering method (FCM) [4,5]. It uses fuzzy partitioning so that each pattern vector can belong to all clusters with different membership grades between 0 and 1. The input parameter of the algorithm is the number of clusters. Each cluster resulting from the classification corresponds to a different damage mechanism identified in the material. In order to associate each output cluster of the algorithm to the corresponding damage mechanism, the distributions of the principal features such as amplitude are computed. The distributions of the features of each obtained cluster are compared to other results found in the bibliography relative to characteristics of damage types of composite materials [2,3,8,10]. Thus, we can associate each resulting cluster to the corresponding damage type.

Then, a principal component analysis is applied on the matrix composed of the parameters collected from AE waveforms. PCA is mathematically defined as an orthogonal linear transformation that transforms the data to a new coordinate system so that the greatest variance by any projection of the data comes to lie on the first coordinate (called the first principal component), the second greatest variance on the second coordinate, and so on. PCA is theoretically the optimum transform for a given data in least square terms. Thus, PCA can be used for dimensionality reduction in a data set by retaining the characteristics of the data set that contribute most to its variance. The PCA projection shows the distribution of the data. If the data do not overlap, an automatic classification should be possible. Thus, we can deduce the most relevant descriptors to be used in the clustering. The PCA shows that the temporal descriptors can separate the damage mechanisms. In addition, once the automatic classification is realized with the fuzzy C-means clustering

method, we use the PCA to visualize the clusters of data into a two-dimension subspace.

The fuzzy C-means clustering method requires the knowledge of damage mechanisms in the materials as each cluster corresponds to a different damage mechanism. This method has been validated on well-known unidirectional fibre composite materials and provides fair results even for more complex materials such as cross-ply composites or SMC [9]. This method enables to identify and monitor in real time several damage mechanisms at the microscopic scale.

4 Results

4.2 Damage characterization of 45° unidirectional fiber/matrix composite materials

The composite materials described in this part are unidirectional composites with fiber reinforcement at ±45° to the loading direction. They are experimented under static tensile tests. Different damage mechanisms have been identified on these composite materials from their AE signals [2,10]: matrix cracking and interfacial debonding (see table 1). Figure 2 presents the amplitude histograms of the recorded AE hits (2131 AE hits) and shows two distinct area: one centered around 45dB and the other one around 70dB.

The multivariable analysis is applied in order to discriminate the damage mechanisms according to their AE signals. The fuzzy C-means clustering method is applied with two clusters that correspond to the two mechanisms. The five descriptors used are the energy, the amplitude, the rise time, the counts and the duration of the signals. A PCA is achieved in order to visualize the results in a two-dimension subspace (see Fig. 3a). Two clusters corresponding to matrix cracking and interfacial debonding damage mechanisms have been well identified. This unsupervised clustering method also shows the time dependency of the different damage types in the material (see Fig. 3b). This visualization shows that the matrix cracking is the most important damage mechanism as it begins from the start of the tests and involves much more numerous events than the other mecanism does (it involves 85% of AE events). The interfacial debonding appears at the end of the experiments and their number increases during the tests (15% of AE events). The clustering process shows some good results and presents two advantages: a multivariable analysis and an unsupervised clustering. Several features can be used together in a single multidimensional analysis and no labelled signal

data base in terms of damage mechanism is required a priori for clustering (unsupervised method).

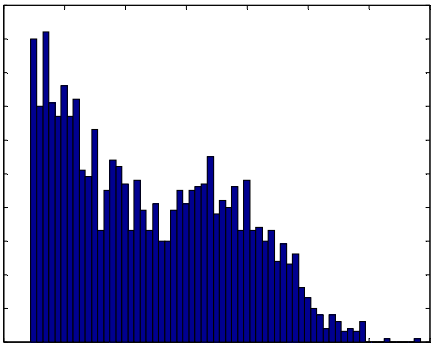

Fig. 2. Static tensile test on 45° unidirectional fiber/matrix composite material: Amplitude histograms of AE hits.

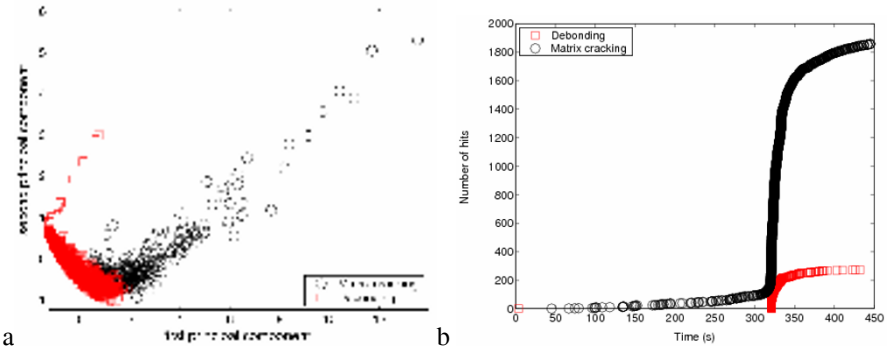

a b

Fig. 3. Static tensile test on 45° unidirectional fiber/matrix composite material: (a) PCA visualization of the fuzzy C-means clustering (90% information kept). (b) Time dependency of the identified damage types.

4.2 Damage characterization of polymer concrete materials

Three-point static bending tests are applied on polymer concrete materials. AE activity increases with the evolution of applied stress during the experiment and becomes very important near the failure of the material (see Fig. 4).

Multivariable AE data analysis enables to identify three clusters corresponding to three damage mechanisms identified in this material (see Fig. 5a). The main characteristics of those identified signals are presented in table 1. Their principal features are similar to those observed in fiber/matrix composite materials. Figure

5b presents the time dependency of the different damage types. Matrix crackings and interfacial debondings appear from the start of the experiment and their number increases till the failure of the material. Gravel failures appear only at the end of the experiment and lead to the final failure. 90% of AE signals correspond to matrix cracking signals, 9% correspond to gravel/resin debonding and 1% are referring to gravel failure signals.

Table 1. Principal characteristics of AE hits identified as matrix cracking and interfacial debonding signals on fiber/matrix composite and polymer concrete materials.

Composite material	Damage mechanism	Amplitude	Rise time	Energy	Duration
Fiber/matrix composite	Matrix cracking	35-55 dB	>0.04 ms	$<10^3$ J	≈0.2 ms
	Interfacial debonding	60-80 dB	<0.01 ms	$>10^4$ J	≈0.05 ms
Polymer concrete	Matrix cracking	35-60 dB	>0.04 ms	$<10^3$ J	<0.2 ms
	Interfacial debonding	50-90 dB	<0.02 ms	$>10^4$ J	0.2-0.4 ms
	Gravel failure	95-100 dB	<0.03 ms	$>10^6$ J	≈0.1 ms

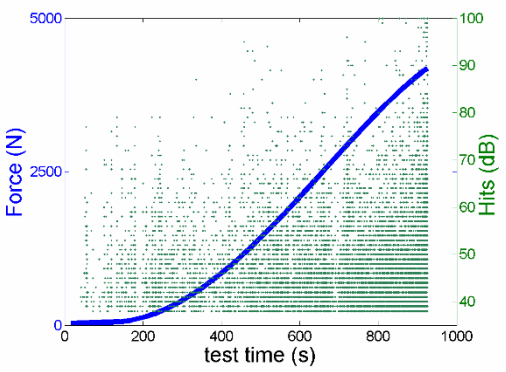

Fig. 4. Load over time of three-point static bending test and amplitude distribution of AE hits of polymer concretes.

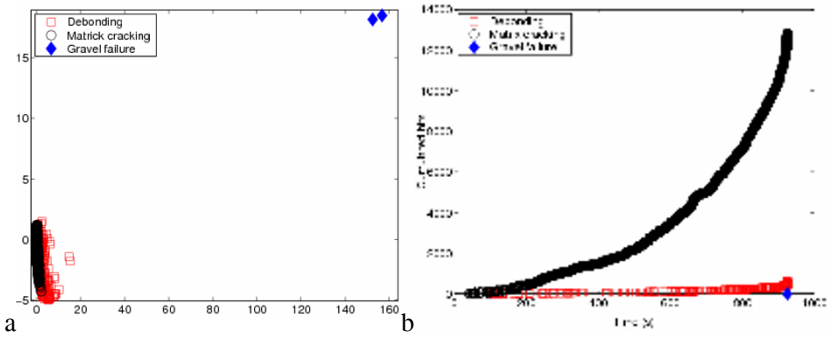

Fig. 5. Polymer concretes : (a) PCA visualization of the fuzzy C-means clustering (91% information kept). (b) Time dependency of the identified damage types.

The identified damage mechanisms are highlighted in figure 6 with post-test micrograph and photography of the failure area.

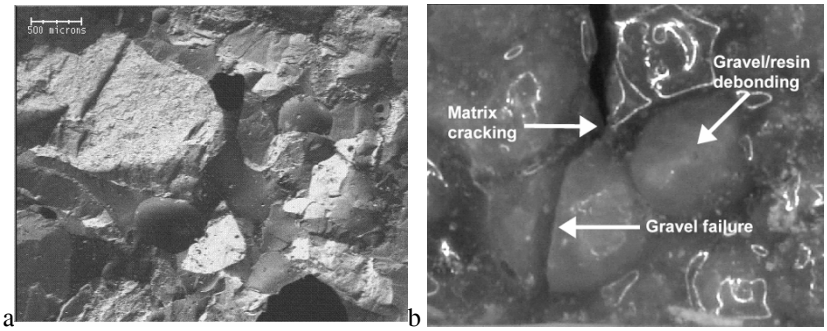

Fig. 6. (a) Post-test SEM (Scanning Electronic Microscope) micrograph of polymer concrete sample. (b) Post-test optical photography of matrix cracking, gravel failure and gravel/resin interfacial debonding.

4.3 Wavelet analysis of AE data

4.3.1 Time-scale analysis of AE data of composite materials

AE source identification of composite materials is usually based on temporal features of AE waveforms. However, AE signals generated within local displacements inside materials (microcracks, etc) are generally not stationary. That is why wavelet transforms are applied in order to identify the different damage mechanisms as, in addition, the temporal descriptors are not always relevant. The two types of wavelet transforms: continuous and discrete are well adapted to our problem [7,9] and are used to extract quantitative descriptors in order to improve the discrimination of damage mechanisms within composite materials.

The continuous wavelet transform (CWT) of a signal f(t) is defined as follows [7]:

$$CW_f(a,b) = \frac{1}{\sqrt{a}} \int_{-\infty}^{+\infty} f(t)\psi^*\left(\frac{t-b}{a}\right)dt, \quad (1)$$

with the scale parameter a, the time translation factor b, the analyzing wavelet ψ and * represents the complex conjugation.

The discrete wavelet transform (DWT), which enables to decompose each signal on a wavelet basis, is defined as [7]:

$$DWT_f(j,k) = \int_{-\infty}^{+\infty} f(t)\psi^*_{j,k}(t)dt, \qquad \psi_{j,k}(t) = 2^{-j/2}\psi(2^{-j}t - k), \tag{2}$$

with the scale parameter j, the time translation factor k, the analyzing wavelet ψ and the analyzed signal f(t). The DWT decomposes f(t) on a wavelet basis referring to different continuous frequency bands, called wavelet levels [7]. The original signal passes through two complementary filters and two signals are obtained, corresponding to the approximation and detail coefficients. The approximations are the high scale, low frequency components of the signal in the band $\left[0 \quad \frac{f_e}{2^{j+1}}\right]$. The details are the low scale, high frequency components in the band $\left[\frac{f_e}{2^{j+1}} \quad \frac{f_e}{2^j}\right]$. f_e denotes the sampling frequency and j is the level of decomposition.

These two wavelet transforms are used to extract new time-scale descriptors based on the moduli of CWT and DWT coefficients corresponding to the most energetic scales. More details about the definition and the validation of these new features can be found in a previous study [9]. The first feature extracted from the CWT is the sum of the square moduli of CWT coefficients defined as [9]:

$$f_1(a, I_b) = \sum_b |CW_f(a,b)|^2, b \in I_b. \tag{3}$$

The second feature is the maximum of the square moduli of CWT coefficients [9]:

$$f_2(a, I_b) = \max |CW_f(a,b)|^2, b \in I_b. \tag{4}$$

f_1 and f_2 are calculated for each scale on a limited time duration I_b. This duration is set from an adaptive threshold which corresponds to a percentage (10%) of the maximum amplitude of the wavelet coefficients. The duration of the AE signal I_b corresponds to the time during which the amplitude of the wavelet coefficients goes beyond the threshold. Then the features corresponding to the most energetic scale are selected as new descriptors.

The DWT could also provide new relevant descriptors to add in the clustering analysis. Thus, an another feature is defined: the maximum of the square detail coefficients for each level of decomposition. This new descriptor is defined as follows [9]:

$$f_3(j) = \max_k (DWT_f(j,k)^2), \quad (5)$$

with $DWT_f(j,k)$ detail wavelet coefficients of each level of decomposition j. This descriptor f_3 is calculated for the levels of decomposition with the most significant amplitudes.

4.3.2 Clustering of fiber/matrix composite materials

The analysis is applied to AE events collected from a static three-point bending test on an actual material as cross-ply composite material. Two damage mechanisms, matrix cracking and interfacial debonding are identified on AE events. The typical characteristics of AE hits representative of damage mechanisms are presented in table 1.

FCM is applied with two clusters corresponding to the two damage types. The traditional temporal AE features are first used to build patterns (see Fig. 1). A PCA is achieved in order to visualize the results in a two-dimension subspace (see Fig. 7a). The PCA projection shows that two clusters are well identified but some patterns of the two different clusters are mixed with each other. Thus, with the temporal descriptors, the separation between the patterns is not effective in this area. In order to improve the clustering, new relevant descriptors defined from wavelet analyses are used to build patterns used for the automatic classification.

The PCA visualization of the clustering obtained on the same AE data set but with time-scale feature are presented in figure 7b. The damage mechanisms are well identified in the material. Indeed, the PCA projection highlights the similarities between the patterns. In addition, there is no overlap between the patterns belonging to each cluster with these time-scale descriptors. Thus, the data classificiation and the identification of the different damage mechanisms are improved.

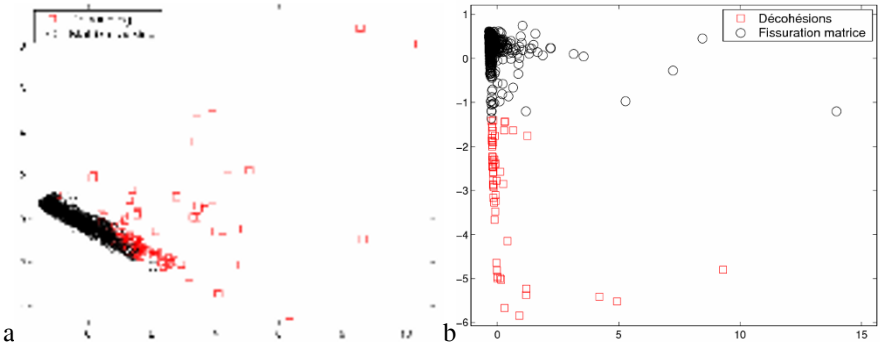

Fig. 7. PCA visualization of the fuzzy C-means clustering of three-point bending test on cross-ply composite material : (a) with temporal descriptors (90% information kept). (b) with time-scale descriptors (94% information kept).

5. Conclusion

Fuzzy C-means clustering method has been coupled with a principal component analysis to discriminate the different damage mechanisms from the AE signals and to visualize the division into classes. Clustering, applied with the typical temporal descriptors of AE waveforms, permits to identify the different damage mechanisms in model and complex composite materials. Wavelet analyses applied to transient AE signals permits to define new relevant time-scale descriptors. The use of these new descriptors in the clustering method improves the identification of damage mechanisms of complex composite materials. This method also leads to highlight the time evolution of damage types in these materials till the final failure. Thus, the most critical damage sources in a composite material can be identified. The identification of damage sources with time could permit to estimate the remaining life time of composite materials.

References

1. K. Ono, "Acoustic emission", *Encyclopedia of acoustics*, Wiley (1997)
2. M. Giordano, A. Calabro, C. Esposito, A. Lizza, A. D'amore, L. Nicolais, "An acoustic emission characterization of the failure modes in polymer composite materials", *Comp. Sci. and Techn*. 58, 1923-28 (1997)
3. S. Barre, M.-L. Benzeggagh, "On the use of acoustic emission to investigate damage mechanisms in glass-fiber reinforced Polypropylene", *Comp. Sci. and Techn*. 52, 369–376 (1994)
4. B. Dubuisson, "Diagnostic, intelligence artificielle et reconnaissance des formes", *Hermès Sci. Pub.* (2001)
5. J.C. Bezdek, "Pattern recognition with fuzzy objective function algortithms", *Plenum Press*, New-York (1981)
6. I.T. Jolliffe, "Principal Component Analysis", *Springer-Verlag* (1986)
7. S. Mallat, "A wavelet tour of signal processing", *New York: Academic Press* (1998)
8. T.H. Loutas, V. Kostopoulos, C. Ramirez-Jimenez, M. Pharaoh, "Damage evolution in center-holed glass/polyester composites...", *Comp. Sci. and Techn*. 66 1366–1375 (2006)
9. A. Marec, J.-H. Thomas, R. El Guerjouma, "Damage characterization of polymer-based composite materials: Multivariable analysis and wavelet transform for clustering acoustic emission data", *Mechanical Systems and Signal Processing,* In press (2008)
10. N. Godin, S. Huguet, R. Gaertner, "Integration of the Kohonen's self-organising map and k-means algorithm for the segmentation of the AE data collected during tensile tests on cross-ply composites", *NDT&E International* 38, 299–309 (2005)

Propagation of elastic waves in a fluid-loaded anisotropic functionally graded waveguide: Application to ultrasound characterization of cortical bone

Cécile Baron and Salah Naili

Abstract Non-destructive evaluation of heterogeneous materials is of major interest not only in industrial but also in biomedical fields. In this work, the studied structure is a three-layered one: a laterally heterogeneous anisotropic solid layer is sandwiched between two acoustic fluids. An original method is proposed to solve the wave equation in such a structure without using a multilayered model for the plate. This method is based on an analytical solution, the matricant, explicitly expressed under the Peano expansion form. We validate this approach for the study of a fluid-loaded anisotropic plane waveguide with two different fluids on each side. This configuration corresponds to the axial transmission technique to the ultrasound characterization of cortical bone *in vivo*.

1 Introduction

A lot of natural media have unidirectional varying elastic properties. The mantel crust, the oceans and cortical bone are some of these functionally graded media. Scientists focused on the advantages presented by this type of materials in terms of mechanical behavior and since the 80's, they developed industrial Functionally Graded Materials (FGM) particularly exploited in high-technology and biomedical

Cécile Baron
Laboratoire de Mécanique Physique, UMR CNRS 7052, B2OA
Faculté des Sciences et Technologie, Université Paris 12 – Val de Marne
61, Avenue du Général de Gaulle, 94010 Créteil cedex, FRANCE
e-mail: cecile.baron@univ-paris12.fr

Salah Naili
Laboratoire de Mécanique Physique, UMR CNRS 70 52, B2OA
Faculté des Sciences et Technologie, Université Paris 12 – Val de Marne
61, Avenue du Général de Gaulle, 94010 Créteil cedex, FRANCE
e-mail: naili@univ-paris12.fr

applications. Consequently, the non-destructive evaluation of these materials is a key issue. Surface and guided waves play a major role in non-destructive testing and evaluation of complex structures. Several studies are dedicated to the leaky Lamb wave propagation in fluid-loaded plates [4, 5, 6]. In all these studies, the media are homogeneous or multilayered. In this work, we introduce a general method to take into account the continuous property variation in an anisotropic waveguide. This method is based on the knowledge of an analytical solution of the wave equation, the matricant, explicitly expressed *via* the Peano series. To the best of our knowledge, this is the first method to evaluate the mechanical behavior of a fluid-loaded anisotropic waveguide with continuously varying properties without modelling the FGM plate as a multilayered plate.

In this work, we first present the method and its setup with fluid-structure interaction; then we proceed to the validation of the method by comparing our results to the dispersion curves obtained from classical schemes on homogeneous waveguides (isotropic and anisotropic). Two advantages of the method are underlined: i) an asymmetric fluid-loading may be taken into account without modifying the scheme for the numerical solution; ii) the influence of the property gradient on the mechanical behavior of the waveguide may be investigated. Finally, we get onto the relevancy of this model applied to the ultrasound characterization of cortical bone by the axial transmission technique.

2 General formulation of the problem

We consider an elastic parallel plate waveguide of thickness d sandwiched between two perfect fluids f_1 and f_2, of respective mass densities ρ_{f_1} and ρ_{f_2}, and, of respective velocities c_{f_1} and c_{f_2}. The interfaces between the fluids and the plate are infinite planes parallel to the $(\mathbf{x}_1, \mathbf{x}_2)$-plane. Therefore, we assume that the structure is two-dimensional and that the guided waves travel in the plane $x_2 = 0$ (see Fig. 1); in the following parts, this coordinate is implicit and is omitted in the mathematical expressions.

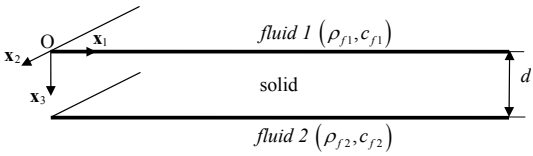

Fig. 1 Geometrical configuration of the waveguide.

The elastic plate is supposed to be anisotropic and is liable to present continuously varying properties along its thickness ($\mathbf{x}_3$-axis). These mechanical properties are represented by the elasticity tensor $\mathbb{C} = \mathbb{C}(x_3)$ and the mass density $\rho = \rho(x_3)$.

2.1 System equations

2.1.1 The wave equation in the fluid f_n (for $n = 1$ or 2)

In the fluid f_n, the characteristic equations are written as:

$$\begin{cases} -\dfrac{\partial p^{(n)}}{\partial x_j} = \rho_{f_n} \dfrac{\partial^2 u_j^{(n)}}{\partial t^2}, \\ p^{(n)} = K_{f_n} \mathtt{div}\, \mathbf{u}^{(\mathbf{n})}, \end{cases} \tag{1}$$

where $\mathbf{u}^{(n)}$ and $p^{(n)}$ respectively represent the displacement vector and the pressure in the fluid f_n; its compressibility and velocity are respectively K_{f_n} and $c_{f_n} = \sqrt{K_{f_n}/\rho_{f_n}}$. The operator $\mathtt{div}$ is the divergence.

The solutions of the system (1) for the fluid f_n are sought under the form:

$$\mathbf{f}_n(x_1, x_2; t) = \mathbf{A}_n(x_3) \exp \imath(k_1 x_1 + k_3^{(n)} x_3 - \omega t), \tag{2}$$

where k_1 is the wavenumber along the $\mathbf{x}_1$-axis, $k_3^{(n)}$ is the wavenumber along the $\mathbf{x}_3$-axis in the fluid f_n and ω is the angular frequency.

We consider an incident wave reaching the plate at an angle θ_1 from the $\mathbf{x}_3$-axis in the fluid f_1. The incident displacement-field is defined in the following form, assuming that its amplitude is normalized:

$$\mathbf{u}_I^{(1)} = \begin{pmatrix} \sin\theta_1 \\ 0 \\ \cos\theta_1 \end{pmatrix} \exp \imath(k_1 x_1 + k_3^{(1)} x_3 - \omega t), \tag{3}$$

with $\sin\theta_1 = k_1 c_{f_1}/\omega$ and $\cos\theta_1 = k_3^{(1)} c_{f_1}/\omega$. From this, the expression of the reflected displacement-field $\mathbf{u}_R^{(1)}$ in f_1 and of the transmitted displacement-field $\mathbf{u}_T^{(2)}$ in f_2 are deduced:

$$\begin{aligned} \mathbf{u}_R^{(1)} &= R \begin{pmatrix} \sin\theta_1 \\ 0 \\ -\cos\theta_1 \end{pmatrix} \exp \imath(k_1 x_1 - k_3^{(1)} x_3 - \omega t), \\ \mathbf{u}_T^{(2)} &= T \frac{c_{f_2}}{c_{f_1}} \begin{pmatrix} \sin\theta_1 \\ 0 \\ \cos\theta_1 \end{pmatrix} \exp \imath(k_1 x_1 + k_3^{(2)} x_3 - \omega t). \end{aligned} \tag{4}$$

The incident, reflected and transmitted pressure fields, respectively noted $p_I^{(1)}$, $p_R^{(1)}$ and $p_T^{(2)}$ are deduced from the expressions (3) and (4) and the second equation of the system (1).

2.1.2 The wave equation in the plate waveguide

The body forces in the solid plate are neglected. The momentum conservation equation associated with the constitutive law of linear elasticity (Hooke's law) gives the following equations:

$$\begin{cases} \dfrac{\partial \sigma_{ij}}{\partial x_j} = \rho \dfrac{\partial^2 u_i}{\partial t^2}, \\ \sigma_{ij} = \dfrac{1}{2} C_{ijk\ell} \left(\dfrac{\partial u_k}{\partial x_\ell} + \dfrac{\partial u_\ell}{\partial x_k} \right) \end{cases} \tag{5}$$

where u_i (for $i = 1, ..., 3$) and σ_{ij} (for $i, j = 1, ..., 3$) respectively represent the components of the displacement-field $\mathbf{u}$ and of the stress σ. The solutions are sought for the vectors of displacement $\mathbf{u}$ and traction σ_{i3} (for $i = 1, ..., 3$) (assumed to be harmonic in time t and space along the $\mathbf{x}_1$-axis) under the form:

$$\mathbf{f}(x_1, x_3; t) = \mathbf{A}(x_3) \exp \imath (k_1 x_1 - \omega t), \tag{6}$$

2.1.3 Fluid-loading interface conditions

The conditions at both interfaces $x_3 = 0$ and $x_3 = d$ are the continuity of the normal displacement and the one of the normal stresses. We consider that the fluids f_1 and f_2 are perfect, consequently, the shear stresses are zero at the interfaces ($\sigma_{13}(x_1, 0; t) = \sigma_{13}(x_1, d; t) = 0$ and $\sigma_{23}(x_1, 0; t) = \sigma_{23}(x_1, d; t) = 0$). The following relations are obtained:

$$\begin{cases} u_3(x_1, 0; t) = u_3^{(1)}(x_1, 0; t), \quad u_3(x_1, d;\, t) = u_3^{(2)}(x_1, d; t), \\ \sigma_{33}(x_1, 0; t) = -p^{(1)}(x_1, 0; t), \quad \sigma_{33}(x_1, d; t) = -p^{(2)}(x_1, d; t). \end{cases} \tag{7}$$

2.2 A closed-form solution: the matricant

Introducing the expression (6) in the equation (5), we obtain the wave equation under the form of a second-order differential equation with non-constant coefficients. For particular forms of geometrical profiles, this equation has analytical solutions expressed with special functions (Bessel or Hankel functions) [18]. But in the general case, there is no analytical solution to the problem thus formulated. The most current methods to solve the wave equation in unidirectionally heterogeneous media are derived from the Thomson-Haskell method [9, 17]. These methods are appropriate for multilayered media [10, 11, 12, 19]. But, for continuously varying media, these techniques mean to replace the continuous profiles of properties by step-wise functions. Thereby the studied problem becomes an approximate one, even before the resolution step; the accuracy of the solution as its validity domain are hard to evaluate. Moreover, the multilayered model of the waveguide creates some "virtual"

interfaces likely to induce artefacts. In order to deal with the exact problem, that is to keep the continuity of the properties variation, the wave equation is re-written under the form of an ordinary differential equations system with non-constant coefficients for which an analytical solution exists: the matricant [1].

We consider that the plate is orthotropic which allow to decouple the P-SV (Pressure - Shear Vertical) waves, polarized in the propagation plane $(\mathbf{x}_1,\mathbf{x}_3)$ and the SH (Shear Horizontal) waves polarized along $\mathbf{x}_2$-axis. The incident media f_1 is a perfect fluid, only the P-SV waves travel in the plate. Applying a spatio-temporal Fourier transform on (x_1,t) of the displacement field (noted $\hat{\mathbf{u}}(k_1,x_3;\omega)$) and on the traction field (noted $\hat{\sigma}_{i3}(k_1,x_3;\omega)$ for $i=1,...,3$), the wave equation becomes a matrix system expressed using the Thomson-Haskell parametrization of the Stroh formalism [16] and the Voigt notation ($C_{ijk\ell}$ for $i,j,k,\ell=1,...,3$ is replaced by c_{IJ} for $I,J=1,...,6$):

$$\frac{d}{dx_3}\eta(x_3)=\imath\omega\mathbf{Q}(x_3)\eta(x_3), \tag{8}$$

that is

$$\frac{d}{dx_3}\begin{pmatrix}\imath\omega\hat{u}_1\\ \imath\omega\hat{u}_3\\ \hat{\sigma}_{13}\\ \hat{\sigma}_{33}\end{pmatrix}= \tag{9}$$

$$\imath\omega\begin{pmatrix}0 & s_1 & 1/c_{55}(x_3) & 0\\ -c_{13}(x_3)/c_{33}(x_3)s_1 & 0 & 0 & 1/c_{33}(x_3)\\ \rho(x_3)-s_1^2\zeta(x_3) & 0 & 0 & -c_{13}(x_3)/c_{33}(x_3)s_1\\ 0 & \rho(x_3) & -s_1 & 0\end{pmatrix}\begin{pmatrix}\imath\omega\hat{u}_1\\ \imath\omega\hat{u}_3\\ \hat{\sigma}_{13}\\ \hat{\sigma}_{33}\end{pmatrix},$$

with the relations:

$$\zeta(x_3)=c_{11}(x_3)-\frac{c_{13}^2(x_3)}{c_{33}(x_3)},\quad k_1=\omega s_1, \tag{10}$$

where s_1 is the x_1-component of the slowness. The matrix $\mathbf{Q}$ includes all the information about the heterogeneity of the waveguide because it is expressed from the plate mechanical properties $(\rho(x_3),\mathbb{C}(x_3))$ and from two acoustical parameters (s_1,ω). The wave equation thus formulated has an analytical solution expressed between a reference point $(x_1,0,x_3^0)$ and some point of the plate $(x_1,0,x_3)$ in the propagation plane. This solution is called the matricant and is explicitly written under the form of the Peano series expansion:

$$\mathbf{M}(x_3,x_3^0)=\mathbf{I}+(\imath\omega)\int_{x_3^0}^{x_3}\mathbf{Q}(\xi)d\xi+(\imath\omega)^2\int_{x_3^0}^{x_3}\mathbf{Q}(\xi)\Big(\int_{x_3^0}^{\xi}\mathbf{Q}(\xi_1)d\xi_1\Big)d\xi+..., \tag{11}$$

where $\mathbf{I}$ is the identity matrix of dimension $(4,4)$. We underline that the $\imath\omega$-factorization leads up to a polynomial form of the matricant. The $\imath\omega$-polynomial coefficients are matrices independent of ω.

Using the propagator property of the matricant through the plate thickness, the state-vector (defined in (9)) at the second interface $\eta(d)$ is evaluated from the state-vector at the first interface $\eta(0)$ as follows:

$$\eta(d) = \mathbf{M}(d,0)\eta(0). \tag{12}$$

The fluid-structure interaction is taken into account *via* the interface conditions (7) used after a spatio-temporal Fourier transform on (x_1,t). The condition to obtain a non-trivial solution to the equation (12) leads to the following relation:

$$\imath\omega\hat{u}_1(k_1,0;\omega)\times M_{13} + \imath\omega\hat{u}_3(k_1,0;\omega)\times M_{32} + \hat{\sigma}_{33}(k_1,0;\omega)\times M_{34} = 0, \tag{13}$$

where M_{ij} (for $i,j = 1,...,4$) represent the components of the matrix $\mathbf{M}$. The displacement component $\hat{u}_1(k_1,0;\omega)$ can be expressed as a linear combination of $\hat{u}_3(k_1,0;\omega)$ and $\hat{\sigma}_{33}(k_1,0;\omega)$ and thus the system (12) of dimension 4 is reduced to a matrix system of dimension 2:

$$\eta(d) = \begin{pmatrix} P_1 & P_2 \\ P_3 & P_4 \end{pmatrix} \eta(0), \qquad \text{where } \eta(x_3) = \begin{pmatrix} \imath\omega\hat{u}_3 \\ \hat{\sigma}_{33} \end{pmatrix}. \tag{14}$$

with the relations:

$$\begin{aligned} P_1 &= M_{22} - M_{21}\frac{M_{32}}{M_{31}}, \quad P_2 = M_{24} - M_{21}\frac{M_{34}}{M_{31}}, \\ P_3 &= M_{42} - M_{41}\frac{M_{32}}{M_{31}}, \quad P_4 = M_{44} - M_{11}\frac{M_{34}}{M_{31}}. \end{aligned} \tag{15}$$

The interface conditions (7) are transformed in the Fourier domain (k_1,ω). The expressions of the displacement and the pressure in the fluids, so that the one of the displacement and traction fields in the solid plate (14), are substituted in the transformed interface conditions. We obtain the following matrix equation:

$$\begin{pmatrix} \imath\omega s_3^{(1)} c_{f_1} & 1 & 0 & 0 \\ -\imath\omega\rho_{f_1} c_{f_1} & 0 & 1 & 0 \\ 0 & P_1 & P_2 & -\imath\omega s_3^{(2)} c_{f_2} \exp(\imath\omega s_3^{(2)} d) \\ 0 & P_3 & P_4 & -\imath\omega\rho_{f_2} c_{f_2} \exp(\imath\omega s_3^{(2)} d) \end{pmatrix} \begin{pmatrix} R \\ \alpha_1 \\ \alpha_2 \\ T \end{pmatrix} = \begin{pmatrix} \imath\omega s_3^{(1)} c_{f_1} \\ \imath\omega\rho_{f_1} c_{f_1} \\ 0 \\ 0 \end{pmatrix}, \tag{16}$$

where $\mathbf{s}^{(n)} = \mathbf{k}^{(n)}/\omega$ is the slowness-vector in the fluid f_n ($n = 1$ or 2); the quantities α_1 and α_2 are respectively the amplitudes of the displacement-field and of the traction-field in the waveguide at the interface $x_3 = 0$. We deduce the analytical expressions of the complex reflection and transmission coefficients ($\hat{R}(s_1,x_3;t)$ and $\hat{T}(s_1,x_3;t)$ respectively):

$$\hat{R} = \frac{(P_3 - P_1 Z_2 + P_4 Z_1 - P_2 Z_1 Z_2)}{(P_3 - P_1 Z_2 - P_4 Z_1 + P_2 Z_1 Z_2)},$$
$$\hat{T} = \frac{-2Z_2(\rho_{f_1} c_{f_1}/\rho_{f_2} c_{f_2})(P_1 P_4 - P_2 P_3)}{(P_3 - P_1 Z_2 - P_4 Z_1 + P_2 Z_1 Z_2)} \exp(-\imath\omega s_3^{(2)} d), \tag{17}$$

with $Z_n = \rho_{f_n}/\sqrt{1/c_{f_n}^2 - s_1^2}$ (for $n = 1$ or 2).

3 Validation

The aim of this sub-section is to check that the Peano expansion of the matricant is well-adapted to study fluid-loaded waveguides. We take into account the fluid-structure interaction in different configurations of homogeneous plates comparing the results obtained from the numerical implementation of the Peano expansion of the matricant to results taken from the literature.

The numerical evaluation of P_1, P_2, P_3 and P_4 requires us to truncate the Peano series and to numerically calculate the integrals. Thus, the error can be estimated and controlled [1]. We retained 70 terms in the series and evaluate the integrals over 100 points using the Simpson's rule (fourth-order integration method). The expressions (17) give the frequency spectrum (modulus and phase) of the reflection coefficient for different incidences (s_1 varies from zero – normal incidence – to $1/c_{f_1}$ corresponding to the critical incidence in the fluid f_1). A lot of works detailed the relationship between the poles and the zeroes of the reflection coefficient and the leaky Lamb waves dispersion curves [5, 6].

The results of sub-section 3.1 compare the dispersion curves obtained by seeking the poles of the reflection coefficient (17) and the results taken from the literature or from closed-form solution.

3.1 Validation for a homogeneous and isotropic or anisotropic fluid-loaded plate

The method is tested by plotting the dispersion curves (variation of the phase velocity *versus* frequency-thickness product) for an isotropic aluminium plate immersed in water. The data in the paper of [5] is used. The results obtained (not shown) by the present method are in perfect agreement with the results presented by them [5].

Taking into account the anisotropy does not change the scheme for the numerical solution of wave equation with the matricant. We consider a transverse isotropic plate immersed in water. For that configuration, [14] developed a method to obtain an analytical solution. By using the data from this paper, the results obtained (not shown) with the present method are in perfect agreement with theirs.

3.2 Asymmetric loading and heterogeneous waveguide

The formalism presented here to solve the wave equation in an unidirectionally graded medium presents two main advantages: without changing the scheme to obtain the numerical solution we can take into account i) an asymmetric loading and ii) the unidirectional continuous heterogeneity.

3.2.1 Isotropic homogeneous plate and asymmetric loading $(f_1 \neq f_2)$

The mechanical behavior of the plate is different for symmetric and asymmetric loadings. For example, in the symmetric loading case, there is a unique critical frequency and a unique phase velocity value v_φ in the plate, which corresponds to the propagation velocity in the fluid $(v_\varphi = c_{f_1} = c_{f_2})$, for which the displacements and the stresses at the interfaces are quasi-null; whereas in the asymmetric loading $(f_1 \neq f_2)$, there are two critical frequencies and two values of the phase velocity in the plate for which the structure does not respond [7]. The validation is done on an isotropic aluminium plate with the following properties: $\rho = 2.79$ g.cm^{-3} ; the longitudinal and transverse waves velocities are respectively $v_L = 6.38$ mm.μs^{-1} and $v_T = 3.10$ mm.μs^{-1}. The characteristic properties of the fluid f_1 correspond to those of water: $\rho_{f_1} = 1$ g.cm^{-3} and $c_{f_1} = 1.485$ mm.μs^{-1}; the characteristic properties of the fluid f_2 correspond to glycerine: $\rho_{f_2} = 1.26$ g.cm^{-3} and $c_{f_2} = 1.920$ mm.μs^{-1}. This configuration is the same as the one studied by [8]. The modulus of the reflection coefficient *versus* the incident angle is plotted in the Fig. 2 for a fixed frequency-thickness product ($f \times d = 4.7$ MHz.mm).

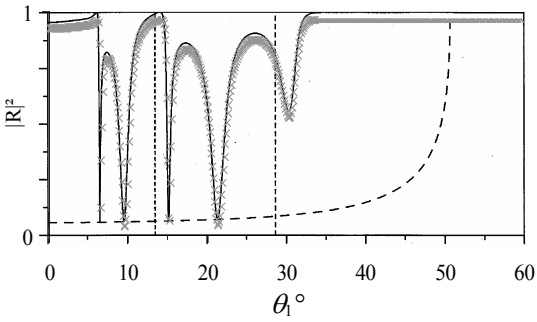

Fig. 2 Reflection coefficient modulus for an asymmetrically fluid-loaded aluminium plate (water and glycerine) *versus* incident angle: in dark lines results published in [8], in grey crosses the reflection coefficient modulus calculated from (17). The vertical lines (dashed) represent the two critical angles for longitudinal waves and transverse waves. The dashed curve correspond to the resonant amplitudes [8].

This figure shows the perfect agreement between our results and the ones presented by [8].

3.2.2 Influence of the property gradient on the frequency spectrum of the reflection coefficient

The main characteristic of the formalism developed in this study is the possibility to take into account a continuous variation of the mechanical properties of a structure along one space direction (here, it is the thickness of the waveguide). The influence of a linear gradient of properties (corresponding to a 10%-increase of the porosity and a 10%-decrease of the propagation velocities) in a transverse isotropic bone plate immersed in water is investigated. Its properties are reported in Tab. 1.

Table 1 Elastic properties of transverse isotropic bone plate with linearly varying properties along the $\mathbf{x}_3$-axis between the planes $x_3 = 0$ and $x_3 = d$.

	ρ (g.cm^{-3})	C_{11} (GPa)	$C_{22} = C_{33}$ (GPa)	$C_{13} = C_{12}$ (GPa)	C_{44} (GPa)	$C_{55} = C_{66}$ (GPa)
$x_3 = 0$	1.9	30.04	24.6	10	6.16	9.2
$x_3 = d$	1.81	23.18	18.98	7.72	4.75	7.1

The frequency spectrum of the reflection coefficient is plotted in Fig. 3 for an incidence close to the critical incidence of longitudinal waves in the plate, which corresponds to the formation of the wave called lateral wave [3] ($\theta_1 \sim 21.93$ degrees (thin grey line and black circles) and $\theta_1 \sim 23.08$ degrees (thin black line)).

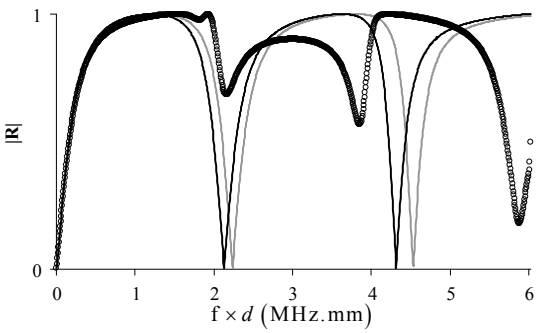

Fig. 3 Frequency spectrum of the reflection coefficient modulus for a homogeneous plate whose properties are those at $x_3 = 0$ (grey line), for a homogeneous plate whose properties are the average of the properties through the plate thickness (black line) and for a linearly varying plate (empty circles).

This figure shows evidence that the behavior of the reflection coefficient modulus is sensibly the same for frequencies between 0 and 1.8 MHz. Beyond this value, the behavior is clearly different.

4 Perspectives

From this study, the transient response of a fluid-loaded plate is considered. The frequency spectrum of the reflection coefficient is calculated for incidences between the normal and critical incidences for compression waves in the fluid f_1. Thus, the plate transfer function is calculated in the Fourier domain (x_1-wavenumber, frequency): $\hat{R}(k_1, x_3; \omega)$. A double inverse Fourier transform on (k_1, ω) is applied on $\hat{R}(k_1, x_3; \omega)$ to transform into the space-time domain; the temporal signals can be obtained at different points along the propagation $\mathbf{x}_3$-axis: $R(x_1, x_3; t)$.

Lastly, the formalism presented here is well-adapted to deal with wave propagation in anisotropic tubes with radial property gradients [15]. The wave equation keeps the same form as (8), the state vector is expressed from the displacement and traction components in the cylindrical basis and the matrix $\mathbf{Q}$ depends on the radial position r ($\mathbf{Q} = \mathbf{Q}(r)$). In cylindrical homogeneous structures, to take into account an anisotropy more important than transverse isotropy is fussy because there is no analytical solution to the "classical" wave equation (second-order differential equation). The Stroh's formalism (hamiltonian formulation of the wave equation) [16], upon which the Peano expansion of the matricant is based, is a promising alternative solution which allows to consider altogether the geometry (cylinder), the anisotropy and the heterogeneity (radial property gradients) of a medium.

4.1 Relevancy of the method for ultrasound characterization of cortical bone by axial transmission technique

Several studies of demonstrated the heterogeneous nature of the cortical bone, particularly they show evidence the gradual variation of the volumetric porosity (ratio between pores and total volume) across the cortical thickness. Yet, the porosity is intrinsically linked to the macroscopic mechanical behavior of the cortical bone [2]. Therefore, the continuous variation of porosity induces a continuous variation of material properties. Taking into account the gradient should prove itself to be essential in the context of diagnosis and therapeutic monitoring of osteoporosis. Indeed, the gradient characterization would allow to assess geometrical (cortex thickness) and material (elastic coefficients variation) information, which are fundamental parameters to evaluate the bone fragility. For several years, the quantitative ultrasonography (by axial and transverse transmissions) proved itself to be an alternative hopeful technique to evaluate the fracture risk [13]. However, the inter-individual and inter-site variations of bone mechanical properties make the standardization of the protocol of fracture risk evaluation by ultrasound very delicate. In this context, the characterization of a relative variation of mechanical properties in the plate thickness may turn out to be relevant to carry out a "standardized" estimation of bone strength. The axial transmission technique is specially dedicated to the ultrasound characterization of the cortical bone, which represents 80% of the bone mass in hu-

man skeleton, in bone pathologies diagnosis. The corresponding configuration may be modelled by a cortical bone plate with varying properties in the thickness and sandwiched between two different fluids, soft tissues and marrow. According to the results presented in this study, the signals recorded by axial transmission technique, corresponding to the waves reflected by the plate and travelling into the fluid (soft tissues), are sensitive to the gradient (see Fig. 3) and may be exploited to its characterization, then to evaluate the bone fragility. To do so, a parametric study must be carried out to determine which ultrasound parameters, accessible by the axial transmission technique, are the most representative of the property gradients (which modes, at which frequencies ?). When the gradient will be characterized, the second step will be to elaborate a standardized and reliable protocol to evaluate the bone strength by ultrasound measurements in preparation for a clinical application.

References

1. C. Baron. *Le développement en série de Peano du matricant pour l'étude de la propagation d'ondes en milieux continûment variables*. PhD thesis, Universit Bordeaux 1, France, 2005.
2. C. Baron, M. Talmant, and P. Laugier. Effect of porosity on effective diagonal stiffness coefficients (c_{ii}) and anisotropy of cortical at 1 MHz: A finite-difference time domain study. *Journal of Acoustical Society of America*, 122:1810–1817, 2007.
3. E. Camus, M. Talmant, G. Berger, and P. Laugier. Analysis of the axial transmission technique for the assessment of skeletal status. *Journal of the Acoustical Society of America*, 108(6):3058–3065, 2000.
4. D. E. Chimenti and A. H. Nayfeh. Ultrasonic Reflection and Guided Waves in Fluid-Coupled Composite Laminates. *Journal of Nondestructive Evluation*, 9:51–69, 1990.
5. D. E. Chimenti and S.I. Rokhlin. Relationship between leaky Lamb modes and reflection coefficient zeroes for a fluid-coupled elastic layer. *Journal of Acoustical Society of America*, 88:1603–1611, 1990.
6. M. Deschamps and O. Poncelet. Transient Lamb waves: Comparison between theory and experiment. *Journal of Acoustical Society of America*, 107:3120–3129, 2000.
7. J. Dickey, G Maidanik, and H. Uberall. The splitting of dispersion curves for the fluid-loaded plate. *Journal of Acoustical Society of America*, 98:2365–2367, 1995.
8. H. Franklin, E. Danila, and J.-M. Conoir. S-matrix theory applied to acoustic scattering by asymmetrically fluid-loaded elastic isotropic plates. *Journal of Acoustical Society of America*, 110:243–253, 2001.
9. N. A. Haskell. The dispersion of surface waves on multilayered media. *Bulletin of the Seismological Society of America*, 43:377–393, 1953.
10. B. Hosten and M. Castaings. Surface impedance matrices to model the propagation in multilayered media. *Ultrasonics*, 41:501–507, 2003.
11. E. G. Kenneth. A propagator matrix method for periodically stratified media. *Journal of Acoustical Society of America*, 73(1):137–142, 1982.
12. D. Lvesque and L. Pich. A robust transfer matrix simulation for ultrasonic response of multilayered absorbing media. *Journal of Acoustical Society of America*, 92(1):452–467, 1992.
13. F. Marin, J. Gonzales-Macias, A. Diez-Perez, S. Palma, and M. Delgado-Rodriguez. Relationship Between Bone Quantitative Ultrasound and Fractures: a Meta-Analysis. *Journal of Bone and Mineral Research*, 21:1126–1135, 2006.
14. A. H. Nayfeh and D. E. Chimenti. Free Wave Propagation in Plates of General Anisotropic Media. *Journal of Applied Mechanics*, 56:881–886, 1989.

15. A.L. Shuvalov. A sextic formalism for three-dimensional elastodynamics of cylindrically anisotropic radially inhomogeneous materials. *Proceedings of the Royal Society of London A.*, 459:1611–1639, 2003.
16. A. N. Stroh. Steady state problems in anisotropic elasticity. *Journal of Mathematics and Physics*, 41:77–103, 1962.
17. W. T. Thomson. Transmission of elastic waves through a stratified solid medium. *Journal of Applied Physics*, 21:89–93, 1950.
18. V. Vlasie-Belloncle and M. Rousseau. Effect of a velocity gradient on the guided modes of a structure. In *Proceedings of the 5th World Congress on Ultrasonics*, Paris, 7-10 Septembre 2003.
19. L. Wang and S. I. Rokhlin. Stable reformulation of transfer matrix method for wave propagation in layered anisotropic media. *Ultrasonics*, 39:413–424, 2001.

Coherent wave propagation in solids containing spatially varying distributions of finite-size cracks

C. Aristégui, M. Caleap, O. Poncelet, A. L. Shuvalov, Y. C. Angel

Abstract Multiple scattering results usually concern uniform distributions of scatterers. In this work, we evaluate the propagation of SH coherent waves through a non-uniform distribution of parallel flat cracks. The spatial variation of distribution is taken into account via replacing a heterogeneous medium by a stack of effective homogenous layers. Propagation in each layer is governed by the effective acoustic impedance and the effective wave number, which are derived by considering cracks as finite-size scatterers. On this basis, the reflection and transmission coefficients due to non-uniformly distributed scatterers are calculated by using the transfer matrix method. Effect of the distribution profiles is also investigated.

1 Introduction

During last several decades, much work has been done on studying the effective behaviour of heterogeneous media, such as bubbly liquids, fibber-reinforced or/and multi-cracked composite materials. A number of dynamic models has been developed for describing phase velocity and attenuation of coherent elastic plane waves propagating in those media [2, 6, 8, 10].

We focus on shear-horizontal (SH) coherent wave propagation in a damaged medium. The energy loss is assumed to be due to the multiple scattering by the cracks (discontinuous phase) randomly distributed in the lossless host matrix. Significance of this study lies in considering the spatial variation of the crack density. This aspect is taken into account by replacing heterogeneous media by stacks of effective homogenous layers. Each layer is viewed as having uniform distribution with effective bulk parameters. The reflection and transmission responses of such

C. Aristégui, M. Caleap, O. Poncelet, A. L. Shuvalov
Université de Bordeaux, CNRS, UMR 5469, Laboratoire de Mécanique Physique, Talence, F-33405, France, email : c.aristegui@lmp.u-bordeaux1.fr
Y .C. Angel
University of Lyon, Lyon, F-69003, France; University Lyon 1, Lyon, F-69003, France; INSERM, U556, Therapeutic Applications of Ultrasound Laboratory, Lyon, F-69424, France

non-uniform distribution of scatterers concentration are evaluated by using the transfer matrix method. Two approximations of the effective attenuation are also proposed.

2 Effective field parameters for uniform concentration of scatterers

Consider a linearly elastic and isotropic medium containing a random and uniform distribution of identical cracks. They are assumed to be parallel and infinite along the axis $\boldsymbol{y}_2$. Their cross section is constant in the (y_1, y_3) plane. Flat (ribbon-shaped) cracks are regarded as discontinuity lines of width $2a$ [1, 7]. The crack faces are stress-free. The number of cracks per unit area (density) is denoted by η.

An incident monochromatic SH plane wave propagates along the axis $\boldsymbol{y}_3$, normally to the crack faces. Its propagation in the lossless crack-free matrix is governed by the wavenumber $k = \omega / c_T$, where ω is the angular frequency and c_T the phase velocity of SH wave in the matrix.

It is well known that, in presence of multiple scatterers, the coherent plane wave propagation in the two-phase (damaged) medium is described by a complex-valued wavenumber K. The dissipation is assumed to be induced only by the multiple scattering, i.e. the anelastic attenuation is not taken into account. For the axes adopted, the coherent wave is represented by the displacement components.

$$u_1 = u_3 = 0\,,\, u_2 = A\mathrm{e}^{\mathrm{i}(Ky_3 - \omega t)}\,, \tag{1}$$

where A is an amplitude factor and K is the effective wavenumber, which can be related to k in terms of the single-crack scattering amplitudes f. For brevity, the time-factor $\mathrm{e}^{-\mathrm{i}\omega t}$ is omitted in the following. In contrast to the previous works, the cracks are considered here as parallel finite-size scatterers and no longer as line-like scatterers [4]. By writing boundary conditions for the average exciting field on each finite-size crack, Angel and Koba derived a formula for K [2], which can be expressed in terms of the scattering amplitude f, defined in Ref. [5], as follows

$$K^2 = k^2 \left(1 - \eta \frac{4\pi}{k^2} f(0)\right)^{-1}\,. \tag{2}$$

The angular shape function $f(0)$ indicates the far-field response of a single flat crack in the forward direction with respect to plane-wave excitation propagating normally to the crack faces.

Alternatively, the dynamic mechanical behaviour of a two-phase medium subjected to multiple scattering of SH waves can be described macroscopically [3, 9].

Due to the symmetry of cracks and their uniform and parallel arrangement, the damaged medium behaves macroscopically as an orthotropic homogeneous medium. In the heterogeneous slab response established by Angel and Koba [2], we have identified the quantity which plays the role of an acoustic impedance in the homogenous description. On this grounds, we have found that the quantity

$$\Theta = \frac{k}{K} \tag{3}$$

represents the ratio of the effective acoustic impedance of the damaged medium, Z, to that of the matrix, z. In Eq. (3), the wavenumber K is given by Eq. (2).

Note that Eq. (3) agrees well with Eq. (15) of Ref. [3] which has been previously established in the context of Waterman and Truell approach [3, 10]. We recall here that, in the special case of flat cracks, the far-field forward and backward scattering amplitudes of a single scatterer are opposite $\left(f(0) = -f(\pi)\right)$.

The dispersion relation of the coherent plane wave propagating in an infinite homogenous medium (with the effective mass density ρ and the effective shear stiffness μ along the axis $\boldsymbol{y}_3$) is

$$\rho \frac{\omega^2}{K^2} = \mu \,. \tag{4}$$

By using Eqs. (3) and (4) and the following relationship

$$Z = \rho \frac{\omega}{K} = \frac{\mu K}{\omega} \,, \tag{5}$$

we find that

$$\rho = \rho_0 \,, \tag{6}$$

$$\mu = \mu_0 \left(1 - \eta \frac{4\pi}{k^2} f(0) \right), \tag{7}$$

with ρ_0 and μ_0 standing for the mass density and the stiffness of the matrix. Note that the complex-valued bulk parameters ρ and μ depend on the frequency and the crack density η.

For small $\tilde{\omega} = ka$, using the low-frequency expression of the scattering amplitude f given in Ref. [5], it follows that

$$\frac{\mu}{\mu_0} = \left(1 - \phi + \frac{\phi}{4} \tilde{\omega}^2 \ln \tilde{\omega} + O\left(\tilde{\omega}^2\right) \right) - \mathrm{i} \frac{\pi\phi}{8} \tilde{\omega}^2 \left(1 + O\left(\tilde{\omega}^2 \ln \tilde{\omega}\right) \right), \tag{8}$$

where $\phi = \pi\varepsilon$ and $\varepsilon = \eta a^2$ stands for the crack density.

We recall that the formulas (6) and (7) have been derived by viewing the damaged region as a homogenous layer embedded in the matrix. This perspective implies that the bulk parameters (6) and (7), and the linear effective constitutive law $(\sigma_{23} = \mu\varepsilon_{23})$ involving the spectra of the only nonzero stress and strain components (σ_{23} and ε_{23}, respectively), guarantee the coherent displacement and the coherent stress vector to be continuous across each interface.

3 Transfer matrix method

Consider a multilayered medium of thickness h, embedded in the matrix as defined in the previous section, Figure 1. Each of the p parallel layers is characterized by a wavenumber k_j, a shear stiffness μ_j and a constant thickness $d_j = h/p$. The lateral dimensions of the layers are assumed to be infinite. The multilayered stack is subjected to a SH plane wave normally incident on the first layer. The outcoming waves are evaluated at the exit of the last layer. The surrounding matrix is assumed in the form of semi-infinite substrates bonded on both sides of the multilayered medium.

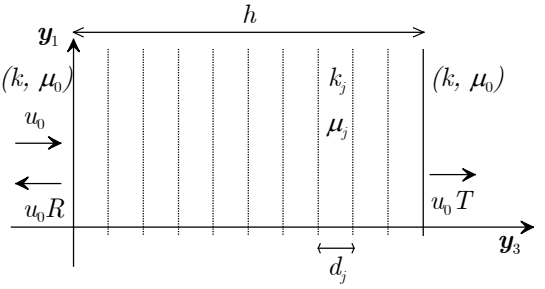

Fig. 1 Schematic representation of a multilayered medium $(h = \sum_j d_j)$

Introduce the SH state vector

$$\boldsymbol{W}(y_3) = \begin{bmatrix} u_2(y_3) \\ \sigma_{23}(y_3) \end{bmatrix}, \tag{9}$$

composed by the out-of-plane displacement u_2 and the shear stress component σ_{23}. The state vectors at both faces ξ_j and ξ_{j+1} of the j^{th} layer can be related as follows

$$\boldsymbol{W}\left(\xi_{j+1}\right) = m_j\left(\omega, k_j, \mu_j, d_j\right)\boldsymbol{W}\left(\xi_j\right), \tag{10}$$

where

$$m_j\left(\omega, k_j, \mu_j, d_j\right) = \begin{bmatrix} \cos k_j d_j & \dfrac{\sin k_j d_j}{k_j \mu_j} \\ -k_j \mu_j \sin k_j d_j & \cos k_j d_j \end{bmatrix}. \tag{11}$$

Invoking the continuity of the state vector (9) at the interfaces between the layers, the state vectors at both edges of the multilayered medium, $y_3 = 0$ and $y_3 = h$, are related as follows

$$\boldsymbol{W}(h) = m(\omega)\boldsymbol{W}(0), \tag{12}$$

where

$$m(\omega) = \prod_{j=p}^{1} m_j\left(\omega, k_j, \mu_j, d_j\right), \tag{13}$$

is the transfer matrix through the layers.

We now consider the wave fields outside the multilayered medium. The incident wave of amplitude u_0 and wavenumber k is reflected by the first interface (amplitude $u_0 R$) and transmitted through the stack of layers (amplitude $u_0 T$). The state vectors $\boldsymbol{W}(0)$ and $\boldsymbol{W}(h)$ are written as

$$\boldsymbol{W}(0) = u_0 \begin{bmatrix} 1+R \\ \mathrm{i}k\mu_0(1-R) \end{bmatrix}, \quad \boldsymbol{W}(h) = u_0 \begin{bmatrix} T\mathrm{e}^{\mathrm{i}kh} \\ \mathrm{i}k\mu_0 T\mathrm{e}^{\mathrm{i}kh} \end{bmatrix}, \tag{14}$$

where $\mu_0 = \rho_0 c_T^2$. Thus, the two unknown amplitudes R and T are evaluated from a system of two equations established by combining Eqs. (10)-(14).

The above-outlined transfer matrix method is applied to damaged layers subjected to multiple scattering by cracks. Each multi-cracked layer is replaced by an appropriate effective homogenous layer. The surrounding medium is the matrix. The dynamic behaviour of each damaged layer, containing η_j cracks per unit area, is governed by the effective wavenumber $K_j\left(\eta_j\right)$ and the effective shear stiffness $\mu_j\left(\eta_j\right)$, $j = 1 \ldots p$, see Eqs. (2) and (7). The reflection and transmission responses of the stack of damaged layers are then evaluated from Eqs. (12) and (14), in which the parameters k_j and μ_j are replaced by $K_j\left(\eta_j\right)$ and $\mu_j\left(\eta_j\right)$. The matrix m in Eq. (12) becomes

$$m\left(\omega, \eta\left(y_3\right)\right) = \prod_{j=p}^{1} m_j\left(\omega, K_j\left(\eta_j\right), \mu_j\left(\eta_j\right), d_j\right), \tag{15}$$

where $\eta\left(y_3\right)$ stands for the spatial function of the crack density over the multilayer depth.

4 Application to non-uniform concentration of cracks

The non-uniform crack density $\eta(y_3)$ of parallel identical flat cracks is introduced by replacing multi-cracked media by stacks of effective homogenous layers with a constant crack density η_j each.

Numerical results are obtained for the space-varying crack density

$$\eta(y_3) = \eta_0 \frac{\mathrm{e}^{-\left(\frac{y_3 - h/2}{\sigma}\right)^2} - \mathrm{e}^{-\left(\frac{h/2}{\sigma}\right)^2}}{1 - \mathrm{e}^{-\left(\frac{h/2}{\sigma}\right)^2}}, \tag{16}$$

for $0 \le y_3 \le h$ (so that $\eta(0) = \eta(h) = 0$), with $\sigma = 0.005$, $h = 30.3\ mm$ and $a = 1\ mm$, see Figure 2. The maximum value of Eq. (16) is taken as $\eta_0 = \eta(h/2) = 30\,000$ cracks$/m^2$. The matrix material is aluminium with $c_T = 3.13\ m/ms$ and $\rho_0 = 2.7\ g/cm^3$.

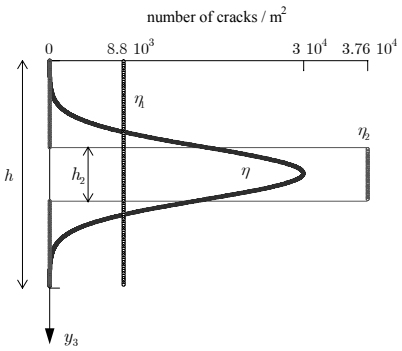

Fig. 2. Profiles of crack density. $\eta(y_3)$ is given by Eq. (16), while $\eta_1(y_3)$ and $\eta_2(y_3)$ satisfy Eq. (18)

4.1 Effect of discretization

The non-uniform multi-cracked medium is viewed as p layers of thickness $d_j = d = h/p$. The moduli of the reflection and transmission coefficients are shown in Figure 3 as functions of the frequency ν for several values of p. Note that the dimensionless frequency $\tilde{\omega} = ka$ is less than 6 when ν is less than 3 MHz. The amplitude of $|R|$ is displayed in the logarithm scale in all the figures.

When the number of layers increases, the values of the crack density at the first and last layers decrease and approach zero. Therefore, the difference between the acoustic impedance of the matrix and those of the 1^{st} and p^{th} tends to zero. While the transmission coefficient is independent of the layer number, some artefacts appear in $|R|$ for frequencies $\nu^{(q)}$ corresponding to the resonances of a single layer.

They can be approximated from the wavelength λ of the incident wave, as follows

$$d_j \approx q\frac{\lambda}{2} \Leftrightarrow \nu^{(q)} \approx q\frac{pc_T}{2h}, \tag{17}$$

where $q = 1,2\ldots$. When the number of layers increases, the resonance frequencies move to higher frequency and therefore depart from the plots. In the following, p is chosen to be equal to 101.

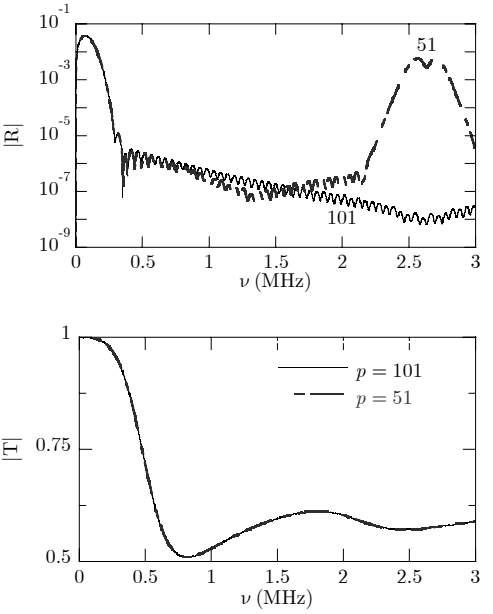

Fig. 3 Moduli of the reflection and transmission coefficients for the space-varying crack density (16). The number of layers takes values $p = 51,101$

4.2 Different profiles of concentration

In this section, we introduce two additional uniform crack densities, $\eta_1(y_3) = \eta_1$ and $\eta_2(y_3) = \eta_2$, which imply the same number of cracks over the range $[0,h]$ as the Gaussian profile (16), see Figure 2. Thus, their mean values are all identical according to

$$\frac{1}{h}\int_0^h \eta(y_3)\,dy_3 = \eta_1 = \eta_2\frac{h_2}{h}. \tag{18}$$

While the thickness of the stack with $\eta_1(y_3) = \eta_1$ is h, the stack thickness for $\eta_2(y_3) = \eta_2$ is chosen such that $h_2 = \sqrt{2}\sigma$. This value corresponds to the distance between the coordinates y_3, where the variation of the profile $\eta(y_3)$ is the highest.

The reflection coefficient calculated for each of the three space-varying crack densities coincides only at very low frequency, when the scatterer location does not affect the response, Figure 4. In turn, the transmission coefficient is almost insensitive to the profiles for any frequency.

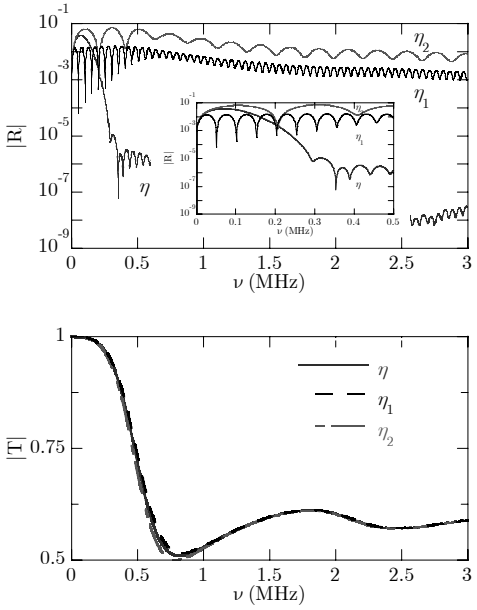

Fig. 4 Moduli of the reflection and transmission coefficients for the three profiles of crack density displayed in Figure 2. The low-frequency part of $|R|$ is zoomed

In the high-frequency limit $(\tilde{\omega} >> 1)$, the effective attenuation $\alpha(\infty)$ of the coherent wave can be expressed in terms of the effective density of cracks $\langle \eta \rangle$ as follows

$$\alpha(\infty) = 2\langle \eta \rangle a\,. \tag{19}$$

Then, we have

$$|T| \to \mathrm{e}^{-2\langle \eta \rangle a\, h}\,,\ (\tilde{\omega} \to \infty)\,. \tag{20}$$

Knowing the stack thickness, one can identify the effective density $\langle \eta \rangle$ from the measurement of the high-frequency limit for $|T|$. In addition, we observe that the curves for $|T|$ in Figure 4 coincide in the high-frequency range. For the two uni-

form crack densities, we have naturally $\langle \eta \rangle = \eta_1$ and η_2, respectively. Thus, Eqs. (18) and (20) yield

$$\langle \eta \rangle = \frac{1}{h}\int_0^h \eta(y_3)\, dy_3 , \tag{21}$$

for the Gaussian profile (16).

4.3 Partial wave decomposition

Individual reflection and transmission coefficients at an interface between the j^{th} and $(j+1)^{th}$ layers are given by

$$R_{j,j+1} = \frac{z_j - z_{j+1}}{z_j + z_{j+1}} \text{ and } T_{j,j+1} = \frac{2z_j}{z_j + z_{j+1}}, \tag{22}$$

where z_j stands for the acoustic impedance of the j^{th} layer, Figure 5. In the special case of multi-cracked layers, z_j depends on the crack density η_j and is evaluated from Eq. (3). The coefficients (22) are used in the Debye serie method of calculating the aggregate reflection and transmission coefficients.

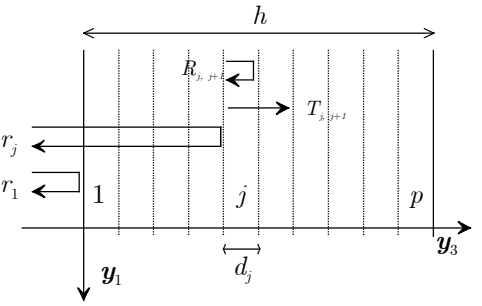

Fig. 5 Partial wave decomposition. Exchanges between the j^{th} and $(j+1)^{th}$ layers: $R_{j,j+1}, T_{j,j+1}$. Specular reflection by the j^{th} interface: r_j

In this context, the spectrum of the forward propagating wave through the first $(j-1)^{th}$ layers, reflected by the j^{th} interface and going back towards the matrix, Figure 5, can be expressed as

$$\begin{cases} r_1 = R_{0,1} \\ r_j = R_{j-1,j} \mathrm{e}^{2\mathrm{i}\sum_{q=1}^{j-1} K_q(\eta_q) d_q} \prod_{q=1}^{j-1} T_{q-1,q} T_{q,q-1}, \quad 2 \le j \le p+1 \end{cases} \tag{23}$$

with $R_{p,p+1} = R_{p,0}$. The properties of the surrounding matrix are indicated by the subscript 0.

Figure 6 shows a comparison between the reflection coefficient R of the multilayered medium and the sum of the specular reflections (23) by all the $p+1$ interfaces. A good agreement between these predictions outlines that the reverberations inside each single layer are negligible for a large number of layers, hence a low contrast between them.

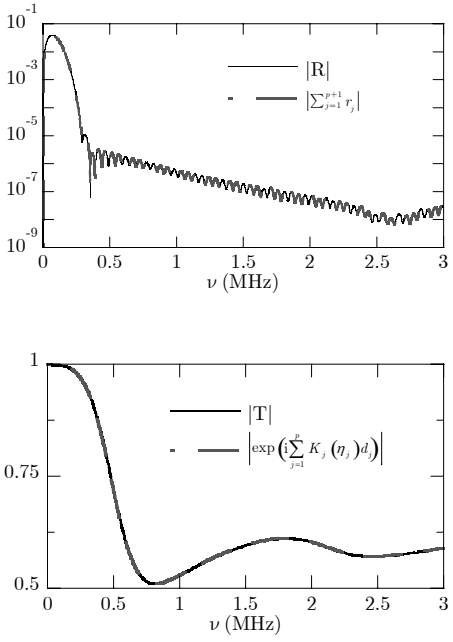

Fig. 6 Moduli of the reflection and transmission coefficients for the space-varying crack density (16). Approximation obtained by neglecting the reverberations inside each single layer: (a) $\left|\sum_{j=1}^{p+1} r_j\right|$, with Eq. (23); (b) Eq. (24)

The effect of the internal reverberations on $|T|$ is examined in a similar way. Figure 6 compares $|T|$ and

$$\left|\exp\left(\mathrm{i}\sum_{j=1}^{p} K_j\left(\eta_j\right) d_j\right)\right|. \tag{24}$$

The two curves match well. The internal reverberations still remain insignificant for the calculation of T.

4.4 Effective attenuation: approximation

For the density profile (16), we assess the effective attenuation α of the multilayered medium from the transmission coefficient T evaluated by using the transfer matrix method described above. Neglecting the difference in the acoustic impedances between the matrix and the damaged region, we have $\mathrm{e}^{-\alpha h} \approx |T|$ and so

$$\alpha \approx -\frac{\ln|T|}{h}. \tag{25}$$

Discarding the reverberation between the layers (thereby disregarding the non-uniformity of the crack density), the effective attenuation can also be evaluated from

$$\alpha \approx \frac{1}{p}\sum_{j=1}^{p} \mathrm{Im}\, K_j\left(\eta_j\right), \tag{26}$$

where the effective wavenumber of the j^{th} layer is given by Eq. (2).

Figure 7 shows the effective attenuation (25) and (26) of the coherent plane wave propagating through the non-uniform density of crack $\eta(y_3)$. The two curves coincide because the reverberation has been discarded.

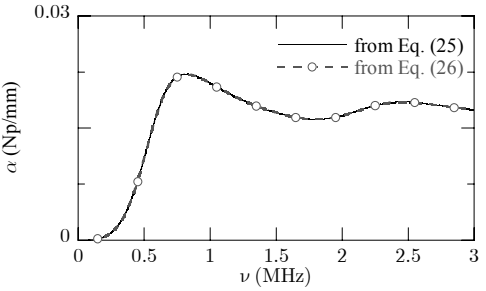

Fig. 7 Assessments (25) and (26) of the effective attenuation of the coherent wave propagating through the profile of space-varying crack density (16)

5 Summary

Propagation of SH coherent wave in a space-varying distribution of parallel flat cracks embedded in an elastic matrix has been investigated. The non-uniform distribution is approximated by a stack of layers each with a uniform distribution.

The reflection response of the Gaussian distribution coincides with that of constant distributions of appropriate value and thickness at low frequency. Interest-

ingly, the transmission at any frequency is not sensitive to the distribution of a given number of cracks.

The impact of the reverberations inside each layer and of the spurious resonance frequencies of the individual layers on the reflection R and transmission T coefficients of the non-uniform distribution can be made negligible.

References

1. Angel, Y. C.: On the reduction of elastodynamic crack problems to singular integral equations. Int. J. Eng. Sci., **26**, 757-764 (1988)
2. Angel, Y. C., Koba, Y. K.: Complex-valued wavenumber, reflection and transmission in an elastic solid containing a cracked slab region. Int. J. Solids Struct., **35**, 573-592 (1998)
3. Aristégui, C., Angel, Y. C.: Effective material properties for shear-horizontal acoustic waves in fiber composites. Phys. Rev. E, **75**, 056607 (2007)
4. Aristégui, C., Caleap, M., Poncelet, O., Golkin, S. V., Shuvalov, A. L.: Coherent elastic wave propagation through non-uniform spatial distributions of cracks. Acoustics'08, ASA EAA SFA, Paris, France, 29 June - 4 July, 2008, 5963-5967, ISBN 978-2-9521105-4-9 (CD).
5. Caleap, M., Aristégui, C., Angel, Y. C.: Further results for antiplane scattering by a thin strip. J. Acoust. Soc. Am., **122**, 1876-1879 (2007)
6. Linton, C. M., Martin, P. A.: Multiple scattering by random configurations of circular cylinders: Second-order corrections for the effective wavenumber. J. Acoust. Soc. Am., **117**, 3413-3423 (2005)
7. Morse, P. M., Rubenstein, P. J.: The diffraction of waves by ribbons and by slits. Phys. Rev., **54**, 895-898 (1938)
8. Robert, S., Conoir, J.-M.: Reflection and transmission process from a slab-like region containing a random distribution of cylindrical scatterers in an elastic matrix. Acustica, **93**, 1-12 (2007)
9. Twersky, V.: Acoustic bulk parameters of random volume distributions of small scatterers. J. Acoust. Soc. Am., **36**, 1314-1329 (1964)
10. Waterman, P. C., Truell, R.: Multiple scattering of waves. J. Math. Phys., **2**, 512-537 (1961)

SPRINGER PROCEEDINGS IN PHYSICS

90 **Computer Simulation Studies in Condensed-Matter Physics XV**
Editors: D.P. Landau, S.P. Lewis, and H.-B. Schüttler

91 **The Dense Interstellar Medium in Galaxies**
Editors: S. Pfalzner, C. Kramer, C. Straubmeier, and A. Heithausen

92 **Beyond the Standard Model 2003**
Editor: H.V. Klapdor-Kleingrothaus

93 **ISSMGE**
Experimental Studies
Editor: T. Schanz

94 **ISSMGE**
Numerical and Theoretical Approaches
Editor: T. Schanz

95 **Computer Simulation Studies in Condensed-Matter Physics XVI**
Editors: D.P. Landau, S.P. Lewis, and H.-B. Schüttler

96 **Electromagnetics in a Complex World**
Editors: I.M. Pinto, V. Galdi, and L.B. Felsen

97 **Fields, Networks, Computational Methods and Systems in Modern Electrodynamics**
A Tribute to Leopold B. Felsen
Editors: P. Russer and M. Mongiardo

98 **Particle Physics and the Universe**
Proceedings of the 9th Adriatic Meeting, Sept. 2003, Dubrovnik
Editors: J. Trampetić and J. Wess

99 **Cosmic Explosions**
On the 10th Anniversary of SN1993J
(IAU Colloquium 192)
Editors: J. M. Marcaide and K. W. Weiler

100 **Lasers in the Conservation of Artworks**
LACONA V Proceedings,
Osnabrück, Germany, Sept. 15–18, 2003
Editors: K. Dickmann, C. Fotakis, and J.F. Asmus

101 **Progress in Turbulence**
Editors: J. Peinke, A. Kittel, S. Barth, and M. Oberlack

102 **Adaptive Optics for Industry and Medicine**
Proceedings
of the 4th International Workshop
Editor: U. Wittrock

103 **Computer Simulation Studies in Condensed-Matter Physics XVII**
Editors: D.P. Landau, S.P. Lewis, and H.-B. Schüttler

104 **Complex Computing-Networks**
Brain-like and Wave-oriented Electrodynamic Algorithms
Editors: I.C. Göknar and L. Sevgi

105 **Computer Simulation Studies in Condensed-Matter Physics XVIII**
Editors: D.P. Landau, S.P. Lewis, and H.-B. Schüttler

106 **Modern Trends in Geomechanics**
Editors: W. Wu and H.S. Yu

107 **Microscopy of Semiconducting Materials**
Proceedings of the 14th Conference, April 11–14, 2005, Oxford, UK
Editors: A.G. Cullis and J.L. Hutchison

108 **Hadron Collider Physics 2005**
Proceedings of the 1st Hadron Collider Physics Symposium, Les Diablerets, Switzerland, July 4–9, 2005
Editors: M. Campanelli, A. Clark, and X. Wu

109 **Progress in Turbulence II**
Proceedings of the iTi Conference in Turbulence 2005
Editors: M. Oberlack, G. Khujadze, S. Guenther, T. Weller, M. Frewer, J. Peinke, S. Barth

110 **Nonequilibrium Carrier Dynamics in Semiconductors**
Proceedings
of the 14th International Conference, July 25–29, 2005, Chicago, USA
Editors: M. Saraniti, U. Ravaioli

111 **Vibration Problems ICOVP 2005**
Editors: E. Inan, A. Kiris

112 **Experimental Unsaturated Soil Mechanics**
Editor: T. Schanz